UNIVERSITY OF Southampton

University of Southampton Research Repository
ePrints Soton

Copyright © and Moral Rights for this thesis are retained by the author and/or other copyright owners. A copy can be downloaded for personal non-commercial research or study, without prior permission or charge. This thesis cannot be reproduced or quoted extensively from without first obtaining permission in writing from the copyright holder/s. The content must not be changed in any way or sold commercially in any format or medium without the formal permission of the copyright holders.

When referring to this work, full bibliographic details including the author, title, awarding institution and date of the thesis must be given e.g.

AUTHOR (year of submission) "Full thesis title", University of Southampton, name of the University School or Department, PhD Thesis, pagination

http://eprints.soton.ac.uk

UNIVERSITY OF SOUTHAMPTON

FACULTY OF ENGINEERING AND THE ENVIRONMENT

Institute of Sound and Vibration Research

Active Control of the Acoustic Environment in an Automobile Cabin

by

Jordan Cheer

Thesis for the degree of Doctor of Philiosophy

December 2012

UNIVERSITY OF SOUTHAMPTON

ABSTRACT

FACULTY OF ENGINEERING AND THE ENVIRONEMENT
Institute of Sound and Vibration Research

Doctor of Philosophy

ACTIVE CONTROL OF THE ACOUSTIC ENVIRONMENT IN AN AUTOMOBILE CABIN

by Jordan Cheer

The acoustic environment in an automobile cabin has a significant effect on the perceived quality of the vehicle. There are two components of the acoustic environment in the automobile cabin: the noise due to automotive processes and the sound produced by the car audio system. In both cases active methods can be employed to improve the acoustic environment and this thesis presents an investigation of both active control of automotive noise and active sound reproduction systems in cars.

In the context of active noise control, cost-effective systems are investigated for the control of both engine noise and road noise. A model of structural-acoustic coupling is first derived and the effects of coupling on the performance of feedforward and feedback controllers is investigated. Feedforward control has been highlighted as a cost-effective method of controlling engine noise. In order to achieve low-cost active control of road noise, however, a number of multi-source, multi-sensor feedback active noise control systems are investigated. A modal feedback control system is investigated and shown to offer significant levels of control of a single dominant resonance. In general, however, a fully multi-input multi-output (MIMO) feedback controller is necessary to achieve control of the multiple resonances present in a road noise disturbance. Measurements have been conducted in a small city car to validate the proposed MIMO feedback controller and a real-time feedforward engine order control system has been implemented.

Active control of sound reproduction has also been investigated with the aim of producing independent listening zones in the front and rear seats of the automobile cabin. Simulations have first been used to investigate the effect of implementing a personal audio system in a car cabin and to compare the performance of acoustic contrast and least squares optimisation strategies. In order to achieve control of the sound field over the full audio bandwidth two arrays are implemented, one employing the four standard car audio loudspeakers and one employing phase-shift loudspeakers mounted to the headrests. The performance of the system is validated using a real-time implementation in a people carrier.

Contents

List of Figures

List of Tables

Declaration of Authorship

I, JORDAN CHEER, declare that the thesis entitled 'Active Control of the Acoustic Environment in an Automobile Cabin' and the work presented in the thesis are both my own, and have been generated by me as the result of my own original research. I confirm that:

- this work was done wholly or mainly while in candidature for a research degree at this University;
- where any part of this thesis has previously been submitted for a degree or any other qualification at this University or any other institution, this has been clearly stated;
- where I have consulted the published work of others, this is always clearly attributed;
- where I have quoted from the work of others, the source is always given. With the exception of such quotations, this thesis is entirely my own work;
- I have acknowledged all main sources of help;
- where the thesis is based on work done by myself jointly with others, I have made clear exactly what was done by others and what I have contributed myself;
- parts of this work have been published as:
  - J. Cheer, S. J. Elliott, Y. Kim, and J.-W. Choi, "The effect of finite sized baffles on mobile device personal audio," in *130th Audio Engineering Society Convention*, (London, UK), 2011.
  - J. Cheer and S. J. Elliott, "The effect of structural-acoustic coupling on the active control of sound in vehicles," in *Proceedings of Eurodyn 2011*, (Leuven, Belgium), 2011.
  - S. J. Elliott, J. Cheer, and M. F. Simón Gálvez, "Personal audio and active control of sound in the environment," in *Proceedings of the 8th International Conference on Informatioin, Communications and Signal Proceesing*, (Singapore), 2011.
  - J. Cheer, M. Abbott, and S. J. Elliott, "Structural-acoustic coupling and psychophysical effects in the active control of noise in vehicles," in *Proceedings of the Institute of Acoustics*, vol. 33, September 2011.

– S. J. Elliott and J. Cheer, “Regularisation and robustness of personal audio systems.” ISVR Technical Memorandum, No. 995, December 2011.

– M. F. Simón Gálvez, S. J. Elliott, and J. Cheer, “A superdirective array of phase-shift sources,” *Journal of the Acoustical Society of America*, vol. 132, no. 2, pp. 746–756, 2012.

– J. Cheer and S. J. Elliott, “Spatial and temporal filtering for feedback control of road noise in a car,” in *Proceedings of the 19th International Congress on Sound and Vibration*, (Vilnius, Lithuania), July 2012.

– J. Cheer, “Using NI CompactDAQ to Investigate the Performance of Active Noise Control in Road Vehicles.” `http://sine.ni.com/cs/app/doc/p/id/cs-14706`, August 2012 (last accessed 8/10/2012).

– J. Cheer, S. J. Elliott, Y.-T. Kim, and J.-W. Choi, “Practical implementation of personal audio in a mobile device,” *Journal of the Audio Engineering Society*, provisionally accepted September 2012.

– S. J. Elliott, J. Cheer, Y.-T. Kim, and J.-W. Choi, “Robustness and regularisation of personal audio systems,” *IEEE Transactions on Audio, Speech, and Language Processing*, vol. 20, pp. 2123–2133, September 2012.

Signed:..... Date:.....

Acknowledgements

Steve Elliott has provided a large input to the work presented in this thesis. He has helped direct the research, provided technical guidance, given me the opportunity to be involved in various projects, provided me with motivation and above all else ensured that I enjoyed my work throughout the last three years. I thank him unreservedly.

A large number of people have helped me in various ways to produce this work and a sincere thank you goes to:

- Mark Abbott for his help in conducting the preliminary in-car measurements for the active noise control systems at the ISVR.
- Marcos Simón Gálvez for his help in conducting the personal audio measurements.
- Maryam Ghandchi-Tehrani for her initial help in developing the real-time feedforward controller.
- The funding for the active noise control work provided by the “Green City Car” project, which is part of the European Commission Seventh Framework Programme.
- The initial funding for the work on personal audio in mobile devices, which was provided by a research and development grant from Samsung. Without this initial impetus the personal audio work presented in this thesis would probably not have been possible.
- The technicians in the ISVR who have helped with equipment and rigs, and provided advice; notably Phil Oxborrow, Antony Wood, Allan Waddilove, Andy Westerman, Chris Oliver and Steve White.
- John Dixon and Matt Parker for their advice prior to the first in-vehicle measurements – I’m sure things would have gone far less smoothly without the insight that they provided.
- Malcolm Smith for lending us the ISVR Consulting automotive lab space on a number of occasions.
- Thank you to my close friends in the ISVR who have helped me in various ways to produce this thesis – Delphine Nourzad, Hugh Hopper and Mark Abbott.

List of Symbols

$\boldsymbol{A}$	$(N \times N)$ Diagonal matrix of acoustic resonant response terms
$\boldsymbol{a}$	Column vector of N complex amplitudes of the acoustic modes
A	Maximum enhancement constraint
a	Audio signal
A_n	Resonant response of the n-th acoustic mode
a_n	Complex amplitude of the n-th acoustic mode
AE	Array effort
$\boldsymbol{B}$	$(K \times K)$ Diagonal matrix of structural resonant response terms
$\boldsymbol{b}$	Column vector of K complex amplitudes of the structural modes
B	Maximum magnitude of plant uncertainty
b	Sum of squared bright zone pressures constraint
B_k	Resonant response of the k-th structural mode
b_k	Complex amplitude of the k-th structural mode
$\boldsymbol{C}$	$(N \times K)$ Matrix of structural-acoustic mode shape coupling coefficients
C	Acoustic contrast
c	Command signal
c_0	Speed of sound
c_{AE}	Array effort constraint
c_E	Individual source effort constraint
$C_{n,k}$	Geometric coupling between the n-th acoustic and k-th structural modes
$\boldsymbol{d}$	Vector of disturbance signals

D Sum of squared dark zone pressures constraint

d Disturbance signal

E Expectation operator (Chapters 4 and 5)

E Young's modulus (Chapter 2)

e Error signal

e' Modified error signal

E_k Total structural kinetic energy

E_p Total acoustic potential energy

e_a Audio reproduction, command following error signal

$\boldsymbol{f}$ Vector of structural forces, f

$\boldsymbol{f}_{am}$ Vector of modal forces due to the reaction force caused by the acoustic pressure acting on the structure

$\boldsymbol{f}_A$ Vector of acoustic reaction forces on the vibrating structure, f_A

$\boldsymbol{f}_p$ Vector of primary structural force excitations

$\boldsymbol{f}_{sm}$ Vector of generalised modal structural external force

$\boldsymbol{f}_s$ Vector of effective structural forces, f_s

f Frequency

f_k Generalised modal structural external force

f_p Primary structural force excitation

f_0 Fundamental frequency

f_c Control frequency

F_s Sampling frequency

$\hat{G}$ Modelled plant response

$\boldsymbol{G}$ Matrix of plant responses

G Plant response

g Filter coefficient representing the plant response

G_0 Nominal plant response

$\boldsymbol{H}$ Matrix of controller responses

^{H} Hermitian, complex conjugate transpose

H Control filter

h Thickness of plate

H_a Command following control filter

H_x Disturbance rejection control filter

$\boldsymbol{I}$ Identity matrix

I Number of filter coefficients

i Index

j $\sqrt{-1}$

J Cost function

J_p Sum of the squared error sensor pressures – Total acoustic potential energy estimate

J_R Sum of the squared error sensor pressures – Regional acoustic potential energy estimate

J_{cost} Generalised cost function including J_p and a term proportional to the control effort

J_C Acoustic contrast maximisation cost function

J_c Composite error signal cost function

J_{LS} Least squares optimisation cost function

K Number of structural modes

k Structural mode number

k_y Structural wavenumber in the y direction

L Number of pressure evaluation positions

l Error sensor number

L_1 Enclosure length

L_2 Enclosure width

L_3 Enclosure height

L_s Number of pressure evaluation positions on the non-rigid structure

L_x Enclosure dimension in the x direction

L_y Panel dimension in the y direction

L_B Number of positions in the bright zone

L_D Number of positions in the dark zone

L_e Number of error sensors

L_T Total number of positions in the bright and dark zones

M Number of secondary sources

m Secondary source number

M_p Number of primary sources

N Number of acoustic modes

n Acoustic mode number (Chapters 2), discrete time iteration number (Chapter 6).

n_1, n_2, n_3 Acoustic modal integers in the three co-ordinate directions

N_{F_c} Number of linearly spaced frequencies within the control bandwidth

N_F Number of linearly spaced frequencies

$\boldsymbol{p}$ Column vector of acoustic pressures at L positions

$\boldsymbol{p}_e$ Column vector of acoustic pressures at L_e error sensors

$\boldsymbol{p}_p$ Column vector of acoustic pressures at L_e error sensors due to the primary excitation

$\boldsymbol{p}_s$ Column vector of acoustic pressures at L_e error sensors due to the secondary excitation

$\boldsymbol{p}_B$ Column vector of acoustic pressures at L_B positions in the bright zone

$\boldsymbol{p}_D$ Column vector of acoustic pressures at L_D positions in the dark zone

$\boldsymbol{p}_T$ Column vector of target acoustic pressures at L_T positions

N_{CW} Number of clockwise encirclements of the Nyquist point

P Number of unstable poles

p Acoustic pressure

p_{c_p} Composite error signal due to the primary source

p_{c_s} Composite error signal due to the secondary sources

p_c Composite error signal

p_d Disturbance pressure

p_e	Error pressure
p_s	Pressure due to the secondary sources
$\boldsymbol{q}$	Vector of acoustic source strengths
$\boldsymbol{q}_{am}$	Vector of generalised modal source strengths due to the acoustic sources
$\boldsymbol{q}_A$	Vector of effective acoustic source strengths, q_A
$\boldsymbol{q}_{s0}$	Column vector of the optimal volume velocities of the M secondary sources
$\boldsymbol{q}_{sm}$	Vector of modal source strengths due to the structural vibration
$\boldsymbol{q}_{st}$	Vector of acoustic source strengths on the vibrating structure, q_{st}
$\boldsymbol{q}_s$	Column vector of the volume velocities of the M secondary sources
q	Volume velocity
q_p	Volume velocity of the primary source
q_s	Volume velocity of the secondary source
q_c	Composite secondary source strength
q_n	Generalised modal acoustic source term
q_{vol}	Distributed volume velocity
$\hat{\boldsymbol{R}}$	Matrix of approximate filtered reference signals
$\boldsymbol{R}$	Matrix of filtered reference signals
$\boldsymbol{r}$	Vector of filtered reference signals
r	Radius
$\boldsymbol{S}$	Diagonal matrix of element areas, ΔS_l (Chapter 2)
$\boldsymbol{S}$	Matrix sensitivity function (Chapters 4 and 5)
$\boldsymbol{S}_{ff}$	Matrix of power and cross spectral densities of the structural disturbance
$\boldsymbol{S}_{pp}$	Matrix of power and cross spectral densities of the pressure disturbance
S	Sensitivity function
s	Wilkinson number
S_F	Surface area of vibrating structure
S_{dd}	Power spectral density of the disturbance signal

S_{ee} Power spectral density of the error signal

S_{xx} Power spectral density of the input signal

S_{xy} Cross spectral density

^{T} Transpose of a vector or matrix

T Complementary sensitivity function

t Time

T_s Sampling period

u Control signal

u_a Audio reproduction, command following control signal

u_x Disturbance rejection control signal

$\boldsymbol{v}$ Vector of loudspeaker drive voltages

V Volume

v Poisson's ratio

$\boldsymbol{w}$ Vector of filter coefficients (Chapter 4, 5, 6)

$\boldsymbol{w}$ Vector of velocities (Chapter 2, 3)

$\boldsymbol{w}_L$ Vector of error sensor weightings

$\boldsymbol{w}_M$ Vector of secondary source weightings

W Feedforward control filter

w Velocity

$\boldsymbol{x}$ Vector of reference signals (Chapter 6)

$\boldsymbol{x} = [x_1, x_2, x_3]$ Vector of co-ordinate positions in the enclosure

x Reference signal

x_Q Quadrature component of the reference signal

x_R In-phase component of the reference signal

$\boldsymbol{y} = [y_1, y_2, y_3]$ Vector of co-ordinate positions on the surface of the vibrating structure

$\boldsymbol{Y}_s$ $(K \times K)$ Matrix of uncoupled structural modal mobilities

$\boldsymbol{Y}_{CS}$ $(L \times L)$ Matrix of acoustic admittance – volume velocity per unit pressure

$\boldsymbol{Y}_L$ $(M \times M)$ Matrix of loudspeaker responses – volume velocity per unit current

$\boldsymbol{Y}_S$ $(L \times L)$ Matrix of uncoupled structural mobilities

Y Structural mobility

y Output signal

$\boldsymbol{Z}_A$ $(L \times L)$ Matrix of uncoupled acoustic impedances

$\boldsymbol{Z}_a$ $(N \times N)$ Matrix of uncoupled acoustic modal impedances

$\boldsymbol{Z}_B$ Matrix of acoustic transfer impedances between M sources and L_B bright zone positions

$\boldsymbol{Z}_D$ Matrix of acoustic transfer impedances between M sources and L_D dark zone positions

$\boldsymbol{Z}_p$ Vector of acoustic transfer impedances between the error sensors and the primary source

$\boldsymbol{Z}'_p$ Vector of transfer responses between the error sensors and the primary force excitation

$\boldsymbol{Z}_s$ Matrix of acoustic transfer impedances between the error sensors and the secondary sources

$\boldsymbol{Z}_{CA}$ $(L \times L)$ Matrix of mechanical impedances

α Convergence coefficient

α_f Frequency dependent convergence coefficient

α_g Frequency independent convergence coefficient

β Control effort weighting parameter

$\Delta\omega_k$ Bandwidth of the k-th structural mode.

$\Delta\omega_n$ Bandwidth of the n-th acoustic mode.

ε Perturbation

ε_n Acoustic mode normalisation factors

κ Condition number with respect to matrix inversion

λ_{AE} Lagrange multiplier governing the array effort constraint

λ_C Lagrange multiplier for the acoustic contrast maximisation problem

λ_m m-th eigenvalue (Chapter 6)

λ_m Lagrange multiplier govenerning the effort constraint for the m-th source (Chapters 7 and 8)

$[\boldsymbol{\phi}]$ $(K \times L)$ matrix of acoustic mode shape functions

$[\boldsymbol{\psi}]$ $(N \times L)$ matrix of acoustic mode shape functions

$\boldsymbol{\Lambda}$ Diagonal matrix of control effort weighting paramters

$\boldsymbol{\phi}$ Column vector of K structural mode shape functions

$\boldsymbol{\psi}$ Column vector of N acoustic mode shape functions

ω Angular frequency

ω_c Angular control frequency

ω_k Resonant angular frequency of the k-th structural mode

ω_n Resonant angular frequency of the n-th acoustic mode

ϕ Angle in the vertical plane

ϕ_k Mode shape function of the k-th structural mode

ψ_n Mode shape function of the n-th acoustic mode

ρ_0 Air density

ρ_s Density of vibrating structure

σ Singular value

θ Angle in the horizontal plane

ζ_k Damping ratio of the k-th structural mode

ζ_n Damping ratio of the n-th acoustic mode

CAN Controller Area Network

CSD Cross Spectral Density

DAQ Data Acquisition

DSP Digital Signal Processing

FFT Fast Fourier Transform

FIR Finite Impulse Response

IFFT Inverse Fast Fourier Transform

IIR Infinite Impulse Response

IMC Internal Model Control

ISVR Institute of Sound and Vibration Rsearch

LMS Least Mean Square

MIMO Multi-Input Multi-Output

OPR Once-Per-Rev

PC Personal Computer

PPF Positive Position Feedback

PSD Power Spectral Density

RMS Root Mean Square

rpm Revolutions per minute

SISO Single Input Single Output

SPL Sound Pressure Level

WFS Wave Field Synthesis

WOT Wide Open Throttle

Chapter 1

Introduction

1.1 The Acoustic Environment in an Automobile Cabin and its Control

The acoustic environment within a car cabin can be separated in to two main aspects: excitation by noise due to automotive processes, such as powertrain, road and wind noise, and the reproduction of audio signals from the car audio system. Although in general the former excitation is unwanted and is described as “noise” and the latter excitation is deliberate and described as “entertainment”, this distinction is not always a clear one. In both of these areas there has been an increasing acknowledgement that the perceived sound quality plays a significant role in consumer preference and, therefore, the success of the car [1, 2, 3]. For example, the quality of the engine noise in some sports cars is certainly seen as a selling point. This acknowledgment has led to significant interest and, therefore, advances in both areas of research.

Although passive acoustic treatments remain dominant in the reduction of automotive noise [4], there has been considerable interest in active noise control measures [5]. This interest has recently been driven by the need to improve the fuel efficiency of vehicles through the use of economical engine designs and by reducing the vehicle’s weight. For example, economical engine designs such as variable displacement, which usually operates by deactivating a number of cylinders [6], result in increased low frequency noise due to the use of a lower number of cylinders and their application is often limited by the acceptable limits of noise, vibration and harshness [7]. Similarly, reducing the weight of a vehicle also results in increased low frequency noise. These increases in low frequency noise are difficult to control using lightweight passive measures, and since active noise control systems are most effective at low frequencies and may be implemented within a car with relatively little increase in weight, they offer a convenient complementary solution. Additionally, active noise control systems offer the ability for the noise control to be adaptive, which is important within the automobile application where the acoustic disturbance is potentially widely variable and additionally the manufacturers may want a different acoustic environment in different models of the same car. The application of active noise control to road vehicles has been investigated for over 20 years [8] and a wide

variety of systems have been proposed to control both road [9] and engine noise [8].

Recent developments in car audio systems relate to both improvements in the sound quality and additional functionality. One area of research that has seen interest for an extended period is frequency response equalisation. An early example is the multiple-point equalisation strategy presented and investigated in the context of a car cabin sized enclosure by Elliott and Nelson in 1989 [10] and this work was extended through practical demonstration by Elliott *et al* in [11]. A more recent example, which develops the ideas presented by Elliott and Nelson, is presented by Carini *et al* in [12]. In addition to the correction of the car audio system's frequency response through equalisation, there has recently been efforts to correct the spatial response in order to compensate for the less than ideal off-centre listening positions and thus improve stereo imaging [13]; this is achieved through the use of all-pass filters implementing a frequency dependent phase shift.

In terms of functionality there are a number of areas where the in-car entertainment system has been enhanced over recent years [14]. These can mainly be related to the introduction of flat panel displays to the car, which allow occupants to watch television and DVDs or play video games; however, coupled with improvements in telecommunication technologies, increased functionality extends to video conferencing and the potential of mobile internet audio in the car [15]. In terms of the car audio system, these developments have led to the desire to implement virtual surround sound systems within the car cabin [14] and personalised rear seat entertainment [16, 17].

Active noise control and audio reproduction within the car environment are potentially complimentary technologies, because of the influence that engine and road noise in a vehicle has on the perceived quality of the car audio system [18, 19]. At low frequencies, in particular, where the automotive noises are generally predominant [20], significant masking of the reproduced audio may result in inaudible or perceptibly uneven bass reproduction [19]. Since the nature of the automotive noise is not constant, this problem cannot be resolved using fixed equalisation strategies and, therefore, it has been highlighted that improved audio quality may be achieved through the use of active noise reduction of automotive noise. This has been taken a step further in the work presented by Wang *et al* [21], who have presented a system that combines an active engine noise control strategy with an audio bass enhancement system.

The connection between active noise control and audio reproduction does not end at their potential complementary nature within the car cabin, but a number of audio systems, such as virtual surround sound reproduction, rely on similar physical processes to the active control of noise. In the same way that active noise control attempts to produce a specific sound field such that the unwanted sound is reduced in level through destructive interference, multichannel audio reproduction systems, such as those discussed for the automotive application by Bai [14], attempt to produce a sound field with specific spatial and temporal characteristics such that the impression of a spatial sound field is achieved; this idea is presented thoroughly by Nelson [22].

Another area of audio reproduction that has similarly strong links with active noise control

concepts is personal audio [23]. This aims to use loudspeaker arrays to create distinct listening areas, or bright zones, whilst minimising the sound level produced outside the listening area, or within the dark zones [24]. The aim of a personal audio system could be to provide an alternative solution to the use of headphones, in situations where either disturbance to those in close proximity to the audio reproduction system is an issue, or where multiple audio programmes are to be reproduced simultaneously in the same acoustic environment. Although personal audio systems based on the type of control methods that are related to active noise control do not appear to have been investigated for the car audio reproduction application, it is clear from the literature that such a system would provide desirable added functionality to car audio systems. For example, it is noted by Crockett *et al* [16] that as rear-seat entertainment systems become more popular the need for personalised headphone reproduction also increases in popularity. However, wearing headphones for prolonged periods may become fatiguing and in certain situations, such as for the driver in the car application, may be dangerous or even illegal [25]. A system that aims to facilitate personal audio reproduction using loudspeakers within the car environment such that different programme material may be heard in different seats is the subject of a patent held by Thigpen [26]; however, the proposed system appears to rely solely on the directivity of the employed "planar magnetic loudspeakers" and their designed interaction with the car cabin acoustic environment through reflections to achieve sound zones. From the limited results presented in the patent, this scheme only achieves significant levels of control at frequencies greater than around 6 kHz, which is not sufficient for most audio reproduction requirements.

The technical link between active noise reduction and active audio reproduction systems can be summarised by the simple control block diagrams presented in Figure 1.1. The variables used in the block diagrams are defined in Table 1.1. Figure 1.1a shows the block diagram for a command following, audio reproduction, control system, in which an audio signal, a, is filtered by the filter, H_a, which is adapted to minimise the error signal, e_a, which is generated by electronically subtracting the command signal from the output of the plant. This control system, therefore, allows a desired signal to be reproduced. In the context of personal audio or spatial audio reproduction this structure of controller is used to produce a desired spatial pressure distribution, which is identical to the aim of the disturbance rejection controller.

Figure 1.1b shows a disturbance rejection control system employing a feedforward structure. In this configuration a reference signal, x, is filtered by the filter, H_x, which is once again adapted to minimise the error signal, e. The error signal in this case is the combination of a disturbance signal, d, and the output signal, y, produced by the filtering of the control signal, u_x, by the plant response G. This feedforward control architecture is used in the active reduction of noise and in terms of a distributed acoustic pressure disturbance the control system attempts to produce an acoustic pressure output y with equal magnitude and spatial distribution to the disturbance but with opposite phase.

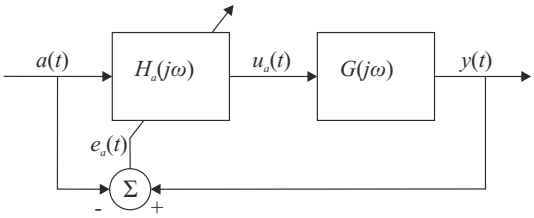

(a) Command following

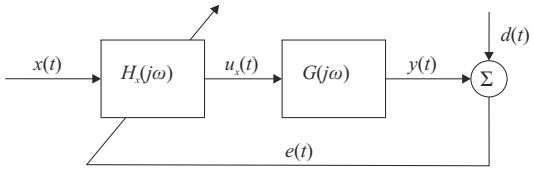

(b) Disturbance rejection

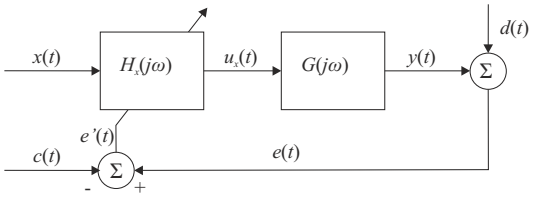

(c) Combined disturbance rejection and command following

Figure 1.1: Control block diagrams. The employed variables are defined in Table 1.1.

Table 1.1: Variables employed in Figure 1.1

Variable	Definition
a	Audio signal
c	Command signal
d	Disturbance signal
e	Error signal
e_a	Audio reproduction, command following error signal
e'	Modified error signal
G	Plant response
H_a	Command following filter response
H_x	Disturbance rejection filter response
t	Time
u	Control signal
u_a	Audio reproduction, command following control signal
u_x	Disturbance rejection control signal
x	Reference signal
y	Output signal

The final control system shown in Figure 1.1c is a combined disturbance rejection and command following architecture. Similarly to the disturbance rejection controller, this system filters a reference signal such that the output control signal interferes with a disturbance signal, however, rather than simply attempting to reject, or cancel the disturbance signal, a specific level of error signal is ensured through the use of the command signal, c. It can be seen from the block diagram in Figure 1.1c that rather than minimising the error signal directly, a pseudo-error signal, e', is minimised which ensures that through the action of the controller the error signal is driven towards the command, or desired signal. This type of controller, which effectively links the disturbance rejection type of control used in active noise control and the command following type of control used in audio reproduction, is effectively used in active noise equalisation [27] or sound-profiling [28]. The aim of sound profiling is to maintain the various engine orders at specified, target levels rather than just attenuating them and, therefore, improve the sound quality of the engine noise. Sound-profiling systems have been a focus of research on active control in vehicles due to the need for audible feedback to the driver from the engine. The use of the combined disturbance rejection and command following controller in this application facilitates the selective rejection and enhancement of engine orders. This allows for the quality of the engine to be controlled in various ways which, as discussed above, is a significant factor in the success of a modern car.

The following two sections provide a review of the work that has been conducted in the control of the automotive acoustic environment. The first section presents a review of active noise control systems that have been developed to control vehicular noise within the car cabin interior. A review of active audio reproduction systems is then presented, with a focus on personal audio systems.

1.2 Active Noise Control in Road Vehicles

The different approaches employed in active noise control systems for application to vehicles are dependent upon both the source of noise that is to be controlled, and whether local or global control of the sound field is to be achieved. The following sections are broken down into the main automotive noise sources within an internal combustion engine driven vehicle. They briefly describe the attributes of the noise sources and provide a review of active noise control systems that have been proposed to control them.

1.2.1 Engine Noise

Despite the need for greener modes of transport, 99% of road vehicles with four or more wheels employ a reciprocating, four stroke, internal combustion engine [20]. Although vehicles with alternative power sources, such as electric battery or fuel cell, are becoming more common and are likely to be significantly quieter than combustion engines, it appears that the internal combustion engine will remain predominant for a significant period of time [20, 29]. This is

particularly true with the availability of technological developments that increase the efficiency of the traditional internal combustion engine such as: hybrid cars, which at least partially use a traditional internal combustion engine [29]; variable cylinder management, which automatically deactivates some of the engine's cylinders according to the driving conditions [30]; or simply smaller more fuel efficient engine designs [31].

The noise produced by the internal combustion engine is dominated by that due to the combustion process and the piston crank mechanism [20]. The noise production related to the piston crank mechanism results from the impact of components, such as the pistons and their liners, and is therefore an impulsive noise with a flat spectrum and greater high frequency content than the noise produced by the combustion process [20]. The noise produced by the combustion process is directly related to the rotational speed of the engine and is, therefore, tonal in nature [32]. In addition to being dependent on the engine speed, the specific spectrum of the noise produced is dependent on a number of variables such as the engine capacity, the number of cylinders, and the engine load [20, 32]. However, in the context of this thesis, and specifically the work presented in Chapter 6 regarding in-car measurements, there are two simple relationships between engine type and the resulting combustion noise that will be produced.

The empirical relationship between average engine noise level and engine size can be expressed in terms of the number of cylinders and the individual capacity of the cylinders measured in litres. For example, for a petrol engine [20],

$$\text{Sound power level} \approx 10\log_{10}(\text{no. of cylinders}) + 23\log_{10}(\text{cylinder capacity})\,\text{dB}. \tag{1.1}$$

This relationship indicates that for an equivalent total engine capacity a vehicle with a larger number of inherently smaller cylinders will produce a lower level of combustion noise; for example, the sound power radiated by a 4 cylinder engine would be approximately 4 dB lower than for a 2 cylinder engine with the same overall capacity.

The spectrum produced by a specific engine can also be related to the number of cylinders. For a four stroke engine the fundamental frequency is given by,

$$f_0 = \frac{\text{rotational speed}}{2 \times 60} \times \text{no. of cylinders}, \tag{1.2}$$

where the rotational speed is measured in revolutions per minute (rpm) and, therefore, the division by 60 converts to revolutions per second, and the division by two relates to the fact that for a four stroke engine the rapid pressure rise related to combustion occurs every other engine rotation, thus producing a full spectrum of harmonics with a fundamental at half the engine rotation frequency, which is often referred to as the first engine order [20]. This means that for a two-cylinder engine the fundamental frequency would be at the engine rotation frequency, which is the first engine order; for a four cylinder engine the fundamental frequency would be at twice the engine rotation frequency, which is the second engine order; and for a six-cylinder

engine the fundamental frequency would be at three times the engine rotation frequency, which corresponds to the third engine order.

Engine Noise Control Systems

From the description of the two main noise sources in the engine it is evident that the combustion noise process is most suitable for treatment using active noise control strategies. This is because it is both tonal in nature and causes greater problems at lower frequencies compared to the impulsive nature of the noise produced by the piston crank mechanism, which is more easily controlled using passive measures. Additionally, since the noise production mechanism is directly related to the engine speed it is possible to obtain a reference signal from either the ignition circuit, a tachometer, or the Controller Area Network (CAN) bus and, therefore, apply feedforward control strategies. In comparison to reference signals obtained from transducers, such as microphones or accelerometers, this type of reference signal is not influenced by the control signal and, therefore, an entirely feedforward control system can be used.

An early implementation of active engine noise control was presented by Elliott *et al* in 1988 [8]. This system consisted of driving two loudspeakers with a version of the engine speed reference signal that was filtered adaptively such that the sum of the squared pressures at four error microphones was minimised; a block diagram of a simple, single channel implementation of such a control system is presented in Figure 1.2. The adaptation of the filter coefficients in [8] used a simple steepest decent algorithm that achieved convergence times of around 0.1 seconds and, therefore, allowed for the variations in engine noise due to engine speed and load variations. The performance of the system was reported for three different cars and reductions in the pressure level at the engine firing frequency were reported between 10 and 15 dB throughout the cabin.

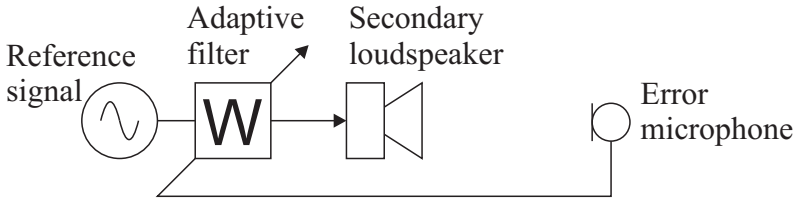

Figure 1.2: Simple single channel feedforward active noise control system.

The system presented in [8] was developed further by introducing additional error sensors and loudspeakers and implementing control of multiple harmonics of the engine firing frequency [33], however, the principles of the control system remained largely the same as that reported in [8]. The first production implementation of an active engine noise control system was reported in 1992 by researchers from Nissan [34], however, the system employed loudspeakers, amplifiers and processors separate from the car audio system and due to this lack of integration was expensive to implement and could not achieve any significant weight saving.

Active engine noise control systems have more recently been commercially implemented

in production vehicles by Honda [35], Toyota [36], GMC [37], Acura [38] and Audi [39]. The Honda active engine noise control system employs two error microphones and the car audio loudspeakers to reduce the increase in noise that occurs when the engine switches from using 6 cylinders to using 3. Using the car audio loudspeakers reduces the cost of implementing the active noise control and, therefore, makes it a more financially viable option. The Toyota system employs three error microphones and it appears that three of the car audio woofer loudspeakers are employed – two in the front doors and one in the rear parcel shelf – however, this is not completely clear from the literature. The Toyota system has been implemented in order to control the increase in noise that results from running the engine at a particularly low rotational frequency [36]. The systems employed by GMC and Accura appear to be developed by Bose [40] and employ a similar combination of microphones and the car audio loudspeakers to reduce unwanted low frequency engine noise. Finally, the system implemented by Audi is designed to compensate for the change in sound quality due to switching between 8-cylinder and 4-cylinder operation and is implemented in conjunction with active engine mounts [39]. This system employs four error microphones installed in the headliner of the cabin and uses four door mounted woofers and 1 rear subwoofer which are part of the audio system. As well as employing the standard car audio loudspeakers, this system employs the car audio digital signal processing and, therefore, is fully integrated.

Although significant levels of engine order reduction may be achieved using an active control system, it may not be desirable to achieve maximal attenuation of engine noise. This is due to the driver's need for audible feedback in order to operate the vehicle safely and the desire of the car manufacturer to achieve a certain "sound quality". In this situation, as detailed in Section 1.1, an *active noise equaliser* or sound-profiling control method may be used, which both retain a residual error with a specified spectrum and may thus facilitate active sound quality control [27, 28].

The early active noise equalisation system proposed by Kuo and Ji [27] employed the filtered-reference least mean squares (LMS) algorithm in conjunction with a pseudoerror signal, which enables the noise level to be driven to a target level rather than minimised. The proposed system is able to control a harmonic spectrum based on a single error signal, and it is shown that the level of the individual harmonics can be independently cancelled, attenuated, unaltered, or enhanced. Such a system enables the engine orders to be individually controlled in level and thus tuned to improve the sound quality of the engine. The active noise equaliser has been further developed by Kuo [41] in order to facilitate spectral shaping of broadband disturbances and multichannel active noise equalisation, for implementation where equalising at a single error sensor position is not suitable – for example, in a car cabin. The multichannel active noise equaliser is more thoroughly presented by Diego *et al* [42]. The active noise equaliser control method has, however, been shown to be very sensitive to estimation error in the plant model used in the filtered-reference LMS algorithm. These errors may result in overshoot, which is the amplification of out-of-band frequencies, or system instability [43, 28, 44]. Consequently, a variety of alternative control strategies have been proposed to achieve active

sound quality control with reduced overshoot and increased stability [45, 28, 46].

An interesting implementation of active sound quality control to a mass production vehicle has been presented by Kobayashi *et al* [47]. This system combines the operation of an active noise control system designed to reduce engine boom, with a system to control the engine sound quality during acceleration. The system operates in its active noise control mode at lower engine speeds, where the vehicle is either idling or cruising, however, at higher engine speeds, which occur during acceleration, the active sound quality control system operates. The active sound quality control system aims to synthesise a "sporty sound" during acceleration and achieves this by adaptively modifying the level of the individual engine orders with a dependency on the engine speed [47].

1.2.2 Intake and Exhaust Noise

Intake noise is produced by the radiation of the pressure pulse produced by the sudden restriction to air flow caused by the closing of the engine inlet valves [20]. Exhaust noise is also produced by the radiation of a pressure pulse, however, in this case it is produced by the rapid release of pressure from the combustion process [20]. Since both noise processes are related to the engine firing frequency it can be appreciated that they are both dominated by low-frequency harmonic content [20].

Intake and Exhaust Noise Control Systems

Intake and exhaust noise control is predominantly implemented using passive acoustic elements such as the air expansion chamber and the currently more popular multi-chamber attenuators consisting of two or three quarter wave helmholtz resonators [20]. Active control of both intake and exhaust noise has been demonstrated [48] and an active helmholtz resonator system has also been investigated [49]; however, according to Thompson and Dixon durability and cost remain an issue [20]. An active exhaust system has recently been presented in [50] and it has been shown that significant reductions in both weight and volume can be achieved whilst maintaining the performance achieved by the alternative passive system. However, as in [20], this recent work also highlights that reductions in cost and industrialisation of the actuator are required in order to make mass production viable.

1.2.3 Road-Tyre Noise

Road-tyre noise is a result of the interaction between the road surface and the tyre design, and can vary by up to 10 dB depending on the specific tyre design [20]. The noise production mechanisms can be separated into two main areas: air pumping and vibration induced noise [20].

Air pumping can be described from two perspectives: the air pumping caused by the tyre tread and the air pumping due to the roughness of the road surface. For a smooth road surface the noise is mainly generated by tread pumping, which is a result of air being forced out of the

tyre tread as a patch of the tyre comes into contact with the road surface and being sucked back into the tread as the patch leaves the road surface [20]. Conversely, on a rough road surface with a smooth tyre surface pumping occurs, which is the reverse process with the tyre forcing air in and out of the cavities in the road [20]. In practice it is evident that the noise produced will be due to a combination of these two processes, and although it is dominated by high frequencies, its level is dependent on the size of the road and tyre cavities, the load on the tyre and the pressure in the tyre [20].

Vibrations are induced in the tyres due to the non-uniformity of road surfaces and irregularities in the tyre tread pattern [20]. These vibrations may directly radiate exterior noise, or propagate through the tyre and suspension to produce broadband noise with both random and tonal components in the vehicle cabin [20, 51, 52]. Tangential excitation of the tyre cavity through both impacts and slip-stick mechanisms, which occur as part of the tyre is deflected and released as it comes into contact with the road surface, have been attributed to mid-high frequency noise. Radial excitation, which is largely due to the road surface, however, has been linked to low-frequency excitation and is, therefore, a potential target for active noise control strategies. Although this type of noise is generally random, for directly radiated noise its spectral shape is altered by the structural and acoustic response of the tyre, and for structure borne noise its spectral shape is modified by both the response of the tyre and the complete structural propagation path.

Road-Tyre Noise Control Systems

Due to the random nature of road-tyre noise and the complex propagation path between structural excitation and the acoustic noise produced in the car cabin the active control of road-tyre noise using feedforward control poses a greater challenge than the feedforward control of engine noise [52, 32]. Reference signals for feedforward road-tyre noise control systems have been obtained from accelerometers mounted to the vehicle's suspension and bodywork [9, 51]. The coherence between the obtained reference signals and the error signals within the car cabin imposes a direct limitation on the level of noise reduction that can be achieved [9, 51]. Sutton *et al* [9] state that, on a range of vehicles, road tests have shown that the coherence between a single accelerometer and the sound pressure in the car cabin is often below 30% and this can be related to the multiple sources of road-tyre noise, the multiple directions of vibrations that cannot be detected with a single accelerometer, and the other noise sources that may not be detected by accelerometers – for example, wind noise (see Section 1.2.4).

In order to improve the coherence between the reference signal and the interior sound pressure it is necessary to increase the number of accelerometers employed and also carefully select their locations [9]. Sutton *et al* indicate that in general at least six accelerometer signals are necessary to provide adequate coherence and this requirement is also replicated by Oh *et al* [52]. Heatwole and Bernhard [53] present a method of selecting the reference sensors based not only on the coherence but on both the maximum potential control and the relative convergence

rate.

The system implemented by Sutton *et al* employed six accelerometers positioned around the suspension system of a small, lightweight family car so as to detect vibrations in the vertical, lateral and longitudinal directions and thus achieve a good coherence [9]. Additionally, the sensor positions were chosen to provide maximum time advance, such that sufficient time for the signal processing to take place before the noise reaches the location of the car's occupants was available [9]. The proposed active noise control system employed two loudspeakers, positioned in the standard car audio positions in the front doors of the vehicle, and two microphones positioned in each of the front headrests. The system thus only attempted control for the front seat occupants and reductions of around 7 dB in the A-weighted sound pressure level were achieved over a bandwidth of 100-200 Hz [9]. Sutton *et al* [9] also propose a second control system that is able to improve upon both the bandwidth and level of control, however, it requires the loudspeakers to be repositioned from the standard audio system locations to the headrests. This system, therefore, attempts local control and achieves a zone of quiet which is a shell-like sphere surrounding the secondary, controlling source as described in [54, 55]. The dimensions of a 10 dB zone of quiet within a diffuse field have been shown to be limited to around a tenth of the acoustic wavelength and, therefore, quiet zones with useful dimensions are limited to a maximum frequency of around 500 Hz [54, 55]. For the local control strategy presented by Sutton *et al* an increase in the level of control to around 10 dB was achieved and the bandwidth of control was extended up to 400 Hz.

Although active feedforward control systems are feasible and may provide significant levels of noise reduction, the need for multiple accelerometers to provide a suitable reference signal results in an expensive system even if the car audio loudspeakers were employed. One commercial implementation which is directly based on the work presented in [9] is available jointly through Harman and Lotus Engineering [56], however, it is unclear how widely used this system is in practice. As a result of the high cost of a feedforward road noise control system, interest has arisen in implementing road-tyre noise cancellation using a feedback system, as this avoids the need for separate reference sensors. Feedback control of road noise has been the focus of a body of work presented by Adachi and Sano, for example [57, 58], and this research has culminated in a mass-production system implemented in the Honda Accord estate car which is presented by Sano *et al* in [59].

The feedback control system proposed by Sano *et al* [59] attempts to control a 40 Hz boom in the front seats of an estate car, which corresponds to the anti-node of the first longitudinal enclosure mode. The feedback system employs a single error microphone, positioned under the front seat around the anti-node of the first longitudinal mode, and the two front door audio system loudspeakers, driven in-phase, to reduce the level of the boom in the front seats by 10 dB. However, when operating alone this feedback strategy causes the level of the 40 Hz boom noise to be increased by 3 dB in the rear seats. Therefore, Sano *et al* [59] propose a second control loop consisting of a fixed feedforward controller which uses the feedback system's error microphone as a reference signal in order to limit noise amplification in the rear

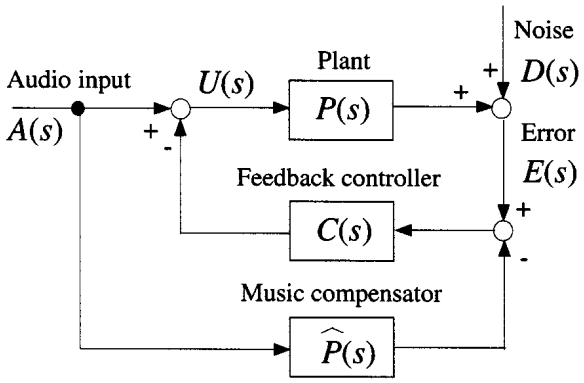

Figure 1.3: Feedback controller and music compensator proposed by Sano *et al* [59] (©IEEE 2001).

seats using the two audio system loudspeakers positioned in the rear doors. The control system thus achieves a 10 dB reduction of the problematic boom in the front seats without increasing the sound level in the rear seats where the boom noise is not a problem.

A potential issue with implementing an acoustic feedback control strategy within the car cabin is that it is not selective and, therefore, will not only cancel unwanted noise signals but will also cancel the programme reproduced by the car audio system around the targeted noise cancellation frequency. To avoid this problem Sano *et al* [59] propose a "music compensator" which, as shown in Figure 1.3, estimates the audio signal produced at the error microphone using a model of the acoustic plant response between the loudspeakers and the error microphone, $\hat{P}$, and subtracts this from the measured error signal; this ensures that the signal due to the audio programme is not cancelled. It is interesting to note that Sano *et al* acknowledge the improvement in audio quality that results from reducing the road booming noise and this may be related back to the discussion presented in Section 1.1 regarding the effects of car noise on audio quality.

1.2.4 Wind Noise

A further source of noise in vehicles is wind noise, which increases in proportion to road speed to the power of six [20]. Consequently, it becomes the predominant component of interior noise at speeds above 100 kmh^{-1} [60]. Wind noise can be separated into a number of separate noise production mechanisms [60]:

1. Aerodynamic noise due to the vehicle moving through air at mid to high speeds. This creates a turbulent boundary layer over much of the vehicle's surface and the associated pressure fluctuations, which vibrate the vehicle structure, produce noise within the vehicle [20]. This noise type is mainly related to the shape of the vehicle and is broadband with a bias towards low frequencies in the range 31.5 to 63 Hz.

2. Aerodynamic noise due to turbulent air flow through holes. This noise source is con-

trolled by the quality of the seals around openings such as windows and doors. The spectrum of the noise is similar to that due to 1.

3. Exterior varying wind conditions also produce aerodynamic noise, however, the noise is fluctuating so is distinct from that due to the vehicle motion. Due to the largely impulsive nature of exterior wind noise the spectrum is dominated by frequencies greater than around 300 Hz.

4. Air flow over open windows or sunroofs when coupled to the car cabin may result in narrowband beating noise due to the system behaving similarly to a helmholtz resonator; this type of noise is referred to as flow oscillations. It should be noted that the noise source is potentially significant at lower road speeds than the other three sources.

Wind Noise Control Systems

Although wind noise is a predominant source of interior noise at high vehicle speeds, it does not appear to have been as widely considered as the other noise sources for the application of active noise control. This may be due to the lower level of wind noise in vehicles under the majority of operating conditions – i.e. lower speeds and with the windows and sunroof closed. That said, Stothers *et al* have presented an adaptive feedback system that controls sunroof flow oscillations, which may produce high level narrowband noise [61]. The system proposed by Stothers *et al* employed an adaptive feedback controller with a filtered-reference LMS algorithm and achieved around 30 dB reduction in a 25 Hz tone produced by sunroof flow oscillations. The feedback control system did result in some increases in the broadband noise of around 10 dB at around 20 Hz, which was presumably a result of spillover. Additionally, by attempting to reduce the controller delay by not using anti-aliasing and reconstruction filters, some less significant increases in the broadband noise also occured at higher frequencies due to distortions.

1.3 Active Control of Reproduced Sound

As discussed in Section 1.1 there are both strong practical and technical links between the active control of noise and the active reproduction of sound, including both spatial audio and personal audio. The following sections present a review of both spatial audio and personal audio reproduction. The spatial audio review considers the implementation of such systems in car cabins, as this has been an area of active research. The personal audio review, however, provides a more general discussion, as the implementation of personal audio systems for sound reproduction in vehicle cabins does not appear to have been widely covered in the literature.

1.3.1 Spatial Audio Reproduction

Spatial audio reproduction may refer to any audio system which provides the listener with a spatial impression of the reproduced sound. This may refer to the perception of distance that can be achieved from the captured reverberation in a monophonic audio reproduction, or to the horizontal localisation that can be achieved from a two-channel stereo reproduction system [62]. In the context of this thesis the focus is on controlling the acoustic environment within a car cabin using active techniques and, therefore, the spatial audio reproduction systems that are of particular interest are those that attempt to generate a specific sound field using methods based on those presented in Figure 1.1. Spatial audio reproduction systems employing such control techniques are distinct from conventional multichannel surround sound systems which use conventional time and amplitude panning techniques [62]. Two specific methods which essentially employ the type of control techniques shown in Figure 1.1a are binaural reproduction over loudspeakers [63, 64] and Wave Field Synthesis (WFS) [65].

Binaural Reproduction Over Loudspeakers

Binaural reproduction over loudspeakers has been widely investigated and operates by producing a sound field at the listener's ears which is ideally equal to the sound field that would occur in the real environment [64]. It can, therefore, be appreciated that in simple terms the implementation of a binaural reproduction system may be achieved using a two-channel implementation of the command following control architecture presented in Figure 1.1a, where the command signals are the sound pressures produced in the real sound field at the listener's ears and the control filters both compensate for the effects of the plant response and implement cross-talk cancellation. One method of implementing such a system is presented by Takeuchi and Nelson [64] and employs a standard inverse filtering technique where the matrix of filters is generated by calculating the inverse of the plant matrix, which consists of transfer responses between each loudspeaker and each ear position. In practice, however, the inversion of the plant responses leads to a number of issues such as a loss in dynamic range and poor robustness to small errors and room reflections [64]. Practical solutions to these problems are investigated in the same publication and this work has resulted in a commercial system [66].

Wave Field Synthesis

In comparison to binaural reproduction over loudspeakers, WFS aims to reproduce wave fronts from a large array of loudspeakers that are identical to the real wave fronts of the sound field to be reproduced [65]. Therefore, WFS produces a sound field through which the listener can move whilst still perceiving the intended spatial sound field. Such a system has a potentially significant advantage compared to binaural reproduction which tends to produce a small listening area, or sweet-spot.

WFS is based on the Huygens' principle which states that any point of a wave front can be considered as a secondary source [65]. Therefore, it can be appreciated that any wave front,

and therefore sound field, can theoretically be synthesised using a continuous and infinite array of loudspeakers. However, in practice a discrete and finite length array of loudspeakers must be used to reproduce the wave fronts and, therefore, WFS will suffer from spatial aliasing due to the discrete array, and truncation effects due to its finite length [65]. Spatial aliasing will occur at frequencies where the separation between the loudspeakers is greater than half the reproduced wavelength and this means that very small inter-element loudspeaker spacing is required to cover the full audio bandwidth. Array truncation results in secondary wave fronts to be radiated from the ends of the loudspeaker array which are delayed and attenuated with respect to the desired wave front [65]. These so called "edge events" can be reduced through the use of a weighting function [65]. It should also be noted that spatial aliasing effects will also occur in the recording of the wave fronts using a finite array of microphones [65].

Car Audio Spatial Sound Reproduction

In the context of car audio there is a significant number of luxury vehicles with multichannel surround sound systems employing standard panning techniques [14]. However, the implementation of spatial sound reproduction techniques, such as the two discussed above, have seen little implementation within cars. In terms of the binaural reproduction method, although the largely fixed seating positions in a car cabin may be ideally suited to the small sweet-spot produced, to generate a sweet-spot at each seating position would require a large number of loudspeakers and, consequently, a complex system. Although the WFS technique does not result in a small sweet-spot, it still requires a large number of loudspeakers for implementation in order to avoid spatial aliasing effects. For example, the "Audi Sound Concept" system, which implements WFS in an Audi Q7, uses 62 loudspeakers as shown in Figure 1.4 [67]; this is clearly impractical for mass production car audio systems. A further problem with both the binaural reproduction and WFS methods is that the availability of suitable audio recordings is limited and, therefore, in order to use these systems with the vast majority of commercial sound recordings either an up or down mixing algorithm is required depending on the source programme material.

A number of more practical methods of implementing spatial audio within the automotive environment have recently been presented by Bai and Lee [14]. The four presented systems use the four standard car audio loudspeakers to reproduce standard 5.1-channel surround sound [68]. Two of the proposed systems employ an inverse filtering method, as used in binaural reproduction over loudspeakers, and the other two systems employ a simpler method using weighting and delay of the audio input signals [14]. The two methods employing inverse filtering are designed to receive either 2-channel stereo or 5.1-channel surround sound audio recordings. The 2-channel stereo inverse filtering system employs a method of upmixing to produce the effect of a 5.1-channel surround sound recording. Bai and Lee show through subjective listening tests that the performance of the inverse filtering methods reduces when listening zones are required for a number of occupants in the car cabin [14]. This is a result

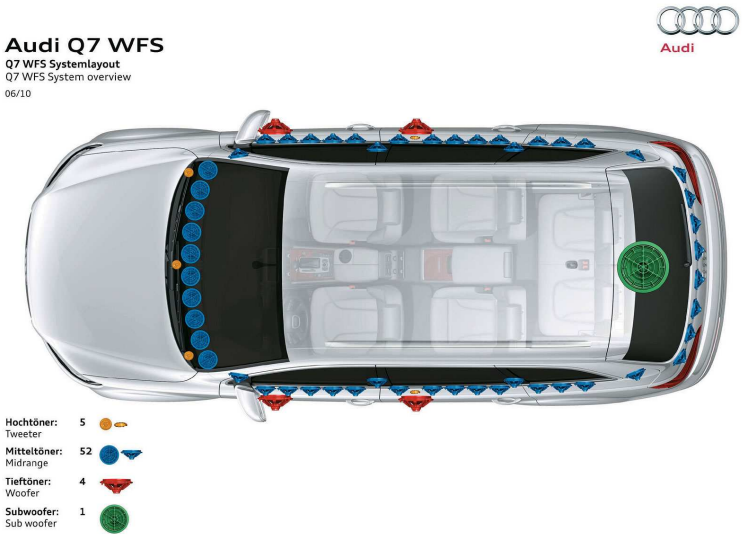

Figure 1.4: Audi sound concept system (reproduced from [67]).

of both the limited number of loudspeakers available and the complexity of designing inverse filters for multiple listening zones [14].

The second method proposed by Bai and Lee, which is again implemented for both 2-channel and 5.1-channel programme material, attempts to avoid the small sweet-spot and complexity issues associated with the inverse filtering method. The second method feeds the four car audio loudspeakers with a weighted combination of either the left and right signals from a 2-channel recording or the 5.1 channels from a surround sound recording and delays the signal to the rear loudspeakers. The weightings and delays are set to give an impression to the occupants of the car of a 5.1-channel surround sound reproduction regardless of the input audio programme. Although this method significantly reduces the complexity of the reproduction system compared to the inverse method, the subjective tests presented in [14] show that the inverse methods are preferred. These results highlight that although the inverse methods are complex, this is traded off for a superior performance.

1.3.2 Personal Audio

Personal audio systems aim to generate listening zones that are confined to a specific region, this may be to improve the privacy of the user, reduce annoyance to nearby listeners, or allow multiple audio programmes to be listened to within the same acoustic space. Personal audio is based on the use of constructive and destructive interference to create listening zones and quiet zones and, therefore, has many technical similarities to the active control of noise, as discussed in Section 1.1. Although the development of personal audio systems to produce personalised listening zones within cars has yet to be widely discussed in the literature or implemented in commercial systems, it has been highlighted in [16] that such a system is of current interest. An early investigation into personal audio reproduction in a car cabin has been presented in [69] in which a method of optimally selecting the loudspeaker positions is presented and a

recent preliminary study has considered the subjective requirements of such a system [70]. The following sections will review previous work in the field of personal audio to form a basis for investigating the application of personal audio to a car audio system.

Combining Active Sound Control and Loudspeaker Arrays

The first significant paper that considers the personal audio problem is presented by Druyvesteyn and Garas [71]. The proposed system employs both active control and beamforming strategies to create a listening zone adjacent to a quiet zone. The system aims to allow two audio programmes to be reproduced with minimal disturbance to each other within the same room. The beamformer, which is a delay and sum type array, is designed such that whilst maintaining the sound pressure level in the listening zone the pressure level in the quiet zone is minimised. This is achieved by steering the array's directivity, as described in [72], such that a null of the pattern is directed toward the quiet zone. The practical study presented in [71] employs an array of 21 loudspeakers at a distance of 0.5 m from the listening zone positioned to form the arc of a circle and the centre of the quiet zone is 1.5 m from the centre of the listening zone. The array achieves a significant reduction in the sound pressure level (SPL) in the quiet zone compared to a single loudspeaker between 1 and 4 kHz. The performance of the array is limited at higher frequencies due to the finite separation between the loudspeakers and at low frequencies due to the length of the array [72]. At higher frequencies, Druyvesteyn and Garas propose that the directivity of the loudspeakers, which results from their finite dimensions [73], should be employed to achieve the required directivity. However, at lower frequencies these authors propose the use of an active feedforward control strategy to minimise the sound level in the quiet zone.

The proposed active sound control strategy employed in [71] uses an additional array of three loudspeakers that are positioned in between the listening and quiet zones, 0.5 m from the centre of the quiet zone. The feedforward control strategy uses the filtered-reference LMS algorithm to optimise three adaptive filters such that the three loudspeakers minimise the SPL in the quiet zone that results from the programme being reproduced in the listening zone; the audio programme is thus used as the reference signal. This control strategy is identical to that employed for the control of engine noise in the car enclosure by [8] and thus the physical limits are identical. The practical study presented by Druyvesteyn and Garas indicates that below 1 kHz the active control strategy achieves between 6 and 11 dB reduction in the quiet zone SPL, which is comparable to that achieved by the array at higher frequencies.

It is indicated by Druyvesteyn and Garas that the proposed combined active control and beamforming strategy achieved a ratio between the SPLs in the listening and quiet zones of around 20 dB over the frequency range 250-4000 Hz. According to the subjective studies on personal sound presented in [23], an effective personal audio strategy should achieve a ratio of levels greater than 11 dB but preferably around 20 dB. Therefore, it can be appreciated that the proposed combined strategy is effective, however, it is also clear that it requires a significant number of loudspeakers in order to achieve this control. Therefore, more recent developments

in personal audio reproduction have moved towards superdirective, or optimal, beamforming techniques. Superdirective beamforming can achieve an increase in the directivity of an array for a given number and spacing of array elements [74] and, therefore, not rely on the combination of control approaches considered in [71].

Superdirective Beamforming

Superdirective, or optimal beamforming control strategies have been the focus of research in array signal processing since the first half of the 20^{th} century [75]. In terms of personal audio sound reproduction a number of different optimal control strategies have been proposed such as brightness maximisation [24], sound power minimisation [76], energy difference maximisation [77] and least squares optimisation [78, 79], although the most widely employed and investigated method has been acoustic contrast control [24]. The acoustic contrast control strategy proposed by Choi and Kim is based on the optimisation of the source strengths of an array of sources such that the ratio of the acoustic potential energy in a bright, or listening zone to that in a dark, or quiet zone is maximised; an example of this acoustical problem is presented in Figure 1.5. This optimisation ensures that for the defined source geometry the array minimises the sound radiated to the dark zone whilst maintaining the level in the bright zone.

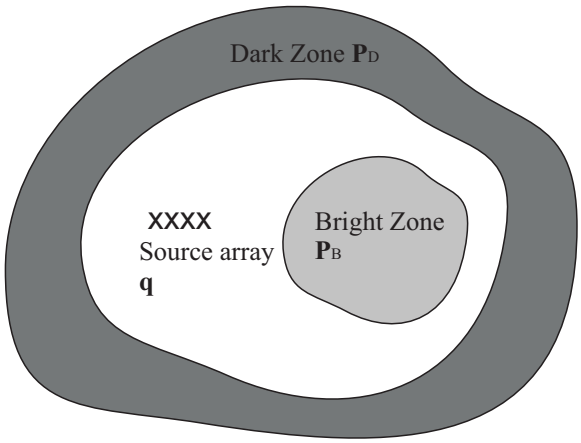

Figure 1.5: An example of a two-dimensional acoustic contrast control problem [80].

Personal Audio Headrest

The method of acoustic contrast control, described above, has been applied to a practical problem by Elliott and Jones [81]. The considered application is where two listeners are seated adjacent to one another in an aircraft or vehicle type scenario listening to different audio programmes, as depicted in Figure 1.6. The reproduction of an audio signal in one seat whilst minimising its level in an adjacent seat – that is, maximising the acoustic contrast between the two seats – is initially investigated using the control system depicted in Figure 1.7. This control strategy is identical in formulation to the feedforward noise control strategy depicted in Figure 1.1b and employed in engine noise control [8], with the engine noise disturbance being

replaced with the known audio signal. The headrest control system employs the loudspeakers already in the left hand headrest as secondary sources to cancel the pressure produced at microphones p_5 to p_8 by the primary source. This control system is shown to achieve significant levels of reduction over the left hand seating region at low frequencies; however, at frequencies where the separation between the primary and secondary sources becomes comparable to the acoustic wavelength the quiet, or dark zone becomes localised around the error microphones [81].

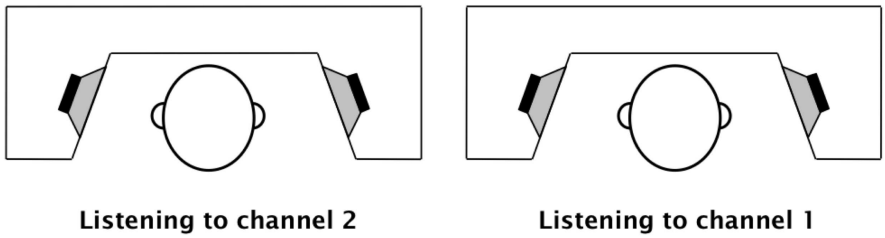

Figure 1.6: Personal audio headrest problem in which adjacent listeners are listening to different audio programmes (after [81]).

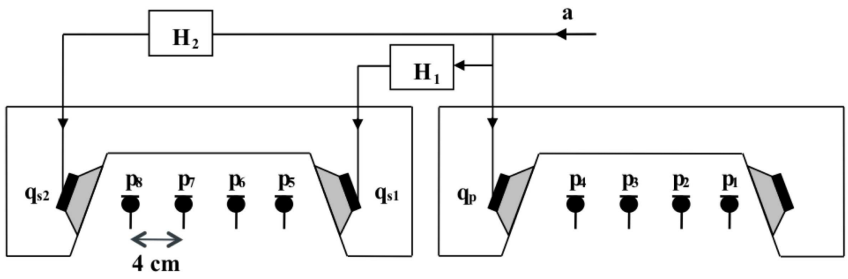

Figure 1.7: Control strategy in which the loudspeakers in the left headrest are employed as secondary sources to cancel the sound produced in that seat by the signal, *a*, which is being reproduced in the right hand seat (after [81]).

The problem of localised zones of quiet is similar to that experienced in active noise control [55], however, in the personal audio problem where the primary source's position is known it is possible to locate the secondary source close to the primary and thus achieve a much broader bandwidth of control. This solution is investigated by Elliott and Jones using the secondary source position presented in Figure 1.8. The performance of this system is investigated using monopole simulations, synthesis using measured transfer responses in an anechoic environment and a real-time implementation in a small room.

The monopole simulations confirm that a dark zone with useful spatial extent is achievable up to a significantly higher frequency of 4 kHz, and an increase in the acoustic contrast compared to a single source of 25 – 30 dB is predicted up to 2 kHz. The synthesised performance of the system depicted in Figure 1.8 using transfer responses measured in an anechoic chamber shows a comparable level of contrast control to the monopole simulations, predicting 20 dB

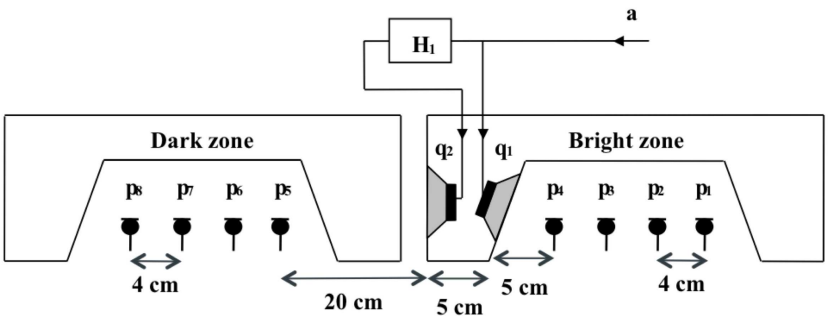

Figure 1.8: Control strategy in which a secondary loudspeaker is mounted next to the primary loudspeaker in order to cancel the sound produced in the left hand seat by the signal, *a*, which is being reproduced by the primary loudspeaker in the right hand seat (after [81]).

improvement between 70 and 300 Hz which then falls to around 15 dB at 1 kHz. Elliott and Jones draw the conclusion that, although simple, monopole simulations provide useful guidance at lower frequencies when designing such systems although accurate predictions are not possible due to the un-modelled influence of the headrests, heads and finite-sized loudspeakers [81].

A real-time implementation of the personal audio system depicted in Figure 1.8 is also presented by Elliott and Jones and its performance is evaluated when it is positioned in a small room. The performance of this system is very close to that predicted by the synthesis using the transfer responses measured in an anechoic chamber, which is due to the acoustic responses between the microphones and loudspeakers being dominated by the direct sound field and, therefore, not differing significantly between the two acoustic environments.

Although Elliott and Jones present a practicable personal audio system with high levels of acoustic contrast performance in [81], in a wide variety of situations in which this system may be applicable there are more than two listeners; for example, in a typical car there may be five occupants, or significantly more in an aircraft cabin. Therefore, the personal audio headrest system has been developed further in a later publication by Jones and Elliott in which two dark zones are defined at two seat locations as shown in Figure 1.9 [76].

The work presented by Jones and Elliott [76] investigates the use of three control strategies to achieve multiple dark zones: acoustic contrast control, brightness maximisation, and sound power minimisation. The brightness maximisation control strategy suffers from the constraint it imposes on the use of self-cancelling arrays, which are generally required to achieve superdirective performance [82], and, therefore, does not perform well in the scenario presented in Figure 1.9. Jones and Elliott [76] show that when there are a few predefined dark zones the acoustic contrast control method performs significantly better than the sound power minimisation strategy. This is due to its ability to steer localised zones of quiet towards the predefined dark zones and for the geometry presented in Figure 1.9 an increase in the acoustic contrast between the bright and dark zones of 20 dB is achieved up to around 1 kHz.

For the case where the number of dark zones becomes larger, Jones and Elliott indicate

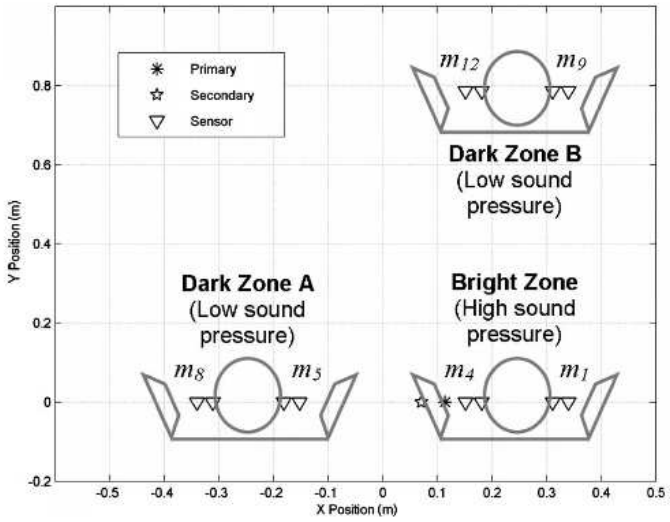

Figure 1.9: Personal audio problem with multiple dark zones (reproduced from [76]).

that the solution given by the acoustic contrast control strategy approaches that given by the sound power minimisation strategy [76]. Therefore, in such an application the sound power minimisation strategy may be more convenient to implement as it only requires the response between the individual sources to be known and does not require the acoustic response to all of the dark zone locations. This may be useful in a large aircraft application, or in an application where the dark zone locations are not predefined.

Personal Audio in a Small Video Monitor

A further technology that may benefit from personal audio systems is personal computers (PCs). This includes both laptops that are frequently used in public spaces or desktop PCs that, in many schools, universities and workplaces, are positioned in large rooms with multiple workstations. The use of acoustic contrast control to generate a personal sound zone for the user of a 17-inch monitor is presented by Chang *et al* [83]. The proposed system employs a broadside array of 9 loudspeakers mounted on either the top or bottom of the monitor as depicted in Figure 1.10a and attempts to generate a bright and dark zone geometry as shown in Figure 1.10b. Using the acoustic contrast optimisation strategy an acoustic contrast of greater than 19 dB is demonstrated in an anechoic environment between 800 Hz and 5 kHz. This level of contrast achieves the levels required to generate subjectively acceptable listening zones according to the study presented in [23], however, there are a number of potential practical issues with the system presented by Chang *et al*.

Firstly, the defined bright and dark zone geometry shown in Figure 1.10b does not consider rear radiation from the system. In a realistic scenario a PC monitor may often be positioned in front of a wall or if a laptop were used in a public space there is just as likely to be people behind the device as to its sides, therefore the rear radiation is likely to have a significant impact

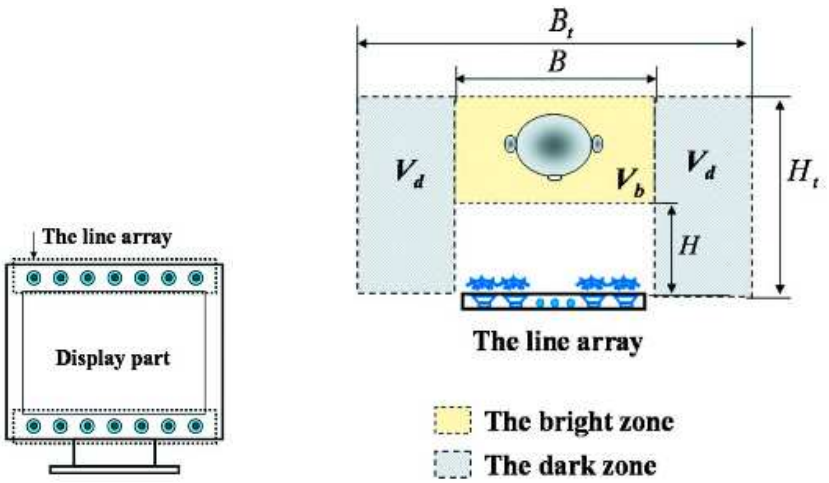

(a) Personal audio system for a monitor.

(b) Geometry of the bright and dark zones.

Figure 1.10: The personal audio system presented in [83] (reproduced from [83]).

on the performance of the system. The symmetry of the broadside array geometry employed in [83] means that for monopole-like sources the sound radiated to the front and the rear of the array will inherently be equal. At low frequencies simple closed-back loudspeakers employed in a practical system will be monopole-like and, therefore, since the bright zone is at the front of the array an unwanted high level zone will also be created at the rear of the array. In order to avoid this effect a more complex array with loudspeakers distributed in the front-to-back dimension or directional loudspeaker units would be required; this has been investigated in [84].

A further area neglected in the personal audio system proposed in [83] is the effect of the actual monitor on the performance of the system. Although the free field assumption is reasonable on the basis that the user is within a short distance of the system and, therefore, the direct sound is dominant over reflections from the walls of the room, since the monitor is in the nearfield of the loudspeakers and also close to the user it is likely to have a significant effect on the system's performance. It has been shown by Cheer *et al* [85, 86], that in the case of a mobile device, the body of the device, which forms a finite-sized baffle, has a significant effect on the high frequency performance of an array optimised using acoustic contrast control. Chang *et al* do consider the scattering effects of the user's head on the performance of the system in a later publication [87] and develop a system that improves on the original system for the practical case when the system is actually in use. However, the effects of the monitor itself are also likely to have a significant effect on the array performance.

The personal audio system presented in [83] is extended to a two-channel system in [88] where the array is used to generate a separate bright zone at each ear of the user and thus facilitate cross-talk cancellation in a personal audio system. The system is able to achieve up to 20 dB of channel separation between the left and right ear bright zones, however, the potential issues discussed above are not addressed.

Personal Audio for Mobile Devices

Mobile devices such as mobile phones, PDAs, portable games consoles and DVD players are widely used in public spaces and, therefore, audio reproduction using a standard loudspeaker system may lead to issues of both user privacy and annoyance for nearby listeners. The generation of a personal sound zone is, therefore, of significant interest in this area and a number of different technologies have been explored to solve this problem. For example, the parametric array [89] has been applied to a mobile device by Nakashima *et al* [90] and achieves such a high level of directivity control that crosstalk between left and right ears is less than 30 dB below 2 kHz. However, the high power requirements, the need for a large number of transducers and the potential health risks [91] limit its practicability in a mobile device.

The use of phase-shift loudspeakers, as reviewed by Holmes [92], have also been investigated for the application of personal audio in a mobile device by Cheer [93]. This work shows that an efficient hypercardioid source is achievable using a single driver and a rear opening with a resistive material covering, however, this is shown to be difficult to achieve over a wide frequency range due to the frequency dependent properties of the rear-port material. That said, the directivity of the developed phase-shift loudspeakers have been employed in arrays to achieve an increased personal audio performance [84, 94].

The use of the acoustic contrast maximisation control strategy to determine the optimum driving signals for an array of 2, 3 and 4 sources in a line array configuration has been investigated by Elliott *et al* for implementation in a mobile device [80]. This work considers a point bright zone as shown in Figure 1.11 and a dark zone that consists of a sphere of pressure evaluation positions separated by 15° surrounding the array – a cross section of which is also shown in Figure 1.11. Monopole simulations are used to demonstrate a trade-off in the number of sources in the array between increasing the acoustic contrast and limiting the electrical power. For example it is shown that a three-source array can reduce the radiated sound power by 11 dB but requires 50 times the electrical power of a single source, and although a four-source array can reduce the radiated sound power by 14 dB it requires around 630 times the electrical power of a single source [80]. Furthermore, it is shown through simulations employing measured transfer responses that as the number of sources in the array is increased the optimal solutions become increasingly sensitive to practical inaccuracies that occur in the driver responses and positions. Therefore, optimal line arrays with greater than two sources are shown to be impractical for a mobile device application not only because of the large power requirements but also due to their low robustness. Improving the robustness of optimal arrays by limiting their sensitivity to practical inaccuracies in transducer positions and responses [95] has been achieved using matrix regularisation for antenna arrays [96], sensor arrays [97] and loudspeaker arrays [98]; the use of regularisation to improve the robustness of optimised personal audio systems has been investigated and is presented in [99].

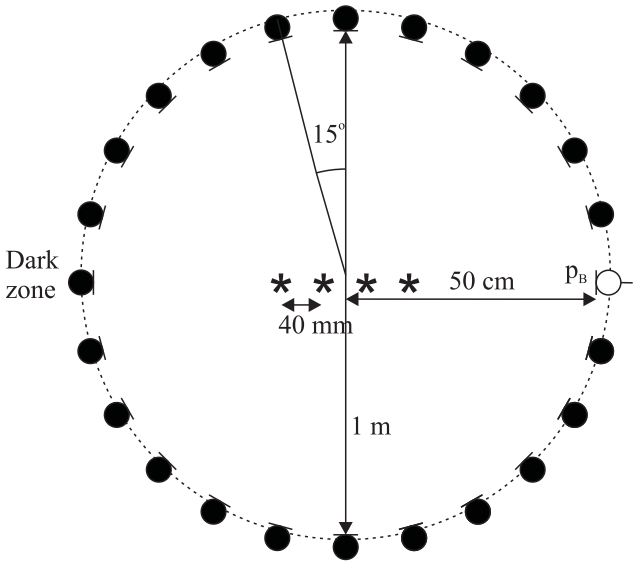

Figure 1.11: Cross-section through the three-dimensional geometric arrangement considered in [80].

Personal Audio in Enclosures

In order to implement a personal audio system within a car cabin environment it is important to consider the implementation of such a system in an enclosed space. Although the vast majority of work has been conducted based on the assumption of a free-field acoustic environment, the implementation of a personal audio system in an enclosed space is presented by Wen *et al* [100]. The investigated personal audio system employs the brightness maximisation [24], or maximum control gain control strategy [100] to optimise an array of 13 sources arranged as three intersecting line arrays forming a star-shaped array positioned in a rectangular enclosure with a volume of 81 m^3. The presented results show that the optimal array significantly outperforms a standard delay-and-sum type beamformer, as described in [101], when the bright zone is positioned beyond the reverberation radius, where the direct and reverberant sound energies are equal [102], in the enclosure. This result can be expected since the delay-and-sum beamformer does not take in to account the influence of the room on the radiated sound field, whereas the optimal array is designed using the acoustic transfer responses between the sources and bright zone positions within the room and, therefore, can attempt to compensate for the influence of the room.

The work presented by Wen *et al* only presents single frequency results and, therefore, it is not possible to determine how the acoustic environment effects the effective operating frequency range of the personal audio system. Moreover, with respect to the implementation of a personal audio system in a car cabin it is important to consider both the use of a distributed array of sources – i.e. the standard car audio loudspeakers – and the generation of multiple bright and dark zones. Additionally, while in the context of free-field personal audio systems the power requirements have been thoroughly considered [80, 82, 99], no consideration of the room's effect on power requirements has been mentioned in the current literature regarding

personal audio in enclosures.

1.4 Thesis Structure and Objectives

This thesis focuses on the development of acoustic active control systems for both noise reduction and audio reproduction in a car cabin environment. From the preceding literature review it is evident that although active noise control systems have been implemented for both engine and road noise control there is a significant need to improve the cost effectiveness and integrability of these systems. This is particularly true for road noise control systems, which have had little commercial implementation since the most technically effective systems require a large number of accelerometers to achieve significant levels of control. Therefore, in the context of noise control, this thesis investigates integrable and cost-effective controllers for both engine and road noise reduction.

There are strong technical links between active noise control and active sound reproduction systems, such as spatial audio and personal audio. The application of spatial audio systems employing active control techniques to car audio reproduction has begun to be investigated both commercially [67] and academically [14]. The implementation of personal audio in car audio systems has, however, not been widely presented in the literature. Therefore, the second main aim of this thesis is to investigate the implementation of a personal audio system within a car cabin. The specific aim of the personal audio system is to allow different audio programmes to be auditioned in different seats in the car.

The structure of the thesis is as follows:

Chapter 2

The acoustic environment in the car cabin is known to be dependent on the coupling between the structure and the enclosure [103]. Prior to the investigation of active noise control strategies and personal audio reproduction systems, this chapter describes a model of structural-acoustic coupling based on modal interactions which is used to derive an elemental model of structural acoustic coupling in Appendix A. The elemental model is used to investigate the effects of a non-rigid structure on the acoustic environment within a car cabin sized enclosure. The results of these simulations are supported by a set of experiments conducted on a car cabin mock-up.

Chapter 3

Feedforward control strategies offer a convenient method of controlling engine noise due to the availability of a reference signal from the reciprocating engine. This chapter investigates two feedforward control strategies – global and regional control – using the model of structural-acoustic coupling derived in Chapter 2. The effects of structural-acoustic coupling on the control strategies are investigated and three primary source excitations are considered: acoustic

point source, structural point force and structural excitation by an acoustic plane wave. Once again, the simulations are supported by experimental results from a car cabin mock-up.

Chapter 4

Feedback active noise control strategies offer a potential method of controlling road noise without the need for the additional accelerometers that are required in a feedforward road noise control system. This chapter presents a review of both single-input single-output (SISO) and multi-input multi-output (MIMO) feedback control theory. A review of modal feedback control is also presented and two internal model control (IMC) formulations of a modal controller employing the standard car audio loudspeakers and the same error sensors that are used in the feedforward engine noise control system investigated in Chapter 3 are presented. Methods of optimising the two control systems are described and the performance of the two control strategies is calculated for a number of primary disturbance conditions.

Chapter 5

To improve the potential control achievable of road noise in the car cabin environment this chapter investigates a fully MIMO IMC feedback controller. The investigated MIMO feedback controller also employs the car audio loudspeakers and the same error sensors that are used in the feedforward control system, however, the signal processing requirements are significantly higher than for the modal control strategies. A method of optimising the proposed feedback controller is presented and the performance of the controller is calculated for a number of primary disturbance conditions.

Chapter 6

Following the investigations of feedforward and feedback active noise control strategies for engine and road noise respectively, a series of measurements are conducted on a small city car. These measurements include a set of transfer response measurements between the car audio loudspeakers and microphones, as well as a set of engine and road noise measurements. Using this measured data feedforward and MIMO feedback controllers are designed and the performance of the active noise control strategies is simulated. Subsequently, the feedforward engine noise control system is implemented in the small city car and the results of real-time operation are presented. A discussion regarding the real-time implementation of the MIMO feedback control system is also presented.

Chapter 7

This chapter presents an investigation of the implementation of a personal audio system in a car cabin sized enclosure. The performance of both distributed and nearfield loudspeaker arrays is simulated and the effects of the enclosure on their performance are investigated through the

comparison of monopole simulations in free-field and modal environments. Based on these findings a personal audio system suitable for the car audio application is proposed. Two alternative control strategies are also detailed and formulations are derived for constraining either the overall electrical power or the electrical power required by individual sources. The performance of the two control strategies is compared in the context of the car cabin personal audio system in terms of both personal audio performance and the conditioning of the solutions.

Chapter 8

Based on the findings of Chapter 7 the practical implementation of a personal audio system in real car cabin in investigated. This process first involves the specification of a loudspeaker array that is capable of producing different audio programmes in the front and rear seats of a car cabin. The response of the array is then measured in the car cabin and these measurements are used to perform offline predictions of the performance of the system and to design practical filters for a real-time implementation. Finally, measurements of the personal audio system operating in real-time are presented.

Chapter 9

The final chapter presents a summary of the conclusions drawn from the work presented in the preceding chapters and provides suggestions for future work in this area.

1.5 Contributions

The main original contributions of this thesis are:

1. The investigation of the effects of structural-acoustic coupling on feedforward active noise control. A key contribution in this area is the direct comparison between the control achievable in a rigid and non-rigid enclosure [104, 105].

2. A modal feedback controller employing non-colocated sources and sensors has been proposed and a novel method of optimising the controller and transducer weightings in parallel has been described.

3. Multi-input multi-output feedback control has been investigated for the application of road noise control through both numerical simulations and offline simulations using data measured in a small city car. A method of optimising the controller has been described and validated.

4. A rapidly converging feedforward engine noise control system has been implemented in a two-cylinder car and a novel method of reducing control spillover, employing a variable frequency bandpass filter, has been proposed and empirically tested.

5. The effects of implementing a personal audio system within a car cabin sized enclosure have been investigated.

6. The acoustic contrast control strategy and least squares optimisation method have been derived with constraints on the individual source strengths and these control strategies have been applied to the optimisation of the car cabin personal audio system.

7. A personal audio system has been designed and implemented to achieve bright (listening) and dark (quiet) zones in a car cabin.

A number of publications and conference proceedings have arisen from both the work presented in this thesis and related work carried out during the same time period and these references are given in the declaration of authorship.

Chapter 2

The Effect of Structural-Acoustic Coupling on the Acoustic Environment of an Automobile Cabin

The acoustic sound field at low frequencies in automobile cabins is dependent on the acoustic and structural properties of the cabin enclosure and their interaction through coupling. This has been widely studied [106, 103] and an understanding of the structural-acoustic coupling has been employed to improve the design of the coupled system in terms of noise reduction [107, 108]. This chapter presents an investigation of the effect of structural-acoustic coupling on a car cabin sized enclosure with the aims of a) informing the development of active noise control strategies and personal audio reproduction systems in the subsequent chapters and b) developing a reliable model that can be used in the following chapters.

This chapter first presents the derivation of an analytical model of an enclosure with structural-acoustic coupling and subsequently employs this model to investigate the effects of coupling upon a car cabin sized enclosure's acoustic and structural response. A mock-up of the modelled car cabin enclosure has been constructed using plywood and the results of a series of experiments conducted on this enclosure are presented. These results are used to confirm the reliability of the structural-acoustic model.

2.1 Model of Structural-Acoustic Coupling

The modal model of structural-acoustic coupling, first presented by Dowell and Voss [109], will be derived in this section following the compact matrix formulation of this model presented by Kim and Brennan [110]. The derivation of the coupled response based upon modal-interaction assumes that the coupled response may be described by the combination of the uncoupled acoustic and structural responses. Based on this assumption the influence of the acoustic system on the structural is determined by the acoustic pressure on the surface of the structure and, similarly, the influence of the structural system on the acoustic is determined by the normal

surface acceleration of the structure [111].

The model of structural-acoustic coupling based upon the interaction of the uncoupled acoustic and structural modes has been widely employed to date; however, recent work by Ginsberg [112] has questioned the simplification employed in Dowell's model, which uses the rigid walled enclosure modes as a basis for the pressure field in the coupled enclosure. This simplification leads to the velocity continuity condition not being satisfied at the non-rigid boundaries, which is acknowledged by Dowell *et al* [113] as well as Ginsberg [112]. Due to this potential issue with Dowell's model, Ginsberg presents an alternative model based upon an extension of the Ritz series method which satisfies all continuity conditions [112]. Ginsberg goes on to present a comparison of the two methods and concludes that the simplified method provides accurate solutions for light fluid loading, except at frequencies below the fundamental rigid enclosure mode, whereas the Ritz series method is shown to be accurate in all cases [112]. This therefore suggests that a more rigourous study should employ the Ritz series method, however, Dowell's response to Ginsberg's work highlights two practical points: (1) Dowell's method has been widely verified experimentally and works well in most cases, and (2) Dowell's method offers lower computational burden [114]. In response to this Ginsberg states that the computational advantage only exists where the rigid-walled modes of the enclosure can be determined analytically [115]. For the work presented in this chapter, and the following chapters employing the presented model, a rectangular acoustic enclosure will be considered and, therefore, since the rigid-walled modes are straightforward to calculate, Dowell's simplified model will be employed in order to keep the computational load to a minimum. Additionally, since the fluid in the acoustic domain for the considered problem is air, the fluid loading is likely to be light compared to, for instance, an underwater acoustics problem. Therefore, as detailed by Ginsberg [112] the accuracy of Dowell's model will be sufficient.

The issue of employing hard walled boundary conditions was also investigated by Bullmore [116] who compared the results of simulations using hard-walled acoustic modes, with fluid damping, and soft-walled acoustic modes, with damping on the surface. He found only small differences in his simulated results. Further supporting the use of Dowell's model.

According to the modal model of the sound field within a rigid walled rectangular enclosure the pressure at a position defined by the vector $\boldsymbol{x}$ may be written in terms of the summation of the complex amplitudes of the acoustic modes, a_n, and the mode shapes ψ_n, as

$$p(\boldsymbol{x}) = \sum_{n=0}^{\infty} a_n \psi_n(\boldsymbol{x}). \tag{2.1}$$

The rigid walled acoustic mode shapes are given by

$$\psi_n(\boldsymbol{x}) = \sqrt{\varepsilon_{n1}\varepsilon_{n2}\varepsilon_{n3}} \cos\frac{n_1\pi x_1}{L_{x_1}} \cos\frac{n_2\pi x_2}{L_{x_2}} \cos\frac{n_3\pi x_3}{L_{x_3}}, \tag{2.2}$$

where x_1, x_2, and x_3 are the co-ordinate directions, L_{x1}, L_{x2} and L_{x3} are the dimensions of the enclosure in the respective co-ordinate directions, n_1, n_2, n_3 denote the trio of model integers,

and ε_{n1}, ε_{n2} and ε_{n3} are normalisation factors used to ensure that the mode shapes form an orthonormal set. For an acoustic source distribution, $q_{vol}(\boldsymbol{x})$, within the enclosure the complex amplitude of the n-th acoustic mode is given by

$$a_n = \frac{\rho_0 c_0^2}{V} A_n \int_V \psi_n(\boldsymbol{x}) q_{vol}(\boldsymbol{x}) \mathrm{d}V, \tag{2.3}$$

where ρ_0 is the ambient air density, c_0 is the speed of sound, V is the volume of the enclosure, and

$$A_n = \frac{\omega}{[2\zeta_n \omega_n \omega + \mathrm{j}(\omega^2 - \omega_n^2)]}, \tag{2.4}$$

where ω is the angular frequency, ζ_n is the damping of the n-th acoustic mode, ω_n is the angular frequency of the n-th acoustic mode, and j is $\sqrt{-1}$. Assuming that the frequency range of interest is limited, it is possible to approximate the acoustic pressure within the enclosure using a finite number of modes, N, and equation 2.1 can then be written in vector notation as

$$p(\boldsymbol{x}) = \boldsymbol{\psi}(\boldsymbol{x})^T \boldsymbol{a}, \tag{2.5}$$

where $\boldsymbol{a}$ is a column vector containing the complex amplitudes of the N acoustic modes and $\boldsymbol{\psi}$ is a column vector of N acoustic mode shapes at position $\boldsymbol{x}$.

According to the modal model of a thin isotropic plate the in-vacuo structural vibration velocity at a position $\boldsymbol{y}$ on the structure may be described by the summation of the complex amplitude of the structural modes, b_k, and the uncoupled structural mode shape functions, ϕ_k, as

$$w(\boldsymbol{y}) = \sum_{k=1}^{\infty} b_k \phi_k(\boldsymbol{y}). \tag{2.6}$$

The mode shape function is dependent on the specific boundary conditions and this will be considered in Section 2.2. The complex amplitude of the k-th structural mode for a distributed force excitation is given by

$$b_k = \frac{1}{\rho_s h S_F} B_k \int_{S_F} \phi_k(\boldsymbol{y}) f(\boldsymbol{y}) \mathrm{d}S, \tag{2.7}$$

where ρ_S is the density of the plate material, h is the plate thickness, S_F is the surface area of the plate, $f(\boldsymbol{y})$ is the distributed force applied to the plate, and

$$B_k = \frac{\omega}{\left[2\zeta_k \omega_k \omega + \mathrm{j}(\omega^2 - \omega_k^2)\right]}, \tag{2.8}$$

where ζ_k is the damping of the k-th structural mode and ω_k is the angular frequency of the k-th structural mode. As for the uncoupled acoustic system, equation 2.6 may be approximated by a finite number of structural modes, K, and can then be written in vector notation as

$$w(\boldsymbol{y}) = \boldsymbol{\phi}(\boldsymbol{y})^T \boldsymbol{b}, \tag{2.9}$$

where $\boldsymbol{b}$ is a column vector containing the complex amplitudes of the K structural modes and $\boldsymbol{\phi}$ is a column vector of K structural mode shapes.

Within an enclosure where the acoustic boundaries are not rigid, but vibrate as plates, the acoustic modes may be excited by both a distribution of acoustic source strengths within the enclosure (as in equation 2.3) and the vibration of non-rigid boundaries. Considering both acoustic and structural source terms the complex amplitude of the n-th acoustic mode is then given by

$$a_n = \frac{\rho_0 c_0^2}{V} A_n \left(\int_V \psi_n(\boldsymbol{x}) q_{vol}(\boldsymbol{x}) \mathrm{d}V + \int_{S_F} \psi_n(\boldsymbol{y}) w(\boldsymbol{y}) \mathrm{d}S \right) \tag{2.10}$$

where $w(\boldsymbol{y})$ is the normal surface velocity of the non-rigid structure. From equation 2.10 the contributions to the n-th acoustic modal amplitude from the acoustical sources, q_{vol}, and structural sources, w, can be clearly identified as the first and second integral terms respectively. For a generalised modal acoustic source term, $q_n = \int_V \psi_n(\boldsymbol{x}) q_{vol}(\boldsymbol{x}) \mathrm{d}V$, equation 2.10 can be written as

$$a_n = \frac{\rho_0 c_0^2}{V} A_n \left(q_n(\boldsymbol{x}) + \int_{S_F} \psi_n(\boldsymbol{y}) w(\boldsymbol{y}) \mathrm{d}S \right). \tag{2.11}$$

Substituting for the structural velocity using equation 2.6 then gives

$$a_n = \frac{\rho_0 c_0^2}{V} A_n \left(q_n(\boldsymbol{x}) + \sum_{k=0}^{\infty} b_k \int_{S_F} \psi_n(\boldsymbol{y}) \phi_k(\boldsymbol{y}) \mathrm{d}S \right). \tag{2.12}$$

From this equation it can be seen that the excitation of the acoustic mode by the non-rigid structure is dependent on the interaction between the structural and acoustic mode shape functions. This is termed geometric coupling and is represented by the integral of the structural and acoustic mode shape functions over the surface of the non-rigid structure:

$$C_{n,k} = \int_{S_F} \psi_n(\boldsymbol{y}) \phi_k(\boldsymbol{y}) \mathrm{d}S. \tag{2.13}$$

For a finite number of structural and acoustic modes, the column vector of complex modal amplitudes, $\boldsymbol{a}$, may be written using the above derivation as

$$\boldsymbol{a} = \boldsymbol{Z}_a (\boldsymbol{q}_{am} + \boldsymbol{q}_{sm}) \tag{2.14}$$

where $\boldsymbol{q}_{am}$ is the vector of modal source strengths due to the acoustic sources; $\boldsymbol{q}_{sm}$ is the vector of modal source strengths due to the structural vibration and is equal to $\boldsymbol{Cb}$, where $\boldsymbol{C}$ is the $(N \times K)$ matrix of structural-acoustic mode shape coupling terms; and the uncoupled acoustic modal impedance matrix, which describes the relationship between the acoustic source excitation and the acoustic pressure in modal coordinates, is $\boldsymbol{Z}_a = \boldsymbol{A}\rho_0 c_0^2 / V$, where $\boldsymbol{A}$ is the $(N \times N)$ diagonal matrix of acoustic resonant response terms given by equation 2.4.

Considering both structural and acoustic force terms the complex amplitudes of the struc-

tural modes may be written as

$$b_k = \frac{1}{\rho_s h S_F} B_k \left(\int_{S_F} \phi_k(\boldsymbol{y}) f(\boldsymbol{y}) \mathrm{d}S - \int_{S_F} \phi_k(\boldsymbol{y}) p(\boldsymbol{y}) \mathrm{d}S \right), \tag{2.15}$$

where $p(\boldsymbol{y})$ is the acoustic pressure evaluated on the plate surface. Once again, as for the acoustic modal complex amplitude, from equation 2.15 the contributions to the k-th structural modal amplitude from the structural force distribution, $f(\boldsymbol{y})$, and the acoustic pressure distribution on the plate, $p(\boldsymbol{y})$, can be identified as the first and second integral terms respectively. The second term is negative since it describes the reaction force to the force acting on the structure due to the acoustic pressure, and thus acts in the opposite direction to the pressure. Defining a generalised modal force $f_k = \int_{S_F} \phi_k(\boldsymbol{y}) f(\boldsymbol{y}) \mathrm{d}S$ and substituting for pressure using equation 2.1 gives

$$b_k = \frac{1}{\rho_s h S_F} B_k \left(f_k - \sum_{n=0}^{\infty} C_{k,n} a_n \right), \tag{2.16}$$

where $C_{k,n} = C_{n,k}^T$. For a finite number of acoustic and structural modes the column vector containing the complex amplitudes of the K structural modes can be written as

$$\boldsymbol{b} = \boldsymbol{Y}_s (\boldsymbol{f}_{sm} - \boldsymbol{f}_{am}), \tag{2.17}$$

where $\boldsymbol{f}_{sm}$ is the vector of generalised modal forces due to the external force distribution $f(\boldsymbol{y})$; $\boldsymbol{f}_{am}$ is the vector of modal forces due to the reaction force caused by the acoustic pressure acting on the structure and is equal to $\boldsymbol{C}^T \boldsymbol{a}$; and the uncoupled structural modal mobility matrix is $\boldsymbol{Y}_s = \boldsymbol{B}/(\rho_s h S_F)$ where $\boldsymbol{B}$ is a $(K \times K)$ diagonal matrix of structural resonant response terms given by equation 2.8.

Substituting equation 2.17 into equation 2.14 for $\boldsymbol{b}$, which forms $\boldsymbol{q}_{sm}$, allows the complex amplitude of the acoustic modes to be written in terms of the direct acoustic and structural excitations, $\boldsymbol{q}_{am}$ and $\boldsymbol{f}_{sm}$ respectively:

$$\boldsymbol{a} = \left[\boldsymbol{I} + \boldsymbol{Z}_a \boldsymbol{C} \boldsymbol{Y}_s \boldsymbol{C}^T \right]^{-1} \boldsymbol{Z}_a (\boldsymbol{q}_{am} + \boldsymbol{C} \boldsymbol{Y}_s \boldsymbol{f}_{sm}). \tag{2.18}$$

Similarly, substituting into equation 2.17 for $\boldsymbol{a}$ using equation 2.14 gives

$$\boldsymbol{b} = \left[\boldsymbol{I} + \boldsymbol{Y}_s \boldsymbol{C}^T \boldsymbol{Z}_a \boldsymbol{C} \right]^{-1} \boldsymbol{Y}_s (\boldsymbol{f}_{sm} - \boldsymbol{C}^T \boldsymbol{Z}_a \boldsymbol{q}_{am}). \tag{2.19}$$

Equation 2.18 may be used to describe the acoustic response of a system with structural-acoustic coupling for various acoustic and structural excitations via substitution into equation 2.5. Similarly equation 2.19 may be used to describe the structural response of a system with structural-acoustic coupling via substitution into equation 2.9.

At this point it is pertinent to observe from equations 2.18 and 2.19 that if the term in square brackets in both instances is approximately equal to the identity matrix, $\boldsymbol{I}$, the system is said to be weakly coupled. This physically implies that the acoustic and structural responses have

limited influence upon each other. More specifically, a system may be described as weakly coupled if either [117]

$$||\boldsymbol{Z}_a \boldsymbol{C} \boldsymbol{Y}_s \boldsymbol{C}^T|| \simeq 0, \tag{2.20}$$

or

$$||\boldsymbol{Y}_s \boldsymbol{C}^T \boldsymbol{Z}_a \boldsymbol{C}|| \simeq 0, \tag{2.21}$$

where $||\cdots||$ denotes a norm of the matrix.

The corresponding analysis using an elemental rather than a modal approach is outlined in Appendix A and provides a method of simulation for more complicated geometries. For example, where multiple walls of the enclosure are non-rigid. The elemental model is employed in the following simulations.

2.2 Numerical Investigation of the Effects of Structural-Acoustic Coupling in an Enclosure

The elemental model derived in Appendix A will be used to investigate how non-rigid structural panels affect the response of the car cabin sized rectangular enclosure presented in Figure 2.1. According to the elemental model, the vector of acoustic pressures, $\boldsymbol{p}$, at the L elements in the non-rigid enclosure is given by equation A.38 which is repeated here for convenience

$$\boldsymbol{p} = [\boldsymbol{I} + \boldsymbol{Z}_A \boldsymbol{Y}_{CS}]^{-1} \boldsymbol{Z}_A (\boldsymbol{q} + \boldsymbol{S} \boldsymbol{Y}_S \boldsymbol{f}), \tag{2.22}$$

where $\boldsymbol{Z}_A$ is the $(L \times L)$ matrix of uncoupled acoustic impedances in the enclosure, $\boldsymbol{Y}_{CS}$ is the $(L \times L)$ matrix of acoustic admittances of the structure, $\boldsymbol{q}$ is the vector of acoustic source strengths, $\boldsymbol{S}$ is the diagonal matrix of element areas, $\boldsymbol{Y}_S$ is the matrix of uncoupled structural mobilities and $\boldsymbol{f}$ is the vector of structural forces. The vector of normal surface velocities on the non-rigid structure is given by equation A.40 and this is again repeated for convenience

$$\boldsymbol{w} = [\boldsymbol{I} + \boldsymbol{Y}_S \boldsymbol{Z}_{CA}]^{-1} \boldsymbol{Y}_S (\boldsymbol{f} - \boldsymbol{S} \boldsymbol{Z}_A \boldsymbol{q}), \tag{2.23}$$

where $\boldsymbol{Z}_{CA}$ is the matrix of mechanical impedances. For this investigation, the enclosure is excited by an acoustic monopole source positioned in a corner of the enclosure, as shown in Figure 2.1, and the acoustic and structural responses will be observed via the acoustic potential energy and the structural kinetic energy respectively. The total acoustic potential energy can be estimated as,

$$E_p \approx \frac{V}{4\rho_0 c_0^2 L} \boldsymbol{p}^H \boldsymbol{p}, \tag{2.24}$$

where L is the number of elements and ^{H} is the complex conjugate, Hermitian, transpose and the total structural kinetic energy over all non-rigid panels can be approximated as,

$$E_k \approx \frac{\rho_s h}{4 L_s} \boldsymbol{w}^H \boldsymbol{w}, \tag{2.25}$$

where L_s is the number of elements which are positioned on the structure.

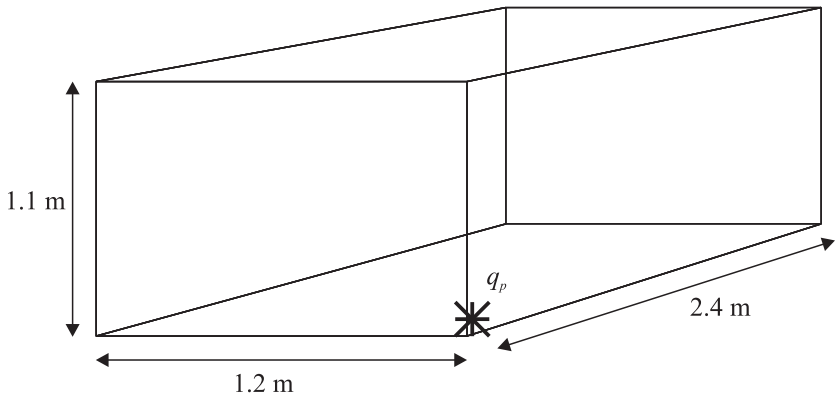

Figure 2.1: Enclosure dimensions and acoustic monopole source position.

The acoustic damping ratio of the enclosure is assumed to be frequency independent and a value of 10% has been used as this is typical of an automotive interior [9]. This estimate is confirmed in the in-car measurements presented in Chapter 6. The properties of the non-rigid panels, which are assumed to be simply supported, are detailed in Table 2.1 and are chosen to be typical of plywood, which will be employed in the later experimental studies presented in Section 2.3. The true boundary conditions are more complicated than simply supported but this assumption provides a reasonable approximation to the true behaviour, and the results are not changed qualitatively if different boundary conditions are used, as discussed in Appendix C. The simulated responses have been generated using 100 acoustic modes and 90 structural modes per non-rigid panel. The elemental spacing has been set such that there are 6 points per wavelength at the maximum frequency of interest – 500 Hz – which results in a total of 2904 points evenly distributed throughout the enclosure. The number of points used to evaluate the structural response is dependent upon the size of the non-rigid structure and, therefore, the number and size of non-rigid panels.

Table 2.1: Non-rigid panel properties

Property	Value
Young's Modulus, E	5×10^9 Nm^{-2}
Panel Thickness, h	12 mm
Poisson's ratio, v	0.3
Panel density, ρ_s	465 kgm^{-3}
Damping ratio, ζ_k	0.05

Prior to employing equations 2.22 and 2.23 it is necessary to define the natural frequencies and mode shape functions of the simply supported panel. The natural frequencies of a simply

supported panel are given by [118]

$$\omega_k = \sqrt{\frac{Eh^2}{12\rho_s(1-\nu^2)}}\left[\left(\frac{k_{y1}\pi}{L_{y_1}}\right)^2 + \left(\frac{k_{y2}\pi}{L_{y_2}}\right)^2\right], \tag{2.26}$$

where L_{y_1} and L_{y_2} are the dimensions of the panel in the y_1 and y_2 co-ordinate directions respectively and k_{y1} and k_{y2} are wavenumbers in the y_1 and y_2 directions. The orthonormal mode shape functions of the simply supported panel are given as [118]

$$\phi_k(y_1,y_2) = 2\sin\left(\frac{k_{y1}\pi y_1}{L_{y_1}}\right)\sin\left(\frac{k_{y2}\pi y_2}{L_{y_2}}\right). \tag{2.27}$$

Before employing the model to simulate the system described here, a number of simulations were carried out using structural-acoustic systems described in the literature in order to confirm that the results of the implemented code agreed with the previous work. For both the modal model and elemental model the results agree with the work presented by Kim *et al* in [117, 110, 119], which considers an enclosure with a non-rigid roof. However, neither the modal or elemental models produce the same results as presented by Mohammad [120], where a small section of the floor is non-rigid. The results of the modal and elemental models implemented for a system with a small non-rigid section of floor do produce the same results as one another, and further consideration of the results presented by Mohammad compared to previous work suggests the possibility of an error in Mohammad's calculations. That is, despite the non-rigid structure employed by Mohammad being considerably smaller than that employed by Kim and the enclosure being considerably larger, the geometric coupling coefficients quoted by Mohammad are consistently of greater magnitude than in the work of Kim. This is not as expected since from equation 2.22, for example, it can be seen that the effect of coupling upon the pressure is dependent upon the size of the $\boldsymbol{Z}_A\boldsymbol{Y}_{CS}$ term compared to unity and since $\boldsymbol{Y}_{CS}$ is proportional to the non-rigid surface area and $\boldsymbol{Z}_A$ is inversely proportional to the volume of the enclosure it can be appreciated that for a smaller non-rigid panel and/or a larger acoustic enclosure the effect of coupling should reduce. Additionally, since the results of Kim *et al* [117, 110, 119] are supported by physical measurements, and Mohammad's are not, it is assumed that the implemented models are correct. This will be supported in the following section through experimental validation.

2.2.1 The Effect of a Single Non-Rigid Roof Panel

The majority of previous work on structural-acoustic coupling has considered the case where there is a single non-rigid panel or wall [109, 121, 122, 123, 124, 125, 126, 127]. Therefore, simulations of a single non-rigid roof panel will be presented first. The benefit of first investigating the effects of a single non-rigid panel is that the causes of the changes in the acoustic and structural responses are more easily attributable than when there are multiple non-rigid panels with different modal responses; this will be investigated in the following section.

For the internal acoustic excitation source, with a volume velocity of 10^{-5} m^3s^{-1} and positioned in the corner of the rectangular enclosure as shown in Figure 2.1, Figure 2.2 shows the total acoustic potential energy and the total structural kinetic energy within the enclosure with a non-rigid roof panel. The acoustic and structural responses have been calculated for both the fully coupled and weakly coupled cases. In the weakly coupled case the terms in square brackets in equations 2.22 and 2.23 have been set to the identity matrix, as discussed at the end of Appendix A. From Figure 2.2a it can be seen that the acoustic potential energy is only significantly affected at frequencies below around 100 Hz.

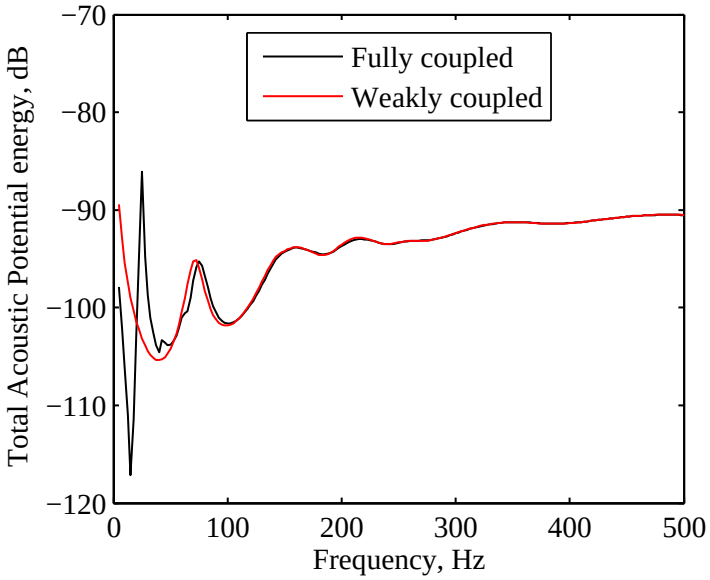

(a) Total acoustic potential energy.

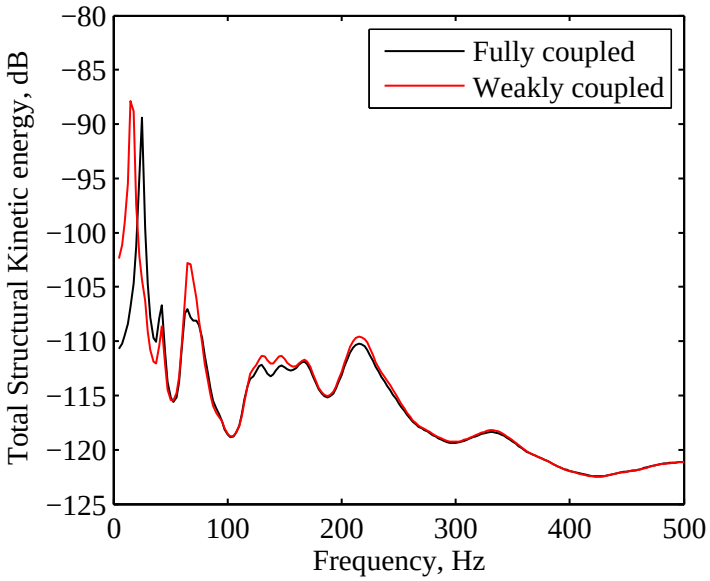

(b) Total structural kinetic energy.

Figure 2.2: Simulated acoustic and structural response of the acoustic enclosure with a flexible roof panel when excited at different frequencies by a single internal acoustic monopole source with a volume velocity of 10^{-5} $\mathrm{m}^3\mathrm{s}^{-1}$.

At frequencies around the $(1,1)$ structural mode it can be seen from Figure 2.2b that the effect of a fully coupled system is to increase the *apparent* frequency of the mode. The magnitude of this effect may be explained by considering the natural frequencies of the first acoustic and structural modes, and the geometric coupling coefficient between these two modes; these values are presented in Table 2.2. For the $(0,0,0)$ acoustic mode and the $(1,1)$ structural mode the magnitude of the geometric coupling is significant compared with the other geometric coupling coefficients presented in Table 2.2 and, therefore, the interactions between these two modes *may* be significant. However, this is not the only parameter that determines the mag-

nitude of the coupling effect, and the relative natural frequencies and bandwidths of the two modes are also important as described by the condition for a well-coupled mode according to Fahy [121]:

$$2|\omega_n - \omega_k| < (\Delta\omega_n + \Delta\omega_k) \tag{2.28}$$

where $\Delta\omega_n$ and $\Delta\omega_k$ are the bandwidth of the n-th acoustic and k-th structural modes respectively. In the case of the compliant acoustic mode, calculating the bandwidth is not feasible since the natural frequency is at 0 Hz so no lower frequency half-power point may be determined. It can, however, be appreciated that based on the proximity of the two mode's natural frequencies and the geometric coupling coefficient they will interact.

The effect of the interaction between an acoustic mode and a structural mode upon the resultant structural-acoustic coupled modes is described by Craggs [106]. He states that if the structure is mass-controlled the frequency of the fully-coupled enclosure mode will increase in frequency compared to the rigid walled case, while the fully-coupled structural mode will decrease in frequency. For a stiffness-controlled boundary the frequency of the fully-coupled enclosure mode will decrease compared to the rigid walled case, while the fully-coupled structural mode will increase in frequency. A structural mode is mass-controlled if its natural frequency is lower than that of the acoustic mode since the acoustic mode will predominantly excite the structural mode in its mass controlled region. Similarly, if the structural mode's natural frequency is above that of the acoustic mode it will be stiffness-controlled since the acoustic mode will predominantly excite the structural mode in its stiffness-controlled region. Therefore, in relation to the $(0,0,0)$ acoustic and $(1,1)$ structural modes it can be appreciated that the effect of this particular coupling will decrease the apparent natural frequency of the enclosure mode through an increase in effective mass. This is the effect that can be seen in Figure 2.2a at frequencies below the dip in the acoustic potential energy at 16 Hz. A more detailed analysis of the modal interaction in this case is presented in Appendix B.

Table 2.2: Coupling coefficients, modal integers, and natural frequencies of the first eight acoustic and first nine structural modes.

Mode number		Structural	1	2	3	4	5	6	7	8	9
	Integers		(1, 1)	(2, 1)	(3, 1)	(1, 2)	(2, 2)	(4, 1)	(3, 2)	(5, 1)	(4, 2)
Acoustic		Frequency (Hz)	16	26	42	55	65	65	81	94	104
1	(0, 0, 0)	0	2.3344	0	0.7781	0	0	0	0	0.4669	0
2	(1, 0, 0)	71	0	2.2009	0	0	0	0.8804	0	0	0
3	(0, 1, 0)	143	0	0	0	2.2009	0	0	0.7336	0	0
4	(2, 0, 0)	143	-1.1005	0	1.9808	0	0	0	0	0.7336	0
5	(0, 0, 1)	156	-3.3014	0	-1.1005	0	0	0	0	-0.6603	0
6	(1, 1, 0)	160	0	0	0	0	2.0751	0	0	0	0.8300
7	(1, 0, 1)	172	0	-3.1126	0	0	0	-1.2450	0	0	0
8	(2, 1, 0)	202	0	0	0	-1.0375	0	0	1.8676	0	0

2.2.2 The Effect of Multiple Non-Rigid Panels

In a practical enclosure, such as a car cabin, it is likely that there will be multiple non-rigid panels, therefore, the elemental model will be employed to investigate the effect of multiple non-rigid panels. The first system to be considered is the same acoustic enclosure as previously with both non-rigid roof and floor panels. Both panels have identical properties and, therefore, their respective structural modes are identical. Figure 2.3a shows the total acoustic potential energy within the enclosure when the fully coupled system is excited by the monopole 10^{-5} $\mathrm{m}^3\mathrm{s}^{-1}$ volume velocity source as previously. From this plot and with reference back to Figure 2.2a it can be seen that the effects of structural-acoustic coupling remain limited to frequencies below around 100 Hz.

Comparing the two sets of data presented in Figure 2.3a indicates that the effect of introducing the non-rigid floor panel is to increase the effects of the structural-acoustic coupling for the single roof panel described previously. For example, the significant peak relating to the $(1,1)$ structural mode at 26 Hz for the non-rigid roof system is slightly increased in magnitude and the frequency is shifted up to 30 Hz. The increase in the natural frequency of this structural mode can also be seen in the total structural kinetic energy, which is presented in Figure 2.3b; however, due to the relative phase of the roof and floor panel velocities and their interaction via the acoustic enclosure there is a slight reduction in the magnitude of the total structural kinetic energy.

Referring back to the total acoustic potential energy plot it can be seen that due to the inclusion of the second non-rigid panel the natural frequency of the first longitudinal acoustic mode has been increased in frequency by a further 2.5 Hz to 77.5 Hz. It is also pertinent to note that, as expected, the inclusion of the second panel produces a larger variation in the acoustic potential energy at around 42 Hz and 60 Hz, where weaker panel resonances occur, but since both panels have the same properties the effects of these modes become more significant.

From Figure 2.3b it can be seen that the total structural kinetic energy – that is, the sum of the total kinetic energy in both the roof and floor panels – is increased for frequencies greater than approximately 100 Hz. However, at lower frequencies it can be seen that the change in kinetic energy is lower and at some frequencies the total kinetic energy in the two panels is reduced compared to the single non-rigid roof panel. This can be related to the interaction between the two flexible panels and the acoustic enclosure.

Although it has been shown how an acoustic enclosure's response is affected by the inclusion of two non-rigid panels with identical properties, it is perhaps more practically orientated in the context of a car cabin to consider an enclosure where all panels are non-rigid. Although the structure of a car cabin is unlikely to be homogeneous – for instance, the structural-acoustic coupling between the windows and the cavity will be significantly different to that between large metal panels, such as the roof, and the cavity – it is useful in terms of understanding the physical problem to consider the simple rectangular enclosure with all panels being constructed of the same non-rigid material. Since there are three different sized panels in the

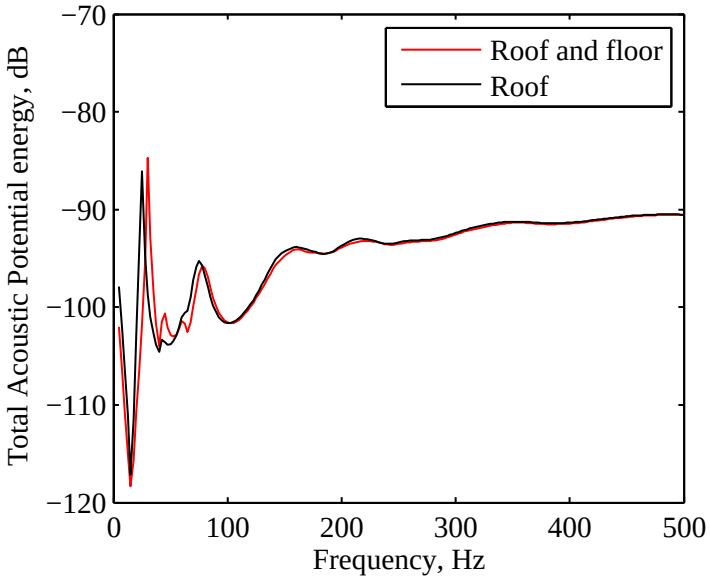

(a) Total acoustic potential energy.

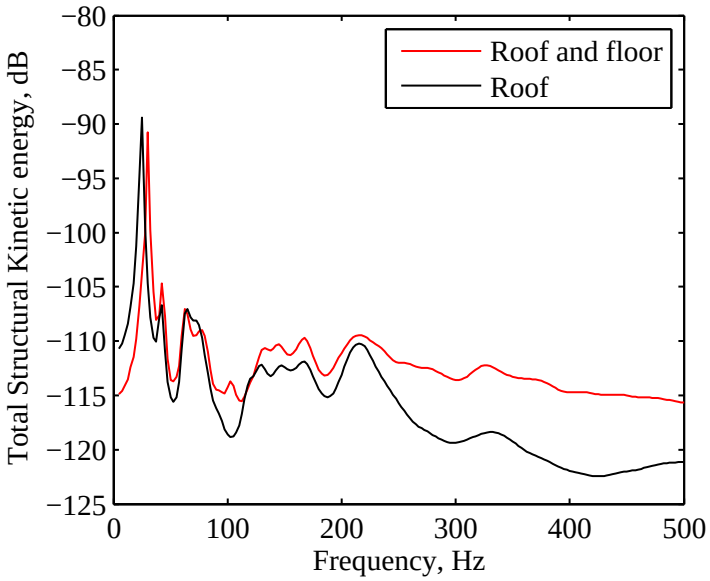

(b) Total structural kinetic energy.

Figure 2.3: Simulated acoustic and structural response of the acoustic enclosure with flexible roof and floor panels when excited at different frequencies by a single internal acoustic monopole source with a volume velocity of 10^{-5} m^3s^{-1}.

rectangular enclosure, investigating the coupled response will enable the effects of structural-acoustic coupling to be observed where there are multiple structural components (or panels) having different mode shapes and frequencies, as well as different positioning relative to the acoustic mode shapes of the enclosure.

Figure 2.4 shows the total acoustic potential energy and total structural kinetic energy for the structural-acoustic system where all panels are non-rigid and have the properties presented in Table 2.1; that is, the enclosure is a plywood rectangular box with the dimensions presented in Figure 2.1. Both plots in Figure 2.4 show the respective energies for the weakly coupled and fully coupled cases. From these plots it can be seen that the effects of structural-acoustic coupling occur over a wider bandwidth than for the single roof panel case considered above, as expected.

From Figure 2.4a it can be seen that significant variations between weakly and fully coupled analyses now occur up to around 200 Hz. Additionally, more peaks in the fully coupled energy spectrum occur for this completely non-rigid enclosure, which may be explained by the larger number of structural modes in the low frequency bandwidth where coupling effects are more significant; that is, due to the multiple panel dimensions now included, 38 structural modes occur below 100 Hz compared to the eight shown in Table 2.2. From the acoustic potential energy plot it can also be seen that, as before, the first longitudinal acoustic mode has been shifted up in frequency, however, in this case the resonance appears at 85 Hz. This may be explained by the significantly increased number of structural modes that are lower in frequency than the first longitudinal acoustic mode, and which may, therefore, depending on their geometric coupling and frequency proximity to the acoustic mode, more significantly increase its effective stiffness and thus natural frequency. It is also clear that, although the fully coupled analysis of the entirely non-rigid enclosure shows a greater number of variations in the acoustic potential energy, the magnitude of the resonances and anti-resonances is either equal to, or lower than for the single non-rigid panel system considered previously.

Figure 2.4b shows the total kinetic energy in all of the panels. From this plot it can be seen that at high frequencies there is little difference between the weakly and fully coupled analyses. This result may be related to the fact that, as noted previously, at higher frequencies the effects of structural acoustic coupling tend to be limited due to low coupling between structural and acoustic modes. At frequencies below around 170 Hz there are some frequencies where the fully coupled analysis indicates that the total structural kinetic energy has increased and some where it has decreased.

The effect of different panel boundary conditions on the response of the structural-acoustic coupled system is investigated in Appendix C and, although the details of the interaction differ, the general form of the results is similar to those for the simply supported panels as discussed herein.

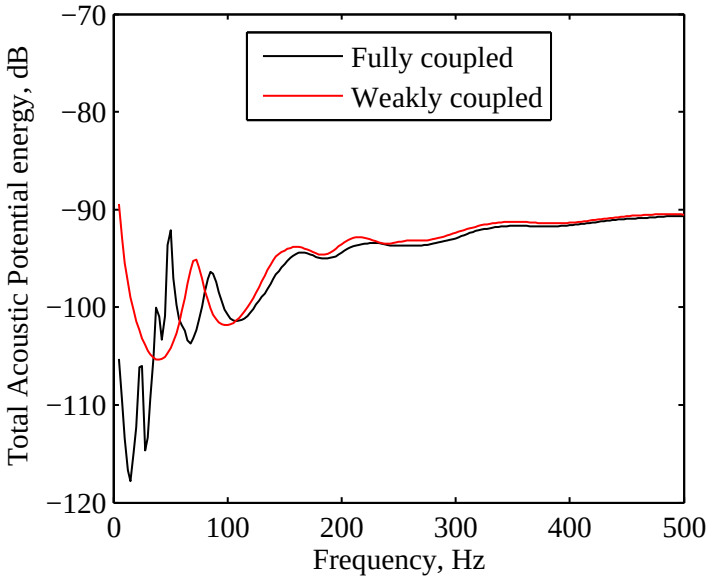

(a) Total acoustic potential energy.

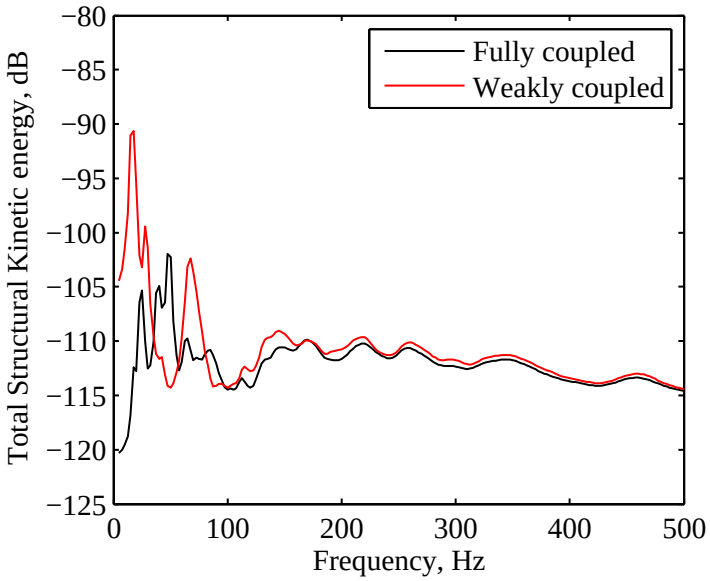

(b) Total structural kinetic energy.

Figure 2.4: Simulated acoustic and structural response of the acoustic enclosure with all non-rigid panels being flexible when excited at different frequencies by a single internal acoustic monopole source with a volume velocity of 10^{-5} m^3s^{-1}.

2.3 Experimental Investigation of the Effects of Structural-Acoustic Coupling in an Enclosure

The effect of structural-acoustic coupling upon the response of a car cabin sized rectangular plywood enclosure has been investigated using an elemental model of the enclosure in the previous section. In order to confirm these results the modelled enclosure has been constructed and is pictured in Figure 2.5. The internal dimensions of the enclosure are $2.4 \times 1.2 \times 1.1$ m and it has been constructed from 12 mm thick plywood. The measurement results presented below are therefore comparable to those presented for the simulated system.

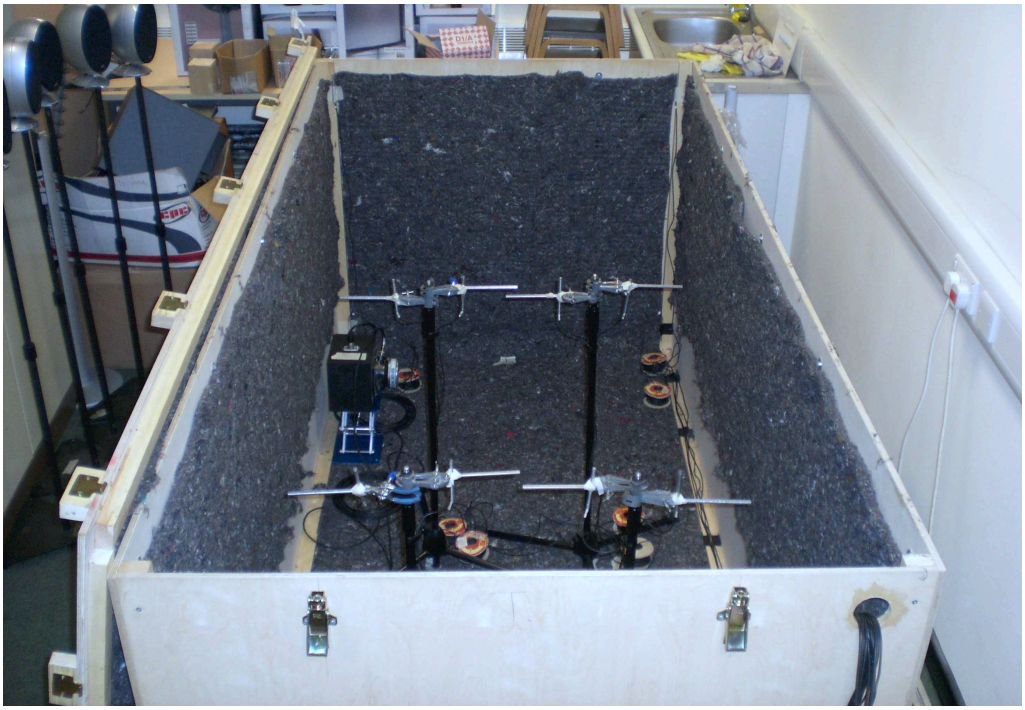

Figure 2.5: Plywood rectangular mock-up of the car cabin with the roof removed and cotton-felt damping in place. The volume velocity source is shown in position $\boldsymbol{x}_{s1}$

The acoustic response of the plywood enclosure was measured and these results will be discussed initially. Secondly the structural response of the panels which form the enclosure was measured in order to confirm that their damping is comparable to that assumed in the simulations. A comparison between the simulation and experimental results will then be presented.

2.3.1 Acoustic Response of the Car Cabin Mock-up

Methodology

The characterisation of the car cabin mock-up has been achieved through the measurement of the frequency response between each of the sixteen microphones – 8 positioned in the corners of the enclosure (see Figure 2.6) and 8 at the hypothetical headrest positions (see Figure 2.5) – and the primary and secondary sources, whose positions are also depicted in Figure 2.6. A

block diagram of the measurement setup is presented in Figure 2.7 and the equipment used is detailed in Appendix D. For the measurement of the acoustic transfer impedances in the enclosure a volume velocity source [128] has been used for both the primary and secondary sources. This allows the acoustic transfer impedance between each error sensor and the source positions to be determined. The data has been acquired using the Matlab Data Acquisition Toolbox and the subsequent analysis of the data has also been conducted within Matlab. For each source position measurement the volume velocity source was driven by band-limited white noise with a cut-off frequency of 12 kHz and 250 seconds of data was acquired in order to permit significant averaging. The data was sampled at a frequency of 25.6 kHz and the anti-aliasing filters were set accordingly by the acquisition system.

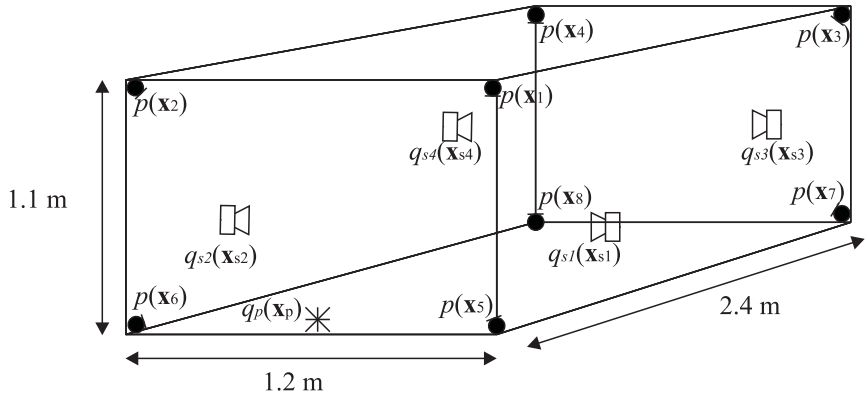

Figure 2.6: Rectangular enclosure showing dimensions and the positions of the sources and sensors.

Using the measured volume velocity and calibrated pressure data the acoustic transfer impedance between each error sensor position and each source position has been calculated as

$$Z(\boldsymbol{x}_{sensor}|\boldsymbol{x}_{source}) = \frac{S_{xy}}{S_{xx}}, \tag{2.29}$$

where S_{xy} is cross spectral density (CSD) between the input volume velocity and the output pressure and S_{xx} is the input power spectral density (PSD).

Results

The acoustic response of the enclosure was first measured within the plywood box with no additional acoustic damping – i.e. bare plywood walls – however, it was found that the acoustic damping was significantly lower than the 10% that has been assumed typical of a car cabin based on [9]. Therefore, the cotton-felt damping, which can be seen in Figure 2.5, was attached to the walls of the enclosure and the response was remeasured. The input (volume velocity source) and output (sensor pressure) PSDs and coherence are presented in Figure 2.8 for the response measured between the secondary source q_{s3} – which corresponds to the rear

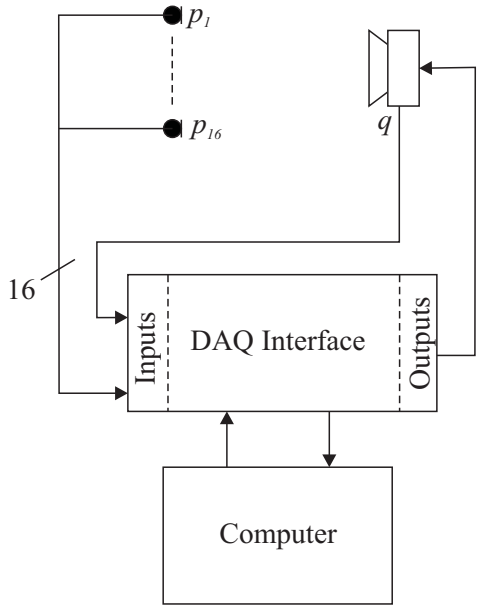

Figure 2.7: Block diagram of the acoustic transfer impedance measurement setup.

left loudspeaker in a car – and error sensor $p(\boldsymbol{x}_1)$ whose positions are depicted in Figure 2.6. From this plot it can be seen that a coherence close to 1 has been achieved across the frequency range of interest for active noise control except at frequencies below around 40 Hz where, from the plot of S_{xx}, it can be seen that the output of the volume velocity source rolls off. This plot highlights the accuracy of the conducted measurements.

Using equation 2.29 the acoustic transfer impedances between each volume velocity source input and each error sensor pressure have been calculated. Figure 2.9 shows the magnitude and phase of the acoustic transfer impedance between source q_{s3} and error sensor $p(\boldsymbol{x}_1)$. This plot clearly shows the modal nature of the enclosure's acoustic response and in comparison to the simulated acoustic transfer impedance for the fully coupled enclosure, which is presented for reference in Figure 2.10, it can be seen that the resonances in the response remain clearly defined up to a much higher frequency and at low frequencies the resonances are less well damped. Calculating the damping of the first longitudinal mode for the acoustic impedance presented in Figure 2.9, which occurs at 76 Hz, using the half-power method indicates that the damping is around 2.2%. This is significantly lower than the frequency independent 10% damping assumed in the simulations, however, it is a significant increase compared to the enclosure without additional damping, which exhibited 0.95% damping of the first acoustic mode. That said, it can be seen from comparing the measurement and simulation results presented in Figures 2.9 and 2.10 respectively that the general characteristics of the response, particularly at frequencies below around 150 Hz, are similar. For example, there is a peak in both responses around 75 Hz, which corresponds to the first longitudinal acoustic mode, and at lower frequencies there are a number of lightly damped resonances that correspond to structural vibrations.

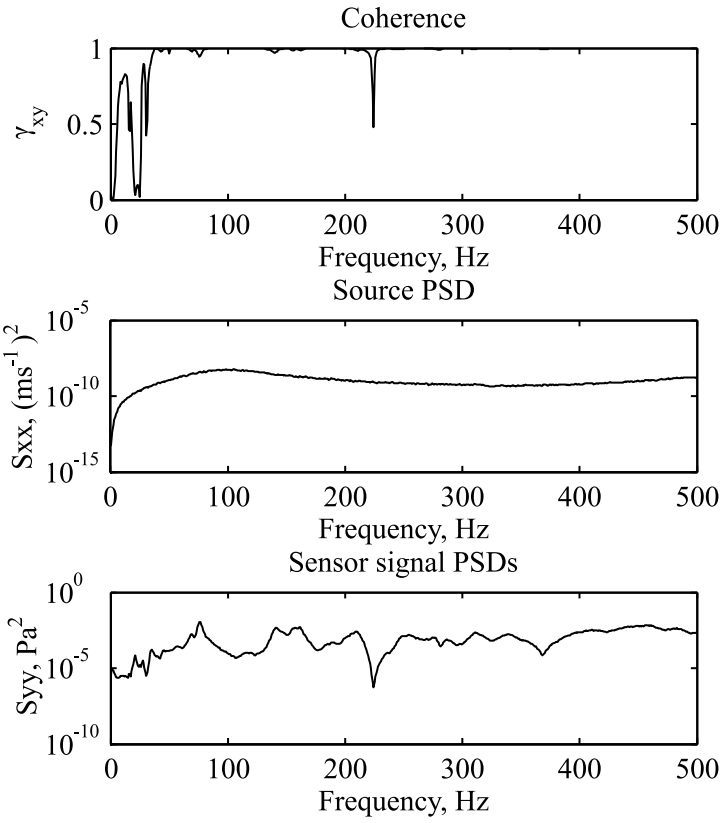

Figure 2.8: Coherence and power spectral densities for acoustic transfer impedance measurement between secondary source q_{s3} and error sensor $p(\boldsymbol{x}_1)$ with cotton-felt damping in the enclosure.

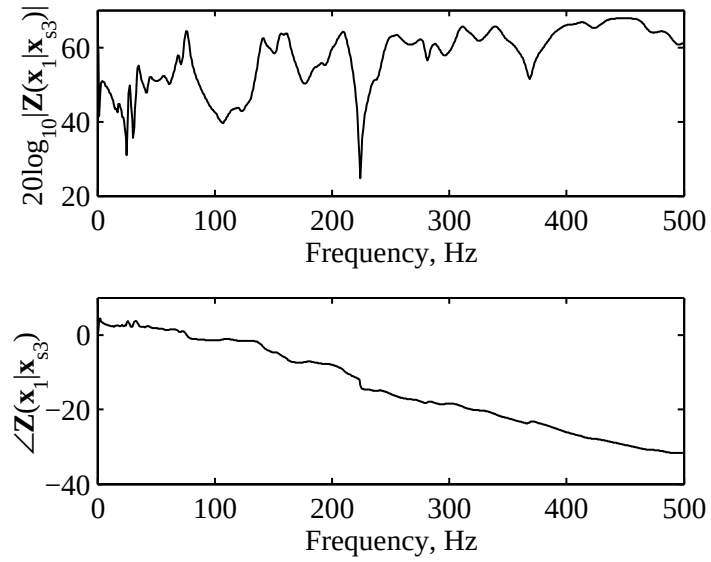

Figure 2.9: Measured acoustic transfer impedance from the secondary source q_{s3} to error sensor $p(\boldsymbol{x}_1)$.

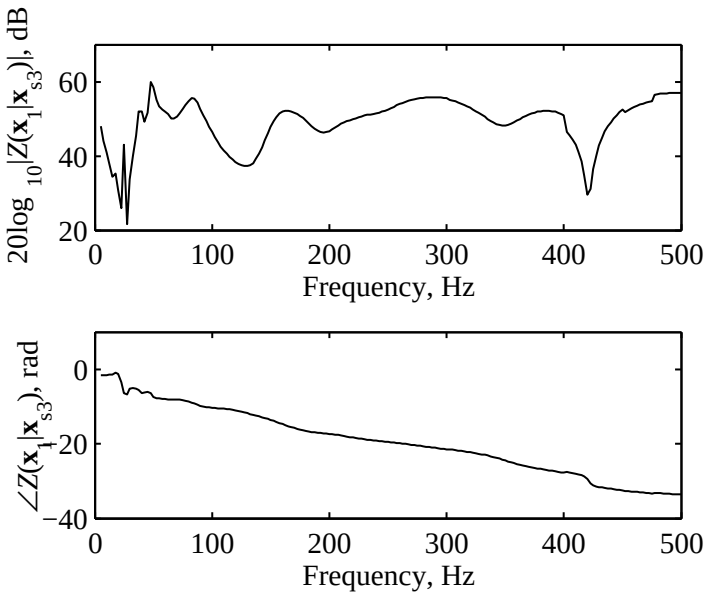

Figure 2.10: Simulated acoustic transfer impedance from the secondary source q_{s3} to error sensor $p(\boldsymbol{x}_1)$ according to the elemental model of structural-acoustic coupling.

Due to the acoustic damping being lower than that assumed in the theoretical simulations an additional set of measurements were conducted with a set of 30 cm deep foam wedges covering the floor of the enclosure, which provides a significant increase in the volume of acoustic damping material. At low frequencies, where the acoustic damping of the enclosure is significantly lower than that assumed in the theoretical investigations, a 1.1% increase in the acoustic damping of the first longitudinal mode was achieved. This small improvement can be related to the general rule of thumb regarding acoustic absorption treatments which states that, in order to provide significant absorption at a specific frequency the material must be comparable to the acoustic wavelength at that frequency. At the first longitudinal mode, 76 Hz in this case, the acoustic wavelength is 4.4 m and thus, based on the rule of thumb, significant absorption would be very challenging to add. From this brief consideration of the acoustic damping within the enclosure it is clear that the assumed frequency independent damping of 10% employed in the model is difficult to achieve at frequencies around the first few acoustic modes in the car cabin mock-up. In an actual car environment a level of damping closer to the assumed 10% may be achieved due to the presence of larger absorbing structures such as the seats and passengers, this will require confirmation in Chapter 6.

Due to the difficulty of positioning sources and sensors within the enclosure when the foam wedges are positioned on the floor, and since they only provide a small increase in the acoustic damping around the modes of interest, the response of the mock-up enclosure with cotton-felt applied to the walls but without the additional foam wedges will be considered from here onwards.

In addition to the absolute properties of the car cabin mock-up enclosure it is interesting to observe how sensitive the acoustic response of the enclosure is to changes in the structural

system. To investigate the sensitivity of the structural-acoustic coupled system the acoustic response has been measured with an additional mass of 12.8 kg placed on the enclosure roof. Figure 2.11 shows the acoustic transfer impedance between source q_{s3} and error sensor $p(\boldsymbol{x}_1)$ both with and without the additional mass. From this plot it can be seen that the additional mass has caused the significant peak at 76 Hz to be increased in frequency by around 1.5 Hz and decreased in amplitude by around 5 dB. This effect can be related to the change in the mode shapes of the roof panel due to the additional mass and the consequential change in their coupling with the acoustic enclosure modes causing the frequency of the acoustic modal resonance to be altered. The change in the structural response of the roof panel as a result of the added mass can also be seen from the additional resonance at 12.5 Hz that has been introduced.

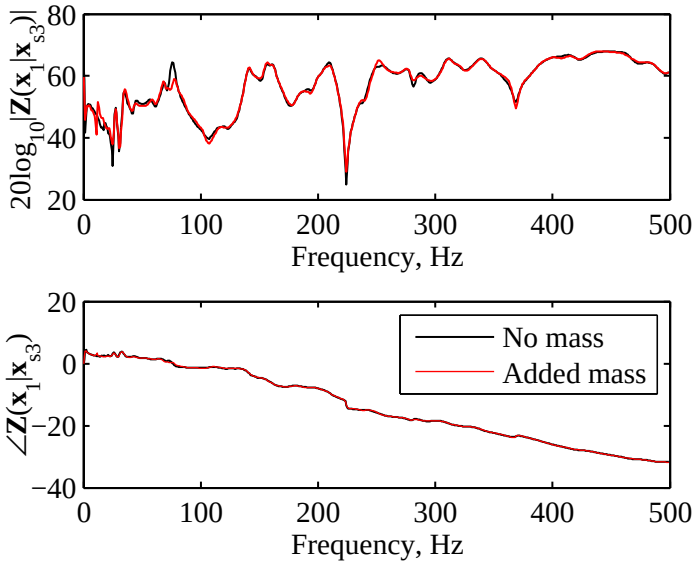

Figure 2.11: Measured acoustic transfer impedance from the secondary source q_{s3} to error sensor $p(\boldsymbol{x}_1)$ with unloaded roof panel (—) and with additional 12.8 kg mass (—).

2.3.2 Structural Response of the Car Cabin Mock-up

Methodology

In addition to investigating the consistency between the measured and simulated acoustic systems it is pertinent to confirm the assumptions made in the theoretical model regarding the characteristics of the structural system. Therefore, the structural mobility has been measured using the equipment detailed in Appendix D. The same setup as depicted in Figure 2.7 has been used for the structural measurements, however, the excitation source has been replaced with a shaker and the error sensors have been replaced by a single accelerometer. The point mobility of both the large side wall and the end wall of the enclosure have been measured. The position of the shaker for the end wall mobility measurement is pictured in Figure 2.12, the

accelerometer was fixed to the inside wall of the enclosure at the position of excitation. These measurements have been conducted both prior and subsequent to the cotton-felt damping being attached to the inside walls of the enclosure.

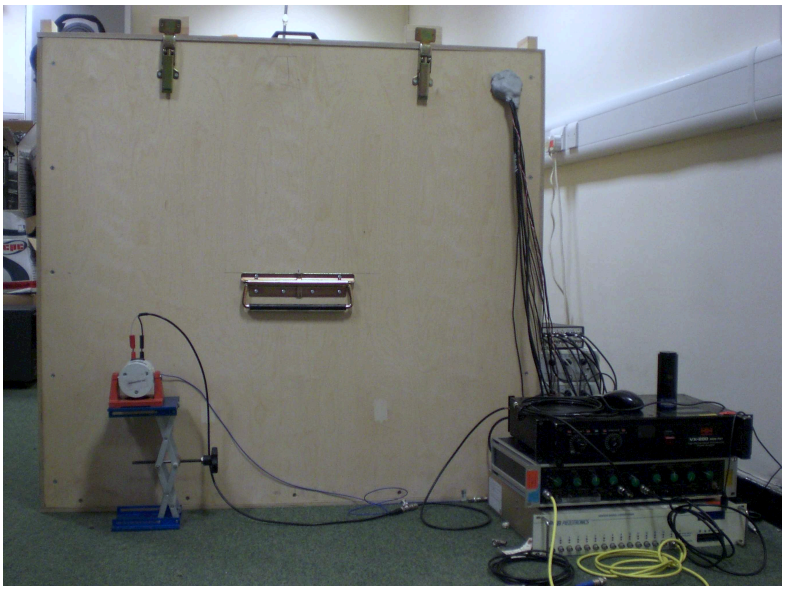

Figure 2.12: Structural response measurement setup.

Results

Figure 2.13 shows the magnitude and phase of the structural mobility, Y – that is, the velocity per unit force – for the large side-wall panel before the application of the cotton-felt damping. From this plot it can be seen that the structural damping is low, and using the half-power estimation method gives a damping ratio of $\zeta_k \simeq 1.25\%$ for the large panel when the average damping of the first nine modes is calculated. For the small end-wall panel the damping ratio is estimated based on the first 10 modes as $\zeta_k \simeq 1.18\%$. This damping ratio is approximately 25% of the value assumed in the simulations.

Repeating the structural measurement of the large side-wall panel once the cotton-felt had been attached resulted in an increase in the average damping of the first nine modes to 2.85%. Additionally the damping in a number of individual modes was increased to around 5%. Since only low frequency, clearly distinct modes were considered in the damping estimate it is likely that the damping factor at higher frequencies will be greater than this estimate. Therefore, this suggests that the 5% structural damping assumed for the simulations employing the fully coupled model is not an unreasonable approximation.

2.3.3 Comparison between Simulated and Measured Enclosure Response

Comparison between the acoustic transfer impedances presented in Figures 2.9 and 2.10 provides an indication that, although the acoustic damping is significantly lower in the car-cabin

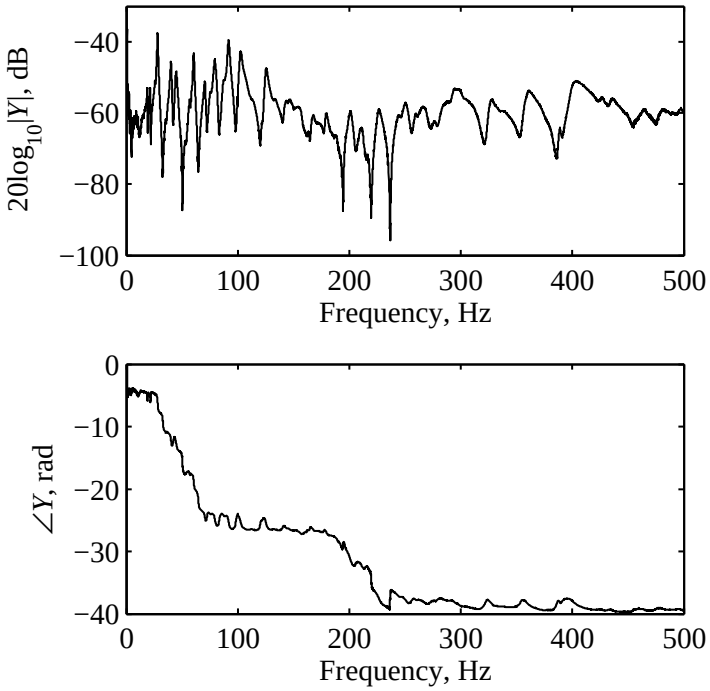

Figure 2.13: Measured point mobility of the large side-wall panel.

mock-up, the simulated and measured responses are similar in character. However, it is also interesting to observe how the acoustic potential energy estimate, J_p, within the simulations and experiments differs. Figure 2.14 shows the estimated acoustic potential energy according to simulations employing the elemental model of structural-acoustic coupling and the measured plywood enclosure; simulated results are shown for both the original acoustic damping of $\zeta_n = 0.1$, which is assumed to be comparable to a car interior according to [9], and a reduced acoustic damping of $\zeta_n = 0.02$, which is closer to that measured in the enclosure. From this plot it can be seen that, at frequencies below the first longitudinal acoustic mode which occurs at around 75 Hz for all three systems, both simulated systems have peaks and nulls that are comparable in magnitude to those observed in the measured system, although the specific frequencies of resonances differ due to inaccuracies in defining the boundary conditions in the model. It can also be seen from Figure 2.14 that the first longitudinal acoustic mode occurs at a similar frequency in the measured and both simulated systems, however, it is clear that the measured system has a much lower damping than the system simulated in the previous sections of this chapter. This lack of damping in the mock-up enclosure can also be seen at higher frequencies. In order to confirm that this difference in the response is a result of the lower level of acoustic damping the response of the enclosure with a frequency independent damping of $\zeta_n = 0.02$ has been calculated and the result is shown by the dashed black line in Figure 2.14. The simulated response with a lower level of acoustic damping shows similar peaks and dips in the acoustic potential energy estimate to those measured in the car cabin mock-up and this simulation thus supports the reliability of the elemental model of structural-acoustic coupling.

The specific frequencies of the resonances in the simulated system, however, do not align with those in the car cabin mock-up and this is due to a number of factors that are not taken into account in the relatively simple model. For example, the exact boundary conditions are unknown and the acoustic and structural damping are both likely to be frequency dependent. The detailed effects of structural-acoustic coupling are notoriously difficult to predict in practical implementations, and it is the qualitative effects which are, in any case, most important here.

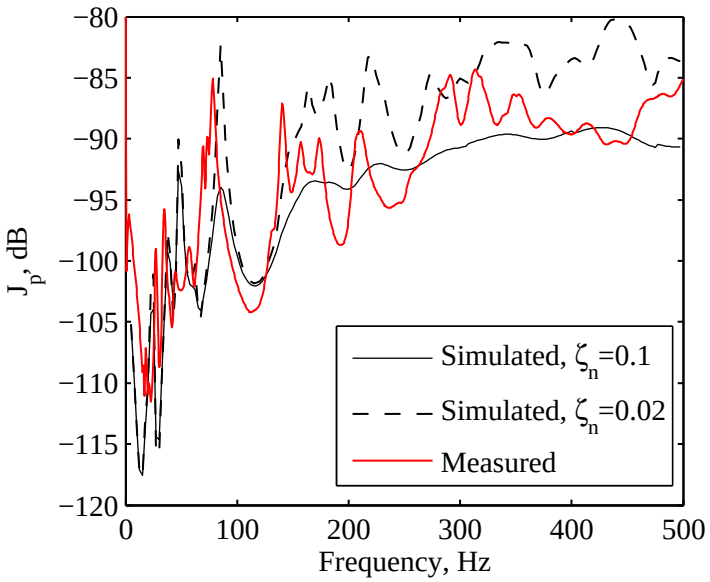

Figure 2.14: Acoustic potential energy estimate, J_p, produced by a single internal acoustic source for the system simulated with the original acoustic damping of $\zeta_n = 0.1$ (—) and a reduced acoustic damping of $\zeta_n = 0.02$ (- -) and the measured response of the car cabin mock-up (—).

2.4 Summary

This chapter has first derived a model of structural-acoustic coupling based on the theory of modal interactions first presented by Dowell and Voss in 1963 [109] and widely employed in the modelling of structural-acoustic systems since. The structural-acoustic model of modal interactions has then been employed to develop an elemental model, which more conveniently represents an entire system and this is presented in Appendix A. The elemental model of structural-acoustic coupling more easily allows multiple non-rigid surfaces to be modelled, which has largely been overlooked in the theoretical investigations presented in the literature, which tend to consider a single non-rigid wall or panel. The elemental model of a structural-acoustic system has been employed to simulate the response of a non-rigid car cabin sized enclosure constructed from plywood and the effects of structural-acoustic coupling on the system response are investigated.

Using the simulations it has been shown that the effects of structural-acoustic coupling are

most significant at low frequencies where the spatial variation in the structural mode shapes is lower, as this results in a high magnitude of geometric coupling between the acoustic and structural mode shape functions. However, it has also been shown that the magnitude of the variations between a weakly and fully coupled analysis are also dependent upon the relative spacing of the resonant frequencies of the acoustic and structural modes and this means that a large geometric coupling coefficient does not necessarily indicate a high level of coupling.

The effect of coupling between acoustic and structural modes has been observed through the presented simulations and it has been shown that if coupling is only significant between a single acoustic and structural mode then the resulting effect on the response is to shift the resonant frequencies of the two modes apart. This effect can be explained by considering whether one mode excites the other in its mass controlled region – i.e. above resonance – or in its stiffness controlled region – i.e. below resonance. For example, it has been shown that if mode *a* excites mode *b* in its mass controlled region the effective mass of mode *b* will be increased and, therefore, its resonance frequency will decrease. However, at the same time mode *b* will be exciting mode *a* in it stiffness controlled region which will increase its effective stiffness and thus increase the natural frequency of mode *a*. As the number of interacting modes increases, which occurs as the number of non-rigid walls is increased, it becomes more difficult to relate resonance frequency shifts to particular modal interactions.

In addition to shifting the resonant frequencies of structural and acoustic modes it has also been shown in Appendix B that there is a corresponding shift in the pressure minima within the enclosure. Specifically, the nodal line of a mode occurs at the same position but at a different frequency due to the change in the resonant frequency through coupling. When a coupled enclosure mode is increased in frequency the pressure minima move away from the non-rigid structure as if the enclosure were effectively decreased in size, whereas for a decrease in the resonant frequency the pressure minima move toward the non-rigid structure as if the enclosure were increased in size.

The effect of multiple non-rigid panels has been investigated and, as expected, introducing an increased number of non-rigid panels results in more complex variations between the weakly and fully coupled analyses and, of specific interest, an increasingly significant shift in the apparent frequency of the first longitudinal acoustic mode. For completeness the effect of structural-acoustic coupling upon an enclosure with clamped non-rigid panels has also been simulated and although the specific effects differ to the simply supported case it has been shown that the general, qualitative effects in terms of the bandwidth that is affected and the influence of multiple non-rigid panels are essentially the same as for the simply supported case; these results are presented in Appendix C.

The car cabin sized rectangular plywood enclosure that has been simulated in this chapter has also been constructed and a series of measurements have been conducted to compare its response to that predicted according to the elemental model of structural-acoustic coupling and to provide transfer responses with which to predict the performance of active noise control strategies in the following two chapters. The presented results indicate that the acoustic damping is

significantly lower than the 10% assumed in the simulations; however, on the basis of previous publications that present in-car measurements, the damping assumed in the simulations will be maintained. The suitability of the assumed acoustic damping will be confirmed in Chapter 6. However, to confirm the validity of the elemental model of the structural-acoustic coupled system the response of the enclosure with reduced acoustic damping has also been simulated. Through comparison with the measured response of the car cabin mock-up it has been shown that although specific features are not accurately modelled the general characteristic behaviour is well modelled. The structural response of the car cabin mock-up has also been measured and it has been shown that the level of damping in the final mock-up configuration with cotton felt damping applied to the walls is comparable to the 5% frequency independent damping assumed in the simulations.

Overall, the effects of structural-acoustic coupling are seen to be strongest at low frequencies, where there are significant interactions between the structural and acoustic modes. Although it is very difficult to predict the details of these interactions in an experimental arrangement, the qualitative effects, of increasing the natural frequency of the first longitudinal acoustic mode and generally making the acoustic response more complicated, are clearly seen in both the simulations and mock-up experiments.

Chapter 3

Feedforward Active Noise Control

Acoustic feedforward control, as indicated in Section 1.2, uses a reference signal to drive a filter that creates a secondary signal which is used to drive a secondary source or sources such that the sound level at error sensor positions is minimised. The need for a reference signal means that feedforward active noise control is more suited to certain applications than others. For example, in the road vehicle noise control application it was highlighted in Section 1.2 that feedforward control of engine noise has been more successful than the feedforward control of road noise, due to the ease of obtaining a coherent reference signal directly from the engine. Although a reference signal for feedforward control of road noise can be obtained from a set of accelerometers, this is expensive and therefore unsuitable for mass production. Since the aim of this part of the thesis is to investigate the development of active control solutions that are highly integrable with the standard electronic systems of mass produced vehicles the focus of feedforward control shall be on engine noise control.

For simplicity of implementation and interpretation, the active control strategies considered within this chapter are only for single frequency tonal excitation. The results will therefore only strictly apply to the control of primary sources whose waveform is deterministic and where, therefore, causality constraints need not be considered; for example, engine order noise. If random sources, such as road noise, were to be considered causality is very important [33]. This chapter also concentrates mainly on the acoustic performance of feedforward control systems, rather than the behaviour of the control algorithms. In addition to the causality assumptions, the simulation results presented in this chapter will assume that:

1. a perfect reference signal is available at each frequency; that is, the coherence between the reference and error signals is unity.

2. the secondary sources have a perfectly flat frequency response.

Based on these assumptions the following results will show the best case scenario for each of the control systems investigated.

This chapter presents the investigation of two control arrangements – global and regional control. For each of the investigated control systems the performance will first be presented

through simulations employing the elemental model of structural-acoustic coupling derived in Section 2.1. Subsequently, the performance of the control systems will be *synthesised* using the acoustic transfer impedances measured in the plywood car-cabin mock-up as described in Section 2.3. Prior to conducting the investigation of feedforward control strategies, however, a review of feedforward active noise control in structural-acoustic coupled systems will be presented.

3.1 Active Noise Control in Structural-Acoustic Coupled Systems

The effect of structural-acoustic coupling on active noise control in a car cabin has previously been considered by Mohammad [120]. This work considered the case where a small area ($0.1\ m^2$) of a rectangular car cabin sized enclosure's structure was non-rigid and, therefore, the effects of structural-acoustic coupling were significantly lower than in an actual car. Additionally, as discussed in Section 2.2 there appears to be a possible error in the structural-acoustic model employed by Mohammad.

A more significant amount of work in the field of active noise control in structural-acoustic coupled systems has been presented considering the use of active noise control to minimise the low-frequency propeller noise transmitted through an aircraft fuselage into the cabin [129]. The active control of noise transmission into a rectangular enclosure with a single non-rigid wall or panel using a force actuator as the control source has been thoroughly investigated by Pan *et al*: an analytical study where the energy in the enclosure is minimised is presented in [129], an experimental study of the same problem using error microphones positioned within the enclosure is presented in [130], and an investigation into the effect of the control force actuator position on the non-rigid panel is presented in [131]. The main finding of this body of work is that the control system operates via two distinct mechanisms. Firstly, for a panel controlled resonance, where the interior sound pressure is dominated by the radiation from a panel mode, the acoustic energy in the enclosure is minimised by minimising the amplitude of the panel vibration at the radiating mode [129, 130]. Conversely, for a cavity controlled mode the structural control force is used to alter the panel velocity distribution and specifically adjusts the panel radiation such that the real part of the radiated power is minimised [129]. Although this second control mechanism minimises the sound energy within the enclosure [129], or the pressure level at discrete error sensors [130], it may result in an increase in the amplitude of panel vibration and a corresponding increase in the sound pressure level in the nearfield of the vibrating panel [129, 130].

In the context of active noise control in the car cabin it has been discussed in Section 1.2 that, in terms of integration into the standard vehicle environment, it is ideal if the standard car audio loudspeakers were employed as the control sources. Kim and Brennan investigate the use of both internal acoustic and structural control sources in the active control of sound transmission into a rectangular enclosure with a single non-rigid wall [119]. This work shows through both simulations and experimentation that control using a single structural force actua-

tor allows control of the sound pressure level in the enclosure at resonances where the response is dominated by the panel vibration modes. Conversely, the use of an internal acoustic control source, such as a loudspeaker, facilitates control of the sound pressure level in the enclosure at resonances where the response is dominated by the acoustic enclosure modes. As a result of these observations, Kim and Brennan investigate the combined use of structural and acoustic sources and show that such a configuration is able to more effectively control the transmission of sound into the enclosure since both structurally and acoustically dominated modes are controllable [119].

In comparison to the transmission problem considered by both Pan *et al* [129, 130, 131] and Kim and Brennan [119], where the excitation is an external plane acoustic wave, the noise produced in the car cabin may be a result of both structural and acoustical noise sources (see Section 1.2). Therefore, this will be considered in the context of the feedforward control strategies investigated in the following sections. Additionally, although there are a significant number of publications relating to the development of active noise control strategies for structural-acoustic coupled systems, an area that does not appear to be thoroughly covered is a direct comparison between active noise control in a rigid walled enclosure, as in [33], and active control of sound in an enclosure with structural-acoustic coupling, as in [119], therefore, this will also be considered in the following sections.

3.2 Global Feedforward Control

Global feedforward control aims to minimise the sound pressure level at all points throughout an enclosure and is, therefore, usually expressed as minimising the total acoustic potential energy within the enclosure. The global control of sound fields in rigid walled enclosures has been thoroughly investigated and Nelson and Elliott present a comprehensive review in Chapter 10 of [33]. This review first considers the direct control of the total acoustic potential energy using a single control source and highlights that in order to control a specific acoustic mode the source must not be positioned on a nodal line of that mode; that is, the source will only achieve control if it couples into the mode to be controlled. As the sound field becomes more complex, for example as the frequency is increased or the enclosure geometry becomes more complex, it becomes more difficult for a single source to couple into all modes and achieve control. Therefore, Nelson and Elliott show that by employing multiple control sources, and thus allowing the sources to couple into a higher number of acoustic modes, control up to a higher frequency may be achieved.

As well as investigating the influence of the control source configuration on the global control of enclosed sound fields when the acoustic potential energy is minimised directly, Nelson and Elliott present an investigation of the more practical case of employing discrete error sensors to estimate the acoustic potential energy through the sum of squared error sensor pressures. Using discrete error sensors it is shown that, similarly to the need for control sources to couple into the acoustic modes, the error sensors must be able to *observe* an acoustic mode

to be able to achieve control and to also ensure that the control system does not enhance the acoustic mode. This requires that the sensors are not positioned on nodal lines and, as for the control sources, in order to achieve this for higher frequencies or more complex enclosures, it is necessary to employ multiple error sensors. It is specifically highlighted that in a rectangular enclosure a set of corner error microphones will avoid the nodal lines and, therefore, provide a good estimate of the acoustic potential energy. In a more complex enclosure geometry, such as the car cabin, it is not possible to chose such convenient error sensor positions.

The final key area that is addressed in the review presented by Nelson and Elliott is a discussion of the enclosure characteristics that determine the high frequency limit of global control. It is stated that the limit of global control is generally related to the separation between the acoustic modes and their damping. These two properties can be described by the modal overlap, which quantifies the number of modes that are significantly excited in an enclosure at any single excitation frequency and is defined as the average number of modes whose natural frequencies fall within the bandwidth of any one mode at a given excitation frequency. For an acoustic enclosure the modal overlap increases in proportion to the cube of the excitation frequency for oblique modes and, therefore, rapidly becomes quite large. Although it may be possible for a single secondary source to suppress any dominant mode provided that it can couple with that mode, controlling a single mode may result in other modes being excited, particularly where the modal overlap is high. Therefore, as the modes move closer together it becomes necessary for both the sources and sensors to couple into more modes, which is achieved by increasing the number of transducers. However, since the modal overlap increases rapidly with frequency the number of necessary sources quickly becomes impractical and, therefore, global active control is limited to lower frequencies.

The following simulations of global feedforward control will focus on the areas covered by the review presented by Nelson and Elliott [33] and thus facilitate the comparison between control in a rigid and non-rigid walled enclosure.

3.2.1 Controller Formulation

Global feedforward control aims to minimise either the total acoustic potential energy, which is given according to the elemental model by equation 2.24, or an estimate of the total acoustic potential energy which is given by

$$J_p = \frac{V}{4\rho_0 c_0^2 L_e} \boldsymbol{p}_e^H \boldsymbol{p}_e, \tag{3.1}$$

where L_e is the number of error sensors and $\boldsymbol{p}_e$ is the column vector of acoustic pressures at the error sensors. The global feedforward control strategy employing discrete error sensors is shown in Figure 3.1 for the case where a single secondary source is driven by the reference signal filtered by a filter, W, which is adapted to minimise the defined cost function.

From Figure 3.1 it can be seen that the error sensor pressures result from the summation of

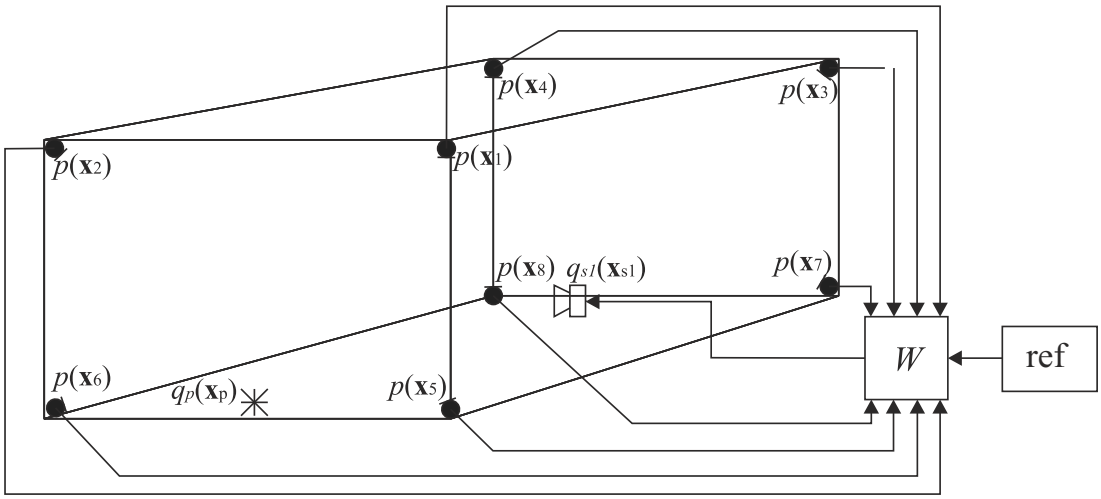

Figure 3.1: Global feedforward control system employing a single secondary source and eight error sensors.

the primary and control, or secondary sources such that $\boldsymbol{p}_e$ can be expressed as

$$\boldsymbol{p}_e = \boldsymbol{p}_p + \boldsymbol{p}_s, \tag{3.2}$$

where $\boldsymbol{p}_p$ and $\boldsymbol{p}_s$ are the vectors of pressures at the error sensors due to the primary and secondary excitations respectively. For an acoustic primary source the error sensor pressures are given by

$$\boldsymbol{p}_e = \boldsymbol{Z}_p q_p + \boldsymbol{Z}_s \boldsymbol{q}_s, \tag{3.3}$$

where $\boldsymbol{Z}_p$ is the $(L_e \times 1)$ vector of acoustic transfer impedances between the error sensors and the primary source, $\boldsymbol{Z}_s$ is the $(L_e \times M)$ matrix of acoustic transfer impedances between the error sensors and the M secondary sources, q_p is the primary source strength, and $\boldsymbol{q}_s$ is the column vector of secondary source strengths. According to the elemental model of structural-acoustic coupling presented in Appendix A, the acoustic transfer impedances are given by

$$\boldsymbol{Z}_s \text{ or } \boldsymbol{Z}_p = [\boldsymbol{I} + \boldsymbol{Z}_A \boldsymbol{Y}_{CS}]^{-1} \boldsymbol{Z}_A, \tag{3.4}$$

which is the pressure per unit volume velocity derived from equation A.19. Alternatively, for a structural primary exciation the vector of error sensor pressures is given by

$$\boldsymbol{p}_e = \boldsymbol{Z}'_p f_p + \boldsymbol{Z}_s \boldsymbol{q}_s, \tag{3.5}$$

where f_p is the force of the primary structural excitation and $\boldsymbol{Z}'_p$ is the transfer response between the primary force excitation and the acoustic error sensors. According to equation A.38 the transfer response between the primary force excitation and the error sensor pressures is given by

$$\boldsymbol{Z}'_p = [\boldsymbol{I} + \boldsymbol{Z}_A \boldsymbol{Y}_{CS}]^{-1} \boldsymbol{Z}_A \boldsymbol{S} \boldsymbol{Y}_S, \tag{3.6}$$

which is the pressure produced per unit force.

The cost function given by the total acoustic potential energy estimate, J_p, or in fact that given by the total acoustic potential energy, E_p, can be expressed in Hermitian quadratic form. For the acoustic potential energy estimate this is achieved by substituting either equation 3.3 for an acoustic primary excitation or 3.5 for a structural primary excitation into equation 3.1 and rearranging. For an acoustic excitation that is

$$J_p = \left[\boldsymbol{q}_s^H \boldsymbol{Z}_s^H \boldsymbol{Z}_s \boldsymbol{q}_s + \boldsymbol{q}_s^H \boldsymbol{Z}_s^H \boldsymbol{Z}_p q_p + q_p^H \boldsymbol{Z}_p^H \boldsymbol{Z}_s \boldsymbol{q}_s + q_p^H \boldsymbol{Z}_p^H \boldsymbol{Z}_p q_p\right], \tag{3.7}$$

where the constant term in equation 3.1 has been neglected as it does not affect the optimal solution. The vector of optimal secondary source strengths is then given by differentiating J_p with respect to the real and imaginary parts of $\boldsymbol{q}_s$, as defined in [33], and equating to zero; this gives

$$\boldsymbol{q}_{s0} = -\left[\boldsymbol{Z}_s^H \boldsymbol{Z}_s\right]^{-1} \boldsymbol{Z}_s^H \boldsymbol{Z}_p q_p. \tag{3.8}$$

For a structural primary source the optimal vector of secondary source strengths is given by equation 3.8, however, $\boldsymbol{Z}_p'$ is substituted for $\boldsymbol{Z}_p$, and for a single primary force excitation f_p is substituted for q_p, or for a distributed force excitation $\boldsymbol{f}_p$ is substituted for q_p. For the case where the total acoustic potential energy is minimised $\boldsymbol{Z}_p$, $\boldsymbol{Z}_s$ and $\boldsymbol{Z}_p'$ become the transfer impedances and responses between the respective sources and all positions in the enclosure.

In a practical scenario it may be necessary to not only minimise the cost function, J_p, but to also impose a constraint on the electrical power required by the control system. This can be achieved by minimising the generalised cost function given by the sum of J_p and a term proportional to the sum of squared source strengths, or control effort [132]:

$$J_{cost} = J_p + \beta \boldsymbol{q}_s^H \boldsymbol{q}_s, \tag{3.9}$$

where β is the real and positive control effort weighting parameter. In this case the vector of optimal secondary source strengths is given by

$$\boldsymbol{q}_{s0} = -\left[\boldsymbol{Z}_s^H \boldsymbol{Z}_s + \beta \boldsymbol{I}\right]^{-1} \boldsymbol{Z}_s^H \boldsymbol{Z}_p q_p. \tag{3.10}$$

The effect of a non-zero control effort weighting parameter is to regularise the optimal solution given by equation 3.10 and thus improve the numerical conditioning of the optimisation problem. Physically, varying the control effort weighting parameter achieves a trade-off between the minimisation of J_p and the required control effort.

3.2.2 Control of an Internal Acoustic Primary source

Simulated Performance

The acoustic enclosure modelled in Chapter 2 will be employed here to investigate the limits on the optimal feedforward controller. The dimensions of this enclosure and the positions

of the secondary sources and corner error microphones were presented in Figure 2.6, but the dimensions are provided in Table 3.1 for convenience. Excitation of the acoustic enclosure by an internal acoustic primary source positioned at co-ordinates $\boldsymbol{x} = [0, L_2/2, 0]$, as shown in Figure 3.1, will be considered first. Using equation 3.8 the vector of optimal secondary source strengths can been calculated such that either the total acoustic potential energy within the enclosure, given by equation 2.24, or the sum of squared error sensor pressures is minimised using either a single secondary source positioned at $\boldsymbol{x}_{s1}$ or all four secondary sources positioned in the standard car audio loudspeaker positions, which are also shown in Figure 2.6. As in Chapter 2, in order to ensure the reliability of the results whilst keeping the computation times to a reasonable length, 6 elements have been used per wavelength and a total of 100 acoustic modes and 90 structural modes per non-rigid panel have been used.

Table 3.1: Enclosure dimensions

Length	L_1	2.4m
Width	L_2	1.2m
Height	L_3	1.1m

Figure 3.2 shows the result of minimising the total acoustic potential energy produced by the internal acoustic primary source shown in Figure 3.1 using a single secondary source positioned at $\boldsymbol{x}_{s1}$ in both the rigid (red) and non-rigid (black) enclosures. From this plot it can be seen that despite the significant differences in the rigid and non-rigid enclosures' uncontrolled responses (solid lines), which are identical to those presented in Figure 2.4a, the responses after control (dashed lines) are almost identical. As discussed above, Nelson and Elliott [33] have related the upper frequency limit of global control in a rigid walled enclosure to the acoustic modal overlap and, therefore, from Figure 3.2 it can be seen that the non-rigid enclosure does not appear to significantly affect this relationship. This may be explained by the limited influence the non-rigid enclosure walls have on the acoustic response at higher frequencies for an acoustic source excitation, which is discussed in Chapter 2. If the primary excitation were structural and structural modes were excited up to a higher frequency, then the limit on global active control may be affected; this will be investigated in Section 3.2.3.

It may be possible to increase the bandwidth of global active control by increasing the number of secondary sources and Figure 3.3 shows the result of minimising the total acoustic potential energy within the enclosure using the four secondary sources positioned at the standard car audio positions shown in Figure 2.6. From this plot it can be seen that the controlled responses of the two enclosures are once again very similar and a significant level of global control has been achieved in both cases up to around 200 Hz. Multiple secondary sources are able to provide increased control by coupling into a larger number of modes compared to a single source. At higher frequencies where a single secondary source may not control the global sound field due to the problem of controlling one mode whilst enhancing another,

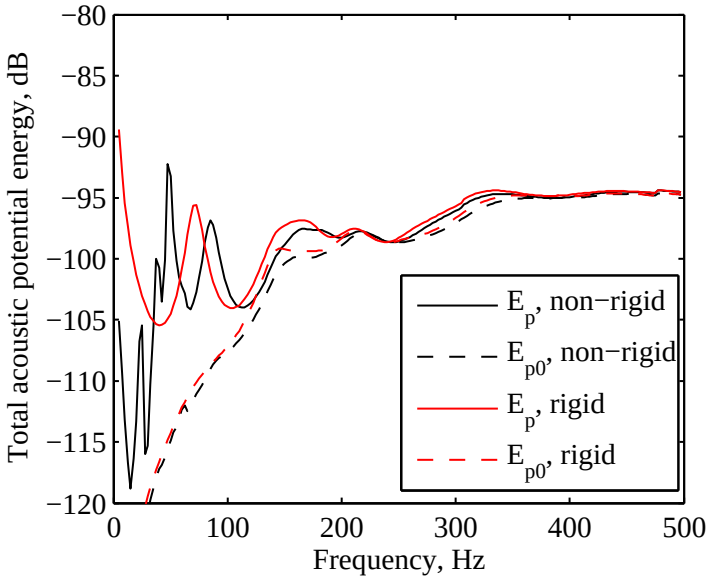

Figure 3.2: Total acoustic potential energy in the rigid (red lines) and non-rigid (black lines) enclosures when driven by a primary acoustic source alone, E_p, (solid lines) and when the total acoustic potential energy has been minimised using a *single secondary source* positioned at $\boldsymbol{x}_{s1}$ (dashed lines) as shown in Figure 2.6, E_{p0}.

it may be possible for a number of secondary sources to reach a compromise. For example, while one source may enhance a mode whilst providing control of another, the introduction of an additional secondary source may be able to limit this enhancement and thus facilitate greater control overall within the restrictions of minimising the total acoustic potential energy. This can be seen at excitation frequencies of around 180 Hz, where 3 acoustic modes have similar natural frequencies and are controllable by four secondary sources, as shown in Figure 3.3, but not by one secondary, as shown in Figure 3.2. The frequency dependence of the modal overlap means that increasing the number of secondary sources by a factor of four only increases the bandwidth of control by less than a factor of two.

It is interesting to note that global control at all frequencies may be achieved by collocating the primary and secondary sources. For example, it is shown in [33] that 20 dB of attenuation is attainable up to a specified frequency for a similar situation to that presented above if the secondary source is within $\lambda/4$ of the primary source. This significant level of control is achievable due to the primary and secondary sources coupling into the modes similarly, which is ensured by the quarter wavelength source spacing experiencing no nodal lines between the two sources. However, in a real noise control application this arrangement is unlikely to be practicable. This is firstly because practical sources, such as loudspeakers, are of finite size and, therefore, cannot be collocated, and more importantly the primary sound field in a vehicle is unlikely to be produced by a single locatable source. This physical limit, however, is important in the generation of personal listening zones using active control techniques and this will be investigated in Chapters 7 and 8.

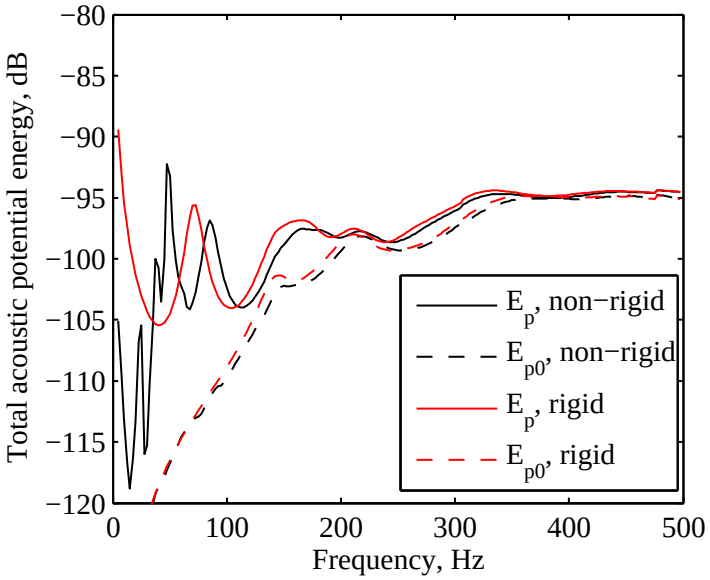

Figure 3.3: Total acoustic potential energy in the rigid (red lines) and non-rigid (black lines) enclosures when driven by a primary acoustic source alone, E_p, (solid lines) and when the total acoustic potential energy has been minimised using the *four secondary sources* (dashed lines) positioned as shown in Figure 2.6, E_{p0}.

On a similar line of discussion it is important to highlight that since a point source has been used for the primary excitation for the results presented herein, due to the relatively close proximity of the primary and secondary sources, particularly for the single secondary source arrangement, control up to a higher frequency may be experienced than if the primary disturbance were a realistic distributed source. Therefore, as stated previously with relation to the assumptions made within this section, the presented results should be considered the best-case scenario.

In practice it is necessary to use a number of error sensors in order to provide, for example, an estimate of the global acoustic potential energy such that the feedforward control system optimises the secondary sources' volume velocities to minimise the pressures at the error sensors. Using equation 3.8 the secondary source strength, or strengths, have been calculated that minimise the sum of the squared pressures at eight error sensors positioned in the corners of the enclosure. The total acoustic potential energy before and after control in the rigid and non-rigid enclosures using a single secondary source positioned at $\boldsymbol{x}_{s1}$ is presented in Figure 3.4. From this plot it can be seen that the controlled responses in the rigid and non-rigid enclosures are, once again, almost identical. Through comparison with Figure 3.2 it can be seen that the level of significant control is almost identical. At frequencies above around 200 Hz the controlled responses based on minimising the estimate of the total acoustic potential energy begin to differ from those based on minimising the total acoustic potential energy and small enhancements in the total acoustic potential energy occur. These enhancements result due to the control system minimising the pressure at a discrete number of locations and this spatial sampling allows the control system to produce enhancements at locations away from the error sensors. From Fig-

ure 3.4 it can be seen that the enhancements are less than 1 dB, which is because the use of the corner error sensors has provided a reasonable estimate of the total acoustic potential energy.

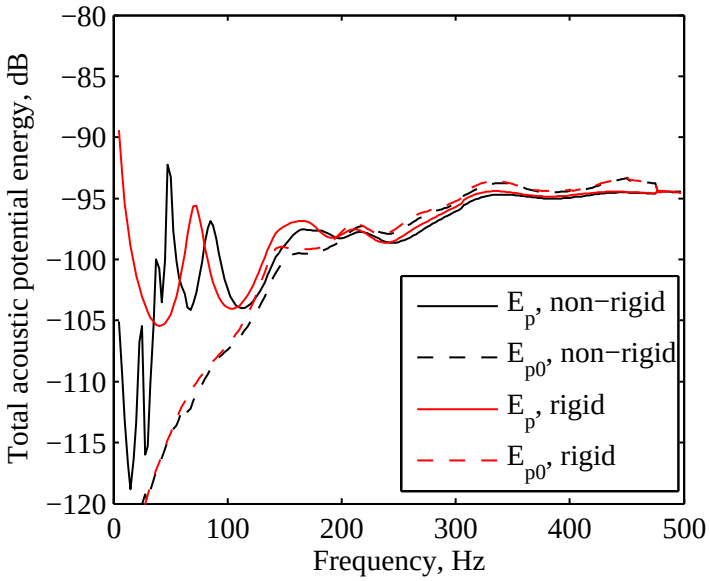

Figure 3.4: Total acoustic potential energy in the rigid (red lines) and non-rigid (black lines) enclosures when driven by a primary acoustic source alone, E_p, (solid lines) and when the sum of the eight squared corner error sensor pressures, shown in Figure 2.6, has been minimised using a *single secondary source* positioned at $\boldsymbol{x}_{s1}$ (dashed line), E_{p0}.

Figure 3.5 shows the change in the total acoustic potential energy in the rigid and non-rigid enclosures when the sum of eight squared corner error sensor pressures is minimised using four secondary sources. From this plot it can be seen that, similarly to when the total acoustic potential energy was minimised directly, the level of control below 200 Hz has been increased compared to the single secondary source case. However, it is also evident that significant enhancements in the total acoustic potential energy have been introduced by the control system at frequencies above 200 Hz. These enhancements are again a result of the spatial sampling imposed through the use of discrete error sensors, but they are more significant here than for the single source control system. This is because the four source control system has greater spatial flexibility. That is, because the four secondary sources couple into more acoustic modes than the single secondary source, they are able to achieve more significant control of the acoustic potential energy estimate, J_p, which is the cost function being minimised, as shown in Figure 3.6. Consequently, at higher frequencies, where the acoustic potential energy estimate is less accurate, while the single secondary source controller becomes largely inactive, the control system employing four secondary sources continues to attempt control and thus produces enhancements in the total acoustic potential energy. In a practical feedforward control system these enhancements could be avoided by limiting the upper frequency of control.

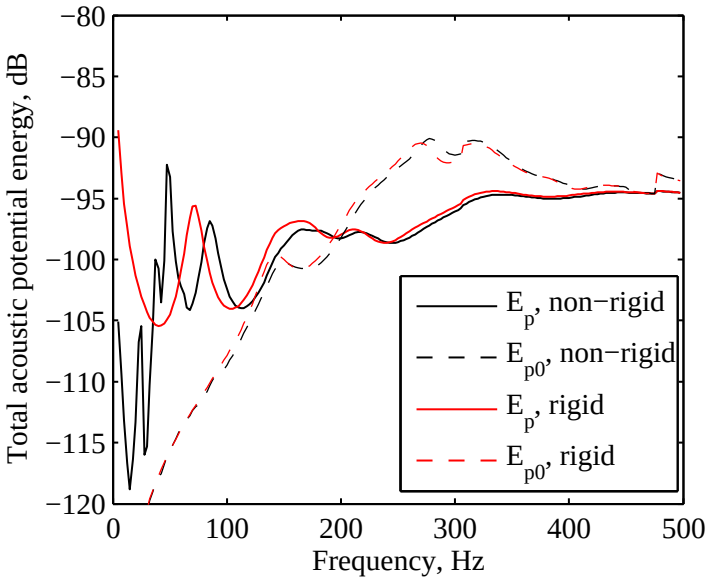

Figure 3.5: Total acoustic potential energy in the rigid (red lines) and non-rigid (black lines) enclosures when driven by a primary acoustic source alone, E_p, (solid lines) and when the sum of the eight squared corner error sensor pressures, shown in Figure 2.6, has been minimised using the *four secondary sources* (dashed line), E_{p0}.

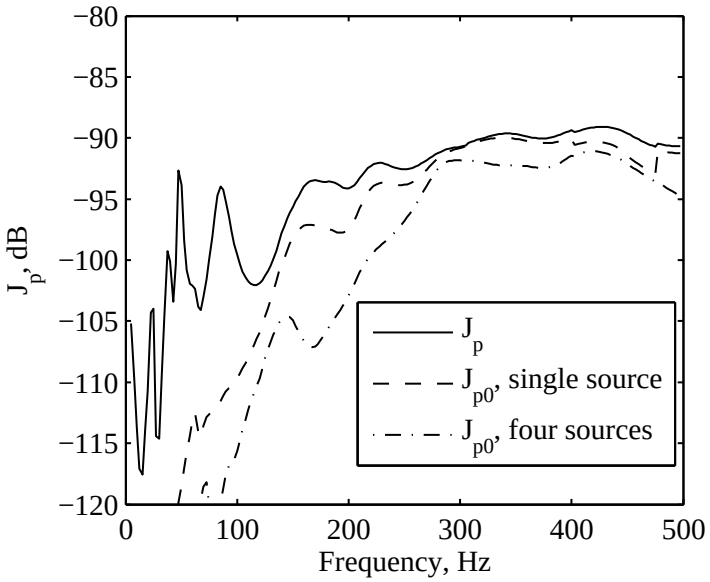

Figure 3.6: The cost function, J_p calculated from the eight corner error sensors in the simulated non-rigid enclosure when driven by a primary source alone, E_p (—) and when the sum of the eight squared corner error sensor pressures has been minimised using a single secondary source (- -) and four secondary sources (— · —), E_{p0}.

Synthesised Performance in the Car Cabin Mock-up

To support the findings of the simulations of global feedforward active noise control in a non-rigid enclosure the performance of the global feedforward control strategy has been synthesised using the acoustic transfer impedances measured between the primary and secondary sources and the sensors in the plywood car cabin mock-up, as detailed in Section 2.3.1. The primary source is, as in the simulated results presented above, an internal acoustic disturbance provided by a volume velocity source positioned as shown in Figure 3.1.

The change in the acoustic potential energy estimate, J_p, due to the action of the secondary volume velocity sources optimised according to the global feedforward control strategy using the eight corner error sensors is presented in Figure 3.7; the plot shows the reduction in J_p achieved by both a single secondary source positioned at $\boldsymbol{x}_{s1}$ and by the four car audio loudspeaker positioned sources, as shown in Figure 2.6. From this plot it can be seen that, for the single secondary source case, a significant reduction in J_p is achieved at frequencies below around 100 Hz, which is consistent with the simulations employing the fully coupled enclosure model. At the first longitudinal mode, 76 Hz in this case, J_p is reduced by approximately 26 dB, however, for the simulations employing the fully coupled enclosure model the reduction in the first longitudinal mode is approximately 18 dB (see Figure 3.6). This difference in reduction can be attributed to the significantly lower acoustic damping in the car-cabin mock-up enclosure compared to that assumed in the model. Repeating the simulations employing damping consistent with the measured system – that is, 1.2% acoustic and 2.29% structural damping – shows a reduction in J_p of 28 dB, which is much closer to the experimental results; these simulation results are presented in Figure 3.8. It is interesting to note that, in both the model simulations and the simulations employing the measured data, the acoustic potential energy estimate at the first longitudinal mode is reduced to around -110 dB. This further supports the observation that the additional reduction in the simulations employing the measured data is due to the lower acoustic damping in the mock-up enclosure.

Figure 3.7 also shows the reduction in J_p when all four sources are used to minimise the sum of the squared corner error sensor pressures. From this data it can be seen that, as for the simulated results, significant reductions are achieved up to around 200 Hz. It can also be seen that reasonable reductions are achieved at some frequencies up to 500 Hz. Although the simulations of global feedforward control using the elemental model indicate some control of J_p at higher frequencies, as shown in Figure 3.6, the level of control shown according to the simulations using measured responses is significantly greater. Through the simulations presented previously it has been shown that although the cost function, J_p, may be reduced at higher frequencies, this does not translate in to a global reduction in acoustic energy and results from the optimised secondary sources producing small zones of quiet around the error sensor positions. For the measurement based simulations this process can be investigated by plotting the acoustic potential energy estimated using all 16 pressure measurement positions – that is, the eight cor-

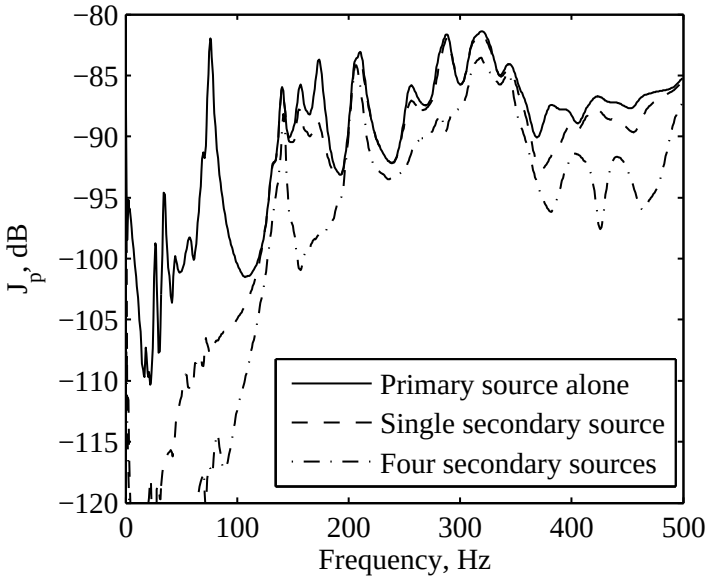

Figure 3.7: The cost function, J_p, calculated from the eight corner measurement positions in the car cabin mock-up before (—) and after global feedforward control using a single secondary volume velocity source positioned at $\boldsymbol{x}_{s1}$ (- -) and four secondary volume velocity sources positioned as shown in Figure 2.6 (- · -) to minimise the sum of the eight squared corner error sensor pressures.

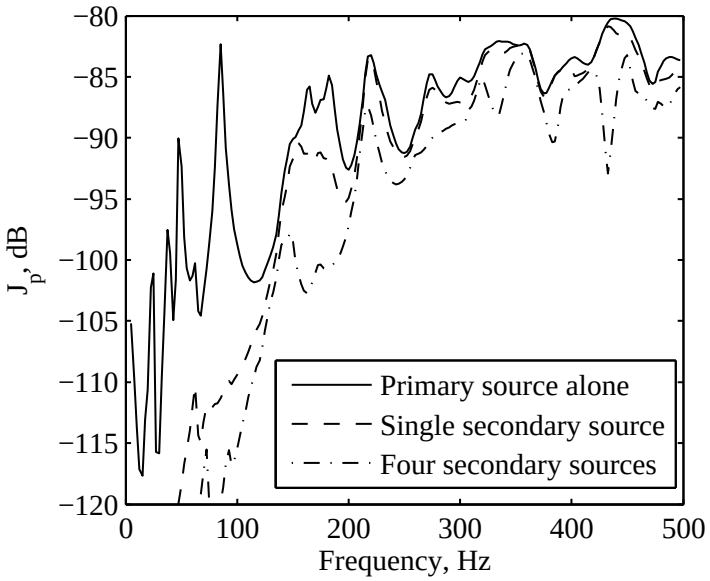

Figure 3.8: The cost function, J_p, calculated from the eight corner error sensors in the simulated non-rigid enclosure before (—) and after global feedforward control using a single secondary volume velocity source positioned at $\boldsymbol{x}_{s1}$ (- -) and four secondary volume velocity sources positioned as shown in Figure 2.6 (- · -) to minimise the sum of the eight squared corner error sensor pressures according to the simulated enclosure with acoustic damping of 1.2% and structural damping of 2.29%, which is consistent with car cabin mock-up.

ner error sensors and the eight headrest sensors – this is presented in Figure 3.9. From this plot it can be seen that the reductions in the estimated acoustic potential energy have been reduced, therefore indicating that the significant reductions observed in Figure 3.7 at frequencies greater than around 200 Hz can be related to the controller producing zones of quiet around the eight corner error sensors. It is interesting to note from Figure 3.9 that despite including the eight headrest sensor positions, only very limited enhancement of the acoustic potential energy estimate has resulted. The significant enhancements in the total acoustic potential energy that were observed in the simulated results shown in Figure 3.5 when four secondary sources were used to minimise the cost function, J_p, have not been reproduced in the synthesised results shown in Figure 3.9 because these synthesised results show an acoustic potential estimated using 16 discrete sensor positions and, therefore, although no significant enhancements are observed in this value, there may be significant enhancements in pressure at positions remote from these sensor locations. However, since it is the pressure level at the headrests that is important, these synthesised results indicate that the effect of spatial sampling introduced by only employing error signals provided by the eight corner sensors has not detrimentally affected the system's performance.

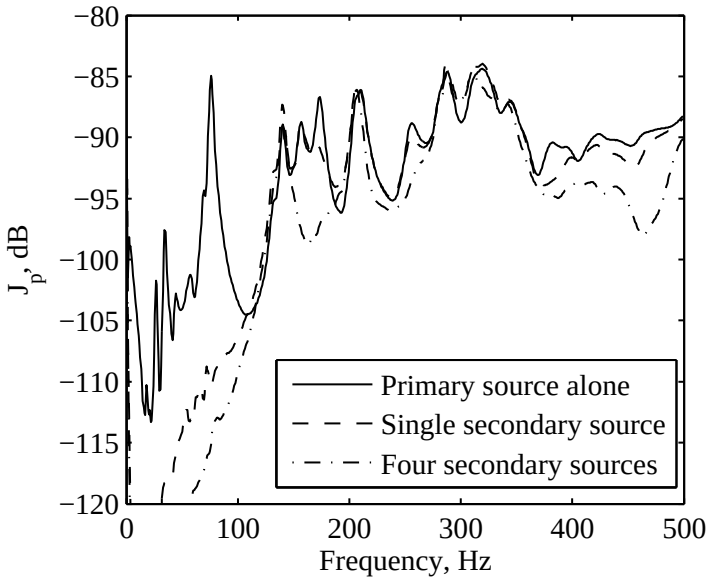

Figure 3.9: Estimated total acoustic potential energy calculated using all 16 measurement positions in the car cabin mock-up before (—) and after global feedforward control using a single secondary volume velocity source positioned at $\boldsymbol{x}_{s1}$ (- -) and four secondary volume velocity sources positioned as shown in Figure 2.6(- · -) to minimise the sum of the eight squared corner error sensor pressures.

3.2.3 Control of a Structural Primary Source

In a car environment the primary noise excitation may be either airborne or structure borne, as discussed in Section 1.2. Therefore, in addition to controlling a direct acoustic excitation of the

structural-acoustic coupled enclosure and car-cabin mock-up, the investigation of controlling a structural primary excitation using the car audio loudspeakers is also of interest. This section will investigate control of a single, primary, point force, f_p, acting on the end wall of the rectangular enclosure, as shown in Figure 3.10, and also the excitation of the end wall by an incident acoustic plane wave, as shown in Figure 3.11. These excitations correspond to an excitation of the bulkhead in a practical, car cabin situation.

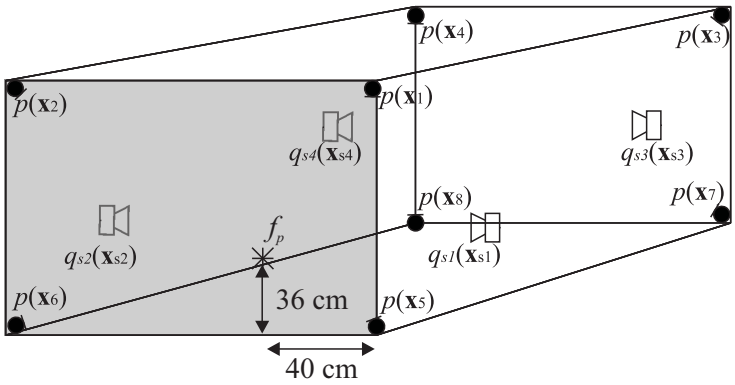

Figure 3.10: Rectangular enclosure showing the standard secondary source positions, corner error sensors and the structural force excitation, indicated by a star, on the grey panel.

Formulation

For the case of a primary structural point force excitation the optimal secondary source strengths are given according to equation 3.8 as

$$\boldsymbol{q}_{s0} = -\left[\boldsymbol{Z}_s^H \boldsymbol{Z}_s\right]^{-1} \boldsymbol{Z}_s^H \boldsymbol{Z}'_p f_p. \tag{3.11}$$

For the case of an incident acoustic plane wave, as shown in Figure 3.11, a distributed structural force occurs and this can be modelled according to the elemental model by the force at the centre of each element. Assuming a time-harmonic pressure fluctuation the sound pressure incident on the outside of the panel at co-ordinate position $\boldsymbol{y} = (y_1, y_2)$ and at a single frequency is given by

$$p(\boldsymbol{y}) = \hat{p}\mathrm{e}^{-\mathrm{j}\left(\mathrm{k}_{y_1}\mathrm{y}_1 + \mathrm{k}_{y_2}\mathrm{y}_2\right)}, \tag{3.12}$$

where $\hat{p}$ is the amplitude of the incident wave and the wavenumbers in the y_1 and y_2 directions are given by

$$k_{y_1} = \frac{\omega}{c_0} \sin\theta \cos\phi \tag{3.13}$$

$$k_{y_2} = \frac{\omega}{c_0} \sin\theta \sin\phi, \tag{3.14}$$

where θ is the angle of incidence in the horizontal plane and ϕ is the angle of incidence in the vertical plane. The force produced by the incident pressure at the i-th element on the panel

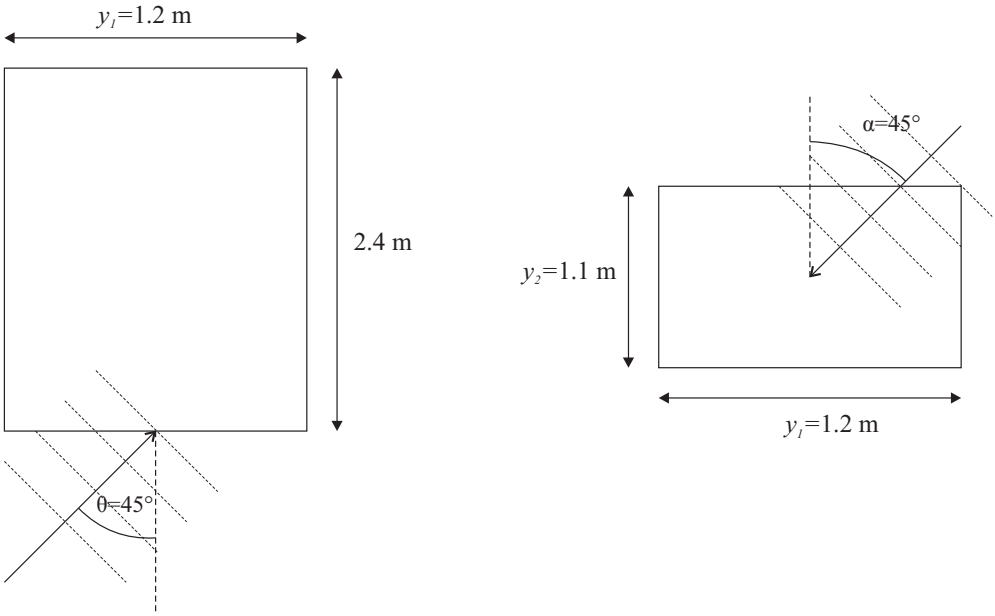

(a) Horizontal plane showing enclosure from above.

(b) Vertical plane showing enclosure from the end.

Figure 3.11: Acoustic plane wave angle of incidence in the horizontal and vertical planes.

surface is then given by

$$f_p(\boldsymbol{y}_i) = 2S_i p(\boldsymbol{y}_i), \tag{3.15}$$

where S_i is the surface area of the i-th element and the multiplication by 2 is due to the doubling in pressure on the surface of the panel due to the assumption of blocked forces on the panel surface [111]. The optimal secondary source strengths can then be calculated as,

$$\boldsymbol{q}_{s0} = -\left[\boldsymbol{Z}_s^H \boldsymbol{Z}_s\right]^{-1} \boldsymbol{Z}_s^H \boldsymbol{Z}_p' \boldsymbol{f}_p. \tag{3.16}$$

Simulated Performance: Point Force

Using equation 3.11 the optimal secondary source strengths have been calculated to minimise the sum of the squared pressures at the eight corner error sensors when the non-rigid enclosure is excited by a primary point force excitation of 5×10^{-2} N acting on the end panel of the rectangular enclosure as shown in Figure 3.10. Figure 3.12 shows the total acoustic potential energy within the enclosure prior to control, E_p, and after control, E_{p0}, using a single secondary source and four secondary sources. From this plot it can be seen that significant reduction in the acoustic potential energy has been achieved at frequencies below around 200 Hz for both the single and multiple secondary source systems. However, in both cases there are two resonances at 65 and 112 Hz that have not been controlled. In comparison to Figures 3.4 and 3.5 it is interesting to observe that, although the upper frequency of control remains similar, the difference in performance between the single and multiple source control systems is more significant at frequencies below 60 Hz. This is a result of the increased spatial complexity

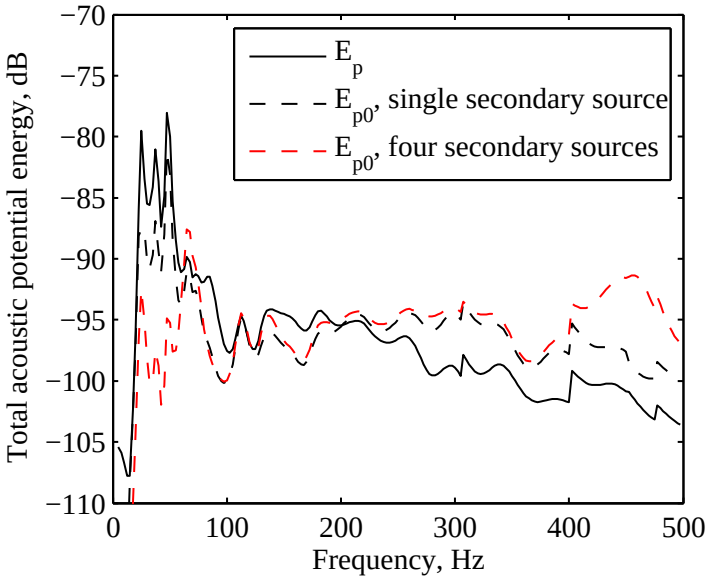

Figure 3.12: Total acoustic potential energy in the simulated non-rigid enclosure when driven by a primary structural point force alone (—) and when the sum of the eight squared corner error sensor pressures, shown in Figure 3.10, has been minimised using a single secondary source (- -) and the four secondary sources (- -).

introduced by the radiating structural modes, which can be observed at low frequencies.

At frequencies higher than around 200 Hz it can be seen from Figure 3.12 that feedforward active control using either a single or four secondary sources results in enhancements in the acoustic potential energy. This is due to the spatial sampling that results from estimating the acoustic potential energy from eight error sensors, as previously observed in Figure 3.5 for an acoustic primary excitation. Figure 3.13 shows the corresponding reduction in the acoustic potential energy estimate, J_p, as a result of controlling the primary field produced by the point force structural excitation using a single secondary source and four secondary sources. From this plot it can be seen that enhancements in J_p do not occur, which indicates that the enhancements in E_p are due to the creation of quiet zones around the error sensors as discussed previously.

Synthesised Performance in the Car Cabin Mock-up: Point Force

In order to support the results presented in Figures 3.12 and 3.13, the performance of the global feedforward control strategy in the car cabin mock-up shown in Figure 2.5 has been synthesised using an electrodynamic shaker to excite the end wall of the mock-up and a primary force excitation of 1×10^{-3} N. Figure 3.14 shows the acoustic potential energy estimated using the 16 microphones positioned in the car cabin mock-up. Comparing this plot to the simulation results presented in Figure 3.12 shows that the level and bandwidth of control are comparable, although the specific details of the responses are changed.

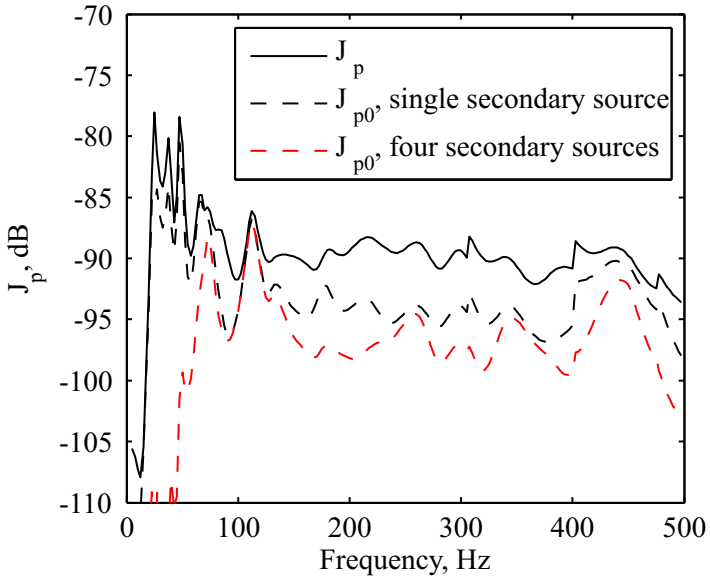

Figure 3.13: The cost function, J_p, calculated from the eight corner error sensors in the simulated non-rigid enclosure when driven by a primary structural point force alone (—) and when the sum of the eight squared corner error sensor pressures has been minimised using a single secondary source (- -) and four secondary sources (- -).

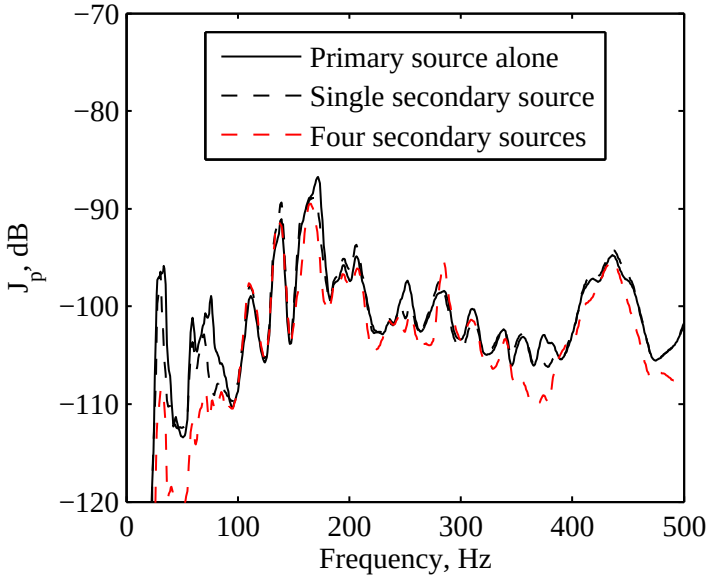

Figure 3.14: The cost function, J_p, calculated from the eight corner measurement positions in the car cabin mock-up when driven by a primary structural force alone (—) and when the sum of the eight squared corner error sensor pressures has been minimised using a single secondary volume velocity source positioned at $\boldsymbol{x}_{s1}$ (- -) and four secondary volume velocity sources positioned as shown in Figure 2.6 (- -) .

Simulated Performance: Plane Wave

Using equation 3.16 the optimal secondary source strengths have been calculated to minimise the sum of the squared pressures at the eight corner error sensors when the non-rigid enclosure is excited by an acoustic plane wave with an amplitude of 1 Pa incident at an angle of $\theta = 45^\circ$ and $\phi = 45^\circ$ on the end panel of the rectangular enclosure as shown in Figure 3.11. The total acoustic potential energy that results from minimising the cost function, J_p, is presented in Figure 3.15 for control using a single secondary source and four secondary sources. From this plot it can be seen that the upper frequency at which reduction in the total acoustic potential energy is achieved is around 100 Hz. In this case it can be seen that the first longitudinal acoustic mode has been excited and using the four source system there are no resonances below 100 Hz that are uncontrollable. There is also less enhancement which, as will be shown below, is because the internal sound field is less complicated and fewer higher order modes are excited.

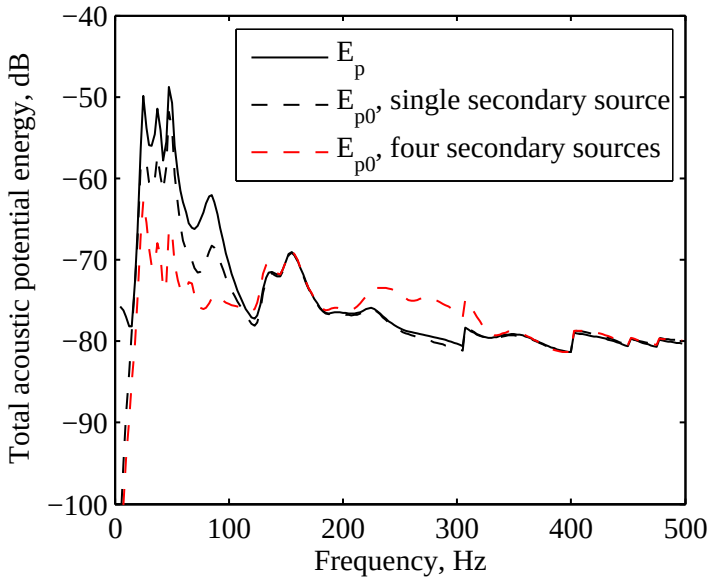

Figure 3.15: Total acoustic potential energy in the simulated non-rigid enclosure when driven by a primary acoustic plane wave excitation of the end panel alone (—) and when the sum of the eight squared corner error sensor pressures, shown in Figure 3.10, has been minimised using a single secondary source (- -) and the four secondary sources (- -).

3.2.4 Comparison of Primary Excitation Sources

Further explanation of the differences between the control achievable for the two different structural primary excitations presented in Figures 3.12 and 3.15 and that achievable for an internal acoustic primary excitation presented in Figures 3.4 and 3.5, can be gained by plotting the level of acoustic potential energy in each acoustic mode for the three different primary excitations. Figure 3.16 shows the normalised acoustic potential energy in the first ten acoustic modes at frequencies up to 300 Hz for the internal acoustic, external acoustic plane wave and

point force structural excitations. From Figure 3.16a it can be seen that the internal acoustic source predominantly excites either the compliant, $(0,0,0)$ acoustic mode or the first longitudinal, $(1,0,0)$ acoustic mode at frequencies below around 100 Hz. This relates to the significant levels of control that are achievable with either a single or four secondary sources (see Figures 3.4 and 3.5 respectively). At higher frequencies it can be seen from Figure 3.16a that an increasing number of acoustic modes are significantly excited and, consequently, control with a finite number of sources becomes unfeasible.

Figure 3.16b shows the acoustic potential energy in each acoustic mode for a primary point force excitation. From this plot it can be seen that, similarly to the internal acoustic excitation, at frequencies below around 100 Hz the $(0,0,0)$ and $(1,0,0)$ acoustic modes are excited most significantly; however, for the point force excitation it can be seen that a number of the higher-order acoustic modes are also significantly excited over narrower bandwidths. For example, at around 65 Hz eight of the ten presented acoustic modes show a significant level of excitation. This is due to structural modes radiating into the enclosure and explains the limited level of control that is achievable using a single secondary source, as shown in Figure 3.12. At higher frequencies the level of excitation of the acoustic modes is not as significant as for the internal acoustic source. This can be related to the reduction in the kinetic energy of the panel at higher frequencies, as observed in Section 2.2, and the consequent low level of acoustic mode excitation. However, the number of significantly excited modes is comparable to that for the internal acoustic excitation and, therefore, control remains unachievable.

The final subplot in Figure 3.16 shows the normalised acoustic potential energy for the first 10 acoustic modes for an external acoustic plane wave excitation. From this plot it can be seen that although the compliant and first longitudinal modes remain significantly excited at frequencies below 100 Hz, as for the other two excitation sources, the majority of the acoustic modes are not significantly excited. This corresponds to the results presented in Figure 3.15 where it can be seen that the acoustic potential energy due to the primary external acoustic plane wave is dominated by the response below 100 Hz and except for the peak at around 150 Hz, which can also be observed in Figure 3.16c, there are no significant peaks in the response at higher frequencies. Figure 3.16c would suggest that control should be achievable since there do not appear to be multiple significantly excited modes, however, extending the colormap range allows a significant number of low level modes to be observed at higher frequencies. Despite only being weakly excited these overlapping modes remain uncontrollable and, therefore, the acoustic control is still limited to low frequencies for the external primary plane wave.

3.3 Regional Feedforward Control

It has been shown in the previous section that significant levels of global control are largely limited to frequencies around the first longitudinal acoustic mode for the predefined secondary source positions. In a car environment global control of the sound field may be an unnecessary

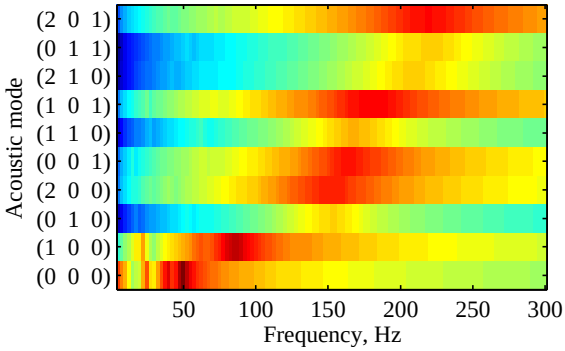

(a) Internal acoustic excitation.

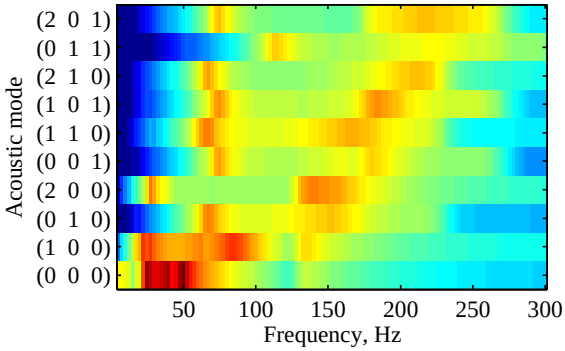

(b) Point force structural excitation

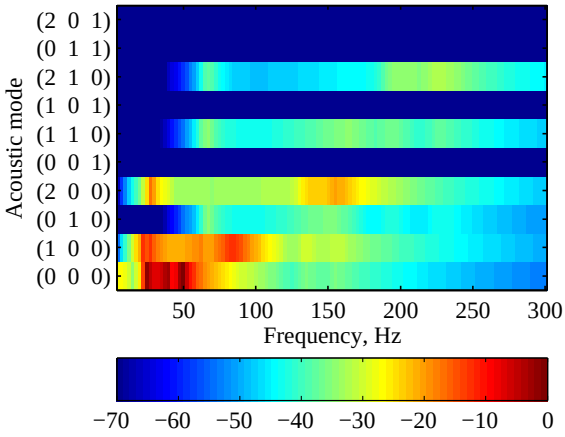

(c) External acoustic plane wave excitation

Figure 3.16: The normalised acoustic potential energy in the enclosure for each acoustic mode for three different excitation sources.

target since the positions of the driver and passengers within the car are largely fixed. Therefore, a more practically optimised system may be to minimise the acoustic potential energy within a specified region around the head positions of the car's occupants. Figure 3.17 shows the geometry of a regional control system indicating both the positions of the error sensors and two rectangular regions within which the acoustic potential energy will be evaluated to determine the performance of the systems. The error sensor positions have been defined to correspond approximately with the positions of the car seat headrests and the standard car audio loudspeaker positions, presented in Figure 2.6, will be used for compatible comparison to the global control simulations. As the effects of different primary source excitations have already been considered in the context of global feedforward control, the regional feedforward control strategy will only be investigated for an acoustic primary source excitation for conciseness.

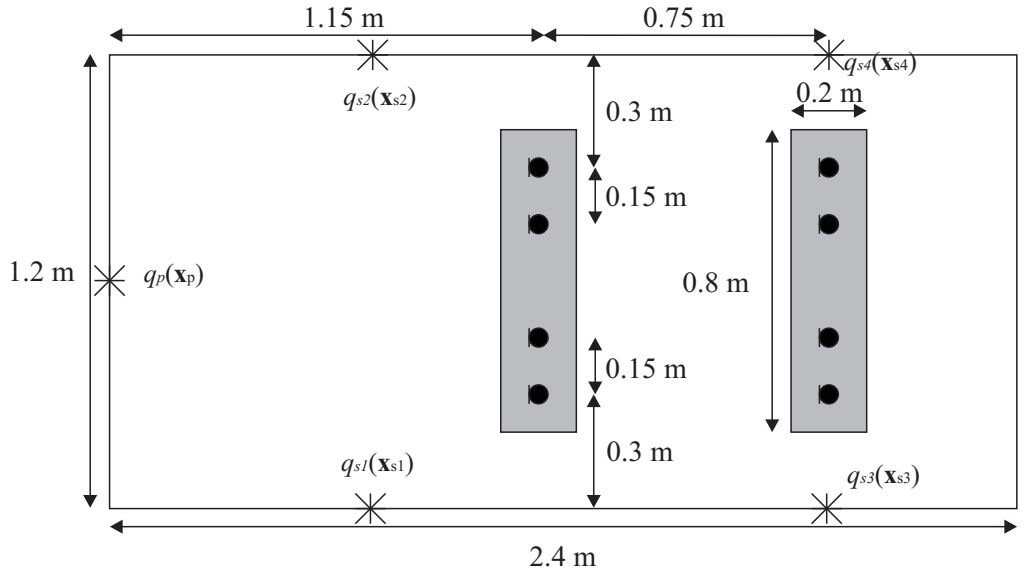

Figure 3.17: Regional control geometry viewed from above showing the positions of the four front and four rear error sensors as well as the rectangular regions within which the potential energy, E_R, is evaluated – the height of all error sensors is 0.9 m and the rectangular control zone is defined in the vertical direction between 0.8 and 1.0 m. The positions of the control sources are also shown.

3.3.1 Controller Formulation

The aim of a regional control system is to reduce the pressure within a specified region, therefore, the cost function, J_R, will be defined as the sum of the squared error sensor pressures within the control regions:

$$J_R = \boldsymbol{p}_e^H \boldsymbol{p}_e. \tag{3.17}$$

Following the formulation presented in Section 3.2.1 for the global feedforward control strategy, the vector of optimum source strengths is given as in equation 3.8 by

$$\boldsymbol{q}_{s0} = -\left[\boldsymbol{Z}_s^H \boldsymbol{Z}_s\right]^{-1} \boldsymbol{Z}_s^H \boldsymbol{Z}_p q_p. \tag{3.18}$$

A potential issue with the regional feedforward control strategy is that, due to the position of the error sensors away from the corners of the enclosure they may not couple in to certain acoustic modes and this will result in enhancements in the controlled acoustic potential energy. This problem can be avoided by increasing the number of error sensors to provide coupling with more acoustic modes, however, this may reduce the regional property of the control system and would also increase the cost and weight of a practical system. An alternative method of limiting enhancements that may occur within the operating bandwidth of the control system is to employ a control effort weighting parameter, β, in the cost function, as discussed in Section 3.2.1, which modifies the optimum solution from equation 3.18 to:

$$\boldsymbol{q}_{s0} = -\left[\boldsymbol{Z}_s^H \boldsymbol{Z}_s + \beta \boldsymbol{I}\right]^{-1} \boldsymbol{Z}_s^H \boldsymbol{Z}_p q_p. \tag{3.19}$$

The effect of employing the control effort weighting parameter is to limit the secondary source strengths and thus avoid significant enhancements, however, this will also restrict the achievable control.

3.3.2 Control of an Internal Acoustic Primary Source

Simulated Performance

The investigated regional control system aims to minimise the sum of the squared pressures at the eight error sensors depicted in Figure 3.17. Figure 3.18 shows the sum of the squared pressures, J_R, at the eight error sensors within the two control regions both prior to control and once the source strengths of the four loudspeakers have been optimised according to equation 3.19 with a regularisation parameter of $\beta = 10^5$, which has been chosen to ensure that the regional acoustic potential energy, E_R, is not enhanced at any frequency. From this plot it can be seen that significant levels of control are achieved at the error sensors up to 400 Hz. In a practical scenario it is also important to consider the effect of control over a larger region than at the eight discrete error sensors, due to movement of the car occupants and variable seating positions. Therefore, Figure 3.19 shows the total acoustic potential energy within the two control regions before and after control. From this plot it can be seen that a significant level of control is achieved up to around 340 Hz and it is also clear that at around 220 Hz there is an uncontrollable bandwidth. Without the regularisation parameter, β, the regional acoustic potential energy is enhanced over this bandwidth indicating that this uncontrollability is due to a single, or multiple acoustic modes being unobservable by the eight error sensors.

The results in Figure 3.19 show that regional feedforward control offers the potential of increasing the controllable bandwidth compared to global feedforward control by almost one octave – that is, from around 180 to 320 Hz. Additionally, it is important to note in terms of a realisable system that the increased performance of the regional system employing eight error sensors has been achieved with no increase in the number of error sensors or secondary

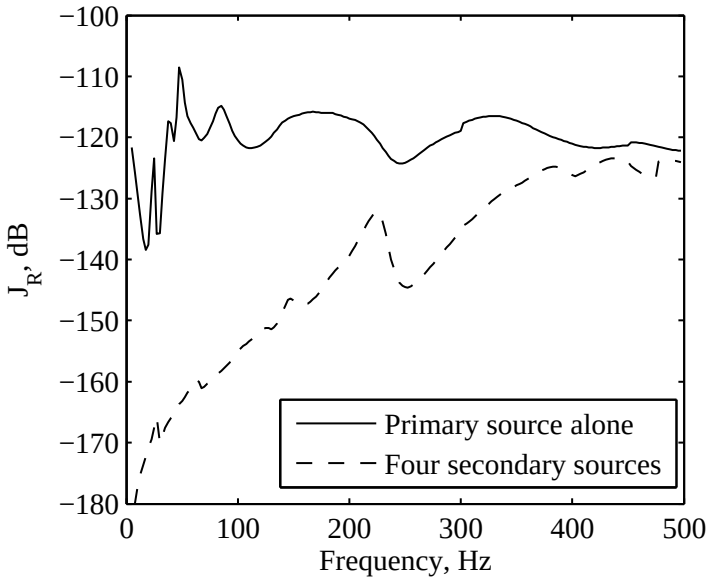

Figure 3.18: The cost function, J_R, calculated from the eight headrest error sensors in the simulated non-rigid enclosure before (—) and after regional feedforward control using four secondary volume velocity sources positioned as shown in Figure 2.6 to minimise the sum of the eight squared headrest error sensor pressures with $\beta = 10^5$ (- -).

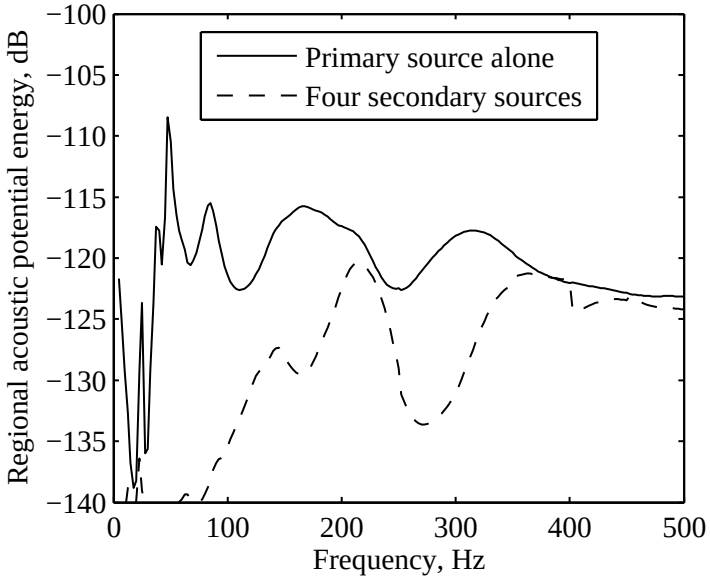

Figure 3.19: The acoustic potential energy *within the control regions*, E_R, evaluated in the simulated non-rigid enclosure when driven by a primary source alone (—) and when J_R has been minimised using the four secondary sources shown in Figure 2.6 with a control effort weighting parameter of $\beta = 10^5$ (- -).

sources, and no alteration to the standard car audio loudspeaker positions.

In addition to the reduction in regional acoustic potential energy it is also interesting to observe how the global potential energy within the enclosure is affected by the action of the regional control system employing the eight error sensors presented in Figure 3.17; this is shown in Figure 3.20. From this plot it can be seen, somewhat surprisingly, that similar levels of global control have been achieved by the regional system as have been achieved for the global control system with eight error sensors shown in Figure 3.5. This may, in retrospect, be expected since identical secondary source positions are employed and the error sensor positions used in the regional control system provide similar coupling to the first longitudinal acoustic mode to that which is achieved by the eight corner error sensors employed in the global system. It is, however, notable that the enhancements at higher frequencies are not greater for the regional control system than for the global system. However, this is due to the use of the regularisation parameter, β, to limit the control effort and, therefore, the enhancements due to unobservable modes.

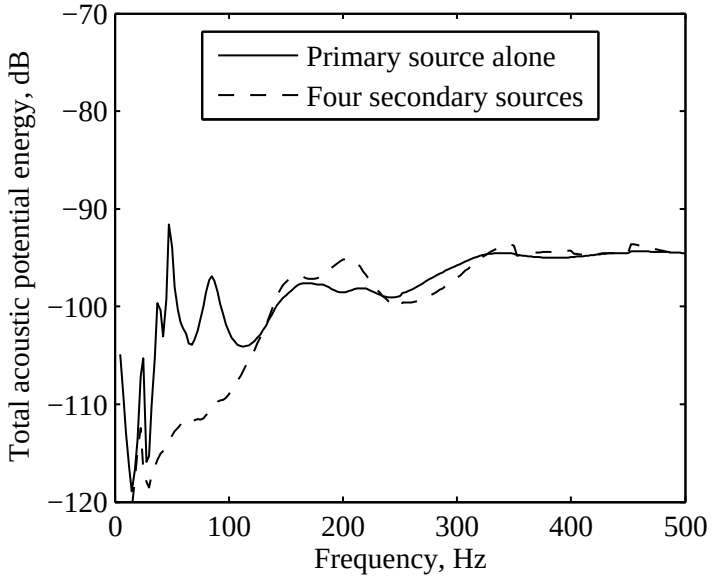

Figure 3.20: The *total* acoustic potential energy within the simulated non-rigid enclosure when driven by a primary source alone (—) and when J_R has been minimised using the four secondary sources shown in Figure 2.6 with a control effort weighting parameter of $\beta = 10^5$ (- -).

Synthesised Performance in the Car Cabin Mock-up

To support the findings of the simulations presented above, the performance of the regional feedforward control strategy has been synthesised using the acoustic transfer impedances measured between the primary and secondary acoustic sources and the sensors in the plywood car cabin mock-up, as detailed in Section 2.3.1.

Figure 3.21 shows J_R, the sum of squared pressures in the control regions as given by

equation 3.17 in the car cabin mock-up before control and when J_R has been minimised using the four secondary sources and a control effort weighting parameter of $\beta = 10^5$. From this plot it can be seen that using the four car audio loudspeaker positioned sources to minimise J_R achieves significant reductions up to around 450 Hz, which is comparable to that presented in the simulations above. Comparing the simulation results presented in Figure 3.18 to those presented in Figure 3.21 it can be seen that the bandwidth and level of control is comparable between the simulated and synthesised result, however, it can be seen that in the synthesised results presented in Figure 3.21 there are modes at around 140 and 210 Hz that are difficult to control.

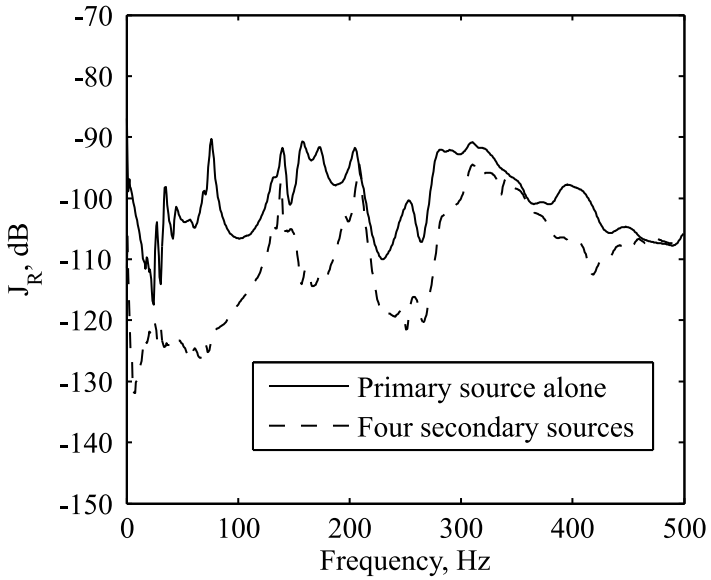

Figure 3.21: The cost function, J_R, calculated from the eight headrest measurement positions in the car cabin mock-up before (—) and after regional feedforward control using four secondary volume velocity sources positioned as shown in Figure 2.6 to minimise the sum of the eight squared headrest error sensor pressures (- -) with a control effort weighting parameter of $\beta = 10^5$.

To determine the effect of the synthesised regional feedforward control on the global sound field within the car cabin mock-up, Figure 3.22 shows the acoustic potential energy estimated using the eight corner error sensors, as in the global feedforward control system. From this plot it can be seen that global control is still maintained up to around 100 Hz where the acoustic response is dominated by the first longitudinal mode, however, at higher frequencies there are a number of enhancements in the acoustic potential energy that are comparable in magnitude to those predicted in the simulation results presented in Figure 3.20.

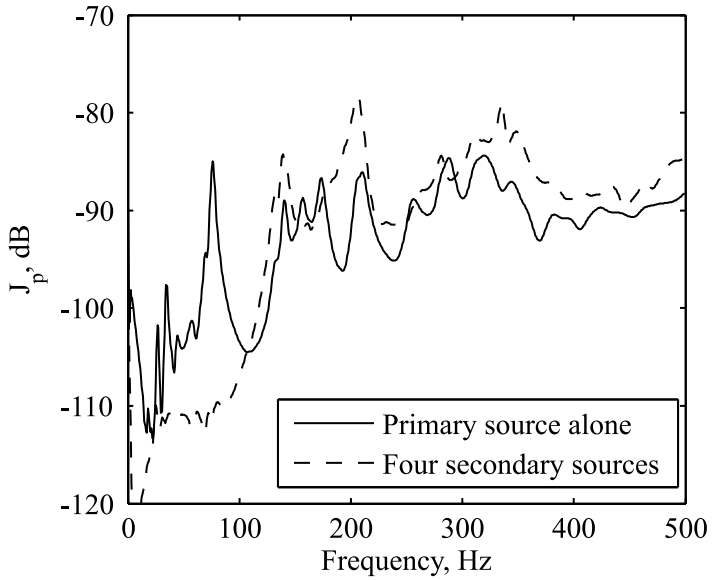

Figure 3.22: Total acoustic potential energy estimated using the eight corner measurement positions in the car cabin mock-up before (—) and after regional feedforward control using four secondary volume velocity sources positioned as shown in Figure 2.6 (- -) to minimise the sum of the eight squared headrest error sensor pressures with a control effort weighting parameter of $\beta = 10^5$.

3.4 Summary

The active control of engine noise in a car cabin interior using a feedforward active noise control strategy has been highlighted as a potentially low-cost and integrable noise control solution and this chapter has investigated the behaviour of optimal feedforward control strategies. To allow the physical limits of the feedforward control strategies to be investigated clearly by avoiding the complexity of a real car cabin the model of a rectangular enclosure detailed in Chapter 2 has been employed to simulate the performance of the control strategies. Despite being comparatively simple to understand compared to the response of a real car enclosure, the model derived in Chapter 2 still allows the effects of structural-acoustic coupling, which are predominant in a vehicle, to be investigated. The car cabin mock-up, presented in Figure 2.5, has been used to synthesise the control systems' performance and thus support the presented simulation results.

Global feedforward control of the total acoustic potential energy produced by an internal acoustic primary excitation has first been investigated, as this allows the effects introduced by employing a finite number of error sensors to be separated from the effects of the number of secondary sources. The presented simulations indicate that for both a single and four secondary sources the global feedforward control strategy is largely unaffected by the change in the enclosure response due to structural-acoustic coupling. That is, the shift in modal resonance frequencies and the additional radiating structural modes do not significantly alter the controlled responses. Therefore, the relationship between the number of secondary sources

and the control bandwidth, as previously shown by Nelson and Elliott [33] for the rigid walled enclosure, is unaffected by structural-acoustic coupling.

A practical control system cannot directly minimise the acoustic potential energy, therefore, simulations have also been presented in which the sum of the squared pressures at eight error sensors positioned in the corners of the enclosure is minimised using feedforward control. The presented simulations once again show little difference between the rigid and non-rigid enclosure controlled responses and the level of control at low frequencies is comparable to that achieved when the total acoustic potential energy is minimised directly. However, at higher frequencies enhancements in the total acoustic potential energy result due to the spatial sampling inherent when using a finite number of error sensors. The high frequency enhancements due to spatial sampling are more significant when an increased number of secondary sources are employed, which is a result of the increased coupling achieved by a larger number of sources. However, these enhancements could simply be avoided by setting a high frequency limit to the controller in a practical system.

To confirm the simulated results a series of results have been synthesised using transfer responses measured in the car cabin mock-up shown in Figure 2.5. Despite the difference in acoustic and structural damping the presented simulations have shown comparable control bandwidths to the simulated performances. The level of pressure reduction has also been validated through simulations of the enclosure with acoustic and structural damping close to that of the mock-up.

In the real car environment the primary noise source may be acoustic or may also be due to structural excitation. Therefore, simulations have been presented for both a point force structural excitation and an external acoustic plane wave excitation. For the point force structural excitation it has been shown that significant reductions in the acoustic potential energy are limited to frequencies below around 200 Hz, which is comparable to the internal acoustic excitation, although there are a number of resonances below 200 Hz that are not controllable. Additionally, although a more significant increase in the level of reduction occurs between one and four secondary sources compared to the internal acoustic excitation, there is no increase in the control bandwidth. This also occurs for the external acoustic plane wave excitation of the enclosure, where the bandwidth of control is limited to below 100 Hz for both the one and four source control systems. Investigating the contributions from the individual acoustic modes for each of the three primary source excitations considered has highlighted the cause of the limited bandwidth increase between using a single and multiple secondary sources for the two structural excitations. Specifically, for the point force structural excitation the radiation from the structure excites higher order acoustic modes at a lower frequency than the internal acoustic excitation and, therefore, increases the effective modal overlap and limits the level of control. For the external acoustic plane wave excitation, although there are significantly less strongly excited modes than both other excitation sources, there are a larger number of overlapping weakly excited modes that again limit the control bandwidth.

From the investigation of global feedforward control the effects of a non-rigid enclosure

have been investigated and validated and the change in control performance for various primary field excitations has been investigated. From these investigations it has been shown that regardless of the structural-acoustic coupling or primary excitation, significant reductions in the acoustic potential energy are largely limited to frequencies around and below the first longitudinal acoustic mode. In order to improve the bandwidth of control a second feedforward control strategy has been investigated that attempts to control the sound in the regions surrounding the car's occupants' heads. This control strategy reduces the volume over which the acoustic energy is to be reduced and, therefore, allows enhancements to occur outside of the specified control regions. This reduces the constraints on the control system and allows the bandwidth of control to be increased.

The performance of the regional feedforward control strategy has been investigated through both simulations using the model of structural-acoustic coupling and synthesis using the transfer responses measured in the car cabin mock-up. Using four secondary sources positioned at the standard car audio loudspeaker positions and eight error sensors positioned at the four headrest positions, the acoustic potential energy within the control regions has been shown to be significantly reduced at frequencies up to 370 Hz. This is around a doubling in the upper frequency limit of control compared to the global feedforward control strategy. A potential issue with the regional feedforward control strategy is that, due to the positions of the error sensors, it is susceptible to unobservable modes that result in enhancements in the regional acoustic potential energy. However, it has also been shown that these effects may be limited through the use of a control effort weighting parameter. The control effort weighting parameter limits the control effort that is used and, therefore, effectively provides a trade-off between control performance and control effort. In practice it may be possible to schedule the control effort weighting based on the pressures at additional microphones positioned remotely from the regional control zones.

Chapter 4

Modal Feedback Control

Whereas feedforward methods can be used to control engine noise in cars, the attenuation of road noise is more suited to a feedback control solution, as discussed in Chapter 1. Sano *et al* [59] have implemented a feedback system in a Honda station wagon to control drumming noise (low-frequency road noise) in the front seats at around 40 Hz, which is the first longitudinal acoustic mode of the vehicle in question. The proposed system also requires a simple fixed feedforward system to ensure that the sound level in the rear of the vehicle is not increased and achieves a 10 dB reduction in the drumming noise in the front seats whilst not enhancing the sound level in the rear; this system has been reviewed in Section 1.2.3. Feedback control directly employs the signals from error sensors to drive the secondary sources via a controller, as shown in Figure 4.1 for a single input single output (SISO) system. Since the error sensor signal is fed back to the secondary source, the system cannot be optimised on a frequency-by-frequency basis, as in feedforward control and the whole frequency response must be considered.

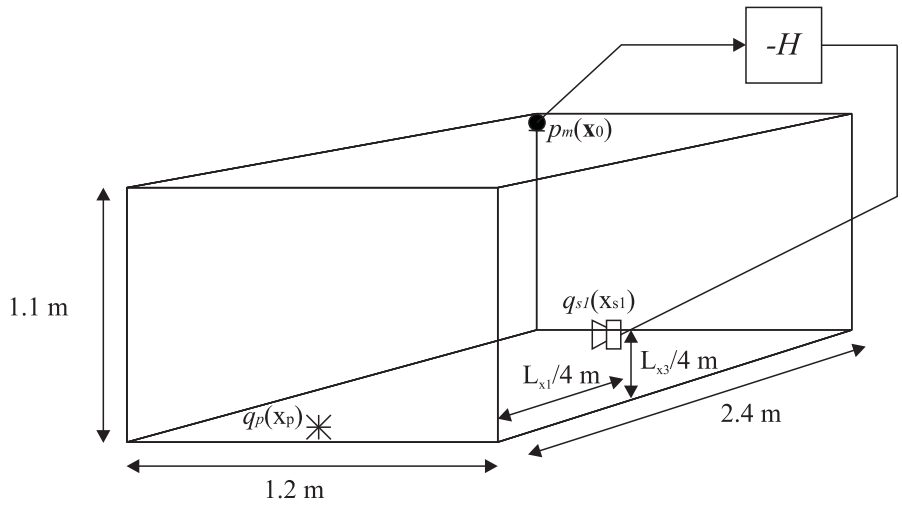

Figure 4.1: Simple single channel feedback control system.

The use of a single-source, single-sensor feedback control system has been widely investigated and the performance limitations are well documented [132, 133, 134]. Such control systems are widely employed in active noise cancelling headphones and, due to the small spacing between the error sensor and the loudspeaker, they can provide significant noise reduction up to frequencies of around 1 kHz [135]. However, since the performance of feedback control systems is limited by their stability, which is in turn significantly limited as the delay in the system is increased [136], feedback active control using a widely spaced error sensor and loudspeaker, as shown in Figure 4.1 calculated from the fully-coupled simulation, will not be able to achieve control over a wide bandwidth. To demonstrate this limitation Figure 4.2 shows the Nyquist plot of the feedback control system presented in Figure 4.1, in which the loudspeaker and microphone are separated by a distance of 1.02 m, giving a delay of 3 ms, where the feedback gain has been set based on the simplified Nyquist stability criterion in which it is assumed that the plant and controller are stable – as discussed in Section 4.3.1 below. Figure 4.3 shows the resulting change in the total acoustic potential energy. By reducing the distance between the control source and the error sensor the delay due to acoustic propagation can be reduced. This allows a wider bandwidth of control to be achieved, but only local control around the microphone is generally achieved and thus it is difficult to achieve a significant level of control throughout the seating region in a car sized enclosure. These limitations are evident in the feedback control system described by Sano *et al* [59] in which the region of acoustic energy reduction is limited to the front seats of the car cabin and the bandwidth of control is limited to the first longitudinal acoustic mode.

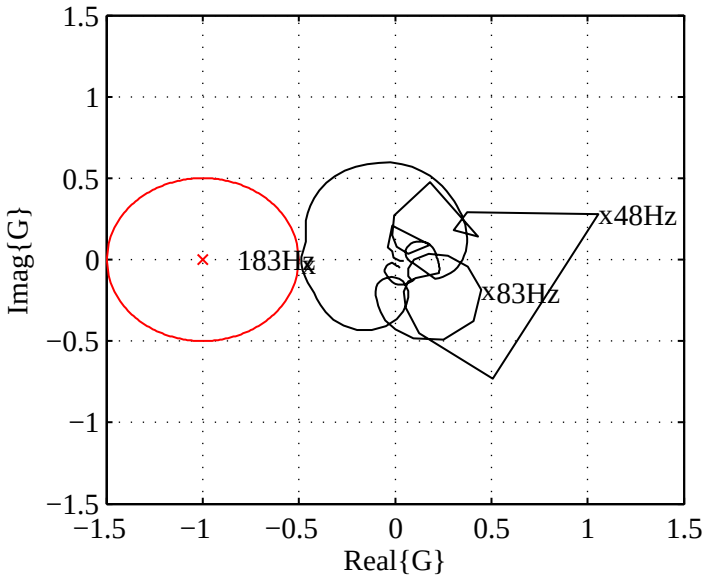

Figure 4.2: Nyquist plot of the open-loop transfer response, calculated for the full coupled enclosure, with a gain of $H = 2.5 \times 10^{-2}$ for a secondary source positioned at $\boldsymbol{x}_s = [L_1/4, 0, L_3/4]$ and an error sensor positioned at $\boldsymbol{x}_0 = [0, 0, L_3]$. The $(-1, j0)$ Nyquist point and region of 6 dB enhancement are also shown.

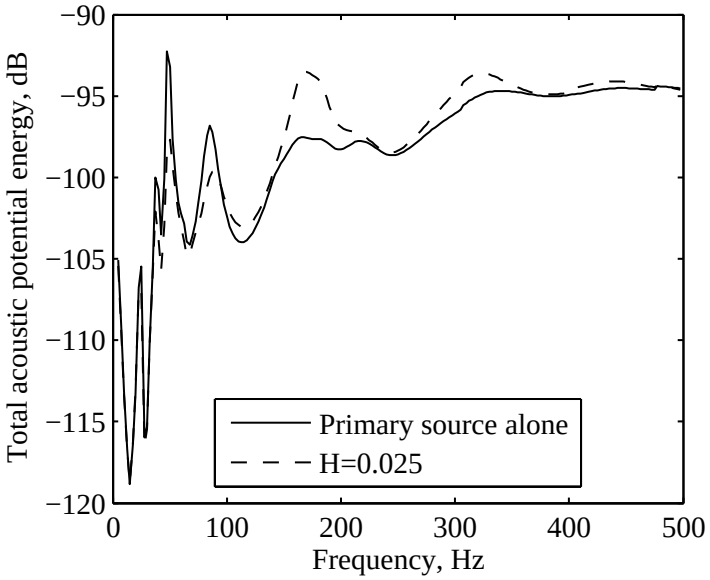

Figure 4.3: The total acoustic potential energy in the flexible walled enclosure for the feedback control system employing a secondary source positioned at $\boldsymbol{x}_s = [L_1/4, 0, L_3/4]$ and an error sensor positioned at $\boldsymbol{x}_0 = [0, 0, L_3]$.

A feedback control system with loudspeakers positioned close to the head of the cars' occupants may be able to provide a significant level and bandwidth of broadband random noise control. Such a system has been detailed in [134], but, as highlighted in Section 1.2, it may be difficult to integrate such a system into the standard car electronic systems.

This chapter investigates the use of feedback active noise control strategies that employ secondary sources positioned at the standard car audio loudspeaker positions and the same microphones that are used in the feedforward control system investigated in the previous chapter as error sensors. The aim of the investigated systems is to improve on the performance reported by Sano *et al* [59] by achieving global control of the sound field. Two modal feedback control systems are investigated which only require a single filter, which offers a significant computational saving in terms of both the optimisation of the controller and its implementation compared to the 32 filters required by a fully multi-input, multi-ouput (MIMO) controller employing eight error microphones and four loudspeakers. Since the modal controllers only require a single filter they may be implemented using a fully analogue system and, therefore, avoid the delays inherent in a digital implementation. Despite the reductions in the controller complexity, however, the two modal feedback control systems are only predicted to achieve significant levels of control in the structural-acoustic coupled enclosure if there is a dominant acoustic mode.

4.1 A Review of Modal Control

Modal structural control strategies can be divided into two distinct areas: positive position feedback (PPF) control [137] and modal filtering [138, 139]. PPF control employs a collo-

cated actuator and sensor pair, which ensures the system is minimum phase, similarly to direct velocity feedback. In comparison to direct velocity feedback, PPF only requires a structural displacement measurement and, therefore, can be implemented with strain-based sensors such as piezoelectric patches, which are free from the low frequency dynamics that cause instability problems in direct velocity feedback [137]. PPF control attempts to control individual modes by feeding the structural displacement measurement through a modally tuned resonant filter, with damping significantly greater than the structural mode's damping. The combined response of the modally tuned filter and the structure give a 180° phase shift at the resonance frequency and thus positive feedback results in cancellation of the structural response at the targeted mode. Multiple modes can be controlled using PPF through the use of multiple modally tuned filters.

The use of an acoustic modal control signal has direct analogies to modal structural control as reviewed by Fuller *et al* [140]. Vibration control using the modal filtering method employs discrete sensor measurements to estimate the modal response of particular target modes whilst rejecting interference from other modes [139]. Modal filtering is achieved through the linear combination of the sensor signals, with the phase and amplitude of each sensor signal set depending on its position relative to the mode shape of the targeted mode. Modal filtering is thus a form of spatial filtering [139] and the modal error signals have been employed in both feedforward [139] and feedback [141] control systems. The estimated modal response is used by a controller to determine the modal force with which to drive an array of actuators in order to add damping to the targeted mode. In theory the method of modal filtering can completely decouple all of the system's modes and, therefore, control of any targeted mode may be achieved without affecting any other mode in the system – i.e. control can be achieved without any spillover [142]. However, in practice only a finite number of sensors and actuators can be used and, therefore, both observation and control spillover result [142, 143]. A number of methods of avoiding, or at least limiting the effects of spillover have been proposed [144, 143, 139].

Modal control systems have also been applied to acoustic systems and there are a number of papers that implement such a system both in an aircraft fuselage [145, 146] and a rocket fairing [147]. These systems all employ an array of collocated transducer pairs that are weighted such that the energy dissipation is emphasised in targeted modes. This is achieved by weighting the arrays such that the poles of the targeted modes are well separated from the zeros and, therefore, an increase in the closed-loop performance is achieved [145]. The first of these papers, which applies the control system with 8 transducer pairs to reducing the noise in an aircraft fuselage, achieves 6 dB of control at the second acoustic mode and 3 dB of control at the third acoustic mode; however, it is worth noting that these modes occur at 46 and 71 Hz respectively and, therefore, have a much greater spacing than the modes in a car cabin sized enclosure. The control scheme employed phase compensation to increase the control bandwidth, which is limited by transducer dynamics [148], and an optimal feedback control strategy was employed to set the feedback gains based on a cost function that balanced the control effort with the

reduction in pressure at each of the microphones [145].

The later two publications [146, 147] employ identical control systems to each other, however, the system is applied to different acoustical problems: [146] attempts control in an aircraft fuselage and [147] is a feasibility study of implementing the control strategy outlined in [146] to control noise in a rocket fairing, where the noise levels may be up to 140 dB. The two control systems employ 16 pairs of collocated transducers that are weighted, as in [145], to emphasise energy dissipation in a targeted mode. It is indicated that the spatial weighting has been determined for each transducer pair from the real part of the frequency response at the targeted modal frequency measured between the error sensors and an arbitrarily positioned loudspeaker. Additionally, a method by which multi-mode control can be achieved is presented. The main difference between the work presented in [145] and that presented in [146, 147] is that an H_2 control law is employed. The control law was designed to emphasise control over the specified modal bandwidth and produce roll-off above the control bandwidth [147]. This increases the stability of the controller by reducing the sensitivity to noise and modelling errors at higher frequencies and, therefore, the potential performance is increased. However, to ensure that the controller does not simply achieve local control, an additional array of "performance" sensors are required in the design of the controller. Within the aircraft fuselage the proposed system achieves a maximum reduction of 6 dB using the single mode controller and an average reduction of 4 dB over 5 targeted modes using the multi-mode controller at the performance sensors [146]. The system implemented in the rocket fairing achieved similar levels of control with values ranging from 6 to 12 dB with little spillover [147]; the increased performance can be related to the increased number of transducer pairs per unit volume.

The result of generating a composite 'modal' error signal in a rectangular enclosure such as that considered in the previous chapter of this thesis can be understood by considering the positions of the nodal planes relative to the positions of the error sensors. For a control system employing eight corner error sensors in a rectangular, rigid walled enclosure, in order to improve the sensing of the first longitudinal acoustic mode, whose nodal line is shown by the grey plane in Figure 4.4, it is necessary to invert the polarity of the microphones positioned at x_3, x_4, x_7 and x_8 relative to microphones x_1, x_2, x_5 and x_6, as shown in Figure 4.4, such that the eight error signals will be in-phase and achieve enhanced sensitivity to this mode. For the next nine acoustic modes – seven of which are shown in Figure 4.5 (b-g) – these polarity inversions will result in their contributions to the composite error signal being cancelled. The next lowest acoustic mode whose sensitivity would be enhanced by the generation of the 'modal' error signal targeting the $(1,0,0)$ mode is the $(3,0,0)$ mode shown in Figure 4.5 (h).

In addition to modal control using modal filtering methods, the concept of PPF control has been applied to acoustic control in a number of acoustic systems [149, 150, 151]. In comparison to structural PPF the acoustic actuators typically have significant dynamics in the frequency range of control, the source and sensor cannot be truly collocated, and the signal fedback is not

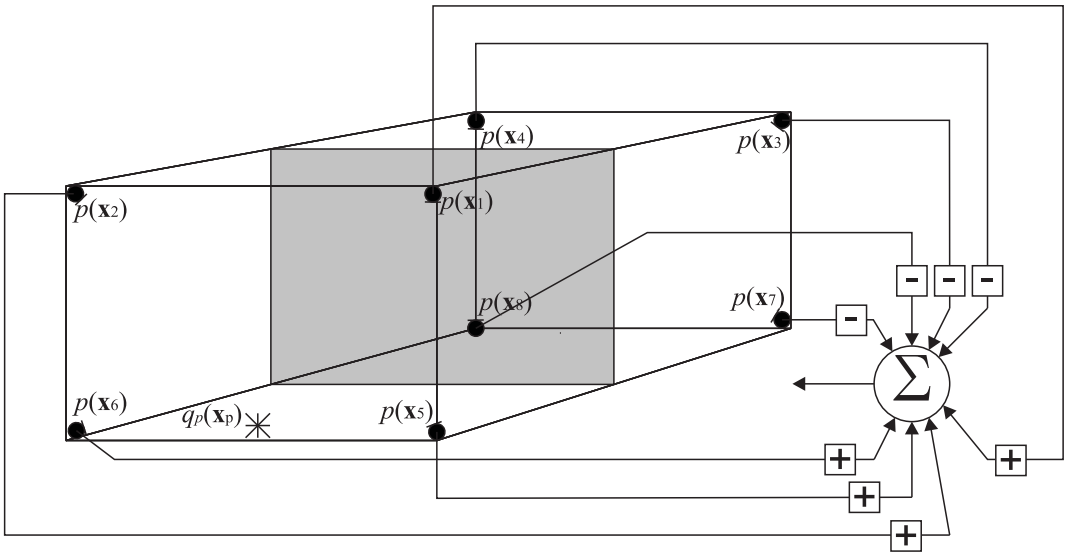

Figure 4.4: Modal feedback control system with transducer weights set to control the first longitudinal acoustic mode.

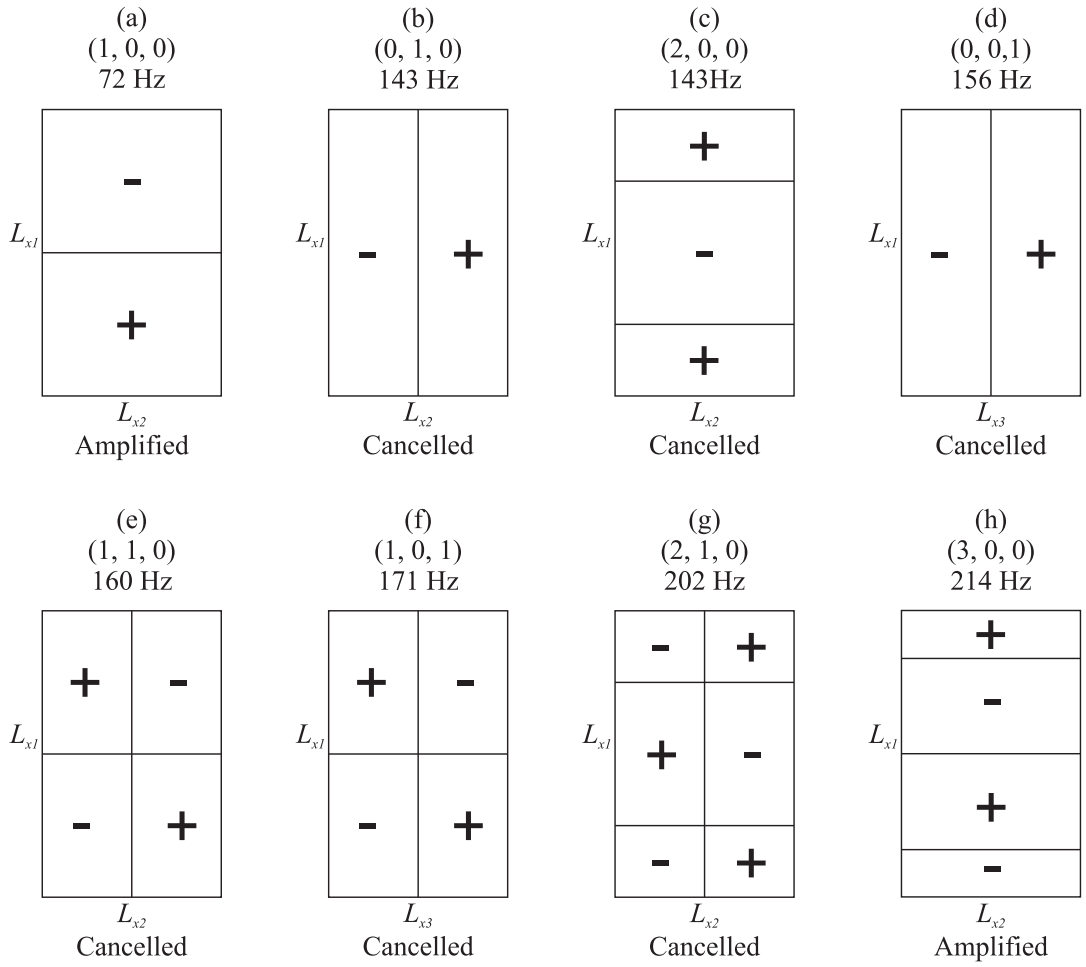

Figure 4.5: The positions of the nodal lines for the first seven modes (a - g) and the position of the nodal lines for the 11th mode (h), for the rectangular enclosure and the effect of the modal error sensor on the measured amplitudes of these modes (amplified/cancelled).

the position (or displacement) but the acoustic pressure. Despite these differences the structure of the acoustic PPF-type controller and the operating principles are the same as for structural PPF. That is, the signal from the error sensor is fedback to the loudspeaker via a modally tuned resonant filter which, when placed in series with the acoustic modal resonance, gives a 180° phase shift and, therefore, achieves cancellation of the targeted acoustic mode using a positive feedback gain.

The work presented by Bisnette *et al* [151] investigates the use of both modally tuned low-pass and bandpass PPF-type filters employed in conjunction with an all-pass filter, which is tuned to compensate for the loudspeaker's phase response and ensure that the 180° phase-shift is achieved at the targeted modal frequency. Bisnette *et al* apply the proposed control system to an acoustic duct and their results indicate that a single mode controller can achieve up to 8 dB reduction in the pressure throughout the duct, with a small amount of spillover in a higher order mode. The multi-mode controller is reported to achieve an average reduction of 4 dB across the first four modes, with 1 dB spillover at the fifth mode. It is also highlighted that, although the low-pass filter achieves good performance for the single mode controller, where the 40 dB/decade high frequency roll-off limits instability and spillover, for multi-mode control the bandpass filter, despite providing only 20 dB/decade roll-off at high and low frequencies, performs better. For multi-mode control the bandpass filter reduces interaction between adjacent modes and specifically reduces the interaction with lower frequency modes, which limits the performance of multi-mode control systems, whilst still providing the high frequency roll-off that improves system stability.

The PPF-type control system presented by Creasy *et al* [150] is similar to that presented by Bisnette *et al* [151], however, in addition to the second-order low-pass PPF filter, sixth-order high-pass and second-order low-pass Butterworth filters are also employed. The cut-on frequency of the high-pass filter is set to the zero preceding the targeted mode, and the cut-off frequency of the low-pass filter is set to the zero following the targeted mode. The resonance frequency of the PPF filter is also set close to the zero following the targeted mode and its damping is set to be approximately an order of magnitude greater than that of the targeted mode [150]. This combination of filters gives an 80 dB/decade high-frequency roll-off and a 120 dB/decade roll-on at low frequencies. The effect of these filters is to reduce the low-frequency spillover that may occur in multi-mode control using a PPF filter and improve system stability. The use of higher-order filters has previously also been presented by Smith [152]. Additionally, the system proposed in [150] implements an adaptation scheme, such that the controller can adapt to changes in the modal frequencies. For the application to an acoustic duct it is shown that the proposed adaptation strategy continues to absorb energy over five modes whilst the frequencies of the acoustic modes are varied by up to 20%. The performance of the proposed control system is implemented in a launch vehicle payload fairing in [149] and it is shown that pressure level reductions of 3.3 dB over a bandwidth of 100 to 250 Hz are maintained with 5% variation in the modal frequencies using a 6 mode controller.

From the preceding literature review it is evident that it may be possible to achieve a sig-

nificant level and bandwidth of control using a modal-based feedback control strategy, whilst reducing the computational demand of the controller compared to a fully multi-input, multi-output (MIMO) controller. Therefore, this chapter will investigate the use of multiple error sensors to generate a composite, 'modal' error signal which will be used to drive multiple secondary sources via a feedback controller. The spatial weighting of the sensor array is comparable to that employed in the modal filtering method, however, unlike the systems presented in [145, 146, 147] the source and sensors will not be collocated. This non-collocation is partially due to the fixed positioning of the car audio loudspeakers and their sub-optimal positioning with regard to error sensor locations, however, in the context of the modal feedback control system, if non-collocation of sensors and actuators is practical then the need for a second "performance" array of sensors, as required in the optimal feedback control systems presented in [146, 147], would be unnecessary.

It is important to note that all of the acoustical systems within which modal control strategies have been employed in the above references are lightly damped and have well spaced modes at low frequencies where active noise control is practicable. In the context of the car cabin enclosure, however, the assumed damping is significantly greater and the modal overlap becomes more significant at low frequencies. The effect that these differences in the acoustical system have on the performance of modal control systems will be illustrated in the following sections.

4.2 Controller Formulation

A block diagram of the multi-sensor, multi-source modal feedback control system is presented in Figure 4.6a and an implementation of the system in the rectangular enclosure employed in Chapters 2 and 3 is presented in Figure 4.7. The feedback control system consists of M loudspeakers and L_e discrete error sensors, which may also be employed in a feedforward engine noise control system, and in this instance is used to control a single acoustic mode. The composite error signal, p_c, is generated through the weighted summation of the signals from the L_e discrete error microphones. This weighted summation is implemented via the $(L_e \times 1)$ vector of real, frequency independent, error sensor weightings, $\boldsymbol{w}_L$, and can be expressed in terms of the $(L_e \times 1)$ vector of pressures at the error sensors, $\boldsymbol{p}_e$, as

$$p_c(j\omega) = \boldsymbol{w}_L^T \boldsymbol{p}_e(j\omega), \tag{4.1}$$

where ^{T} denotes the matrix transpose and the vector of pressures at the error sensors is given by the summation of the $(L_e \times 1)$ vectors of pressures due to the primary disturbance, $\boldsymbol{p}_p$, and the control, or secondary sources, $\boldsymbol{p}_s$, so that

$$\boldsymbol{p}_e(j\omega) = \boldsymbol{p}_p(j\omega) + \boldsymbol{p}_s(j\omega). \tag{4.2}$$

The composite error signal, p_c, is filtered by the negative feedback controller, $-H$, to give the composite secondary source strength

$$q_c(j\omega) = -H(j\omega)p_c(j\omega). \tag{4.3}$$

The composite source strength is then sent to the M secondary sources, via the $(M \times 1)$ vector of real, frequency independent source weightings, $\boldsymbol{w}_M$, which gives the vector of secondary source strengths as

$$\boldsymbol{q}_s(j\omega) = \boldsymbol{w}_M q_c(j\omega). \tag{4.4}$$

The secondary source strengths are related to the vector of pressures due to the secondary sources, $\boldsymbol{p}_s$, via the $(L_e \times M)$ matrix of acoustic transfer impedances between the secondary sources and the error sensors, $\boldsymbol{Z}_s$, and thus equation 4.2 can be expanded to give,

$$\boldsymbol{p}_e(j\omega) = \boldsymbol{p}_p(j\omega) + \boldsymbol{Z}_s(j\omega)\boldsymbol{q}_s(j\omega). \tag{4.5}$$

Substituting equations 4.1, 4.3 and 4.4 into equation 4.5 and rearranging gives the vector of error sensor pressures as

$$\boldsymbol{p}_e(j\omega) = \left[\boldsymbol{I} + \boldsymbol{Z}_s(j\omega)\boldsymbol{w}_M H(j\omega)\boldsymbol{w}_L^T\right]^{-1} \boldsymbol{p}_p(j\omega), \tag{4.6}$$

where $\boldsymbol{I}$ is an $(L_e \times L_e)$ identity matrix. The $(L_e \times L_e)$ matrix sensitivity function of the L_e input, M output feedback controller is given by

$$\boldsymbol{S}(j\omega) = \left[\boldsymbol{I} + \boldsymbol{Z}_s(j\omega)\boldsymbol{w}_M H(j\omega)\boldsymbol{w}_L^T\right]^{-1}, \tag{4.7}$$

and the open-loop response is given by

$$\boldsymbol{Z}_s(j\omega)\boldsymbol{w}_M H(j\omega)\boldsymbol{w}_L^T, \tag{4.8}$$

where the L_e input, M output controller response is given by $\boldsymbol{H}(j\omega) = \boldsymbol{w}_M H(j\omega)\boldsymbol{w}_L^T$. However, substituting equation 4.5 into equation 4.1 gives the composite error signal as

$$\begin{aligned} p_c(j\omega) &= \boldsymbol{w}_L^T \boldsymbol{p}_p + \boldsymbol{w}_L^T \boldsymbol{Z}_s(j\omega)\boldsymbol{q}_s, \\ &= p_{c_p} + \boldsymbol{w}_L^T \boldsymbol{Z}_s(j\omega)\boldsymbol{q}_s, \end{aligned} \tag{4.9}$$

where p_{c_p} is the composite primary pressure. Substituting for the secondary source strengths using equations 4.3 and 4.4 then gives the composite error signal as

$$p_c(j\omega) = \left[1 + \boldsymbol{w}_L^T \boldsymbol{Z}_s(j\omega)\boldsymbol{w}_M H(j\omega)\right]^{-1} \boldsymbol{w}_L^T \boldsymbol{p}_p(j\omega), \tag{4.10}$$

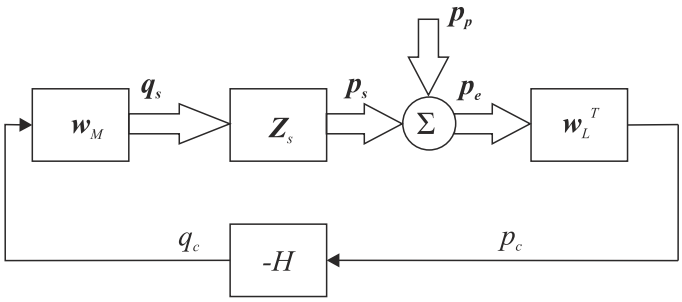

(a) Block diagram of the multi-source, multi-sensor modal feedback control system.

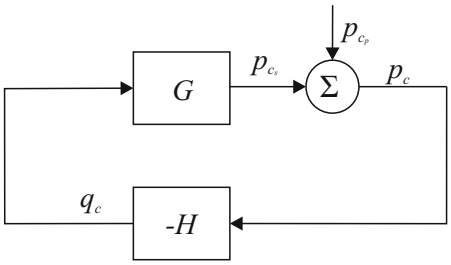

(b) Block diagram of the single-input, single-output modal feedback control system.

Figure 4.6: Block diagrams of the modal feedback controller

where the scalar sensitivity function of the composite system is given as

$$S_c(j\omega) = \left[1 + \mathbf{w}_L^T \mathbf{Z}_s(j\omega)\mathbf{w}_M H(j\omega)\right]^{-1}. \tag{4.11}$$

The open-loop response of the composite system is given by

$$\mathbf{w}_L^T \mathbf{Z}_s(j\omega)\mathbf{w}_M H(j\omega). \tag{4.12}$$

where the composite plant is given by $\mathbf{w}_L^T \mathbf{Z}_s(j\omega)\mathbf{w}_M = G(j\omega)$ and the controller response is simply given by H. Therefore, despite employing L_e error sensors and M secondary sources, it can be seen that the performance and stability of the single-mode controller may be determined using the relatively more straightforward SISO controller design methods and the simplified block diagram for this formulation is shown in Figure 4.6b.

4.3 Robust Stability Constraints

4.3.1 Single-Input Single-Output Robust Stability

The design of SISO feedback control systems, such as the SISO controller shown in Figure 4.6b, can be achieved using the definitions of the closed and open loop responses. The closed-

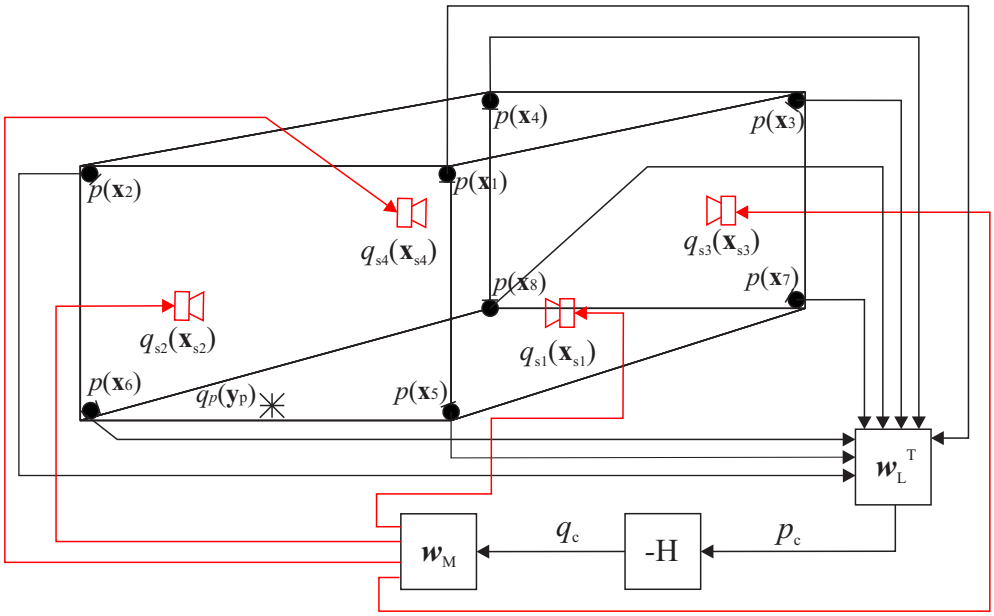

Figure 4.7: Multi-source, multi-sensor modal feedback control system.

loop response for a general SISO system is given by

$$S(j\omega) = \frac{p_e(j\omega)}{p_d(j\omega)} = \frac{1}{1+G(j\omega)H(j\omega)}, \tag{4.13}$$

where p_e is the error pressure, p_d is the disturbance pressure, $G(j\omega)$ is the frequency response of the plant and $H(j\omega)$ is the frequency response of the controller and the open-loop response is given by

$$G(j\omega)H(j\omega). \tag{4.14}$$

To design a feedback controller it is necessary ensure that the closed-loop system is stable. Assuming at this stage that both the plant and controller are themselves stable, the closed-loop stability criterion for a SISO feedback controller can be observed from the sensitivity function given by equation 4.13. If $G(j\omega)H(j\omega)$ was equal to -1 then the response of the feedback controller, which is governed by the sensitivity function, would become unbounded and the controller would be unstable [132]. This leads to the definition of the Nyquist stability criterion, which states that the polar plot of the open-loop response must not enclose the Nyquist point, $(-1,0)$, as ω increases from $-\infty$ to $+\infty$ [153].

In a practical system where the open-loop response may be subject to variations it is typical to set the feedback gain to allow the system to remain stable despite these variations. The use of gain and phase margins provide a common method of designing a stable feedback controller, however, there are situations under which a system may have both large gain and phase margins but still become unstable if there is a change in both the gain and phase of the system. A system that remains stable despite changes in both the gain and phase is said to be robustly stable [132]. To ensure robust stability a feedback system may be designed using an unstructured model of the plant uncertainties [132]. Plant uncertainties are the changes that occur in the nominal

response of the open-loop system, $G_0(j\omega)$ – that is, the response with no uncertainty. These changes in the nominal response produce regions of uncertainty around the nominal open-loop frequency response at each frequency and these may be described by a disc of uncertainty [132]. Robust stability may then be ensured by designing the feedback system such that the discs of uncertainty at each frequency do not encircle the Nyquist point.

Using the model of unstructured plant uncertainty the disc of uncertainty at each frequency may be described by a circle with a centre point $G_0(j\omega)H(j\omega)$ and a radius $B(\omega)|G_0(j\omega)H(j\omega)|$, where B is the maximum magnitude of the plant uncertainty. The robust stability criterion then requires that

$$|1+G_0(j\omega)H(j\omega)| > B(\omega)|G_0(j\omega)H(j\omega)| \qquad \forall\omega, \tag{4.15}$$

which states that the distance from the centre of the circle to the Nyquist point must be greater than the radius of the circle for all, $\forall$, frequencies. Rearranging equation 4.15 gives

$$\frac{|G_0(j\omega)H(j\omega)|}{|1+G_0(j\omega)H(j\omega)|} < \frac{1}{B(\omega)} \qquad \forall\omega,, \tag{4.16}$$

$$|T_0(j\omega)| < \frac{1}{B(\omega)} \qquad \forall\omega,, \tag{4.17}$$

where T_0 is the complementary sensitivity function and is related to the sensitivity function by [132]

$$S_0(j\omega) + T_0(j\omega) = 1. \tag{4.18}$$

4.3.2 Multi-Input Multi-Output Robust Stability

Although only a SISO modal controller is considered in Section 4.2 it is useful at this stage to also discuss the robustness constraint in the context of a MIMO controller since, as will be shown below, it is perhaps beneficial to formulate the modal controller as a MIMO system. The closed-loop response of the MIMO feedback controller shown in Figure 4.8 is given following equation 4.6 as

$$\boldsymbol{p}_e(j\omega) = [\boldsymbol{I}+\boldsymbol{G}(j\omega)\boldsymbol{H}(j\omega)]^{-1}\,\boldsymbol{p}_p(j\omega), \tag{4.19}$$

where $\boldsymbol{G}(j\omega)$ is the matrix of plant responses and $\boldsymbol{H}(j\omega)$ is the matrix of controller responses and the term in square brackets is the sensitivity function, $\boldsymbol{S}(j\omega)$. The stability of a MIMO feedback control system can be determined based on a generalisation of the Nyquist criterion discussed above in the context of SISO systems, where it is again assumed that both the plant and controller are themselves stable. The details of this generalisation are detailed in Appendix F, however, it is pertinent to highlight that the stability of the closed-loop MIMO system is guaranteed by ensuring that the loci of the eigenvalues of the open-loop response matrix, $\boldsymbol{G}(j\omega)\boldsymbol{H}(j\omega)$ do not encircle the $(-1,0)$ point [132].

In a practical system, where the open-loop responses may be subject to some variations, it is again necessary to derive a robust stability condition. In the MIMO feedback system this con-

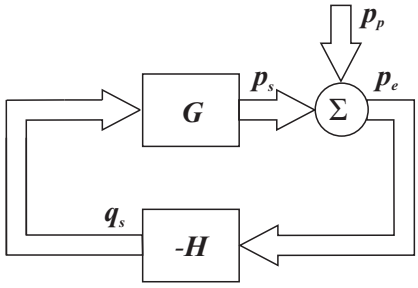

Figure 4.8: Block diagram of the multichannel feedback control system.

dition is significantly more complex than for the SISO case, as plant uncertainties due to input and output perturbations cannot always be combined to form a simple uncertainty description [154]. The problem of lumping input and output uncertainties is discussed in Appendix F, however, in the following simulations it is convenient to assume that the plant uncertainty can be modelled as output uncertainty. In the simulation scenario any plant uncertainty is artificially defined and, therefore, defining the multichannel plant uncertainty as output uncertainty loses no generality, but does allow a convenient condition for robust stability. The condition for robust stability in the case of unstructured output uncertainty is given by [132]

$$\bar{\sigma}[\boldsymbol{T}_0(j\omega)] < \frac{1}{B(j\omega)} \qquad \forall\omega, \tag{4.20}$$

where $\bar{\sigma}[\cdots]$ indicates the maximum singular value of the associated matrix and $\boldsymbol{T}_0(j\omega)$ is the multichannel complementary sensitivity function of the nominal plant and is given by

$$\boldsymbol{T}_0(j\omega) = [\boldsymbol{I} + \boldsymbol{G}_0(j\omega)\boldsymbol{H}(j\omega)]^{-1}\boldsymbol{G}_0(j\omega)\boldsymbol{H}(j\omega). \tag{4.21}$$

4.4 Enhancement Constraints

4.4.1 Single-Input, Single-Output Enhancement Constraint

When designing a feedback controller it is often desirable to also enforce a limit on the maximum enhancement of the primary disturbance signal. In the context of the SISO controller a constraint on the enhancement in the error signal can be ensured by limiting the sensitivity function given by equation 4.13 to be less than a maximum value of A. The sensitivity function governs the response between the error and the disturbance signals and this constraint thus ensures that the disturbance signal is not enhanced by more than a factor of A. This enhancement constraint can be expressed as [132]

$$|1 + G_(j\omega)H(j\omega)| > \frac{1}{A} \qquad \forall\omega, \tag{4.22}$$

and can be interpreted geometrically as a circle of radius $1/A$ centred on the Nyquist point through which the locus of the open-loop response should not pass in order to ensure a maximum enhancement of A. That is, for $A = 2$, provided the open-loop response does not pass

through this circle a maximum enhancement of 6 dB will be ensured.

4.4.2 Multi-Input, Multi-Output Enhancement Constraints

It is again convenient to extend the discussion of enhancement to MIMO systems here, even though only SISO modal controllers are initially being considered, since it will be used later.

According to equation 4.19 the sensitivity function of the MIMO feedback controller is given by

$$\boldsymbol{S}(j\omega) = [\boldsymbol{I} + \boldsymbol{G}(j\omega)\boldsymbol{H}(j\omega)]^{-1}, \tag{4.23}$$

and this again describes the response between the primary disturbance and the error signal; $\boldsymbol{p}_p$ and $\boldsymbol{p}_e$ in the controller shown in Figure 4.8. Therefore, as in the SISO case, it is possible to use the sensitivity function to define a constraint on the maximum enhancement in the disturbance signal. A possible constraint on out of band enhancements is provided by constraining the maximum singular value of the sensitivity function to be less than the desired enhancement factor, A, where A is greater than unity; that is

$$\bar{\sigma}[\boldsymbol{S}(j\omega)] < A \qquad \forall\omega. \tag{4.24}$$

However, the maximum singular value of the sensitivity function is related to the ratio of the 2-norms of the primary disturbance vector, $\boldsymbol{p}_p(j\omega)$, and the error vector, $\boldsymbol{p}_e(j\omega)$, by [132]

$$\bar{\sigma}[\boldsymbol{S}(j\omega)] \geqslant \frac{||\boldsymbol{p}_e(j\omega)||_2}{||\boldsymbol{p}_p(j\omega)||_2}, \tag{4.25}$$

and therefore this enhancement constraint is potentially somewhat conservative with respect to the enhancements in the sum of the squared pressures.

In the context of the MIMO system a less conservative constraint on the maximum enhancement can be approached from two directions by either directly limiting the enhancement in the sum of squared error sensor pressures or the enhancement in the individual error sensor pressures. The constraint on the maximum enhancement in the sum of the squared error sensor pressures can be expressed for a random noise disturbance as

$$\frac{E\left(\boldsymbol{p}_e^H(j\omega)\boldsymbol{p}_e(j\omega)\right)}{E\left(\boldsymbol{p}_p^H(j\omega)\boldsymbol{p}_p(j\omega)\right)} < A \qquad \forall\omega, \tag{4.26}$$

where E is the expectation operator and A is the maximum enhancement limit, such that for a value of $A = 4$ the maximum enhancement in the sum of the squared error signals is limited to 6 dB. This constraint can be rewritten using the trace, which is the sum of the diagonal elements of a square matrix, as

$$\frac{\text{trace}\left[E\left(\boldsymbol{p}_e(j\omega)\boldsymbol{p}_e^H(j\omega)\right)\right]}{\text{trace}\left[E\left(\boldsymbol{p}_p(j\omega)\boldsymbol{p}_p^H(j\omega)\right)\right]} < A \qquad \forall\omega. \tag{4.27}$$

Since the error sensor pressures, $\boldsymbol{p}_e$, can be related to the primary pressures using the sensitivity function as

$$\boldsymbol{p}_e(j\omega) = \boldsymbol{S}(j\omega)\boldsymbol{p}_p(j\omega), \tag{4.28}$$

the constraint on the maximum enhancement can be expressed in terms of the disturbance and the sensitivity function as

$$\frac{\text{trace}\left[E\left(\boldsymbol{S}(j\omega)\boldsymbol{p}_p(j\omega)\boldsymbol{p}_p^H(j\omega)\boldsymbol{S}^H(j\omega)\right)\right]}{\text{trace}\left[E\left(\boldsymbol{p}_p(j\omega)\boldsymbol{p}_p^H(j\omega)\right)\right]} < A \qquad \forall\omega. \tag{4.29}$$

The expectation of the outer product is defined as the matrix of power and cross spectral densities

$$\boldsymbol{S}_{pp}(j\omega) = E\left(\boldsymbol{p}_p(j\omega)\boldsymbol{p}_p^H(j\omega)\right), \tag{4.30}$$

and, therefore, the constraint on the maximum enhancement in the sum of squared pressures can finally be expressed as

$$\frac{\text{trace}\left[\boldsymbol{S}(j\omega)\boldsymbol{S}_{pp}(j\omega)\boldsymbol{S}^H(j\omega)\right]}{\text{trace}\left[\boldsymbol{S}_{pp}(j\omega)\right]} < A \qquad \forall\omega. \tag{4.31}$$

Using equation 4.31 it is possible that a high level of enhancement in the pressure may occur at one error sensor location whilst this is balanced out by a comparable level of attenuation at another error sensor. This may be detrimental to the subjective performance of the control system and, therefore, it is pertinent to also consider constraining the maximum enhancement in the individual error sensor pressures. This constraint may be expressed for a random disturbance at the l-th error sensor as

$$\frac{E\left(|p_{e_l}(j\omega)|^2\right)}{E\left(|p_{p_l}(j\omega)|^2\right)} < A \qquad \forall\omega, \tag{4.32}$$

where if $A = 4$ the maximum enhancement in the squared pressure at the l-th error sensor due to control is 6 dB. This constraint can be expressed for all error sensors using a matrix formulation as

$$\max\left[\text{diag}\left(\boldsymbol{D}(j\omega)E(\boldsymbol{p}_e(j\omega)\boldsymbol{p}_e^H(j\omega))\right)\right] < A, \tag{4.33}$$

where the diag of an $(N \times N)$ square matrix $\boldsymbol{A}$ is defined as

$$\text{diag}\left(\boldsymbol{A}\right) = \left[\begin{array}{cccc} A_{11} & A_{22} & \cdots & A_{NN} \end{array}\right]^T, \tag{4.34}$$

and the matrix $\boldsymbol{D}$ is defined at a single frequency as the diagonal matrix

$$\boldsymbol{D} = \left[\begin{array}{cccc} \frac{1}{E(|p_{p_1}|^2)} & 0 & 0 & 0 \\ 0 & \frac{1}{E(|p_{p_2}|^2)} & 0 & 0 \\ 0 & 0 & \ddots & 0 \\ 0 & 0 & 0 & \frac{1}{E(|p_{p_L}|^2)} \end{array}\right]. \tag{4.35}$$

Substituting for $\boldsymbol{p}_e$ using equations 4.28 and 4.30 the constraint on the maximum enhancement of the pressure at any one error sensor can be expressed as

$$\max\left[\text{diag}\left(\boldsymbol{D}(j\omega)\boldsymbol{S}(j\omega)\boldsymbol{S}_{pp}(j\omega)\boldsymbol{S}^H(j\omega)\right)\right] < A. \tag{4.36}$$

4.5 Internal Model Control

Internal Model Control (IMC) allows the feedback control problem to be reformulated as an equivalent feedforward problem and, therefore, the design of the feedback controller may be achieved using feedforward control design methods [132, 155]. This provides a convenient method of designing optimal feedback controllers and as shown in [156] it can be used to formulate the optimisation of a feedback controller with both H_2 and H_∞ constraints. The IMC method will be applied to the design of the modal feedback control system which can be formulated as either a SISO or MIMO controller and, therefore, the SISO and MIMO formulations of an IMC architecture will be detailed.

4.5.1 Single-Input, Single-Output Internal Model Control

Figure 4.9a shows the standard feedback control block diagram and Figure 4.9b shows the system employing an IMC architecture, where the complete feedback controller, $-H$, is contained within the dashed lines and consists of the control filter W and the modelled plant response $\hat{G}$. The response of the feedback controller is given by

$$H(j\omega) = \frac{-W(j\omega)}{1+\hat{G}(j\omega)W(j\omega)}, \tag{4.37}$$

where W is the control filter and the resulting sensitivity function is given by

$$S(j\omega) = \frac{p_e(j\omega)}{p_d(j\omega)} = \frac{1+\hat{G}(j\omega)W(j\omega)}{1-\left[G(j\omega)-\hat{G}(j\omega)\right]W(j\omega)}. \tag{4.38}$$

Assuming that the plant model is perfect, then the feedback signal is equal to the primary disturbance and, therefore, effectively acts as a perfect reference signal to drive the control filter, W. Under this assumption the sensitivity function becomes

$$S(j\omega) = 1+G(j\omega)W(j\omega), \tag{4.39}$$

and the control filter, W, operates as a feedforward controller and, therefore, can be designed using standard feedforward techniques [155, 132].

As in Chapter 3, the feedforward controller, W, can be designed to minimise the squared error signal which, for a random disturbance signal, is given by

$$S_{ee}(j\omega) = E\left(p_e(j\omega)^H p_e(j\omega)\right) = |1+G(j\omega)W(j\omega)|^2 S_{dd}(j\omega), \tag{4.40}$$

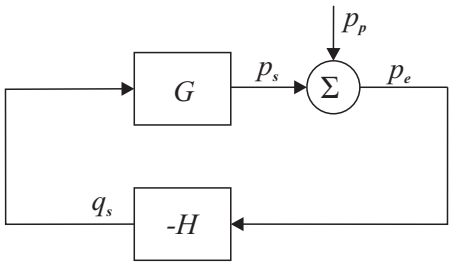

(a) Standard SISO Feedback Controller

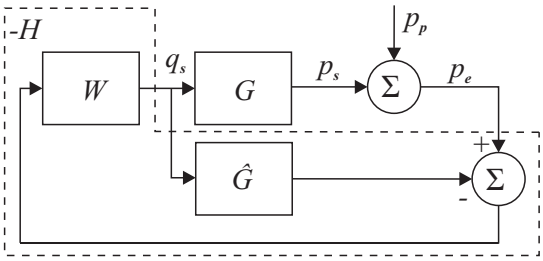

(b) IMC SISO Feedback Controller

Figure 4.9: Block diagrams of a standard and IMC SISO feedback control system

where S_{dd} is the spectral density of the disturbance. However, despite IMC allowing a feedback controller to be reformulated as a feedforward system, in a practical active noise control system the plant model will not be perfect and a degree of feedback will be present in the system [155]. This leads to potential stability problems and the need to enforce robust stability constraints in the controller design [155, 132]. For the SISO IMC controller the robust stability constraint derived in Section 4.3.1 can be expressed by substituting 4.37 into equation 4.16 and assuming that the modelled plant response is equal to the nominal response to give

$$|G_0(j\omega)W(j\omega)| < \frac{1}{B(\omega)} \qquad \forall\omega. \tag{4.41}$$

Similarly, the disturbance enhancement constraint given by equation 4.22 can be written in terms of the IMC controller as

$$\frac{1}{|1+G_0(j\omega)W(j\omega)|} > \frac{1}{A} \qquad \forall\omega. \tag{4.42}$$

Thus, by combining the minimisation of the mean squared error, $S_{ee}(j\omega)$, with the requirements of maintaining the robustness and enhancement constraints, the IMC formulation can be used to design a robust feedback controller.

Up to this point it has been assumed that both the plant and controller are open-loop stable, however, this is not a general requirement of IMC and it is possible that the design process may produce a controller that is open-loop unstable but closed-loop stable. Therefore, a more general definition of the Nyquist stability criterion that does not assume open-loop stability is required. The more general definition of the Nyquist stability criterion is that the closed-loop system should have no unstable, right-half plane zeros [155, 133]. This criterion can be

expressed as [155]

$$N_{CW} = -P, \tag{4.43}$$

where N_{CW} is the number of clockwise encirclements of the $(-1,0)$ point by $G_0(j\omega)H(j\omega)$ and P is the number of unstable poles of the open-loop response. Therefore, in the case when the plant and controller are stable there should be no encirclements of the $(-1,0)$ point, as detailed in Section 4.3.1. However, for each unstable pole in the open-loop response the locus of the open-loop response $G(j\omega)H(j\omega)$ must encircle the $(-1,0)$ point in the anti-clockwise direction to ensure closed-loop stability.

In an acoustic control scenario it is reasonable to assume that the open-loop plant is stable, however, according to equation 4.37 an unstable pole in the feedback controller, $H(j\omega)$, can be related to an unstable zero in the response $G_0(j\omega)W(j\omega)$. In a practical real-time system, the use of an unstable controller would be difficult to realise since it would not be possible to measure the response of the open-loop controller and, therefore, it would be difficult to ensure that the expected closed-loop performance would be achieved. This issue has been discussed in the context of an active headrest system employing a virtual microphone by Tseng *et al* [157] and in order to ensure a stable open-loop controller an additional design constraint was proposed that limits the response of the open-loop controller to be on the right hand side of the Nyquist point. This design constraint can be expressed as

$$\Re\{G_0(j\omega)W(j\omega)\} > -1 \quad \forall\omega. \tag{4.44}$$

This design constraint can also be included in the optimisation of the controller using the IMC architecture along with the robustness and enhancement constraints.

4.5.2 Multi-Input, Multi-Output Internal Model Control

The design of MIMO feedback controllers is significantly more demanding than SISO controllers since in the multichannel feedback case the open and closed loop responses are governed by matrices and, therefore, require the use of matrix norms rather than scalar norms [132]. A wide variety of methods have been proposed for designing multichannel feedback controllers [154] and a particularly practical method of designing a robustly stable controller, which is relatively simple from the designers perspective, has been proposed by McFarlane and Glover [158]. This design method, referred to as McFarlane-Glover loop-shaping, combines the characteristics of classical loop-shaping and H_∞ design. The designer first specifies weighting functions that shape the open-loop magnitude response in order to achieve the required performance criterion, such as disturbance rejection at low frequencies and robust stability at high frequencies, and then a controller is designed using H_∞ methods to robustly stabilise the shaped plant. The difficulty in implementing this control method is that it requires a state-space model of the plant and, therefore in a complex system, such as the acoustic control problem considered here, it is difficult to implement an accurate model of the practical plant that can

also be solved using the McFarlane-Glover method. IMC allows a multichannel feedback controller to be designed without the need for predefining weighting functions and may avoid the need for a complex model of the plant [134]. The block diagram of the multichannel IMC feedback controller is shown in Figure 4.10.

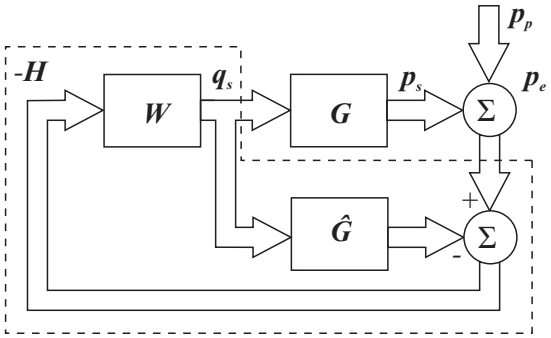

Figure 4.10: Block diagram of the mutlichannel feedback control system in which the feedback control is implemented using an internal modal control architecture.

For the MIMO IMC controller, the response of the complete feedback controller, $\boldsymbol{H}$, which is contained within the dashed lines in Figure 4.10, is given by

$$\boldsymbol{H}(j\omega) = -\left[\boldsymbol{I} + \boldsymbol{W}(j\omega)\hat{\boldsymbol{G}}(j\omega)\right]^{-1}\boldsymbol{W}(j\omega), \tag{4.45}$$

where $\boldsymbol{W}$ is the $(M \times L_e)$ control filter matrix and $\hat{\boldsymbol{G}}$ is the $(L_e \times M)$ matrix of modelled plant responses. Assuming that the plant model is equal to the nominal plant response the vector of error signals is given by substituting equation 4.45 into equation 4.19 and rearranging to give

$$\boldsymbol{p}_e(j\omega) = \left[\boldsymbol{I} + \boldsymbol{G}_0(j\omega)\boldsymbol{W}(j\omega)\right]\boldsymbol{p}_p(j\omega), \tag{4.46}$$

and the nominal matrix sensitivity function of the controller in Figure 4.10 is given by [155, 132]

$$\boldsymbol{S}_0(j\omega) = \boldsymbol{I} + \boldsymbol{G}_0(j\omega)\boldsymbol{W}(j\omega). \tag{4.47}$$

The IMC architecture has allowed the feedback controller to be reformulated as a feedforward system, where the disturbance signal is equal to the reference signal provided that the plant model is perfect. The nominal performance of the controller can, therefore, be designed using feedforward control techniques. However, in comparison to feedforward control, since the reference signals are equal to and, therefore, completely coherent with the disturbance signals, there are no limitations on the controller performance imposed by coherence [132].

In a practical active noise control system the plant model will not be perfect and there will, therefore, be a degree of feedback in the system. This feedback leads to potential stability issues and the need to enforce stability constraints by 'detuning' the nominal feedforward controller [155]. The robust stability constraint for the MIMO IMC controller is given by assuming that the modelled plant is equal to the nominal plant response and substituting equation 4.45 into

equation 4.21 and substituting the result into equation 4.20, which gives

$$\bar{\sigma}[\boldsymbol{G}_0(j\omega)\boldsymbol{W}(j\omega)] < \frac{1}{B(\omega)} \qquad \forall\omega, \tag{4.48}$$

where $\boldsymbol{G}_0(j\omega)\boldsymbol{W}(j\omega) = \boldsymbol{T}_0(j\omega)$ is the complementary sensitivity function [155].

The three different approaches to enforcing a constraint on the maximum disturbance enhancement detailed in Section 4.4.2 can be obtained for the IMC controller architecture by substituting equation 4.47 into equations 4.24, 4.31 and 4.36.

4.6 Minimising the Modal Error Signal

The general design method for the modal feedback controller requires the transducer weightings, $\boldsymbol{w}_L$ and $\boldsymbol{w}_M$, and the feedback controller, H, to be set such that the open-loop response is maximised over the frequencies where the targeted modes occur, whilst minimising the response at other frequencies and maintaining a robustly stable system, as described in the previous section. Previous work on acoustic modal control has achieved this design process in two stages – first selecting the transducer weightings and then designing the response of the controller (see for example [146, 147]). This design approach has also been investigated within the work leading to this thesis and a novel method of selecting the transducer weightings has been proposed by the author in [159]. This method defines the sensor weightings by maximising the response between the composite source strength, q_c, and the composite pressure due to the secondary sources, p_{c_s}, over the frequency range where control is required whilst minimising this response at all other frequencies. The source weightings are defined by maximising the response between the composite source strength, q_c, and the pressures produced at the error sensors by the secondary sources, $\boldsymbol{p}_s$, over the frequency range where control is required whilst minimising this response at all other frequencies. This method of defining the transducer weightings, or spatial filtering, is combined with a simple temporal filtering method employing a modally tuned all-pass and bandpass filter as in [151] and initial results using this method have been presented at ICSV19 in [159]. The method of defining the transducer weightings is presented and discussed in Appendix H.

The main limitation of the controller design strategy discussed in Appendix H is that due to the separate design of the transducer weightings and feedback controller they do not guarantee a system which is optimal overall. Therefore, a method of optimising the transducer weightings and controller response in parallel has been developed. This method of designing the modal feedback controller uses IMC and an optimisation routine following the method proposed by Rafaely and Elliott in [156].

4.6.1 Controller Design and Optimisation

There are two methods by which the modal feedback controller presented in Figure 4.6a may be formulated using an IMC architecture. In the first method the transducer weightings are

included in the IMC controller modelling path, as shown in Figure 4.11, and this leads to the modal error signal being minimised. Using this formulation and assuming that the modelled plant is equal to the nominal plant, that is $\hat{\boldsymbol{G}}(j\omega) = \boldsymbol{G}_0(j\omega)$, the response of the complete SISO feedback controller is given by

$$H(j\omega) = \frac{-W(j\omega)}{1 + \boldsymbol{w}_L^T \boldsymbol{G}_0(j\omega)\boldsymbol{w}_M W(j\omega)}, \tag{4.49}$$

where the nominal plant is given by the combination of the nominal acoustic response, $\boldsymbol{Z}_{s0}$ and the loudspeaker response, $\boldsymbol{Y}_L$, as

$$\boldsymbol{G}_0(j\omega) = \boldsymbol{Z}_{s0}(j\omega)\boldsymbol{Y}_L(j\omega). \tag{4.50}$$

In contrast to feedforward control, in order to rigorously investigate feedback control it is necessary to include a model of the secondary sources' responses. Including a model of the secondary sources' responses ensures that, as in a practical system, the magnitude of the open-loop frequency response tends to zero at high frequencies [132]. This allows the stability of the system to be confirmed whilst only modelling a limited frequency range. That is, provided the magnitude of the open-loop response rolls off at high frequencies, it is possible to assume that the system's stability will not be affected by the high frequency response. Inclusion of the secondary sources' responses is also necessary as the additional phase-lag that they introduce to the system will have an effect on the stability and, therefore, the predicted performance of the feedback active noise control system. In this instance the response of the secondary source loudspeakers will be modelled using a second-order, SDOF, system, which is included in the model via $\boldsymbol{Y}_L(j\omega)$, and the details of the loudspeaker model are presented in Appendix E.

The controller formulation presented in Figure 4.11 conveniently leads to the minimisation of the composite error signal, p_c, which is given by substituting equation 4.49 into equation 4.10 as

$$p_c(j\omega) = \left[1 + \boldsymbol{w}_L^T \boldsymbol{G}_0(j\omega)\boldsymbol{w}_M W(j\omega)\right] \boldsymbol{w}_L^T \boldsymbol{p}_p(j\omega). \tag{4.51}$$

The aim of the modal feedback controller in this case is to minimise the mean-square of the composite error signal. For a random noise disturbance, such as road noise, this cost function can conveniently be defined as [132]

$$J_c(j\omega) = E\left(p_c(j\omega)p_c^*(j\omega)\right), \tag{4.52}$$

where E is the expectation operator and * indicates the complex conjugate operation. Substituting equations 4.51 and 4.30 into equation 4.52 gives

$$J_c(j\omega) = \left[1 + \boldsymbol{w}_L^T \boldsymbol{G}_0(j\omega)\boldsymbol{w}_M W(j\omega)\right] \boldsymbol{w}_L^T \boldsymbol{S}_{pp}(j\omega)\boldsymbol{w}_L \left[1 + W^*(j\omega)\boldsymbol{w}_M^T \boldsymbol{G}_0^H(j\omega)\boldsymbol{w}_L\right]. \tag{4.53}$$

Since the IMC controller is a SISO system, the cost function to be minimised, given by equation

4.53, can be rewritten as

$$J_c(j\omega) = |1 + \boldsymbol{w}_L^T \boldsymbol{G}_0(j\omega)\boldsymbol{w}_M W(j\omega)|^2 \boldsymbol{w}_L^T \boldsymbol{S}_{pp}(j\omega)\boldsymbol{w}_L. \tag{4.54}$$

In comparison to the work presented by Rafaely and Elliott [156] and standard feedback control, the cost function for the modal control system not only requires the optimisation of the control filter, but also the transducer weights. From equation 4.54 it can be seen that the cost function is not quadratic with respect to the transducer weights. However, the cost function appears to be convex, as suggested by the simulations reported below, and, therefore, has a global minimum provided that the sensor weighting vector is constrained to be non-zero and within specific bounds such that any overall gain required in the feedback loop is implemented by the control filter and not the transducer weightings. This can be achieved by constraining the transducer weights such that

$$\begin{aligned} \boldsymbol{w}_L^T \boldsymbol{w}_L &= 1, \\ \boldsymbol{w}_M^T \boldsymbol{w}_M &= 1. \end{aligned} \tag{4.55}$$

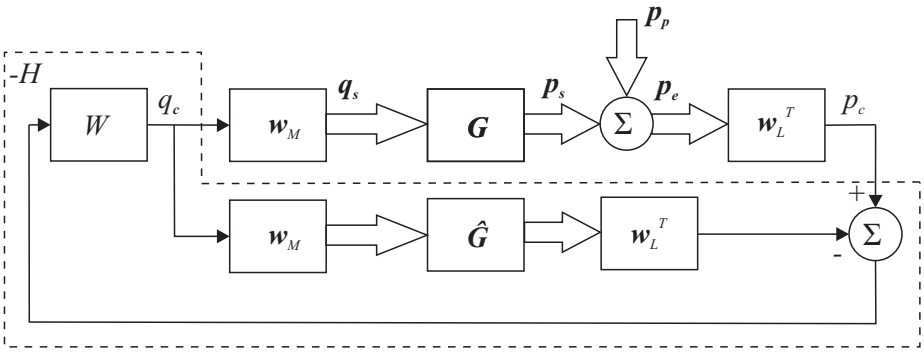

Figure 4.11: Block diagram of the multi-source, multi-sensor modal feedback control system implemented using an internal model control (IMC) architecture with the transducer weights in the modelling path.

The robust stability, disturbance enhancement and controller stability constraints for the IMC controller in Figure 4.11 can be derived by substituting equation 4.49 into equations 4.16, 4.22 and 4.44 respectively. The robust stability constraint for the single mode controller is given by

$$|\boldsymbol{w}_L^T \boldsymbol{G}_0(j\omega)\boldsymbol{w}_M W(j\omega)| < \frac{1}{B(j\omega)} \quad \forall\omega, \tag{4.56}$$

and the disturbance enhancement constraint is given by

$$|1 + \boldsymbol{w}_L^T \boldsymbol{G}_0(j\omega)\boldsymbol{w}_M W(j\omega)| < A \quad \forall\omega, \tag{4.57}$$

where, for the controller in Figure 4.11, it is the enhancement of the composite error signal that

is limited. The open-loop controller stability constraint is given by

$$\Re\{\boldsymbol{w}_L^T \boldsymbol{G}_0(j\omega)\boldsymbol{w}_M W\} > -1 \quad \forall\omega. \tag{4.58}$$

In a real-time system it is important for the controller to be causally constrained [132] and this can be achieved in the IMC feedback controller by defining the control filter, W, as a finite impulse response (FIR) filter as in feedforward control [132]. In the modal control system W can be implemented as a single FIR filter with a vector of I coefficients, $\boldsymbol{w}$. The optimisation of the FIR control filter in a standard feedback controller could be achieved using the analytical methods developed for feedforward controllers as described in [132]. However, to minimise the cost function whilst also maintaining the robust stability and disturbance enhancement constraints is more complex and in the case of the modal feedback controller it is also necessary to optimise the transducer weightings. This constrained minimisation can be achieved by discretising the design problem in the frequency domain and solving using an optimisation strategy. This method has been employed by Rafaely and Elliott [156] to design a SISO IMC feedback controller for an active headrest application with an H_2 performance criterion and both H_2 and H_∞ constraints. In the SISO headrest system the control filter is implemented as an FIR filter and, therefore, the cost function and constraints become convex functions of the filter coefficients. The optimal solution of this convex optimisation problem is calculated by discretising the frequency responses of the nominal plant, control filter, and constraint functions and using sequential quadratic programming to calculate the optimal solution. The same convex optimisation problem has also been solved using an iterative gradient-descent method in place of the sequential quadratic programming in [160] and achieved essentially the same results [132]. Frequency discretisation had previously been proposed in [161] and employed in an acoustic application in [162]. This method of IMC controller design and optimisation will be extended to the modal feedback controller.

By discretising the frequency responses of the plant and controller at N_F linearly spaced frequency intervals between 0 Hz and the maximum frequency of the system, the design objective can be expressed using equations 4.54 through to 4.58. However, if the primary disturbance is known to be dominant over a specific frequency range, or control is required over a predefined frequency range, then the optimisation problem can be modified such that maximal disturbance attenuation is achieved over a specified bandwidth whilst the constraints are maintained over the full bandwidth. If the lower and upper bounds of the bandwidth over which disturbance attenuation is required are defined as f_1 and f_2 respectively and the number of discrete frequency

points in this interval is N_{F_c}, then the optimisation problem can be expressed as

$$\begin{aligned}
\min_{\boldsymbol{w}} \quad & \frac{1}{N_{F_c}} \sum_{f=f_1}^{f_2} |1+\boldsymbol{w}_L^T \boldsymbol{G}_0(f)\boldsymbol{w}_M W(f)|^2 \boldsymbol{w}_L^T \boldsymbol{S}_{pp}(f)\boldsymbol{w}_L, \\
\text{subject to} \quad & \boldsymbol{w}_L^T \boldsymbol{w}_L = 1, \\
& \boldsymbol{w}_M^T \boldsymbol{w}_M = 1, \\
& \left|\boldsymbol{w}_L^T \boldsymbol{G}_0(f)\boldsymbol{w}_M W(f) B(f)\right| < 1 \quad \forall f, \\
& \left|1+\boldsymbol{w}_L^T \boldsymbol{G}_0(f)\boldsymbol{w}_M W(f)\right| \frac{1}{A} < 1 \quad \forall f \\
& \Re\{\boldsymbol{w}_L^T \boldsymbol{G}_0(j\omega)\boldsymbol{w}_M W\} > -1 \quad \forall f.
\end{aligned} \tag{4.59}$$

In order to solve this optimisation problem using sequential quadratic programming the cost function must be convex and the constraints must be affine [163]. As detailed above, the cost function appears be convex when the transducer weightings are suitably constrained, however, the optimisation described by equation 4.59 is with respect to the filter coefficients and, therefore, as in [164] it is important to show that the use of sequential quadratic programming is appropriate. Since the discretised frequency response of the control filter is linearly related to the filter coefficients as

$$\boldsymbol{W}(f) = \frac{1}{N_F} \sum_{i=0}^{I-1} \boldsymbol{w}_i e^{-j2\pi i f/N_F}, \tag{4.60}$$

then the optimisation problem is also convex with respect to the filter coefficients. Therefore, the optimal controller will be calculated using sequential quadratic programming [163] which has been implemented in Matlab using the built-in function *fmincon* in Matlab v2010b.

A significant advantage of the frequency domain design of the feedback controller described by equation 4.59 compared to other popular feedback controller design methods, such as McFarlane-Glover loop-shaping [158], is that the required variables can be determined directly from experimental data. That is, there is no need for weighting functions to be defined by the designer and there is no need to calculate an accurate state-space model of the plant. However, to ensure that the optimisation described in equation 4.59 actually achieves the optimal result with respect to the real-world problem, it is important to select the number of frequencies at which the optimisation is defined, N_F, to be large enough such that the frequency responses are represented accurately in the discretised domain, whilst not being so large that the optimisation problem is made unnecessarily complex [156]. This can be achieved by ensuring that the impulse responses of the discretised functions decay away and thus have negligible amplitude at the end of their responses [164]. It is also important that the length of the FIR control filters, I, is set sufficiently long such that the solution is optimal. This can be achieved by gradually increasing I until the performance of the optimised controller does not improve [162, 156].

4.6.2 Control of an Internal Acoustic Primary Source

The modal feedback controller with four secondary sources and eight error microphones positioned in the corners of the non-rigid walled rectangular car cabin sized enclosure has been optimised according to equation 4.59 for the case when there is a single acoustic primary disturbance positioned at $\boldsymbol{x} = [0, L_2/2, 0]$ as shown in Figure 2.6. The frequency range considered is 0 to 500 Hz and the frequency range of the cost function has been limited to frequencies below 115 Hz by setting $f_1 = 0$ and $f_2 = 115$ in the optimisation. This control bandwidth limits control to frequencies where the response is dominated by the first longitudinal acoustic mode. If the control bandwidth is increased, although the controller can continue to minimise the modal, composite error signal, it is not capable of achieving reductions in the sum of squared error sensor pressures since the response at higher frequencies is not dominated by a single acoustic mode. The frequency responses have been discretised at $N_F = 198$ frequencies and the control filter's length has been set to $I = 64$. These parameters have been chosen as outlined above to ensure that a close to optimal solution is obtained without unnecessary computational expense. The robust stability constraint, given by equation 4.56, has been set to $B = 0.5$ and the disturbance enhancement constraint given by equation 4.57 has been set to $A = 2$. The resulting response and performance of this controller are presented in Figure 4.12.

Figures 4.12a and 4.12b show the robustness and enhancement constraints given by equations 4.56 and 4.57 respectively. In each case the black dashed line shows the level above which the constraints are violated. From these two plots it can be seen that the optimised controller maintains both the robustness and enhancement constraints. Figure 4.12c shows the Nyquist plot of the open-loop response, $\boldsymbol{w}_L^T \boldsymbol{G}_0(j\omega)\boldsymbol{w}_M H$, and it can be seen that the $(-1, 0)$ point is not encircled indicating a stable closed loop controller. Figure 4.12d shows the Nyquist plot of the open-loop IMC controller, $\boldsymbol{w}_L^T \boldsymbol{G}_0(j\omega)\boldsymbol{w}_M W$, and it can be seen that this is also stable and has been constrained such that the stability constraint given by equation 4.58 is maintained. Figure 4.12e shows the change in the composite error signal, p_c, as a result of the feedback controller. From this plot it can be seen that narrowband reductions of up to 20 dB have been achieved and over the bandwidth of the first longitudinal acoustic mode at 85 Hz reductions of up to 12 dB are achieved. The controller is thus doing a good job of attenuating the composite error signal it was designed to control within the imposed constraints. The effect of this controller on the overall sound field in the enclosure can be estimated from the sum of the squared error sensor pressures, J_p. Figure 4.12f shows this before and after control and from this plot it can be seen that the reduction of the composite error signal directly translates into a reduction in J_p of 12 dB around the first longitudinal acoustic mode. However, although the enhancement constraint on the *composite* error signal is satisfied, it can be seen from this plot that enhancements of up to around 15 dB are produced in the sum of the squared pressures. Therefore, despite the significant levels of attenuation at about 85 Hz, these significant enhancements at higher frequencies will limit the use of this control strategy.

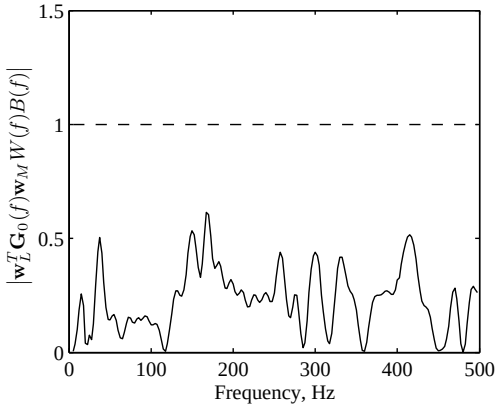

(a) Robust stability measure given by equation 4.56.

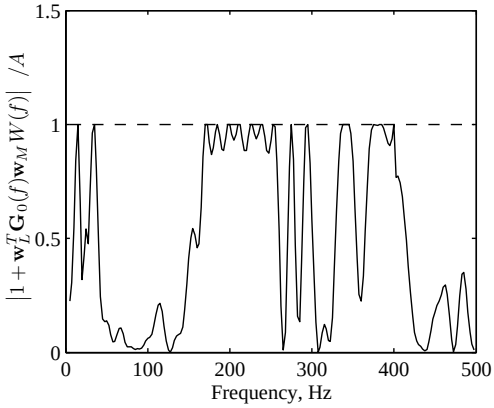

(b) Error signal enhancement measure given by equation 4.57.

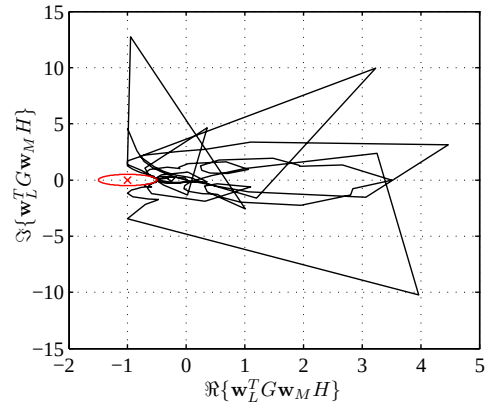

(c) The Nyquist plot of the open-loop frequency response.

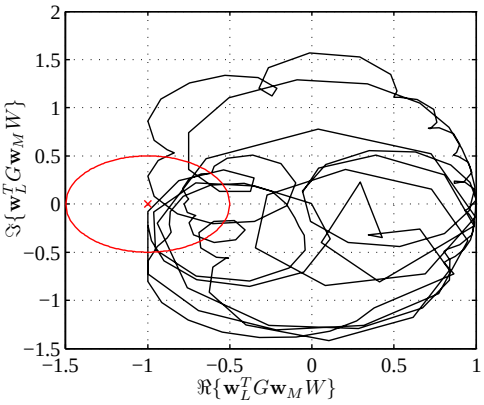

(d) The Nyquist plot of the IMC controller.

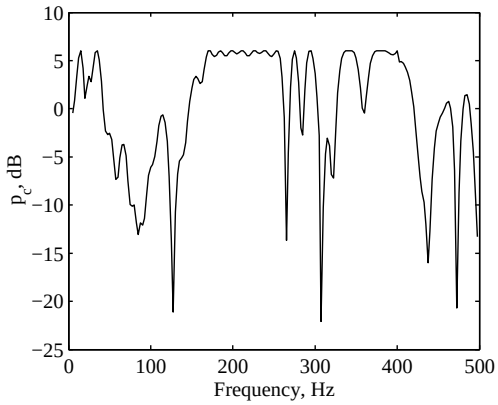

(e) The change in the composite error signal, p_c, due to feedback control plotted in decibels.

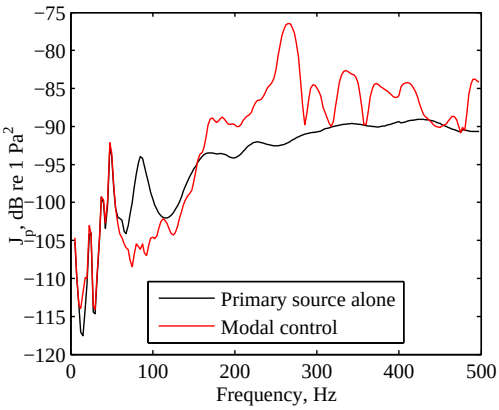

(f) The cost function, J_p, calculated from the eight corner error sensors when driven by a primary internal acoustic source alone (—) and when p_c has been minimised (—).

Figure 4.12: The performance of the IMC feedback controller with an $I = 64$ coefficient FIR control filter, transducer weighting in the modelling path, a robust stability constraint given by equation 4.56, an enhancement constraint given by equation 4.57, and a cost function frequency range of 0 to 115 Hz optimised to control an internal acoustic primary source positioned as shown in Figure 2.6.

4.7 Minimising the Sum of Squared Error Signals

An alternative method of formulating the modal feedback controller presented in Figure 4.6a using the IMC architecture is to include the transducer weightings in the control path, as shown in Figure 4.13. This results in a more complex optimisation problem as the feedback controller now has L_e inputs and M outputs, however, it allows the controller to be optimised and constrained based on the sum of the squared error signals directly.

4.7.1 Controller Design and Optimisation

Assuming again that the modelled plant is equal to the nominal plant response, the response of the MIMO IMC feedback controller is given following equation 4.45 as

$$\boldsymbol{H}(j\omega) = -\left[\boldsymbol{I} + \boldsymbol{w}_M W(j\omega)\boldsymbol{w}_L^T \boldsymbol{G}_0(j\omega)\right]^{-1} \boldsymbol{w}_M W(j\omega)\boldsymbol{w}_L^T, \tag{4.61}$$

where the MIMO control filter in equation 4.45 is given by

$$\boldsymbol{W}(j\omega) = \boldsymbol{w}_M W(j\omega)\boldsymbol{w}_L^T. \tag{4.62}$$

The input error signal to the MIMO controller in Figure 4.13 is the vector of error signals $\boldsymbol{p}_e$ and, therefore, with this controller formulation the error sensor pressures can be minimised directly. The vector of error signals is given by

$$\boldsymbol{p}_e(j\omega) = \left[\boldsymbol{I} + \boldsymbol{G}_0(j\omega)\boldsymbol{w}_M W(j\omega)\boldsymbol{w}_L^T\right] \boldsymbol{p}_p(j\omega), \tag{4.63}$$

where the bracketed term is equivalent to the sensitivity function given by equation 4.47 for the MIMO IMC controller. Despite the additional complexity of optimising the controller presented in Figure 4.13, it can be shown that implementing a fixed feedback controller designed using this method is no more demanding than using the IMC formulation of the modal controller shown in Figure 4.11. From Figure 4.6a it can be seen that in the standard feedback configuration the MIMO feedback controller is given by

$$\boldsymbol{H}(j\omega) = \boldsymbol{w}_M H(j\omega)\boldsymbol{w}_L^T, \tag{4.64}$$

and, therefore, by equating equations 4.64 and 4.61, rearranging and cancelling it can be shown that the SISO feedback control filter's frequency response, $H(j\omega)$, is still given by equation 4.49 despite the additional complexity of the IMC controller.

The aim of the controller in Figure 4.13 can be defined as minimising the sum of the mean-square error signals, as in the feedforward controller in Chapter 3. Using the trace of a square matrix, which is the sum of its diagonal elements, the cost function to be minimised can be written as [132]

$$J_p(j\omega) = \text{trace}\left[E\left(\boldsymbol{p}_e(j\omega)\boldsymbol{p}_e^H(j\omega)\right)\right]. \tag{4.65}$$

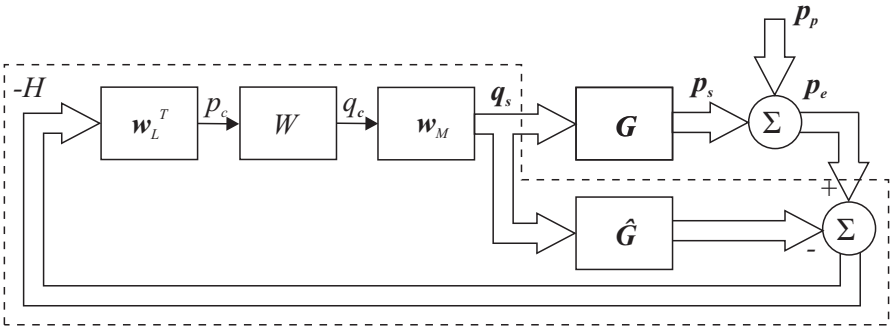

Figure 4.13: Block diagram of the multi-source, multi-sensor modal feedback control system implemented using an internal model control (IMC) architecture with the transducer weights in the control path.

Substituting equation 4.63 into equation 4.65 gives

$$J_p(j\omega) = \text{trace}\left[\left[\boldsymbol{I}+\boldsymbol{G}_0(j\omega)\boldsymbol{w}_M W(j\omega)\boldsymbol{w}_L^T\right]\boldsymbol{S}_{pp}(j\omega)\left[\boldsymbol{I}+\boldsymbol{G}_0(j\omega)\boldsymbol{w}_M W(j\omega)\boldsymbol{w}_L^T\right]^H\right], \quad (4.66)$$

where $\boldsymbol{S}_{pp}(j\omega)$ is the matrix of power and cross spectral densities of the primary disturbance given by equation 4.30. This can be expanded to give

$$\begin{aligned} J_p(j\omega) = \text{trace}\big[&\boldsymbol{G}_0(j\omega)\boldsymbol{w}_M W(j\omega)\boldsymbol{w}_L^T\boldsymbol{S}_{pp}(j\omega)\boldsymbol{w}_L W^*(j\omega)\boldsymbol{w}_M^T\boldsymbol{G}_0^H(j\omega)+\cdots \\ &\boldsymbol{G}_0(j\omega)\boldsymbol{w}_M W(j\omega)\boldsymbol{w}_L^T\boldsymbol{S}_{pp}(j\omega)+\boldsymbol{S}_{pp}(j\omega)\boldsymbol{w}_L W^*(j\omega)\boldsymbol{w}_M^T\boldsymbol{G}_0^H(j\omega)+\boldsymbol{S}_{pp}(j\omega)\big]. \end{aligned} \quad (4.67)$$

From equations 4.66 and 4.67 it can be seen that the cost function in this case is quadratic with respect to both the control filter and the transducer weightings, therefore, the design problem can once again be solved using convex optimisation techniques. However, to ensure that their is a unique solution the transducer weightings should be constrained according to equation 4.55.

The robust stability constraint for the IMC controller in Figure 4.13 can be derived by substituting equation 4.62 into equation 4.48 to give

$$\bar{\sigma}\left[\boldsymbol{G}_0(j\omega)\boldsymbol{w}_M W(j\omega)\boldsymbol{w}_L^T\right] < \frac{1}{B(\omega)} \qquad \forall\omega, \quad (4.68)$$

where the bracketed term is the complementary sensitivity function. In the following simulations the constraint on the maximum enhancement in the individual error signals will be used, since it is this constraint that gives the ideal performance. The alternative MIMO enhancement constraints will be investigated more thoroughly in the context of the fully MIMO feedback controller in the following chapter. For the modal controller the constraint on the maximum enhancement in the individual error sensor pressures is given by substituting equation 4.62 into equation 4.36 to give

$$\max\left[\text{diag}\left(\boldsymbol{D}(j\omega)\boldsymbol{S}_0(j\omega)\boldsymbol{S}_{pp}(j\omega)\boldsymbol{S}_0^H(j\omega)\right)\right] < A \quad \forall\omega, \quad (4.69)$$

where $\boldsymbol{S}_0$ is the complex sensitivity function for the controller shown in Figure 4.13 and is

given by

$$\boldsymbol{S}_0 = \left(\boldsymbol{I} + \boldsymbol{G}_0(j\omega)\boldsymbol{w}_M W(j\omega)\boldsymbol{w}_L^T\right). \tag{4.70}$$

The design of the modal IMC feedback controller with the transducer weights in the control path can be achieved using the same method as discussed for the modal IMC feedback controller with the transducer weights in the model path, which followed the work presented in [156]. Using this approach the SISO control filter, W, is implemented as an I coefficient filter, $\boldsymbol{w}$, and the optimisation is implemented in the discrete frequency domain. Using this method the design objective can be expressed using equations 4.58, 4.55, 4.67, 4.68 and 4.69 as

$$\begin{aligned}
\min_{\boldsymbol{w}} \quad & \frac{1}{N_{F_c}} \sum_{f=f_1}^{f_2} \text{trace}\left[\boldsymbol{G}_0(f)\boldsymbol{w}_M W(f)\boldsymbol{w}_L^T \boldsymbol{S}_{pp}(f)\boldsymbol{w}_L W^*(f)\boldsymbol{w}_M^T \boldsymbol{G}_0^H(f) + \cdots\right. \\
& \left. \boldsymbol{G}_0(f)\boldsymbol{w}_M W(f)\boldsymbol{w}_L^T \boldsymbol{S}_{pp}(f) + \boldsymbol{S}_{pp}(f)\boldsymbol{w}_L W^*(f)\boldsymbol{w}_M^T \boldsymbol{G}_0^H(f) + \boldsymbol{S}_{pp}(f)\right], \\
\text{subject to} \quad & \boldsymbol{w}_L^T \boldsymbol{w}_L = 1, \\
& \boldsymbol{w}_M^T \boldsymbol{w}_M = 1, \\
& \bar{\sigma}\left[\boldsymbol{G}_0(f)\boldsymbol{w}_M W(f)\boldsymbol{w}_L^T B(f)\right] < 1 \quad \forall f, \\
& \max\left[\text{diag}\left(\boldsymbol{D}(f)\boldsymbol{S}_0(f)\boldsymbol{S}_{pp}(f)\boldsymbol{S}_0^H(f)\right)\right]\frac{1}{A} < 1 \quad \forall f, \\
& \Re\{\boldsymbol{w}_L^T \boldsymbol{G}_0(j\omega)\boldsymbol{w}_M W\} > -1 \quad \forall f.
\end{aligned} \tag{4.71}$$

where the cost function has once again been defined over a set bandwidth between f_1 and f_2 to allow the controller to target a specific frequency range. This process also has the effect of reducing the optimisation space and therefore increasing the speed of the optimisation.

4.7.2 Control of an Internal Acoustic Primary Source

The modal feedback controller with four secondary sources and eight error microphones positioned in the corners of the non-rigid walled rectangular car cabin sized enclosure has been optimised according to equation 4.71 for the case when there is a single acoustic primary disturbance positioned at $\boldsymbol{x} = [0, L_2/2, 0]$ as shown in Figure 2.6. The frequency range considered is 0 to 500 Hz and the frequency range of the cost function has been limited to frequencies below 200 Hz by setting $f_1 = 0$ and $f_2 = 200$ in the optimisation. This control bandwidth has been selected based on the bandwidth controllable using the feedforward control strategy in the previous chapter, and avoids the controller attempting to achieve localised regions of control around the error microphones at higher frequencies and consequently limiting the control achievable over the practical low frequency bandwidth. The frequency responses have again been discretised at $N_F = 198$ frequencies and the control filter's length has again been set to $I = 64$. These parameters are consistent with the alternative formulation of the modal controller considered in Section 4.6. The robust stability constraint, given by equation 4.68, has been set to $B = 0.5$ and the disturbance enhancement constraint given by equation 4.69 has been set to $A = 4$, which gives a maximum enhancement in the individual squared error sensor pressures

of 6 dB. The resulting response and performance of this controller are presented in Figure 4.14.

From Figures 4.14a and 4.14b it can be seen that the robustness and enhancement constraints are maintained. The Nyquist plot of the open-loop response is shown in Figure 4.14c and it can be seen that the control system is stable. Figure 4.14d shows the Nyquist plot of the IMC controller and it can be seen that the additional constraint to ensure a stable open-loop controller given by equation 4.58 is not active. Figure 4.14e shows the sum of squared error sensor pressures before and after control. From this plot it can be seen that, although the level of control at the first longitudinal acoustic mode at 85 Hz has been reduced compared to the controller investigated in Figure 4.12, the bandwidth of control has been increased up to 200 Hz; this is due to the increase in the cost function bandwidth, but it is important to highlight that the controller optimised to minimise the sum of the squared error sensor pressures can achieve identical levels of control at the first longitudinal mode to the results presented in Figure 4.12 if the control bandwidth is limited. In comparison to the IMC modal feedback controller optimised to minimise the modal error signal, it can be seen that the enhancement constraint has ensured that the high frequency enhancements in the sum of the squared error sensor pressures are limited. As an independent check that global control has been achieved, Figure 4.14f shows the total acoustic potential energy in the non-rigid walled rectangular enclosure before and after control. From this plot it can be seen that significant reductions in the total acoustic potential energy are also achieved at the first longitudinal mode, while the reductions at frequencies above 120 Hz are reduced in comparison to those shown in J_p, but the enhancements at high frequencies remain limited.

The performance of the modal feedback controller has also been synthesised using the transfer responses measured in the car cabin mock-up, as detailed in Section 2.3. These results show similar levels of control and a similar control bandwidth to the simulation results. The similarity between the control achieved in the simulated and measured mock-up enclosures has previously been highlighted in Section 3.2.2 in the context of feedforward control and therefore these results are not included here.

4.7.3 Control of Multiple Uncorrelated Structural Primary Forces

The aim of the feedback control system is to control the noise due to road-tyre interactions. As discussed in Chapter 1, the generated vibrations propagate through the structure of the car and are then radiated into the car cabin. This means that the primary disturbance due to road noise will be generated by a number of uncorrelated primary forces. Therefore, it is important to investigate the performance of the IMC modal feedback controller when the non-rigid enclosure is excited by multiple uncorrelated primary forces. For the case when there are M_p uncorrelated structural primary forces the matrix of power and cross spectral densities of

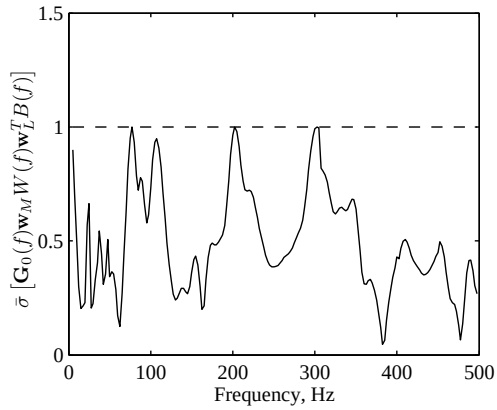

(a) Robust stability measure given by equation 4.68.

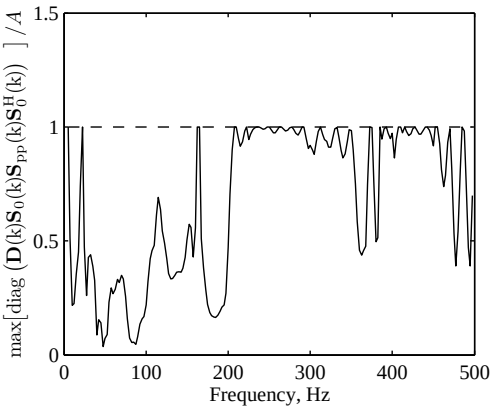

(b) Disturbance enhancement measure given by equation 4.69.

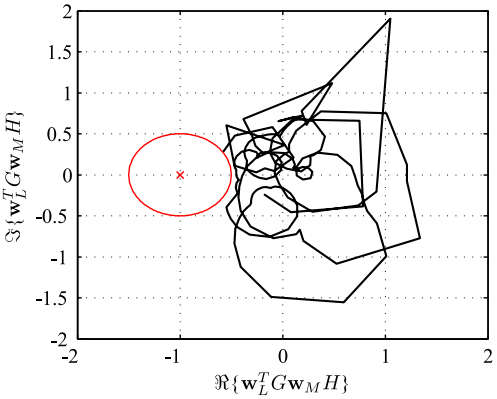

(c) The Nyquist plot of the open-loop frequency response.

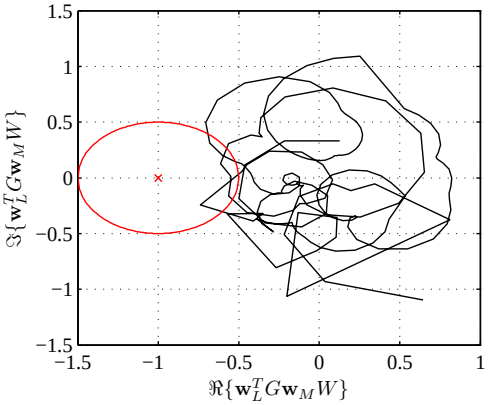

(d) The Nyquist plot of the IMC controller.

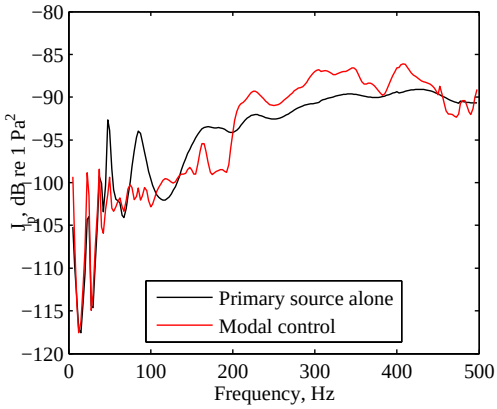

(e) The cost function, J_p, calculated from the eight corner error sensors when driven by a primary internal acoustic source alone (—) and when J_p has been minimised (—).

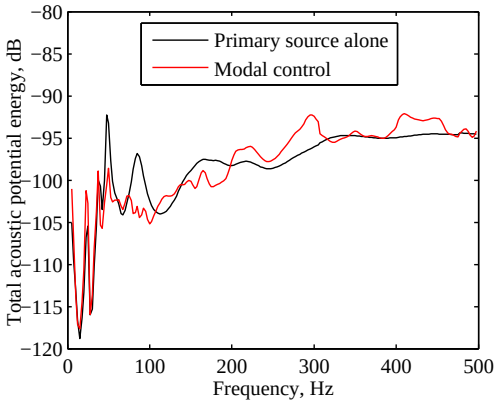

(f) The total acosutic potential energy, E_p, when the non-rigid walled enclosure is driven by a primary internal acoustic source alone (—) and when J_p has been minimised (—).

Figure 4.14: The performance of the IMC feedback controller with an $I = 64$ coefficient FIR control filter, transducer weighting in the control path, a robust stability constraint given by equation 4.68, an enhancement constraint given by equation 4.69, and a cost function frequency range from 0 to 200 Hz optimised to control an internal acoustic primary source positioned as shown in Figure 2.6.

the primary pressure field given by equation 4.30 can be expressed as

$$\begin{aligned}\boldsymbol{S}_{pp}(j\omega) &= E\left(\boldsymbol{p}_p(j\omega)\boldsymbol{p}_p^H(j\omega)\right), \\ &= E\left(\boldsymbol{Z}'_p(j\omega)\boldsymbol{f}_p(j\omega)\boldsymbol{f}_p^H(j\omega)\boldsymbol{Z}'_p(j\omega)\right), \\ &= \boldsymbol{Z}'_p(j\omega)\boldsymbol{S}_{ff}(j\omega)\boldsymbol{Z}'_p(j\omega), \end{aligned} \tag{4.72}$$

where $\boldsymbol{S}_{ff}(j\omega)$ is the $(M_p \times M_p)$ matrix of power and cross spectral densities of the M_p primary structural excitations and for a set of uncorrelated structural sources is a diagonal matrix.

Figure 4.15 shows the performance of the IMC modal controller optimised to minimise the sum of squared error sensor pressures produced when the floor of the non-rigid enclosure is driven by 18 uncorrelated primary point forces positioned as shown in Figure 4.16. The enhancement is again limited at each individual microphone, as discussed in Section 4.4.2. From Figures 4.15a and 4.15b it can be seen that the modal controller has maintained the robustness and stability constraints. Figures 4.15c and 4.15d show the Nyquist plots of the open-loop response and the IMC controller and from these two plots it can be seen that the system is both closed and open loop stable. Figure 4.15e shows the cost function, J_p, before and after modal feedback control. From this plot it can be seen that significant levels of attenuation are achieved at frequencies below around 100 Hz and the significant resonance at around 40 Hz is reduced by around 16 dB. However, the resonance that is excited at 70 Hz is not controllable by the modal feedback controller. There are enhancements in J_p at higher frequencies, however, these are once again limited to around 6 dB.

Figure 4.17 shows the transducer weightings and FIR filter coefficients for the modal controller optimised to minimise the sum of the squared error sensor pressures produced by the 18 uncorrelated structural excitations. These results are presented to highlight the simplicity of implementing the modal feedback controller and will provide a comparison to the MIMO feedback controller investigated in the following chapter. From the microphone weightings shown in Figure 4.17a it can be seen that microphones 3-8 are all summed in-phase and with similar magnitudes whilst the phase of microphones 1 and 2 is inverted and the magnitude of their weighting is significantly lower than for the rest of the microphones. This can be related to the dominance of the resonances in the uncontrolled response presented in Figure 4.15e that occur below the first longitudinal mode and, therefore, excite the compliant mode of the enclosure. The loudspeaker weightings shown in Figure 4.17b result in the four loudspeakers being driven in-phase with each other which can also be related to the dominance of the compliant acoustic mode, however, the front two loudspeakers (1 and 2) are driven with around half the amplitude of the rear loudspeakers. The coefficients of the single 64 coefficient FIR filter are presented in Figure 4.17c and it can be seen that the filter response has largely decayed to zero over this length indicating that the filter length is adequate.

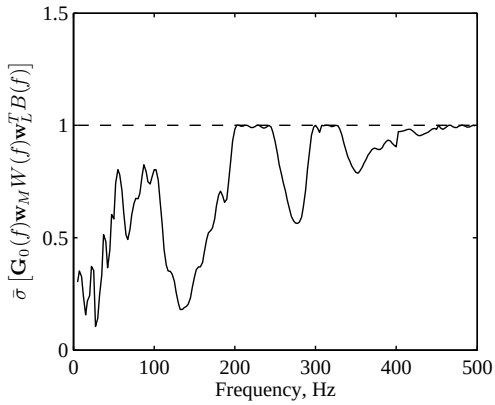

(a) Robust stability measure given by equation 4.68 which must be less than 1 at all frequencies to ensure the robust stability constraint is satisfied with a plant uncertainty of $B = 0.5$.

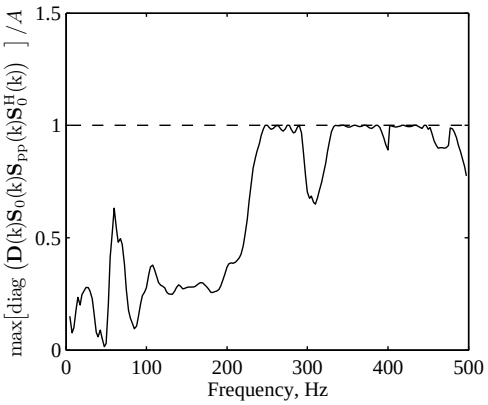

(b) Maximum individual squared disturbance pressure enhancement measure given by equation 4.69 which must be less than 1 at all frequencies to ensure the individual squared disturbance pressures are not enhanced by more than a factor of $A = 4$.

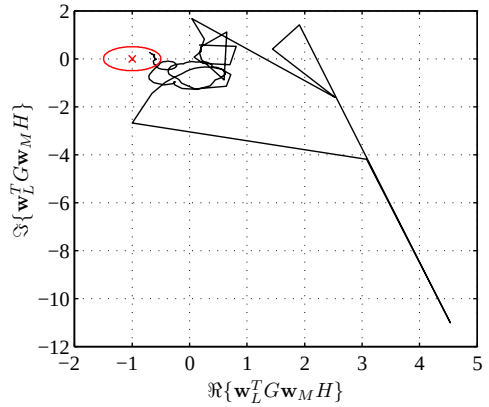

(c) The Nyquist plot of the open-loop frequency response.

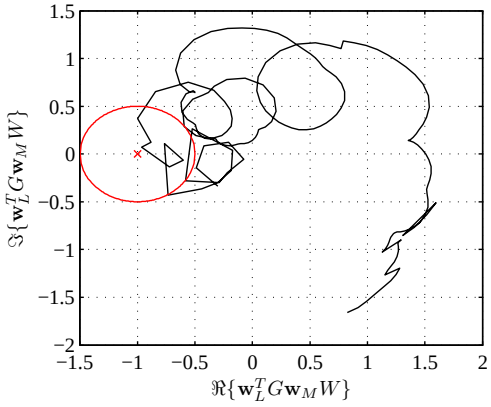

(d) The Nyquist plot of the IMC controller.

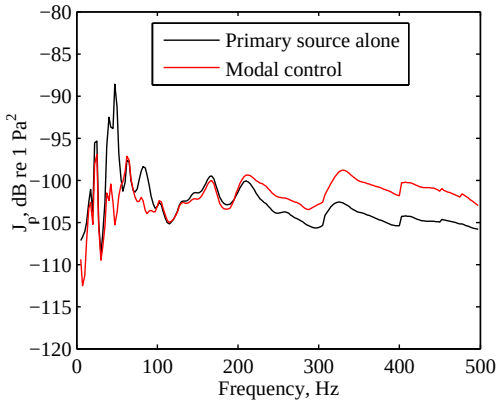

(e) The cost function, J_p, calculated from the eight corner error sensors when driven by a primary excitation alone (—) and when J_p has been minimised (—).

Figure 4.15: The performance of the IMC feedback controller with an $I = 64$ coefficient FIR control filter, transducer weighting in the control path, a robust stability constraint given by equation 4.68, an enhancement constraint given by equation 4.69, and a cost function frequency range from 0 to 200 Hz optimised to control the pressures produced in the simulated non-rigid walled enclosure when driven by 18 uncorrelated structural excitations positioned as shown in Figure 4.16.

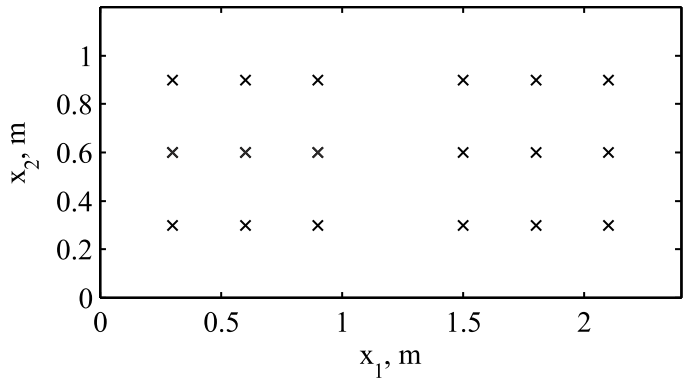

Figure 4.16: Positions of the 18 primary structural excitations on the floor of the non-rigid walled enclosure.

4.8 Summary

The use of feedback control to control road noise in the car cabin has been highlighted as a potentially low-cost noise control solution that can be integrated with feedforward control systems for engine noise control. Previous work has shown that feedback control can achieve significant levels of road noise control in the front seats of a car cabin [59]. This chapter has investigated alternative feedback control strategies that may be able to achieve significant levels of global control. To achieve global control it is necessary to employ both multiple sensors and sources, as in feedforward control, however, a fully MIMO feedback controller requires both significant computational time to optimise and a large number of filters to implement. Therefore, modal feedback control has been investigated as a potential method of achieving global noise control whilst limiting the signal processing requirements.

The standard modal feedback controller has initially been formulated and standard feedback control theory has been presented for both SISO and MIMO feedback control systems. In addition to the standard robustness and enhancement constraints, a constraint on the enhancement in the individual error signals has been derived, which perhaps provides a more practically optimal constraint. Design of the modal feedback controller using IMC has been highlighted as a convenient method of designing the modal feedback controller since the optimisation of the controller does not require the designer to specify weighting functions or calculate an accurate state-space model.

Using the IMC architecture leads to two alternative formulations of the modal feedback controller, both of which lead to convex cost functions which allow the controllers to be conveniently optimised. The first formulation, in which the transducer weightings are included in the modelling path, operates on the modal error signal and therefore optimisation and enhance-

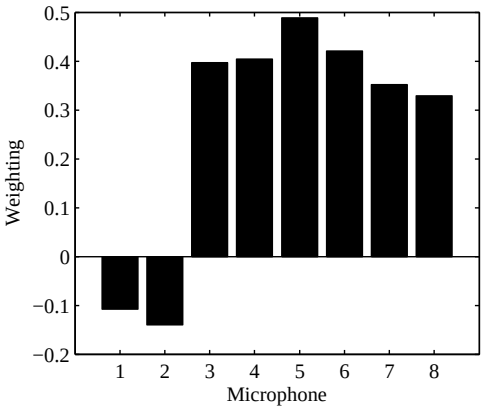

(a) Microphone weightings, $\boldsymbol{w}_L$.

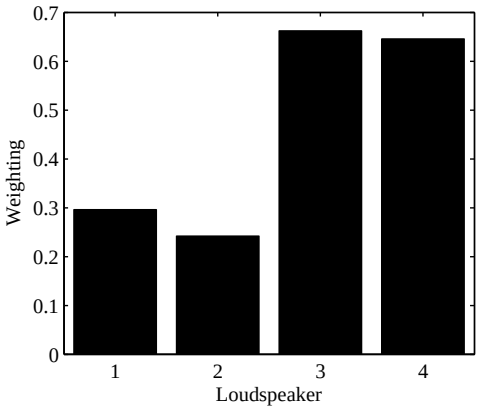

(b) Loudspeaker weightings, $\boldsymbol{w}_M$.

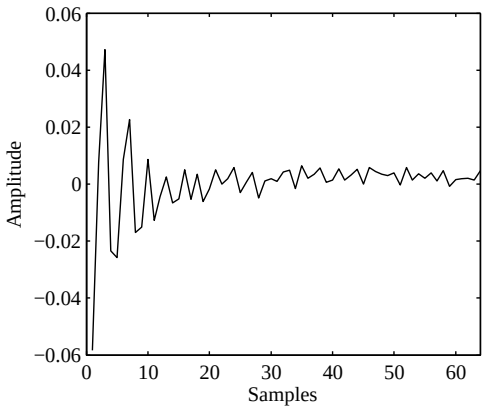

(c) FIR filter coefficients, $\boldsymbol{w}$.

Figure 4.17: The transducer weightings and filter coefficients for the modal IMC controller optimised to minimise the sum of the squared error sensor pressures when the non-rigid walled enclosure is excited by 18 uncorrelated structural excitations positioned as shown in Figure 4.16.

ment constraints are based on the modal error signal. A method of designing the controller has been proposed which formulates the problem as a convex optimisation problem using an FIR control filter and frequency discretisation, and calculates the filter coefficients and transducer weightings using sequential quadratic programming. The performance of this control strategy and design method has been assessed for the system employing the four car audio loudspeaker positioned sources and the eight corner error sensors in the rectangular car cabin sized enclosure with non-rigid walls; this allows the levels of control to be compared to those presented for the feedforward engine noise controller in the previous chapter. From these simulations it has been shown that significant levels of global reduction are achievable at the targeted acoustic mode, however, since the enhancement constraint is only enforced on the modal error signal, significant levels of enhancement are produced in the sum of the squared error sensor pressures at frequencies above the targeted mode.

A second formulation of the modal feedback controller using the IMC architecture is then described, in which the transducer weightings are included in the control path. This formulation operates on the actual error signals and, therefore, optimisation is based on the sum of the squared error signals and the enhancement in the individual error sensor pressures can be enforced. The design of the controller has again been formulated as a convex optimisation problem with an FIR control filter and frequency discretisation, and has been solved using sequential quadratic programming. This controller does not increase the requirements of a practical fixed feedback controller, compared to the modal controller based on minimising the model error signal. However, the controller optimised to minimise the sum of the squared error signals is able to achieve significant levels of control of a primary acoustic disturbance over a bandwidth comparable to feedforward control.

The two formulations of the modal feedback controller are physically identical systems and, therefore, require the same number of filters to be implemented. However, the two formulations lead to different optimisation strategies and this means that the second formulation, in which the transducer weightings are included in the control path, leads a more practically useful solution. It should be highlighted, however, that this optimisation is more time consuming than that required for the first formulation in which the modal error signal is minimised.

The performance of the modal feedback controller in controlling multiple uncorrelated structural primary sources is also simulated, as this disturbance is closer to that produced by road noise. These simulations have shown that significant levels of control of multiple uncorrelated structural excitations is achievable, however, due to the complexity of the sound field the bandwidth of control is limited to frequencies where a single acoustic resonance dominates the enclosure's response.

In the majority of practical car cabin environments the response is unlikely to be dominated by a single acoustic resonance, except in estate cars where the length of the cabin is significantly greater than the height and width. Therefore, although significant control performance may be achieved in applications where individual dominate resonances occur, the applicability of the modal feedback control strategies investigated in this chapter may be limited in the car

cabin road noise application. Therefore, the following chapter will extend the investigation of feedback control using multiple sensors and sources to a fully MIMO controller.

Chapter 5

Multi-Input, Multi-Output Feedback Control

Although the modal feedback control strategy presented in the previous chapter is able to achieve significant levels of control when a single resonance dominates the system response, this is not generally the case in a practical car cabin environment. Therefore, the implementation of a fully multi-input, multi-output (MIMO) feedback controller will be investigated in this chapter, again using the model of the non-rigid walled rectangular enclosure. The MIMO feedback controller will still utilise the standard car audio loudspeakers and the same error sensors that are used in the feedforward control system investigated in Chapter 3 and, therefore, be effectively integrated into the standard car systems; however, the computational requirements will be significantly increased compared to SISO modal controller.

Multichannel feedback control has been widely investigated and although the design of such controllers is more complex than SISO feedback systems, a wide variety of optimal design processes have been described [154]. The application of a MIMO feedback system to the control of road noise has been suggested by Elliott and Sutton [136], however, although the theory in this paper covers the MIMO implementation, the practical example of controlling road noise is only demonstrated for a SISO controller. The use of MIMO feedback control in the context of active noise control in structural-acoustic systems has also been considered by Kim [117], however, although the theory regarding a MIMO feedback controller is detailed, the performance is not investigated due to the computational burden of calculating the optimal controller. Computational power has significantly increased since the late 1990s when [136] and [117] were published and, therefore, it is important to investigate the use of a MIMO feedback controller for the active control of road noise in a car cabin. Although the real-time implementation of such a system may still be slightly out of reach, due to the digital signal processing (DSP) requirements, the offline calculation of the controller performance remains of interest as its implementation may be feasible using future developments in DSP and it also provides a benchmark for the modal feedback controllers investigated in the previous chapter.

5.1 Controller Formulation

A block diagram of the MIMO feedback control system for the active noise control application is presented in Figure 5.1 and an implementation of the system in the rectangular enclosure employed previously is presented in Figure 5.2. The feedback control system consists of M loudspeakers and L_e error sensors, which, in a practical application, may be common to the feedforward noise control system investigated in Chapter 3. From Figure 5.1 it can be seen that the $(L_e \times 1)$ vector of pressures at the error sensors is given by the summation of the pressures due to the primary disturbance, $\boldsymbol{p}_p(j\omega)$, and the control, or secondary sources, $\boldsymbol{p}_s(j\omega)$, so that

$$\boldsymbol{p}_e(j\omega) = \boldsymbol{p}_p(j\omega) + \boldsymbol{p}_s(j\omega). \tag{5.1}$$

The pressures due to the secondary sources can be expressed as

$$\boldsymbol{p}_s(j\omega) = \boldsymbol{Z}_s(j\omega)\boldsymbol{q}_s(j\omega), \tag{5.2}$$

where $\boldsymbol{Z}_s(j\omega)$ is the $(L_e \times M)$ matrix of acoustic transfer responses between the secondary sources and the error sensors and $\boldsymbol{q}_s(j\omega)$ is the $(M \times 1)$ vector of secondary source strengths. The secondary source strengths are generated by driving the L_e input M output feedback controller, $-\boldsymbol{H}(j\omega)$, with the vector of error sensor pressures and then driving the M loudspeakers with the output from the feedback controller. The response of the M loudspeakers can be described by the $(M \times M)$ diagonal matrix $\boldsymbol{Y}_L(j\omega)$, which contains the volume velocity produced per unit input current to each loudspeaker. The secondary source strengths can thus be written as

$$\boldsymbol{q}_s(j\omega) = -\boldsymbol{Y}_L(j\omega)\boldsymbol{H}(j\omega)\boldsymbol{p}_e(j\omega). \tag{5.3}$$

Substituting equations 5.2 and 5.3 into equation 5.1 and rearranging gives

$$\boldsymbol{p}_e(j\omega) = \left[\boldsymbol{I} + \boldsymbol{Z}_s(j\omega)\boldsymbol{Y}_L(j\omega)\boldsymbol{H}(j\omega)\right]^{-1}\boldsymbol{p}_p(j\omega), \tag{5.4}$$

where the complete plant response including the acoustic and loudspeaker responses is given by

$$\boldsymbol{G}(j\omega) = \boldsymbol{Z}_s(j\omega)\boldsymbol{Y}_L(j\omega), \tag{5.5}$$

the open-loop response is given by

$$\boldsymbol{G}(j\omega)\boldsymbol{H}(j\omega) = \boldsymbol{Z}_s(j\omega)\boldsymbol{Y}_L(j\omega)\boldsymbol{H}(j\omega), \tag{5.6}$$

and the sensitivity function is given by

$$\begin{aligned}\boldsymbol{S}(j\omega) &= \left[\boldsymbol{I} + \boldsymbol{Z}_s(j\omega)\boldsymbol{Y}_L(j\omega)\boldsymbol{H}(j\omega)\right]^{-1}, \\ &= \left[\boldsymbol{I} + \boldsymbol{G}(j\omega)\boldsymbol{H}(j\omega)\right]^{-1}.\end{aligned} \tag{5.7}$$

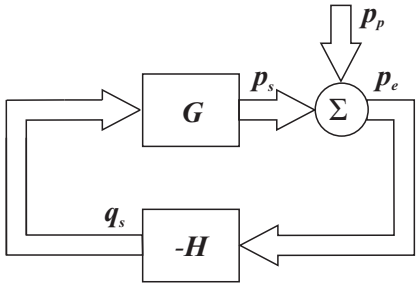

Figure 5.1: Block diagram of the multichannel feedback control system.

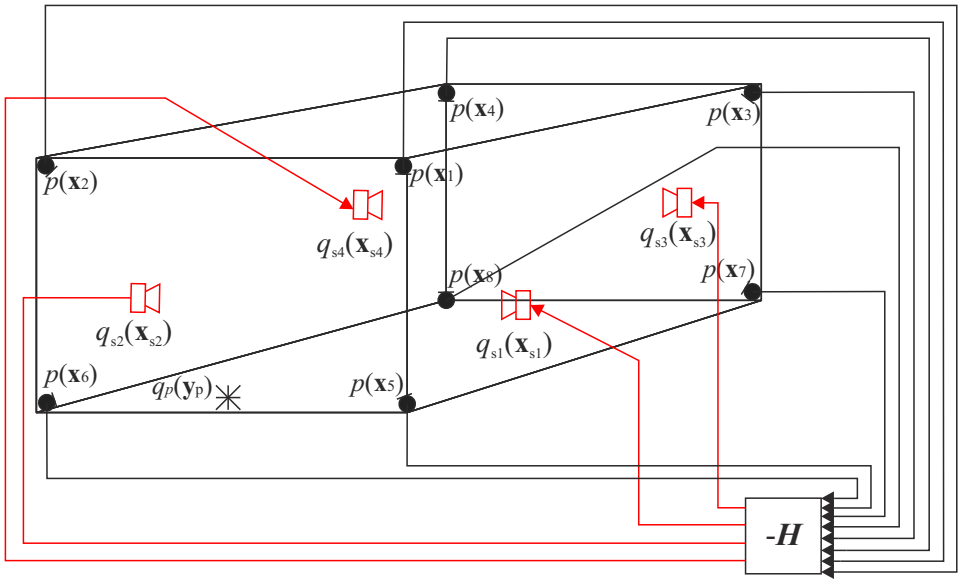

Figure 5.2: Mutli-input, multi-output feedback control system in the rectangular enclosure.

The sensitivity function is the response between the primary disturbance and the error signal, $\boldsymbol{p}_p$ and $\boldsymbol{p}_e$ in this case. Therefore, in the active noise control application it is desirable for the sensitivity function to be small such that the error signal is reduced [132]. However, the sensitivity function is related to the complementary sensitivity function, $\boldsymbol{T}(j\omega)$, by [155]

$$\boldsymbol{S}(j\omega) + \boldsymbol{T}(j\omega) = \boldsymbol{I}, \tag{5.8}$$

and, as shown in Section 4.3.2, in order for the controller to be robust it is necessary for $\boldsymbol{T}(j\omega)$ to be small. Therefore, equation 5.8 describes the trade-off between performance and robustness which is inherent in feedback control systems.

5.2 Controller Design and Optimisation

The aim of the MIMO feedback controller in the considered application is identical to that of the feedforward controller considered in Chapter 3. That is, to minimise the sum of the mean-squared pressures at the error sensors. For a random noise disturbance, such as road noise, this

cost function can be expressed as [132]

$$J_p(j\omega) = \text{trace}\left[E\left(\boldsymbol{p}_e(j\omega)\boldsymbol{p}_e^H(j\omega)\right)\right]. \tag{5.9}$$

If the MIMO feedback controller is formulated using the IMC architecture as discussed in Section 4.5.2 then the MIMO feedback controller can be conveniently designed following the methods employed in the previous chapter. The cost function for the MIMO feedback controller in this case is given by substituting equation 4.46 into equation 5.9 gives the cost function as

$$J_p(j\omega) = \text{trace}\left[E\left(\left[\boldsymbol{I}+\boldsymbol{G}(j\omega)\boldsymbol{W}(j\omega)\right]\boldsymbol{p}_p(j\omega)\boldsymbol{p}_p^H(j\omega)\left[\boldsymbol{I}+\boldsymbol{G}(j\omega)\boldsymbol{W}(j\omega)\right]^H\right)\right]. \tag{5.10}$$

Evaluating the expectation operator then gives the cost function as

$$J_p(j\omega) = \text{trace}\left[\left[\boldsymbol{I}+\boldsymbol{G}(j\omega)\boldsymbol{W}(j\omega)\right]\boldsymbol{S}_{pp}(j\omega)\left[\boldsymbol{I}+\boldsymbol{G}(j\omega)\boldsymbol{W}(j\omega)\right]^H\right]. \tag{5.11}$$

Equation 5.11 can then be expanded to give the cost function as

$$\begin{aligned} J_p(j\omega) =& \text{trace}\left[\boldsymbol{G}(j\omega)\boldsymbol{W}(j\omega)\boldsymbol{S}_{pp}(j\omega)\boldsymbol{W}^H(j\omega)\boldsymbol{G}^H(j\omega)\right. \\ &\left.+\boldsymbol{G}(j\omega)\boldsymbol{W}(j\omega)\boldsymbol{S}_{pp}(j\omega)+\boldsymbol{S}_{pp}(j\omega)\boldsymbol{W}^H(j\omega)\boldsymbol{G}^H(j\omega)+\boldsymbol{S}_{pp}(j\omega)\right]. \end{aligned} \tag{5.12}$$

Differentiating equation 5.12 with respect to the real and imaginary parts of $\boldsymbol{W}(j\omega)$ as defined in [132] gives

$$\frac{\partial J_p}{\partial \boldsymbol{W}_R} + j\frac{\partial J_p}{\partial \boldsymbol{W}_I} = 2\left[\boldsymbol{G}^H(j\omega)\boldsymbol{G}(j\omega)\boldsymbol{W}(j\omega)\boldsymbol{S}_{pp}(j\omega)+\boldsymbol{G}^H(j\omega)\boldsymbol{S}_{pp}(j\omega)\right], \tag{5.13}$$

where $\boldsymbol{W}_R$ and $\boldsymbol{W}_I$ are the real and imaginary parts of $\boldsymbol{W}$ respectively. By equating equation 5.13 to zero and solving for $\boldsymbol{W}(j\omega)$ at each frequency it is possible to calculate the optimal unconstrained controller response for the nominal plant. By differentiating equation 5.13 with respect to the real and imaginary parts of $\boldsymbol{W}$, the Hessian of the cost function is obtained as

$$2\left[\boldsymbol{G}^H(j\omega)\boldsymbol{G}(j\omega)\boldsymbol{S}_{pp}(j\omega)\right], \tag{5.14}$$

and since both $\boldsymbol{G}^H(j\omega)\boldsymbol{G}(j\omega)$ and $\boldsymbol{S}_{pp}(j\omega)$ are positive definite then the cost function, J_p, is convex and has a unique global minimum [163].

In a real-time system it is important for the controller to be causally constrained [132] and, therefore, it cannot be directly calculated by setting the derivative of the cost function to zero at each frequency. Control filter causality can be achieved in the IMC feedback controller by defining the control filter as an FIR filter as in the previous chapter. In the MIMO feedback control system $\boldsymbol{W}$ can be implemented as an ML_e bank of FIR filters each with I coefficients. For the road noise control system employing the 8 error sensors and 4 secondary sources consistent with the feedforward control system this results in a bank of 32 FIR filters. These ML_eI time domain filter coefficients can be expressed by the $(ML_eI \times 1)$ vector of filter coefficients,

$\boldsymbol{w}$, given by

$$\boldsymbol{w} = \begin{bmatrix} \boldsymbol{w}_0^T & \boldsymbol{w}_1^T & \cdots & \boldsymbol{w}_M^T \end{bmatrix}^T. \tag{5.15}$$

where $\boldsymbol{w}_m$ is the $(L_e I \times 1)$ vector of coefficients related to the m-th source

$$\boldsymbol{w}_m = \begin{bmatrix} \boldsymbol{w}_{m1}^T & \boldsymbol{w}_{m2}^T & \cdots & \boldsymbol{w}_{mL_e}^T \end{bmatrix} \tag{5.16}$$

and $\boldsymbol{w}_{ml}$ is the $(I \times 1)$ vector of coefficients related to the m-th source and l-th sensor

$$\boldsymbol{w}_{ml} = \begin{bmatrix} w_{ml1} & w_{ml2} & \cdots & w_{mlI} \end{bmatrix} \tag{5.17}$$

and w_{mli} is the i-th coefficient of the filter between the m-th source and l-the sensor.

The calculation of the FIR control filters to minimise the sum of the squared pressures, given by equation 5.12, can be achieved using the methods developed for feedforward controllers as described in [132]. However, to minimise this cost function whilst also maintaining the robust stability and disturbance enhancement constraints is more complex. This constrained minimisation can be achieved by discretising the design problem in the frequency domain and solving using an optimisation strategy as discussed in Section 4.6. This method of IMC controller design and optimisation will be extended to the MIMO feedback controller.

By implementing the control filters as a bank of FIR filters and discretising the frequency responses at N_F linearly spaced frequency intervals between 0 Hz and the maximum frequency of interest, which would be the Nyquist frequency, $Fs/2$, in a digital system, the design objective can be expressed using the cost function given by equation 5.12, the robust stability constraint given by equation 4.48 and one of the disturbance enhancement constraints given by equations 4.24, 4.31 or 4.36. If the primary disturbance is known to be dominant over a specific frequency range, or control is required over a predefined frequency range, then the optimisation problem can be modified such that the maximal disturbance attenuation is achieved over a specified bandwidth, whilst the constraints are maintained over the full bandwidth; this has been applied to the modal controllers investigated in the previous chapter. If the lower and upper bounds of the bandwidth over which disturbance attenuation is required are defined as f_1 and f_2 respectively and the number of discrete frequency points in this interval is N_{F_c}, then

the optimisation of the MIMO controller can be defined for the nominal plant responses as

$$\begin{aligned}
\min_{\boldsymbol{w}} \quad & \frac{1}{N_{F_c}} \sum_{f=f_1}^{f_2} \text{trace}\left[\boldsymbol{G}_0(f)\boldsymbol{W}(f)\boldsymbol{S}_{pp}(f)\boldsymbol{W}^H(f)\boldsymbol{G}_0^H(f)\right. \\
& \left. +\boldsymbol{G}_0(f)\boldsymbol{W}(f)\boldsymbol{S}_{pp}(f)+\boldsymbol{S}_{pp}(f)\boldsymbol{W}^H(f)\boldsymbol{G}_0^H(f)+\boldsymbol{S}_{pp}(f)\right] \\
\text{subject to} \quad & \bar{\sigma}[\boldsymbol{G}_0(f)\boldsymbol{W}(f)B(f)] < 1 \quad \forall f, \\
\text{and} \quad & \bar{\sigma}[\boldsymbol{S}_0(j\omega)]\frac{1}{A} < 1 \quad \forall f, \\
\text{or} \quad & \frac{\text{trace}\left[\boldsymbol{S}_0(j\omega)\boldsymbol{S}_{pp}(j\omega)\boldsymbol{S}_0^H(j\omega)\right]}{\text{trace}\left[\boldsymbol{S}_{pp}(j\omega)\right]A} < 1 \quad \forall f, \\
\text{or} \quad & \max\left[\text{diag}\left(\boldsymbol{D}(f)\boldsymbol{S}_0(f)\boldsymbol{S}_{pp}(f)\boldsymbol{S}_0^H(f)\right)\right]\frac{1}{A} < 1 \quad \forall f. \qquad (5.18)
\end{aligned}$$

It has been shown following equations 5.12 through to 5.14 that the cost function is convex (and specifically quadratic) with respect to the control filters' frequency responses and since the discretised frequency responses of the control filters are linearly related to the FIR filters according to equation 4.60, then the optimisation problem is also convex with respect to the filter coefficients. The optimisation problem can therefore be solved using sequential quadratic programming as in the modal controller optimisations detailed in Sections 4.6.1 and 4.7.1.

5.3 Control of a Single Internal Acoustic Primary Source

The non-rigid walled enclosure, modelled in Chapter 2, will be employed here to investigate the MIMO feedback control strategy. The dimensions of this enclosure and the positions of the secondary sources and corner error microphones are shown in Figure 2.6. Excitation of the acoustic enclosure by an acoustic primary source positioned at $\boldsymbol{x} = [0, L_2/2, 0]$, as shown in Figure 2.6, will be considered in this section and will be used to compare the alternative multichannel enhancement constraints described in Section 4.4.2 . These simulations will provide a direct comparison to those presented in Section 3.2.2 for the feedforward controller and in Section 4.7.2 for the modal feedback controller optimised to minimise the sum of the squared error sensor pressures.

5.3.1 Comparison of the Alternative Multichannel Enhancement Constraints

The multichannel feedback control system with four secondary sources and eight error microphones positioned in the corners of the non-rigid walled rectangular car cabin sized enclosure has been optimised using the method described by equation 5.18 for the case when there is a single acoustic primary disturbance. The frequency range considered is 0 to 500 Hz and the cost function has been limited to frequencies below 200 Hz by setting $f_1 = 0$ and $f_2 = 200$ in equation 5.18, which is consistent with the bandwidth employed in the modal feedback controller optimised to minimise the sum of squared error sensor pressures in Section 4.7. The frequency responses have been discretised at $N_F = 198$ frequencies and the control filter lengths

have been set to $I = 64$; these parameters have been chosen as outlined in Section 4.6.1 to ensure an optimal solution is obtained without unnecessary computational expense. The robust stability constraint, given as

$$\bar{\sigma}[\boldsymbol{G}_0(f)\boldsymbol{W}(f)] < \frac{1}{B(f)}, \tag{5.19}$$

has been set to a frequency independent value of $B = 0.5$, which ensures that the eigenvalues of the open-loop plant response have a gain margin of 3.5 dB and a phase margin of 30° [132]. In a practical system B could be determined from measurements of the plant under different conditions as in [156]. The controller has been optimised for the three different disturbance enhancement constraints detailed in Section 4.4.2, in each case the maximum enhancement in the relevant value has been limited to 6 dB. The three enhancement constraints are summarised here for convenience:

1. Constraint on the maximum singular value of the sensitivity function:

$$\bar{\sigma}[\boldsymbol{S}_0(j\omega)] < A \tag{5.20}$$

2. Constraint on the maximum enhancement in the sum of squared error sensor pressures:

$$\frac{\text{trace}\left[\boldsymbol{S}_0(j\omega)\boldsymbol{S}_{pp}(j\omega)\boldsymbol{S}_0^H(j\omega)\right]}{\text{trace}\left[\boldsymbol{S}_{pp}(j\omega)\right]} < A \tag{5.21}$$

3. Constraint on the maximum enhancement in the individual error sensor pressures:

$$\max\left[\text{diag}\left(\boldsymbol{D}(f)\boldsymbol{S}_0(f)\boldsymbol{S}_{pp}(f)\boldsymbol{S}_0^H(f)\right)\right] < A \tag{5.22}$$

Figure 5.3 shows the four optimisation constraints given by equations 5.19 through to 5.22 for the three controllers optimised according to the three different enhancement constraints. In each of the four plots the results of the controller optimised with the enhancement constraint given by equation 5.20 are shown in red, the results of the controller optimised with the enhancement constraint given by equation 5.21 are shown in blue, and the results of the controller optimised with the enhancement constraint given by equation 5.22 are shown in green. The black dashed lines in each plot show the level above which the various constraints are violated.

From Figure 5.3a it can be seen that all three optimised controllers respect the robustness constraint. It can be seen that the magnitude of the largest singular value of the complementary sensitivity function for all three controllers is largest at frequencies between around 50 and 250 Hz. This is approximately the frequency range over which both the amplitude of the disturbance is significant and the controller is optimised to achieve control. It can also be seen from the blue line in Figure 5.3a that the controller optimised with the constraint on the enhancement in the sum of the squared pressures is the only one of the three controllers that

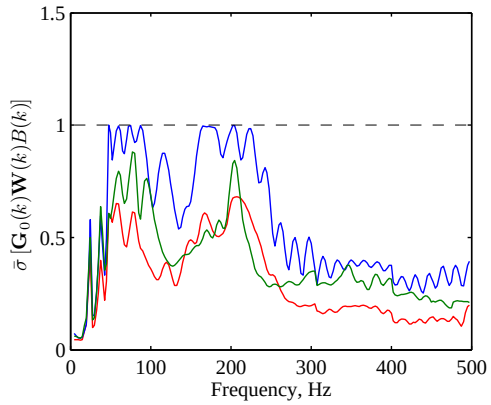

(a) Robust stability measure given by equation 5.19 which must be less than 1 at all frequencies to ensure the robust stability constraint is satisfied with a plant uncertainty of $B(k)$.

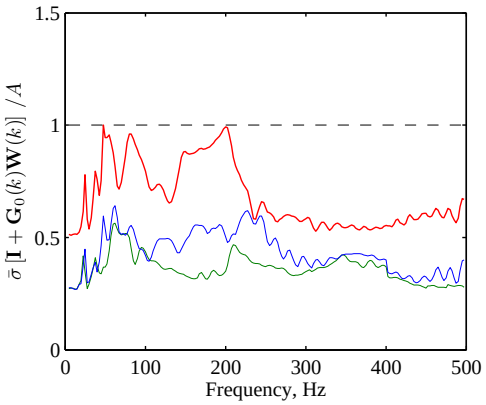

(b) Maximum singular value disturbance enhancement measure given by equation 5.20 which must be less than 1 at all frequencies to ensure the disturbance corresponding to the maximum singular value is not enhanced by more than a factor of A.

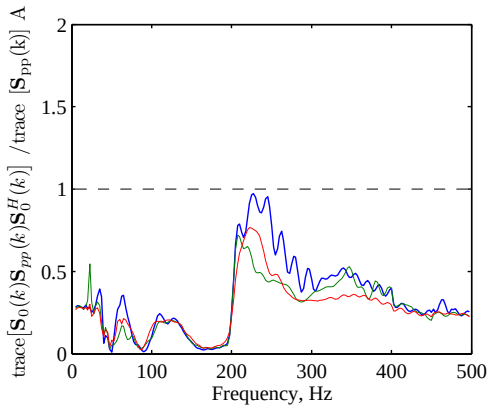

(c) Sum of squared disturbance pressures enhancement measure given by equation 5.21 which must be less than 1 at all frequencies to ensure the sum of squared disturbance pressures is not enhanced by more than a factor of A.

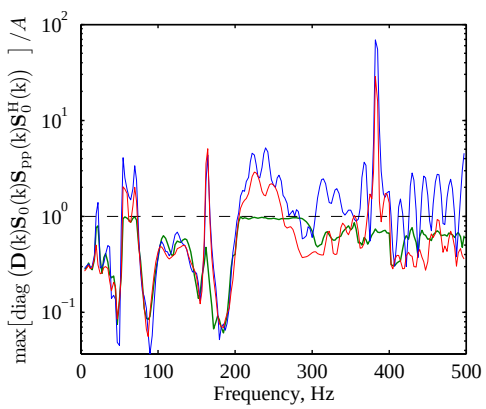

(d) Maximum individual squared disturbance pressure enhancement measure given by equation 5.22 which must be less than 1 at all frequencies to ensure the individual squared disturbance pressures are not enhanced by more than a factor of A.

Figure 5.3: The results of the MIMO IMC controller designed with a robust stability constraint and three different enhancement constraints given by equations 5.20, maximum singular value, (—), 5.21, maximum sum of squared pressues, (—) and 5.22, maximum individual pressure, (—) to control an internal acoustic primary source positioned as shown in Figure 2.6.

reaches the robustness constraint limit and, therefore, this controller is the least robust of the three designed systems.

Figure 5.3b shows the maximum singular value of the sensitivity function, given by equation 5.20, for the three controllers. From this plot it can be seen that all three controllers respect this constraint. The controller optimised specifically with the maximum singular value enhancement constraint, shown by the red line, exactly maintains this constraint at a number of frequencies below 200 Hz, whilst the other two controllers have a significant margin to the constraint limit over the full bandwidth. The maximum enhancement in the sum of squared pressures for the three controllers is shown in Figure 5.3c. From this plot it can be seen that the maximum enhancement in the sum of squared pressures is similar for all three controllers and the maximum enhancements occur between around 200 and 250 Hz. In each system the constraint is not reached meaning that the maximum enhancement in the sum of squared pressures is below 6 dB in all three systems; however, the enhancement is greatest for the controller optimised with this constraint, which is shown by the blue line. The final enhancement criterion, defined by the maximum enhancement in the individual squared pressures and given by equation 5.22, is shown in Figure 5.3d which, due to the large range of values for the two controllers not optimised with this constraint, is plotted using a logarithmic y-axis. From this plot it can be seen that this enhancement constraint is significantly exceeded by the two controllers with enhancement constraints given by equations 5.20 and 5.21, while the controller optimised with a constraint on the maximum enhancement in the individual pressures maintains this constraint.

From the results presented in Figure 5.3 it has been shown that the controllers optimised according to each of the three enhancement constraints maintain both robust stability and their respective enhancement constraints. Furthermore, all three controllers maintain the constraints imposed by equations 5.20 and 5.21 while the constraint on the maximum enhancement in the individual error sensor pressures is significantly violated by the two controllers not optimised according to this constraint, particularly at about 370 Hz. To determine the implications of these different constraints on the control performance, Figure 5.4 shows the cost function, J_p, given by equation 5.9 for the uncontrolled system and for the three controllers. From this plot it can be seen that all three controllers achieve significant reductions in J_p at frequencies below around 200 Hz, whilst enhancements in the cost function occur at frequencies above 200 Hz as expected from the results presented in Figure 5.3c. The controller optimised with a constraint on the maximum enhancement in the sum of squared pressures, which is once again shown by the blue line in Figure 5.4, achieves reductions up to 12 dB in both the structural resonance that occurs at 55 Hz and the first longitudinal acoustic mode at 85 Hz, and up to 10 dB at frequencies between around 150 and 200 Hz. The other two controllers, shown by the red and green lines in Figure 5.4, achieve maximum reductions of between around 8 and 10 dB. However, as previously shown in Figure 5.3c the levels of enhancement in J_p that occur mainly at frequencies above 200 Hz are lower for these two controllers.

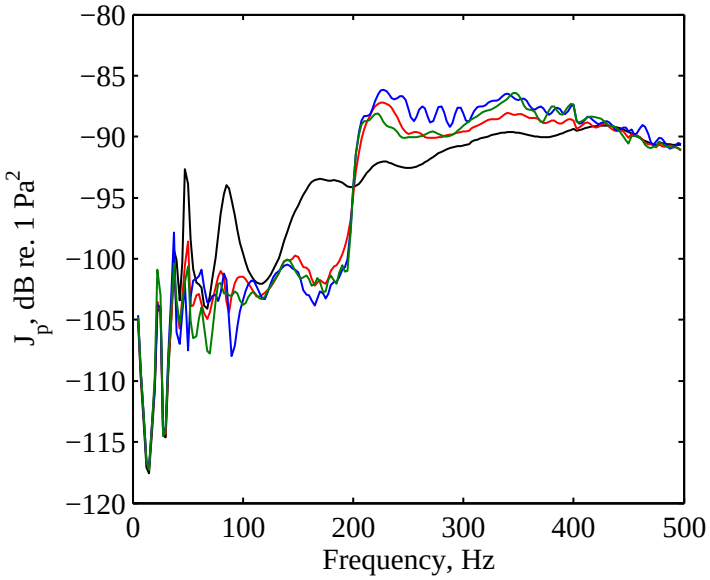

Figure 5.4: The cost function, J_p, calculated from the eight corner error sensors in the simulated non-rigid walled enclosure when driven by a primary source alone (—) and when J_p has been minimised using the MIMO IMC controller designed with a constraint on the maximum singular value enhancement (—), the maximum enhancement in the sum of the squared pressures (—) and the maximum enhancement in the individual squared pressures (—).

To determine how the three controllers affect the global sound field within the non-rigid walled enclosure Figure 5.5 shows the total acoustic potential energy in the enclosure. These results are directly comparable to those presented in Figure 3.5 for the equivalent feedforward control system and in Figure 4.14f for the modal feedback controller optimised to minimise the sum of squared error sensor pressures. From Figure 5.5 it can be seen that all three controllers maintain significant levels of control at the structural resonance at 55 Hz and the first longitudinal mode at 85 Hz and the levels of control are comparable to those achieved by the modal feedback controller optimised to minimise the sum of squared error sensor pressures. As previously observed for both the feedforward and modal feedback controllers, the global control at frequencies above the first longitudinal mode is limited to around 4 dB. It is interesting to note that the controller optimised with a constraint on the maximum enhancement in the individual error sensor pressures (shown by the green line) achieves a slightly greater reduction in the total acoustic potential energy than the other two controllers whilst maintaining the lowest level of enhancement at higher frequencies. This is a result of this enhancement constraint avoiding high levels of pressure at some error sensors being compensated for by low levels at others, and thus giving a more uniform reduction in the pressure. This is similar to the performance achieved by the feedforward controller which minimises the maximum error signal [165].

From the results presented in Figures 5.3 through to 5.5 it has been shown that the three enhancement constraints given by equations 5.20, 5.21 and 5.22 achieve very similar levels of control. It has been shown that the controller optimised according to equation 5.21, which limits the maximum enhancement in the sum of squared error sensor pressures, achieves the

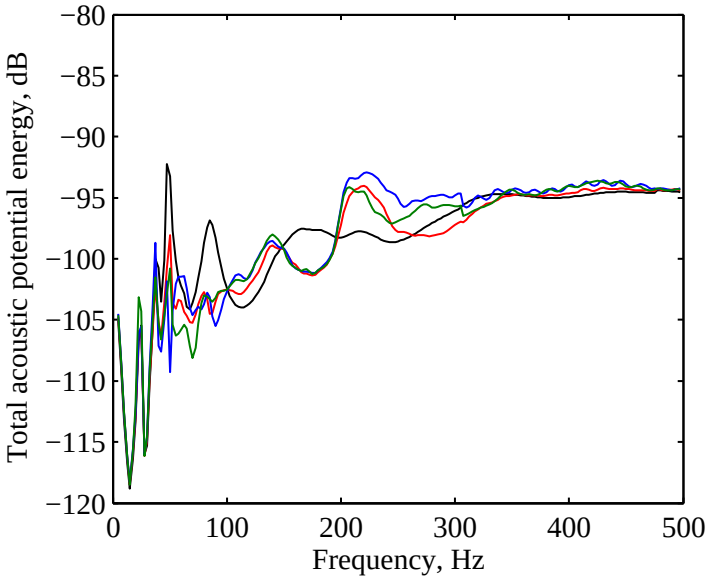

Figure 5.5: Total acoustic potential energy in the non-rigid enclosure when driven by a primary source alone (—) and when J_p has been minimised using the MIMO IMC controller designed with a constraint on the maximum singular value enhancement (—), the maximum enhancement in the sum of the squared pressures (—) and the maximum enhancement in the individual squared pressures (—).

highest levels of reductions in the cost function, J_p, but is also the least robust of the three controllers and produces significant levels of enhancement at individual error sensors. This is also a problem with the controller optimised with the enhancement constraint given by equation 5.20. The controller optimised with the constraint on the maximum enhancement in the individual sensor pressures, given by equation 5.22, inherently avoids this problem whilst not significantly reducing the performance assessed according to the cost function J_p. The controller optimised with this enhancement constraint also benefits from improvements in the levels of global control, which can be attributed to the more uniform reduction in the error sensor pressures that this constraint tends to produce. Due to these benefits the enhancement constraint at the individual error sensors will be employed in the following investigations.

5.4 Control of Multiple Uncorrelated Structural Primary Forces

In the car cabin environment the primary disturbance due to road noise will be generated by a number of uncorrelated primary forces – as discussed in Chapter 1. Therefore, it is important to investigate the performance of the MIMO IMC feedback control system when the non-rigid enclosure is excited by multiple uncorrelated primary forces. This can be achieved as detailed in Section 4.7.3.

The performance of the MIMO controller optimised for a primary disturbance produced by 18 uncorrelated primary forces positioned on the floor of the enclosure as shown in Figure 4.16 has been simulated and the results are presented in Figure 5.6; these results are directly

comparable to those presented in Figure 4.15. From the plots in Figure 5.6 it can be seen that both constraints are maintained and the enhancement constraint is maintained with a significant margin. This result indicates that the level of enhancements in the individual squared pressures are below around 3 dB. From Figures 5.6c and 5.6d it can be seen that significant reductions in the cost function are achieved by the optimised controller at frequencies below around 100 Hz.

In comparison to the performance of the modal feedback control system, presented in Figure 4.15, it can be seen that, between around 20 and 100 Hz, where significant levels of control are achieved, the MIMO controller is able to control all of the resonances, whereas the modal feedback controller is not able to control the resonance at 70 Hz. Additionally, it can be seen that the MIMO controller does not produce significant enhancements in the sum of the squared pressures, whereas the modal feedback controller produces significant enhancements at higher frequencies. The improvements in the control achieved by the MIMO controller compared to the modal controller can be attributed to the increased complexity. That is, while the modal controller attempts to achieve the best global control using single composite error and control signals, the MIMO controller directly employs the error signals from the eight error sensors and drives the four sources with independent signals. This, however, results in a significantly more complex controller which requires a model of the interaction between the four loudspeakers and eight error microphones in the plant, $\hat{\boldsymbol{G}}$, and 32 FIR filters to be implemented in $\boldsymbol{W}$; the response of these control filters for the MIMO controller optimised to minimise the sum of the squared pressures produced by the 18 uncorrelated structural excitations are presented in Figure 5.7.

5.5 Summary

This chapter has built upon the work presented in the previous chapter by presenting an investigation of the design and performance of a fully MIMO feedback controller employing four sources positioned at the standard car audio loudspeaker locations and the eight corner error sensors consistent with the global feedforward controller investigated in Chapter 3. The formulation of the MIMO feedback controller is first presented and then through the use of an IMC architecture the controller design problem is formulated as a convex optimisation in the frequency domain using FIR filters and frequency discretisation. The MIMO feedback controller requires a bank of ML_e FIR filters with I coefficients, which corresponds to 32 FIR filters with 64 coefficients in the 4 source, 8 error sensor system investigated in this chapter and also requires an accurate model of the plant responses.

The performance of the MIMO feedback controller has been investigated in the modelled non-rigid car cabin sized rectangular enclosure. Although the aim of the controller is to control road noise, the control of an internal acoustic primary disturbance has initially been simulated

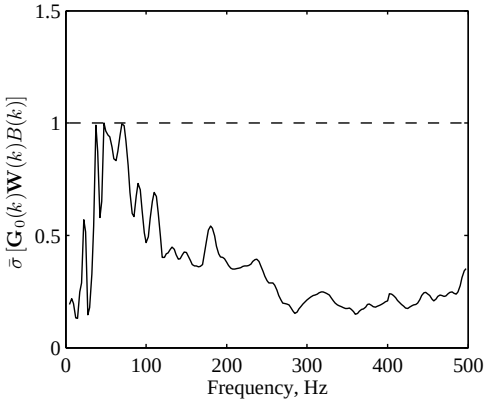

(a) Robust stability measure given by equation 5.19 which must be less than 1 at all frequencies to ensure the robust stability constraint is satisfied with a plant uncertainty of $B = 0.5$.

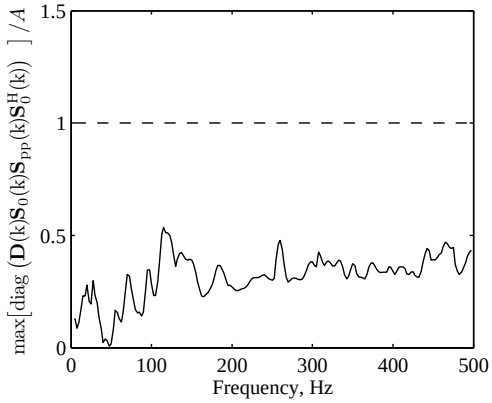

(b) Maximum individual squared disturbance pressure enhancement measure given by equation 5.22 which must be less than 1 at all frequencies to ensure the individual squared disturbance pressures are not enhanced by more than a factor of $A = 4$.

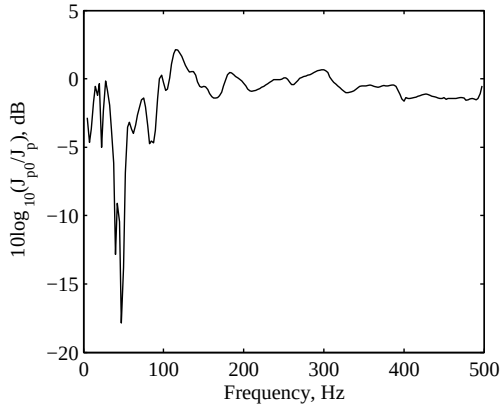

(c) The cost function after control, J_{p0}, plotted in decibels relative to the cost function due to the primary alone, J_p, calculated from the eight corner error sensors.

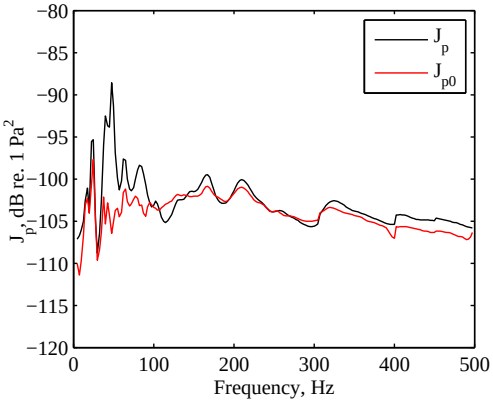

(d) The cost function, J_p, calculated from the eight corner error sensors when driven by a primary excitation alone (—) and when J_p has been minimised (—).

Figure 5.6: The results of the MIMO IMC controller designed with a robust stability constraint and a constraint on the maximum enhancement in the individual error microphone pressures in the simulated non-rigid walled enclosure when driven by 18 uncorrelated structural excitations positioned as shown in Figure 4.16

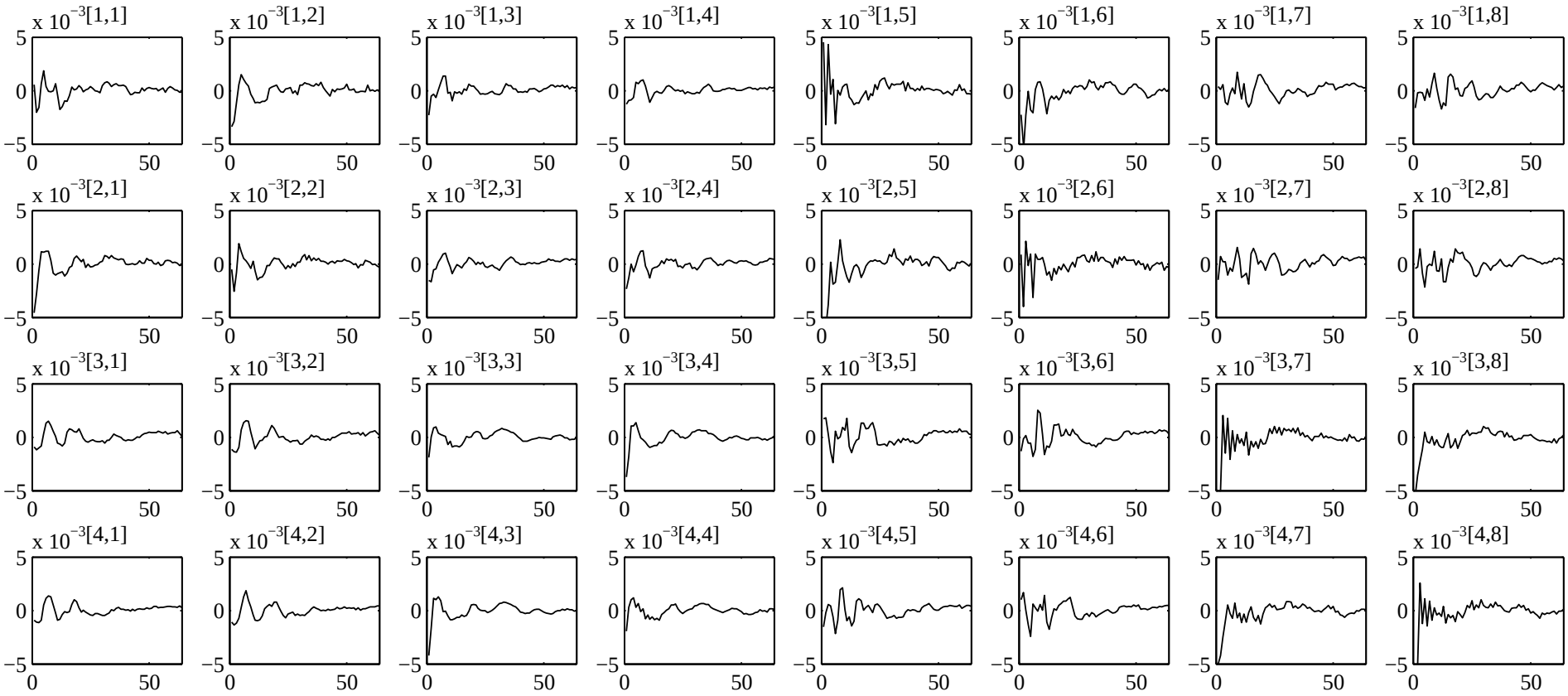

Figure 5.7: The filter coefficients for the 32 FIR filters for the MIMO IMC feedback controller with four loudspeakers and eight error microphones optimised to minimise the sum of the squared error sensor pressures when the non-rigid walled enclosure is excited by 18 uncorrelated structural excitations positioned as shown in Figure 4.16.

to allow a comparison of the three multichannel enhancement constraints derived in Chapter 4. This comparison has shown that the controllers optimised with the three enhancements constraints all maintain the constraints on both the maximum singular value of the sensitivity function and the maximum enhancement in the sum of the squared error sensor pressures; however, the constraint on the maximum enhancement in the individual error sensor pressures is significantly violated by the two controllers optimised according to the other two constraints. This indicates that these controllers will produce significant enhancements in the pressures at certain error sensors in order to achieve an increase in the reduction of the cost function. It is also shown that the controller optimised with a constraint on the maximum enhancement in the individual error sensor pressures achieves larger reductions in the total acoustic potential energy and this can be related to the more uniform reduction in pressure achieved by enforcing this constraint.

The performance of the MIMO feedback controller in controlling a structural primary excitation has been simulated and it has been shown that control of an increased number of resonances compared to the modal feedback controller is possible. Additionally, when the non-rigid enclosure is excited by multiple uncorrelated point forces, the optimised MIMO feedback controller is able to control all resonances within the control bandwidth up to around 100 Hz whilst producing significantly lower levels of spillover at higher frequencies compared to the modal controller.

From the results presented in this chapter it has been shown that the MIMO IMC feedback controller using acoustic secondary sources is capable of achieving significant levels of control of multiple uncorrelated structural excitations, which suggests that control of road noise in a practical car cabin environment may be physically achievable. However, in each scenario considered in the presented simulations, the controller has been optimised to control a specific disturbance spectrum and a perfect plant model has been assumed. The effect of practical variations in these parameters has not be explicitly investigated, although the robust stability constraint will ensure the controller is robust to some variations in the plant. The robustness of the controller to variations in the disturbance spectrum, which may be produced by changes in road surface, and the plant response will be investigated in the following chapter in a real car environment.

Chapter 6

Experimental Investigation of Active Noise Control

The previous three chapters have investigated feedforward and feedback active noise control through both simulations and experiments in a car cabin mock-up. It has been shown that where a suitable reference signal is available, such as in engine noise control systems, feedforward active noise control may provide a significant level of low frequency attenuation, and is largely unaffected by the effects of structural-acoustic coupling and primary source excitation. When a reference signal is not conveniently available, such as in the control of the random disturbance produced by road noise, feedback active noise control is a more practical control method. Chapter 4 has investigated a SISO feedback control system employing both spatial and temporal filtering, which is based on modal feedback control strategies, and it has been shown that levels of global control comparable to the feedforward control strategy are achievable when a single acoustic mode dominates the response. In order to improve the bandwidth and level of control achievable using a feedback control system, a MIMO feedback controller has been investigated in Chapter 5. This MIMO feedback controller has been shown to be able to achieve a bandwidth of control comparable to the feedforward controller and it has been specifically shown that the feedback controller is able to achieve control of multiple uncorrelated structural excitations, which is consistent with the primary disturbance in a road noise control system. Following on from this work, this chapter investigates the performance of the feedforward control of engine noise and the feedback control of road noise using the MIMO feedback controller in a small city car.

This chapter first investigates the acoustic environment in the small city car through measurements of both the plant responses and primary disturbances, which include both engine and road noise. These measurements are then used to perform offline simulations of the performance of the feedforward and MIMO feedback controllers. The results of feedforward controller simulations are used to inform the design and implementation of a real-time feedforward engine noise control system, whose performance is measured in the small city car. Although the real-time implementation of the MIMO feedback controller is not presented, some discussion

is provided as to its practicality.

The presented results relate to a small city car with a two-cylinder 875 cc petrol engine and all measurements have been conducted at an automotive test facility by the author using equipment from the Institute of Sound and Vibration Research (ISVR) as detailed in Appendix D. A second set of preliminary measurements were also conducted on a similar car but with a four-cylinder 1200 cc petrol engine at the ISVR. The four-cylinder measurements were intended as a practice run before travelling to the test facility to conduct the measurements on the 'green city car' and, therefore, they are not presented here.

6.1 Characterisation of the Car Cabin Acoustic Environment

The setup employed for the measurements presented in the following sections is shown in the block diagram presented in Figure 6.1. As for the measurements of the car cabin mock-up presented in Chapter 2, the system consists of 16 microphones – 8 positioned at the nominal corners of the car cabin, examples of which are shown in Figure 6.2, and 8 positioned at the headrests of the car seats as shown in Figure 6.3. The positions of the 16 microphones are summarised in Table 6.1. Two secondary sources have been employed in the measurements – the volume velocity source previously employed in the measurements presented in Chapter 2 [128] and the car audio loudspeakers. Figure 6.1 shows a dashed connection which provides the volume velocity signal and is, therefore, only employed for the measurements using the volume velocity source and not the car audio loudspeakers. The positions of the standard car audio loudspeakers in the green city car are shown in Figure 6.4 and these secondary source positions are also used for the volume velocity source measurements. A further important element of the setup presented in Figure 6.1 is the Once-Per-Rev (OPR) reference signal which provides a reference for the feedforward control system simulations. For the measurements conducted on the two cylinder car, a measurement of the speed was also taken during the road noise measurements using a global positioning system. It should also be noted that the necessary anti-aliasing and reconstruction filters are implemented by the data acquisition (DAQ) device and a sample rate of 2.56 kHz has been used for all measurements. This gives a Nyquist frequency of 1.28 kHz and provides sufficient bandwidth for the active noise control systems to be validated. The frequency response measurements were made by driving a secondary source with pink noise and using an H_1 estimate, equal to the cross spectral density between the microphone and drive signal divided by the power spectral density of the drive signal.

Table 6.1: Microphone positions

	Position
Microphone 1	Front offside roof
Microphone 2	Front nearside roof
Microphone 3	Rear offside roof
Microphone 4	Rear nearside roof
Microphone 5	Front offside floor
Microphone 6	Front nearside floor
Microphone 7	Rear offside seat
Microphone 8	Rear nearside seat
Microphone 9	Driver outer right headrest
Microphone 10	Driver inner left headrest
Microphone 11	Front passenger inner right headrest
Microphone 12	Front passenger outer left headrest
Microphone 13	Rear nearside passenger outer right headrest
Microphone 14	Rear nearside passenger inner left headrest
Microphone 15	Rear offside passenger inner right headrest
Microphone 16	Rear offside passenger outer left headrest

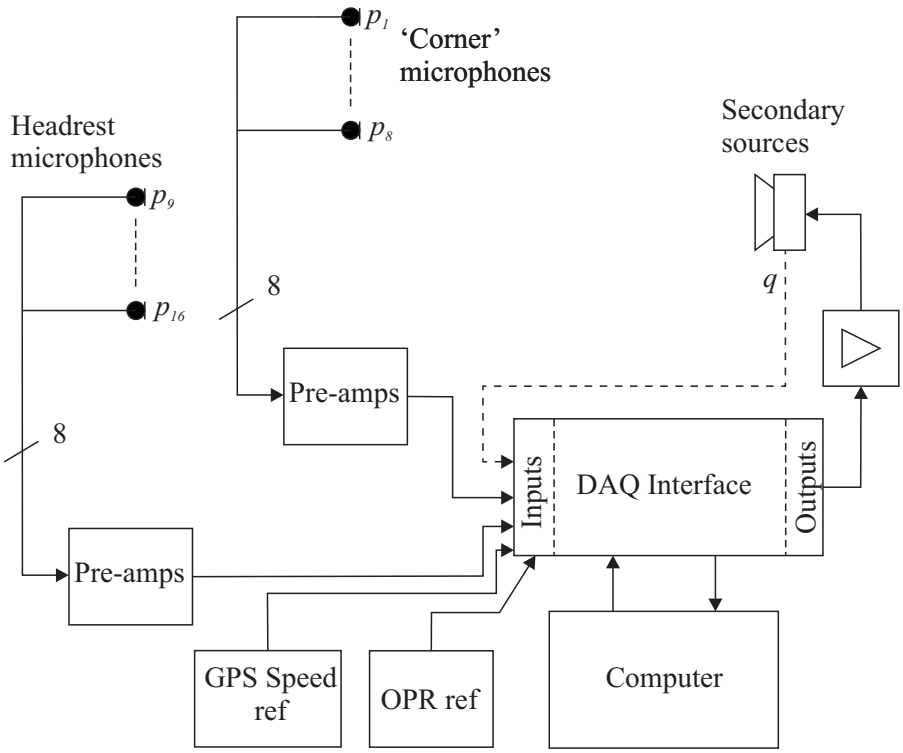

Figure 6.1: Block diagram of the in-car acoustic environment measurement setup. The secondary sources are either a volume velocity source, or the car audio loudspeakers, in which case the dashed connection indicating the volume velocity measurement, is not present. The Once-Per-Rev (OPR) reference signal is provided from the engine tachometer.

(a) Front roof ‘corner’ microphone position (b) Rear ‘corner’ microphone positions

Figure 6.2: ‘Corner’ microphone positions

(a) Front headrest microphone positions (b) Rear headrest microphone positions

Figure 6.3: Headrest microphone positions

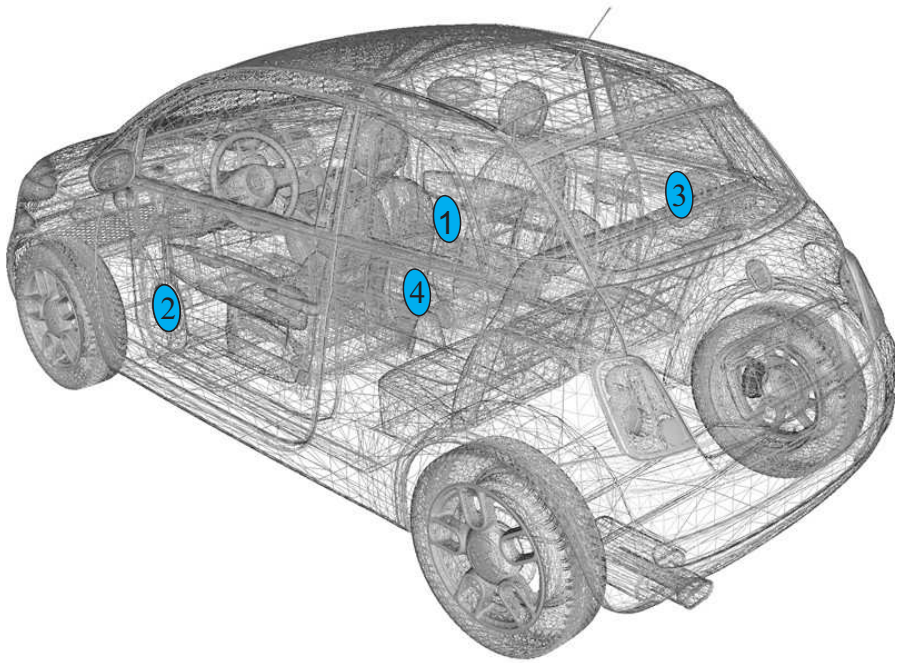

Figure 6.4: The positions of the standard car audio loudspeakers in the green city car cabin (note: the measurements were conducted in a right-hand-drive vehicle) (modified from [166]).

6.1.1 Plant Response

Using the setup shown in Figure 6.1 the acoustic transfer response between the volume velocity source positioned close to the car audio loudspeakers' positions, as shown in Figure 6.4, and the 16 microphone positions has been measured. Figure 6.5 shows the acoustic transfer response between source position 1 and microphone 9 positioned at the driver's right ear when the car cabin has two occupants, one in each front seat. From this plot it can be seen that there is no significantly dominant resonance in the cabin for this source and sensor combination and it can be seen that the damping is comparable to the 10% assumed in the earlier simulations (see Figure 2.10 for example). The high magnitude of the acoustic transfer impedance at low frequencies is a result of noise in the measurements due to the low output of the volume velocity source at low frequencies; this is confirmed by the low values of the coherence at these frequencies. The results for the other microphone positions and the three other secondary source positions show similar characteristics and, therefore, are not presented.

The results presented in Figure 6.5, and those corresponding to the other source positions, do not show the significant low frequency resonances which were observed in the rectangular enclosure simulations and measurements shown in Figures 2.10 and 2.9 respectively. This is more than likely because the car's sound package has been designed to avoid such resonances and, therefore, an ideal scenario would be to measure the car's response with a significantly reduced sound package to determine the acoustical problems that may be solved using active control techniques rather than the passive measures currently in place; this, however, was not possible for practical reasons.

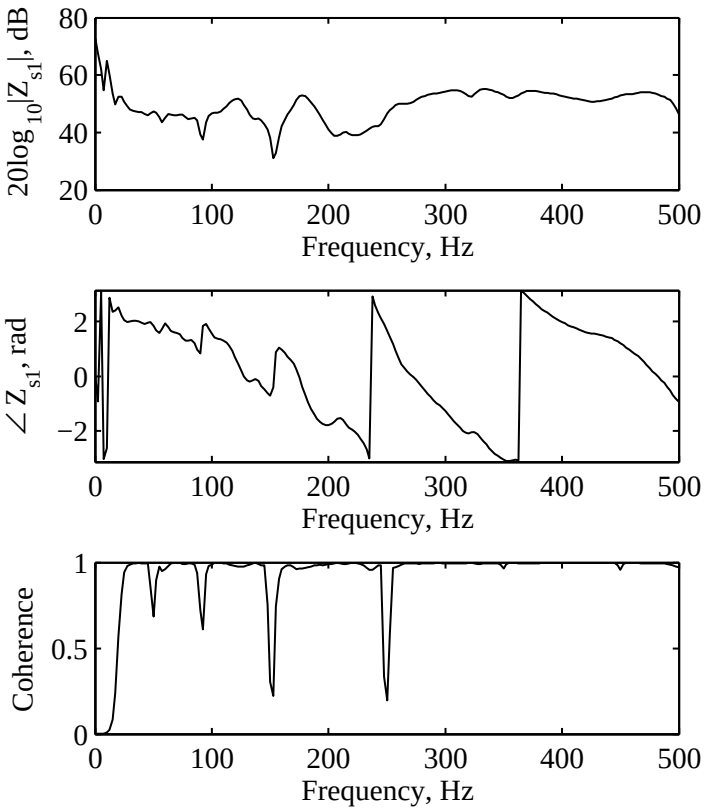

Figure 6.5: The acoustic transfer response between the volume velocity source at position 1 and the pressure at microphone 9 positioned at the driver's outer right headrest.

In a low-cost active noise control system it is necessary to use the car audio loudspeakers as secondary sources. Therefore, to determine the suitability of the standard car audio loudspeakers the response between the voltage input to the loudspeakers and the pressures produced at the 16 microphone positions has been measured. The response between loudspeaker 1 and microphone 9 is presented in Figure 6.6. From this plot it can be seen that the pressure produced by the loudspeaker rolls off at frequencies below around 70 Hz. This suggests that the loudspeaker's resonance occurs at around 70 Hz, which may affect the stability of the feedback control system and may result in difficulties in reproducing the required sound pressure levels for both feedforward and feedback control at frequencies significantly below around 70 Hz.

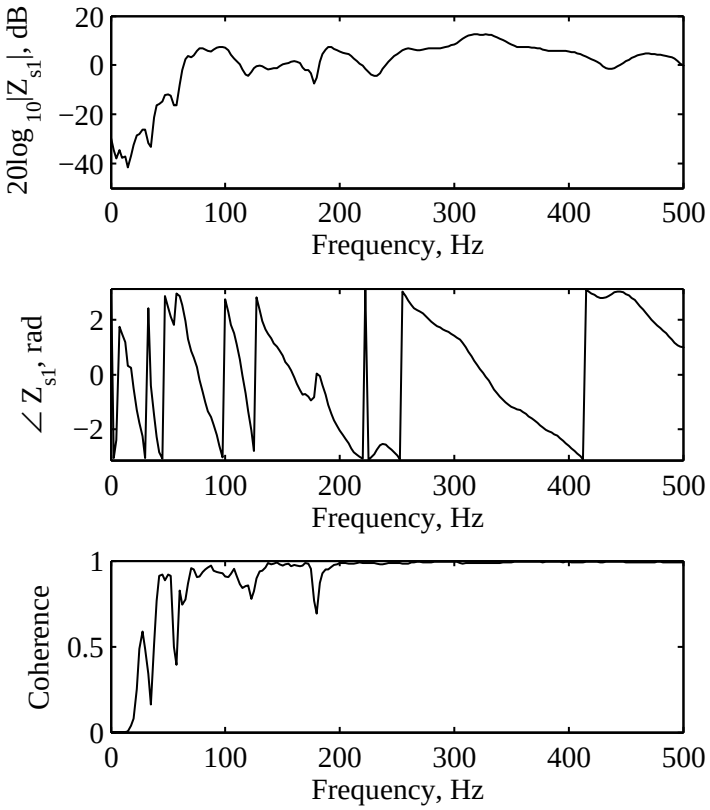

Figure 6.6: Transfer response between the voltage input to car audio loudspeaker 1 and the pressure at microphone 9 positioned at the driver's outer right headrest.

To determine the maximum sound pressure levels that could be reproduced by the standard car audio loudspeakers, and therefore to indicate whether they will be able to generate the required cancelling pressures at the error sensors, a series of measurements were conducted where the four car audio loudspeakers were each driven with sine waves at 50, 100, 200 and 300 Hz. Two loudspeaker drive conditions have been investigated:

1. Constant drive at 5 volts for 10 seconds.

2. Ramp up in voltage with a peak of 14 volts.

The constant drive at 5 volts has been selected to provide an indication of the maximum steady-state sound pressure level reproducible and the ramp-up in voltage to 14 volts has been used to provide an indication of the short term, or peak voltage that may be applied to the loudspeakers without damaging the drivers. Figure 6.7 shows the mean sound pressure level produced at the 16 microphones under the two voltage drive conditions for the four car audio loudspeakers. From this plot it can be seen that the mean sound pressure level produced under both constant and peak voltage drive conditions is consistently lower at 50 Hz for all four loudspeakers. This is a result of the loudspeakers' resonances being at around 70 Hz and, therefore, the pressure per unit input volt is lower. The pressure produced by each loudspeaker for a constant input voltage level of 5 volts at 100, 200 and 300 Hz is between 90 and 105 dB, while the mean pressure level produced by a peak input voltage of 14 volts is between 102 and 112 dB, and these pressures are reasonably consistent with a linear response. It should be noted, however, that although the response at the driving frequency increased reasonably linearly with excitation voltage, at input voltages above about 1 volt a number of harmonics were produced by buzzing of the loudspeakers in their enclosures. This would severely limit the use of these loudspeakers for active control, since in reducing low frequency noise the loudspeakers would generate high frequencies, which may be more annoying.

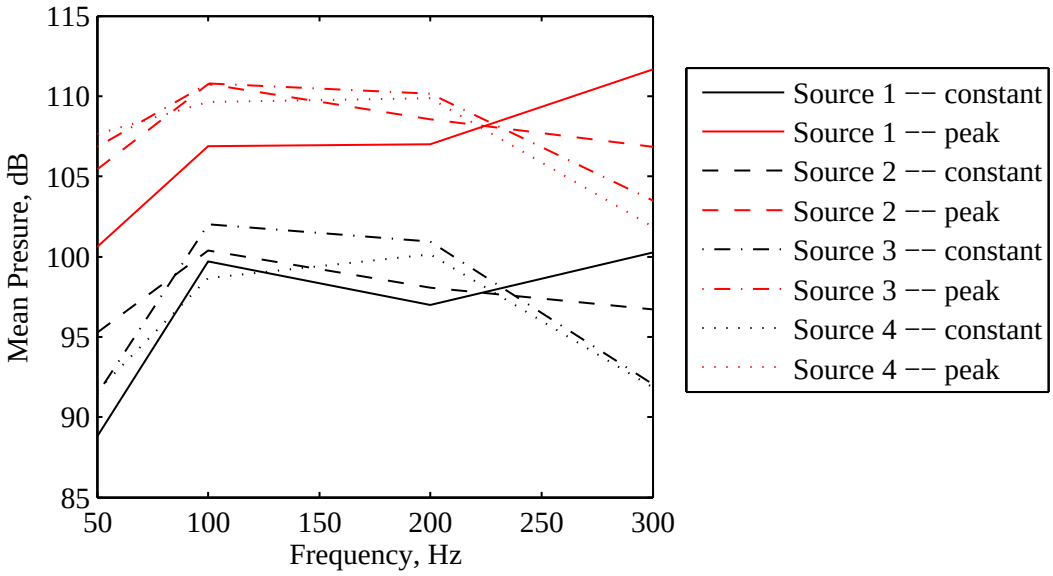

Figure 6.7: The mean sound pressure level produced at the 16 microphones by each of the loudspeakers for a constant drive level of 5 volts (black lines) and for a short-term peak input voltage of 14 volts (red lines).

In a practical scenario the car cabin will have at least a driver and possibly up to four additional passengers. Therefore, the transfer response between the voltage input to the loudspeaker and the pressure at the 16 microphones has also been measured when there is both either a driver or a driver and a front seat passenger in the vehicle. Figure 6.8 shows the acoustic transfer response between loudspeaker 1 and microphone 9, which is at the driver's right

ear, for the three different occupancy conditions measured. From this plot it can be seen that at frequencies below around 190 Hz the effect of varying the number of occupants is minimal, while at higher frequencies there are some significant variations in the magnitude and phase of the response. These results will be employed in offline simulations of the active control systems to test the robustness of the controllers to variations in the plant responses.

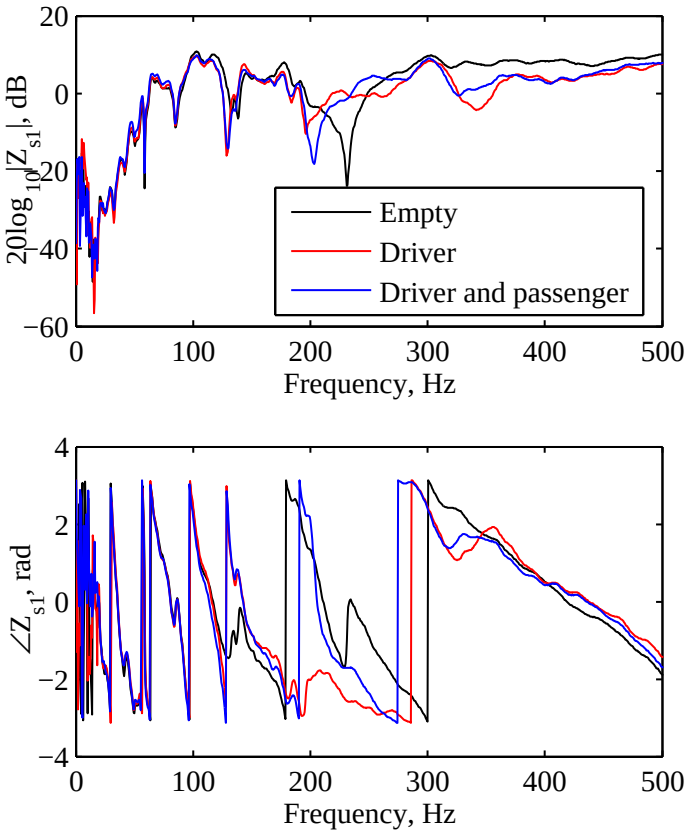

Figure 6.8: Transfer response between the voltage input to car audio loudspeaker 1 and microphone 9 (driver left ear) for three occupancy conditions: empty (—); driver (—); driver and passenger (—).

6.1.2 Engine Noise

To investigate the potential performance of the feedforward active noise control strategy, the pressure at the 16 microphone positions has been measured under a number of different engine conditions with the vehicle on the rolling road in a hemi-anechoic chamber. The different engine test conditions are detailed in Table 6.2. Measurements of the engine noise produced for a constant engine speed have been measured both out of gear and under load, this is to provide a consistent set of constant engine speed measurements; that is, due to the gearing of the vehicle it was not possible to run the engine at all desired speeds in the same gear.

Figure 6.9 shows the spectrum of the acoustic potential energy estimated from the 16 mi-

Table 6.2: Rolling road engine noise measurement conditions.

Engine Speed (rpm)	Condition (i)	Condition (ii)
1000	Out of gear	2nd gear
2000	Out of gear	3rd gear
3000	Out of gear	2nd gear
4000	Out of gear	3rd gear
5000	Out of gear	3rd gear
Engine run-up 1000 – 6000	WOT 2nd gear	WOT 3rd gear

crophones, E_p, at engine speeds of 1000, 2000, 3000, 4000 and 5000 rpm whilst out of gear. The frequency of the n-th engine order is given by

$$f_n = n \times \frac{\text{rpm}}{60}. \tag{6.1}$$

From Figure 6.9a it can be seen that only the first engine order has been significantly excited in this case, however, the resonance occurs at 20 Hz which does not correspond to the first engine order at an engine speed of 1000 rpm, which should be 16.6 Hz. This difference is because the engine speed was not accurately maintained at 1000 rpm during the measurements.

From Figures 6.9b through to 6.9e it can be seen that a full series of engine orders are excited. At 2000, 3000 and 4000 rpm the first engine order has the highest level and occurs at 33, 50 and 66 Hz respectively. At 5000 rpm, however, the second engine order, which occurs at 170 Hz, is the highest level order. A general trend can be seen from the results shown in Figure 6.9 in which the level of the engine orders becomes more constant with increasing engine speed.

Although the previous results show an indication of the engine noise spectrum produced at discrete engine speeds with no load on the engine, it is also interesting to observe the spectrum produced at various speeds when the engine is under load. Figure 6.10 shows the spectrum of the acoustic potential energy estimated from the 16 microphone pressure measurements for 1000, 2000, 3000, 4000 and 5000 rpm in various gears when the car is on a loaded rolling road. From these plots it can be seen that, in general, the spectrum produced is more complex than that produced by the out of gear engine. Narrowband peaks occur at frequencies not corresponding to integer engine orders and broader spectral peaks are also produced. For example, in Figure 6.10b at around 130 Hz a broad spectral peak can be observed. For the engine noise measurements under load the front wheels of the vehicle rotate and interact with the rolling road and this may produce additional noise not directly related to the engine. The interactions between the rolling road and the tyre will not be reproduced identically when the car is driven on a real road and, therefore, some of these non-integer engine orders may not occur in a real driving scenario. Although half engine orders may be produced by single cylinder variations or uneven exhaust pipe lengths [167], it is not clear if these effects are present here.

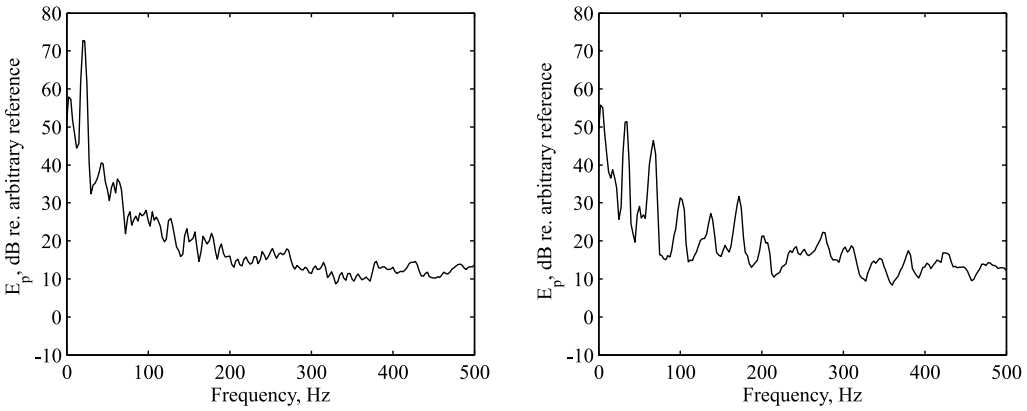

(a) 1000 rpm

(b) 2000 rpm

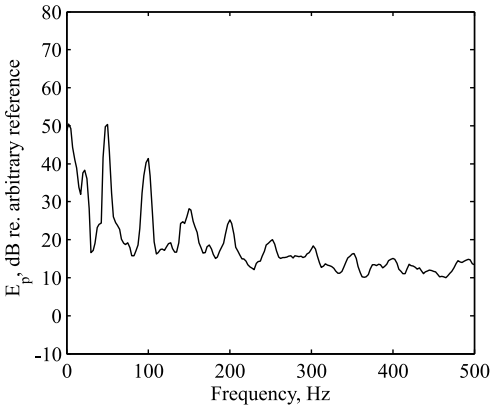

(c) 3000 rpm

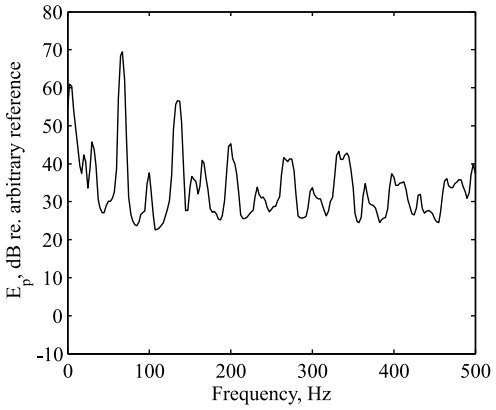

(d) 4000 rpm

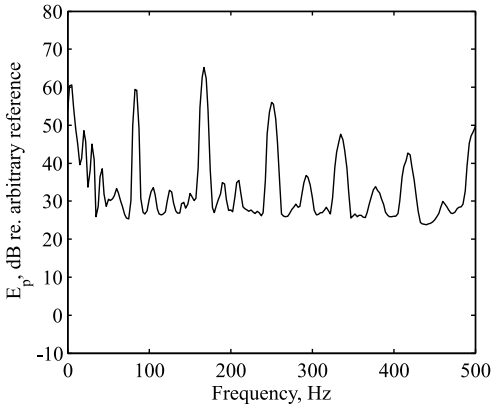

(e) 5000 rpm

Figure 6.9: The spectrum of the acoustic potential energy estimated from the 16 pressure measurements for various constant unloaded (out of gear) engine speeds.

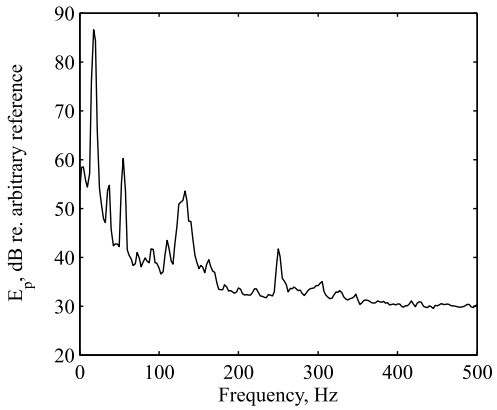

(a) 1000 rpm, 2nd gear

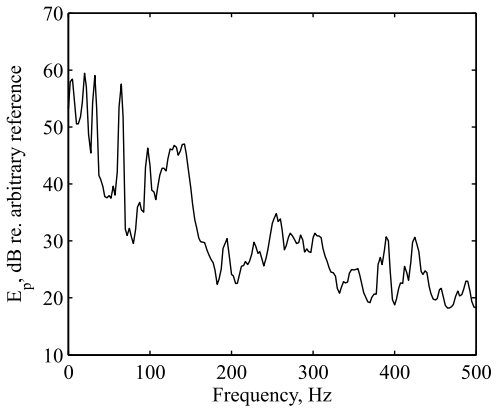

(b) 2000 rpm, 3rd gear

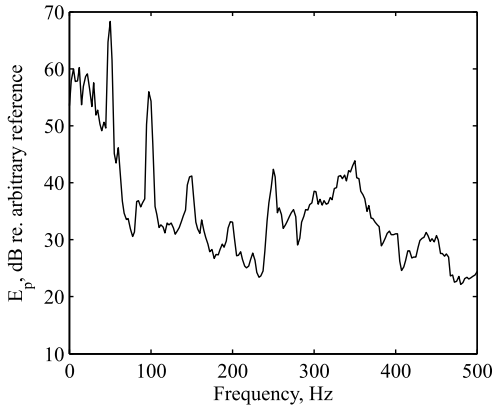

(c) 3000 rpm, 2nd gear

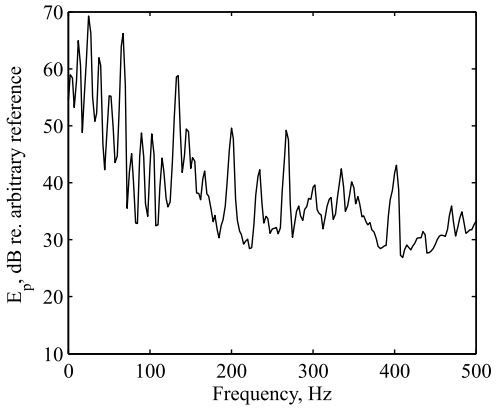

(d) 4000 rpm, 3rd gear

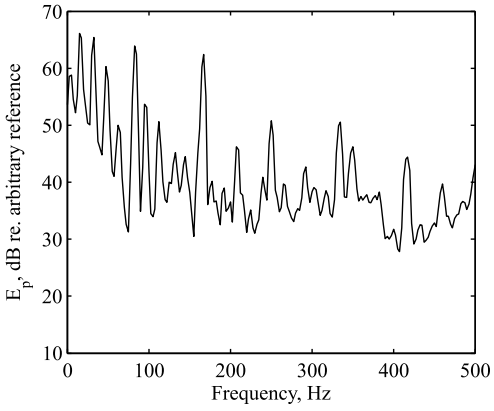

(e) 5000 rpm, 3rd gear

Figure 6.10: The acoustic potential energy estimated from the 16 pressure measurements for various constant engine speeds in various gears.

An overall picture of the engine noise and the components that require control can be obtained from the sound pressures produced during an engine run-up. This has been measured and Figures 6.11 and 6.12 show the plots of the change in the acoustic potential energy spectrum estimated using the 16 microphone measurements as the engine is accelerated from 1500 through to 6000 rpm in 2nd and 3rd gears respectively. These graphs were calculated using short term spectral estimates of different data blocks using the Matlab function *spectrogram*. From Figure 6.11 it can be seen that at engine speeds below 2500 rpm the first engine order dominates the spectrum, which is the order with a frequency of 100 Hz at 6000 rpm. At around 2500 rpm a sub-harmonic resonance at half the frequency of the first engine order produces a significant acoustic potential energy, but this half order becomes low in level again at around 3000 rpm. At around 3000 rpm some additional sub-harmonic components become significant, however, it is thought that they are related to the interaction between the vehicle and the rolling road, and would not be reproduced under standard road driving conditions. As the engine speed is increased further, the level of the first engine order tends to reduce and at around 4000 rpm the second engine order becomes dominant. The third, fourth and fifth engine orders are also clear in Figure 6.11, but their level is significantly below the first and second orders.

Figure 6.12 shows the acoustic potential energy for an engine run-up in 3rd gear. From this plot it can be seen that the first engine order produces a significant level throughout the range of engine speeds and at around 4000 rpm the level of the second engine order again becomes more dominant. At around 2500 rpm the half engine order is significantly excited and remains at a significant level until 3500 rpm. In comparison to the run-up in 2nd gear it can be seen that a full spectrum of half engine orders are also excited at levels comparable to the 3rd, 4th and 5th engine orders.

From the results presented in this section it is evident that the most significant contribution to the engine noise is the first engine order. At higher engine speeds the second engine order becomes more significant and, consequently, the engine begins to sound more like a four-cylinder. A further feature of the engine noise that has been highlighted from the results presented in this section is the presence of a half order which is significant in level, however, it occurs at a relatively low frequency and, therefore, controlling this order may not offer a significant subjective improvement.

6.1.3 Road Noise

To investigate the possible reductions in road noise that may be achieved using the MIMO feedback control system, measurements of the pressure produced at the 16 microphone positions while driving on two road surfaces – pavè and a rough road – have been conducted. Measurements have been conducted on the two road surfaces under two driving conditions:

1. Constant speed

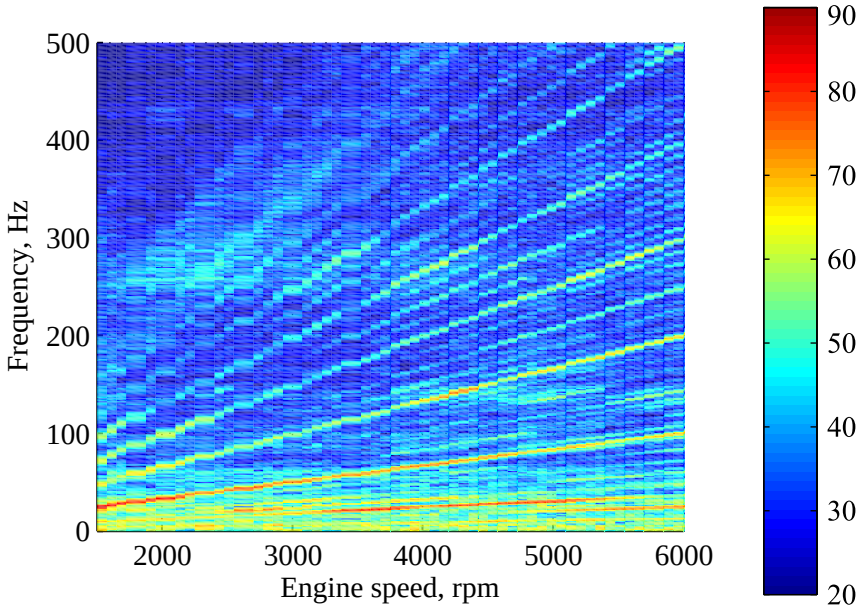

Figure 6.11: The acoustic potential energy estimated from the 16 pressure measurements plotted in decibels with reference to an arbitrary reference level for an engine run-up in 2nd gear

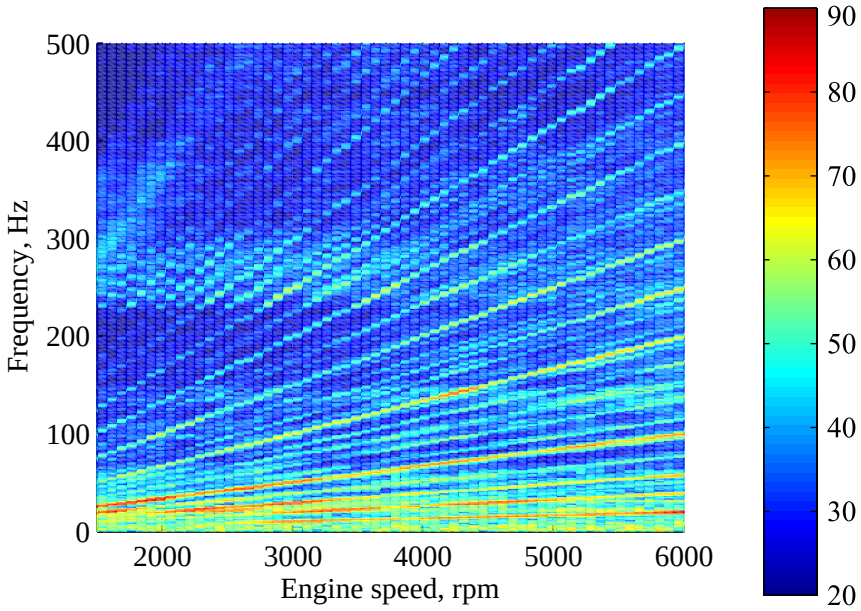

Figure 6.12: The acoustic potential energy estimated from the 16 pressure measurements plotted in decibels with reference to an arbitrary reference level for an engine run-up in 3rd gear

2. Coast down

The first driving condition provides a static noise spectrum, however, although these measurements are dominated by road noise since the load on the engine is relatively low at constant speed, the pressure levels also contain a contribution from the engine. The second driving condition allows a reduction in the engine noise contributions since the engine can be unloaded during the measurement. The details of the complete set of road noise measurements conducted is presented in Table 6.3

Table 6.3: Road noise measurement conditions

Surface	Test Condition	Speed
Pavè	Constant	50 km/h
	Cost down	55 – 45 km/h
Rough road	Constant	50 km/h
		75 km/h
		100 km/h
	Coast down	55 – 45 km/h
		80 – 70 km/h
		100 – 95 km/h

Figure 6.13 shows the A-weighted acoustic potential energy estimated using the 16 pressure measurements in the car cabin when the car is driven at a constant speed of 50 km/h on the pavè surface and on the rough road at constant speeds of 50, 75 and 100 km/h. The A-weighted spectrum has been presented since this allows a simple, informed judgement of the components of the road noise that contribute most significantly to the perceived noise. From this plot it can be seen that for all four constant speed measurements there is a significant broadband peak in the spectrum from 80 to 180 Hz. This peak is most significant for the measurements conducted on the pavè surface and, therefore, to be sure that the dominance of this peak on the pavè surface is not due to the constant road speed during the measurement and the size of the pavè blocks, Figure 6.14 shows the spectrum of the estimated acoustic potential energy during the coast down from 55 to 45 km/h. From this plot it can be seen that the broadband peak from 80 to 180 Hz is relatively constant with road speed and, therefore, is unlikely to be a result of the specific pavè block dimensions.

The constant road speed measurements shown in Figure 6.13 show a second frequency range with two significant narrowband peaks between 230 and 260 Hz, although the specific frequencies differ between the different driving conditions. These peaks can be related to the first tyre cavity resonance and the two resonance peaks are produced due to the tyre loading and resulting deformation producing a non-symmetrical structure [168]. The variation in the two spectral peaks is due to the Doppler effect and in general this causes the lower frequency resonance to decrease in frequency with increasing road speed, whilst the higher frequency

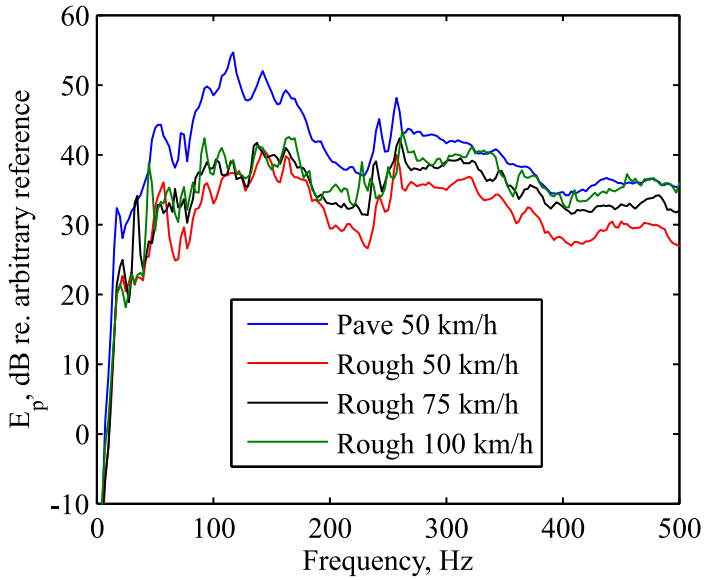

Figure 6.13: The A-weighted acoustic potential energy estimated from the 16 microphone measurements for a constant road speeds on the pavè and rough road.

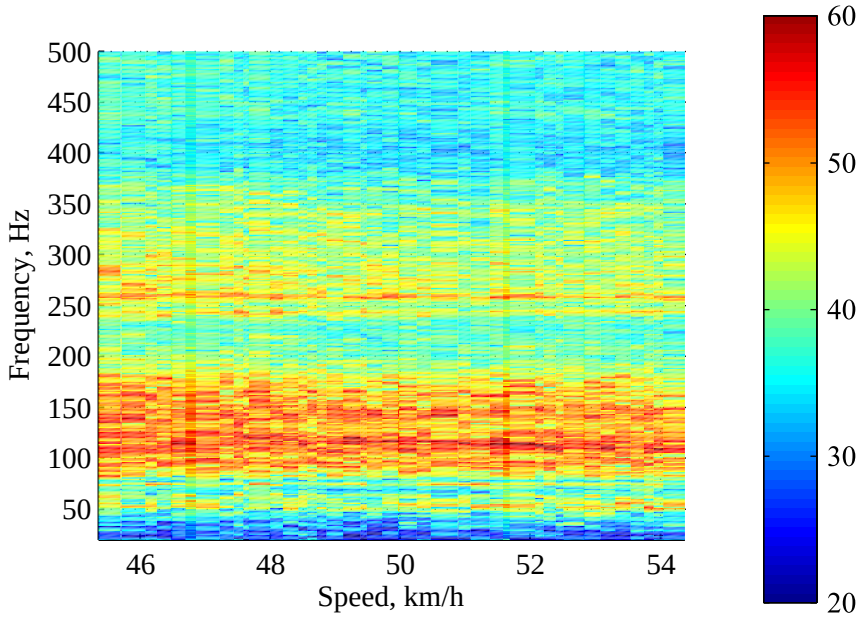

Figure 6.14: The A-weighted acoustic potential energy estimated from the 16 microphone measurements for a coast down from 55 to 45 km/h on the pavè plotted in decibels with reference to arbitrary reference level.

resonance increases in frequency [168].

From the results presented in this section it has been shown that there are two frequency regions where the reduction of road noise is required. These are between 80 and 180 Hz, where a structural resonance produces a broadband peak, and between around 230 and 260 Hz, where the tyre cavity resonance produces two narrowband peaks. Based on the results of the MIMO feedback control simulations presented in Chapter 5, the control of the tyre cavity resonances will not be achievable using the proposed feedback active noise control system due to their

relatively high frequency. The control of the broadband peak between 80 and 180 Hz, however, may be achievable using the proposed MIMO feedback controller and this will be investigated in Section 6.3.

6.2 Feedforward Control of Engine Noise

6.2.1 Offline Control Simulations

It has been shown in the results presented in Section 6.1.2 that the predominant source of engine noise is the first engine order. Therefore, optimal feedforward control of this engine order has been simulated using the engine run-up in third gear and the acoustic transfer responses measured using the volume velocity source. The feedforward control performance has been calculated using the short term Fourier transform of the engine run-up data such that within each time block it can be assumed that the engine speed is constant and, therefore, the control of the sound due to the first engine order can be calculated at a single frequency. In a practical system, where the engine speed would not necessarily be constant, it is necessary to track the engine speed using the rpm reference signal, however, for these initial control performance indications this is unnecessary.

Global Control

As detailed in Section 3.2.1, the optimal solution for an overdetermined control system, where the number of error sensors is greater than the number of secondary sources, gives the optimal secondary source strengths as

$$\boldsymbol{q}_{s0} = \left[\boldsymbol{Z}_s^H \boldsymbol{Z}_s + \beta \boldsymbol{I}\right]^{-1} \boldsymbol{Z}_s^H \boldsymbol{p}_e. \tag{6.2}$$

Using this optimal solution, Figure 6.15 shows the change in the sum of the squared pressures at the eight 'corner' error microphones, J_p, and the change in the sum of the squared pressures at all 16 microphones, E_p, when the four secondary sources are optimised to minimise the sum of the squared pressures at the eight corner error sensors, as in the global feedforward control simulations in Chapter 3. So that

$$J_p = \frac{1}{8} \sum_{m=1}^{8} |p_m|^2, \tag{6.3}$$

$$E_p = \frac{1}{16} \sum_{m=1}^{16} |p_m|^2, \tag{6.4}$$

where the first 8 microphones are those used in the control system. From this plot it can be seen that both J_p and E_p are reduced by up to 20 dB at low frequencies, with an average reduction of perhaps 10 dB. The level of control tends to reduce with increased engine speed, however, there are a number of frequency bands where a sudden drop in engine order reduction is observed. These can be attributed to both the change in the level of the primary disturbance

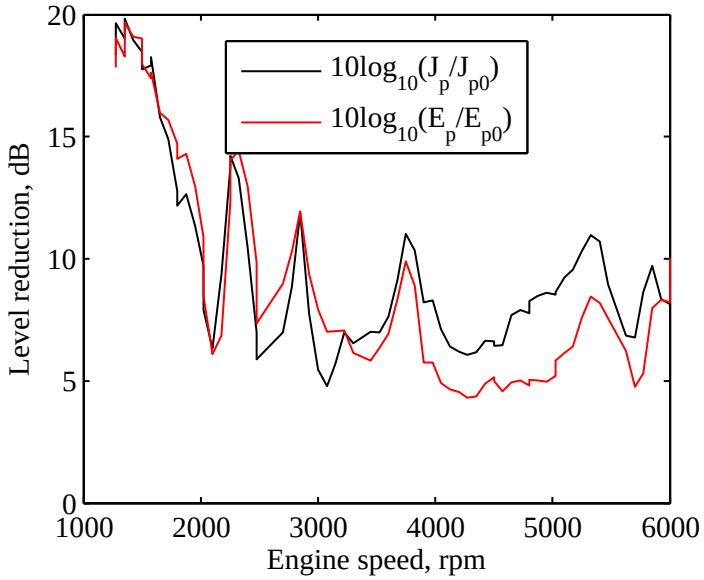

Figure 6.15: The change in the sum of the squared pressures due to the first engine order at the eight 'corner' error sensors, J_p, (—) and at all 16 microphone positions, E_p, (—) when the four loudspeakers are driven to minimise J_p.

with engine speed, and the coupling between the loudspeakers and the acoustical modes of the cabin. Despite the variations in control with engine speed, a reduction in the sum of the squared pressures at all 16 microphones of greater than 5 dB is achieved at all presented engine speeds.

Figure 6.16 shows the acoustic potential energy estimate, E_p, before and after optimal feedforward control of J_p at the first engine order. From this plot it can be seen that the variation in the level of the first engine order during the engine run-up has been reduced. The reductions in both J_p and E_p shown in Figures 6.15 and 6.16 are consistent with the results of the simulations in the rectangular enclosure presented in Chapter 3, where the reductions were most significant at low frequencies and reduced with increasing frequency as the number of excited acoustic modes increases.

It has been shown in Figures 6.15 and 6.16 that a significant level of control of the first engine order is possible. However, in a practical system it is also necessary to determine whether the required loudspeaker input voltages are within the range of the employed loudspeakers. For the standard car audio loudspeakers the pressures produced by a constant voltage sine wave input have been measured and are presented in Figure 6.7. Using the measurements of the pressure produced at 100 Hz by a 5 volt input to the loudspeakers and the sound pressures required to achieve the control of the first engine order presented above, the voltage input to the four car audio loudspeakers has been calculated and is presented in Figure 6.17. The estimation of this voltage has been calculated using the loudspeaker transfer responses presented in Figure 6.6 and a calibration factor calculated from the single frequency responses at 100 Hz.

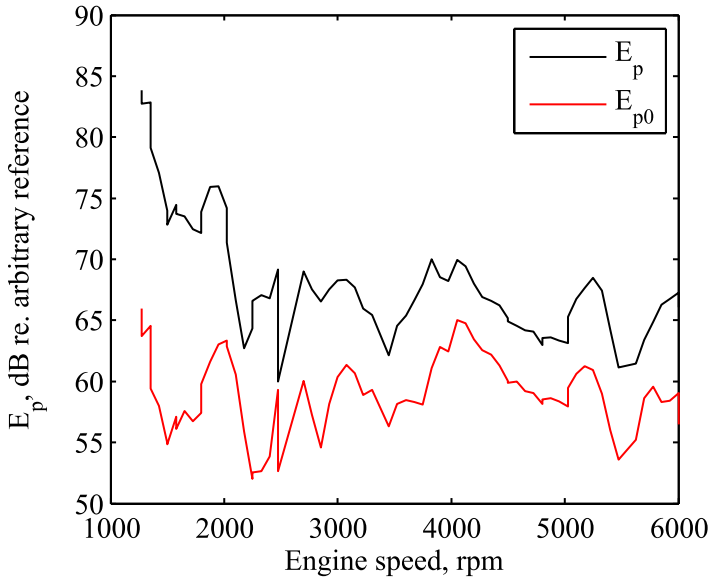

Figure 6.16: The acoustic potential energy estimated from the 16 pressure measurements due to the first engine order with no control (—) and when the four secondary sources have been optimised to minimise J_p (—) .

The validity of this single frequency calibration factor has been verified by using calibration factors calculated from the other single frequency responses, which showed a maximum variation in the calculated required voltage of 3 dB. From this plot it can be seen that for all four loudspeakers the voltage input required is greatest at low engine speeds, however, the predicted levels do not reach the 1 volt input level that produced significant buzzes in the vehicle.

Regional Control

It has been shown in Chapter 3 that by employing a regional control system, where the acoustic potential energy or pressures within a defined smaller region are minimised, it is possible to increase the bandwidth and levels of control compared to a global control system. Therefore, using the measurements in the small city car the performance of a feedforward control system that is optimised to minimise the sum of the squared pressures at the eight headrest microphones using the four car audio loudspeakers has been predicted. Figure 6.18 shows the resulting change in the sum of the squared pressures at the eight headrest error microphones, J_R, and the change in the sum of the squared pressures at all 16 microphones, E_p. From this plot it can be seen that between around 1200 and 6000 rpm in excess of 20 dB reduction is achieved in the sum of the squared pressures at the 8 headrest microphones. However, from the red line in Figure 6.18, which shows the sum of the squared pressures at all 16 microphone positions, it can be seen that global reductions are only achieved at lower engine speeds. This is consistent with the results presented in Chapter 3 where, although global reductions are achieved by the regional feedforward controller at low frequencies, significant enhancements are introduced

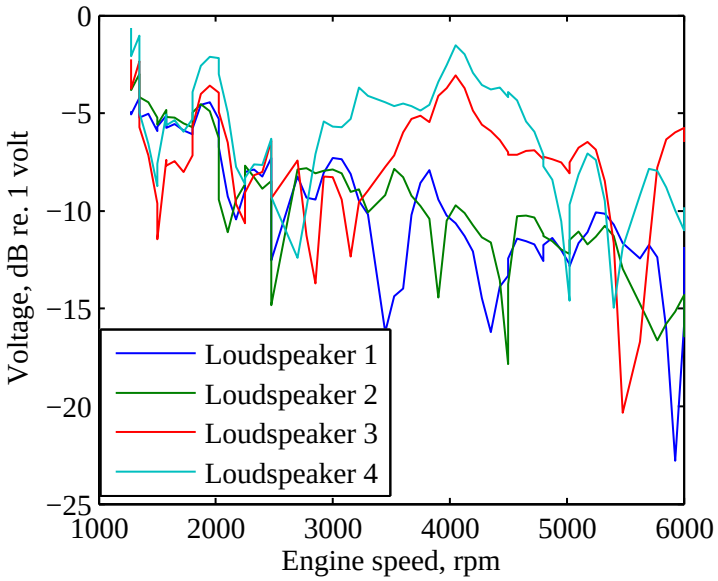

Figure 6.17: The estimated voltage input to the four loudspeakers required to achieve control of the first engine order at the eight 'corner' error microphones as the engine speed is increased from 1200 to 6000 rpm. The voltage is plotted in decibels relative 1 volt.

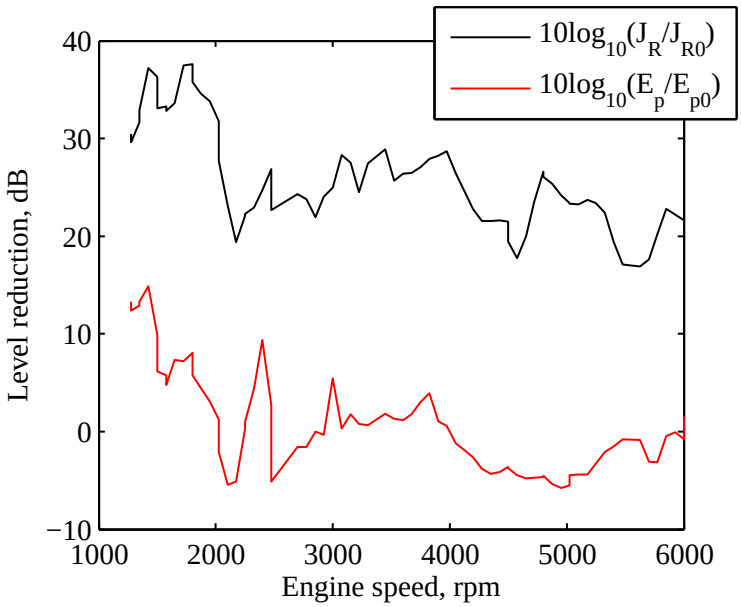

Figure 6.18: The change in the sum of the squared pressures due to the first engine order at the eight headrest error microphones, J_R, (—) and at all 16 microphone positions, E_p, (—) when the four loudspeakers are driven to minimise J_R.

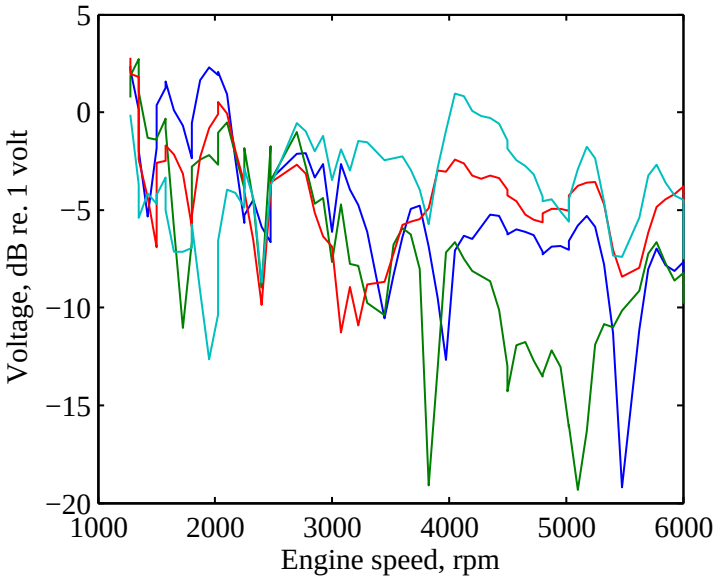

Figure 6.19: The estimated voltage input to the four loudspeakers required to achieve control of the first engine order at the eight headrest error microphones as the engine speed is increased from 1200 to 6000 rpm. The voltage is plotted in decibels relative 1 volt.

particularly at frequencies where unobservable modes occur.

Despite the enhancements in the sum of the squared pressures at all 16 microphones, the regional control strategy does offer a potentially significant improvement in the levels of control achievable at the locations of the car cabin's occupants'. Therefore, it is again important to determine whether the required loudspeaker input voltages are within the limits of the car audio loudspeakers. Figure 6.19 shows the voltage input to the four car audio loudspeakers required by the regional control system plotted in decibels relative to 1 volt. From this plot it can be seen that the voltage input required to achieve the levels of control presented in Figure 6.18 are greater than 1 volt at some engine speeds and, therefore, may produce additional harmonics as discussed in Section 6.1.1.

Due to the significant performance increase between the global and regional feedforward control strategies that has been predicted using the offline simulations, it is desirable to implement the regional feedforward control strategy in a real-time system. However, it has been shown that the car audio loudspeakers will probably produce additional harmonics at the required voltage drive levels. In a future implementation it may be possible to avoid these problems through improving the car audio loudspeakers' mounting system or by increasing the damping of the interior car door panels. To avoid this problem in the implemented real-time system a separate set of closed-back loudspeakers will be employed at positions close to the standard car audio loudspeakers. However, since it will not be possible to position a loudspeaker in the foot-well of the driver due to safety, it is necessary to determine whether removing this loudspeaker from the control system will have a significant effect on the control performance or required voltage levels. Additionally, in order to reduce the computational de-

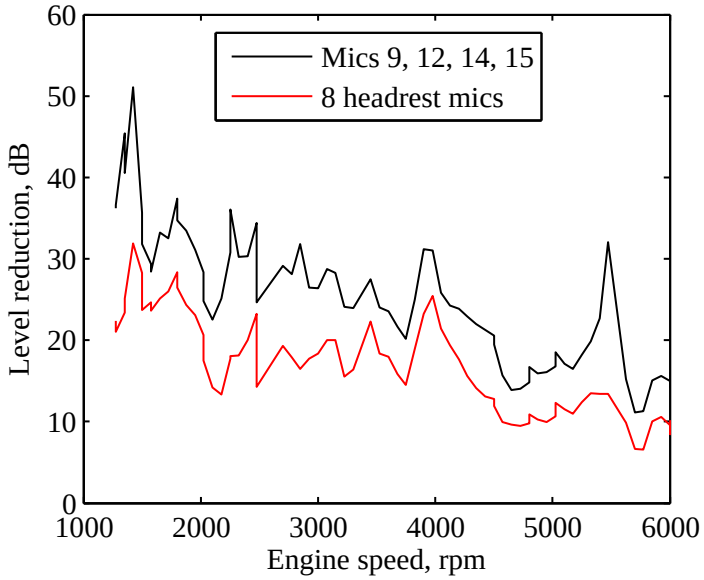

Figure 6.20: The change in the sum of the squared pressures due to the first engine order at the four headrest error microphones 9, 12, 14, and 15 (—) and at all eight headrest microphone positions (—) when the three loudspeakers positioned at locations 2, 3 and 4 in Figure 6.4 are driven to minimise the pressures at microphones 9, 12, 14, and 15.

mand of the real-time controller, the effect of reducing the number of error sensors to four, with one at each headrest position will also be calculated. Figure 6.20 shows the change in the sum of the squared pressures at the eight headrest microphones and at microphones 9, 12, 14 and 15 when the sum of the squared pressures at these microphones has been minimised using the three car audio loudspeakers positioned at locations 2, 3 and 4 shown in Figure 6.4. From this plot it can be seen that a significant level of control has been achieved at the four error microphones, however, the important result is that significant levels of control are also achieved at all eight headrest microphone positions. Additionally, the use of three control loudspeakers does not appear to significantly reduce the levels of control within the bandwidth of the first engine order. Figure 6.21 shows the required voltage input to the three control loudspeakers and it can be seen from this plot that, although there are variations in the voltage required by each of the loudspeakers compared to those shown in Figure 6.19 for the 4 loudspeaker system, the maximum level required by each loudspeaker is not significantly affected. The real-time implementation of this control system will therefore be investigated.

6.2.2 Design and Implementation of a Real-Time Controller

Up to this point the performance of the feedforward controller has been predicted in the frequency domain using the least-squares solution. To implement real-time feedforward control of engine noise it is necessary to be able to track the changes in the frequency and spatial distribution of the primary field that occur as the engine speed and load is varied. This can be

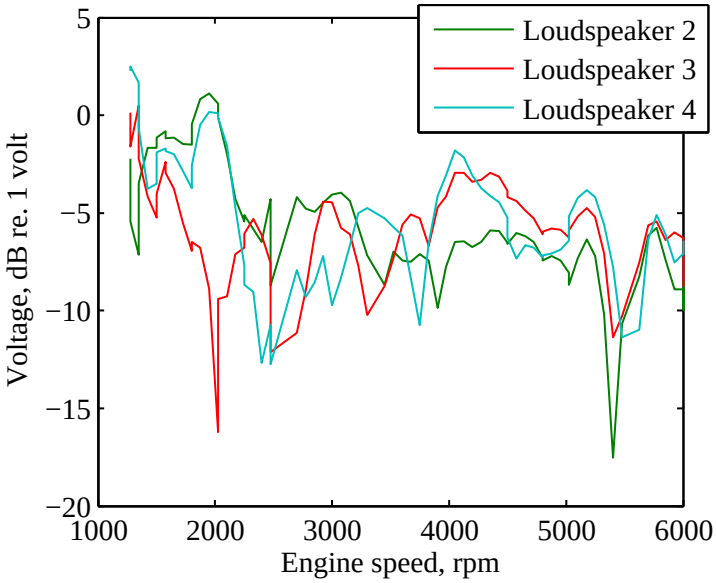

Figure 6.21: The estimated voltage input to the four loudspeakers required to achieve control of the first engine order at the eight headrest error microphones as the engine speed is increased from 1200 to 6000 rpm. The voltage is plotted in decibels relative 1 volt.

achieved by making the control filters adapt over time to minimise the mean-sqaure error. If the control filters are implemented as FIR filters then, since the error surface for such filters has a quadratic shape, it is possible to converge toward the global optimum by adjusting the control filter coefficients by a small amount in the direction of the negative gradient of the cost function with respect to the filter coefficient [132]; this adaptive process is referred to as the steepest descent algorithm. A widely used, simple and robust implementation of steepest descent algorithm is the LMS algorithm in which the filter coefficients are updated based on the instantaneous estimate of the gradient rather than an averaged estimate [132]. The LMS algorithm is given by [132]

$$\boldsymbol{w}(n+1) = \boldsymbol{w}(n) + \alpha \boldsymbol{x}(n) e(n), \tag{6.5}$$

where n is the iteration number, $\boldsymbol{w}$ is the vector of I FIR control filter coefficients, α is the convergence coefficient, $\boldsymbol{x}$ is vector of reference signals over the past I samples and e is the error signal.

The Filtered-Reference LMS Algorithm

Although a wide variety of algorithms have been proposed and employed to adapt the filter coefficients in a feedforward active noise control system, the filtered-reference LMS algorithm has probably been most widely employed. Since the filtered-reference LMS algorithm is simple to implement and particularly efficient for tonal noise control problems [132] it will be employed here in the implementation of the engine noise controller.

In the context of feedforward active noise control it is necessary to modify the LMS al-

gorithm since the error signal input to the controller has been filtered by the plant response and, therefore, is no longer aligned in time with the reference signal. The error and reference signals can be aligned in time by pre-filtering the reference signal using an estimate of the plant response and this results in the filtered-reference LMS algorithm [132].

The filtered-reference LMS algorithm has been derived in a number of widely available publications [132, 169] and it will be presented here for the specific case of controlling a single frequency using L_e error sensors, M control sources and I coefficient FIR filters modelling the plant responses. The single frequency control problem can be efficiently solved using a filtered-reference LMS controller with two adaptive weights controlling the in-phase and quadrature components of the control signals, as described in [170]. The in-phase component of the reference signal at the control frequency f_c is given by

$$x_R(n) = \cos(2\pi f_c n T_s) \tag{6.6}$$

where T_s is the sample period, and the quadrature component of the reference signal is given by

$$x_Q(n) = \sin(2\pi f_c n T_s). \tag{6.7}$$

The following derivation will be presented using the control notation, as apposed to the acoustic notation used in the earlier chapters, since this nomenclature is more widely used in this context.

By assuming that the control filter coefficients vary slowly with time compared to the plant dynamics, in the discrete time domain the vector of error signals at the n-th sample is approximated by [132]

$$\boldsymbol{e}(n) = \boldsymbol{d}(n) + \boldsymbol{R}(n)\boldsymbol{w}(n), \tag{6.8}$$

where $\boldsymbol{e}(n)$ is the vector of $(L_e \times 1)$ error signals, $\boldsymbol{d}(n)$ is the vector of $(L_e \times 1)$ disturbance signals, $\boldsymbol{w}(n)$ is the vector of $(2M \times 1)$ control filter coefficients and $\boldsymbol{R}(n)$ is the $(L_e \times 2M)$ matrix of filtered reference signals. The vector of $2M$ control filter coefficients is given by

$$\boldsymbol{w} = \left[\boldsymbol{w}_1^T, \boldsymbol{w}_2^T, \cdots, \boldsymbol{w}_M^T\right]^T, \tag{6.9}$$

where the two filter coefficients related to the m-th source are

$$\boldsymbol{w}_m = \left[w_{m_R}, w_{m_Q}\right]^T, \tag{6.10}$$

where w_{m_R} is the in-phase filter coefficient and w_{m_Q} is the quadrature filter coefficient. The

matrix of filtered reference signals is given by

$$\boldsymbol{R}(n) = \begin{bmatrix} \boldsymbol{r}_1^T(n) \\ \boldsymbol{r}_2^T(n) \\ \vdots \\ \boldsymbol{r}_{L_e}^T(n) \end{bmatrix}, \tag{6.11}$$

where $\boldsymbol{r}_l$ is the $(2M \times 1)$ vector

$$\boldsymbol{r}_l(n) = \left[r_{l1_R}, r_{l1_Q}, \cdots, r_{lM_R}, r_{lM_Q} \right], \tag{6.12}$$

and r_{lm_R} is the in-phase reference signal filtered by the plant response from error sensor l to secondary source m and r_{lm_Q} is the quadrature reference signal filtered by the plant response from error sensor l to secondary source m. The in-phase reference signal is given by

$$r_{lm_R}(n) = \sum_{j=0}^{J-1} g_{lmj} x_R(n-j), \tag{6.13}$$

where g_{lmj} is j-th coefficient of the J coefficient FIR filter which represents the plant response between the l-th error sensor and m-th secondary source to arbitrary accuracy. The quadrature reference signal is given by

$$r_{lm_Q}(n) = \sum_{j=0}^{J-1} g_{lmj} x_Q(n-j), \tag{6.14}$$

The aim of the multichannel adaptive controller is to minimise the sum of the squared error signals. The instantaneous sum of the squared error signals is given by

$$J_p(n) = \boldsymbol{e}^T(n)\boldsymbol{e}(n) = \boldsymbol{w}^T(n)\boldsymbol{R}^T(n)\boldsymbol{R}(n)\boldsymbol{w}(n) + 2\boldsymbol{w}^T(n)\boldsymbol{R}^T(n)\boldsymbol{d}(n) + \boldsymbol{d}^T(n)\boldsymbol{d}(n), \tag{6.15}$$

and as detailed above the LMS algorithm attempts to minimise this cost function by adjusting each control filter coefficient in the direction of the negative gradient of the cost function with respect to the filter coefficients. The derivative of equation 6.15 with respect to the filter coefficients is

$$\frac{\partial J_p(n)}{\partial \boldsymbol{w}(n)} = 2\left[\boldsymbol{R}^T(n)\boldsymbol{R}(n)\boldsymbol{w}(n) + \boldsymbol{R}^T(n)\boldsymbol{d}(n) \right], \tag{6.16}$$

$$= 2\boldsymbol{R}^T(n)\boldsymbol{e}(n), \tag{6.17}$$

and therefore the filtered-reference LMS algorithm, which describes the adaptation of the filter coefficients, is given by

$$\boldsymbol{w}(n+1) = \boldsymbol{w}(n) - \alpha\boldsymbol{R}^T(n)\boldsymbol{e}(n). \tag{6.18}$$

In practice the matrix of filtered reference signals is obtained using a model of the plant responses and the matrix of filtered reference signals is known only approximately as, $\hat{\boldsymbol{R}}(n)$,

where the degree of accuracy in this case is dependent on the I coefficient FIR plant modelling filters. The filtered-reference LMS algorithm using the model of the plant responses is

$$\boldsymbol{w}(n+1) = \boldsymbol{w}(n) - \alpha\hat{\boldsymbol{R}}^T(n)\boldsymbol{e}(n). \tag{6.19}$$

To implement the filtered-reference LMS algorithm it is necessary to determine suitable values of the convergence coefficient α, since this parameter determines both the stability of the controller and its performance. That is, a relatively low value of α will give a slow convergence speed, but a small error, whilst a relatively large value of α will give a faster convergence but may compromise the minimisation of the error signal. A method of combining these two properties using a convex combination of two adaptive LMS filters has recently been proposed in [171], however, this increases the computational demand and will therefore not be considered in this work.

The convergence condition of the multichannel filtered-reference LMS algorithm has been derived for example in [132] and for the general case of a stochastic disturbance signal is given by

$$0 < \alpha < \frac{2\Re(\lambda_m)}{|\lambda_m|^2} \qquad \forall \quad \lambda_m, \tag{6.20}$$

where λ_m are the eigenvalues of the matrix $E\left[\hat{\boldsymbol{R}}^T(n)\boldsymbol{R}(n)\right]$. However, for a tonal controller where the reference signal, x, is a pure tone, it is the eigenvalues of the matrix $\hat{\boldsymbol{G}}^H(j\omega_c)\boldsymbol{G}(j\omega_c)$ at the frequency of the disturbance signal, ω_c, that are relevant and, therefore, it can be seen that the maximum convergence coefficient is a function of frequency. Although a constant value of α may be selected which ensures a stable controller at all frequencies, it is possible to improve the performance of the controller by employing a frequency dependent convergence coefficient. In the engine noise control system the convergence coefficient can be scheduled on the engine speed via the reference signal. The filtered-reference LMS algorithm can then be rewritten with a time varying convergence coefficient as

$$\boldsymbol{w}(n+1) = \boldsymbol{w}(n) - \alpha(n)\hat{\boldsymbol{R}}^T(n)\boldsymbol{e}(n), \tag{6.21}$$

where the value of $\alpha(n)$ is given by

$$\alpha(n) = \alpha_g\alpha_f(f) \tag{6.22}$$

where α_g is a frequency independent value that is used to allow a general trade-off between convergence and accuracy, while α_f is the frequency dependent convergence coefficient that is scheduled on the frequency of the disturbance signal, and is set according to the maximum bound given by equation 6.20 using the largest eigenvalue of $\hat{\boldsymbol{G}}^H(j\omega_c)\boldsymbol{G}(j\omega_c)$.

Total Control Effort Constraint

In a practical control scenario it may be necessary to not only minimise the cost function, J_p, but to also impose a constraint on the electrical power required by the control system. This can be achieved by minimising the generalised cost function given by the sum of J_p and a term proportional to the control effort, as detailed in Section 3.2.1 in the context of a frequency domain, least-squares optimisation. For a tonal controller, in the time domain the cost function with a constraint on the control effort can be expressed as

$$J_{cost}(n) = \boldsymbol{e}^T(n)\boldsymbol{e}(n) + \beta \boldsymbol{w}^T(n)\boldsymbol{w}(n), \tag{6.23}$$

so that,

$$J_{cost}(n) = \boldsymbol{w}^T(n)\boldsymbol{R}^T(n)\boldsymbol{R}(n)\boldsymbol{w}(n) + 2\boldsymbol{w}^T(n)\boldsymbol{R}^T(n)\boldsymbol{d}(n) + \boldsymbol{d}^T(n)\boldsymbol{d}(n) + \beta \boldsymbol{w}^T(n)\boldsymbol{w}(n), \tag{6.24}$$

where β is the control effort weighting parameter and the sum of the squared filter coefficients, $\boldsymbol{w}^T(n)\boldsymbol{w}(n)$, is proportional to the sum of the squared control signals. With this new cost function the instantaneous gradient is given by

$$\frac{\partial J_{cost}(n)}{\partial \boldsymbol{w}(n)} = 2\left[\boldsymbol{R}^T(n)\boldsymbol{e}(n) + \beta \boldsymbol{w}(n)\right], \tag{6.25}$$

and the filtered-reference LMS algorithm with the modelled plant filtered reference is given by

$$\boldsymbol{w}(n+1) = (1 - \alpha(n)\beta)\boldsymbol{w}(n) - \alpha \hat{\boldsymbol{R}}^T(n)\boldsymbol{e}(n). \tag{6.26}$$

Individual Control Effort Constraints

Although the total control effort constraint has been widely used, in practice it is the individual amplifiers or loudspeakers that often limit the performance of the control system. Therefore, it is perhaps more practically useful to impose a constraint on the individual control effort for each secondary source and this has been proposed in [172]. In this case the cost function to be minimised can be expressed as

$$\begin{aligned} J_{cost}(n) &= \boldsymbol{e}^T(n)\boldsymbol{e}(n) + \sum_{m=1}^{M} \beta_m \boldsymbol{w}_m^T(n)\boldsymbol{w}_m(n) \\ &= \boldsymbol{w}^T(n)\boldsymbol{R}^T(n)\boldsymbol{R}(n)\boldsymbol{w}(n) + 2\boldsymbol{w}^T(n)\boldsymbol{R}^T(n)\boldsymbol{d}(n) + \boldsymbol{d}^T(n)\boldsymbol{d}(n) + \sum_{m=1}^{M} \beta_m \boldsymbol{w}_m^T(n)\boldsymbol{w}_m(n), \end{aligned} \tag{6.27}$$

where β_m is the control effort weighting parameter related to the m-th source and $\boldsymbol{w}_m^T(n)\boldsymbol{w}_m(n)$ is the sum of the squared filter coefficients for the m-th source. The instantaneous gradient

vector is then given by

$$\frac{\partial J_{cost}(n)}{\partial \boldsymbol{w}(n)} = 2\left[\boldsymbol{R}^T(n)\boldsymbol{e}(n) + \boldsymbol{\Lambda}\boldsymbol{w}(n)\right], \tag{6.28}$$

where $\boldsymbol{\Lambda}$ is a diagonal matrix containing the $2M$ vector of control effort weightings $\boldsymbol{\beta} = [\beta_1, \beta_1, \beta_2, \beta_2, \cdots, \beta_M, \beta_M]$ on the diagonal. The filtered-reference LMS algorithm is then modified to give

$$\boldsymbol{w}(n+1) = (1 - \alpha(n)\boldsymbol{\Lambda})\boldsymbol{w}(n) - \alpha\hat{\boldsymbol{R}}^T(n)\boldsymbol{e}(n), \tag{6.29}$$

Elliott and Baek [172] propose to schedule the values of the vector $\boldsymbol{\beta}$ on the instantaneous values of the corresponding individual source control efforts. This is achieved by defining a maximum control effort for each source, P_L, and scheduling each of the weighting parameters, $\beta_m(n)$, such that they are zero when $\boldsymbol{w}_m^T(n)\boldsymbol{w}_m(n) < 0.9P_L$, and increase in proportion to $\boldsymbol{w}_m^T(n)\boldsymbol{w}_m(n) - 0.9P_L$ at levels above $0.9P_L$; this piecewise linear scheduling function is shown in Figure 6.22 by the red line. Although this method appears to work in the simulations presented in [172], when implemented in the real-time controller the switching between the two scheduling states produced audible oscillations in the error signal. Therefore, the control effort parameters were instead scheduled using an inverse barrier type function as

$$\beta_m(n) = \left| \frac{1}{P_L - \boldsymbol{w}_m^T(n)\boldsymbol{w}_m(n)} - \frac{1}{P_L} \right|, \tag{6.30}$$

such that as $\boldsymbol{w}_m^T(n)\boldsymbol{w}_m(n)$ tends towards the limit, P_L, the effort weighting tends towards a very large value and if $\boldsymbol{w}_m^T(n)\boldsymbol{w}_m(n)$ is much less than the limit then the effort weighting tends towards a very small value. This inverse barrier type scheduling function is shown in Figure 6.22 by the solid black line and due its continuously varying nature avoids the oscillating effects produced by the piecewise scheduling function. For the time varying effort weighting the update algorithm becomes

$$\boldsymbol{w}(n+1) = (1 - \alpha(n)\boldsymbol{\Lambda}(n))\boldsymbol{w}(n) - \alpha\hat{\boldsymbol{R}}^T(n)\boldsymbol{e}(n). \tag{6.31}$$

In addition to the scheduling based on an absolute power limit it is also important to limit the voltage sent to the loudspeakers at frequencies below their operable range. Therefore, a second scheduling method has also been introduced which increases the value of the control effort weighting parameters as the disturbance frequency goes below the limit of the loudspeakers. In this case the control effort parameters have been scheduled such that if the frequency of disturbance is greater than some limit, f_L, then the effort weighting parameters due to this constraint are zero, whilst if the disturbance frequency is lower than the limit then

$$\beta_m(n) = \frac{f_L - f(n)}{f_L}. \tag{6.32}$$

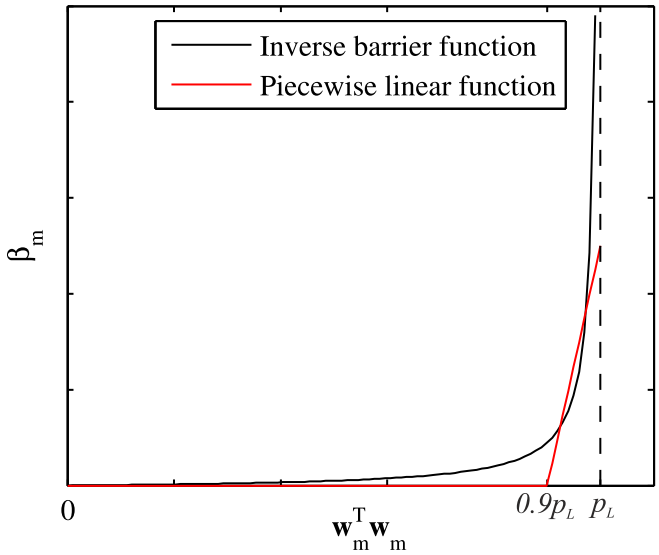

Figure 6.22: Effort weighting parameter, β_m, scheduling functions.

The two effort weighting parameters scheduled on equation 6.30 and 6.32 are summed in the controller.

6.2.3 Performance of the Real-Time Controller in a Laboratory Setup

To test the performance of the proposed control strategy in an controllable environment, the regional feedforward control system with 4 error microphones and 3 control loudspeakers was implemented in the laboratory, as shown in Figure 6.23. The controller is based around a DSpace DS-1103 board and the control algorithm has been implemented using Simulink. Details of the Simulink implementation are presented in Appendix I. To avoid aliasing in the error signals and reconstruction artefacts in the control signals anti-aliasing filters and reconstruction filters were employed with a cut-off frequency of 200 Hz. These were implemented using first-order analogue low-pass filters and are able to provide adequate roll-off at the Nyquist frequency due to the high sampling rate of the system – 8 kHz – relative to the disturbance and their specification is detailed in Section D.4.2. The control system was used to control a single tone generated within the DSpace system and reproduced by an 18-inch volume velocity source, which was positioned approximately equal distance from the error microphones as the control loudspeakers, as depicted in Figure 6.23.

From Figure 6.23 it can be seen that loudspeakers 1 and 2 were KEF B200G drivers which have a 183 mm diameter cone and were mounted in closed-back cabinets with an internal volume of approximately 0.01 m^3 and their full specification is provided in Section D.4.3. Loudspeaker 3 was a larger KEF B300B driver with a 288 mm diameter cone mounted in a closed-back cabinet with an internal volume of 0.026 m^3 and its full specification is provided in Section D.4.4. The low frequency limit, f_L, used to schedule the power constraint given by

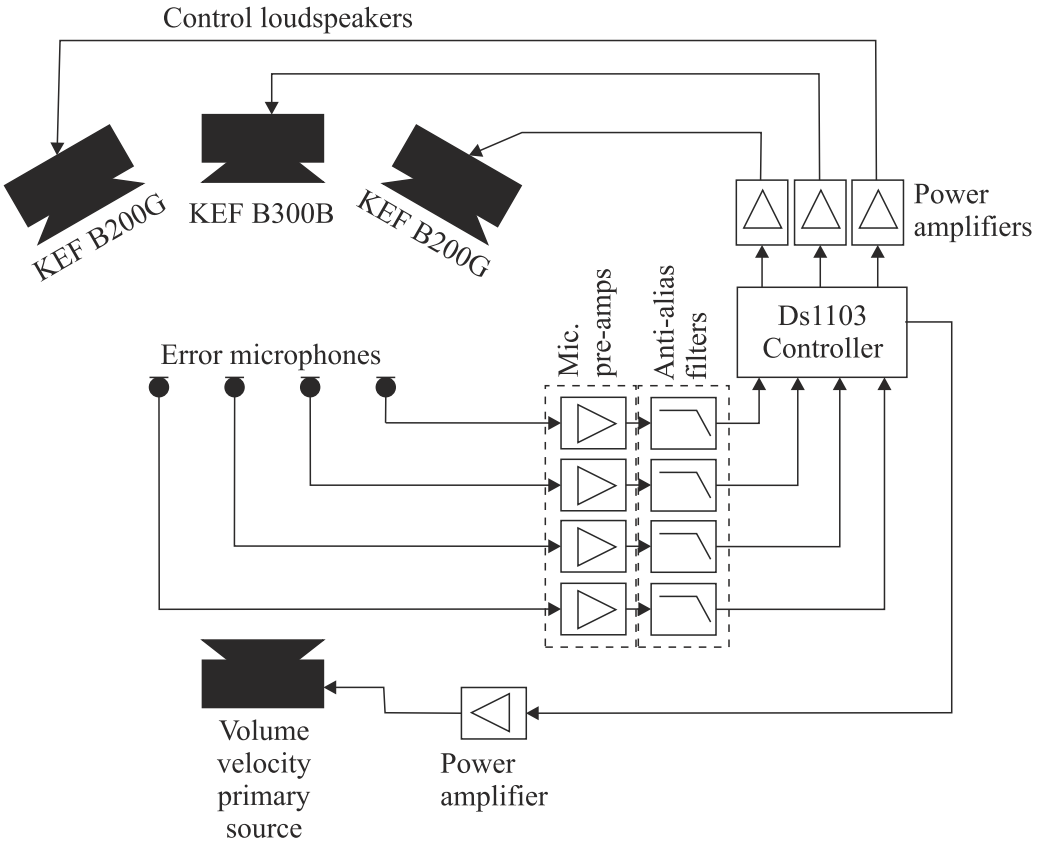

Figure 6.23: The feedforward control system implemented in the lab with three control loudspeakers, four error microphones and a primary disturbance produced by a single 18-inch volume velocity source.

equation 6.32 was set at 25 Hz for loudspeakers 1 and 2 and 20 Hz for loudspeaker 3.

Plant Response

To implement the feedforward controller using the filtered-reference LMS algorithm it is necessary to implement a model of the plant response. Therefore, the response between the input voltage to each loudspeaker and the resulting output voltage from each error microphone has been measured. The responses measured between each of the loudspeakers and the microphones are presented in Figure 6.24. From Figures 6.24a and 6.24b, which show the responses for the two smaller loudspeaker units, it can be seen that the magnitude responses begin to roll-off at around 95 Hz, which corresponds to the resonance of the KEF B200G loudspeaker driver in the closed-back enclosure. The magnitude response of the larger loudspeaker unit, which is shown in Figure 6.24c, begins to roll-off at frequencies below around 75 Hz which corresponds to the resonance of the KEF B300B driver in the larger closed-back enclosure. For all three loudspeakers it can be seen that at frequencies above around 200 Hz the measured responses begin to roll-off due to the anti-aliasing and reconstruction filters.

The phase responses shown in Figure 6.24 show an increasing lag with frequency with an overall delay of around 1.5 ms. This delay is due to a combination of the acoustic propagation time between the loudspeaker and the microphone, which is around 1 ms in this case, the delay introduced by the DSpace system's digtal-to-analogue converters and the delay due to the anti-aliasing filters. This delay can also be clearly seen in the impulse response measured between loudspeaker 3 and microphone 2, which is shown by the black line in Figure 6.25.

To implement the filtered-reference LMS controller a model of the measured plant responses is required. In a single frequency control system it is possible to model the plant responses using a two-coefficient filter since the response is only required at a single frequency [132]. If the controller is required to track a varying disturbance frequency a two-coefficient filter plant model may still be employed by using a look-up table indexed according to the disturbance frequency. However, it is straightforward to model the plant responses using fixed FIR filters. The measured plant responses presented in Figure 6.24 were modelled using 60 coefficient FIR filters that accurately represented the magnitude and phase response between around 20 and 100 Hz. This frequency range corresponds to the bandwidth over which the first engine order varies between engine speeds of 1200 and 6000 rpm. Figure 6.26 shows the measured and modelled plant responses between each of the loudspeakers and microphone 2. From these plots it can be seen that over the frequency range of interest the modelled plant responses match the measured responses with reasonable accuracy. At frequencies below around 20 Hz the accuracy of the FIR filters begins to significantly reduce, however, this is below the operating frequency of the control system and, therefore, will not degrade performance. The remaining FIR plant model filters show similar properties to those shown in Figure 6.26 and,

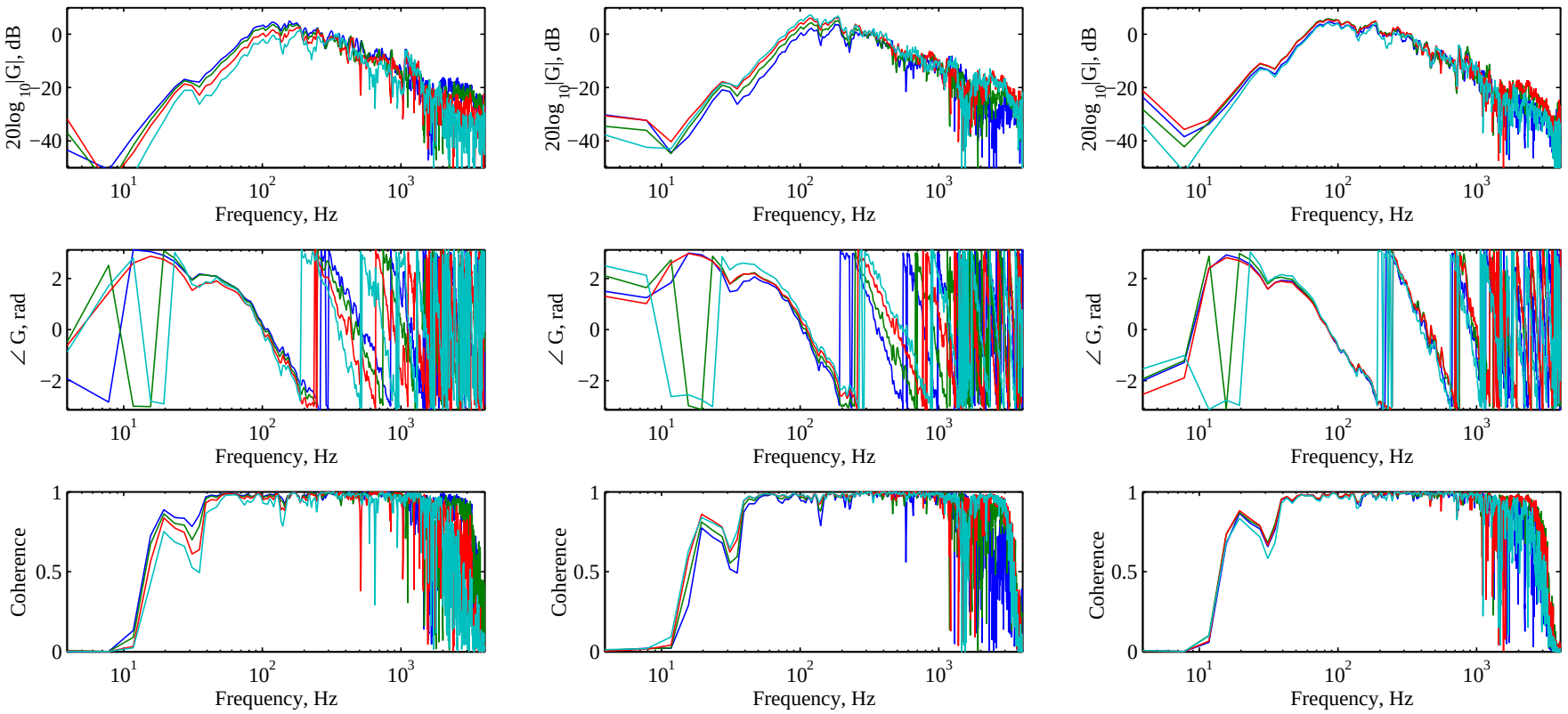

(a) Loudspeaker 1 – KEF B200G

(b) Loudspeaker 2 – KEF B200G

(c) Loudspeaker 3 – KEF B300B

Figure 6.24: The plant response measured between each control loudspeaker and the four error microphones in the laboratory setup in Figure 6.23: Mic. 1 (—), Mic. 2 (—), Mic. 3 (—), Mic. 4 (—)

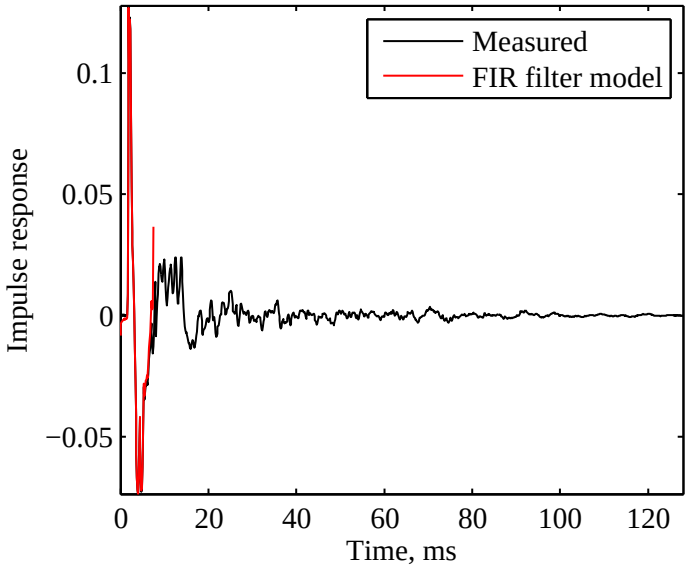

Figure 6.25: Impulse response of the plant measured between loudspeaker 3 and microphone 2 (—) and the impulse response of the 60 coefficient FIR filter used to model the plant (—) at the 8 kHz sample rate.

therefore, are not presented.

It is also interesting to compare the measured and modelled impulse responses and Figure 6.25 shows the measured and modelled impulse responses between loudspeaker 3 and microphone 2. From this plot it can be seen that the FIR filter accurately models the early response of the system where the magnitude is large.

Frequency dependent convergence coefficient

To implement the filtered-reference LMS controller with a frequency dependent convergence coefficient it is necessary to calculate the maximum stable value of α as a function of frequency. According to equation 6.20, for a tonal controller the maximum convergence coefficient is dependent on the eigenvalues of the plant response matrix and the modelled plant response matrix. If the model of the plant is perfect then the maximum value of the convergence coefficient, α_{max}, is given at each frequency by

$$\alpha_{max} = \frac{2\Re(\lambda_{max})}{|\lambda_{max}|^2}, \tag{6.33}$$

where λ_{max} is the maximum eigenvalue of the matrix $\boldsymbol{G}^H\boldsymbol{G}$; the maximum convergence coefficient over frequency for this case is shown by the black dashed line in Figure 6.27. If the model of the plant is not perfect, as in a practical system, then the maximum convergence coefficient is again given by equation 6.33, however, λ_{max} corresponds to the maximum eigenvalue of the matrix $\hat{\boldsymbol{G}}^H\boldsymbol{G}$. The maximum convergence coefficient in this case is shown by the red dashed line in Figure 6.27 and it can be seen that due to the inaccuracies in the plant model the maximum convergence coefficient has been reduced at low frequencies compared to perfect plant

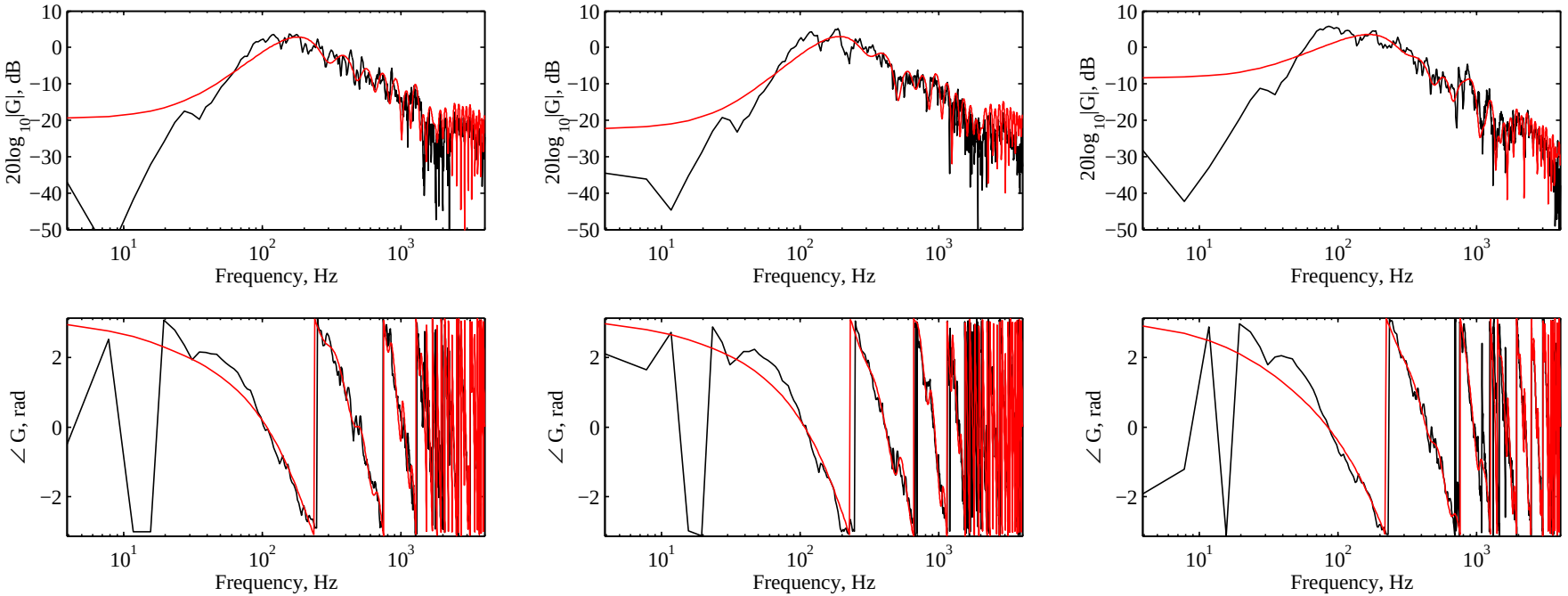

(a) Loudspeaker 1 to mic. 2

(b) Loudspeaker 2 to mic. 2

(c) Loudspeaker 3 to mic. 2

Figure 6.26: The measured (—) plant response measured between each control loudspeaker and error microphone 2 in the laboratory setup in Figure 6.23 and the corresponding model plant responses modelled with FIR filter with 60 coefficients (—).

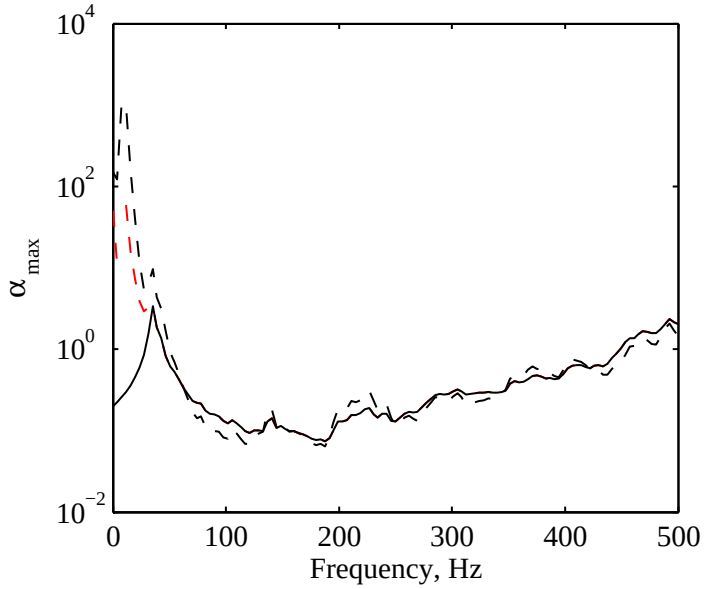

Figure 6.27: The maximum value of the convergence coefficient according to the eigenvalues of the measured plant matrix, $\boldsymbol{G}^H\boldsymbol{G}$, (- -), the eigenvalues of the measured and modelled plant matrix, $\hat{\boldsymbol{G}}^H\boldsymbol{G}$, (- -) and the eigenvalues of the measured and modelled plant with frequency dependent regularisation factor, β_f, introduced to avoid overdriving the loudspeakers at very low frequencies.

model case.

The maximum convergence coefficient is also affected by the control effort weighting parameter [132]. The effect of the control effort parameter scheduled on the instantaneous control effort, as detailed in equation 6.30, cannot be calculated in advance since it is dependent on the disturbance and although an online calculation process could be performed, it would be computationally demanding due to the eigenvalue calculation. However, the effect of the control effort parameter scheduled on the disturbance frequency, as detailed in equation 6.32, can be calculated in advance. In this case the maximum value of the convergence coefficient is again given by equation 6.33, however, λ_{max} corresponds to the maximum eigenvalue of the matrix $\hat{\boldsymbol{G}}^H\boldsymbol{G}+\boldsymbol{\Lambda}$, where $\boldsymbol{\Lambda}$ is, in this case, the diagonal matrix containing the 3 control effort weightings β_1, β_2 and β_3 which are calculated according to equation 6.32 at each frequency. The maximum convergence coefficient in this case is shown by the solid black line in Figure 6.27 and it can be seen that at frequencies below around 25 Hz, where the power constraint becomes active for loudspeakers 1 and 2, the maximum convergence coefficient is significantly reduced. In practice the difference in performance between the controller implemented with the maximum convergence coefficients shown by the solid black and dashed red lines in Figure 6.27 was not significant, which is thought to be related to the limited control effort at such low frequencies.

Controller Performance

The performance of the implemented controller has initially been measured with the primary source driven at 33, 50, 66, 83 and 100 Hz, which correspond approximately to the frequency of the first engine order at engine speeds of 2000, 3000, 4000, 5000 and 6000 rpm. The primary source has been driven such that the power constraint is not active ($\mathbf{\Lambda} = \mathbf{0}$) and the frequency independent convergence coefficient has been set by trial and error to $\alpha_g = 0.01$, which ensures that the controller remains stable despite variations in the plant response introduced by covering individual microphones. The envelope of the sum of the squared error signals has been calculated using the Hilbert transform and the resulting convergence at the 5 discrete frequencies is shown in Figure 6.28 for the controller switched on at $t = 0$. From these plots it can be seen that the speed of convergence increases with frequency. For example, for a disturbance at 100 Hz the sum of the squared error signals has been reduced by 20 dB within 20 msec, while at 66 Hz a 20 dB reduction is achieved after 80 msec. The maximum level of attenuation also tends to increase with frequency. For example, at 33 Hz a maximum reduction of around 20 dB is achieved, whilst at 100 Hz the maximum attenuation is around 25 dB. The limit on the performance at low frequencies can be related to the lower signal-to-noise ratio in both the plant response measurements, as can be seen from the coherence plots in Figure 6.25, and during the real-time controller operation.

To determine the performance of the individual source control effort constraints governed by equation 6.30 the response of the control system at 66 Hz with an effort constraint of $P_L = 1$ has been measured and the results are presented in Figure 6.29 along with the response of the unconstrained controller. From 6.29a it can be seen that the introduction of the control effort constraint does not affect the initial convergence speed of the controller, however, it is clear that the overall attenuation has been limited to around 11 dB compared to around 25 dB. Figure 6.29b shows the envelope of the control signals for the three loudspeakers both with and without the power constraints. From this plot it can be seen that the control signal driving loudspeaker 3 (shown by the dot-dashed lines) has been significantly reduced as a result of the power constraint, while the control signal driving loudspeaker 2 (shown by the dashed lines) has been slightly reduced. The control signal driving loudspeaker 1 has, however, increased as a result of the power constraint. The large reduction in the control signal driving loudspeaker 3 can be related to the large magnitude of the unconstrained control signal compared to the other two control signals. The increase in the control signal driving loudspeaker 1 indicates that due to the significant limit on loudspeaker 3 the controller attempts to improve the levels of control by increasing this control signal. Figure 6.29c shows the values of β for the three control channels and it can be seen that there is an initial transient in each of the parameters before they reach a steady state value.

In the car cabin environment it is necessary for the controller to track the engine speed in order to achieve control of the first engine order during normal driving conditions. Although it

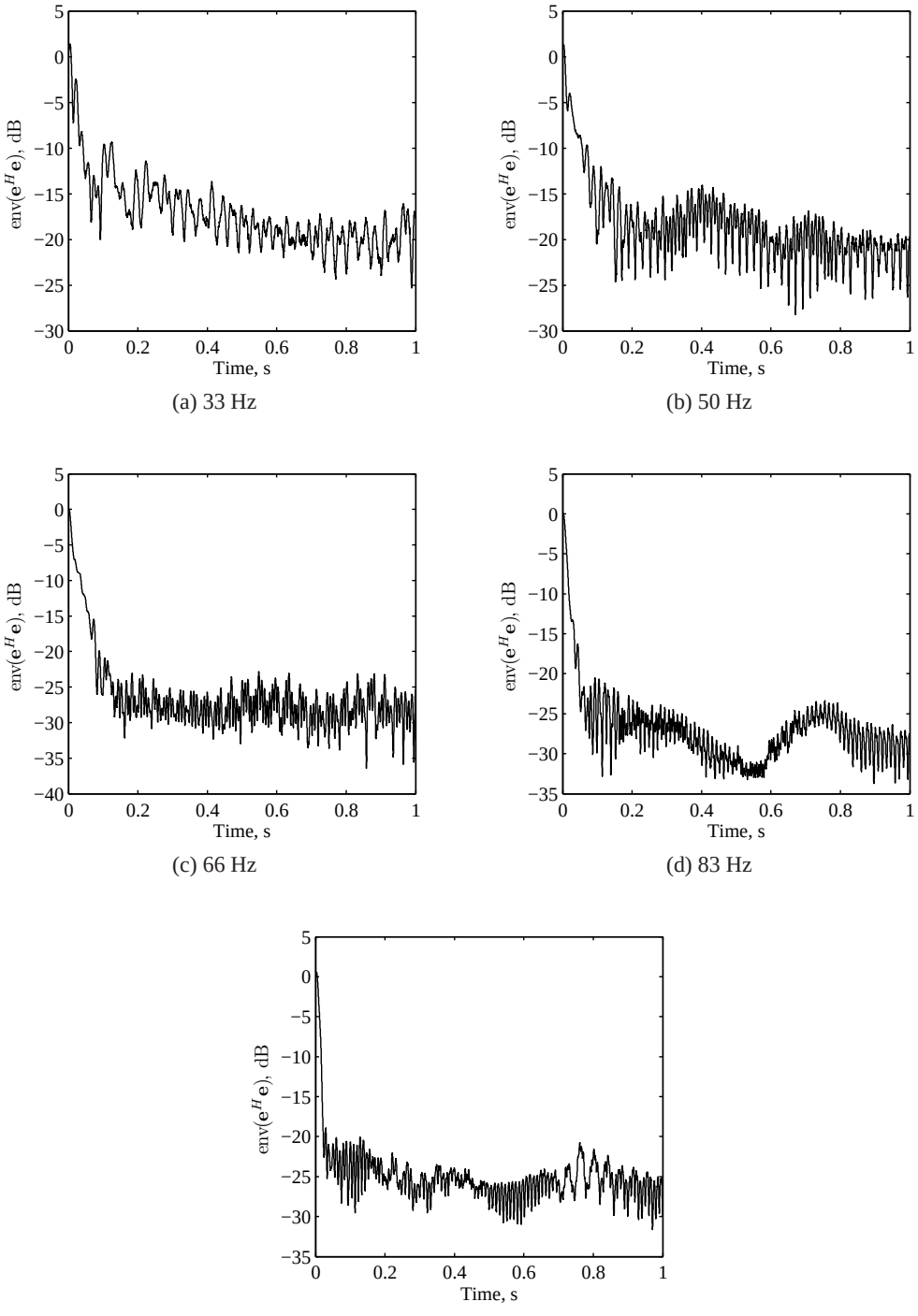

(a) 33 Hz

(b) 50 Hz

(c) 66 Hz

(d) 83 Hz

(e) 100 Hz

Figure 6.28: The envelope of the sum of squared error signals calculated using the Hilbert transform for constant single frequency disturbance signals for the laborartory controller with $\alpha_g = 0.01$.

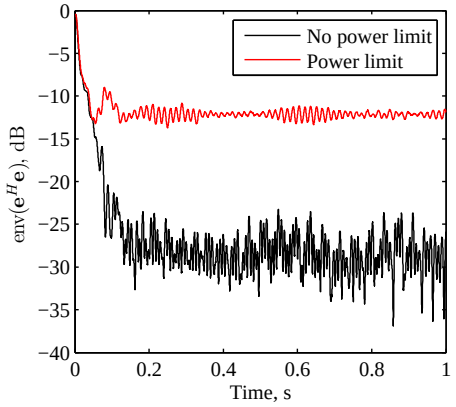

(a) The envelope of the sum of squared error signals.

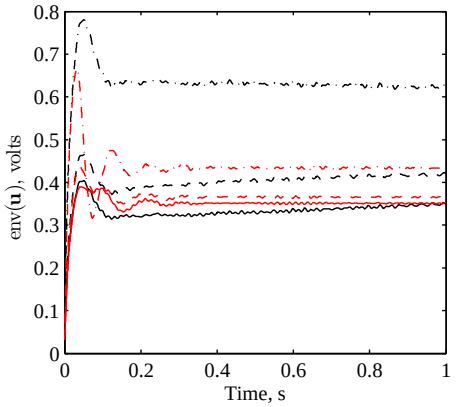

(b) The envelope of the control signals. The black lines show the case with no power limit and the red lines show the case with a power limit. The signals corresponding to source 1 are solid, source 2 are dashed and source 3 are dot-dashed.

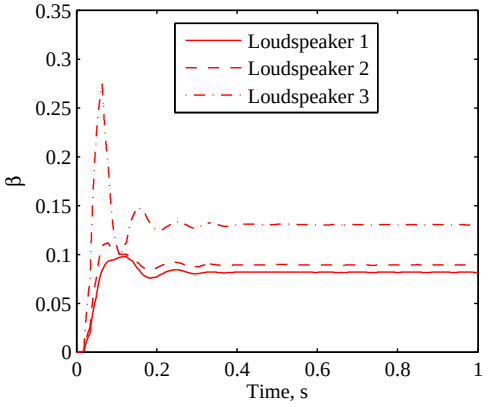

(c) The regularisation parameter β for the case when the power is limited.

Figure 6.29: The response of the feedforward controller for $\alpha_g = 0.01$ without a power limit and with a power limit of $P_L = 1$ with β scheduled according to equation 6.30.

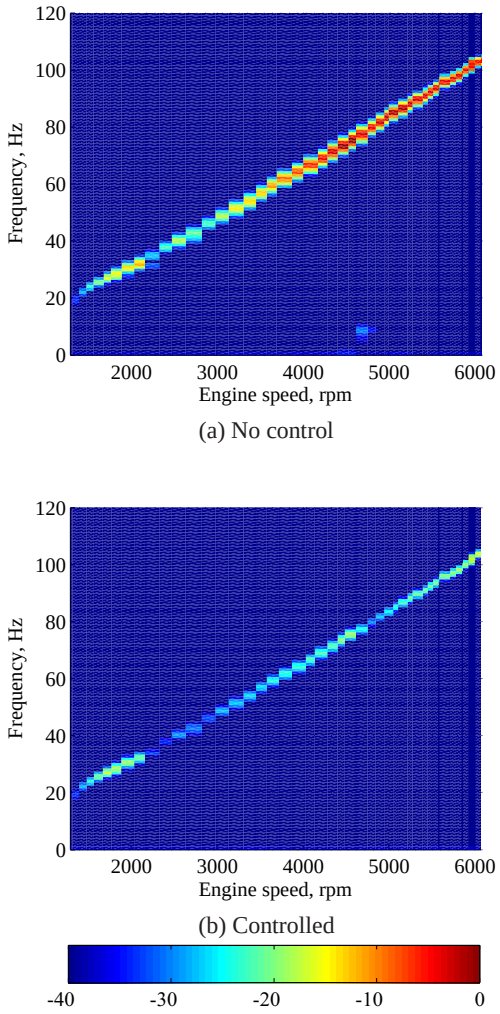

Figure 6.30: The cost function J_p plotted in decibels normalised to the maximum level for the first engine order synthesised from the measured engine run-up signal both without control (a) and with control (b).

has been shown by the convergence plots in Figure 6.28 that the controller is able to converge rapidly at discrete frequencies, it is also important to measure its ability to track a time varying primary disturbance. A primary disturbance containing a tone at the frequency of the first engine order during an engine run-up from 1200 to 6000 rpm has been synthesised based on the measurements presented in Figure 6.12 and the performance of the controller has been measured. Figure 6.30 shows the sum of the squared error signals. From these two plots it can be seen that reductions in the sum of the squared error signals are achieved at engine speeds greater than 1500 rpm. The levels of control are significantly greater at higher engine speeds, as expected from the single frequency measurements. The performance of the controller can be more clearly seen from Figure 6.31a, which shows the level at the frequency of the first engine order with and without control. The change in the control effort weighting parameter for the three control channels is shown in Figure 6.31b and it can be seen that the limited low frequency performance is due to the frequency dependent control effort constraint.

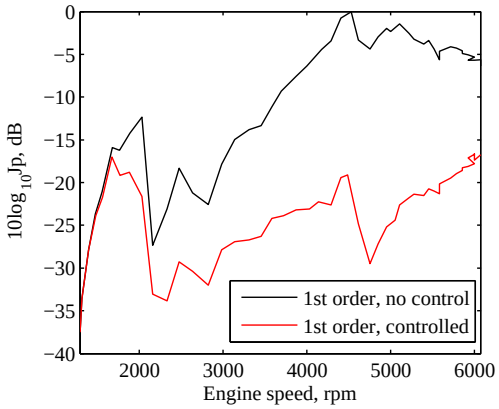

(a) The cost function J_p due to the first engine order.

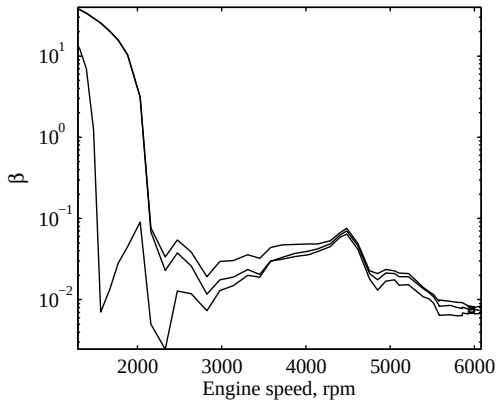

(b) The frequency dependent regularisation parameter β_f.

Figure 6.31: The performance of the feedforward controller during a synthesised engine run-up.

6.2.4 Performance of the Real-Time Controller in the Car Cabin

The feedforward active control system has also been implemented in the two-cylinder 875 cc green city car described in Section 6.1. The controller setup is depicted in Figure 6.32 and is identical to the controller employed in the laboratory measurements presented in the previous section, however, in this instance an additional input is provided for the tacho reference signal, which is a once-per-rev signal obtained from the engine.

The four error microphones were positioned at each of the four headrests in the car and thus the controller attempts to achieve control for all occupants of the car. The two front control microphones were positioned at the co-driver's left ear and the driver's right ear (in the right-hand drive vehicle), as shown by the outer two microphones in Figure 6.3a. The two rear control microphones were positioned at the left ear of the passenger behind the driver and the right ear of the passenger behind the co-driver, as shown by the inner two microphones in Figure 6.3b. The control microphone locations are summarised in Table 6.4.

Table 6.4: Microphone positions

	Position
Microphone 1	Driver outer right headrest
Microphone 2	Front passenger outer left headrest
Microphone 3	Rear nearside passenger inner left headrest
Microphone 4	Rear offside passenger inner right headrest

It was indicated through the measurements presented in Section 6.1.1 that at driving voltages above about 1 volt the standard car audio loudspeakers in the green city car produced a number of harmonics due to the buzzing of the loudspeakers in their enclosures. This would limit the use of these loudspeakers for active control, since in reducing low frequency noise the loudspeakers would generate high frequencies that may be more annoying than the original uncontrolled noise. To avoid this problem in the demonstration and measurement of the feedforward controller, the 3 KEF drivers mounted in closed-back enclosures employed in the laboratory setup were positioned in the car cabin. Several loudspeaker positions were investigated. The most successful one had one KEF B200G loudspeaker positioned in the front passenger foot-well (position 2 in Figure 6.4) and a second KEF B200G loudspeaker positioned on the rear offside seat (position 4 in Figure 6.4), both loudspeakers were positioned close to the corresponding car audio loudspeakers. The larger third loudspeaker, a KEF B300B, was positioned at the rear nearside seat (position 3 in Figure 6.4). The loudspeaker positions are summarised in Table 6.5.

Table 6.5: Loudspeaker descriptions and positions

	Position	Description
Source 1	Front offside foot-well	183 mm diameter cone
Source 2	Rear offside seat	183 mm diameter cone
Source 3	Rear nearside seat	288 mm diameter cone

Plant Responses

The transfer responses measured between the three loudspeakers and the four microphones are shown in Figure 6.33. From these plots it can be seen that, as in the laboratory experiments, the three loudspeakers roll-off at frequencies below their respective resonance frequencies and at frequencies above 200 Hz where the anti-aliasing filters limit the responses. In order to be able to achieve significant levels of active control it is necessary for the loudspeakers to be able to reproduce a sound pressure level comparable to that produced at the microphones by the engine. The first engine order produces a tone between 16 Hz and 100 Hz as the engine speed increases between 1000 rpm and 6000 rpm, therefore, all three loudspeakers will largely be operating in the region where their responses are rolling off below resonance. The low frequency limit quoted by KEF for both the B200G and the B300B is 25 Hz, however, the maximum linear excursion for the B300B is twice that for the B200G, at 12mm. These frequency limits mean that the ability to control the first engine order at speeds below around 1500 rpm will be limited, however, the high linear excursions achievable at low frequencies should allow adequate pressure levels to be produced to facilitate control.

To implement the controller described in Section 6.2.2 the measured plant responses have each been modelled using a 90 coefficient FIR filter. It was necessary to employ a higher order filter in the car cabin environment than in the laboratory implementation due to the more complicated plant responses. This requirement meant that the sampling frequency of the control system had to be reduced to 5 kHz in order to be able to run on the available DSpace system. The frequency responses of the measured and modelled plant responses between the three loudspeakers and microphone 2 are presented in Figure 6.34. From these plots it can be seen that between around 10 Hz and 100 Hz the measured plant responses have been accurately modelled in both magnitude and phase. The other modelled plant responses are similar to those presented in Figure 6.34 and therefore, are not presented.

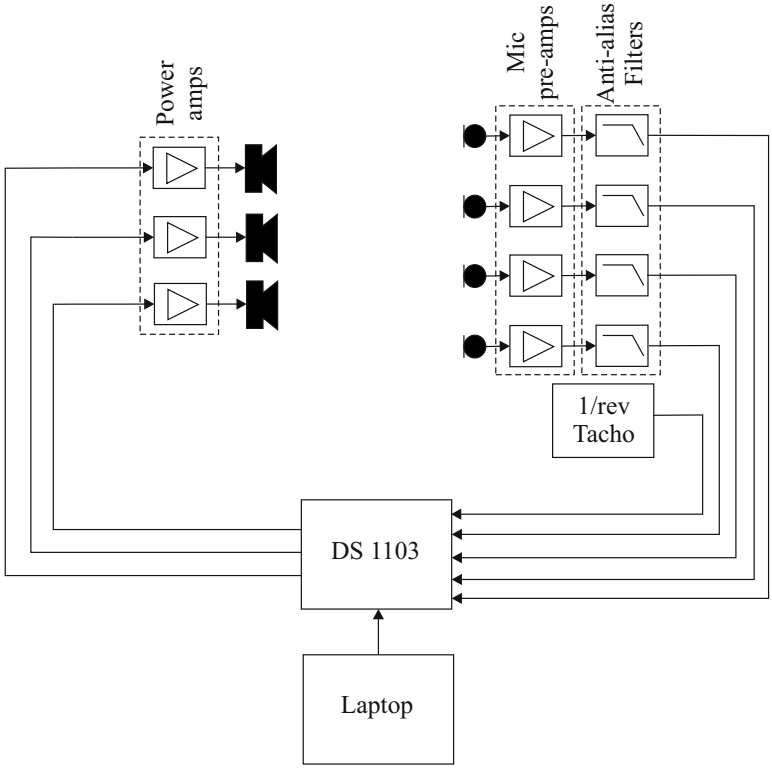

Figure 6.32: Feedforward controller setup consisting of four error microphones and 3 control loudspeakers used in the vehicle . The once-per-rev signal is obtained directly from the engine.

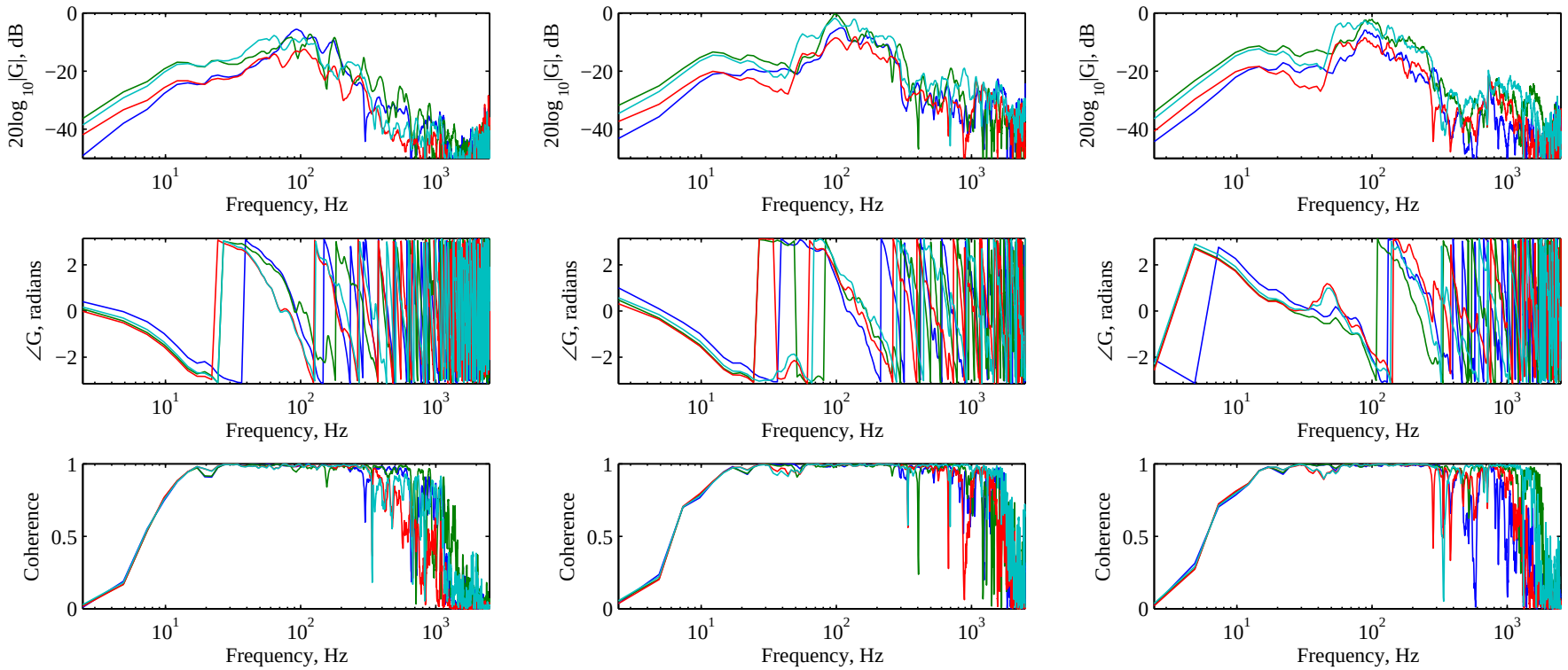

(a) Source 1 (b) Source 2 (c) Source 3

Figure 6.33: Measured plant response between each source and the four error microphones: Front nearside headrest (—), Front offside headrest (—), Rear nearside headrest (—), Rear offside headrest (—)

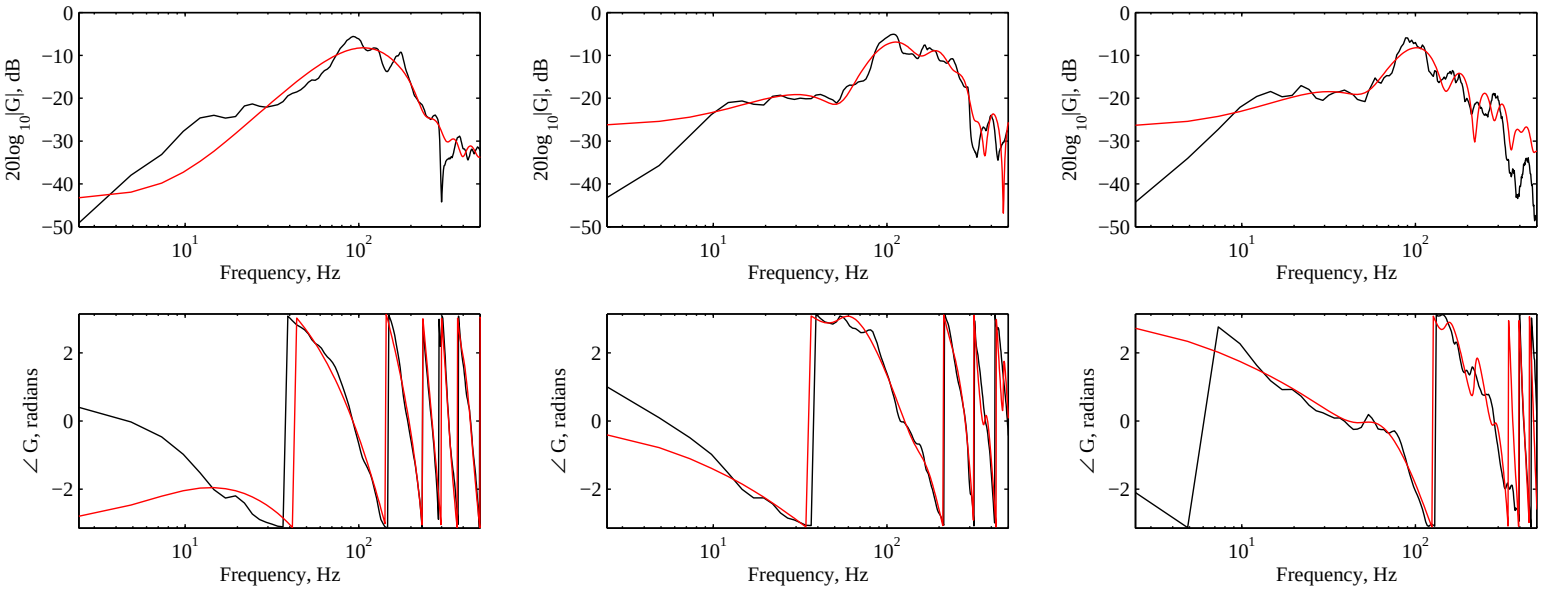

(a) Source 1 to error 1

(b) Source 2 to error 1

(c) Source 3 to error 1

Figure 6.34: The measured (—) plant response between each control loudspeaker and error microphone 1 in the car cabin and the corresponding model plant responses modelled with FIR filters with 90 coefficients (—).

Controller Performance

The performance of the controller was measured under a number of operating conditions. Figure 6.35 shows the sum of the squared error sensor pressures for a slow run-up, over about 3 minutes, in third gear for three conditions: (a) no control, (b) control with a convergence coefficient of $\alpha = 0.01$, and (c) control with a convergence coefficient of $\alpha = 0.001$. The greatest degree of control at the first engine order is obtained with $\alpha = 0.01$, but it can also be seen that around 7 dB enhancement of the second engine order was produced between 2000 and 3000 rpm and some of the fractional orders are also enhanced between 2000 and 4000 rpm. By reducing the frequency independent convergence coefficient, α_g, to 0.001 these enhancements can be reduced, as shown in Figure 6.35c, however, due to the slower convergence the level of control of the first engine order is also reduced. The effect of reducing the convergence coefficient can be more clearly seen from the two plots in Figure 6.36; Figure 6.36a shows the sum of the squared error sensor pressures at the first engine order, and Figure 6.36b shows the sum of the squared error sensor pressures at the second engine order. From Figure 6.36a it can be seen that with $\alpha_g = 0.01$ the controller achieves a reduction in the first order of around 10 dB at engine speeds below around 3300 rpm, however, this is significantly reduced when the convergence coefficient is set to $\alpha_g = 0.001$ and almost no control is achieved at engine speeds above around 4200 rpm. From Figure 6.36b, which shows the change in the second engine order, it can be seen that significant enhancements occur between 2000 rpm and 3000 rpm when $\alpha = 0.01$, however, these are reduced when $\alpha = 0.001$. In comparison to the corresponding offline simulation results presented in Section 6.2.1, and specifically Figure 6.20, it can be seen from the results presented in Figure 6.36a that the level of control achievable in the real-time system is significantly lower than in the offline simulations. This can be related to the lack of power constraints, external noise and finite precision limitations in the offline simulations. However, the levels of control achieved in the real-time system are comparable to those achieved in similar engine noise control systems in previous work, see for example [8, 21].

From the results presented in Figures 6.35 and 6.36 it is evident that the faster the convergence of the feedforward controller, the greater the levels of enhancement produced. The generation of these enhancements can be understood by considering the production of the control signals. The control signals are generated by filtering the reference signals, which contain only the first engine order, with the adaptive filters which are adapted in proportion to the error signals which contain all of the engine orders. This adaptation of the filter coefficients essentially produces a feedback loop in the system and this has been analysed in [173] by treating the adaptive feedforward controller as an equivalent feedback system. However, this effect can also be simply demonstrated by considering a SISO controller with only an in-phase control filter, as shown in Figure 6.37. Without loss of generality it can be assumed that the filtered

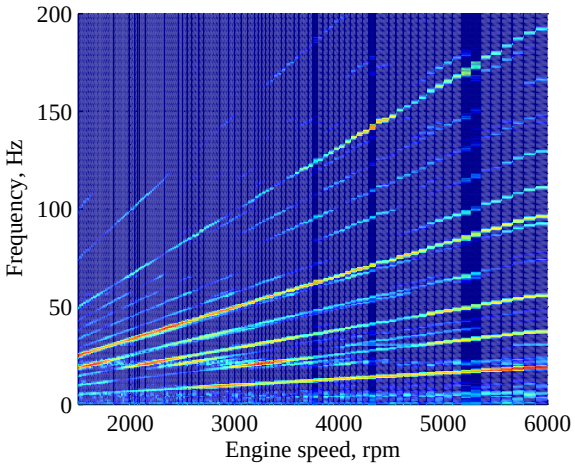

(a) ANC off

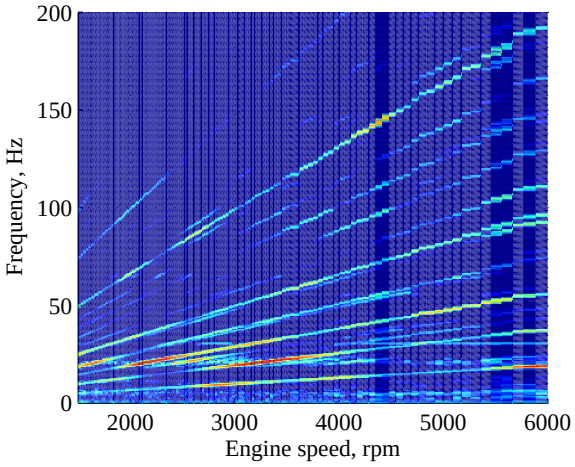

(b) ANC on, $\alpha_g = 0.01$

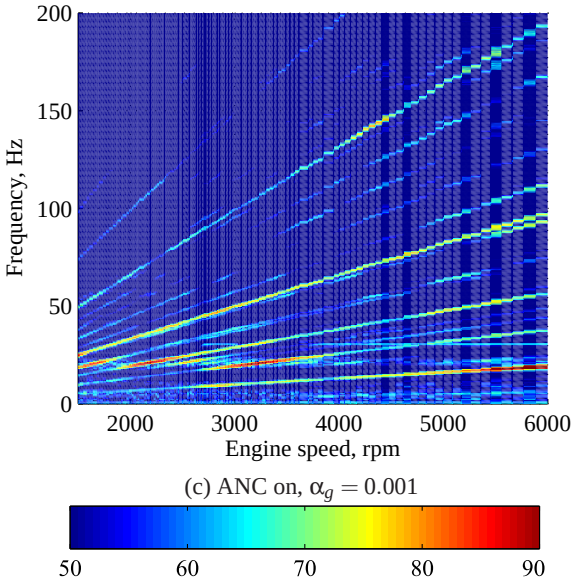

(c) ANC on, $\alpha_g = 0.001$

Figure 6.35: The sum of the squared error sensor pressures plotted in decibels relative to an arbitrary reference level for a slow engine run-up in 3rd gear.

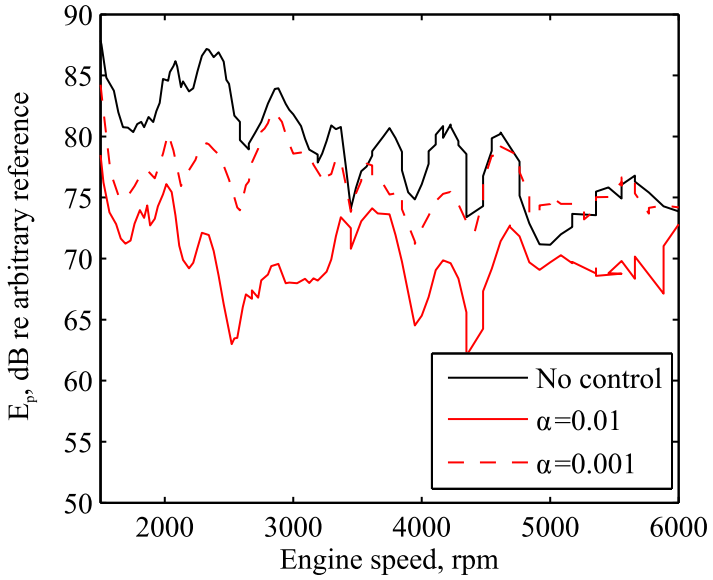

(a) First engine order.

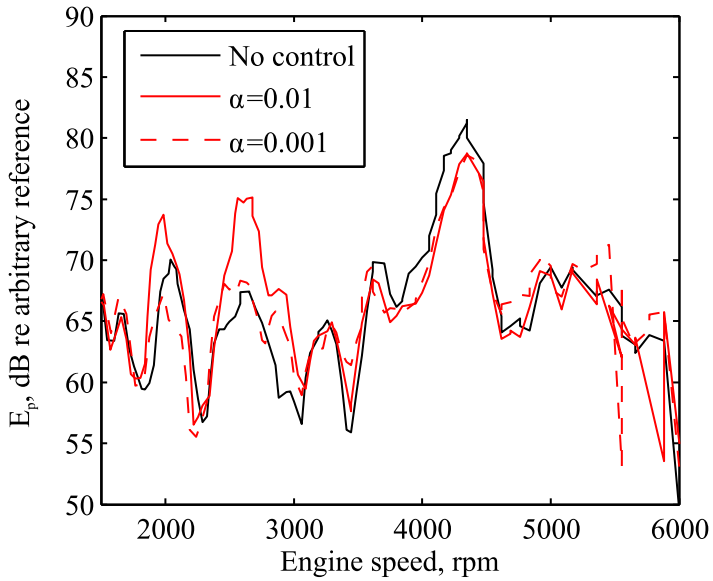

(b) Second engine order.

Figure 6.36: The sum of the squared error sensor pressures at a single engine order plotted in decibels relative to an arbitrary reference level for a slow engine run-up in 3rd gear with the active noise control system off (—) and on with $\alpha_g = 0.01$ (—) and with $\alpha_g = 0.001$ (- -).

reference signal is given by

$$\begin{aligned} r(n) =& g\cos(\omega_c nT_s + \phi_g) \\ =& g\left(\cos(\omega_c nTs)\cos\phi_g + \sin(\omega_c nT_s)\sin\phi_g\right), \end{aligned} \tag{6.34}$$

where g and ϕ_g are the amplitude and phase of the modelled plant response at the control frequency, f_c. The SISO version of the filtered-reference LMS update equation, given for the MIMO case by equation 6.21, is

$$w(n+1) = w(n) - \alpha e(n) r(n), \tag{6.35}$$

and the control filter output is

$$u(n+1) = w(n+1)\cos(\omega_c nT_s). \tag{6.36}$$

By substituting equation 6.34 into equation 6.35 and substituting the result into equation 6.36 the control signal can be expressed as

$$u(n+1) = w(n)\cos(\omega_c nT_s) - \alpha e(n) g\left(\cos(\omega_c nTs)\cos\phi_g + \sin(\omega_c nT_s)\sin\phi_g\right)\cos(\omega_c nT_s). \tag{6.37}$$

and using trigonometric identities this can then be re-written as

$$u(n+1) = w(n)\cos(\omega_c nT_s) - \alpha e(n)\frac{g}{2}\left(\cos\phi_g + \cos(2\omega_c nT_s)\cos\phi_g + \sin(2\omega_c nT_s)\sin\phi_g\right). \tag{6.38}$$

From this equation it can be seen that the first term produces a signal at the control frequency, but the three terms in brackets produce components that are proportional to the error signal. The first term is directly proportional to the error signal, while the second and third terms are modulated versions of the error signal. The magnitude of the terms dependent on the error are also proportional to the convergence coefficient, α, and so will be more important as this becomes larger in systems that adapt more quickly. This analysis helps to explain the enhancements observed in the results presented in Figure 6.36a. The effects on the control signal can be seen from the spectrum of the sum of the squared control signals during the slow engine run-up in third gear with $\alpha_g = 0.01$ presented in Figure 6.38. From this plot it can be seen that, although at a significantly lower level than the first engine order, harmonics are present in the control signals and can be related to the enhancements observed in Figure 6.35b. The issue of enhancements has been briefly discussed in the context of an engine noise control system in [39], however, no clear analysis or solution is provided. It is evident from the presented results and analysis that to improve the performance of the controller it is necessary to reduce the harmonics related to the error signal whilst maintaining a fast convergence. This problem has previously been solved using cascading adaptive filters in [173] and a recursive least squares based controller in [174] leads to a similar controller, however, an alternative

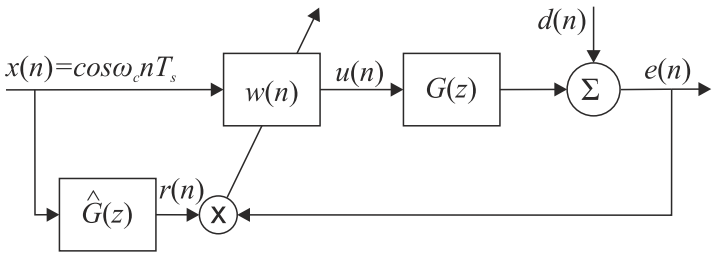

Figure 6.37: Block diagram of a single-input single-output in-phase feedforward controller.

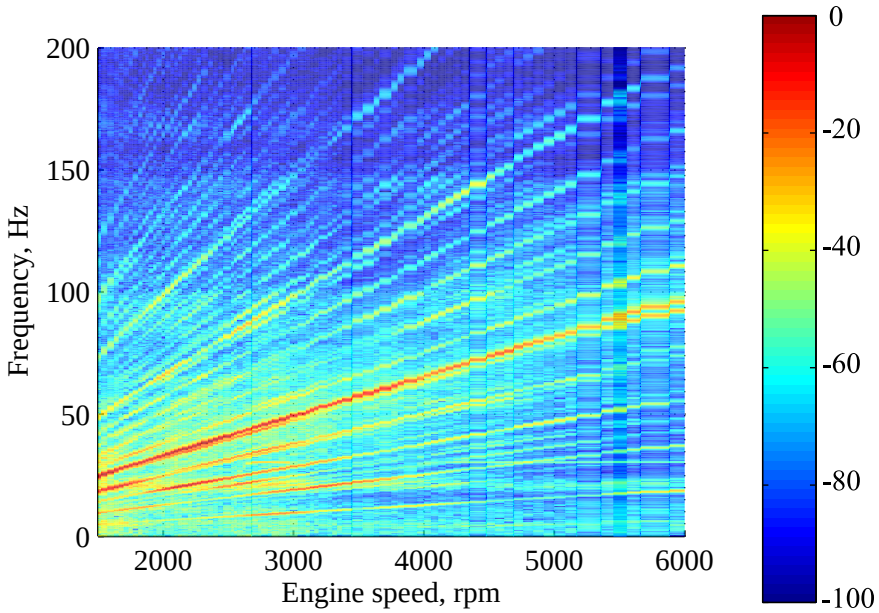

Figure 6.38: The sum of the squared control signals plotted in decibels relative to 1 volt for a slow engine run-up in 3rd gear with $\alpha_g = 0.01$.

method is proposed here.

Modified Controller

To reduce the levels of enhancement produced by the standard feedforward controller whilst also maintaining a fast convergence speed and high levels of control at the first engine order, a modification to the standard filtered-reference LMS algorithm has been implemented. This modified controller employs a second-order Infinite Impulse Response (IIR) bandpass filter at the control outputs to reduce the level of the control signals at frequencies away from the control frequency. The bandpass filter response has been specified in the z-domain as [175]

$$H_{BP}(z) = \frac{\left(\frac{1-r^2}{1+r^2}\right) sz^{-1} - (1-r^2)z^{-2}}{1 - sz^{-1} + r^2 z^{-2}}, \tag{6.39}$$

where

$$0 \ll r < 1 \tag{6.40}$$

$$-2r < s < 2r, \tag{6.41}$$

r is the pole radius which determines the bandwidth of the filter and s determines the resonance frequency according to

$$\omega_0 = \cos^{-1}\left(\frac{s}{1+r^2}\right). \tag{6.42}$$

This filter implementation allows the resonance frequency of the filter to be adapted according to a single term and, therefore, the bandpass filter response is able to track the frequency of the first engine order and provide attenuation of the additional harmonics produced by the standard controller. The parameter r has been set to 0.99, which gives a narrow filter bandwidth and thus significant attenuation of the harmonics. The bandpass filter specified according to equation 6.39 also has unity gain and zero phase at its resonance frequency [175] and, therefore, will not modify the plant response provided that the frequency tracking is accurate, although it does introduce a group delay.

Modified Controller Performance

Figure 6.39 shows the performance of the modified controller during a slow run-up in third gear with a convergence coefficient of $\alpha = 0.01$. From this plot it can be seen that, in comparison to the results for the standard controller, while significant control of the first engine order is still achieved, the enhancement at the second order has been significantly reduced. The fractional orders are still somewhat enhanced, due to the limited roll-off achieved by the bandpass filter at these frequencies. Figure 6.40 shows the sum of the squared pressures at the first and second engine orders before and after control and it can be seen that comparable levels of control of the first order are achieved compared to those presented in Figure 6.36a for the standard controller while the second engine order is not significantly affected. Figure 6.41 shows the performance of the modified and standard controllers for a fast engine run-up, over about 45 seconds, in third gear and it can be seen that in this case the modified controller still produces enhancements at the second engine order at a comparable magnitude to the standard controller. This is a result of the group delay introduced by the bandpass filter, however, to understand this behaviour would require further investigation of the modified controller which was not possible due to limited time during the measurements.

To gain more insight in to the effect of the bandpass filter on the controller performance Figure 6.42 shows the sum of the squared error sensor pressures at the first engine order at 5 constant engine speeds when the two controllers are switched on at $t = 1$ sec. From these plots it can be seen that the convergence of the algorithm does not appear to be significantly affected

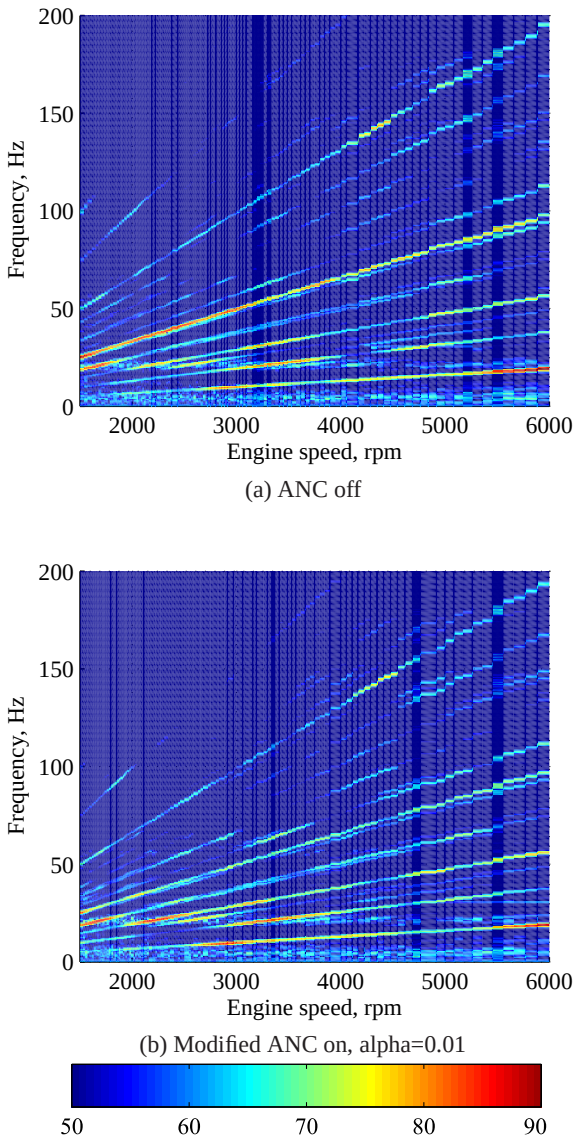

Figure 6.39: The sum of the squared error sensor pressures plotted in decibels relative to an arbitrary reference level for a slow engine run-up in 3rd gear.

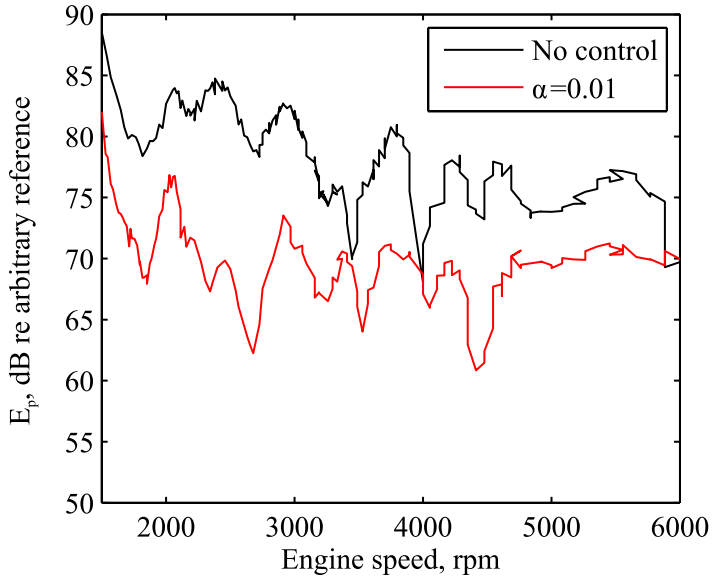

(a) First engine order.

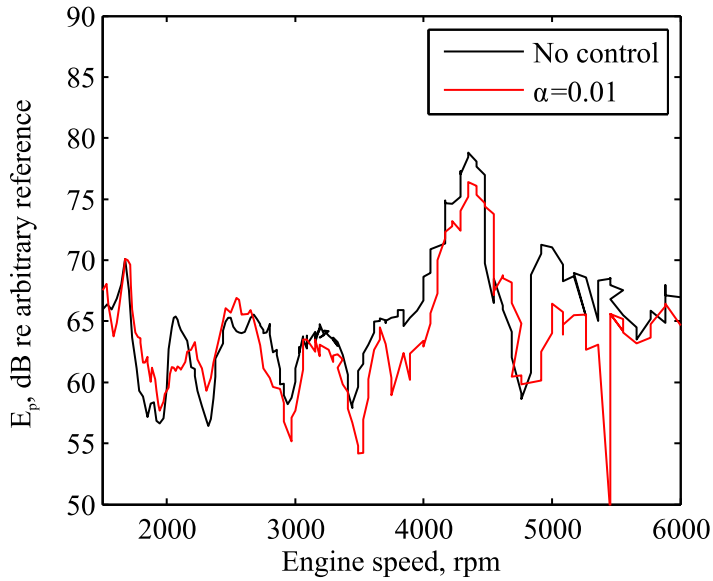

(b) Second engine order.

Figure 6.40: The sum of the squared error sensor pressures at a single engine order plotted in decibels relative to an arbitrary reference level for a slow engine run-up in 3rd gear with the modified active noise control system off (—) and on with $\alpha_g = 0.01$ (—) .

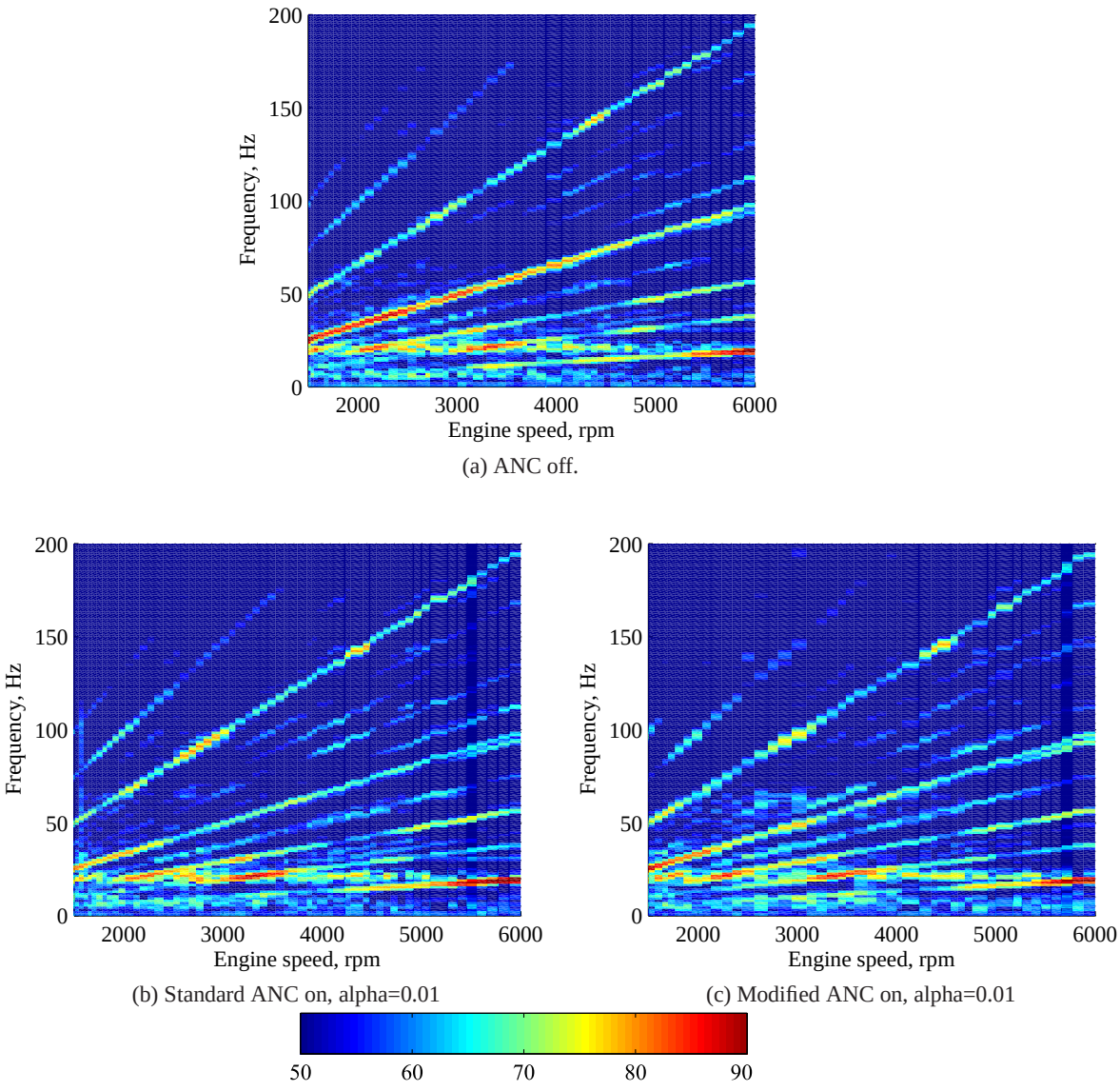

(a) ANC off.

(b) Standard ANC on, alpha=0.01

(c) Modified ANC on, alpha=0.01

Figure 6.41: The sum of the squared error sensor pressures plotted in decibels relative to an arbitrary reference level for a fast engine run-up in 3rd gear.

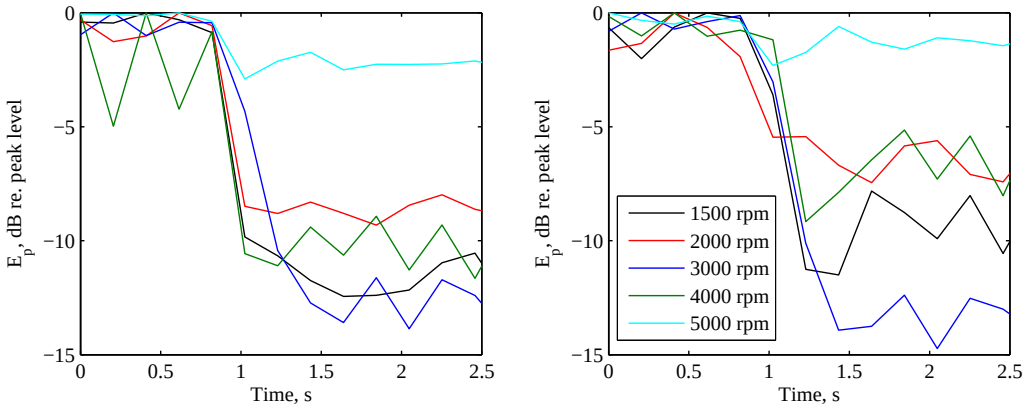

(a) Standard controller.

(b) Modified controller with bandpass filter.

Figure 6.42: Response of the active noise controllers switched on at t=1 at 1500 (—), 2000 (—), 3000 (—), 4000 (—) and 5000 rpm (—) in 3rd gear.

by the bandpass filter and is around 20 msec at most engine speeds. However, it is difficult to observe the effect of the bandpass filter in this experimental configuration and simulations of this modified controller would provide further insight into its operation. Also, it can be seen that in general the maximum levels of control have been slightly reduced by the modified controller. The operating limitations of the modified controller are not completely clear from the presented results, however, the reduced performance may be related to the group delay introduced by the bandpass filter and this is consistent with the comparable control system presented in [173]. In the formulation presented here, the bandpass filter delay could be compensated for in the controller by including a duplicate of the bandpass filter in the plant modelling path, although time did not allow this modification to be tested and this would still reduce the speed of convergence.

6.3 Feedback Control of Road Noise

It has been shown in Section 6.1.3 that the road noise component that may benefit from active noise control has a broadband peak between around 80 and 180 Hz. From the acoustic transfer responses presented in Figure 6.5, however, it is evident that the responses at around these frequencies do not correspond to a single lightly damped acoustic mode. Acoustic modal feedback control with spatial weighting has previously been mostly employed in systems where well defined modes produce noise problems, however, in the vehicle environment the noise problem is due to the spectrum of noise produced by the interaction between the road and the vehicle and this excites a number of acoustic modes. Therefore, the control systems investigated in Chapter 4, employing spatially weighted microphone and loudspeaker arrays, will not be suitable for this application. The fully MIMO feedback control system investigated in Chapter 5, however, is capable of controlling the noise produced in an enclosure by multiple uncorrelated structural excitations. Therefore, despite the complexity of this control system its performance in the small city car will be investigated using offline simulations.

6.3.1 Offline Control Simulations

The MIMO feedback control system, employing the four car audio loudspeakers and the eight 'corner' error microphones, has been optimised as in Chapter 5 according to the optimisation:

$$\begin{aligned}
\min_{\boldsymbol{w}} \quad & \frac{1}{N_{F_c}} \sum_{f=f_1}^{f_2} \text{trace} \left[\boldsymbol{G}_0(f)\boldsymbol{W}(f)\boldsymbol{S}_{pp}(f)\boldsymbol{W}^H(f)\boldsymbol{G}_0^H(f) \right. \\
& \left. + \boldsymbol{G}_0(f)\boldsymbol{W}(f)\boldsymbol{S}_{pp}(f) + \boldsymbol{S}_{pp}(f)\boldsymbol{W}^H(f)\boldsymbol{G}_0^H(f) + \boldsymbol{S}_{pp}(f) \right] \\
\text{subject to} \quad & \bar{\sigma}[\boldsymbol{G}_0(f)\boldsymbol{W}(f)B(f)] < 1 \quad \forall f, \\
\text{and} \quad & \max \left[\text{diag} \left(\boldsymbol{D}(f)\boldsymbol{S}_0(f)\boldsymbol{S}_{pp}(f)\boldsymbol{S}_0^H(f) \right) \right] \frac{1}{A} < 1 \quad \forall f,
\end{aligned} \tag{6.43}$$

where the main minimisation is of the mean square pressures at the microphones, the first constraint is to provide robust stability and the second constraint is to limit the enhancement in the individual error sensor pressures. The frequency bandwidth has been set to $f_1 = 80$ and $f_2 = 180$ to target the broadband peak in the road noise measured in the small city car, the frequency responses have been discretised at $N_F = 513$ frequencies and the control filter lengths have been set to $I = 128$. The filter length and resolution of the frequency discretisation have been set to ensure an optimal solution is obtained without unnecessary computational expense, as discussed in Chapter 5. The robust stability constraint has been set to $B = 0.5$ and the individual enhancement constraint has been set to $A = 4$, which gives a maximum enhancement of 6 dB in the squared pressure at each error microphone. The controller has been optimised for the nominal plant measured with two front seat occupants and the primary disturbance produced when the car is driven on the pavè road surface at 50 km/h.

Figure 6.43 shows the nominal performance of the optimised feedback controller. From Figure 6.43a it can be seen that the robust stability constraint has been maintained, whilst

Figure 6.43b indicates that the enhancement constraint has not been reached. This indicates that the enhancements in the squared pressures at the error microphones will be less than 6 dB. Figure 6.43c shows the nominal performance of the optimised MIMO IMC feedback controller. That is, the sum of the squared pressures at the eight 'corner' error microphones before and after control, and from this plot it can be seen that the cost function has been reduced by up to 6 dB within the targeted bandwidth, while enhancements occur at frequencies above and below the targeted bandwidth where the level of the primary disturbance is low. The change in the cost function can be seen more clearly from Figure 6.43d, which shows the cost function after control plotted with reference to the cost function prior to control. Figure 6.43d also shows the change in the sum of the squared pressures at all 16 microphones in the car cabin and it can be seen that the level of control in the targeted bandwidth, about 3 dB, is not significantly different to that achieved in J_p. This indicates that the control is achieved throughout the car cabin enclosure.

In Chapter 5 the performance of the MIMO feedback controller was simulated in the non-rigid walled rectangular enclosure and the results are shown in Figure 5.6. This simulation predicted a peak reduction in J_p of around 17 dB and an average reduction over the control bandwidth of around 5 dB. The slight decrease in the average reduction over the control bandwidth, from 5 dB in the simulated enclosure to 3 dB in the real car cabin, can be related to the higher number of resonances in the practical car cabin. To provide control of a higher number of resonances it is necessary to increase the order of the feedback controller. The lower peak reduction achieved in the practical car cabin can be related to the higher levels of damping of low frequency resonances. That is, in the rectangular enclosure the peak reduction is achieved at around 50 Hz where there is a strongly radiating structural resonance, such resonances do not occur in the carefully designed practical car cabin and, therefore, the maximum levels of reduction achievable using the active control system are lower.

In a practical implementation the control effort required to drive the loudspeakers is important and this has been estimated, as in Section 6.2.1, using the measurements of the standard car audio loudspeakers presented in Section 6.1.1. Figure 6.44 shows the control effort required to achieve the levels of control presented in Figure 6.43 for the feedback controller operating while the car is driven at 50 km/h over the pavè road surface. From this plot it can be seen that the control effort is significantly below the limits of the standard car audio loudspeakers, which are capable of driving up to 1 volt without producing additional harmonics. This control effort is lower than required in the engine noise control system, which can be related to both the lower maximum level of primary disturbance and the lower levels of control.

The results presented in Figure 6.43 correspond to the performance of the controller when the modelled plant response and the plant response used to optimise the controller are identical to the actual plant response. This is unrealistic and therefore to estimate the robustness of the performance of the controller optimised according to the plant response measured with two

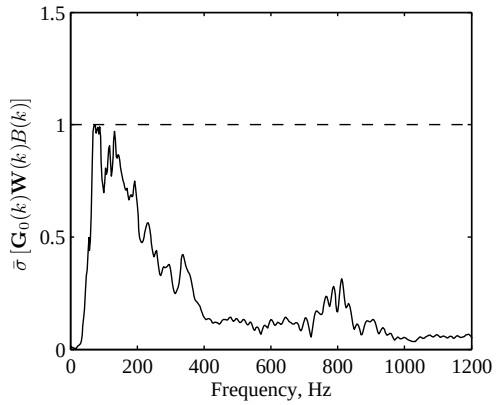

(a) Robust stability measure, which must be less than 1 at all frequencies to ensure the robust stability constraint is satisfied with a plant variation of $B = 0.5$.

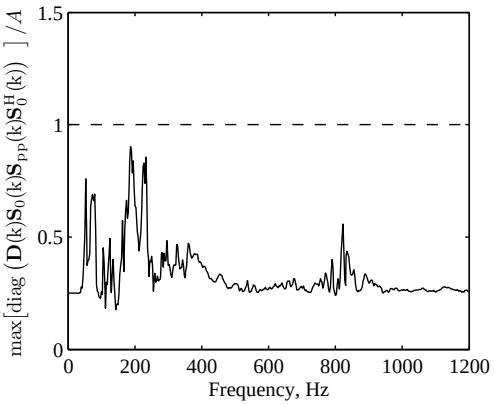

(b) Maximum individual squared disturbance pressure enhancement measure, which must be less than 1 at all frequencies to ensure the individual squared disturbance pressures are not enhanced by more than a factor of $A = 4$.

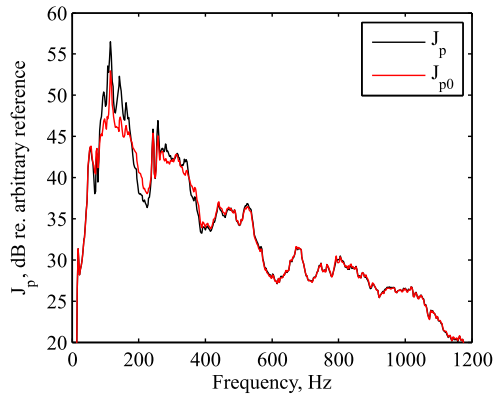

(c) The cost function, J_p, calculated from the eight 'corner' error microphones before (—) and after control (—).

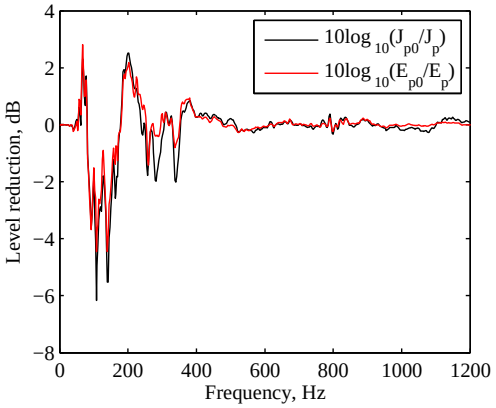

(d) The cost function calculated from the eight 'corner' error microphones after control, J_{p0}, plotted in decibels relative to the cost function before control J_p (—) and the sum of the squared pressures calculated from all 16 microphones after control, E_{p0}, plotted in decibels relative to the sum of the squared pressures before control E_p (—).

Figure 6.43: The results of the MIMO IMC controller designed with a robust stability constraint and a constraint on the enhancement in the individual error microphone pressures in the car cabin enclosure with two front seat occupants when driven over the pavè road surface at 50 km/h.

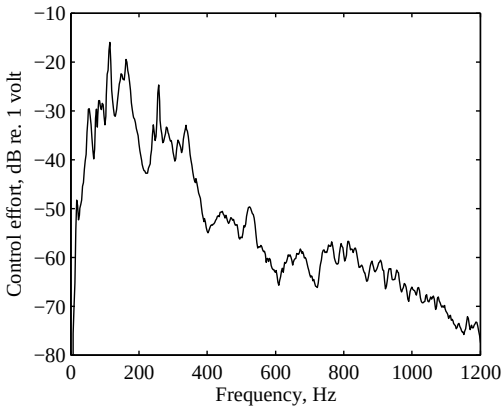

Figure 6.44: The estimated control effort required by the MIMO IMC controller when used to minimise the sum of the squared pressures at the eight 'corner' error microphones in the car when driven over the the pavè road surface at 50 km/h plotted in decibels relative to 1 volt.

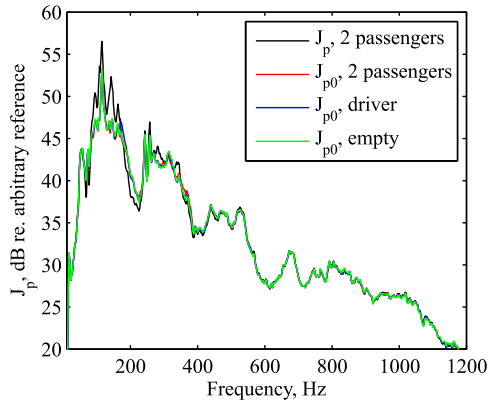

Figure 6.45: The cost function, J_p, calculated from the eight 'corner' error microphones before (—) and after control for the nominal plant response with two front seat occupants (—) and for the plant responses measured with a driver (—) and no occupants (—).

front seat occupants, the performance of this controller has been calculated using the plant responses measured when only the driver is present and when the car is unoccupied; these results are presented in Figure 6.45. From this plot it can be seen that the controlled response is not significantly affected by the changes in the plant response, which indicates that the designed controller is robust to variations in the plant response. However, it should be highlighted that the three measured plant response conditions may not represent the most extreme variations in the car cabin environment that may occur in practice. For example, the plant response may be more significantly altered by the opening of windows and in order to implement this control system in practice a more thorough investigation of plant variations would be necessary, as in [39]. If a more complete set of plant responses were measured then the robust stability constraint B could be defined based on the measured plant responses, however, if this were conducted using only the three measured plant responses then an unrealistic controller would be produced.

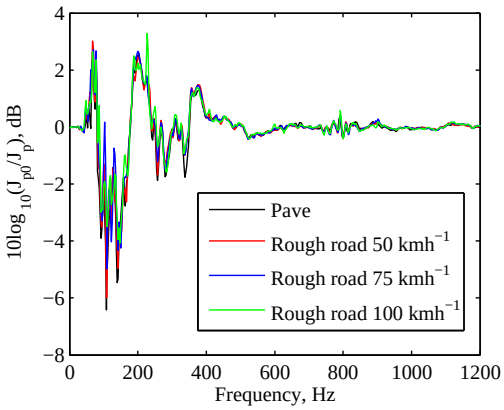

Figure 6.46: The cost function calculated from the eight 'corner' error microphones after control, J_{p0}, plotted in decibels relative to the cost function before control J_p (—) for four different driving conditions.

Since the feedback controller has also been optimised using a single road noise measurement it is also important to investigate how the performance of the controller is affected by changes in the primary disturbance. Therefore, the performance of the feedback controller optimised based on the pavè road surface has been simulated for the other three road conditions presented in Section 6.1.3 and the results are presented in Figure 6.46. From this plot it can be seen that the performance of the controller is relatively unaffected by the changes in the primary disturbance and this can be related to the relatively consistent spectrum of the road noise in the targeted bandwidth despite the changes in road surface and speed, as observed in Section 6.1.3.

6.3.2 Discussion of Real-Time Implementation Requirements

It has been shown through the offline simulations in the previous section that the MIMO IMC feedback controller is able to achieve control of low frequency road noise even through variations in both the plant responses and the disturbance signals, whilst avoiding significant levels of enhancement. To implement the fully coupled feedback controller, from eight microphones to 4 loudspeakers, requires a bank of 32 FIR filters to implement the control filter matrix, $\boldsymbol{W}$, and a further bank of 32 filters to model the plant responses, $\hat{\boldsymbol{G}}$, in the IMC controller formulation. However, in a fixed controller implementation these filters may be combined to form the standard feedback control filter matrix $\boldsymbol{H}$ as

$$\boldsymbol{H}(j\omega) = -\left[\boldsymbol{I} + \hat{\boldsymbol{G}}(j\omega)\boldsymbol{W}(j\omega)\right]^{-1}\boldsymbol{W}(j\omega), \tag{6.44}$$

as described in Chapter 4, and a single bank of 32 filters is then required. This does not appear to be of significant computational expense, since a similar number of filters would be required in a real-time feedforward controller and at the same sampling frequency of 2.56 kHz employed in the offline feedback control simulations, it is possible to implement the MIMO

feedback controller on the DSpace 1103 processing board. However, in the offline simulations the delays inherent in a practical digital implementation of the feedback controller, which will be introduced by the anti-aliasing and reconstruction filters and the digital to analogue and analogue to digital converters, have not been included. These additional delays will limit the bandwidth over which the feedback controller can be applied [132]. This problem has been addressed in the context of road noise control by Elliott and Sutton in [136] who showed that in the SISO feedback control system considered, the overall plant delay had to be kept below around 1.5 ms to achieve significant levels of control.

In order to achieve levels of control comparable to those predicted by the offline simulations it will at least be necessary to operate the control system at a high sample rate in order to keep the delay due to the digital implementation to a minimum. Implementing the controller at a higher sample rate will increase the number of coefficients required in each of the FIR filters and, therefore, significantly increase the computational demand. For example, although implementing the bank of 32 FIR filters with an impulse response of length 50 msec, as employed in the offline simulations, is possible at a sampling frequency of 2.56 kHz on the DSpace DS-1103 board, increasing the sampling rate to reduce the delay due to the anti-aliasing and reconstruction filters and converters to below 1 msec is not possible.

In order to implement the MIMO feedback controller using the DSpace processing board used in this work it seems necessary to either employ a more computationally efficient controller implementation, for example using IIR filters instead of FIR filters, although this will change the design procedure, or use a combined analogue and digital implementation to achieve the speed of an analogue controller with the flexibility of a digital controller. It may also be possible to achieve similar performance without having a fully coupled MIMO controller. Further investigations would be necessary to determine both if and how the proposed fully MIMO feedback controller may be implemented using the currently available digital signal processing capabilities and this is a recommendation for further work.

6.4 Summary

Based on the simulations in the three preceding chapters, this chapter has investigated the practical performance and implementation of the feedforward engine noise control system and the MIMO feedback road noise control system in a small city car with a two-cylinder engine. A series of measurements were conducted in the small city car to understand the acoustic environment in the cabin. Transfer responses were measured between both a volume velocity source positioned adjacent to the car audio loudspeakers and the standard car audio loudspeakers, and 16 microphones. The results of these measurements have confirmed that the 10% acoustic damping assumed in the simulations presented in the previous chapters was appropriate, however, it has also been highlighted that the significant low frequency resonances observed in the rectangular enclosure simulations do not occur, which is likely to be due to the careful design of the car's sound package. Using the array of 16 microphones, measurements of typical engine

and road noise have been conducted on a rolling road and a number of different road surfaces respectively. From these results it was shown that the dominant source of engine noise is due to the first engine order. From the results of the road noise measurements it has been shown that two frequency regions exist where noise control is required: a broadband peak between 80 and 180 Hz, which is due to a structural resonance; and narrowband peaks between 230 and 260 Hz, which are due to the tyre cavity resonance.

Using the measured transfer responses and engine noise data the performance of an optimal feedforward first engine order controller has been predicted using offline simulations. Global control of the first engine order, where the sum of the squared pressures at the 'corner' error microphones is minimised, has first been simulated and reductions of up to 20 dB have been predicted at low frequencies. The level of control generally decreases with increaseing engine speed and these results are consistent with those presented in Chapter 3. To achieve improvements in the level and bandwidth of control, regional control, where the sum of the squared pressures at the headrest error microphones is minimised, has also been simulated. These offline predictions showed that the level of control at the positions of the car cabin's occupants is significantly increased, as previously shown in Chapter 3; however, there is a corresponding increase in the loudspeaker voltage drive levels and the required voltage drive levels may cause the standard car audio loudspeakers to buzz in their enclosures and produce additional undesirable harmonics.

Based on the offline simulations of feedforward engine noise control a practical real-time control system has been designed and implemented using the filtered-reference LMS control algorithm due to its robustness and computational efficiency, although it is noted that alternative algorithms could improve the speed of convergence. To avoid the potential issues of employing the standard car audio loudspeakers a separate array of three loudspeakers, including one subwoofer unit, has been employed and the individual driving voltages have been limited by employing an individual control effort constraint. The performance of the real-time controller has first been studied in a laboratory setup and has subsequently been implemented in the small city car. The implemented feedforward controller achieved levels of first engine order reduction consistent with those predicted in the offline simulations, however, enhancements at other orders were also produced. These enhancements have been related to the effective feedback loop in the controller and are linked to the speed of adaptation. To attempt to reduce these enhancements a modified controller was proposed which employs a variable bandpass filter at the control outputs in order to reduce the components of the control signal at frequencies other than the first engine order. The performance of this modified controller has been measured and the presented results have shown that for slow engine run-ups the enhancements have been reduced, whilst the level of first order control is largely maintained. However, for faster engine-runps the enhancements are not reduced, which has been related to the group delay introduced by the bandpass filter. Further investigation of the proposed modified controller has been suggested in order to fully understand its operation and potential performance.

The MIMO feedback controller, initially investigated in Chapter 5, has also been investi-

gated through offline predictions using the measured transfer responses and road noise data. The MIMO feedback controller has been optimised to achieve control of the broadband peak between 80 and 180 Hz and a reduction in the sum of the squared error microphone pressures of up to 6 dB was predicted, whilst the enhancements in the individual squared pressures was kept below 6 dB. The robustness of the controller to deviations from the nominal plant response and disturbance spectrum were also predicted, and it has been shown that in both cases the designed controller is robust to these variations. However, it has also been highlighted that the considered plant variations are not expected to represent the most significant plant variations that may occur in practice and a more comprehensive study would be required in practice.

Although offline simulations of the MIMO feedback controller have predicted significant levels of control, these simulations have not considered a number of practical limitations. For example, due to its complexity it is necessary to implement the MIMO feedback controller digitally, however, the offline predictions have not taken into account the delays inherent in a digital implementation which will limit the bandwidth of control. It is necessary to minimise these delays in a practical implementation, however, the presented controller cannot be implemented on the currently available digital signal processing hardware with a short enough delay. Therefore, a number of areas of future work have been suggested to allow the real-time implementation of the proposed controller.

Chapter 7

Active Control of Sound Reproduction in an Automobile Cabin

In the previous chapters the active control of unwanted noise due to automotive processes has been investigated. However, as discussed in Chapter 1, the acoustic environment in an automobile cabin is determined by both the automotive noise processes, such as engine and road noise, and the audio reproduced by the car audio system. Therefore, in designing the acoustic environment it is necessary to consider both of these aspects. There are a number of areas of sound reproduction which may benefit from active control methods, such as multi-point equalisation and spatial audio reproduction, and particularly strong links between active noise control methods and personal audio reproduction have been highlighted in Chapter 1. Personal audio reproduction attempts to produce personalised listening zones and this is achieved by driving an array of loudspeakers with an audio signal via a bank of filters which are optimised to produce the desired sound field, as shown by the block diagram in Figure 7.1.

The development of personal audio systems that aim to reproduce sound over a specified region of space whilst minimising the sound reproduced in other regions have seen a significant amount of interest over recent years. This is due to the rapid increase in both the number of methods via which, and the number of environments within which media, including video, audio and telecommunications, may be received. For example, mobile 'phones are now in-

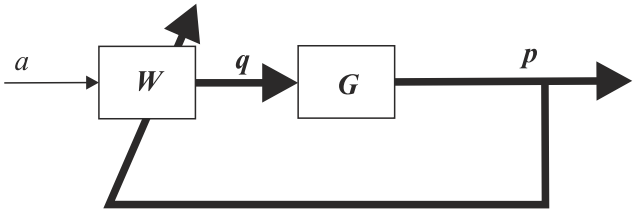

Figure 7.1: Block diagram of the personal audio reproduction problem in which a single channel audio signal, a, is used to drive a bank of control filters, $\boldsymbol{W}$, the output of which is used to drive an array of loudspeakers. The control filters are optimised based on a cost function related to the pressures, $\boldsymbol{p}$, produced at a number of locations.

creasingly used to stream video, listen to audio, or make video calls [176]. Due to the desire to create personalised listening zones, there has been a number of personal audio systems proposed for different applications such as in mobile devices [80, 86] and video monitors [83], and a review of these systems has been presented in Section 1.3.2.

In the automobile cabin environment there is also a desire to implement personalised rear seat entertainment, in part due to the introduction of flat panel displays [16]. Two systems to generate personal listening zones in a car cabin have been presented in patents [26, 17]. The first system patented in 2004 [26] relies on the directivity of "planar magnetic loudspeakers" and their interaction with the car cabin acoustic environment through reflections to generate personalised listening zones. However, the results presented in this patent show that the generation of personal sound zones is only achievable at frequencies greater than around 6 kHz. The second system proposes using "ultrasonic speakers" [17], or parametric arrays [89], to generate personal listening zones in a car cabin. Although the patent does not indicate the performance of the proposed system, based on the high directivity that is achievable using parametric arrays the proposed system is likely to provide a significant level of performance. However, the high power requirements, the need for a large number of transducers and the potential health risks [91] may limit the practicability of this system.

The generation of personal sound zones in applications other than the car cabin environment have successfully employed active sound control techniques that generate a desired sound field through both constructive and destructive interference between the sound fields produced by an array of sources, or loudspeakers, as discussed in Chapter 1. The most widely investigated approach to generating a personal sound zone using an array of loudspeakers is superdirective or optimal beamforming. This chapter will investigate the development of a personal audio system that allows different audio programmes to be reproduced in the front and rear seats of a car cabin environment using these optimal beamforming control strategies.

Although a number of methods of optimising arrays for personal audio reproduction have been proposed, the most widely employed and investigated method has been acoustic contrast control [24]. Therefore, this method will first be reviewed and then a generalisation of acoustic contrast control will be presented that introduces a constraint on the electrical power required by the optimised array. Additionally, a new formulation of the acoustic contrast control strategy with a constraint on the electrical power required by the individual sources will be derived. Although acoustic contrast control provides the optimum performance in terms of the absolute pressure levels reproduced in the control zones, it does not constrain the phase of the produced pressures and, therefore, the audio quality may be poor [78]. This has been considered in [78] in the context of a broadside array of phase-shift loudspeakers and it has been shown that the least squares method, which is widely employed in active noise control, as in Chapter 3, is capable of defining both the magnitude and phase of the reproduced audio whilst maintaining an acoustic contrast that is only slightly reduced compared to contrast maximisation. Therefore, the least squares method will also be detailed and formulations of this method with power constraints will also be derived.

The acoustic contrast control strategy is used here to investigate the physical limitations on generating personal listening zones using both distributed and nearfield arrays in a car cabin sized enclosure. The geometry of the considered enclosure is larger than that employed in Chapters 2, 3, 4 and 5, since the personal audio measurements that are presented in the following chapter were conducted in a larger vehicle due its availability. Figure 7.2 shows an overhead view of the personal audio control geometry with control zones at the front and rear seating positions. The acoustic contrast control strategy will be compared to the least squares optimisation method in the context of the proposed loudspeaker arrays.

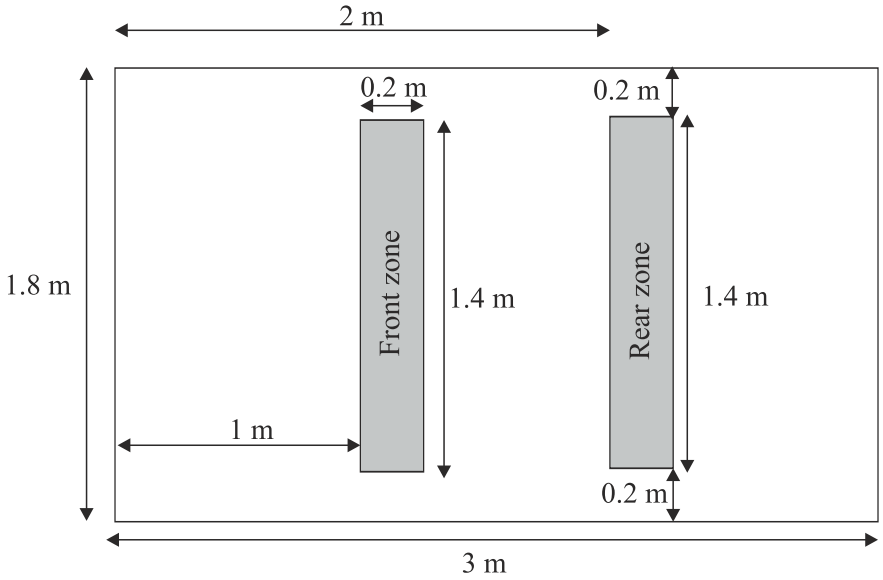

Figure 7.2: Plan view of the car cabin personal audio control geometry at a height of 0.9 m. for a cabin that is 1.2 m high, with cuboid control zones in the front and rear seating regions. the cuboid control zone is defined in the vertical direction between 0.8 and 1.0 m.

7.1 Acoustic Contrast Control

The acoustic contrast control strategy, proposed by Choi and Kim [24], is based on the optimisation of the source strengths of an array of sources such that the ratio of the acoustic potential energy in a bright, or listening zone to that in a dark, or quiet zone is maximised. The acoustic contrast, C, between the bright and dark zones, depicted for a generic problem in Figure 7.3, can be expressed at a given frequency as the ratio of the mean of the modulus squared pressures in the bright and dark zones respectively, that is

$$C = \frac{L_D \boldsymbol{p}_B^H \boldsymbol{p}_B}{L_B \boldsymbol{p}_D^H \boldsymbol{p}_D} = \frac{L_D \boldsymbol{q}^H \boldsymbol{Z}_B^H \boldsymbol{Z}_B \boldsymbol{q}}{L_B \boldsymbol{q}^H \boldsymbol{Z}_D^H \boldsymbol{Z}_D \boldsymbol{q}}, \tag{7.1}$$

where $\boldsymbol{p}_B$ and $\boldsymbol{p}_D$ are the column vectors of pressures in the bright and dark zones respectively, $\boldsymbol{q}$ is the column vector of M source strengths in the array, and $\boldsymbol{Z}_B$ and $\boldsymbol{Z}_D$ are the $(L_B \times M)$ and $(L_D \times M)$ matrices of acoustic transfer impedances from each element in $\boldsymbol{q}$ to each of the L_B

locations in $\boldsymbol{p}_B$ and L_D locations in $\boldsymbol{p}_D$ respectively.

The optimisation of the source strengths, $\boldsymbol{q}$, such that the acoustic contrast is maximised can be cast as a constrained quadratic optimisation in which $\boldsymbol{p}_B^H \boldsymbol{p}_B$ is maximised with the constraint that $\boldsymbol{p}_D^H \boldsymbol{p}_D$ is held constant with a value D. Using the method of Lagrange multipliers this gives the function to be maximised as [177]

$$J_C = \boldsymbol{q}^H \boldsymbol{Z}_B^H \boldsymbol{Z}_B \boldsymbol{q} - \lambda_C (\boldsymbol{q}^H \boldsymbol{Z}_D^H \boldsymbol{Z}_D \boldsymbol{q} - D), \tag{7.2}$$

where λ_C is the Lagrange multiplier and is a positive constant. Differentiating equation 7.2 with respect to the real and imaginary parts of $\boldsymbol{q}$ and equating to zero leads to

$$\lambda_C \boldsymbol{q} = \left[\boldsymbol{Z}_D^H \boldsymbol{Z}_D\right]^{-1} \boldsymbol{Z}_B^H \boldsymbol{Z}_B \boldsymbol{q}, \tag{7.3}$$

where the optimal solution is that $\boldsymbol{q}$ is proportional to the eigenvector corresponding to the largest eigenvalue of the matrix $\left[\boldsymbol{Z}_D^H \boldsymbol{Z}_D\right]^{-1} \boldsymbol{Z}_B^H \boldsymbol{Z}_B$, as shown by Choi and Kim [24], with the absolute value being dependent upon the constraint D. This optimisation ensures that for the defined source geometry the array maximises the sound radiated to the bright zone whilst maintaining the level in the dark zone.

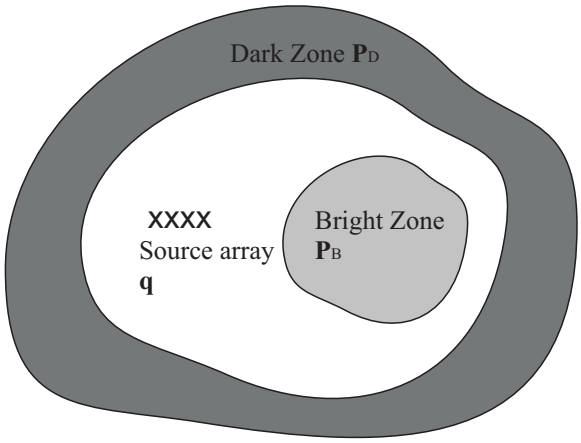

Figure 7.3: An example of a two-dimensional acoustic contrast control problem [80].

7.1.1 Personal Audio Optimisation with an Electrical Power Constraint

Although the acoustic contrast maximisation strategy does inherently ensure that for a defined source array and bright-dark zone geometry the acoustic contrast is maximised, for a practical system, it does not put any constraint on the electrical power required to achieve that contrast. In a practical system this may result in destruction of the loudspeakers, or an excessive electrical power requirement. One method of ensuring that the electrical power required does not become excessively large is proposed by Choi and Kim [24] and is referred to as the *brightness problem*. The brightness problem is based on maximising the acoustic potential energy in the bright zone subject to the constraint that the input electrical power, or array effort, is limited.

Where the array effort[1] is defined as

$$AE = \boldsymbol{q}^H \boldsymbol{q}, \tag{7.4}$$

and is proportional to the electrical power required to drive the array, assuming there are no significant electroacoustic interactions between the transducers [80]. Using the brightness problem control strategy the optimised array will produce the maximum bright zone pressures within the specified power constraints, however, as there is no restriction on the sound field outside of the bright zone this method is not guaranteed to produce a well defined personal sound zone. It is shown by Jones and Elliott [76] that the performance of an array optimised using the brightness problem is dependent upon the orientation of the array relative to the bright and dark zone geometry, but in general the performance is significantly below that achieved using the same array optimised using acoustic contrast control.

An alternative method of limiting the required electrical power whilst maintaining the production of a personal listening zone has been presented by Shin *et al* [77] (see also [178]). The proposed method aims to overcome some of the potential problems associated with the acoustic contrast control strategy by maximising the difference in acoustic energy between a dark and bright zone rather than the ratio, whilst the electrical power is kept constant. This formulation has the advantage of not requiring the calculation of the inverse of any matrix, and thus avoids the associated conditioning problems [77]. This benefit is confirmed by Elliott and Cheer [82] by comparing the conditioning of the energy difference formulation to the conditioning of acoustic contrast maximisation formulated with an additional power constraint. Despite the improved conditioning achieved by the energy difference formulation, it is shown by Elliott *et al* [99] that the performance of the energy difference maximisation control strategy is identical to that achieved by acoustic contrast control with an additional constraint on the electrical power. Therefore, the claims regarding increased radiation efficiency compared to acoustic contrast control in [77] appear to be unfounded. Moreover, despite the improvement in numerical conditioning that is achieved by the energy difference formulation, it is shown in [99] that an indirect formulation of the acoustic contrast control strategy with an additional constraint on the electrical power provides a good compromise between providing a well conditioned solution, and a formulation that allows a trade-off between acoustic contrast and electrical power via a parameter with a well-defined physical meaning. Therefore, the indirect formulation of acoustic contrast control with an additional constraint on the electrical power defined in [99] will be used in the following investigations.

7.1.2 The Indirect Formulation of Power Constrained Contrast Maximisation

The direct formulation of acoustic contrast control has been described by equations 7.2 and 7.3, however, as detailed in [99] there is a second, indirect, formulation in which the maximisation

[1] In the context of active noise control considered in the earlier chapters of this thesis the sum of the squared source strengths is defined as the control effort; however, in the context of active control of sound reproduction the sources do not only perform a controlling function but also a reproduction function and, therefore, it is pertinent to distinguish between the control effort and the array effort

of the acoustic contrast can be formulated as a minimisation problem. The indirect method of contrast maximisation is formulated by minimising $\boldsymbol{p}_D^H \boldsymbol{p}_D$ with the constraint that $\boldsymbol{p}_B^H \boldsymbol{p}_B$ is held constant with a value of b, so that the Lagrangian cost function to be minimised is

$$J_C = \boldsymbol{q}^H \boldsymbol{Z}_D^H \boldsymbol{Z}_D \boldsymbol{q} + \lambda_C (\boldsymbol{q}^H \boldsymbol{Z}_B^H \boldsymbol{Z}_B \boldsymbol{q} - b), \tag{7.5}$$

where the sign of the second term is the opposite of that in equation 7.2 so that λ_C remains a positive constant. Differentiating equation 7.5 with respect to the real and imaginary parts of $\boldsymbol{q}$, equating to zero and assuming that $\boldsymbol{Z}_B^H \boldsymbol{Z}_B$ is invertible yields

$$\lambda_C \boldsymbol{q} = -\left[\boldsymbol{Z}_B^H \boldsymbol{Z}_B\right]^{-1} \boldsymbol{Z}_D^H \boldsymbol{Z}_D \boldsymbol{q}. \tag{7.6}$$

Since the Lagrangian is being minimised with respect to $\boldsymbol{q}$, the solution is equal to the eigenvector corresponding to the smallest eigenvalue of $\left[\boldsymbol{Z}_B^H \boldsymbol{Z}_B\right]^{-1} \boldsymbol{Z}_D^H \boldsymbol{Z}_D$. As $\boldsymbol{Z}_D^H \boldsymbol{Z}_D$ is also assumed to be invertible, however, the smallest eigenvalue of this matrix is equal to the largest eigenvalue of its inverse, $\left[\boldsymbol{Z}_D^H \boldsymbol{Z}_D\right]^{-1} \boldsymbol{Z}_B^H \boldsymbol{Z}_B$, and this formulation gives exactly the same result as the direct formulation given above. However, when a constraint on the electrical power is introduced the direct and indirect formulations lead to two separate solutions and the indirect formulation leads to solutions that are relatively well conditioned and physically meaningful [99].

In the indirect formulation of acoustic contrast control with a constraint on the total power, or array effort, the aim is to minimise the mean square pressure in the dark zone with the constraints that the mean square pressure in the bright zone is equal to b and the array effort, given by equation 7.4, is equal to c_{AE}. The Lagrangian in this case is

$$J_C = \boldsymbol{q}^H \boldsymbol{Z}_D^H \boldsymbol{Z}_D \boldsymbol{q} + \lambda_C \left(\boldsymbol{q}^H \boldsymbol{Z}_B^H \boldsymbol{Z}_B \boldsymbol{q} - b\right) + \lambda_{AE} \left(\boldsymbol{q}^H \boldsymbol{q} - c_{AE}\right) \tag{7.7}$$

where λ_{AE} is the real and positive Lagrange multiplier governing the array effort constraint. The differential of the Lagrangian with respect to the real and imaginary parts of $\boldsymbol{q}$, divided by two, is then

$$\frac{1}{2} \frac{\partial J_C}{\partial \boldsymbol{q}} = \boldsymbol{Z}_D^H \boldsymbol{Z}_D \boldsymbol{q} + \lambda_C \boldsymbol{Z}_B^H \boldsymbol{Z}_B \boldsymbol{q} + \lambda_{AE} \boldsymbol{q}. \tag{7.8}$$

Assuming once again that $\boldsymbol{Z}_B^H \boldsymbol{Z}_B$ is invertible this differential is zero if

$$\lambda_C \boldsymbol{q} = -\left[\boldsymbol{Z}_B^H \boldsymbol{Z}_B\right]^{-1} \left[\boldsymbol{Z}_D^H \boldsymbol{Z}_D + \lambda_{AE} \boldsymbol{I}\right] \boldsymbol{q}. \tag{7.9}$$

The optimal minimum solution is proportional to the eigenvector corresponding to the smallest eigenvalue of $\left[\boldsymbol{Z}_B^H \boldsymbol{Z}_B\right]^{-1} \left[\boldsymbol{Z}_D^H \boldsymbol{Z}_D + \lambda_{AE} \boldsymbol{I}\right]$, which is the largest eigenvalue of

$$\left[\boldsymbol{Z}_D^H \boldsymbol{Z}_D + \lambda_{AE} \boldsymbol{I}\right]^{-1} \boldsymbol{Z}_B^H \boldsymbol{Z}_B. \tag{7.10}$$

The acoustic contrast is independent of the numerical value of λ_C as discussed above, however, in order to ensure that $\boldsymbol{p}_B^H \boldsymbol{p}_B$ has the specific value b the magnitude of $\boldsymbol{q}$ must still be adjusted.

Similarly, the value of λ_{AE} has to be adjusted such that the array effort, $\boldsymbol{q}^H\boldsymbol{q}$, is less than or equal to the specified constant c_{AE}. If the value of $\boldsymbol{q}^H\boldsymbol{q}$ in the unconstrained contrast maximisation problem is less than the value of c_{AE} then the constraint is said to be inactive and λ_{AE} will be zero.

7.1.3 The Indirect Formulation of Contrast Maximisation with Individual Source Power Constraints

Although not currently required here, in some applications the factor limiting the performance of the array may not be the array effort, which is related to the total electrical power required by the array, but instead, by the individual amplifier or loudspeaker limitations. In this instance a constraint is required that limits the electrical power supplied to each individual source in the array. This process has previously been described in the context of feedforward active noise control [172] and has been employed in the practical active engine noise control system whose implementation is detailed in Section 6.2.2. This individual source power constraint would be particularly useful in the context of a personal audio array in which different loudspeaker drivers are used to cover different frequency ranges, as is likely in the car audio application in particular.

Following the indirect formulation of acoustic contrast control detailed above, the constraint on the individual source strengths can be imposed by ensuring that $|q_m|^2$, where q_m is the source strength of the m-th secondary source, is equal to the constant c_E for all m. This optimisation can again be solved using the method of Lagrange multipliers and in this case the Lagrangian is

$$J_C = \boldsymbol{q}^H\boldsymbol{Z}_D^H\boldsymbol{Z}_D\boldsymbol{q} + \lambda_C\left(\boldsymbol{q}^H\boldsymbol{Z}_B^H\boldsymbol{Z}_B\boldsymbol{q} - b\right) + \sum_{m=1}^{M}\lambda_m\left(|q_m|^2 - c_E\right). \tag{7.11}$$

where λ_m are the real and positive Lagrange multipliers governing the M constraints on the individual magnitude squared of the source strengths. The differential of this Lagrangian with respect to the real and imaginary parts of $\boldsymbol{q}$, divided by two, is then

$$\frac{1}{2}\frac{\partial J_C}{\partial \boldsymbol{q}} = \boldsymbol{Z}_D^H\boldsymbol{Z}_D\boldsymbol{q} + \lambda_C\boldsymbol{Z}_B^H\boldsymbol{Z}_B\boldsymbol{q} + \boldsymbol{\lambda}_M\boldsymbol{q}, \tag{7.12}$$

where

$$\boldsymbol{\lambda}_M = \begin{bmatrix} \lambda_1 & 0 & 0 & 0 \\ 0 & \lambda_2 & 0 & 0 \\ 0 & 0 & \ddots & 0 \\ 0 & 0 & 0 & \lambda_M \end{bmatrix}. \tag{7.13}$$

By setting the differential of the cost function to zero and rearranging gives

$$\lambda_C\boldsymbol{q} = -\left[\boldsymbol{Z}_B^H\boldsymbol{Z}_B\right]^{-1}\left[\boldsymbol{Z}_D^H\boldsymbol{Z}_D + \boldsymbol{\lambda}_M\right]\boldsymbol{q}, \tag{7.14}$$

and the optimal solution in this case is proportional to the eigenvector corresponding to the largest eigenvalue of $\left[\boldsymbol{Z}_D^H \boldsymbol{Z}_D + \boldsymbol{\lambda}_M\right]^{-1} \left[\boldsymbol{Z}_B^H \boldsymbol{Z}_B\right]$. Once again, the acoustic contrast is independent of λ_C and this value must simply be adjusted to ensure that the constraint on the sum of the squared bright zone pressures is achieved. However, in comparison to the optimal solution for the cost function in which the total power is constrained, the value of each λ_m has to be adjusted such that $|q_m|^2$ is less than the constraint c_E for all sources. As discussed by Elliott and Baek in the context of active noise control, this problem is much more complicated than finding the single value of λ_{AE} in the total power constraint problem detailed above and this is in part due to a single λ_m affecting the effort supplied to each individual source [172].

Despite the potential complexity of this optimisation problem, due the quadratic nature of the cost function it is convex and may be solved using the optimisation approach employed in [156] and Chapters 4 and 5 of this thesis. For example, by discretsing the problem in the frequency domain it may be solved using sequential quadratic programming, as described in Section 4.6 in the context of the modal feedback controller. Additionally, following this optimisation approach it is possible to design the filters, whose frequency responses are given by $\boldsymbol{q}$, as FIR filters and thus constrain the solution to produce causal filters. The use of causal filters, as opposed to non-causal filters, avoids the use of a modelling delay which may limit the usefulness of the designed personal audio system in a number of applications, such as telecommunications, and may also improve the audio quality by avoiding the pre-ringing that occurs in non-causal filters implemented with a modelling delay [78].

7.2 Least Squares Optimisation

The method of least squares has been widely employed in the context of active noise control [33] and is detailed in the context of feedforward control in Section 3.2.1. The least-squares method has also been widely used in the context of reproduced sound [179, 64] and has been formulated for the personal audio problem by Simón-Gálvez *et al* [78].

In the least squares optimisation of a personal audio system the acoustic transfer impedances to the bright and dark zones are combined into a new matrix, with dimensions $(L_T \times M)$, of the form

$$\boldsymbol{Z} = \begin{bmatrix} \boldsymbol{Z}_B \\ \boldsymbol{Z}_D \end{bmatrix}, \tag{7.15}$$

where $L_T = L_B + L_D$ is the total number of pressure evaluation positions in the bright and dark zones. The vector of pressures at the L_T control points in the bright and dark zones due to the source strengths $\boldsymbol{q}$ of the M sources in the array is then given as

$$\boldsymbol{p} = \boldsymbol{Z}\boldsymbol{q}. \tag{7.16}$$

The least squares problem is then formulated by defining a vector of pressures, $\boldsymbol{p}_T$, which the system aims to produce at the control points. In the context of the personal audio system in

[78] the target pressures are set to zero at the dark zone positions, whilst the target pressures in the bright zone are set, for example, to those produced by the centre source of the array operating in isolation. The assignment of the specific values of the target pressure vector will be dependent on both the control and source geometries and will be investigated below.

Using the vector of target pressures an error vector may be defined as the difference between the target pressures and the actual pressures

$$\boldsymbol{e} = \boldsymbol{p}_T - \boldsymbol{p}, \tag{7.17}$$

and by minimising this value in a least squares sense it is possible to optimise the source strengths, $\boldsymbol{q}$, such that the array produces an approximation of the targeted sound field. This can be achieved by minimising the cost function given by the sum of the modulus squared errors

$$J_{LS} = \boldsymbol{e}^H \boldsymbol{e}. \tag{7.18}$$

Substituting equations 7.16 and 7.17 into equation 7.18 and expanding gives

$$J_{LS} = \boldsymbol{p}_T^H \boldsymbol{p}_T - \boldsymbol{q}^H \boldsymbol{Z}^H \boldsymbol{p}_T - \boldsymbol{p}_T^H \boldsymbol{Z}\boldsymbol{q} + \boldsymbol{q}^H \boldsymbol{Z}^H \boldsymbol{Z}\boldsymbol{q}. \tag{7.19}$$

Differentiating J_{LS} with respect to the real and imaginary parts of $\boldsymbol{q}$, equating to zero and rearranging for the case when $L_T > M$ (i.e. the overdetermined system) gives the vector of optimal source strengths as

$$\boldsymbol{q} = \left[\boldsymbol{Z}^H \boldsymbol{Z}\right]^{-1} \boldsymbol{Z}^H \boldsymbol{p}_T. \tag{7.20}$$

From equation 7.20 it can be seen that the least squares solution to the personal audio problem no longer requires the calculation of an eigenvalue problem, as was required in the case of acoustic contrast control. However, the personal audio performance of an array optimised using the least squares method will be completely dependent on the ability to define the vector of target pressures. Although this is relatively convenient in the freefield personal audio system in [78], this process requires further investigation in more complex problems such as the car audio problem investigated in the following sections.

7.2.1 Power Constrained Least Squares Optimisation

Similarly to the acoustic contrast control strategy, it is also possible to introduce a constraint to the least squares optimisation problem which allows the array effort, or electrical power to be limited. Constraining the array effort given by equation 7.4 to be less than a value c_{AE} gives the cost function for the least squares optimisation as

$$J_{LS} = \boldsymbol{e}^H \boldsymbol{e} + \lambda_{AE} \left(\boldsymbol{q}^H \boldsymbol{q} - c_{AE}\right), \tag{7.21}$$

where λ_{AE} is the real and positive Lagrange multiplier as defined above. Following the derivation of the optimal source strengths for the unconstrained solution, the vector of optimal source

strengths according to the least squares formulation is given by

$$\boldsymbol{q} = \left[\boldsymbol{Z}^H\boldsymbol{Z} + \lambda_{AE}\boldsymbol{I}\right]^{-1}\boldsymbol{Z}^H\boldsymbol{p}_T, \tag{7.22}$$

where the value of λ_{AE} has to be adjusted such that the array effort, $\boldsymbol{q}^H\boldsymbol{q}$, is less than or equal to the specified constant c_{AE}. As in the acoustic contrast method, the effect of the power constraint is to regularise the matrix to be inverted and this solution has previously been employed in both active noise control [132] (see Chapter 3) and personal audio [99].

7.2.2 Least Squares Optimisation with Individual Source Power Constraints

In addition to limiting the overall electrical power it is often also important in practice to limit the individual power required by each source in the array. This optimisation problem has been derived in Section 7.1.3 in the context of acoustic contrast control and it will be detailed here in the context of the least squares formulation.

The constraint on the individual source strengths can be imposed by ensuring that $|q_m|^2$ is equal to the constant c_E for all M sources. This gives the cost function for the least squares optimisation as

$$J_{LS} = \boldsymbol{e}^H\boldsymbol{e} + \sum_{m=1}^{M}\lambda_m\left(|q_m|^2 - c_E\right), \tag{7.23}$$

where λ_m are the real and positive Lagrange multipliers governing the M constraints on the individual magnitude squared of the source strengths. Differentiating with respect to the real and imaginary parts of the source strength gives

$$\boldsymbol{q} = \left[\boldsymbol{Z}^H\boldsymbol{Z} + \boldsymbol{\lambda}_M\right]^{-1}\boldsymbol{Z}^H\boldsymbol{p}_T, \tag{7.24}$$

The problem of choosing the values for the individual elements of $\boldsymbol{\lambda}_M$ is similar to that discussed in Section 7.1.3, which although convex may require iterative solution methods.

7.3 Physical Limits on the Generation of Personal Listening Zones in an Automobile Cabin

The generation of personal listening zones in the car cabin enclosure would ideally be achieved using the standard car audio loudspeakers and, therefore, limit the additional requirements of the system. However, from the investigations of active noise control, particularly in Chapter 3, it is evident that the control of the sound field in an enclosure is limited to low frequencies, where the modal overlap is low. Therefore, the use of a distributed array of sources, such as the standard car audio loudspeakers, to generate personal listening zones in the car cabin enclosure is likely to also be limited to low frequencies. To understand this limit, this section will first investigate the potential performance of distributed arrays of sources attempting to achieve a bright zone in the front of the car cabin sized enclosure whilst achieving a dark zone in the rear

and vice versa. Subsequently, the performance of small arrays of loudspeakers positioned in close proximity to the car cabin's occupants' heads will also be investigated, to increase the high frequency performance.

The geometry of the personal audio problem was presented in Figure 7.2. The dimensions of the enclosure have been specified to be representative of the Ford S-max vehicle that will be employed for the measurement and implementation study detailed in the following chapter. The front and rear control zones used in the simulations presented in the following sections are each defined by a three-dimensional grid of 135 microphones evenly distributed throughout the cuboid control zones as shown in Figure 7.4. The inter-microphone separation is 10 cm in each co-ordinate direction. In a practical implementation, reducing the number of microphones in the control zones may result in zones of control localised around the microphones, as in active noise control [54]; however, in contrast to an active noise control system, the personal audio system does not require the microphones in the real-time implementation and, therefore, the use of a large number of microphones to optimise the system is, perhaps, not unreasonable. In the first instance it was considered more important to investigate separating the audio reproduction for the front and back seats rather than between the left and right hand sides of the car.

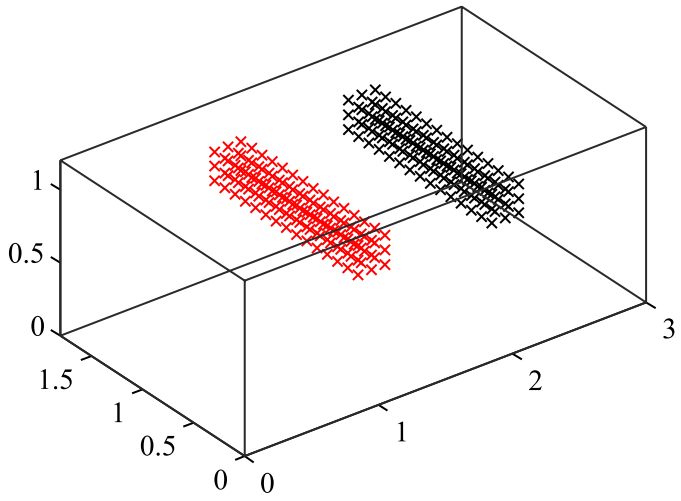

Figure 7.4: Rectangular enclosure showing the enclosure dimensions and the positions of the pressure evaluations in the front (red) and rear (black) control zones.

7.3.1 The Performance of Distributed Loudspeaker Arrays

Previous work has investigated the effect of rooms, or enclosures on the performance of personal audio systems by considering the enclosure's contribution to the sound field as a diffuse field [82]. Although this is a reasonable approximation at frequencies greater than the Schroeder frequency, this approximation will not be valid at the low frequencies where a dis-

tributed array may achieve control. The performance of a personal audio system employing optimal beamforming in a modal sound field has been investigated in [100] using the brightness maximisation control strategy discussed above and described by Choi and Kim [24]. This investigation is limited to the consideration of a single frequency excitation and, therefore, does not provide any insight into how the acoustic environment affects the operating frequency range of the personal audio system. Additionally, no investigation of the effect of the enclosure on the power requirements has been presented. Therefore, the following section will investigate how the performance and power requirements of distributed arrays are affected by the modal sound field. This investigation will be achieved using the weakly coupled, or rigid walled modal model detailed in Chapter 2 since the computational demand is significantly reduced compared to the fully coupled model. Although structural-acoustic coupling may be significant in a car cabin environment, as discussed in Chapter 2, it has been shown in Chapter 3 that feedforward active noise control is largely unaffected by structural-acoustic coupling and, therefore, due to the similarity in operation, personal audio performance is also not expected to be significantly affected; this has been confirmed in Appendix J. The acoustic sources in the array will be modelled as monopoles, as in the active noise control investigations, since this provides a reasonable model of practical loudspeakers at low frequencies [73] and the enclosure has been modelled using 4420 acoustic modes, which includes sufficient modes to accurately model the enclosure up to about 1.2 kHz.

An array of corner sources

The ability of an acoustic source to achieve global control of the sound field in an enclosure can be related to how the source couples into the acoustic modes, as discussed in the context of active noise control in Chapter 3. For example, if the acoustic source is positioned on the nodal line of a particular acoustic mode then the sound field related to that acoustic mode will not be controllable. By positioning monopole sources in the corners of a rectangular enclosure, as shown in Figure 7.5, the distributed array of sources is able to couple in to all of the enclosure's acoustic modes. The ability of this distributed array to maximise the acoustic contrast between the two control zones, also shown in Figure 7.5, has been simulated by optimising the eight source strengths using the unconstrained acoustic contrast control strategy given by equation 7.6 with the array both in the rigid walled rectangular enclosure and in the freefield. Figure 7.6 shows the resulting acoustic contrast and array effort in the two acoustic environments, for two control scenarios where the bright zone is either placed in the front control zone or the rear control zone.

From Figure 7.6a it can be seen that in the freefield the acoustic contrast in both control scenarios is between around 30 and 35 dB at very low frequencies and then begins to roll-off with increasing frequency. The performance of the array does not roll-off constantly with frequency. However, due to the complex source and sensor geometry of the optimised system

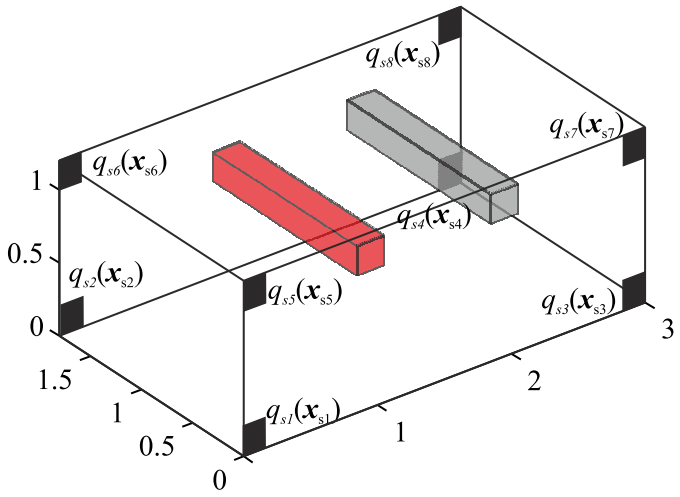

Figure 7.5: Rectangular enclosure showing the positions of the corner monopole sources (indicated by rectangles) and the front (red) and rear (grey) control zones.

it is difficult to relate this roll-off characteristic to one particular parameter as is possible, for example, for simple end-fire [80] or broadside arrays [78]. It can be seen from comparing the red and black lines in Figure 7.6a that, in general, the acoustic contrast is slightly lower when producing a front bright zone than when producing a rear bright zone. This can be related to the slightly closer proximity of the control sources to the rear control zone than to the front control zone and, therefore, the lower source strengths required to produce the desired average bright zone pressure. From the general trend which is observed for both control scenarios, the results show that as the wavelength of the radiated sound gets shorter, the generation of two distinct listening zones becomes more difficult and this can be related to both the physical separation between the sources as well as the relative separation and the orientation of the control zones.

Figure 7.6b shows the corresponding array effort required to achieve the acoustic contrast levels presented in Figure 7.6a. The array effort is plotted in decibels relative to the array effort required to produce the same average bright zone pressure when driving all of the sources in phase. From the freefield results shown in this plot a general trend can again be observed for both control scenarios. At frequencies below around 50 Hz the array effort is relatively constant at around 33 dB when producing a front bright zone and 38 dB when producing a rear bright zone. At frequencies greater than 50 Hz the array effort in both cases begins to roll-off as the array becomes less self-cancelling.

Despite the difficulty in understanding the details of the physical limits on the control system performance in the freefield, these results can still be used to provide a reference for understanding the physical effects introduced by employing the control system in the enclosure. The acoustic contrast performance of the system optimised in the enclosure is shown by the dashed lines in Figure 7.6a for the two control scenarios. From this comparison it can be seen that at

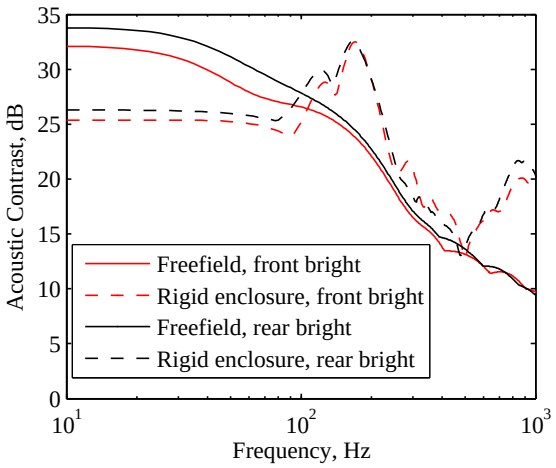

(a) Acoustic contrast.

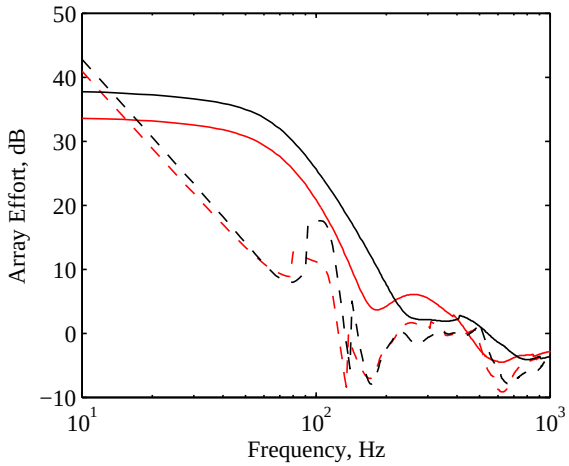

(b) Array effort.

Figure 7.6: Acoustic contrast and array effort plotted as a function of frequency for the array of eight sources positioned in the corners of the car cabin sized rectangular enclosure or freefield region. The array effort is plotted in decibels relative to the array effort required to produce the same average bright zone pressure when driving all sources in phase. The performance of the array is shown in both the freefield (solid lines) and in a rigid walled enclosure (dashed lines) for two control scenarios, where the bright zone is defined as either the front control zone (red lines) or the rear control zone (black lines).

frequencies below 100 Hz, where the response is dominated by individual acoustic modes, the performance of the array is reduced by the effect of the enclosure. This reduction in performance is due to the mode shapes of the compliant, or $(0,0,0)$, acoustic mode, the $(1,0,0)$ mode at 57 Hz and the $(0,1,0)$ mode at 95 Hz which dominate the acoustic response at these low frequencies. In order to produce a bright front and dark rear zone, or vice versa, the array must work against the natural response of the enclosure and this results in a reduced performance and a rise in the array effort at low frequencies, as shown in Figure 7.6b. At higher frequencies the acoustic contrast performance in the enclosure is more varied than in the freefield, although the performance of the array is largely increased. This can again be related to the control geometry and the relative spatial properties of the enclosure's modes where, in this case, the modal response tends to allow an increase in the performance of the array. It can be seen from the array effort plot in Figure 7.6b that at frequencies where the acoustic response of the enclosure is not dominated by the compliant acoustic mode, the array effort is generally lower than in the freefield, and towards the upper limit of the frequency range presented the array effort in the enclosure and freefield are very similar.

Car Audio Source Array

In a practical implementation in a car cabin, it will not be possible to position the loudspeaker array to couple so effectively with a large number of the enclosure's acoustic modes. Therefore, it is important investigate the effects of positioning the array of sources at the nominal car audio loudspeaker positions, as employed throughout the earlier chapters of this thesis. The positions of the four car audio loudspeakers in the rectangular enclosure are shown in Figure 7.7 along with the control zone geometry. Figure 7.8 shows the optimised performance of the car audio loudspeakers in both the freefield and the rigid walled enclosure for the two control scenarios.

Figure 7.8a shows the acoustic contrast achieved by the car audio source array when optimised to produce either a front bright zone or a rear bright zone. From these plots it can be seen that in the freefield the acoustic contrast in both control scenarios is lower than achieved using the corner source array, which can be related to the number of sources in the array, their relative positioning and their positioning relative to the control zones. However, it can also be seen that the performance of the array does not begin to roll-off until above around 200 Hz in both control scenarios, which is an increase compared to the corner source array and can be related to the closer proximity of the sources to the control zones. It is also interesting to highlight that the car audio array achieves a significantly higher level of acoustic contrast when producing a front bright zone than when producing a rear bright zone, which is opposite to the result observed for the corner source array. This effect can be related to the relative positions of the sources to the two control zones in each of the arrays. For the car audio source array the average distance between the sources and the front control zone is significantly less than the average distance between the sources and the rear control zone, whereas for the corner source

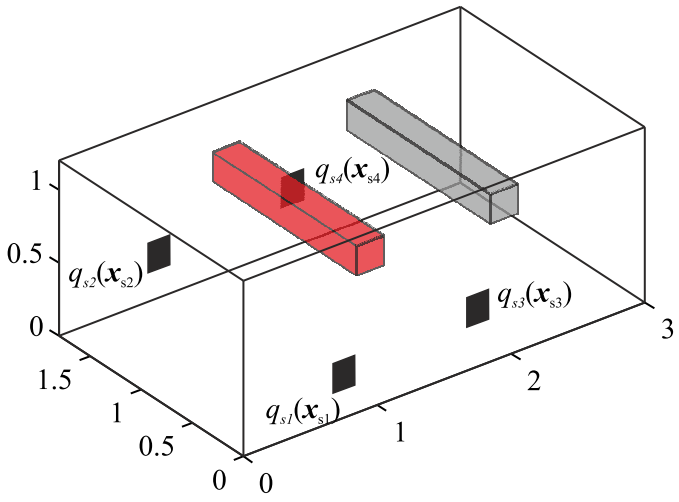

Figure 7.7: Rectangular enclosure showing the positions of the car audio monopole sources (indicated by rectangles) and the front (red) and rear (grey) control zones.

array there is a slightly smaller average distance to the rear control zone than to the front control zone.

Figure 7.8b shows the corresponding array effort required to achieve the acoustic contrast performance presented in Figure 7.8a. The array effort is again plotted in decibels relative to the array effort required to produce the same average bright zone pressure when driving all sources in-phase. From the freefield results shown in this plot it can be seen that the array effort is significantly lower than that required by the corner source array, which can be related to the closer proximity of the sources to the control zones. However, the required array effort follows a similar trend to that required by the corner array; that is, at frequencies below around 50 Hz the array effort is relatively constant for both control scenarios and at frequencies above around 50 Hz the array effort begins to roll-off as the array becomes less capable of producing the specified bright and dark zones.

Figure 7.8a shows the effect of the rigid walled enclosure on the acoustic contrast performance achieved using the car audio source array. It can be seen that the effect of the enclosure on the contrast performance at frequencies below the first longitudinal acoustic mode is not as significant as was observed for the corner source array and in fact the performance is increased when producing a rear bright zone. This can be related to the car audio sources not being symmetrically distributed and, therefore, not all coupling into the acoustic modes identically. At higher frequencies the performance of the car audio array in the enclosure is more varied than in the freefield and the array is unable to achieve a significant level of acoustic contrast at frequencies greater than around 200 Hz for a front bright zone and 120 Hz for a rear bright zone. This limit is consistent with the limit of active noise control in an enclosure as detailed in Chapter 3 and can be related to the array not coupling with a sufficient number of acoustic

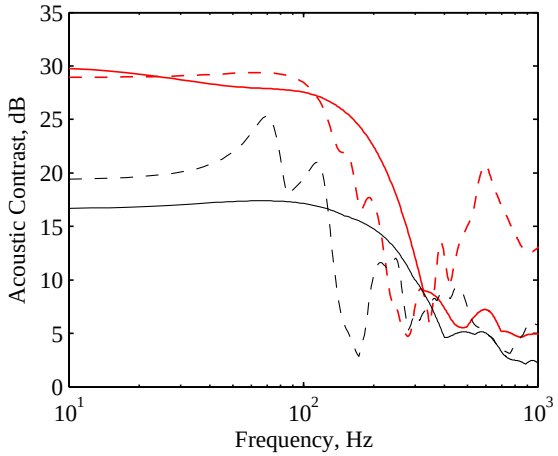

(a) Acoustic contrast.

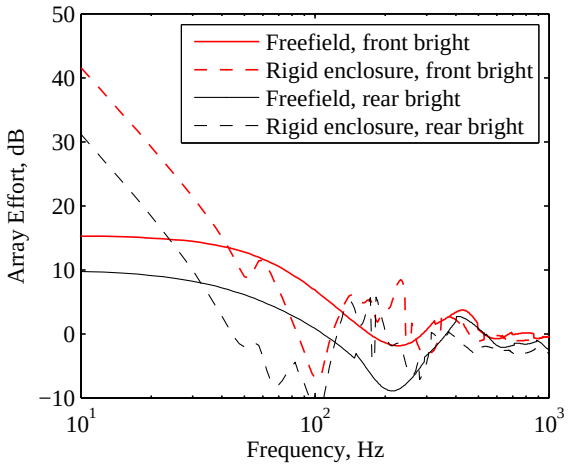

(b) Array effort.

Figure 7.8: Acoustic contrast and array effort plotted as a function of frequency for the array of four sources positioned at the standard car audio loudspeaker positions in the car cabin sized rectangular enclosure or freefield region. The array effort is plotted in decibels relative to the array effort required to produce the same average bright zone pressure when driving all sources in phase. The performance of the array is shown in both the freefield (solid lines) and in a rigid walled enclosure (dashed lines) for two control scenarios, where the bright zone is defined as either the front control zone (red lines) or the rear control zone (black lines).

modes to achieve effective sound field control.

The effect of the enclosure on the required array effort shown in Figure 7.8b is consistent with that shown for the corner source array. At frequencies above around 200 Hz, where the performance of the array is limited, the array effort in the freefield and the enclosure are very similar, while at very low frequencies the required array effort rises significantly due to the compliant acoustic mode. At intermediate frequencies, the array effort required in the enclosure is below that required in the freefield.

7.3.2 The Performance of Nearfield Loudspeaker Arrays

From the results presented in the previous section it has been shown that at higher frequencies, where the number of dominant acoustic modes is large, the generation of personal listening zones using a distributed array of loudspeakers is not feasible. This performance limit is consistent with the high frequency limit on active noise control using a distributed array of sources, such as the car audio loudspeakers and, therefore, to increase the bandwidth of control it is necessary to introduce additional loudspeakers close to the car cabin's occupants' heads, as in the case of local active noise control [180]. Although there may be a frequency range over which these loudpseakers operate in the modal region of the car cabin enclosure's response, due to their proximity to the control zones, at higher frequencies the responses will be dominated by the direct sound from the arrays and, therefore, it is reasonable to neglect the indirect sound due to the enclosure acoustics and use the freefield model to investigate the performance of the array. This approach has previously been employed in the context of local active noise control [180] and for personal audio systems [81] and it has been shown that the use of freefield acoustic monopole models provides a convenient and efficient method of investigating personal audio systems with simulation predictions that provide useful guidance with respect to practical implementations [81, 80]. Therefore, the freefield monopole model will be used along side the modal model to investigate the performance of arrays of sources positioned in the nearfield of the car cabin's occupants' heads. However, it should also be highlighted that although the contributions from the room may be negligible, the effects of objects in close proximity to the arrays may have a significant effect on the performance of the array. This has been shown in the context of a personal audio headrest by Jones and Elliott [181], a personal audio system for implementation on a video monitor by Chang *et al* [87] and a personal audio system in a mobile device by Cheer *et al* [86]. These effects may be modelled using boundary element or finite element numerical modelling methods, but the computational complexity of employing such methods is high and it is therefore difficult to conveniently investigate a number of control geometries. Therefore, these effects will be neglected in this initial numerical investigation.

Compact Arrays

In order to generate independent listening zones in the front and rear seating areas of the car cabin, it is necessary to use a number of sources in close proximity to the control zones. From

previous work it has been shown that the use of a compact endfire array allows a significant acoustic contrast to be achieved whilst employing a small array of loudspeakers. This is important in the car cabin application since mounting large arrays close to the occupants heads may be impracticable due to crash safety and restricting the driver's vision. Therefore, based on the results of the previous work described above, the control geometry presented in Figure 7.9 will be investigated. The control system consists of four two-source endfire arrays each mounted at the centre of the occupants' head positions with an inter-source separation of 4 cm, which is consistent with the previous work in [80]. The contrast is maximised by allowing independent control of each of the eight individual sources within the array.

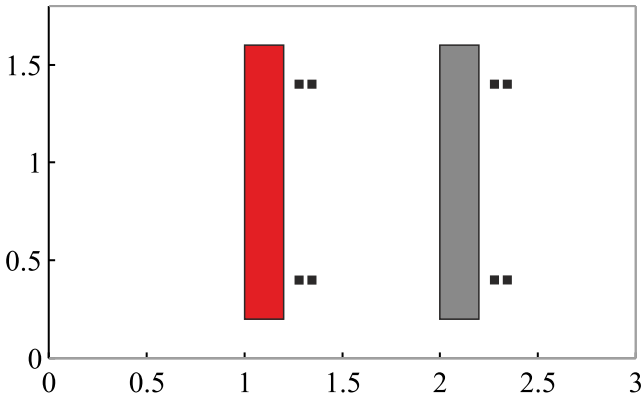

Figure 7.9: Plan view of the rectangular enclosure showing the positions of the four two-source compact source arrays (indicated by rectangles) and the front (red) and rear (grey) control zones.

Figure 7.10 shows the acoustic contrast and array effort according to the modal and freefield simulations for the two control scenarios. The modal simulations are presented up to 1.2 kHz using 4420 acoustic modes, while the freefield simulations are shown up to 10 kHz. From the acoustic contrast results in the freefield it can be seen that in both control scenarios high levels of acoustic contrast performance are achieved at low frequencies. The acoustic contrast gradually reduces with increasing frequency and rolls-off quite rapidly from around 200 Hz. This is significantly lower than the high frequency limit previously observed for the two-source compact array with an inter-source separation of 4cm [80], however, the employed array in this case is not a simple two-source array operating in isolation and therefore the roll-off characteristic is significantly more complicated. Despite this roll-off it can be seen that an acoustic contrast greater than 10 dB is still achieved at 10 kHz for both control scenarios. This acoustic contrast would provide subjectively acceptable performance according to the work presented in [23] and acceptable levels of performance under certain operating scenarios according to [70]. However, it is important to reiterate that the presented simulation results are likely to be quite inaccurate at higher frequencies since the practical effects such as the directivity of the

individual loudspeakers and baffling due to headrests are not considered.

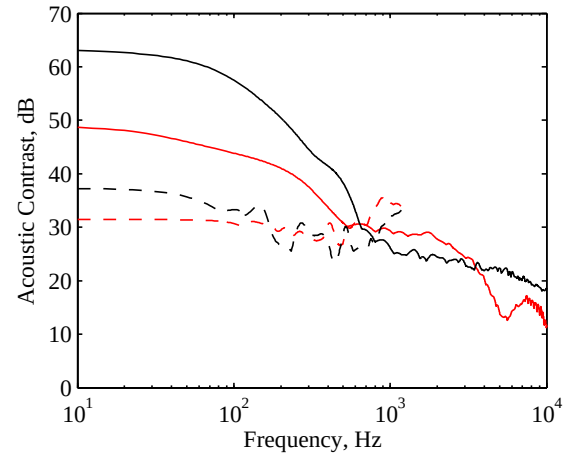

(a) Acoustic contrast.

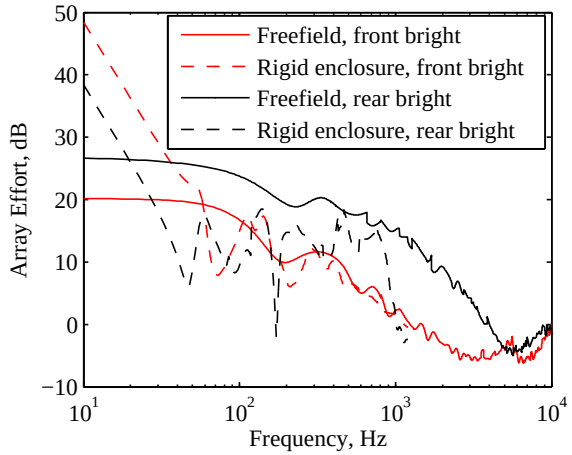

(b) Array effort.

Figure 7.10: Acoustic contrast and array effort plotted as a function of frequency for the array of four two-source compact arrays positioned at the centre of each of the four headrest positions in the car cabin sized rectangular enclosure or freefield region. The array effort is plotted in decibels relative to the array effort required to produce the same average bright zone pressure when driving all sources in phase. The performance of the array is shown in both the freefield (solid lines) and in a rigid walled enclosure (dashed lines) for two control scenarios, where the bright zone is defined as either the front control zone (red lines) or the rear control zone (black lines).

Figure 7.10a also shows the performance of the four two-source compact arrays simulated in the rigid walled enclosure using the modal model. From these results it can be seen that in both control scenarios the acoustic contrast at frequencies below around 500 Hz is significantly below that predicted according to the freefield simulations. However, it appears that as the frequency increases the results of the models converge to a similar predicted performance. This behaviour can also be seen in the array effort results presented in Figure 7.10b, where significant differences are observed between the freefield and modal simulations at low frequencies but reasonably consistent results are shown as the modal density increases.

Broadside Arrays

The use of the compact array geometry presented in Figure 7.9 may provide significant levels of acoustic contrast control, but, if only a single two-source compact array is employed at each headrest position, then the reproduction of two-channel stereo audio programmes will not be possible. Although the reproduction of two-channel stereo will not be considered in detail in this work, due to the added complexities, it is important to consider this future development. The reproduction of a two-channel stereo programme at each listening position may be achieved by employing a two-source compact array at each side of each headrest, however, this results in an array of 16 loudspeakers, which significantly increases the cost of implementing the system. Therefore, it is interesting to investigate the acoustic contrast performance achievable using an array consisting of a single source positioned at each side of each headrest and this geometry is shown in Figure 7.11.

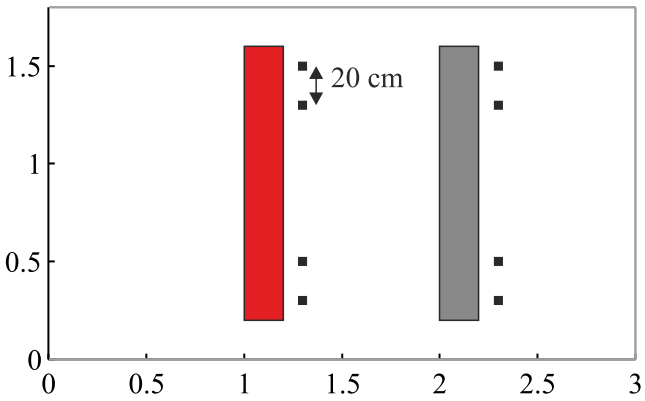

Figure 7.11: Plan view of the rectangular enclosure showing the positions of the four two-source broadside source arrays (indicated by rectangles) and the front (red) and rear (grey) control zones.

The acoustic contrast and array effort for the array geometry presented in Figure 7.11 are presented in Figure 7.12 for the freefield and modal simulations. From the acoustic contrast plot presented in Figure 7.12a it can be seen that in the freefield the proposed array geometry achieves lower levels of acoustic contrast than the four two-source compact arrays in both control configurations. At around 100 Hz the high levels of low frequency contrast begin to roll-off and at frequencies above around 1 kHz the acoustic contrast is between 10 and 15 dB in both control scenarios. From the freefield array effort results presented in Figure 7.12b it is interesting to note that a significantly lower array effort is required, particularly at lower frequencies, than in the compact array system. This can be related to the strongly self-cancelling nature of the compact arrays [80, 99].

As in the compact array simulation results presented in Figure 7.10, the effect of the enclo-

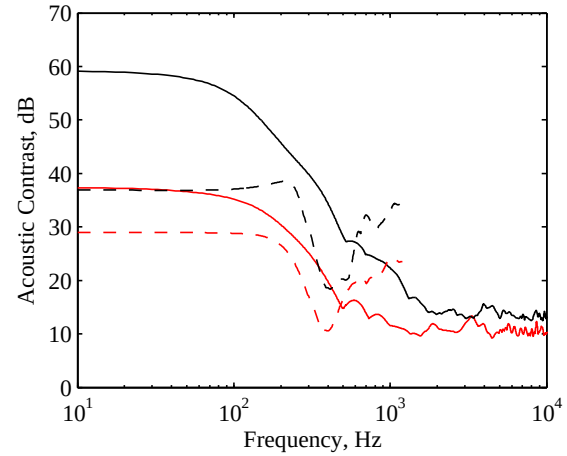

(a) Acoustic contrast.

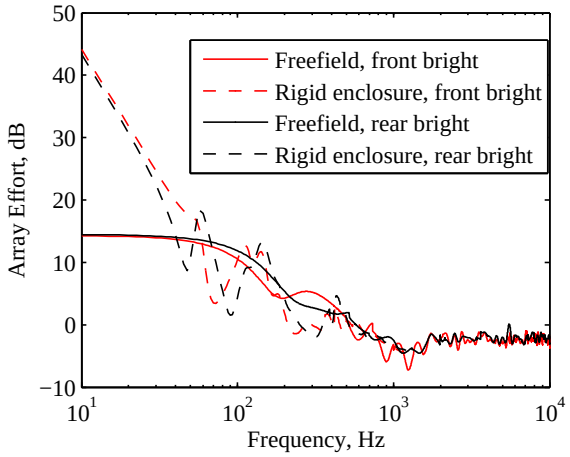

(b) Array effort.

Figure 7.12: Acoustic contrast and array effort plotted as a function of frequency for the array of four broadside arrays each employing two *monopole* sources positioned at the sides of each of the four headrest positions in the car cabin sized rectangular enclosure or freefield region. The array effort is plotted in decibels relative to the array effort required to produce the same average bright zone pressure when driving all sources in phase. The performance of the array is shown in both the freefield (solid lines) and in a rigid walled enclosure (dashed lines) for two control scenarios, where the bright zone is defined as either the front control zone (red lines) or the rear control zone (black lines).

sure on the performance of the array geometry presented in Figure 7.11 is to reduce the predicted acoustic contrast at low frequencies compared to the freefield simulations. Compared to the acoustic contrast performance of the four two-source compact arrays in the enclosure, it can be seen that a lower acoustic contrast is largely achieved by the array presented in Figure 7.11. The array effort for the four two-source broadside arrays shown in Figure 7.12b is significantly greater in the enclosure compared to the freefield at frequencies below around 70 Hz. However, in a practical implementation this array is unlikely to be used at such low frequencies.

Broadside Arrays of Hypercardioid Sources

Although the performance of the broadside array of loudspeakers, as shown in Figure 7.11, is able to achieve significant levels of acoustic contrast whilst also providing the future compatibility for a stereo audio system, the performance of the system is lower than that achieved by the array of four two-source compact arrays. The performance of the compact arrays may be combined with the potential stereo functionality of the broadside arrays by using eight two-source compact arrays, one positioned at either side of each headrest. However, this would require 16 headrest loudspeakers. Previous work by the author [93] has investigated employing phase-shift loudspeakers [92] to achieve a directional source using a single loudspeaker. This is achieved by employing an enclosure with a rear opening in which a resistive material is placed. By specifying the dimensions of the enclosure and the rear opening, and the resistive and compliant properties of the material covering the rear opening, the directivity response of the phase-shift loudspeaker can be altered. If the phase-shift loudspeakers' directivity is tuned suitably, then it may be possible to combine the benefits of the compact and broadside arrays described in the previous sections. That is, the higher contrast performance achieved by the compact arrays may be achievable whilst allowing for future stereo functionality and whilst only using eight loudspeakers. The use of phase-shift loudspeakers in arrays has been investigated in [84, 78].

The directivities of the compact two-source arrays investigated above are a complex function of both frequency and position and, therefore, it is not feasible to attempt to design a phase-shift loudspeaker with these directivities. However, in previous work it has been shown that, when attempting to produce a bright zone at a single point whilst minimising the radiated sound power, the optimum directivity of a two-source endfire array is a hypercardioid [80]. The use of hypercardioid-like phase-shift loudspeakers in an array has been successfully demonstrated in [78] and, therefore, the use of hypercardioid sources will be investigated here for the car audio application.

Simulations of the broadside headrest array geometry presented in Figure 7.11 have been calculated when the individual sources have hypercardioid directivities given by

$$\text{Directivity}(\theta,\phi) = 0.25 + 0.75\cos\theta\cos\phi, \tag{7.25}$$

where θ is the horizontal angle and ϕ is the vertical angle with respect to the look-direction of

the sources. Figure 7.13 shows the acoustic contrast and array effort for the array of hypercardioid sources optimised for the two control scenarios in the freefield and modal environments. From the acoustic contrast plot in Figure 7.13a it can be seen that in the freefield simulations at frequencies below around 200 Hz the performance of the array optimised to produce a front bright zone has not been significantly altered compared to the broadside array simulation results presented in Figure 7.12a, however, the performance of the array when producing a rear bright zone has been reduced by around 8 dB. The performance of the hypercardioid array in the enclosure is not significantly different from the performance of the monopole array, although there are some significant variations in the array effort which appear to be related to conditioning problems (see Section 7.4 below).

At higher frequencies it can be seen from comparing Figures 7.12a and 7.13a that the performance of the array has been increased when producing a bright front zone using the hypercardioid sources as opposed to the monopole sources. However, the use of the hypercardioid sources has slightly reduced the performance of the array attempting to produce a rear bright zone. The corresponding array effort requirements of the hypercardioid source array are presented in Figure 7.13b and it can be seen that they have not been significantly affected by the use of hypercardioid sources.

From the results presented in Figure 7.13 it can be seen that, in this case, the use of hypercardioid sources does not appear to have a significant advantage over employing monopole sources. In practice neither closed-back or phase-shift loudspeakers will maintain the respectively assumed monopole or hypercardioid directivities over the full audio bandwidth. The simulations presented here therefore provide limited insight into the practical performance of these arrays, particularly at higher frequencies where the effects of finite-sized sources and baffling will significantly affect the source direcitivties [86]. Based on the experience gained from previous practical work [93, 84, 78, 86] the phase-shift loudspeakers will be employed in the practical investigation presented in the following chapter and will be considered in the following numerical investigation of the personal audio control strategies.

7.4 Numerical Investigation of Personal Audio Control Strategies

The previous section has investigated the physical limits on generating personal listening zones within a car cabin enclosure. In a practical system there are also limits imposed by the employed control strategy. For instance, although the acoustic contrast control method, detailed in Section 7.1, will achieve the maximum levels of acoustic contrast between the bright and dark zones, it may also limit the audio quality [78]. This problem may be avoided by employing the least squares optimisation method detailed in Section 7.2 as shown in [78] in the context of a broadside array of phase-shift loudspeakers. In [78] the acoustic contrast performance of the array is not significantly reduced by employing the least squares method compared to acoustic contrast control and it is reported that the audio quality is improved. Therefore, this section will

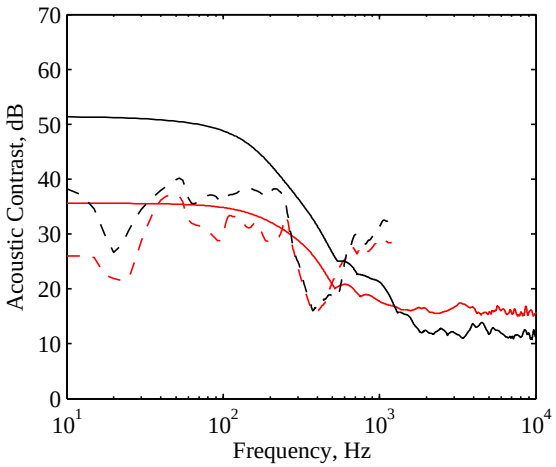

(a) Acoustic contrast.

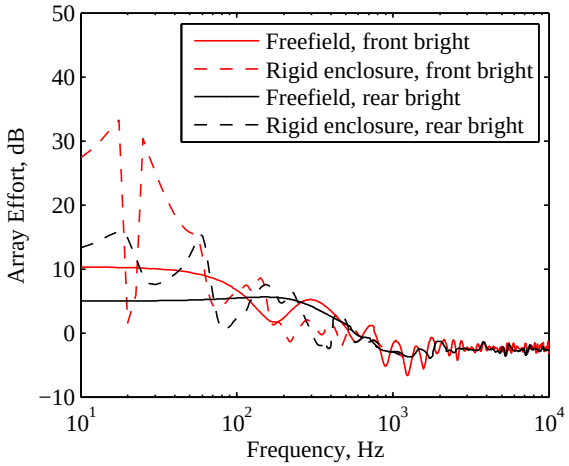

(b) Array effort.

Figure 7.13: Acoustic contrast and array effort plotted as a function of frequency for the array of four broadside arrays each employing two *hypercardioid* sources positioned at the sides of each of the four headrest positions in the car cabin sized rectangular enclosure or freefield region. The array effort is plotted in decibels relative to the array effort required to produce the same average bright zone pressure when driving all sources in phase. The performance of the array is shown in both the freefield (solid lines) and in a rigid walled enclosure (dashed lines) for two control scenarios, where the bright zone is defined as either the front control zone (red lines) or the rear control zone (black lines).

compare the performance predicted according to the least squares optimisation to that predicted according to acoustic contrast control for the car audio loudspeaker array shown in Figure 7.7 and the broadside headrest array employing hypercardioid sources shown in Figure 7.11.

7.4.1 Least Squares Optimisation Target Criterion

As detailed in Section 7.2, to optimise the signals driving the arrays using the least squares optimisation it is necessary to define a vector of target pressures. In the context of the broadside loudspeaker array in [78], the target pressures were set to zero at the dark zone positions and for the bright zone positions were defined as the pressures produced by the loudspeaker at the centre of the array being driven alone. This choice of bright zone target pressures represents the sound field that would be produced by the standard loudspeaker system. In the car audio system, assuming the audio programme to be reproduced is mono, the targeted sound field can be defined following the same principle. For the distributed loudspeaker arrays the bright zone target pressures will be defined as the pressures produced in the bright zone when the sources in the array are driven in-phase. The bright zone target pressures for the optimisation of the nearfield arrays will, however, be defined as the pressures produced in the bright zone when the sources in the four sources in the nearfield of the bright zone are driven in-phase. These definitions of the bright zone target pressures ensure that the optimised arrays do not attempt to compensate for the positions of the loudspeakers and therefore significantly limit the level of acoustic contrast. This would occur, for example, if the bright zone target pressures were set as the pressures produced by the car audio loudspeakers driven in-phase, regardless of the array used for personal audio reproduction.

7.4.2 Numerical Conditioning

In computing problems, such as optimisation, ill-conditioning may describe any computation whose output values are very sensitive to small changes in the input data and, therefore, in the presence of small errors or perturbations an ill-conditioned problem may produce highly inaccurate results. The effects of ill-conditioning have been considered in the context of personal audio systems in a number of publications [82, 84, 99] and more generally in the context of sound field reconstruction [182, 183]. It has been shown that when the optimisation problem is not well conditioned it is susceptible to uncertainties in the transfer responses [82, 99] and in a practical implementation this significantly limits the performance of the array, where transfer response uncertainties are easily produced by variations in the acoustic environment, for example. A comparison between the conditioning of the acoustic contrast and least squares solutions has been presented in [84] in the context of a broadside array of phase-shift loudspeakers, and it was shown that the two control strategies were similarly well conditioned. However, the conditioning is dependent on the defined system and therefore the conditioning of the acoustic contrast control and least squares optimisation will be compared in the context of the car cabin personal audio system.

The conditioning of a matrix may be considered with respect to either the calculation of the inverse of the matrix or the calculation of its eigenvalues. In the acoustic contrast control strategy it is necessary to perform both matrix inversion and eigenvalue calculation, while in the least squares optimisation only matrix inversion is required. The methods of calculating the conditioning with respect to both matrix inversion and the eigenvalue problem will be defined here for use in the following comparison of acoustic contrast control and least squares optimisation.

The condition number of a symmetric matrix with respect to its inverse is given by the ratio of its largest, $\bar{\sigma}$, to its smallest singular value, $\underline{\sigma}$, which is [184],

$$\kappa = \frac{\bar{\sigma}}{\underline{\sigma}}. \tag{7.26}$$

A large condition number compared to unity indicates that the matrix is close to singular and, therefore, the matrix is said to be ill-conditioned and small errors in the elements of the matrix to be inverted will produce large changes in the solution.

The effect of perturbations in the elements of a matrix on its eigenvalues may be described by the Wilkinson number of the matrix [184]. The Wilkinson number corresponding to the *n*-th eigenvalue of the matrix $\boldsymbol{A}$ is given by [185, 186]

$$s(\lambda_n) = |\boldsymbol{y}_n^H \boldsymbol{x}_n|, \tag{7.27}$$

where $\boldsymbol{x}_n$ and $\boldsymbol{y}_n$ are the left and right eigenvectors corresponding to the *n*-th eigenvalue, where $||\boldsymbol{x}_n||_2 = ||\boldsymbol{y}_n||_2 = 1$ and satisfy the equations

$$\begin{aligned} \boldsymbol{A}\boldsymbol{x} &= \lambda \boldsymbol{x}, \\ \boldsymbol{y}^H \boldsymbol{A} &= \lambda \boldsymbol{y}^H, \end{aligned} \tag{7.28}$$

where $\boldsymbol{A}$ is a square Hermitian matrix. For a non-defective matrix $\boldsymbol{A}$, which has a compete set of linearly independent eigenvectors, $s(\lambda)$ is equal to unity, but, for a defective matrix it is necessary to use the Jordan decomposition and $|\boldsymbol{y}^H \boldsymbol{x}|$ is not necessarily equal to unity. The Wilkinson number is the cosine of the angle between the left and right eigenvectors associated with the eigenvalue, λ_n, and is the reciprocal of the *eigenvalue condition number* [185]. For a perturbation of order ε, the perturbation in the eigenvalue, λ_n, can be roughly related to the Wilkinson number by the value $\varepsilon / s(\lambda_n)$ [185]. Therefore, if the Wilkinson number is small compared to unity the problem is ill-conditioned and small perturbations in the elements of the matrix will produce disproportionately large perturbations in the calculated eigenvalues.

7.4.3 Comparison of Acoustic Contrast and Least Squares Control Strategies

Car Audio Source Array

It has been shown through simulations in the previous section that the car audio loudspeaker array in the car cabin sized rectangular enclosure is only capable of achieving significant levels of acoustic contrast at low frequencies. The performance of the array optimised using both the acoustic contrast control and least squares optimisation methods has been calculated using the modal model of the rigid walled rectangular enclosure. The enclosure has again been modelled using 4420 acoustic modes, which includes sufficient modes to accurately model the enclosure response up to about 1.2 kHz. The acoustic contrast and array effort are shown in Figure 7.14 for the two optimisation methods when the four source array is optimised to produce a bright front zone and a dark rear zone; the reverse listening configuration shows similar results and, therefore, these are not presented.

From Figure 7.14a it can be seen that the least squares solution achieves a lower acoustic contrast than the acoustic contrast control strategy particularly at around 100 Hz. Although the acoustic contrast control strategy, by definition, achieves the maximum acoustic contrast possible for the defined control geometry and array configuration, it is possible for the array optimised using the least squares method to achieve a very similar level of contrast depending on the definition of the target pressure vector. It can be seen from Figure 7.14a that at low frequencies, below around 120 Hz, the least squares system is able to achieve levels of acoustic contrast greater than around 11 dB, which is reported to provide adequate separation for personal listening zones according to [23]. From Figure 7.14b it can be seen that the array effort required by the least squares system is also reduced compared to the acoustic contrast controlled system at frequencies below around 150 Hz.

The significant reductions in the array effort required by the least squares optimised array at low frequencies for relatively small reductions in the acoustic contrast performance can be related to the trade-off between the acoustic contrast and array effort. Figure 7.15 shows this trade-off for the case when the power constrained acoustic contrast solution, given by equation 7.9, has been calculated at discrete frequencies with an increasing constraint on the array effort. From this plot can be seen that at 50 Hz, for example, to achieve a contrast of around 24 dB requires an effort of around -4 dB, while increasing the acoustic contrast by 6 dB requires a 13 dB increase in the array effort. Conversely, at 100 Hz it can be seen that a significant increase in acoustic contrast performance is achieved for a small increase in the array effort. This trade-off behaviour has previously been reported in the context of compact arrays in [99].

A great deal of insight into the practical robustness of the optimised personal audio systems can be gained from investigating the conditioning of the calculations, as discussed above. In the acoustic contrast control strategy it is necessary to invert the matrix $\boldsymbol{Z}_D^H \boldsymbol{Z}_D$, while in the least squares solution the inverse of $\boldsymbol{Z}^H \boldsymbol{Z}$ must be calculated. Figure 7.16 shows the condition

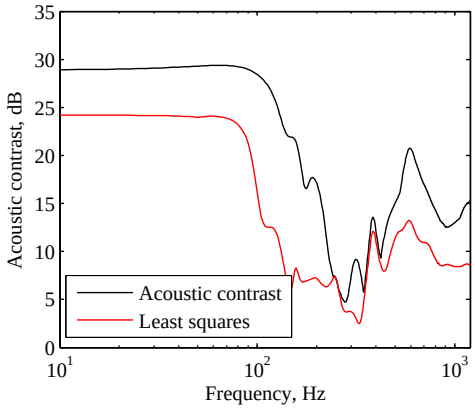

(a) Acoustic contrast between a bright front zone and dark rear zone.

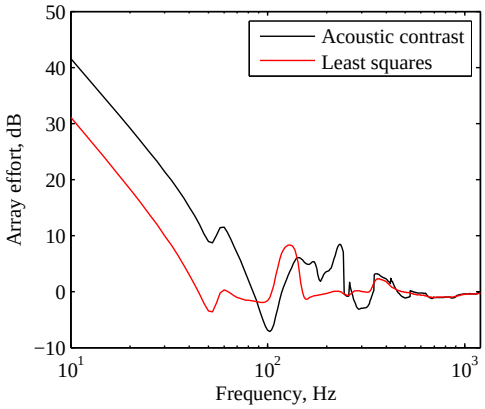

(b) Array effort required to achieve a bright front zone and dark rear zone with the contrast level in Figure 7.14a.

Figure 7.14: Acoustic contrast and array effort plotted as a function of frequency for the array of four sources positioned at the standard car audio loudspeaker positions in the car cabin sized rectangular enclosure. The array effort is plotted in decibels relative to the array effort required to produce the same average bright zone pressure when driving all sources in phase. The performance of the array optimised using both acoustic contrast maximisation (—) and least squares optimisation (—) are shown.

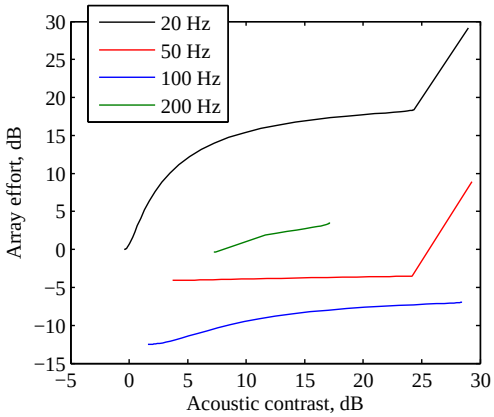

Figure 7.15: The trade-off between the array effort and the acoustic contrast achieved when using the power constrained acoustic contrast control strategy for the car audio source array.

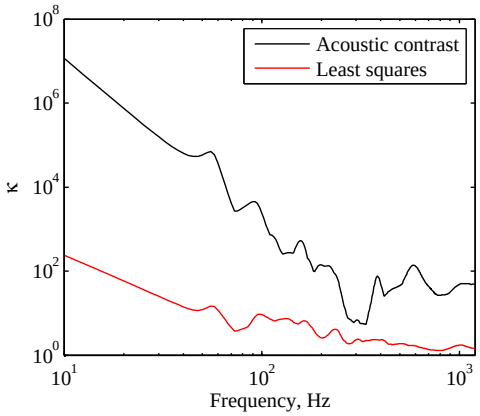

Figure 7.16: The condition number, κ, with respect to the inversion of the $\boldsymbol{Z}_D^H \boldsymbol{Z}_D$ matrix for the acoustic contrast maximisation method (—) and the $\boldsymbol{Z}^H \boldsymbol{Z}$ matrix for the least squares optimisation method (—) for the car audio source array.

number with respect to matrix inversion for these matrices. It can be seen that the condition number for the least squares solution is significantly lower than that for the acoustic contrast solution throughout the presented frequency range. The difference in the condition numbers is most significant at low frequencies, where it has been shown that there is a significant difference between the array efforts required by each solution. The results presented in Figure 7.16 indicate that the least squares solution is better conditioned than the acoustic contrast control strategy and, therefore, will be less susceptible to the errors and uncertainties that will occur in a practical system. If the array effort in the acoustic contrast control strategy is limited to the levels required by the least squares solution then it is possible to improve the conditioning of this problem, as the array effort constraint acts to regularise the matrix to be inverted. However, this will not necessarily improve the audio quality of the system. For example, in [78] despite the similar levels of array effort required by the two solutions, it is reported that the least squares solution still achieves a higher level of audio quality.

In the acoustic contrast control strategy it is also necessary to calculate the eigenvalues of the matrix $\left[\boldsymbol{Z}_D^H \boldsymbol{Z}_D\right]^{-1} \boldsymbol{Z}_B^H \boldsymbol{Z}_B$ and this calculation is also susceptible to conditioning problems. Therefore, although the results presented in Figure 7.16 show a significant advantage in employing the least squares method, it is also interesting to calculate the Wilkinson number given by equation 7.27, which describes the conditioning of the eigenvalues of a matrix. The Wilkinson numbers of the matrix $\left[\boldsymbol{Z}_D^H \boldsymbol{Z}_D\right]^{-1} \boldsymbol{Z}_B^H \boldsymbol{Z}_B$ are presented in Figure 7.17 for the car audio source array. A well conditioned eigenvalue is indicated by a Wilkinson number close to unity and, therefore, from this plot it can be seen that there may be significant numerical problems at low frequencies.

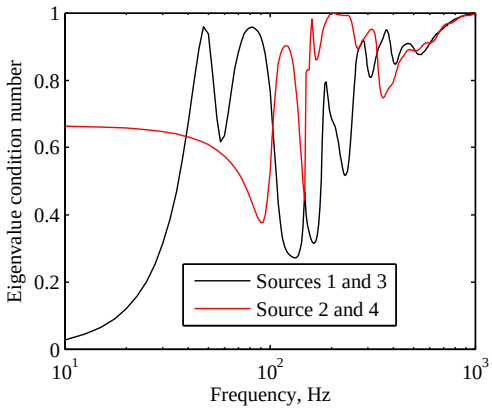

Figure 7.17: The Wilkinson numbers for the matrix $\left[\boldsymbol{Z}_D^H \boldsymbol{Z}_D\right]^{-1} \boldsymbol{Z}_B^H \boldsymbol{Z}_B$ for the car audio source array.

Broadside Arrays of Hypercardioid Sources

Although the simulations of the car audio array in the enclosure indicate significant levels of acoustic contrast at low frequencies, to achieve performance at higher frequencies it is necessary to employ an array of sources in the nearfield of the two listening zones, such as in Figure 7.11. It is interesting to compare the performance of this array employing hypercardioid sources when it is optimised using either the acoustic contrast or least squares strategies. Although the physical limits of this array have been considered using both the modal and freefield models in Section 7.3, the freefield model will be employed here since the difference in performance and conditioning between the two control strategies is not significantly affected by the acoustic environment at higher frequencies.

Figure 7.18 shows the acoustic contrast and array effort achieved by the array of four two-source broadside arrays employing hypercardioid sources when optimised using the acoustic contrast and least squares control strategies. From the acoustic contrast plot in Figure 7.18a it can be seen that at frequencies below around 2 kHz the acoustic contrast optimised array achieves significantly higher levels of acoustic contrast than the array optimised using the least squares method and it can be seen from Figure 7.18b that this significant acoustic contrast performance does not come at the expense of a significantly higher array effort. At frequencies above around 2 kHz both optimisation methods achieve comparable levels of acoustic contrast and array effort; although, as expected, the acoustic contrast for the array optimised using the acoustic contrast optimisation strategy is consistently slightly greater than achieved by the least squares solution. Despite the lower acoustic contrast performance achieved by the least squares optimised array, its acoustic contrast performance is still greater than 13 dB throughout the presented frequency range.

Figure 7.19 shows the condition number, κ, with respect to the inverse of the $\boldsymbol{Z}_D^H \boldsymbol{Z}_D$ matrix for acoustic contrast optimisation and the $\boldsymbol{Z}^H \boldsymbol{Z}$ matrix for least squares optimisation. From this plot it can be seen that the condition number is consistently lower for the least squares method

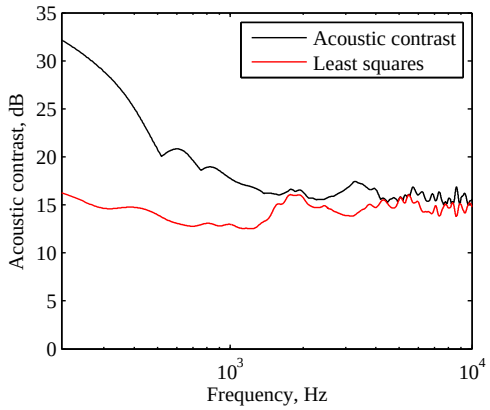

(a) Acoustic contrast between a bright front zone and dark rear zone.

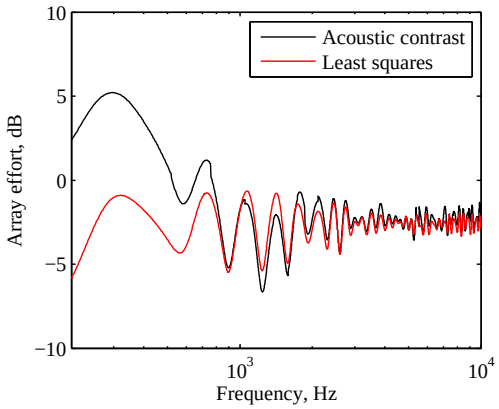

(b) Array effort required to achieve a bright front zone and dark rear zone with the contrast level in Figure 7.14a.

Figure 7.18: Acoustic contrast and array effort plotted as a function of frequency for the array of four broadside arrays each employing two *hypercardioid* sources positioned at the sides of each of the four headrest positions in the car cabin sized rectangular region. The array effort is plotted in decibels relative to the array effort required to produce the same average bright zone pressure when driving all sources in phase. The performance of the array optimised using both acoustic contrast maximisation (—) and least squares optimisation (—) are shown.

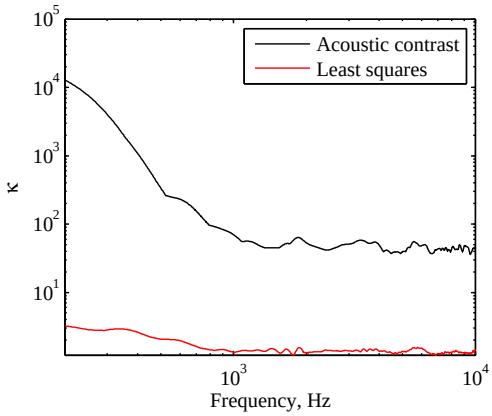

Figure 7.19: The condition number, κ, with respect to the inversion of the $\boldsymbol{Z}_D^H \boldsymbol{Z}_D$ matrix for the acoustic contrast maximisation method (—) and the $\boldsymbol{Z}^H \boldsymbol{Z}$ matrix for the least squares optimisation method (—) for the array of four broadside arrays each employing two *hypercardioid* sources positioned at the sides of each of the four headrest positions in the car cabin sized rectangular region.

and as for the car audio source array this difference is most significant at lower frequencies. At frequencies above around 1 kHz the condition number is almost two orders of magnitude greater for the acoustic contrast method, and this difference increases at low frequencies such that at around 200 Hz the condition number is more than 3 orders of magnitude greater for the acoustic contrast method. From these results it is evident that the least squares solution will be far less susceptible to the errors and uncertainties that will occur in a practical system.

Despite the results presented in Figure 7.19 it is once again interesting to also present the conditioning with respect the eigenvalue calculation in the acoustic contrast optimisation strategy. Figure 7.20 therefore shows the Wilkinson numbers for the matrix $\left[\boldsymbol{Z}_D^H \boldsymbol{Z}_D\right]^{-1} \boldsymbol{Z}_B^H \boldsymbol{Z}_B$. From this plot it can be seen that for all eight eigenvalues the Wilkinson number is reasonably close to unity over the presented frequency range and, therefore, the calculation of the eigenvalues in this case is a relatively well conditioned problem. However, due to the ill-conditioning with respect to the matrix inversion in the acoustic contrast optimisation problem, this is of limited benefit.

7.5 Summary

This chapter used simulations to investigate two key aspects in the design of a personal audio reproduction system for the generation of two independent listening zones in an automobile cabin. Firstly, the physical limits on the generation of personal listening zones in a car cabin sized enclosure have been investigated and then two alternative control strategies have been compared in terms of both acoustic contrast performance and numerical conditioning.

The physical limits on the performance of a distributed loudspeaker array have been investigated by comparing the results of modal and freefield simulations. It has been shown that

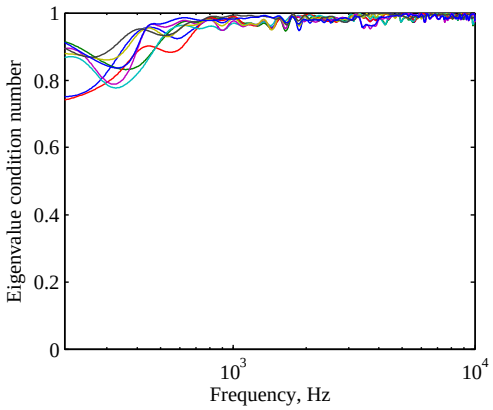

Figure 7.20: The Wilkinson numbers for the matrix $\left[\boldsymbol{Z}_D^H \boldsymbol{Z}_D\right]^{-1} \boldsymbol{Z}_B^H \boldsymbol{Z}_B$ for the array of four broadside arrays each employing two *hypercardioid* sources positioned at the sides of each of the four headrest positions in the car cabin sized rectangular region.

the performance of a distributed source array, such as the standard car audio loudspeakers, is limited to low frequencies where the sources are able to control a significant number of acoustic modes and this limit is consistent with that observed in Chapter 3 in the context of active noise control. It has also been shown that the performance of the distributed source arrays is significantly dependent on whether the natural spatial response of the enclosure supports or conflicts the spatial pressure distribution required by the defined control geometry; although this is perhaps not easily controllable in a practical implementation.

For audio reproduction it is necessary to achieve control over a wider bandwidth than is possible using the car audio loudspeakers. One solution is to use an array of full-range loudspeakers positioned at the headrest of each occupant, as in [81], although, this may lead to safety issues in the car scenario. An alternative solution has therefore been investigated, in which arrays of small loudspeakers positioned close to the car cabin occupants are to be used at high frequencies in combination with the car audio loudspeakers for low frequency control. Two alternative nearfield array geometries have been investigated: one employing compact arrays and one employing broadside arrays. Both configurations show comparable levels of acoustic contrast performance and the effect of the enclosure on both of arrays is most significant at low frequencies, which is related to their proximity to the control zones. Despite the similarity in performance between the two nearfield arrays, the proposed compact array would not be able to achieve stereophonic reproduction without a significant increase in the number of loudspeakers and, therefore, the broadside headrest array is more suitable. To provide a compromise between the performance offered by the compact arrays and the functionality available from the broadside arrays, the use of individual directional sources in the broadside array geometry has also been investigated. The individual sources were modelled as hypercardioids based on previous work, but it was shown that this did not significantly affect the simulated performance.

To implement a personal audio system it is also necessary to optimise the signals driving

the array and this may be achieved using a number of methods as discussed in Chapter 1. Although the acoustic contrast control strategy is inherently capable of achieving the maximum level of acoustic contrast in an ideal system for a given control scenario, it may provide limited audio quality in practice. Previous work has shown that using a least squares control strategy with suitable target pressures may facilitate improved audio quality. Therefore, the acoustic contrast and least squares control strategies have been presented and for both control strategies formulations including constraints on either the array effort or the individual source efforts have been derived; these constrained formulations will be employed in the optimisation of the practical system in the following chapter.

The performance of the acoustic contrast and least squares control strategies has been compared in the context of both the car audio array and the broadside headrest array employing hypercardioid sources. For the car audio loudspeaker array it has been shown that the least squares solution achieves similar levels of acoustic contrast to the acoustic contrast control strategy at low frequencies, where the array is physically capable of achieving significant levels of contrast. However, the least squares solution benefits from a significant reduction in array effort and a significant improvement in the conditioning compared to the acoustic contrast solution. This will provide a more robust implementation in practice. For the broadside headrest array it has been shown that the predicted acoustic contrast of the array optimised according to the least squares strategy is relatively constant with frequency, but at frequencies below around 2 kHz the performance is significantly lower than for the acoustic contrast control strategy. It has also been shown that the conditioning of the least squares solution is significantly better than the acoustic contrast control strategy at all frequencies and the high levels of acoustic contrast predicted for the acoustic contrast control strategy may be unachievable in a practical system subject to uncertainties. Therefore, the least squares solution is a more practical solution which is also expected to provide improved audio quality.

Chapter 8

Experimental Investigation of Active Control of Sound Reproduction in an Automobile Cabin

The previous chapter has investigated both the physical limits on the generation of personal listening zones in a car cabin sized enclosure, and a comparison of the acoustic contrast maximisation and least squares optimisation methods through simulations. It has been shown that a distributed array, such as the standard car audio loudspeakers, is able to achieve significant levels of acoustic contrast at low frequencies, where the number of dominant acoustic modes is low, while acoustic contrast throughout the audio frequency range can be achieved using loudspeakers positioned in the nearfield of the car cabin's occupant's heads. These investigations have been conducted using point source simulations, in either a freefield or modal acoustic environment and, therefore, do not consider all of the practical effects of employing finite sized loudspeakers in a practical car cabin. For example, in a practical implementation the directivity of the loudspeakers will be affected by their finite dimensions [86] and the phase-shift loudspeaker will not behave as a hypercardioid over the full audio frequency range [84]. Additionally, in the car cabin implementation the nearfield headrest arrays will be mounted in close proximity to the car headrests, which will act as a baffle and further influence the directivity and therefore the performance of the array. Although these practical effects could be studied using finite element or boundary element methods, as in [86] for example, in the complicated car cabin acoustic environment it is more convenient to investigate the performance of the proposed array using measurements.

This chapter details the investigation of implementing a personal audio system in a Ford S-Max car cabin with the aim of producing two independent listening zones in the front and rear seating positions. Based on the work presented in the previous chapter two loudspeaker arrays will be investigated to attempt to provide adequate acoustic contrast over the full audio bandwidth – the distributed car audio loudspeaker array and the broadside headrest array employing directional phase-shift loudspeakers. The loudspeaker and microphone array geometries em-

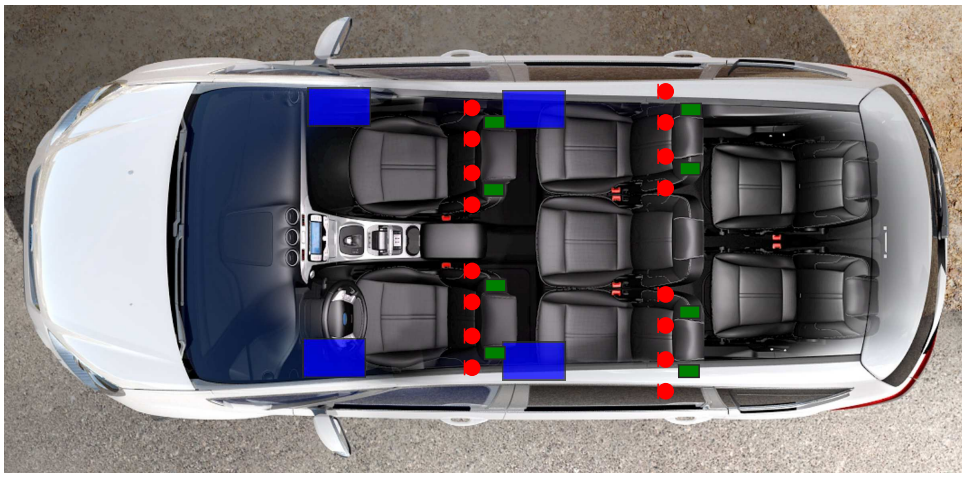

Figure 8.1: Plan view of the Ford S-max showing the positions of the KEF loudspeakers positioned close to the standard car audio loudspeakers' positions as blue rectangles, the phase-shift headrest loudspeakers as green rectangles, and the microphones are shown in red. Note, the vehicle used in the tests was a right-hand drive version. Original image from [187].

ployed are first detailed and then the transfer responses between all of the microphones and loudspeakers are presented. These measurements are used to perform offline predictions of the performance achievable using the arrays. A method of designing practical filters for the real-time implementation is detailed and suitable time domain filter responses are calculated. Finally, the performance of the two arrays was measured and these results are presented and discussed.

8.1 Specification of the Car Cabin Personal Audio System

8.1.1 The Test Vehicle

The vehicle employed in the measurements was a right-hand drive Ford S-max which has a capacity for seven passengers as can be seen from the plan view presented in Figure 8.1. The interior dimensions of the car are approximately 3 m $\times$ 1.8 m $\times$ 1.2m, with an internal volume of approximately 6.48 m^3. These dimensions and the layout of the vehicle are approximately consistent with those employed in the simulations in the previous chapter.

8.1.2 Loudspeaker Array

Based on the simulations presented in the previous chapter two loudspeaker arrays will be investigated. The first array is the car audio loudspeaker array which aims to achieve sound field control at low frequencies and the second is the broadside headrest array employing directional loudspeakers which aims to achieve control at higher frequencies.

(a) Front array setup showing offside KEF loudspeaker.

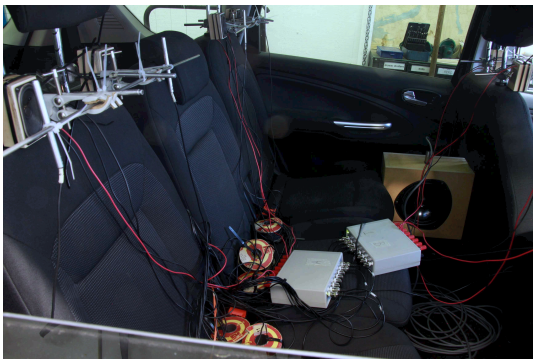

(b) Front array setup showing offside KEF loudspeaker.

(c) Front headrest array setup.

(d) Front and rear headrest array setup.

Figure 8.2: Personal audio loudspeaker and microphone array setup.

Car Audio Loudspeaker Array

The car audio loudspeaker array consists of four KEF B200G drivers which have a 183 mm diameter cone and were mounted in closed-back cabinets with an internal volume of approximately 0.01 m^3. These loudspeakers were positioned adjacent to the standard car audio loudspeakers in the front and rear of the car as shown by the blue rectangles in Figure 8.1 and in the photos presented in Figures 8.2a and 8.2b. These loudspeakers were used instead of the standard car audio loudspeakers to avoid unnecessary difficulty in accessing the standard car audio loudspeakers' connectors.

Headrest Array

The broadside headrest array consists of eight phase-shift loudspeakers, as described in [84], with one loudspeaker mounted to each side of each headrest as shown in the plan presented in Figure 8.1 and in the photos in Figures 8.2c and 8.2d. The dimensions and a photo of the phase-shift loudspeakers are presented in Figure 8.3 and details of the Visaton SC 4.7 loudspeaker driver are provided in Appendix D. As can be seen from Figure 8.3b, the phase-shift loudspeaker enclosure consists of a rear opening in which a resistive material is placed. By specifying the dimensions of the enclosure and the rear opening, and the resistive and compliant properties of the material covering the rear port, the directivity response of the phase-shift loudspeaker can be altered. The design of phase-shift loudspeakers has been investigated

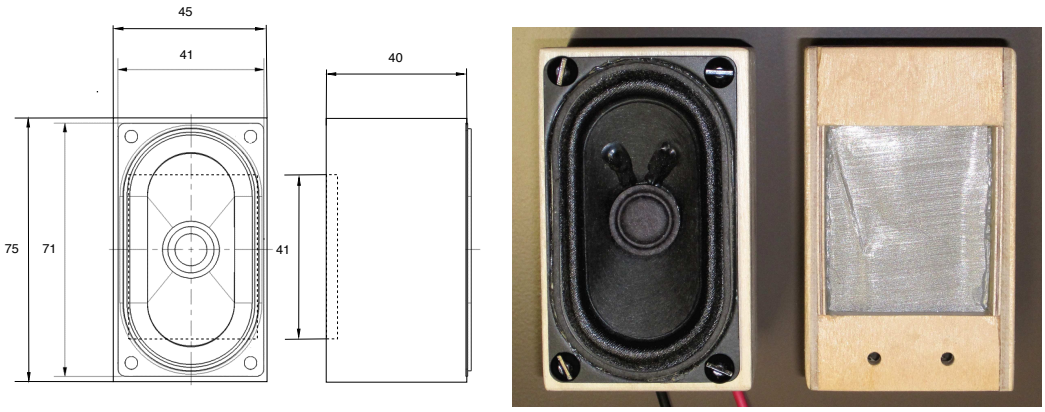

(a) Phase-shift loudspeaker dimensions in mm.

(b) Phase-shift loudspeaker.

Figure 8.3: Dimensions and photo of the phase-shift loudspeaker [84].

and discussed in [93, 84, 92]. The phase-shift loudspeakers employed here were designed in a previous project [84] to produce a hypercardioid directivity pattern. The resistive material positioned covering the rear opening was a fine metal gauze and the size of the opening was empirically determined using a prototype phase-shift loudspeaker with a variable size rear opening. The directivity index of the implemented phase-shift loudspeaker measured in an anechoic chamber is shown in Figure 8.4 along with the directivity index of a theoretical hypercardioid source. The directivity index was measured as the ratio of the squared pressure produced on-axis to the average squared pressures produced at 24 additional positions evenly distributed on a circle surrounding the source in the horizontal plane. From this plot it can be seen that the directivity index of the phase-shift loudspeaker is close to that of a hypercardioid source at frequencies between around 200 Hz, where the loudspeaker begins to operate effectively, and 1 kHz. At frequencies between around 1 kHz and 3.5 kHz the directivity index is negative indicating that the phase-shift loudspeaker radiates more efficiently to the rear of the device. This problem has been solved in subsequent work by Simón Gálvez by introducing high frequency absorption at the rear opening of the phase-shift loudspeaker and these loudspeakers have been employed in [78]. Despite the limited directivity index of the phase-shift loudspeakers shown in Figure 8.3, it is expected that at these frequencies the diffraction effects introduced by the positioning of the loudspeakers in close proximity to the car seats and headrests will significantly alter their directivities. This will require further work to fully understand and, therefore, due to their availability, these phase-shift loudspeakers will be used in this study. The positions of both the headrest and car audio loudspeakers are summarised in Table 8.1.

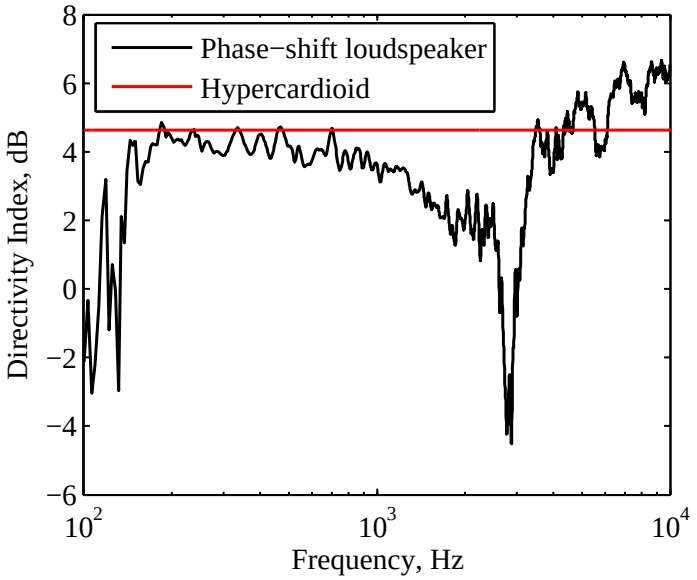

Figure 8.4: The directivity index of the phase-shift loudspeaker and a theoretical hypercardioid source [78].

Table 8.1: Loudspeaker positions

Loudspeaker	Position	Details
1	Driver foot-well	KEF B200G
2	Passenger foot-well	KEF B200G
3	Rear Nearside foot-well	KEF B200G
4	Rear offside foot-well	KEF B200G
5	Driver right headrest	Phase-shift loudspeaker
6	Driver left headrest	Phase-shift loudspeaker
7	Front passenger right headrest	Phase-shift loudspeaker
8	Front passenger left headrest	Phase-shift loudspeaker
9	Rear nearside passenger right headrest	Phase-shift loudspeaker
10	Rear nearside passenger left headrest	Phase-shift loudspeaker
11	Rear offside passenger right headrest	Phase-shift loudspeaker
12	Rear offside passenger left headrest	Phase-shift loudspeaker

8.1.3 Microphone Array

To define the bright and dark zones an array of microphones is used. In the simulations presented in the previous chapter, the two zones were each defined by 135 microphones. To achieve this in practice would require a large number of microphones and acquisition channels, but in practice a lower number of microphones must be used to define the two listening zones, whilst attempting to provide sufficient spatial coverage to avoid the generation of small listening zones. Four microphones were positioned at each headrest, as shown in Figure 8.5, and, therefore, the two listening zones were each defined by 8 microphones. The inner two microphones were separated by around 12 cm and the outer two microphones were spaced a further 8 cm from these microphones. Additionally, to provide some spread in the other two

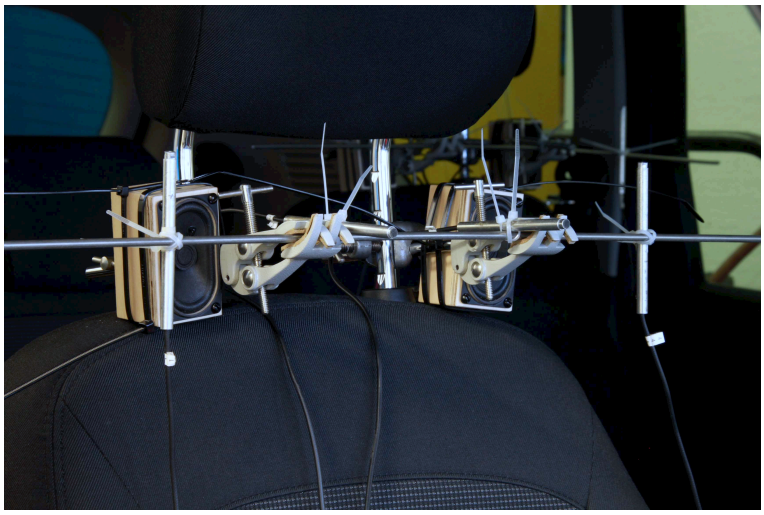

Figure 8.5: The broadside headrest loudspeaker array and the four microphone positions.

dimensions, the outer microphones were positioned around 4 cm above and 4 cm behind the inner two microphones. The positions of the 16 microphones are summarised in Table 8.2.

Table 8.2: Microphone positions

Microphone	Position
1	Driver outer right
2	Driver inner right
3	Driver inner left
4	Driver outer left
5	Front passenger outer right
6	Front passenger inner right
7	Front passenger inner left
8	Front passenger outer left
9	Rear nearside passenger outer right
10	Rear nearside passenger inner right
11	Rear nearside passenger inner left
12	Rear nearside passenger outer left
13	Rear offside passenger outer right
14	Rear offside passenger inner right
15	Rear offside passenger inner left
16	Rear offside passenger outer left

8.2 System Response Measurements

To predict the performance of the proposed personal audio systems and to then design the filters required for the real-time implementation, it is necessary to measure the transfer responses between the voltage input to each of the loudspeakers and the resulting pressure produced at the 16 microphones. This has been done using the setup shown in Figure 8.6. In this setup the

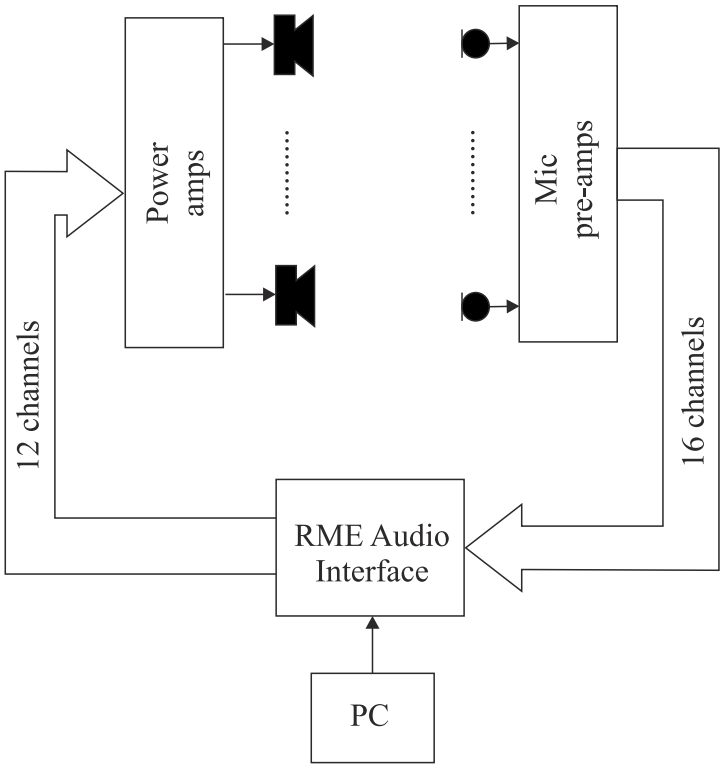

Figure 8.6: Block diagram of the measurement setup used to measure the transfer responses of the personal audio system.

RME audio interface has been used, instead of the DSpace and National Instruments hardware employed in the previous chapters, in order to provide both an adequate number of channels and the necessary anti-aliasing and reconstruction filters. As in Chapter 6 the transfer responses have been measured by driving each of the loudspeakers individually with pink noise and using an H_1 estimate, which is equal to the cross spectral density between each microphone and the drive signal divided by the power spectral density of the drive signal. In this case all of the measurements have been conducted at a sample rate of 48 kHz to allow the full audio bandwidth to be considered.

Car Audio Loudspeaker Array

Figure 8.7 shows the transfer response between the voltage input to loudspeaker 1, in the driver's foot-well, and the pressure produced at all 16 microphone positions. From this plot it can be seen that at frequencies below around 150 Hz the responses are relatively consistent between all of the microphone positions and that the responses begin to roll-off at frequencies below around 100 Hz, which corresponds to the resonance frequency of the KEF B200G loudspeaker in the closed-back enclosure. At higher frequencies more significant variations occur between the responses, due to the increasing number of excited modes, and it can be seen that at around 3 kHz the responses begin to roll-off, which can be related to the high frequency limit of the KEF B200G driver as quoted in the manufacturer's specification, provided in Appendix

D. The responses measured for the other three loudspeakers positioned at the car audio loudspeaker positions are similar to those presented in Figure 8.7, particularly at low frequencies where this array will operate, and therefore they are not presented. It should also be noted that one of the microphone responses, shown by the blue line in Figure 8.7a, appears to differ from the other responses for all loudspeaker excitations. This was not noticed during the measurements and is thought to be due to a fault with the microphone or pre-amp. However, since the set-up was not changed throughout the measurements and the fault only seems to produce a change in the frequency response it is not expected to affect the results.

Headrest Array

The transfer responses between the voltage input to loudspeaker 5, positioned at the driver right headrest, and the pressures produced at microphone positions 2 (driver inner right) and 10 (rear nearside passenger inner right) are presented in Figure 8.8a. From this plot it can be seen that the two responses roll-off at frequencies below around 400 Hz, which corresponds to the resonance frequency of the Visaton SC 4.7 loudspeaker drivers. The responses also begin to roll-off at frequencies above around 4 kHz. It can also be seen from Figure 8.8a that the response to microphone 10, which is in the rear of the car cabin, is around 10 dB below that to microphone 2 on average. This can be related to both the distance between the loudspeaker and the two microphones and the directivity of the loudspeaker and its orientation. To demonstrate this second point, Figure 8.8b shows the transfer responses between the voltage input to loudspeaker 9, positioned at the rear nearside passenger right headrest, and the pressures produced at microphone positions 2 and 10. From this plot it can be seen that the response to microphone 10 is now greater than that to microphone 2 by around 5 dB on average. This level difference is lower than that observed for loudspeaker 5 and this is because the two microphone positions are now both in the forward-direction of the loudspeaker, whereas microphone 10 is in the backward-direction for loudspeaker 5. The responses measured for the other microphones and six headrest loudspeakers are similar in character to those presented in Figure 8.8 and therefore are not presented.

8.3 Frequency Domain Offline Performance Predictions

Using the measured transfer responses as the appropriate elements of the $\boldsymbol{Z}_B$ and $\boldsymbol{Z}_D$ matrices, the optimal filter frequency responses can be calculated in the frequency domain using either the least squares optimisation or the acoustic contrast control strategy. It has been shown in the previous chapter that for the car audio loudspeaker array, the least squares method achieves similar levels of acoustic contrast to the acoustic contrast control strategy but with a lower array effort and improved conditioning. For the broadside headrest loudspeaker array it has also been shown that although a reduction in contrast performance occurs at low frequencies,

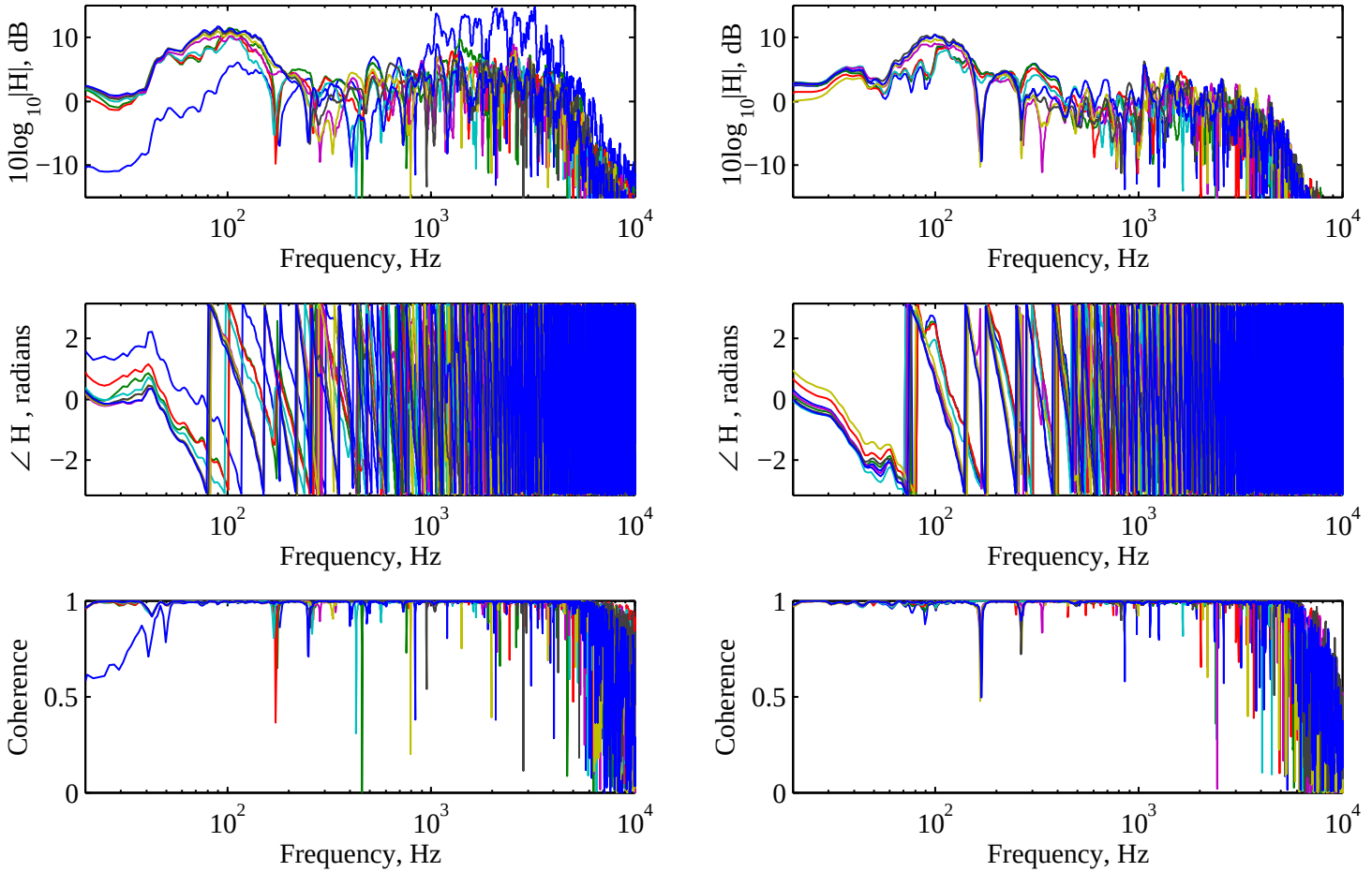

(a) Microphone positions 1 to 8.

(b) Microphone positions 9 to 16.

Figure 8.7: The transfer response between the voltage input to loudspeaker 1 (KEF B200G, driver foot-well) and the pressure produced at microphone positions 1 to 8 (a) and 9 to 16 (b).

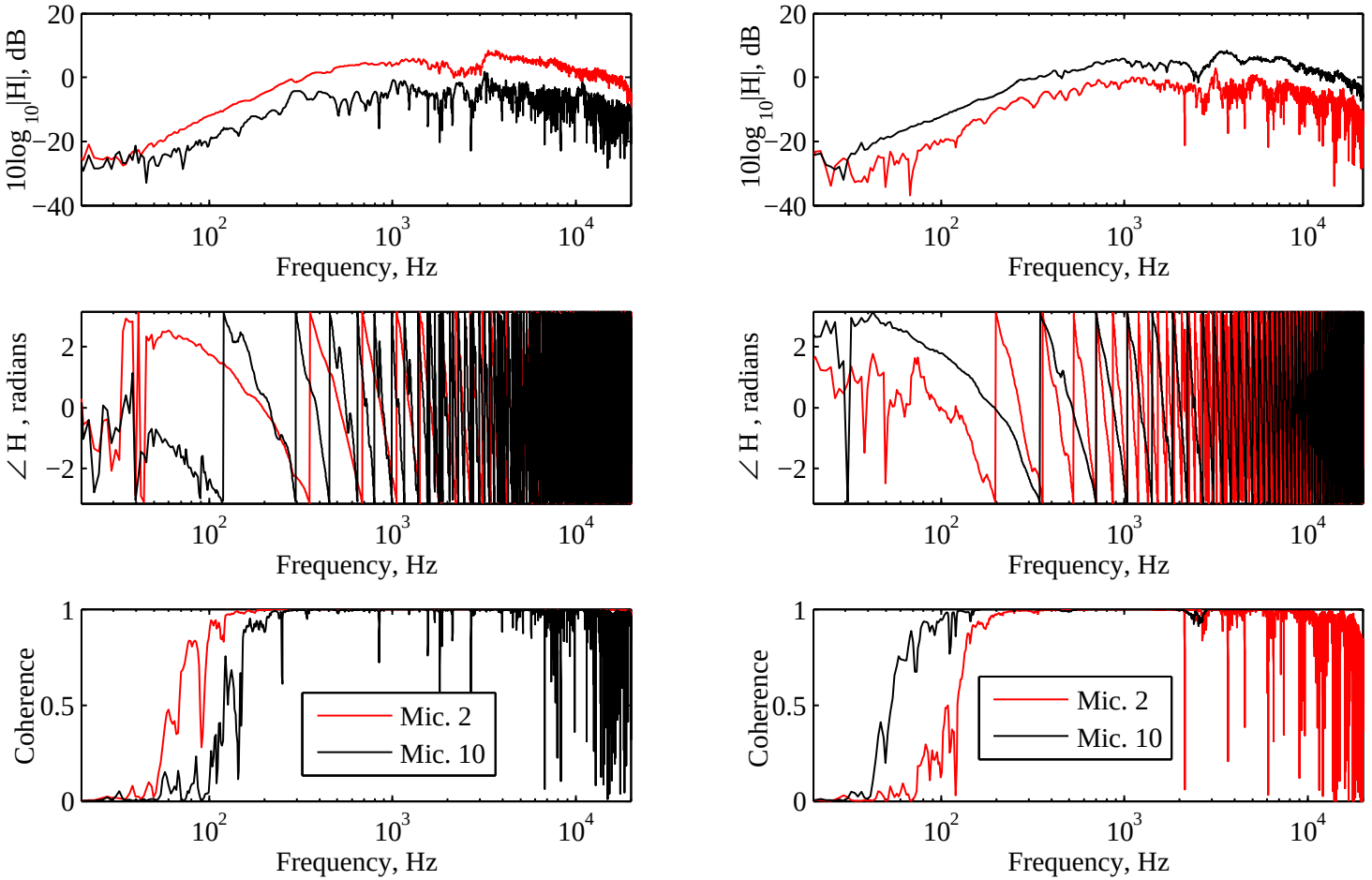

(a) The transfer response between the voltage input to loudspeaker 5 (Phase-shift loudspeaker, driver right headrest) and the pressure produced at microphone positions 2 (driver inner right) and 10 (Rear nearside passenger inner right).

(b) The transfer response between the voltage input to loudspeaker 9 (Phase-shift loudspeaker, nearside rear passenger right headrest) and the pressure produced at microphone positions 2 (driver inner right) and 10 (Rear nearside passenger inner right).

Figure 8.8: Example headrest loudspeaker transfer responses.

the least squares method provides a well conditioned solution with useful levels of control over the audio bandwidth. Therefore, the least squares solution will be employed in the following predictions. The least squares solution is given by equation 7.20, which for a vector of driving voltages, $\boldsymbol{v}$, is

$$\boldsymbol{v} = \left[\boldsymbol{Z}^H \boldsymbol{Z}\right]^{-1} \boldsymbol{Z}^H \boldsymbol{p}_T, \tag{8.1}$$

where

$$\boldsymbol{Z} = \begin{bmatrix} \boldsymbol{Z}_B \\ \boldsymbol{Z}_D \end{bmatrix}$$

and $\boldsymbol{p}_T$ is the vector of target pressures. This optimisation strategy gives the optimal solution with no constraint on the required electrical power and this will be employed in the following predictions to provide an indication of the maximum levels of acoustic contrast achievable. As detailed in Section 7.4.1 of the previous chapter, the target pressures in the dark zone are set to zero and the target pressures in the bright zone are set to the pressures produced when the four sources are driven in-phase for the car audio loudspeaker array, and to the pressures produced when the four phase-shift loudspeakers in the nearfield of the respective bright zones are driven in-phase for the headrest array.

8.3.1 Car Audio Loudspeaker Array

Figures 8.9a and 8.9b show the frequency responses of the filters optimised using the least squares method to achieve a front bright zone and rear bright zone respectively using the four KEF loudspeakers positioned at the car audio loudspeaker locations. The drive levels have been adjusted so that a unit input voltage to the loudspeakers produces a average bright zone SPL of 60 dB re. 2×10^{-5} Pa. From these plots it can be seen that in both control scenarios the four sources are driven at similar levels and the phase responses can be seen to become complicated at frequencies above around 150 Hz. It is also interesting to note that the voltage drive levels at frequencies below around 100 Hz required to produce the front bright zone are lower than those required to produce the rear bright zone. This can be related to the lower average distance between the four car audio loudspeakers and the front zone microphones than to the rear zone microphones.

The performance of the car audio array has been synthesised using the optimal filter responses presented in Figure 8.9 and the principle of linear superposition using the measured frequency responses. Figure 8.10 shows the predicted acoustic contrast and required array effort for the two control scenarios. From the acoustic contrast plot in Figure 8.10a it can be seen that in both control scenarios the four source car audio loudspeaker array achieves significant levels of acoustic contrast at frequencies up to around 200 Hz and then the performance begins to roll-off. The level of acoustic contrast achieved by the array producing a front bright zone is around 10 to 15 dB higher than that achieved by the array optimised to produce a rear bright zone. This trend was also observed in the simulations presented in the previous chapter

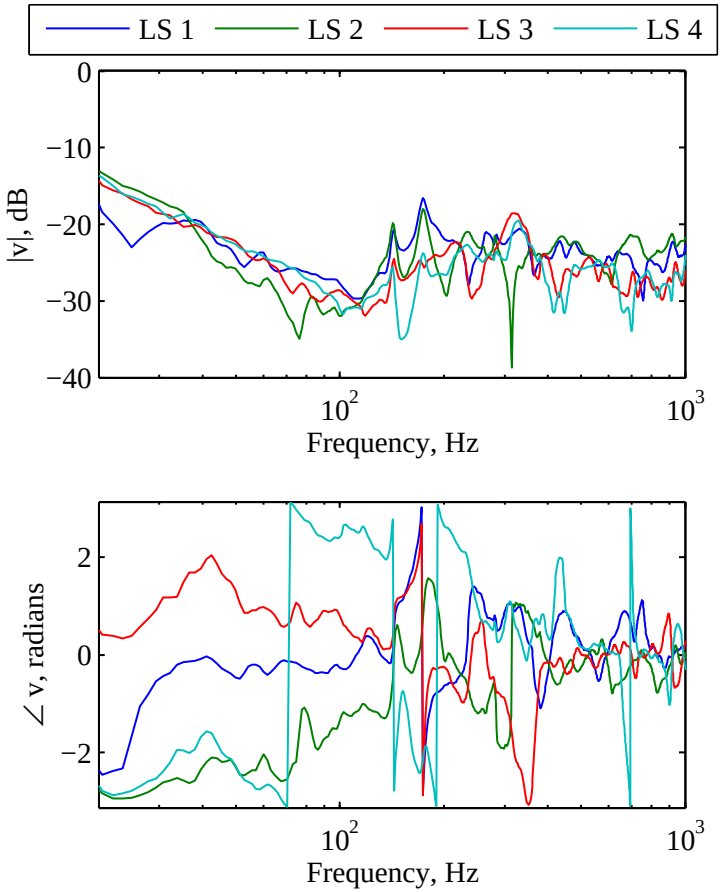

(a) The frequency response of the filters required to produce a front bright zone and a dark rear zone using the four car audio positioned loudspeakers.

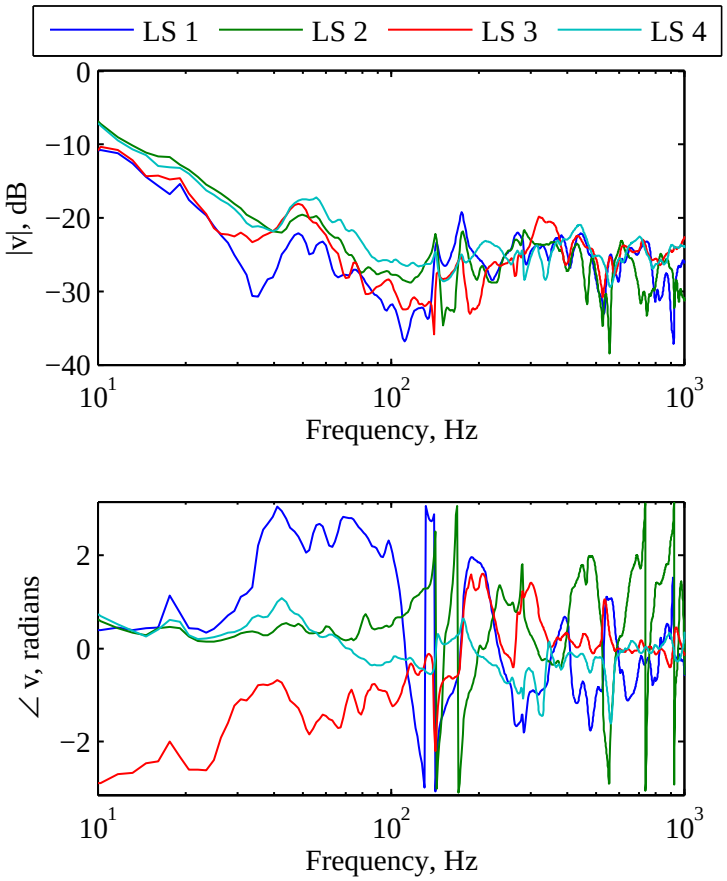

(b) The frequency response of the filters required to produce a dark front zone and a rear bright zone using the four car audio positioned loudspeakers.

Figure 8.9: Least squares optimised filter frequency responses for the car audio loudspeaker array.

and can again be related to the lower average distance between the loudspeakers and the front control zone than to the rear control zone. The simulations shown in Figure 7.8, for example, predict contrast levels at low frequencies of about 29 dB for the front bright zone and 19 dB for the rear bright zone. It can be seen that the performance of the practical system is very close to this prediction, although the upper frequency at which acoustic contrast is achieved when producing a rear bright zone is better in the practical system.

Despite the lower contrast performance when producing a rear bright zone it can be seen from the results in Figure 8.10a that the car audio array may achieve levels of control that would provide subjectively sufficient levels of acoustic contrast according to the subjective studies presented in [23, 70]. However, it is also important to consider the required array effort and this is shown in Figure 8.10b for the two control scenarios. From this plot it can be seen that, except for two narrowband peaks at around 150 Hz and 200 Hz, the required array effort at frequencies within the audio bandwidth, that is above 20 Hz, is below 10 dB relative to a 1 volt input. These levels are comparable to those presented in the previous chapter and suggest that the predicted levels of control may be achievable in practice.

8.3.2 Headrest Loudspeaker Array

Figures 8.11a and 8.11b show the frequency responses of the filters optimised using the least squares method to achieve a front bright zone and rear bright zone respectively using the eight phase-shift headrest loudspeakers while producing an average bright zone SPL of 60 dB re. 2×10^{-5}. In each of these plots the frequency responses related to the front headrest loudspeakers are shown in red and those related to the rear loudspeakers are shown in black. From the plot in Figure 8.11a it can be seen that when generating a bright zone at the front microphones the four front headrest loudspeakers are driven largely in-phase and at similar levels to each other. This is not surprising since this is the way that the target pressures have been defined for the least squares optimisation. The four rear headrest loudspeakers are all driven at around 5 dB below the front loudspeakers and they have a complicated phase-response. These results suggest that the rear loudspeakers are being used to cancel the pressures produced by the front headrest loudspeakers at rear microphone positions.

Figure 8.11b shows the filter responses for the eight headrest loudspeakers when optimised to produce a rear bright zone. From this plot it can be seen that, once again, the four loudspeakers in the nearfield of the bright zone (the rear region in this case) are driven largely in-phase and at a higher level than the front loudspeakers, since this is how the target pressures are defined. However, in this configuration the difference in level between the rear and front loudspeakers' drive levels is lower than when producing a front bright zone. This can be related to the observations made regarding the transfer responses presented in Figure 8.8. That is, the response between the rear loudspeakers and the pressures produced at the front microphones is greater than that between the front loudspeakers and the pressures produced at the rear micro-

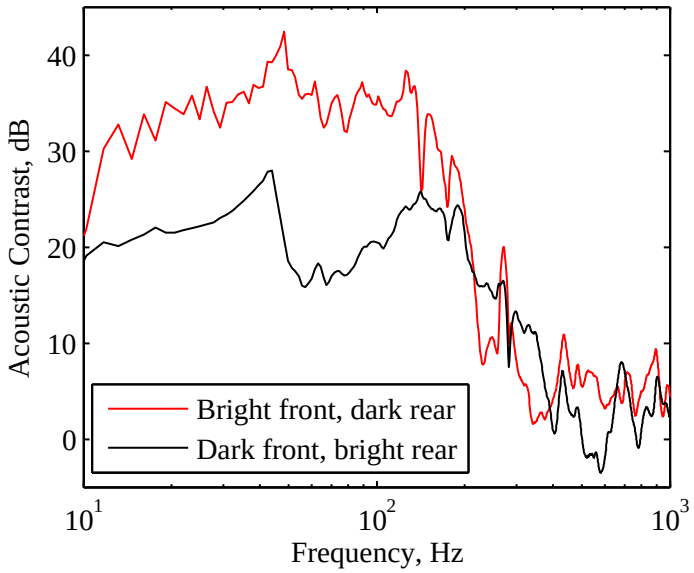

(a) Acoustic contrast.

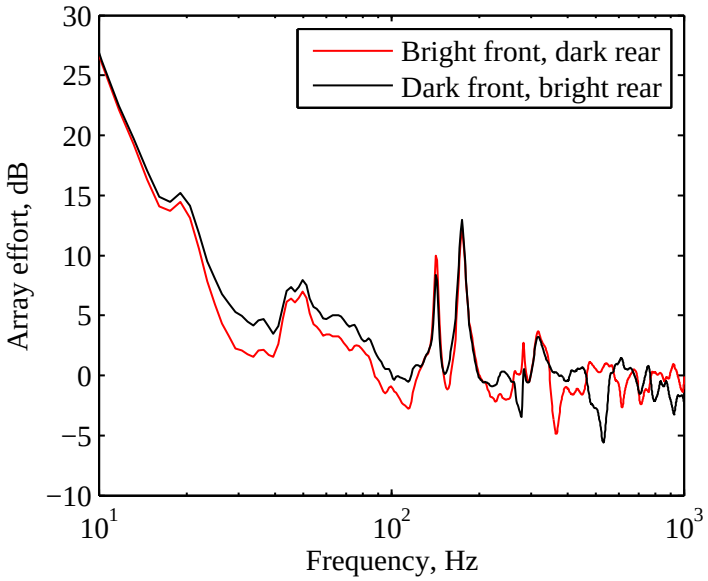

(b) Array effort.

Figure 8.10: The acoustic contrast and array effort plotted as a function of frequency for the array of four car audio positioned loudspeakers optimised to produce a front bright zone (—) and a rear bright zone (—). The array effort is plotted in decibels relative to the array effort required to produce the same average bright zone pressure when driving all loudspeakers in-phase.

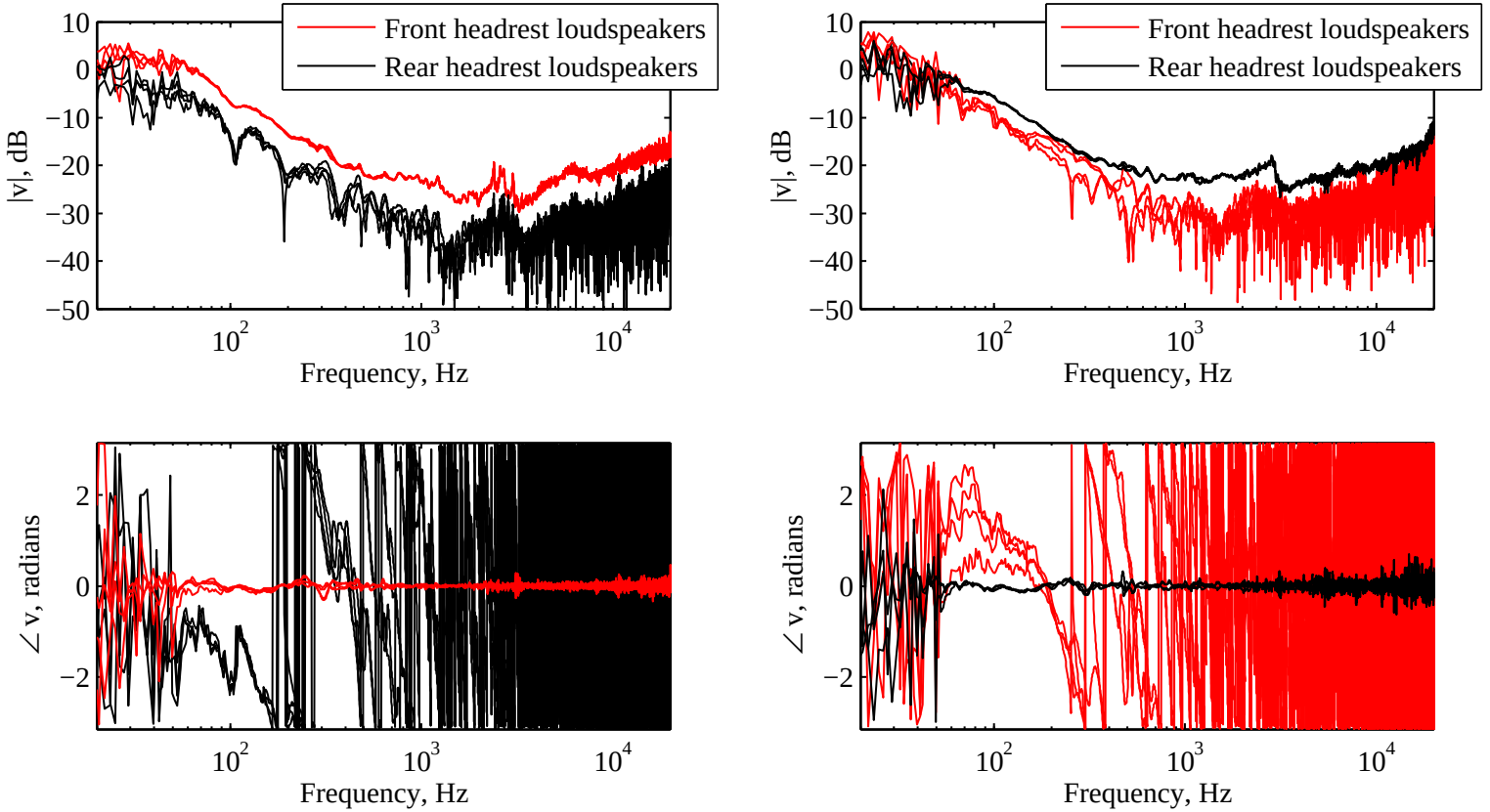

(a) The frequency response of the filters optimised to produce a *front bright* zone and a dark rear zone using the eight headrest phase-shift loudspeakers.

(b) The frequency response of the filters optimised to produce a dark front zone and a *rear bright* zone using the eight headrest phase-shift loudspeakers.

Figure 8.11: Least squares optimised filter frequency responses for the headrest phase-shift loudspeaker array.

phones, and, therefore, the front loudspeakers must be driven harder to achieve cancellation of the pressures produced in the front zone by the rear loudspeakers.

Using the optimal filter responses presented in Figure 8.11 the performance of the optimised headrest loudspeaker array has been synthesised and Figure 8.12 shows the predicted acoustic contrast and required array effort. From the acoustic contrast plot it can be seen that when producing either a front bright or rear bright zone the predicted acoustic contrast is greater than 20 dB at frequencies between 70 Hz and 800 Hz. At around 800 Hz the predicted acoustic contrast for the rear bright zone configuration begins to fall off and, although a significant level of acoustic contrast is maintained up to 20 kHz, the performance falls below the minimum 11 dB level required for a subjectively acceptable performance according to [23] and would only provide adequate acoustic contrast under certain operating scenarios according to [70]. The difference in performance between the two control scenarios can be related to the forward-direction of the phase-shift headrest loudspeakers, the directivity of the individual phase-shift loudspeakers (see Figure 8.4), and the relative positions of the dark and bright zones as discussed in relation to the headrest loudspeaker transfer responses presented in Figure 8.8. From the array effort plot in Figure 8.12b it can be seen that the levels of effort are low, which should be expected as the loudspeakers in the nearfield of the bright zone in each control scenario are driven largely in-phase, which is the array effort reference condition, and the loudspeakers in the nearfield of the dark zone in each case are driven at a lower level. These results are generally similar to the corresponding theoretical predictions shown in Figure 7.13 of the previous chapter, where the contrast level is predicted to be between around 30 and 40 dB at low frequencies and 10 and 20 dB at frequencies above 1 kHz.

To provide further insight into the operation of the headrest loudspeaker array Figure 8.13 shows the acoustic contrast for the two control scenarios when the full array of eight headrest loudspeakers are driven and when only the four loudspeakers in the nearfield of the bright zone are driven using the same filters as for the eight source optimised array. From these plots it can be seen that in both control scenarios significant improvements in the acoustic contrast occur at frequencies below 1 kHz when using all eight loudspeakers, although at higher frequencies only small reductions in the performance occur. This indicates that at higher frequencies the acoustic contrast performance is largely due to the directivity of the phase-shift loudspeakers and the broadside array operation. To improve this performance it would be necessary to increase the number of sources, decrease the inter-element separation or optimise the performance of the phase-shift loudspeakers [84, 78].

Although the high frequency performance of the eight headrest phase-shift loudspeaker array when attempting to produce a bright zone in the rear of the car cabin is perhaps too low to achieve subjectively adequate levels of acoustic contrast, the real-time implementation of this array will be considered along with the car audio source array. Although it was found to be possible to improve the acoustic contrast achieved by the eight source headrest array by using

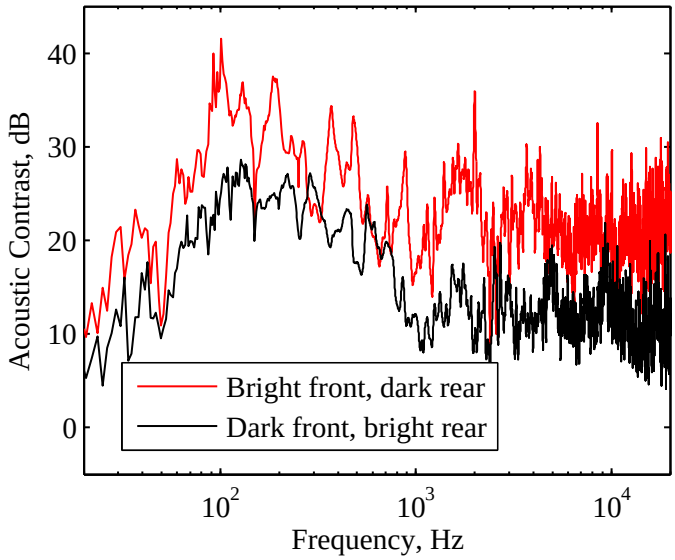

(a) Acoustic contrast.

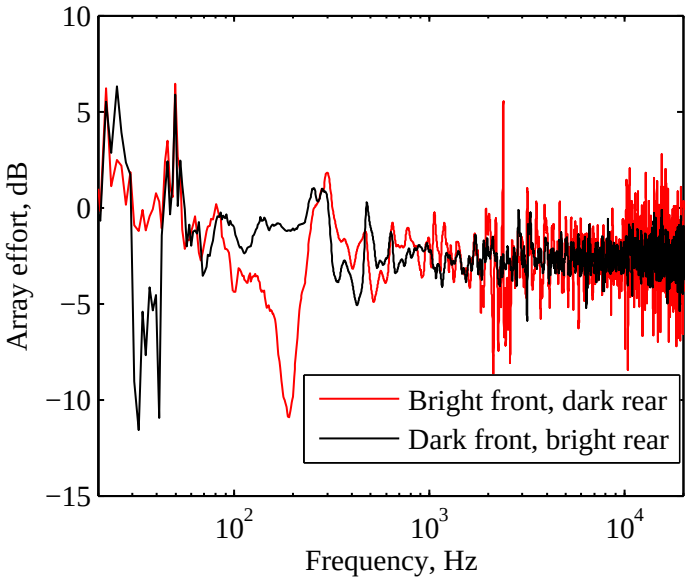

(b) Array effort.

Figure 8.12: The acoustic contrast and array effort plotted as a function of frequency for the array of eight headrest phase-shift loudspeakers optimised to produce a front bright zone (—) and a rear bright zone (—). The array effort is plotted in decibels relative to the array effort required to produce the same average bright zone pressure when driving all loudspeakers in-phase.

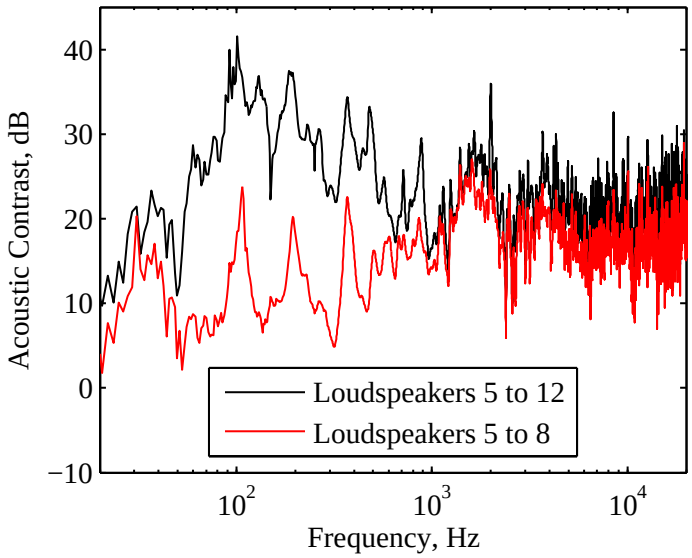

(a) Front bright zone.

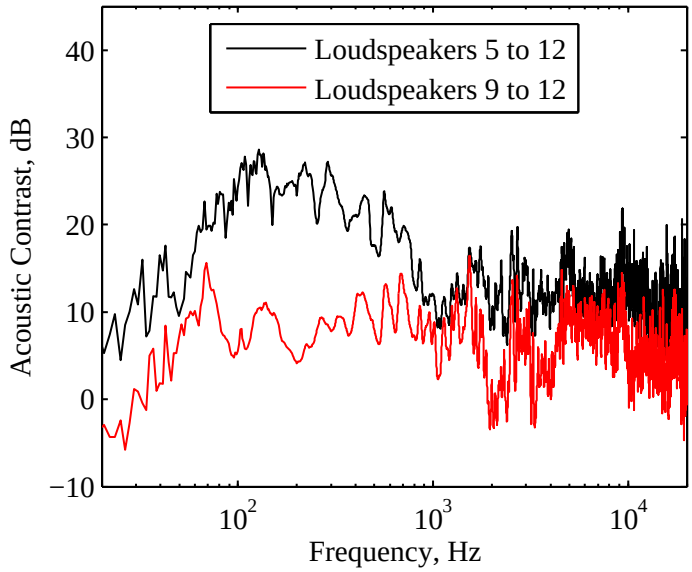

(b) Rear bright zone.

Figure 8.13: The acoustic contrast plotted as a function of frequency for the optimised array of eight headrest phase-shift loudspeakers (—) and for the four headrest loudspeakers in the nearfield of the front (a) and rear (b) bright zones alone (—).

the acoustic contrast optimisation method instead of the least squares optimisation, this leads to a significant reduction in audio quality and, therefore, is of little advantage.

8.4 Time Domain Design and Offline Performance Predictions

The offline predictions presented in the previous section have demonstrated the maximum levels of acoustic contrast control that may be achievable using the two array configurations and the unconstrained least squares optimisation. However, these predictions have been calculated in the frequency domain using filters with no causality constraint. To implement the personal audio system in real-time it is necessary to drive the loudspeakers with real-time signals, which requires the implementation of practical filters. The calculation of the required time-domain filter responses can be achieved using a number of methods, for example it is possible to directly optimise causal filter coefficients, or use the Matlab function *invfreqz* to calculate the filter coefficients via a least squares complex curve fitting algorithm. From previous work by the author [86] it has been shown that the required time domain filter responses may be conveniently calculated via inverse Fourier transformation of the optimal frequency domain filter responses.

8.4.1 Filter Design Method

In the previous section the filters have been designed without any constraint on the required array effort or voltage drive levels. In practice this may lead to excessive voltage levels driving the loudspeakers, particularly when multiple arrays are employed to cover different regions of the audio bandwidth. Therefore, the optimal filters' frequency responses will be calculated using the least squares optimisation with individual source power constraints detailed in Section 7.2.2. In this case the optimal filter responses are calculated as

$$\boldsymbol{v} = \left[\boldsymbol{Z}^H\boldsymbol{Z} + \boldsymbol{\lambda}_M\boldsymbol{I}\right]^{-1}\boldsymbol{Z}^H\boldsymbol{p}_T, \tag{8.2}$$

where $\boldsymbol{\lambda}_M$ is a diagonal matrix of M Lagrange multipliers that can be independently set to fulfil specified constraints on each loudspeaker. A number of constraints have been defined for the car audio and headrest loudspeaker arrays to ensure that the loudspeakers are not driven at high levels for frequencies outside of their operational bandwidths, and that a maximum acoustic contrast of 15 dB is achieved. Although in some circumstances it could be necessary to enforce a constraint on the loudspeaker drive levels within their operational bandwidth, due to the naturally low levels of array effort for the two considered arrays within their operational bandwidths this was unnecessary. The frequency limits of the car audio loudspeaker array have been set based on the low frequency limit of audio reproduction and the high frequency limit of the contrast control problem observed in the previous section. The frequency limits of the headrest array have been based on the low frequency limit of the loudspeakers quoted by the manufacturer and the high frequency limit of audio reproduction. The employed constraints

are summarised in Table 8.3 and the necessary values of $\boldsymbol{\lambda}_M$ have been calculated using the Matlab function *fmincon* and the interior point algorithm.

Table 8.3: Personal audio filter optimisation constraints

Array	Operational Frequency Range	Maximum Contrast
Car audio loudspeaker	$20 < f <$300 Hz	15 dB
Broadside headrest	220 Hz $< f <$ 20kHz	15 dB

Using the frequency responses of the optimal filters designed using the effort constrained least squares optimisation, practical time-domain filter responses have been calculated according to the following method, this has previously been presented in [86]:

1. The optimal frequency responses of each filter have been windowed to ensure zero level at 0 Hz and the Nyquist frequency

2. The frequency domain windowed responses have been Inverse Fast Fourier Transformed (IFFT) to give impulse responses of length

$$I = \left(\frac{Fs}{\Delta f} + 1\right), \tag{8.3}$$

   where Fs is the sample rate and Δf is the separation between adjacent frequency points in the optimal filter frequency responses. Δf is dependent on the length of the Fast Fourier Transform (FFT) used in the calculation of the transfer responses $\boldsymbol{Z}_B$ and $\boldsymbol{Z}_D$ from the measured response data. Δf has been set to 1.4648 Hz which ensures the IFFT has largely decayed to zero over its duration.

3. The filter impulse responses have been shifted to accommodate for the periodicity of the FFT.

4. At this stage a practicable set of filters is available, however, since this method of filter design imposes no constraint on causality, the filters have a response of length $(I-1)/2$ before zero time. This response can be implemented using a modelling delay and, for the employed sample rate and frequency point separation, a modelling delay of 341 ms is required. However, this leads to practical issues in applications such as two-way telecommunications and such a significant pre-echo leads to subjectively poor audio quality [188]. Therefore, it is desirable to truncate the length of the filters in the time domain to reduce the required modelling delay. For both arrays the filters have been truncated to the shortest length possible without significant reductions in the offline predicted acoustic contrast or significant enhancements in the array effort. For the car audio array the filter impulse responses have been truncated to $I = 25000$ which requires a modelling delay of 260 ms and for the headrest array the filters have been truncated to $I = 2000$ which requires a modelling delay of 21 ms.

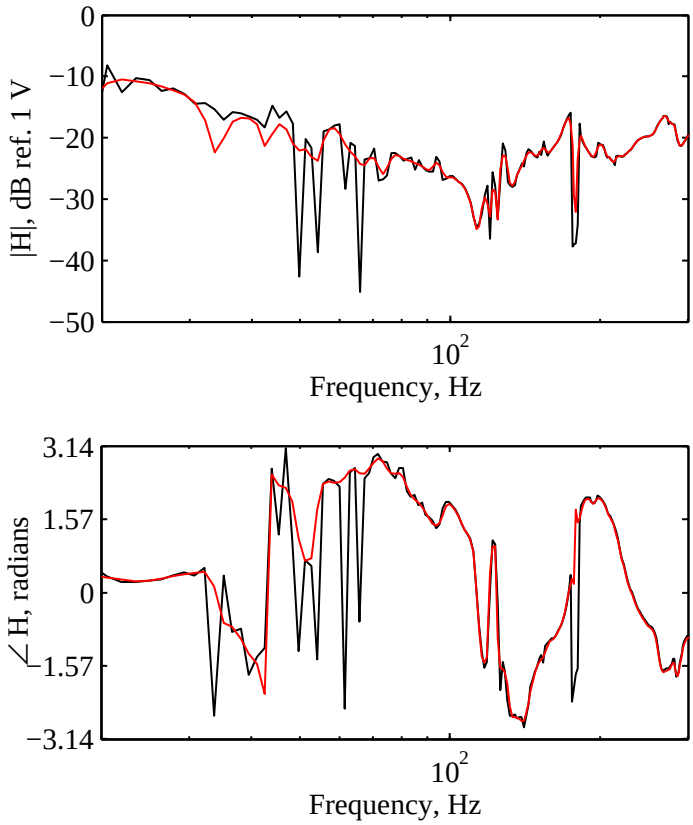

Figure 8.14: The optimal (—) and causal (—) frequency responses of the filter for loudspeaker 1 in the car audio loudspeaker array when producing a rear bright zone.

5. The truncated filter impulse responses have been windowed using a Hanning window to avoid artefacts due to non-zero responses at the start and end of the filters.

8.4.2 Offline Performance Predictions

Car Audio Loudspeaker Array

The frequency response of an example causal filter designed according to the method defined above, with $I = 25000$, is shown in Figure 8.14, along with the optimal frequency domain response for loudspeaker 1, when producing a rear bright zone using the car audio loudspeaker array. From this plot it can be seen that the designed filter accurately matches the optimal filter response except for a number of sharp nulls in both the magnitude and phase response. The effect of these inaccuracies can be determined through offline predictions of the acoustic contrast performance using the time-domain truncated filters. The differences between the other designed filters and the corresponding optimal frequency domain responses are similar to those shown by Figure 8.14 and, therefore, they are not presented.

Using the truncated filters the performance of the car audio loudspeaker array has been predicted for the two control scenarios using offline simulations and the acoustic contrast and

array effort are presented in Figure 8.15 along with the optimal frequency domain results. From these plots it can be seen that the acoustic contrast predicted for the truncated filters is close to that of the optimal filters designed for the performance specifications in Table 8.3, and in fact offers some improvements in acoustic contrast.

Broadside Headrest Loudspeaker Array

The frequency response of an example practical, time-domain truncated filter designed according to the method defined above, with $I = 2000$, is shown in Figure 8.16 along with the optimal frequency domain response for loudspeaker 5 when producing a rear bright zone and a dark front zone using the headrest phase-shift loudspeaker array. From this plot it can be seen that the designed filter accurately matches the optimal filter response at frequencies above around 700 Hz. At lower frequencies the optimal frequency domain filter response has a large number of rapid variations in both the magnitude and phase responses and these are not accurately represented by the time-domain truncated filter. These variations can be more accurately included in the time-domain truncated filters by increasing the length of the filters. However, the performance of the truncated filters is not significantly affected by these inaccuracies. This can be seen from the offline predictions presented in Figure 8.17 for the two control scenarios. In both control scenarios it can be seen from Figure 8.17 that the predicted acoustic contrast using the truncated filters is largely equal to or greater than the frequency domain responses at frequencies greater than 200 Hz where the headrest array is designed to operate and, therefore, it is unnecessary to increase the length of the truncated filters.

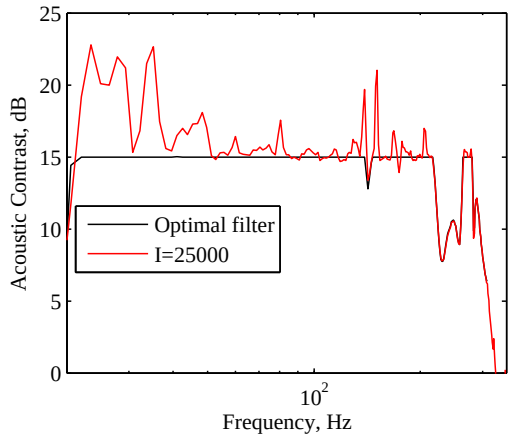

(a) Acoustic contrast between a *front bright* zone and rear dark zone.

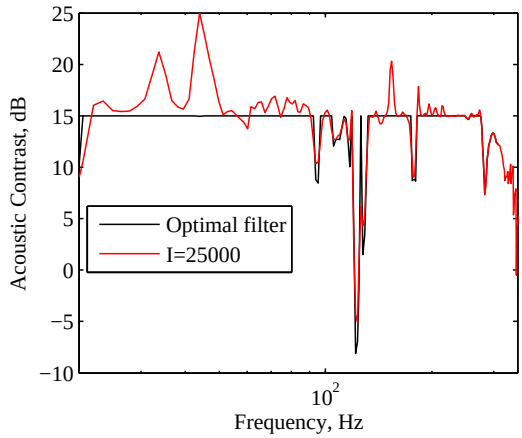

(b) Acoustic contrast between a *rear bright* zone and a front dark zone.

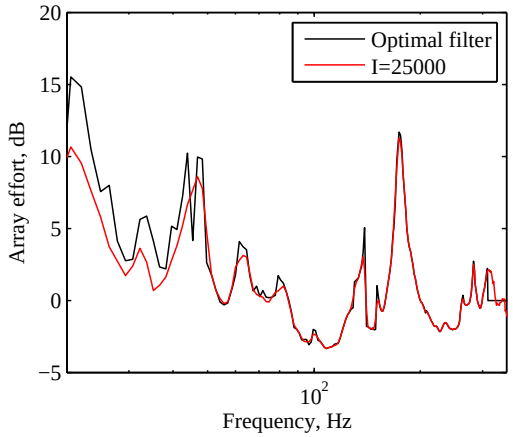

(c) Array effort required to produce a *front bright* zone and rear dark zone.

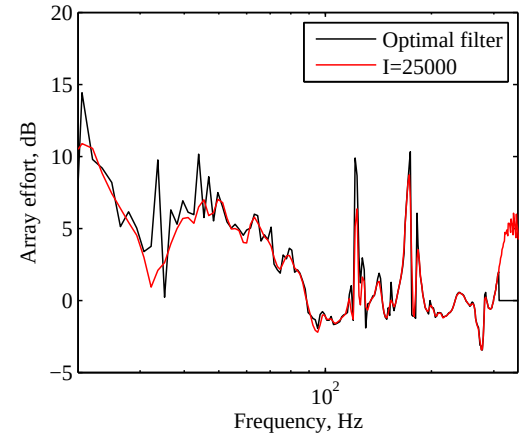

(d) Array effort required to produce a *rear bright* zone and a front dark zone.

Figure 8.15: The acoustic contrast and array effort plotted as a function of frequency for the array of four car audio positioned loudspeakers optimised with the constraints defined in Table 8.3. The performance of the frequency domain optimal filter (—) and the offline predictions using the time-domain filter design (—) are shown. The array effort is plotted in decibels relative to the array effort required to produce the same average bright zone pressure when driving all loudspeakers in-phase.

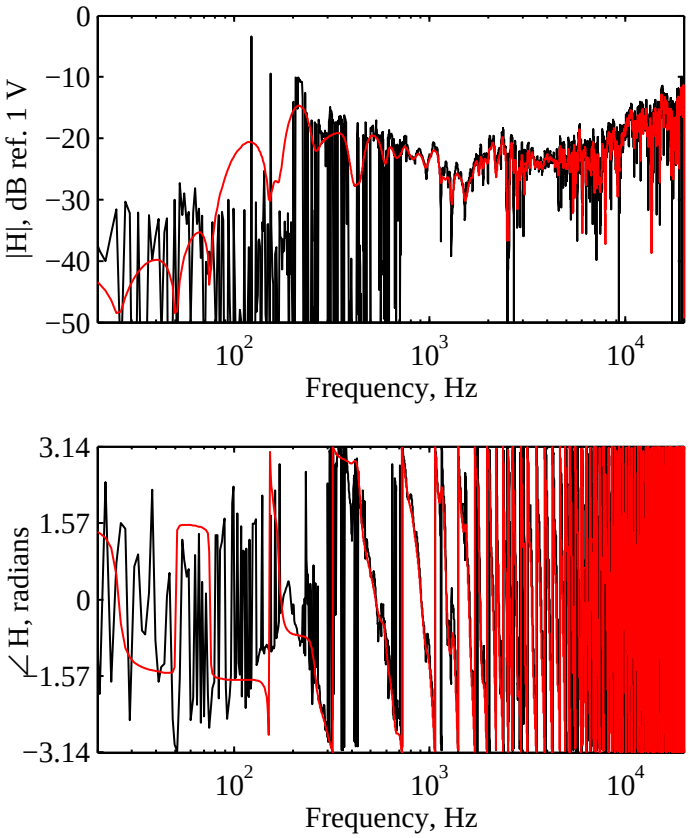

Figure 8.16: The optimal (—) and causal (—) frequency responses of the filter for loudspeaker 5 in the headrest phase-shift loudspeaker array when producing a rear bright zone.

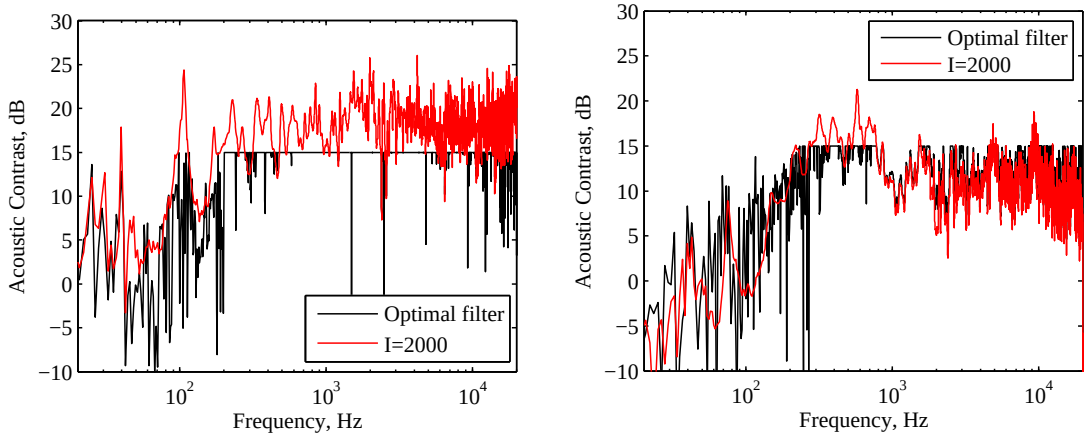

(a) Acoustic contrast between a *front bright* zone and rear dark zone.

(b) Acoustic contrast between a *rear bright* zone and a front dark zone.

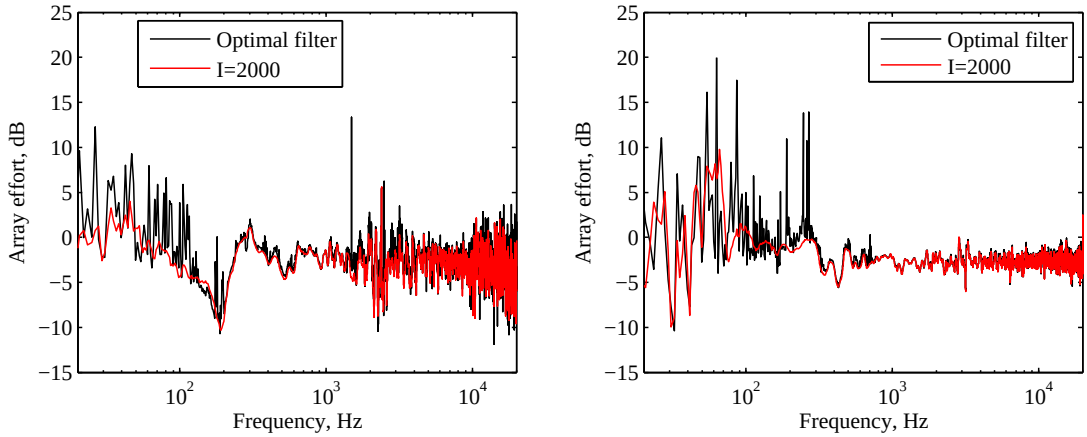

(c) Array effort required to produce a *front bright* zone and rear dark zone.

(d) Array effort required to produce a *rear bright* zone and a front dark zone.

Figure 8.17: The acoustic contrast and array effort plotted as a function of frequency for the array of eight phase-shift headrest loudspeakers optimised with the constraints defined in Table 8.3. The performance of the frequency domain optimal filter (—) and the offline predictions using the time-domain filter design (—) are shown. The array effort is plotted in decibels relative to the array effort required to produce the same average bright zone pressure when driving all loudspeakers in-phase.

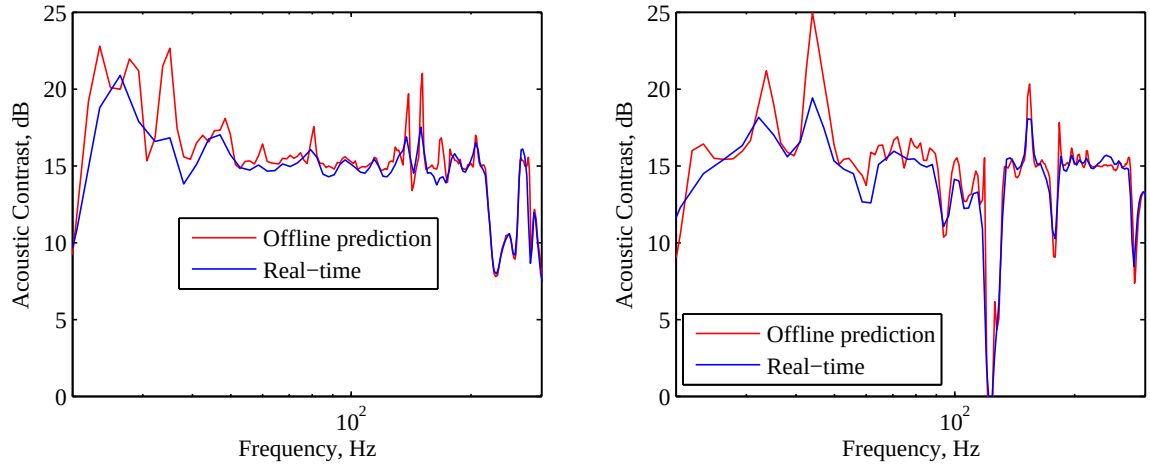

(a) Acoustic contrast between *front bright* and dark rear zones. (b) Acoustic contrast between *rear bright* and dark front zones.

Figure 8.18: The acoustic contrast plotted as a function of frequency for the optimised array of car audio loudspeakers predicted using offline simulations (—) and measured in real-time (—).

8.5 Real-Time System Performance

To confirm the practical performance of the truncated filters the performance of the two loudspeaker arrays has been measured in real-time. The performance of the two arrays when optimised to achieve both front bright and rear bright zones has been measured by driving the loudspeakers in each array simultaneously with a pink noise signal filtered using the associated truncated filters and the pressure levels produced at the 16 microphones defining the bright and dark zones have been measured. The measured acoustic contrast achieved by the car audio loudspeaker array for the two control scenarios is presented in Figure 8.18, along with the performance predicted for the truncated filters in the offline simulations. From these results it can be seen that the acoustic contrast levels achieved by the real-time system are very close to the offline predictions. The level of acoustic contrast control achieved for both control scenarios is practically useful and produces subjectively impressive level differences between the two control zones in informal listening tests.

The measured acoustic contrast achieved by the headrest phase-shift loudspeaker array is presented in Figure 8.19 along with the offline predicted results for the two control scenarios. From Figure 8.19a it can be seen that when a bright zone is produced in the front of the car cabin the measured acoustic contrast closely matches that predicted by offline simulations at frequencies above around 200 Hz. At lower frequencies the measured acoustic contrast rolls-off in comparison to the offline simulations. This is a result of inaccuracies in the measured transfer responses leading to differences between the responses assumed in the design of the filters and the response of the real-time system. However, these low frequency inaccuracies are due to the employed loudspeakers operating range being limited to frequencies above around 200 Hz and, therefore, they are not expected to be able to produce significant pressure levels at

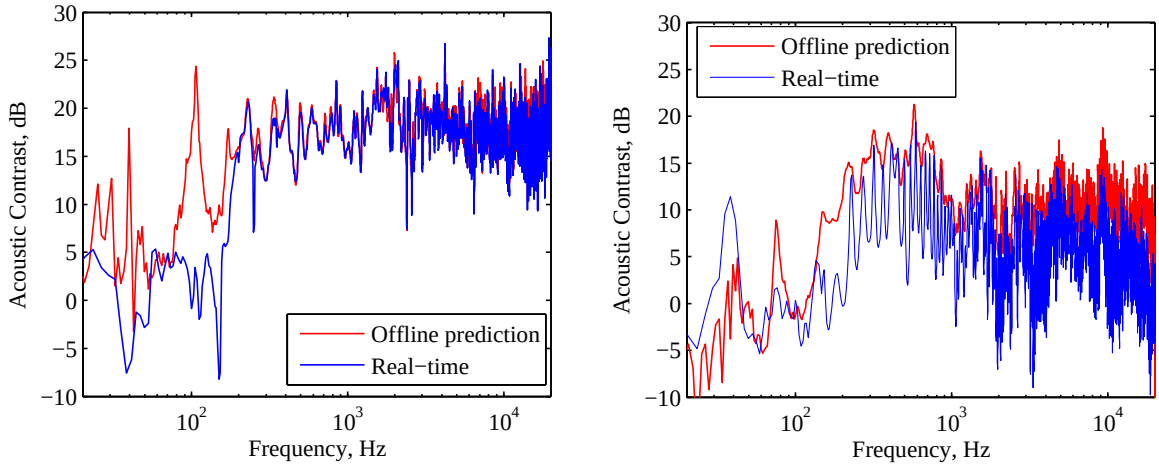

(a) Acoustic contrast between *front bright* and dark rear zones. (b) Acoustic contrast between *rear bright* and dark front zones.

Figure 8.19: The acoustic contrast plotted as a function of frequency for the optimised array of headrest phase-shift loudspeakers predicted using offline simulations (—) and measured in real-time (—).

these frequencies.

The measured acoustic contrast for the headrest loudspeaker array, optimised to produce a bright zone in the rear of the cabin, is presented in Figure 8.19b and it can be seen that there are more significant differences between the offline predictions and the real-time measurements. This can be related to variations in the positions of the loudspeakers between the measurements of the transfer responses and the measurement of the real-time system. These variations were not introduced systematically and, therefore, their magnitude is unknown; however, it does highlight that further investigation into the robustness of the proposed array geometry should be conducted. This may be approached following the previous work on the robustness of compact arrays presented in [99].

8.6 Summary

This chapter has built upon the simulation work presented in the previous chapter by presenting an investigation into the practical implementation and performance of a personal audio system in a car cabin. The aim of the personal audio system was to produce two independent listening zones, one at the positions of the front seat headrests and one at the rear seat headrests. Based on the simulations presented in the previous chapter two loudspeaker arrays have been investigated in order to achieve control over the full audio bandwidth. At frequencies below around 200 Hz an array of four loudspeakers positioned adjacent to the standard car audio loudspeakers has been investigated, and at higher frequencies an array of eight phase-shift loudspeakers mounted at each side of the four headrest positions has been investigated.

The response of the two proposed loudspeaker arrays has first been measured to an array of 16 microphones. Four microphones were positioned at each of the four headrests to define

the bright and dark zones for the optimisation of the loudspeaker arrays. Using the measured transfer responses the optimal filters required to produce both a front bright zone and rear bright zone were calculated in the frequency domain using the unconstrained least squares method defined in Section 7.2, and the performance of the two loudspeaker arrays was predicted using offline synthesis. For the car audio loudspeaker array it has been predicted that significant levels of acoustic contrast control could be achieved at frequencies below around 200 Hz for both control scenarios, which is consistent with the simulation results presented in the previous chapter. The performance of the headrest phase-shift loudspeaker array has also been predicted and, although the results are not as consistent with the simulations presented in the previous chapter, significant levels of acoustic contrast have been predicted. At frequencies between around 200 Hz and 800 Hz a contrast level greater than 20 dB was predicted when producing either a front bright zone or a rear bright zone. However, at higher frequencies the ability of the array to produce a rear bright zone was shown to reduce. This has been related to the orientation and directivity performance of the phase-shift sources and could potentially be improved by optimising the phase-shift loudspeaker design for this application.

To implement the proposed personal audio system in real-time it is necessary to design practical filters and a method of calculating the required time-domain responses from the optimal filters' frequency responses has been presented. The proposed method is based on calculating the inverse Fourier transform of the optimal frequency domain filter responses. It is shown that practical filters can be designed using this method for both the car audio and headrest loudspeaker arrays, however, since no constraint is imposed on the filters' causality, a modelling delay is required. For the headrest loudspeaker array the filter required to achieve significant levels of performance is relatively short and, therefore, the required modelling delay does not significantly affect the applications of the system. However, to achieve significant levels of performance using the car audio loudspeaker array requires a long filter and, therefore, a long modelling delay. This may lead to issues in employing the proposed system in two-way telecommunications applications and, more importantly, may lead to poor audio quality due to audible pre-echos. Despite this potential limitation the performance of the two loudspeaker arrays has been measured in real-time and it has been shown that the two arrays perform as predicted by offline frequency domain simulations. However, it has also been highlighted, in-part through an experimental inconsistency, that the performance of the headrest loudspeaker array is susceptible to variations in the loudspeaker positions. Therefore, to determine the practicability of implementing the proposed personal audio system in a mass production system it is necessary to conduct a study considering the robustness of the two loudspeaker arrays.

Chapter 9

Conclusions and Further Work

9.1 Conclusions

The acoustic environment in automobile cabins is determined by two components: that due to automotive processes, such as engine and road noise, and that due to the audio system, which may be used for entertainment, telecommunications, satellite navigation audio instruction and warning sounds. This thesis has investigated the application of active control solutions to both automotive noise reduction and personal audio reproduction in the automobile cabin. Although these two areas are linked both practically, in terms of the improved quality that each can bring to the car cabin environment, and technically, since they both use an array of loudspeakers to produce a desired sound field, the main conclusions from each area are separated into the two following sections.

9.1.1 Active Noise Control

Active noise control has been highlighted as a potential solution to the increased low frequency noise due to both economical engine designs employing low cylinder counts and low engine speeds, and the push for weight reduction to increase fuel efficiency. However, the cost of active noise control systems, and particularly road noise control systems, has limited their commercial implementation. This thesis has, therefore, focused on investigating cost-effective active noise control systems for both engine and road noise control that can be largely integrated within the automobile's standard electronics.

In the car cabin environment previous work has highlighted the importance of structural-acoustic coupling on the response of the car cabin enclosure at low frequencies where active noise control may be applied and, therefore, an investigation of the effects of structural-acoustic coupling on the response of a car cabin sized enclosure have been investigated. Using both numerical simulations and measurements it has been shown that in a car cabin sized enclosure structural-acoustic coupling introduces additional resonances due to radiating structural modes and changes in both the structural and acoustic modal resonance frequencies and mode shapes. The influence of these changes in the response of a car cabin sized enclosure on the perfor-

mance of feedforward active noise control has been investigated. Through a direct comparison between optimal feedforward control in both rigid and non-rigid enclosures it has been shown that active feedforward control is largely unaffected by the change in the enclosure's response due to structural-acoustic coupling.

In the context of the structural-acoustic coupled enclosure, a comparison between the control of an internal acoustic, external acoustic plane wave and point force structural primary disturbance has been presented. This comparison has shown that for the two structural primary excitations there is only a limited increase in control bandwidth between employing a single secondary source and four secondary sources. This has been linked to the radiation from the structure exciting higher order acoustic modes at lower frequencies than an internal acoustic excitation and this results in an effective increase in the modal overlap and consequent limited bandwidth.

Although feedforward control has been highlighted as a cost-effective method for active engine noise control, feedback control may offer a more cost-effective active road noise control solution. In order to achieve global control it is necessary to use multiple secondary sources and error sensors, however, the implementation of a fully multi-input, multi-output (MIMO) feedback controller is computationally demanding and, therefore, a modal feedback control system has been investigated. Internal model control (IMC) has been used as a convenient method of designing the modal feedback controller and it has been shown that the IMC architecture leads to two alternative formulations of the modal feedback controller. The most useful formulation includes the transducer weightings in the control path and leads to the minimisation of the actual error signals rather than the modal error signal.

A method of designing the modal feedback controller has been proposed which formulates the problem as a convex optimisation using an FIR control filter and frequency discretisation. This design procedure improves upon previous methods of designing modal controllers by calculating both the transducer weightings and control filter in parallel and, therefore, achieving an optimal controller. The optimised modal controller has been shown to achieve significant levels of control when there is a single dominant acoustic resonance, however, the performance of the single-input, single-output controller is limited when multiple resonances occur.

To overcome the limitations of the modal feedback controller, a fully coupled MIMO feedback controller has been investigated. It has been shown that the fully coupled MIMO feedback controller is capable of achieving significant levels of control of multiple uncorrelated structural excitations and, therefore, improves on the modal control strategy. In the context of the proposed MIMO controller three alternative enhancement constraints have been derived, including a constraint on the enhancement in the individual error signals and the more common constraint on the sum of the squared error signals. The performance of these constraints has been compared in the context of the MIMO feedback controller and it has been shown that the novel constraint on the enhancement in the individual error signals provides a controller with a more uniform reduction in pressures and a more practically optimal controller.

To practically validate the performance of feedforward engine noise control and MIMO

feedback road noise control, an experimental study on a small city car with a two-cylinder engine has been presented. Feedforward control of the first engine order has been implemented using a standard filtered-reference LMS algorithm. It has been shown that for fast convergence speeds enhancements of non-controlled engine orders are produced and this has been related to the effective feedback loop in the feedforward controller. These enhancements have been reduced using a modified controller employing a variable bandpass filter on the control outputs. However, the performance of the modified controller is limited when there is fast change in engine speed.

The performance of the MIMO feedback controller to control the road noise in the small city car has been predicted using offline simulations and it has been shown that reductions of low frequency noise of around 3 dB are expected. However, the proposed controller was not implemented in real-time as this was not possible using the available digital signal processing hardware.

9.1.2 Active Sound Reproduction

Active control methods have been highlighted as a potential method of improving audio quality and providing additional functionality in the reproduction of sound in the automobile cabin environment. This thesis has investigated the implementation of a personal audio system in the car cabin, which aims to produce a personal listening zone in either the front or rear seating positions.

The effects of implementing a personal audio system in a car cabin sized enclosure have been investigated through simulations and it has been shown that, similarly to active noise control, the performance of the control system is dependent on how the loudspeakers couple with both the acoustic modes of the enclosure and the bright and dark control zones. This means that the performance of a distributed loudspeaker array, such as the standard car audio loudspeakers, is limited to low frequencies. To achieve control over the full audio bandwidth a number of loudspeaker arrays positioned in the nearfield of the control zones have been investigated and, although the accuracy of the employed point source simulations is limited at high frequencies, an array of four two-source broadside arrays of hypercardioid sources positioned at each headrest has been shown to potentially offer sufficient control.

Previous work has highlighted that significant improvements in audio quality may be achieved by employing least squares optimisation as opposed to acoustic contrast control. A numerical investigation of the acoustic contrast and least squares optimisation strategies has been presented. For the car audio loudspeaker array it has been shown that similar levels of acoustic contrast are achievable using the two optimisation strategies at low frequencies where the array is effective. However, the least squares solution requires a significantly lower array effort and achieves a significant improvement in numerical conditioning, which will result in a more robust system. For the headrest loudspeaker array it has been shown that the acoustic contrast control strategy significantly outperforms the least squares solution at low frequencies in an

ideal scenario. However, due to the poor conditioning of the acoustic contrast solution these high levels of contrast may not be achievable in a practical system subject to uncertainties and the least squares solution is predicted to provide subjectively significant levels of control.

A personal audio system has been implemented in a car cabin employing two loudspeaker arrays optimised using the least squares control strategy to achieve an acoustic contrast of 15 dB and a method of designing practical filters has been proposed. The four standard car audio loudspeakers are employed at low frequencies and are shown to achieve the targeted acoustic contrast level of 15 dB at frequencies up to 200 Hz. An array of eight phase-shift loudspeakers, one mounted at either side of each headrest, is employed to achieve acoustic contrast at higher frequencies and when producing a front bright zone this array is able to achieve the targeted acoustic contrast at frequencies above 200 Hz. However, when producing a rear bright zone the performance of the array is limited at high frequencies due to the directivities of the individual phase-shift loudspeakers.

9.2 Suggestions for Further Work

The work presented in this thesis has highlighted a number of areas for potential future work. The suggestions for future work are separated into the two main areas of focus in the following two sections and a third section considers the integration of the different control systems.

9.2.1 Active Noise Control

Although the modal feedback control strategies investigated in Chapter 4 have limited application in the car environment they may provide significant levels of performance in an application where single acoustic, or structural resonances dominate the system's response. Investigation of the application of the modal controller to an appropriate system would, therefore, be useful to determine the practical performance of these control strategies. This work may initially consider the control of a single acoustic mode in a duct, for example, using a fixed controller but then it would also be interesting to extend this investigation to consider both multi-modal control and adaptive control.

The MIMO feedback controller has been shown to potentially offer significant levels of control of road noise in the automobile application, however, it has been highlighted that the implementation of such a controller has a number of implementation requirements that must be overcome. Therefore, future work could investigate efficient methods of implementing the MIMO feedback controller within the currently available digital signal processing capabilities and minimising the delays through such a controller, which would limit its performance.

The enhancements produced by the standard LMS controller have been reduced during slow engine run-ups using a modified controller with a variable bandpass filter on the control outputs. This controller was designed intuitively and its performance during fast engine run-ups was limited. Future work could more formally analyse the proposed controller's behaviour

and this insight may lead to the design of a controller with a higher level of performance during both steady-state and dynamic engine conditions. This work may be informed by the similar control systems proposed in [173, 174].

Control effort constraints have been successfully scheduled in the real-time feedforward controller, however, the dynamics of this outer control loop are not completely consistent with previous theoretical studies [172]. It is not entirely clear how the dynamics of this outer loop are governed and, therefore, this could be investigated in more detail.

9.2.2 Active Sound Reproduction

The feasibility of generating personal sound zones within a car cabin environment has been successfully demonstrated, although, the performance of the headrest loudspeaker array has been shown to be limited at higher frequencies when producing a rear bright zone. Alternative array geometries could be investigated to improve this performance, or the design of the phase-shift loudspeakers could be refined for the car cabin personal audio system.

In a commercial system it would, at a minimum, be necessary to reproduce stereophonic programme material. Therefore, future work could be conducted to consider the reproduction of stereophonic audio programme within the personal listening zones. Although the headrest loudspeaker array employed here may be suited to binaural reproduction, due to the proximity of the loudspeakers to the ears of the occupants, it may not be ideal for reproduction of standard stereo audio programme material and audio quality requirements may demand the development of audio re-mixing algorithms.

In this thesis the generation of two listening zones within the car cabin has been considered, but significantly increased flexibility could be added by generating four independent listening zones as shown in Figure 9.1. The feasibility of achieving this using the loudspeaker array proposed in Chapters 7 and 8 could be studied and, depending on the results of this work, the proposed personal audio loudspeaker array could be developed.

Previous work on the generation of personal audio zones [78, 86] and the work presented in Chapter 8 of this thesis has implemented the required optimal filtering using a non-causal filter and a modelling delay. This introduces a delay in the audio reproduction and also pre-echos which may reduce basic audio quality [188]. Although the delay introduced by the signal processing may not be a problem in the majority of applications, other than telecommunications, the reduction in audio quality due to the filter pre-echos is of significant importance and can only be reduced using the signal processing strategy employed in this thesis through strong regularisation and truncation of the filter responses [78]. This problem could be overcome if the control filters were designed directly in the time domain and this could be achieved by constraining the filters to be FIR filters and optimising their responses using the convex optimisation with frequency discretisation method that has been employed in this thesis in the design of the feedback controllers.

No formal subjective tests were conducted in this thesis to determine whether the level

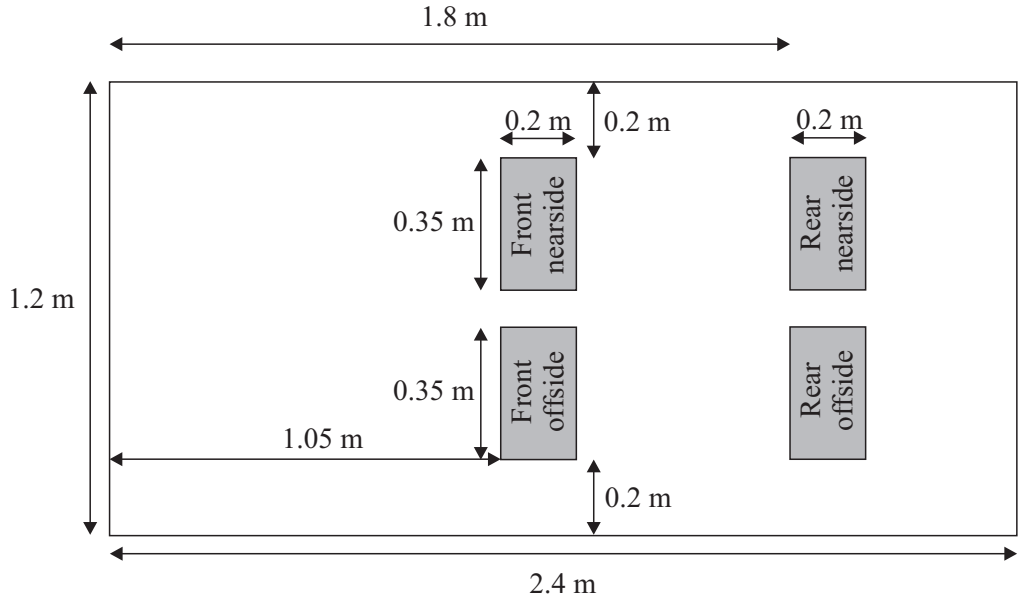

Figure 9.1: Overhead view of the car cabin personal audio control geometry with four control zones in the four seating positions.

of control achieved by the personal audio system produced listening zones that would allow different audio programmes to be listened to in the two control zones comfortably. This would likely to be programme dependent and also dependent on the background noise produced by the vehicle, such as engine and road noise, and, although preliminary results studying this area have been presented by Francombe *et al* [70], further work is needed to understand the subjective requirements of the personal audio system in the automobile environment.

Although the implemented personal audio system has employed the least squares optimisation method, it has been shown that higher levels of contrast performance may be achieved using the acoustic contrast control strategy. A compromise between the least squares and the acoustic contrast control strategies could be achieved using the optimisation method recently proposed in [79], which is a kind of weighted least squares optimisation. The use of this method may allow levels of acoustic contrast to be increased while the audio quality offered by the least squares solution is maintained. However, in order to achieve this, further work would be needed to understand this trade-off in terms of audio quality. It may be that the best way that this trade-off can be understood is by conducting a series of listening tests.

9.2.3 Integration of the Active Noise Control and Active Sound Reproduction Systems

To implement a cost-effective active noise control system for both engine and road noise it is important that the two systems share common system resources and also operate effectively in conjunction with each other. It is also possible that the active noise control and active sound reproduction control systems could be implemented within the same vehicle and, therefore, the combined operation is important to understand. Future work could investigate the potential effect of the feedback control system on the acoustic response of the environment and the

consequent effects on the feedforward control system, the personal audio system and external sound sources such as speech.

A final area of potential development of the work presented in this thesis is to combine the functionality of the active noise control and active sound reproduction systems. For example, with reference to Figure 9.1 it may be desirable to cancel road noise at all seating locations while providing an equalised engine noise to the driver, cancelling the engine noise at all passenger locations and producing independent audio programmes at each seating location. For example, the driver may require personalised warning sounds and satellite navigation instructions, while the rear seat passengers may want to watch a video and the front seat passenger may want to listen to the radio. The development of such a system would require a thorough understanding of the interactions between the various control systems, but would potentially give enough added functionality to motivate automotive manufacturers to provide the additional system requirements which are still difficult to justify purely within the context of active noise control.

Appendix A

Elemental Model

The modal model derived in Section 2.1 may be used to determine the coupled response of the system in modal co-ordinates, however, it is perhaps easier to compute the physical effects of coupling by deriving a model which describes the system behaviour in physical co-ordinates directly. This may be achieved using an elemental model, as described for a vibrating structure by Elliott and Johnson [189] or for a structural-acoustic coupled system by Kim [117]. Such a model enables a system to be considered as a whole, rather than at a single point as in the modal model (see equations 2.5 and 2.9). The elemental model thus lends itself to the modelling of the structural-acoustic coupled system, particularly where multiple panels of the enclosure are non-rigid. The modelling of multiple panels has largely been neglected in the literature, with most theoretical investigations considering a single non-rigid wall or panel [109, 121, 122, 123, 124, 125, 126, 127]. The elemental model can also be used on geometries where there are no simple analytic modal expansions, since the structural and acoustic responses can be calculated using the finite element method, or boundary element method, for example. Therefore, the elemental model will be derived.

The elemental model is based on dividing the system into a number of elements within which the structural and acoustic mode shape functions are approximately constant. The size of the elements must, therefore, be determined based on the frequency range of interest and the precision of the results required – for the same precision but an increased frequency of interest the element size must be reduced. A common rule of thumb is that there should be at least 6 elements within the shortest wavelength considered [111]. At each element the response is represented by the velocity and pressure at the centre of the element. The overall system response can then be determined from the combination of elemental responses.

For an acoustic excitation at a single frequency within the enclosure the vector of acoustic pressures, $\boldsymbol{p}$, at the L elements may be related to the column vector of effective acoustic source strengths at each element, $\boldsymbol{q}_A$, via the $(L \times L)$ uncoupled acoustic impedance matrix $\boldsymbol{Z}_A$; that is

$$\boldsymbol{p} = \boldsymbol{Z}_A \boldsymbol{q}_A. \tag{A.1}$$

The uncoupled acoustic impedance of each element in $\boldsymbol{Z}_A$ is defined as

$$Z_A(i,j) = \frac{p(\boldsymbol{x}_i)}{q_A(\boldsymbol{x}_j)}, \tag{A.2}$$

that is the ratio of the pressure produced at element i due to the effective volume velocity at element j. Using equation 2.1 from the modal model presented in Chapter 2 the acoustic pressure at the i-th element can be written as

$$p(\boldsymbol{x}_i) = \sum_{n=0}^{N} a_n \psi_n(\boldsymbol{x}_i), \tag{A.3}$$

where a_n is given by equation 2.10. Assuming that the effective volume velocity on the j-th element can be approximated as a point volume velocity source acting at the centre of the element, the complex amplitude of the n-th acoustic mode can be written as

$$\begin{aligned} a_n &= \frac{\rho_0 c_0^2}{V} A_n \int_{\Delta V_j} \psi_n(\boldsymbol{x}) q_A(\boldsymbol{x}_j) \delta(\boldsymbol{x} - \boldsymbol{x}_j) \mathrm{d}V \\ &= \frac{\rho_0 c_0^2}{V} A_n \psi_n(\boldsymbol{x}_j) q_A(\boldsymbol{x}_j) \end{aligned} \tag{A.4}$$

where ΔV_j is the volume associated with the j-th element. Substituting equation A.4 into equation A.3 gives the pressure at the i-th element due to the effective source strength as

$$p(\boldsymbol{x}_i) = \frac{\rho_0 c_0^2}{V} \sum_{n=0}^{N} \psi_n(\boldsymbol{x}_i) A_n \psi_n(\boldsymbol{x}_j) q_A(\boldsymbol{x}_j). \tag{A.5}$$

Thus the uncoupled acoustic impedance between the i-th and j-th elements can be written as

$$Z_A(i,j) = \frac{\rho_0 c_0^2}{V} \sum_{n=0}^{N} \psi_n(\boldsymbol{x}_i) A_n \psi_n(\boldsymbol{x}_j). \tag{A.6}$$

This may be written in vector notation for N acoustic modes as

$$Z_A(i,j) = \boldsymbol{\psi}(\boldsymbol{x}_i)^T \boldsymbol{Z}_a \boldsymbol{\psi}(\boldsymbol{x}_j), \tag{A.7}$$

where $\boldsymbol{\psi}(\boldsymbol{x})$ is the $(N \times 1)$ vector of the uncoupled acoustic mode shape functions at co-ordinate position $\boldsymbol{x}$. The complete matrix of uncoupled acoustic impedances may then be written as

$$\boldsymbol{Z}_A = [\boldsymbol{\psi}]^T \boldsymbol{Z}_a [\boldsymbol{\psi}], \tag{A.8}$$

where $[\boldsymbol{\psi}]$ is the $(N \times L)$ matrix of uncoupled acoustic mode shape functions.

An acoustic excitation within the enclosure not only produces an acoustic pressure but may also induce a source strength $\boldsymbol{q}_{st}$ on the elements positioned on the non-rigid structure. These source strengths can be related to the vector of acoustic pressures via the acoustic admittance

matrix, $\boldsymbol{Y}_{CS}$; that is

$$\boldsymbol{q}_{st} = -\boldsymbol{Y}_{CS}\boldsymbol{p}. \tag{A.9}$$

Each element of the acoustic admittance matrix is defined as

$$Y_{CS}(i,j) = -\frac{q_{st}(\boldsymbol{y}_i)}{p(\boldsymbol{y}_j)}, \tag{A.10}$$

that is the ratio of induced structural source strength at element i due to the acoustic pressure at element j. Using the relationship between the volume velocity and velocity of an element

$$q_{st}(\boldsymbol{y}_i) = \Delta S_i w(\boldsymbol{y}_i) \tag{A.11}$$

where ΔS_i is the surface area of the i-th element, equation A.10 can be rewritten as

$$Y_{CS}(i,j) = -\frac{\Delta S_i w(\boldsymbol{y}_i)}{p(\boldsymbol{y}_j)}. \tag{A.12}$$

Using equation 2.6 from the modal model in Chapter 2 the vibration velocity at the i-th element is given as

$$w(\boldsymbol{y}_i) = \sum_{k=1}^{K} b_k \phi_k(\boldsymbol{y}_i), \tag{A.13}$$

where b_k is given by equation 2.15. Based on the assumption of the elemental model that the acoustic pressure and mode shape function are constant over the j-th element, the complex amplitude of the k-th structural mode can be written as

$$\begin{aligned} b_k &= -\frac{1}{\rho_s h S_F} B_k \int_{\Delta S_j} \mathrm{d}S \phi_k(\boldsymbol{y}_j) p(\boldsymbol{y}_j) \\ &= -\frac{1}{\rho_s h S_F} B_k \phi_k(\boldsymbol{y}_j) p(\boldsymbol{y}_j) \Delta S_j. \end{aligned} \tag{A.14}$$

Substituting equation A.14 into equation A.13 gives the vibration velocity of the i-th element due to the acoustic reaction force as

$$w(\boldsymbol{y}_i) = -\frac{1}{\rho_s h S_F} \sum_{k=1}^{K} \phi_k(\boldsymbol{y}_i) B_k \phi_k(\boldsymbol{y}_j) \Delta S_j p(\boldsymbol{y}_j). \tag{A.15}$$

Therefore, the acoustic admittance can be written as

$$Y_{CS}(i,j) = \frac{1}{\rho_s h S_F} \sum_{k=1}^{K} \Delta S_i \phi_k(\boldsymbol{y}_i) B_k \phi_k(\boldsymbol{y}_j) \Delta S_j. \tag{A.16}$$

Once again, for a finite number of structural modes, this may be written in vector notation as

$$Y_{CS}(i,j) = \Delta S_i \boldsymbol{\phi}_i^T \boldsymbol{Y}_s \boldsymbol{\phi}_j \Delta S_j, \tag{A.17}$$

where $\boldsymbol{\phi}_i$ and $\boldsymbol{\phi}_j$ are $(K \times 1)$ vectors of the uncoupled structural mode shape functions at ele-

ments i and j respectively. The complete matrix of acoustic admittance may then be written as

$$\boldsymbol{Y}_{CS} = \boldsymbol{S}[\boldsymbol{\phi}]^T \boldsymbol{Y}_s [\boldsymbol{\phi}] \boldsymbol{S}, \tag{A.18}$$

where $[\boldsymbol{\phi}]$ is the $(K \times L)$ matrix of uncoupled structural mode shape functions and $\boldsymbol{S}$ is the $(L \times L)$ diagonal matrix of element areas, ΔS_l.

Since the effective source strength, $\boldsymbol{q}_A$, is equal to the sum of the excitation source strength, $\boldsymbol{q}$, and the induced source strength, $\boldsymbol{q}_{st}$, the acoustic pressure and induced source strengths can be expressed using equations A.1 and A.9 as

$$\boldsymbol{p} = [\boldsymbol{I} + \boldsymbol{Z}_A \boldsymbol{Y}_{CS}]^{-1} \boldsymbol{Z}_A \boldsymbol{q} \tag{A.19}$$

and

$$\boldsymbol{q}_{st} = -\boldsymbol{Y}_{CS} [\boldsymbol{I} + \boldsymbol{Z}_A \boldsymbol{Y}_{CS}]^{-1} \boldsymbol{Z}_A \boldsymbol{q} \tag{A.20}$$

respectively. Equations A.19 and A.20 may be used to describe the physical response of the structural-acoustic coupled system under direct acoustic excitation. The derivation of the associated equations for the case when there is a direct structural excitation follows.

For an effective structural excitation force, $\boldsymbol{f}_S$, the normal surface velocity of the structure, $\boldsymbol{w}$, is given as,

$$\boldsymbol{w} = \boldsymbol{Y}_S \boldsymbol{f}_S, \tag{A.21}$$

where $\boldsymbol{Y}_S$ is the $(L \times L)$ matrix of uncoupled structural mobilities from force to velocity, which differs by a factor of $-a^2$ from $\boldsymbol{Y}_{CS}$ in equation A.10 where a is the area of the element, and $\boldsymbol{f}_S$ and $\boldsymbol{w}$ are column vectors of their respective values at each of the L elements. The uncoupled structural mobility of each element in $\boldsymbol{Y}_S$ is defined as

$$Y_S(i,j) = \frac{w(\boldsymbol{y}_i)}{f_S(\boldsymbol{y}_j)}, \tag{A.22}$$

which is the ratio of the structural velocity produced at the i-th element due to the effective force at element j. Using equations 2.6 and 2.7 from the modal model and assuming that the effective force on the j-th element can be approximated as a point force the structural velocity at the i-th element can be expressed as

$$\begin{aligned} w(\boldsymbol{y}_i) &= \frac{1}{\rho_s h S_F} \sum_{k=1}^{K} \left[B_k \phi_k(\boldsymbol{y}_i) \int_{\Delta S_j} \phi_k(\boldsymbol{y}) f_S(\boldsymbol{y}_j) \delta(\boldsymbol{y} - \boldsymbol{y}_j) dS \right] \\ &= \frac{1}{\rho_s h S_F} \sum_{k=1}^{K} \phi_k(\boldsymbol{y}_i) B_k \phi_k(\boldsymbol{y}_j) f_S(\boldsymbol{y}_j). \end{aligned} \tag{A.23}$$

The uncoupled structural mobility between the i-th and j-th elements can then be written as

$$Y_S(i,j) = \frac{1}{\rho_s h S_F} \sum_{k=1}^{K} \phi_k(\boldsymbol{y}_i) B_k \phi_k(\boldsymbol{y}_j). \tag{A.24}$$

For a finite number of structural modes this can be written in vector notation as

$$Y_S(i,j) = \boldsymbol{\phi}(\boldsymbol{y}_i)^T \boldsymbol{Y}_s \boldsymbol{\phi}(\boldsymbol{y}_j), \tag{A.25}$$

and the complete matrix of structural mobilities is then given as

$$\boldsymbol{Y}_S = [\boldsymbol{\phi}]^T \boldsymbol{Y}_s [\boldsymbol{\phi}], \tag{A.26}$$

where $[\boldsymbol{\phi}]$ is the $(K \times L)$ matrix of structural mode shape functions.

Similarly to the acoustic excitation case, the structural excitation not only produces a structural velocity but also induces an acoustic reaction force, f_A, at the elements on the non-rigid structure. This reaction force can be related to the structural velocity vector via the mechanical impedance matrix, $\boldsymbol{Z}_{CA}$, which differs by a factor of $1/a^2$ from the acoustic impedance matrix $\boldsymbol{Z}_A$ in equation A.1; that is

$$\boldsymbol{f}_A = \boldsymbol{Z}_{CA} \boldsymbol{w}. \tag{A.27}$$

The coupled acoustic impedance of each element in $\boldsymbol{Z}_{CA}$ can be expressed as the ratio between acoustic reaction force at the i-th element due to the structural velocity at the j-th element as

$$Z_{CA} = \frac{f_A(\boldsymbol{y}_i)}{w(\boldsymbol{y}_j)}. \tag{A.28}$$

Using the relationship between the acoustic pressure and the acoustic reaction force

$$f_A(\boldsymbol{y}_i) = \Delta S_i p(\boldsymbol{y}_i) \tag{A.29}$$

to substitute for f_A this becomes

$$Z_{CA} = \frac{\Delta S_i p(\boldsymbol{y}_i)}{w(\boldsymbol{y}_j)}. \tag{A.30}$$

Once again employing equations 2.1 and 2.10 from the modal model and employing the elemental model's assumption that the velocity and mode shape function are constant over each element, the pressure at the i-th element can be expressed as

$$p(\boldsymbol{y}_i) = \frac{\rho_0 c_0^2}{V} \sum_{n=0}^{N} \psi_n(\boldsymbol{y}_i) A_n \psi_n(\boldsymbol{y}_j) \Delta S_j w(\boldsymbol{y}_j). \tag{A.31}$$

The mechanical impedance between the i-th and j-th element is then given as

$$Z_{CA}(i,j) = \frac{\rho_0 c_0^2}{V} \sum_{n=0}^{N} \Delta S_i \psi_n(\boldsymbol{y}_i) A_n \psi_n(\boldsymbol{y}_j) \Delta S_j, \tag{A.32}$$

which can be expressed in vector form for a finite number of structural modes as

$$Z_{CA}(i,j) = \Delta S_i \boldsymbol{\psi}(\boldsymbol{y}_i)^T \boldsymbol{Z}_a \boldsymbol{\psi}(\boldsymbol{y}_j) \Delta S_j. \tag{A.33}$$

The complete matrix of mechanical impedances is given by

$$\boldsymbol{Z}_{CA} = \boldsymbol{S}[\boldsymbol{\psi}]^T \boldsymbol{Z}_a [\boldsymbol{\psi}] \boldsymbol{S}. \tag{A.34}$$

Since the vector of effective forces acting on the non-rigid structure is given by

$$\boldsymbol{f}_S = \boldsymbol{f} - \boldsymbol{f}_A, \tag{A.35}$$

using equations A.21 and A.27 the structural velocity and acoustic reaction force can be expressed as

$$\boldsymbol{w} = [\boldsymbol{I} + \boldsymbol{Y}_S \boldsymbol{Z}_{CA}]^{-1} \boldsymbol{Y}_S \boldsymbol{f} \tag{A.36}$$

and

$$\boldsymbol{f}_A = \boldsymbol{Z}_{CA} [\boldsymbol{I} + \boldsymbol{Y}_S \boldsymbol{Z}_{CA}]^{-1} \boldsymbol{Y}_C \boldsymbol{f} \tag{A.37}$$

respectively.

For the case where both acoustic, $\boldsymbol{q}$, and structural, $\boldsymbol{f}$, excitations are present, equations A.19 and A.37 may be combined based on the principle of linear superposition to give the vector of pressures as

$$\boldsymbol{p} = [\boldsymbol{I} + \boldsymbol{Z}_A \boldsymbol{Y}_{CS}]^{-1} \boldsymbol{Z}_A (\boldsymbol{q} + \boldsymbol{S}\boldsymbol{Y}_S \boldsymbol{f}), \tag{A.38}$$

and the acoustic reaction forces as

$$\boldsymbol{f}_A = [\boldsymbol{I} + \boldsymbol{Z}_{CA} \boldsymbol{Y}_S]^{-1} (\boldsymbol{S}\boldsymbol{Z}_A \boldsymbol{q} + \boldsymbol{Z}_{CA} \boldsymbol{Y}_S \boldsymbol{f}). \tag{A.39}$$

Similarly, equations A.20 and A.36 may be combined to give the vector of structural velocities as

$$\boldsymbol{w} = [\boldsymbol{I} + \boldsymbol{Y}_S \boldsymbol{Z}_{CA}]^{-1} \boldsymbol{Y}_S (\boldsymbol{f} - \boldsymbol{S}\boldsymbol{Z}_A \boldsymbol{q}) \tag{A.40}$$

and the induced acoustic source strengths on the non-rigid structure as

$$\boldsymbol{q}_{st} = [\boldsymbol{I} + \boldsymbol{Y}_{CS} \boldsymbol{Z}_A]^{-1} (\boldsymbol{S}\boldsymbol{Y}_S \boldsymbol{f} - \boldsymbol{Y}_{CS} \boldsymbol{Z}_A \boldsymbol{q}). \tag{A.41}$$

As in the modal model, the structural-acoustic system is said to be weakly coupled if either of the terms in square brackets are approximately equal to the identity matrix; that is, either, $||\boldsymbol{Z}_A \boldsymbol{Y}_{CS}|| \simeq 0$ or $||\boldsymbol{Y}_S \boldsymbol{Z}_{CA}|| \simeq 0$.

Appendix B

Further Comments on the Response of a Structural-Acoustic Coupled Enclosure with a Single Non-Rigid Panel

From Figure 2.2a it can also be seen that the fully-coupled system exhibits a significant peak in the acoustic potential energy at 26 Hz. From Table 2.2 it can be seen that this corresponds to the natural frequency of the $(2,1)$ structural mode, however, inspecting the magnitude of the velocity distribution on the roof panel, as shown in Figure B.1, it can be seen that the dominant mode at 26 Hz in the fully coupled system is the $(1,1)$ mode. This indicates that the structural-acoustic coupling has increased the natural frequency of the $(1,1)$ structural mode and this effect can also be observed in the structural kinetic energy presented in Figure 2.2b where the dominant resonance shifts from 16 Hz to 26 Hz.

The physical basis for the increase in the natural frequency of the $(1,1)$ structural mode can be understood in terms of its interaction with the $(0,0,0)$ acoustic mode. That is, since the compliant acoustic mode is lower in frequency than the $(1,1)$ structural mode it increases the effective stiffness of the panel through fluid-loading and thus increases its natural frequency.

Based on the interaction between the first acoustic and structural modes, it is apparent that the interaction of two modes causes the two natural frequencies to move apart. This effect is reported by both Craggs [106] and Nefske *et al* [103] in the context of a vehicle cabin. For example, Nefske *et al* demonstrate how varying the uncoupled natural frequency of the tailgate in relation to the uncoupled natural frequency of the enclosure will cause varying shifts in the natural frequencies of both the coupled tailgate and acoustic enclosure.

In addition to the observations already made it can be seen from Figure 2.2a that the frequency of the first longitudinal acoustic mode, which occurs at 71 Hz in the rigid walled case, has been slightly increased in frequency to 75 Hz. Based on the preceding discussion it can be

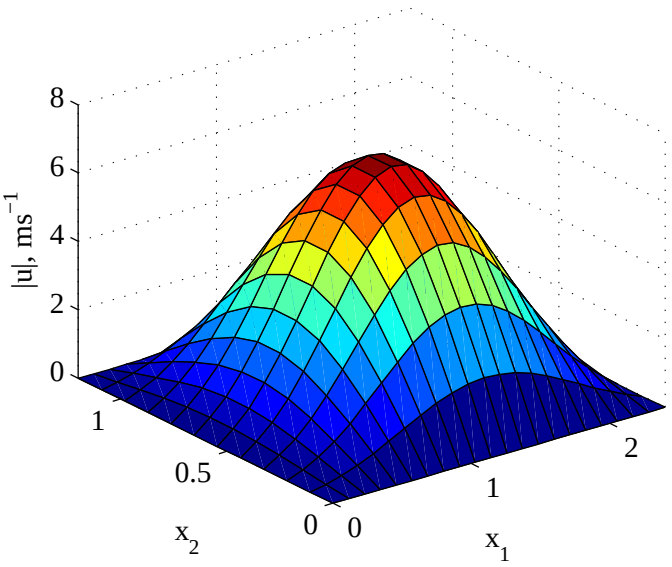

Figure B.1: The magnitude of the structural velocity of the roof panel in the fully coupled system at 26 Hz.

appreciated that this shift must be the result of a structural mode, or modes, that are lower in frequency than the rigid walled acoustic mode but also proximate in frequency and with a significant geometric coupling coefficient. From Table 2.2 it can be seen that both the $(2,1)$ and $(4,1)$ structural modes are lower in frequency than the $(1,0,0)$ acoustic mode and couple geometrically; however, because the $(2,1)$ structural mode is significantly lower in frequency than the first longitudinal acoustic mode compared to the $(4,1)$ structural mode, the observed coupling effects will be dominated by the influence of the $(4,1)$ structural mode. In this instance the increase in frequency can be related to an increased enclosure stiffness.

Referring once again to Figure 2.2a it can be seen that a significant reduction in the acoustic potential energy occurs between the fully and weakly coupled systems at around 16 Hz. The cause of this effect can be explained through equation A.19 which gives the acoustic pressure produced in the enclosure for an acoustic volume velocity excitation; this equation is repeated here for convenience:

$$\boldsymbol{p} = [\boldsymbol{I} + \boldsymbol{Z}_A \boldsymbol{Y}_{CS}]^{-1} \boldsymbol{Z}_A \boldsymbol{q}, \tag{B.1}$$

where $\boldsymbol{Z}_A$ is the matrix of uncoupled acoustic impedance, $\boldsymbol{Y}_{CS}$ is the matrix of acoustic admittances, $\boldsymbol{q}$ is the volume velocity and the coupled acoustic impedance is given by

$$\boldsymbol{Z} = [\boldsymbol{I} + \boldsymbol{Z}_A \boldsymbol{Y}_{CS}]^{-1} \boldsymbol{Z}_A. \tag{B.2}$$

From equations B.1 and B.2 it can be seen that the pressure produced in the coupled enclosure for a given acoustic source strength is directly related to the coupled acoustic impedance, such that a high value of $\boldsymbol{Z}$ will produce a high pressure and vice versa. However, from equation B.2 it can be seen that the coupled impedance is dependent on both the uncoupled, or rigid walled

acoustic impedance, and the acoustic admittance, which, according to equation A.9, relates the acoustic pressure produced by the acoustic source to the source strengths that it induces on the flexible panel. Figure B.2 shows the uncoupled acoustic impedance and admittance, at the point with maximum response, and the resulting coupled acoustic impedance of the rectangular enclosure with a flexible roof panel when only the first acoustic and structural modes are considered. From this plot it can be seen that at 16 Hz the admittance is high due to the structural resonance in the flexible roof panel and according to equation B.2 this produces a low coupled acoustic impedance, as seen in the black line in Figure B.2, and, therefore, a dip in the acoustic potential energy in Figure 2.2a.

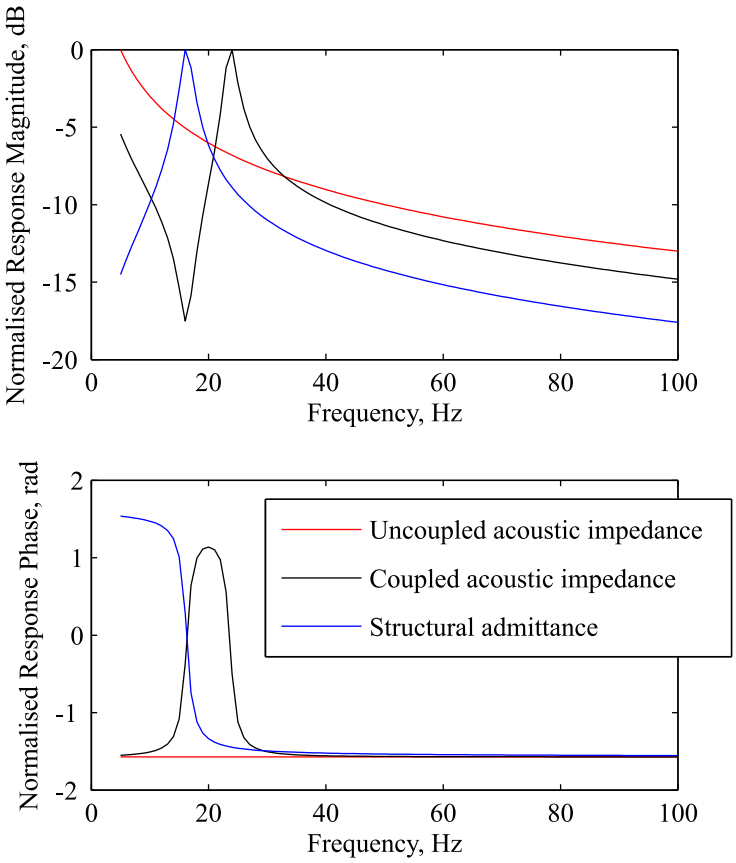

Figure B.2: The coupled and uncoupled acoustic impedances and the acoustic admittance due to the structure in the rectangular enclosure with a flexible roof panel when excited at different frequencies by a single internal acoustic monopole source. The magnitude responses are plotted in decibels relative to the maximum response in order to allow convenient comparison of the results.

In addition to the significant variations between the weakly and fully coupled responses already described, the two plots in Figure 2.2 also show some smaller variations. For example, Figure 2.2a shows a slight peak at 42 Hz, which can be simply related to the radiation of the $(3,1)$ structural mode (see Table 2.2). Figure 2.2b, which shows the total structural kinetic energy, also shows some small variations up to around 250 Hz. These variations are mainly

reductions in the fully coupled kinetic energy compared to the weakly coupled case and can thus be related to the pressure loading on the panel reducing the amplitude of vibration.

In addition to the variation in the natural frequencies due to the effects of coupling, a variation in the mode shape can also be expected. For the $(1,0,0)$ acoustic mode the pressure distribution over a cross-section in the x_1–x_3 plane through the centre of the enclosure is presented in Figure B.3. From this plot it can be seen that there is little displacement in the position of the nodal line between the weakly and fully coupled systems. It can, however, be seen that the fully-coupled system does result in some variation in the pressure distribution away from the nodal line.

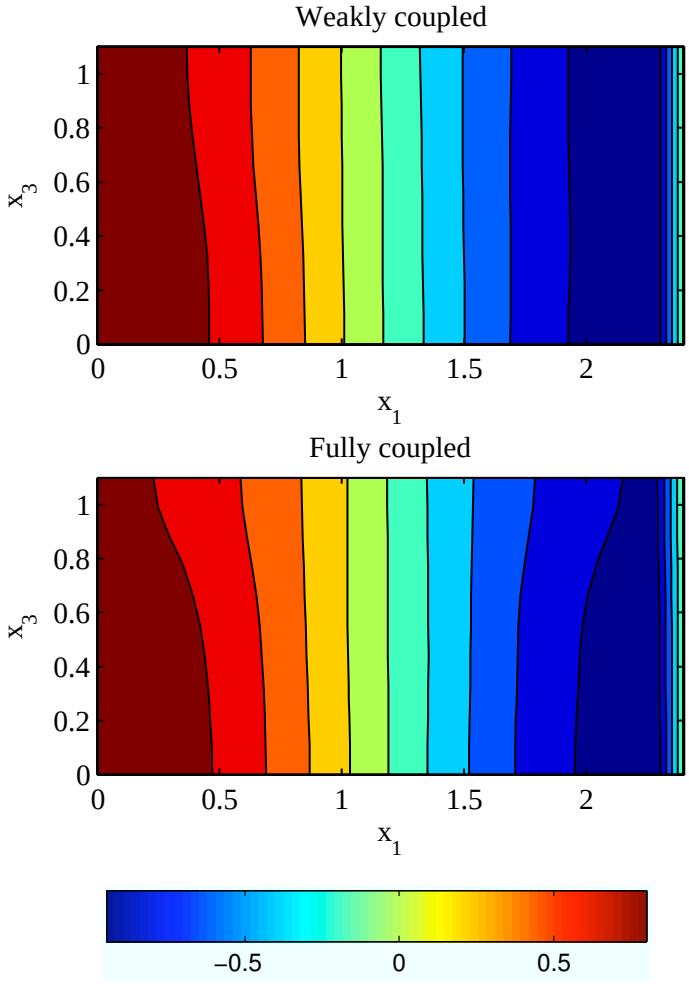

Figure B.3: The pressure distribution over a cross-section in the x_1–x_3 plane through the centre of the enclosure for the first longitudinal acoustic mode occuring at $\sim$ 71 Hz in the weakly coupled case and $\sim$ 75 Hz in the fully coupled case.

Previous investigations into structural-acoustic coupling suggest that a shift in natural frequency should produce a corresponding shift in the nodal line of the mode [106, 103]. For example, a mass-controlled panel, which increases the natural frequency, is expected to move the nodal line away from the panel due to the decreased wavelength [106]. Conversely, for a stiffness-controlled panel mode the nodal line of the acoustic mode is expected to move towards

the boundary [106]. This has not been observed for the $(1,0,0)$ mode, however, it is thought that this is due to the nodal line being perpendicular to the single non-rigid panel. In order to confirm this Figure B.4 shows the pressure distribution in the x_1–x_2 plane at a cross-section through the centre of the enclosure when the rear wall is non-rigid for both 70 Hz and 75 Hz for the weakly and fully coupled cases. In the weakly coupled case

From these plots it can be seen that at 70 Hz (approximately the frequency of the $(1,0,0)$ mode in the weakly coupled case) the pressure minimum is shifted slightly away from the non-rigid rear wall, as expected since the panel is mass-controlled around this frequency. Similarly, at 75 Hz (the approximate natural frequency of the first longitudinal acoustic mode in the fully coupled system) the pressure minimum is further away from the non-rigid rear wall than for the weakly coupled system. However, comparing the position of the pressure minimum for the weakly coupled resonance at 70 Hz and the fully coupled resonance at 75 Hz there is negligible difference in their positions. This thus clarifies the effect of coupling upon the nodal line's position reported previously [106, 103].

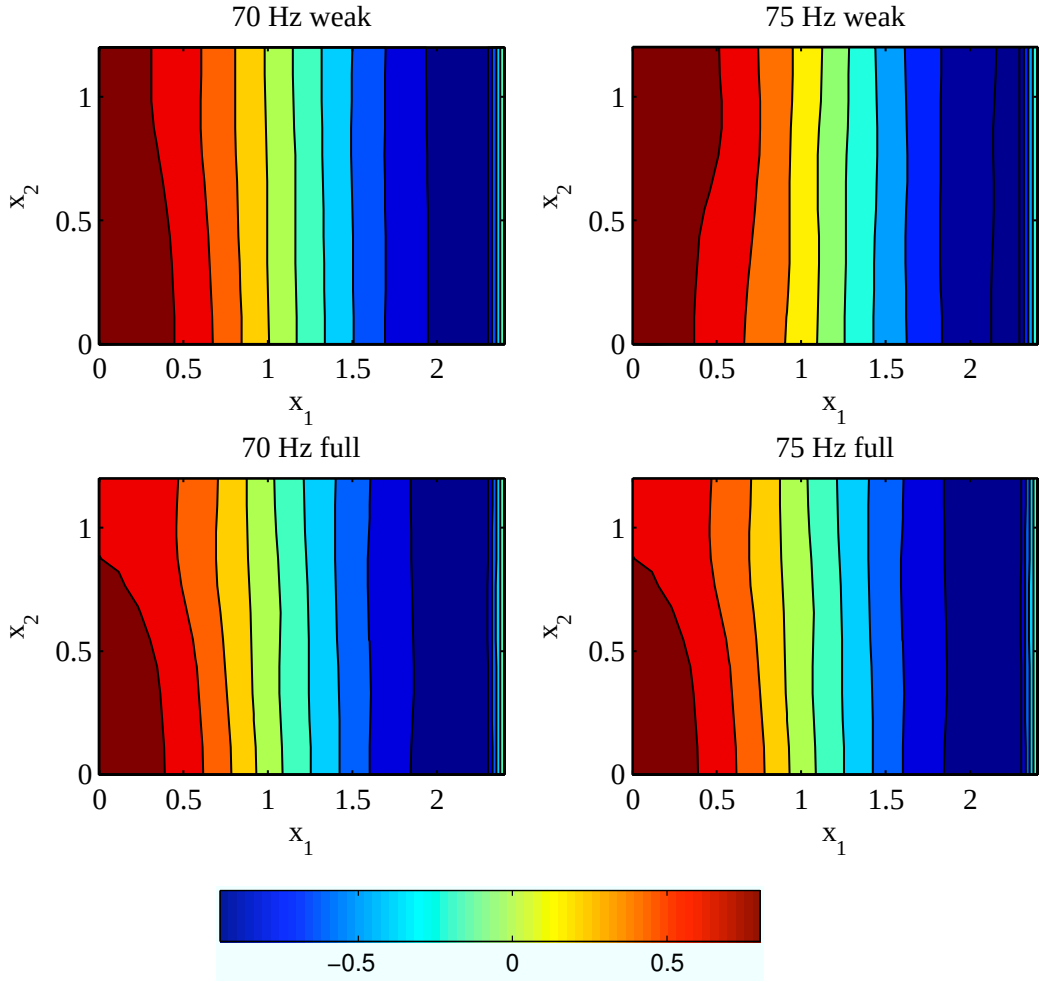

Figure B.4: The pressure distribution over a cross-section in the x_1–x_2 plane through the centre of the enclosure for the first longitudinal mode occuring at $\sim$ 71 Hz in the weakly coupled case and $\sim$ 75 Hz in the fully coupled case.

In order to give an overview of the conditions under which structural-acoustic coupling effects the response of an enclosure with a non-rigid simply supported roof, the magnitude of the geometric coupling coefficients given by equation 2.13 in the modal model have been plotted it Figure B.5 for the first 50 acoustic and first 30 structural modes; this is the same data as presented in Table 2.2 but for a larger number of modes. From this plot it can be seen in general that the geometric coupling coefficients are strongest for low structural mode numbers, where the structural mode shapes are less spatially complex. This observation is consistent with the observations regarding Figure 2.2 where the largest effects of coupling are seen at low frequencies. However, Figure B.5 remains to show large magnitude geometric coupling coefficients at higher acoustic modes than appear to be affected according to the energy plots. This may be explained by the fact that the geometric coupling coefficients only depend upon the geometrical similarity between the acoustic and structural mode shape functions, and are not directly related to the frequency of excitation or the frequencies of the acoustic and structural natural frequencies [190]. That is, for example, although the geometric coupling between the $(1,1)$ structural mode and the $(0,0,2)$ acoustic mode is strong, the natural frequencies of the two modes are widely spaced – 15 Hz and 312 Hz respectively – and, therefore, the acoustic mode does not significantly excite the structural mode and vice versa.

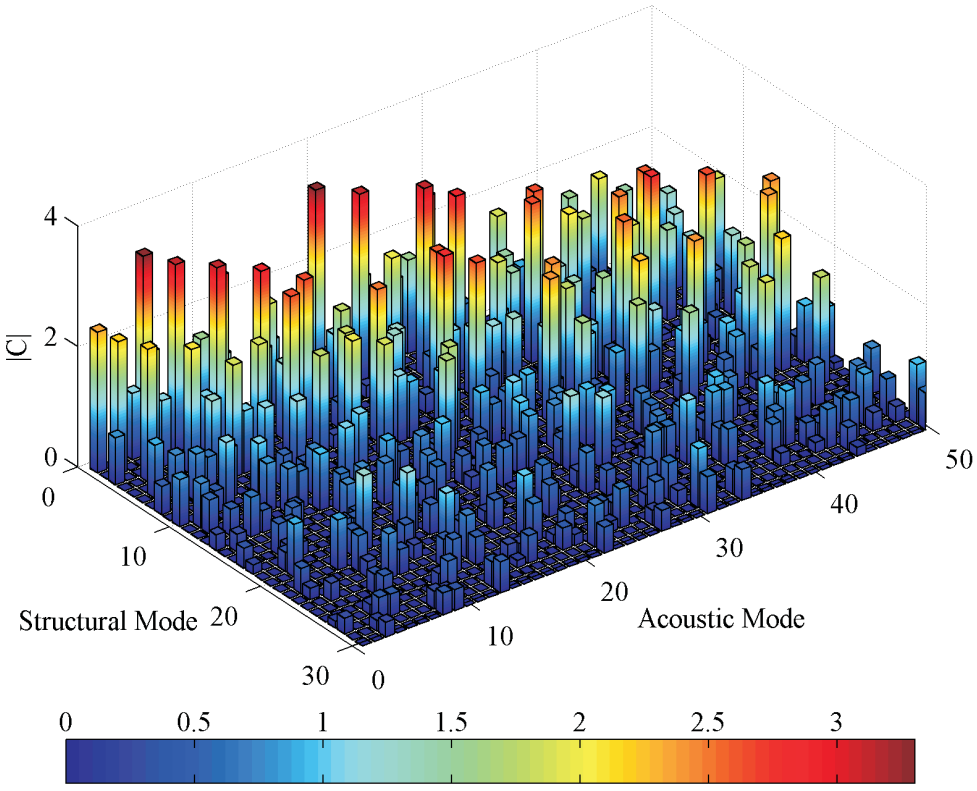

Figure B.5: Magnitude of the geometric coupling coefficients, $|C|$, for the acoustic enclosure with a non-rigid, simply supported roof panel plotted for the first 50 acoustic and first 30 structural modes.

From the presented simulations it is clear that, for the considered enclosure, the effects of structural-acoustic coupling are significant and, therefore, the fully coupled analysis should be employed for further simulations.

Appendix C

The Effect of Boundary Conditions on Structural-Acoustic Response

Although the simulation results presented in Section 2.2 provide an insight into the effects of structural-acoustic coupling, it is also pertinent to consider how the panel boundary conditions change the coupled response. In Section 2.2 simply supported panel boundary conditions have been assumed, in practice the boundary conditions are likely to be somewhere between simply supported and clamped [191]. Therefore, in this section the elemental model will be employed to calculate the structural-acoustic response for systems where the panels are clamped.

C.1 Clamped Boundary Condition Theory

For a clamped panel the resonance frequencies of the k-th structural mode are given by [118],

$$\omega_k = \sqrt{\frac{Eh^2}{12\rho_s(1-\nu^2)}}\left(\frac{\pi}{L_{y_1}}\right)^2 q_k \tag{C.1}$$

where,

$$q_k = \sqrt{G_{y_1}^4(k_1) + G_{y_2}^4(k_2)\left(\frac{L_{y_1}}{L_{y_2}}\right)^4 + 2\left(\frac{L_{y_1}}{L_{y_2}}\right)^2 [H_{y_1}(k_1)H_{y_2}(k_2)]} \tag{C.2}$$

and the values for G_{y_1}, G_{y_2}, H_{y_1} and H_{y_2} are detailed in Table C.1. The mode shape functions of the clamped panel are given by the product of the beam mode shape functions evaluated in the y_1 and y_2 directions [118]. That is,

$$\phi_k(y_1,y_2) = \varphi_{k_1}(y_1)\varphi_{k_2}(y_2), \tag{C.3}$$

where $\varphi_{k1}(y_1)$ is the mode shape function of a beam with the same boundary conditions as the panel under consideration in the y_1 direction and, similarly, $\varphi_{k2}(y_2)$ is the mode shape function of a beam with the same boundary conditions as the panel under consideration in the y_2 direction. The mode shape functions for a beam in the y_1 direction clamped at both ends are given in Table C.2 and the zeros of the 'gamma-functions' are detailed in Table C.3. For the

beam functions in the y_2 direction the indices for the modal integer k and the co-ordinate y are set to 2.

Table C.1: Values for the constants G_{y_1}, G_{y_2}, H_{y_1} and H_{y_2} in equation C.2 for a rectangular panel with all four edges clamped (from [118]) where n is 1 or 2 corresponding to the associated modal integer

k_1 or k_2	G_{y_1} or G_{y_2}	H_{y_1} or H_{y_2}
1	1.506	1.248
> 1	$(k_n + 0.5)$	$(k_n + 0.5)^2 \left(1 - \frac{4}{(2k_n+1)\pi}\right)$

Table C.2: Beam mode shape functions in the y_1 direction for a clamped-clamped beam

For $k_1 = 1,3,5...$ with $i = (k_1+1)/2$	For $k_1 = 2,4,6...$ with $j = k_1/2$
$\varphi_{k_1}(y_1) = \sqrt{2}\left(\cos\gamma_i\left(\frac{y_1}{L_{y_1}} - \frac{1}{2}\right) + \kappa_{k_1}\cosh\gamma_i\left(\frac{y_1}{L_{y_1}} - \frac{1}{2}\right)\right)$	$\varphi_{k_1}(y_1) = \sqrt{2}\left(\sin\gamma_j\left(\frac{y_1}{L_{y_1}} - \frac{1}{2}\right) + \kappa_{k_1}\sinh\gamma_j\left(\frac{y_1}{L_{y_1}} - \frac{1}{2}\right)\right)$
$\kappa_{k_1} = \frac{\sin(\gamma_i/2)}{\sinh(\gamma_i/2)}$ with $\tan(\gamma_i/2) + \tanh(\gamma_i/2) = 0$	$\kappa_{k_1} = -\frac{\sin(\gamma_j/2)}{\sinh(\gamma_j/2)}$ with $\tan(\gamma_j/2) - \tanh(\gamma_j/2) = 0$

Table C.3: Zeros of the gamma-functions employed in Table C.2

k_1	$\tan(\gamma_i/2) + \tanh(\gamma_i/2) = 0$	$\tan(\gamma_j/2) - \tanh(\gamma_j/2) = 0$
1	4.7300	7.8532
2	10.9956	14.1372
3	17.2788	20.4204
4	23.5620	26.7036
5	29.8452	32.9868
$\geqslant 6$	$\frac{(4i-1)\pi}{2}$	$\frac{(4j+1)\pi}{2}$

C.2 Clamped Boundary Condition Simulations

Employing the elemental model from section 2.1 in conjunction with the expressions for the resonant frequencies and mode shapes of the clamped panel the response of the structural-acoustic coupled enclosure with clamped panels to an acoustic source excitation has been computed. Figure C.1 shows the total acoustic potential energy and the total structural kinetic energy for the considered enclosure with a non-rigid clamped roof panel for both the weakly and fully coupled analyses; this plot is directly comparable to the case presented in Figure 2.2 for the simply supported panel. From the plot of total acoustic potential energy, as for the simply supported case, it can be seen that at frequencies lower than around 100 Hz there are significant differences between the weakly and fully coupled analyses, suggesting that a fully coupled analysis is still required for the clamped panel case. It is interesting that by comparing Figure C.1a to Figure 2.2a it can be seen that there are once again two significant variations in the fully coupled response from the weakly coupled response – a peak and a dip. However, for the clamped panel system the dip in the acoustic potential energy has been shifted up to 25 Hz and the peak has been shift up to 45 Hz. The differences between the clamped and simply supported system responses may be related to the associated change in structural resonant frequencies and mode shapes. It can also be seen from the upper plot in Figure C.1 that the first longitudinal mode has been marginally shifted up in frequency, however, the effect is not a significant as was observed for the case with the simply supported panel. In terms of the structural kinetic energy, which is plotted in Figure C.1b for the non-rigid clamped roof panel, it can be seen that once again the effects of structural-acoustic coupling are largely limited to frequencies below around 160 Hz and the most significant variation corresponds to the increase in the natural frequency of the $(1,1)$ structural mode.

Figure C.2 shows the energy plots for the structural-acoustic system where all panels are non-rigid and clamped; this plot is therefore directly comparable to the simply supported case presented in Figure 2.4. From these plots it can be seen that there are obvious characteristic effects of the structural-acoustic coupling regardless of the specific boundary condition employed. For example, it can be seen that the most significant effects are limited to similar low frequency ranges for both boundary conditions. However, it is also clear that the specific narrowband impact of structural-acoustic coupling is significantly dependent upon the panel boundary conditions, which is due to the change in panel mode shapes and resonant frequencies; these are the two properties which, as discussed in Section 2.2, determine the influence of the structural response on the acoustical response and vice versa.

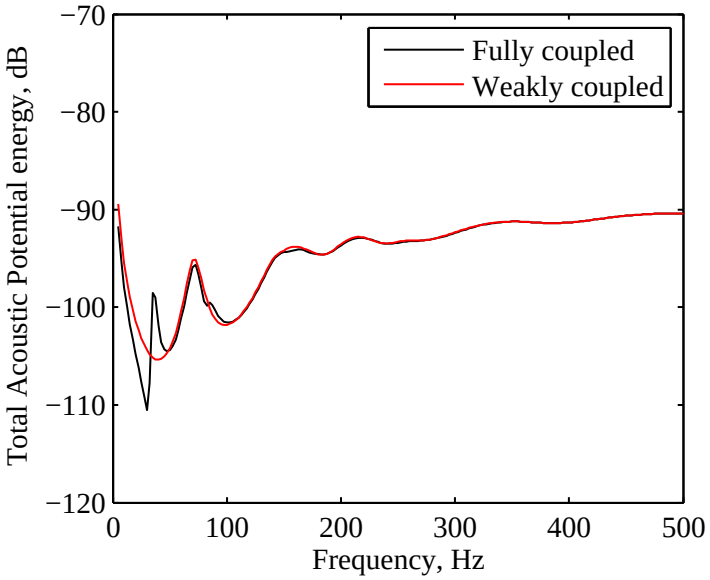

(a) Total acoustic potential energy.

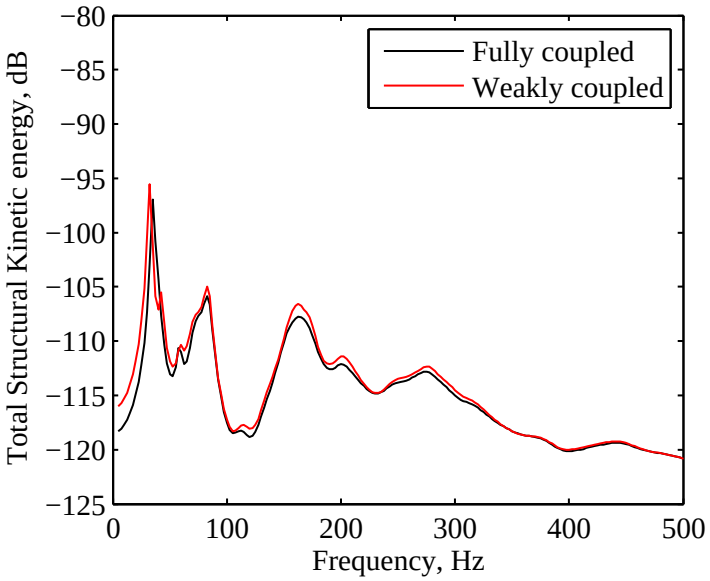

(b) Total structural kinetic energy.

Figure C.1: Simulated acoustic and structural response of the acoustic enclosure with a flexible roof panel with clamped boundary conditions when excited at different frequencies by a single acoustic monopole source with a volume velocity of 10^{-5} m^3s^{-1}.

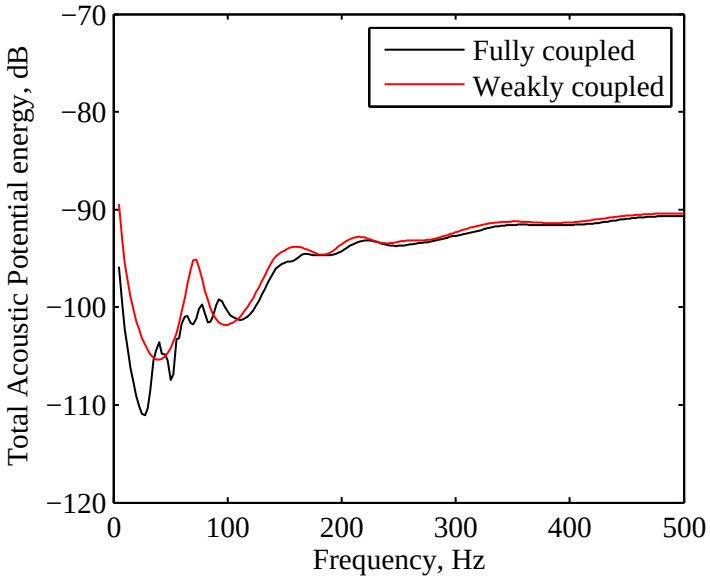

(a) Total acoustic potential energy.

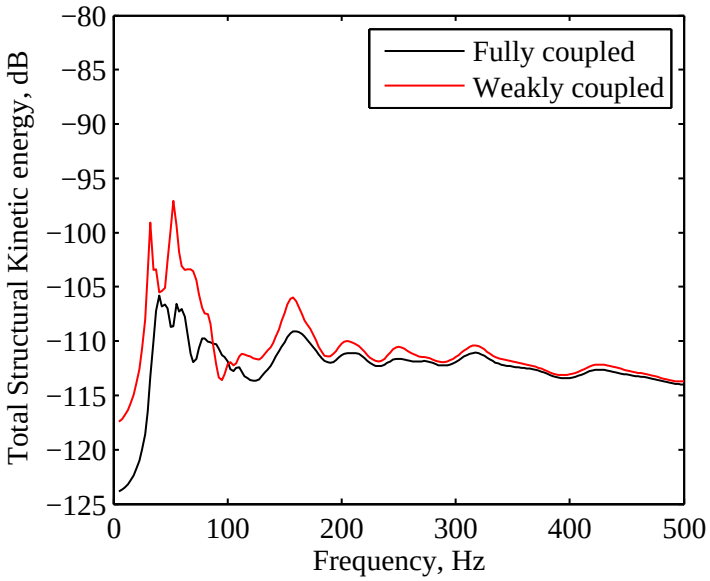

(b) Total structural kinetic energy.

Figure C.2: Simulated response of the acoustic enclosure with all non-rigid panels being flexible with clamped boundary conditions excited by a single acoustic monopole source with a volume velocity of 10^{-5} m^3s^{-1}.

Appendix D

Equipment Lists

D.1 Car Cabin Mock-up and Car Cabin Characterisation Measurements

D.1.1 General Setup

- Laptop running Matlab 2011a with data acquisition toolbox
- National Instruments cDAQ-9178, Compact DAQ 8-slot USB Chassis
- National Instruments 9263, 4-channel output module
- 4 $\times$ National Instruments 9234, 4-channel input module
- Power amplifier: HH Electronic VX-200 (serial no. SV2596)

D.1.2 Acoustic Response Measurement Setup

- Volume velocity source, constructed using KEF B110B SP1057 drivers (custom built enclosure)
- Direct radiator loudspeaker, constructed using KEF B110B SP1057 drivers (custom built enclosure)
- 16 Panasonic WM-063T electret condenser microphones
- 16 electret microphone pre-amplifiers (custom built)
- 1/4” Microphone calibrator

D.1.3 Structural Response Measurement Setup

- Shaker: Ling Dynamic System V201 (serial no. 54587.43)
- Shear Accelerometer: PCB Piezotronics A352C67 (serial no. 59258)

- Force sensor: PCB Piezotronics 208C01 (serial no.21963)
- Sensor signal conditioner: PCB Piezotronics Seriess 481 (serial no. SV3853)

D.2 Real-Time Feedforward Controller Implementation

D.2.1 Equipment List

- Laptop PC running Matlab/Simulink 2010a and DSpace control desk 3.6
- DSpace DS1103 system and break-out board
- 4 Panasonic WM-063T electret condenser microphones
- 4 electret microphone pre-amplifiers
- 1/4” Microphone calibrator
- 2 KEF B220-G loudspeakers mounted in 0.01 m^3 closed-back enclosures
- 1 KEF B300-B loudspeaker mounted in 0.026 m^3 closed-back enclosures
- 2 Behringer iNuke1000 Audio power amplifiers
- 8-channel low-pass filter box

D.3 Active Control of Sound Reproduction Implementation

- RME audio interface (16 input channels and 12 output channels)
- PC running adobe audition
- 16 Panasonic WM-063T electret condenser microphones
- 16 electret microphone pre-amplifiers
- 1/4” Microphone calibrator
- 4 KEF B220-G loudspeakers mounted in 0.01 m^3 closed-back enclosures
- 2 Behringer iNuke1000 Audio power amplifiers (4 channels)
- 8 phase-shift loudspeakers with Visaton SC 4.7 drivers
- 8 custom made class-D amplifiers

D.4 Equipment Specifications

D.4.1 Panasonic WM-063T Electret Condenser Microphones

- Dimensions: 6.0 × 5.0 mm
- Frequency range: 20 Hz – 20 kHz
- Sensitivity: -64 dB ± 3 dB re. 1V/Pa
- Omindirectional

D.4.2 Custom made low-pass filter box

The anti-aliasing filters have been custom made by the ISVR electronics workshop. The filters are first order low-pass filters with a cut-off frequency of 195 Hz – the circuit diagram is shown in Figure D.1.

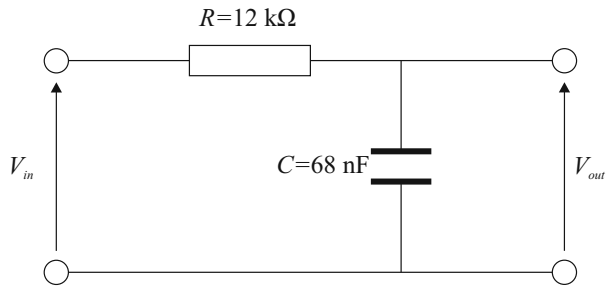

Figure D.1: First order low-pass filter employed as antialiasing filter

D.4.3 KEF B200-G Loudspeaker Data Sheet

KEF DATA SHEET

B200·G

Specification Number SP1075

Low/mid range unit with visco-elastic damped Bextrene diaphragm and high temperature coil assembly, suitable for use where low distortion and high power handling are required.

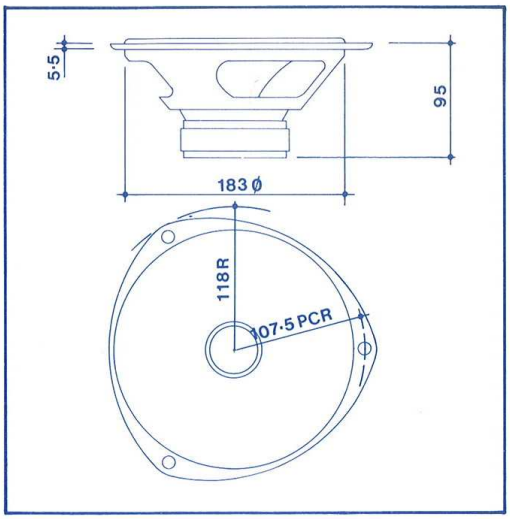

Net weight: 1.35 kg

Nominal impedance: 5 ohms

Nominal frequency range: 25-3,500 Hz

Typical enclosure volumes: Totally enclosed box 20-25 litres

Power handling:
Continuous sine wave 28 V RMS (see note 1)
Programme 150 W (see note 2)

Magnet:
Flux density 1.1 T (11,000 gauss)
Total flux 7.15 x 10^{-4}Wb (71,500 Maxwells)

Voice coil:
Diameter 32.6 mm
Inductance
Max continuous service temperature (30 min) 250°C
Max intermittent temperature (5 sec) 340°C
Nominal DC Resistance, R_{DC} 4.7 ohms (tolerance ± 5%)
Minimum impedance (in nominal frequence range) 5.3 ohms at 160 Hz

Diaphragm:
Effective area, S_D 246 cm²
Effective moving mass, M_D 24.3 g
Max linear excursion, X_D 6 mm peak-peak
Max damage limited excursion 20 mm peak-peak

Free air resonance frequency, f_s:
Nominal 27 Hz

Total mechanical resistance of suspension, R_{MS}:
1.38 mech ohms

Suspension compliance, C_{MS}: 1.4 x 10^{-3} m/N

Force factor, Bl: 6.82 N/A

Damping:
Mechanical Q_M: 3.03
Electrical Q_E: 0.42
Total Q_T: 0.37 (see note 3)

Notes

1 Continuous Power Rating (Pc).

$$Pc = \frac{V^2}{R}$$

V is the RMS voltage which can be applied to the unit continuously without thermal overload of the voice coil. At low frequencies the continuous power rating of the speaker may be reduced because of limitations imposed on diaphragm excursion by the acoustic loading.

2 The programme rating of a unit is equal to the maximum programme rating of any system with which the unit may be safely used in conjunction with the recommended dividing network and enclosure.
The programme rating of any system is the undistorted power output of an amplifier with which the system may be satisfactorily operated on normal programme over an extended period of time.

3 $$Q_M = \frac{2\pi f_S M_D}{R_{MS}} \qquad Q_E = \frac{2\pi f_S M_D}{(Bl)^2/R_{DC}} \qquad \frac{1}{Q_T} = \frac{1}{Q_M} + \frac{1}{Q_E}$$

D.4.4 KEF B300-B Loudspeaker Data Sheet

KEF DATA SHEET

B300·B

Specification Number SP1071

Low frequency unit with visco-elastic damped Bextrene diaphragm and high temperature coil assembly, suitable for use where low distortion and high power handling are required.

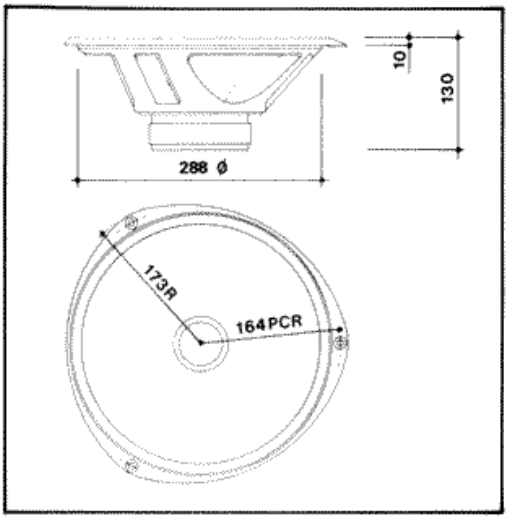

Net weight: 3.75 kg (8 lb 4 oz)

Nominal impedance: 8 ohms

Nominal frequency range: 25-2,000 Hz

Typical enclosure volumes:
Totally enclosed box 65-75 litres
Reflex 90-180 litres

Power handling:
Continuous sine wave 35 V RMS (see note 1)
Programme 200 W (see note 2)

Magnet:
Flux density 1.02 T (10,200 gauss)
Total flux 1.3 mWb (130 k Maxwells)

Voice coil:
Nominal diameter 52 mm
Nominal DC resistance, R_{DC} 6.9 ohms (tolerance ± 5%)
Minimum impedance 7.8 ohms at 120 Hz (in nominal frequency range)
Max continuous service temperature (30 min) 250°C
Max intermittent temperature (5 sec) 340°C

Diaphragm:
Effective area, S_D 520 cm²
Effective moving mass, M_D 73 gm
Max linear excursion, X_D 12 mm peak-peak
Max damage-limited excursion 25 mm peak-peak

Free air resonane frequency, f_s:
Nominal 23 Hz (tolerance ± 5 Hz)

Total mechanical resistance of suspension, R_{MS}:
2.0 mech ohms

Suspension compliance, C_{MS}: 6.6 x 10^{-4} m/N
Equivalent volume of compliance, V_{AS}: 250 litres
Force factor, Bl: 12 N/A

Damping:
Mechanical Q_M 5.3
Electrical Q_E 0.50
Total Q_T 0.46 (see note 3)

Notes

1 Continuous Power Rating (Pc).

$$P_C = \frac{V^2}{R}$$

V is the RMS voltage which can be applied to the unit continuously without thermal overload of the voice coil. At low frequencies the continuous power rating of the speaker may be reduced because of limitations imposed on diaphragm excursion by the acoustic loading.

2 The programme rating of a unit is equal to the maximum programme rating of any system with which the unit may be safely used in conjunction with the recommended dividing network and enclosure.
The programme rating of any system is the undistorted power output of an amplifier with which the system may be satisfactorily operated on normal programme over an extended period of time.

3 $$Q_M = \frac{2\pi f_S M_D}{R_{MS}} \qquad Q_E = \frac{2\pi f_S M_D}{(Bl)^2/R_{DC}} \qquad \frac{1}{Q_T} = \frac{1}{Q_M} + \frac{1}{Q_E}$$

D.4.5 Visaton SC 4.7 Loudspeaker Data Sheet

Table D.1: Visaton SC 4.7 Technical Data [192].

Rated Power	2 W
Maximum Power	4 W
Nominal Impedance	8 Ohm
Frequency response	220 - 20000 Hz
Mean SPL	81 dB (1 W/1 m)
Excursion limit	$\pm$0.5 m
Resonance frequency	420 Hz
Magnetic induction	0.7 T
Magnetic flux	60μWb
Voice coil diameter	14 mm
Height of winding	2 mm
D.C. resistance	7.5 Ohm
Mechanical Q factor	4.92
Electrical Q factor	8.18
Equivalent volume	0.9 l
Effective piston area	45 cm^2
Dynamically moving mass	0.7 g
Force factor	1.2 Tm
Voice coil inductance	0.3 mH

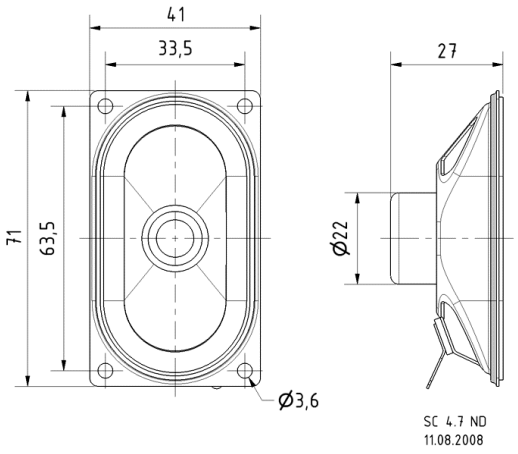

Figure D.2: The dimensions of the Visaton SC 4.7 loudspeaker driver (reproduced from [192]).

Appendix E

Loudspeaker Model

The force, F, produced by a moving coil loudspeaker is related to the input current via the transduction coefficient, ϕ, that is,

$$F = \phi i, \tag{E.1}$$

where i is the current input to the loudspeaker, which is determined by the feedback controller. Assuming that the loudspeaker is current controlled the velocity, u, can be related to the current via the mechanical impedance Z_m:

$$u = \frac{F}{Z_m} = \frac{\phi i}{Z_m}. \tag{E.2}$$

It then follows that the volume velocity per unit current, Y_L, is given by,

$$Y_L = \frac{\phi A_d}{Z_m}, \tag{E.3}$$

where A_d is the area of the diaphragm and the mechanical impedance is given by,

$$Z_m = \frac{S}{\mathrm{j}\omega} + r + \mathrm{j}\omega\mathrm{m} \tag{E.4}$$

where S is the loudspeaker's stiffness, r is the mechanical damping of the loudspeaker, and m is the loudspeaker's moving mass. Therefore, equation E.3 can be written as,

$$Y_L = \frac{\mathrm{j}\omega\phi\mathrm{A_d}}{S(1 + \mathrm{j}2\zeta_\mathrm{L}\frac{\omega}{\omega_\mathrm{n}} - (\frac{\omega}{\omega_\mathrm{n}})^2)} \tag{E.5}$$

where ζ_L is the damping ratio of the loudspeaker. This loudspeaker response is shown in Figure E.1 for the loudspeaker properties detailed in Table E.1. Due to the phase response associated with the loudspeaker system it is necessary to design the loudspeaker's response in order to optimise the control that is achievable within the specified enclosure. The resonance frequency of 50 Hz has been chosen in order to optimise the system's global performance for a rigid walled enclosure with the dimensions and source and sensor positions shown in Figure 4.1; that is, as shown in Figure E.2, the total acoustic potential energy at the first longitudinal mode

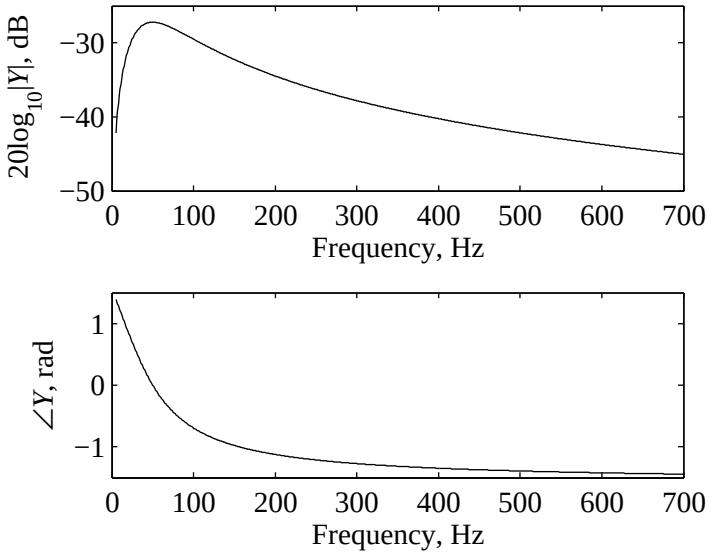

Figure E.1: Frequency response of the second-order SDOF loudspeaker model.

Table E.1: SDOF loudspeaker model properties

f_n	50 Hz
ζ_L	0.9
S	700 Nm^{-1}
ϕ	0.17 N/A
A_d	2.5×10^{-2}

(72 Hz) is minimised when the loudspeaker's natural frequency is chosen to be 50 Hz.

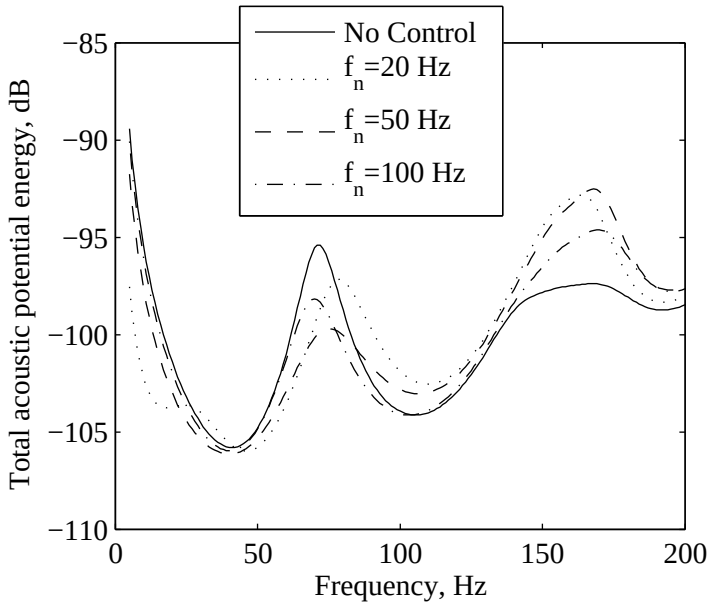

Figure E.2: The total acoustic potential energy within the rigid walled enclosure when minimised using an error sensor positioned at $\boldsymbol{x}_0 = [0, 0, L_3]$ and a secondary source positioned at $\boldsymbol{x}_{s1} = [L_1/4, 0, L_3/4]$ with differing loudspeaker natural resonances.

Appendix F

Multi-Input, Multi-Output Robust Stability

The stability of a multichannel feedback system can be determined based on a generalisation of the Nyquist criterion, which is discussed in the context of SISO systems in Section 4.3.1. The multichannel generalisation of the Nyquist criterion states that the closed-loop system will be stable provided that the locus of the function

$$\det\left[\boldsymbol{I}+\boldsymbol{G}(\mathrm{j}\omega)\boldsymbol{H}(\mathrm{j}\omega)\right], \tag{F.1}$$

does not encircle the origin [132]. However, due to the potential complexity of a multichannel system it is often difficult to predict the effect of gain changes in all of the elements of the controller matrix on the shape of the locus and, therefore, a reliable guide to the relative stability of the system is not provided [132].

A simpler guide to the relative stability of the multichannel feedback system can be obtained by expanding equation F.1 as [132]

$$\det\left[\boldsymbol{I}+\boldsymbol{G}(\mathrm{j}\omega)\boldsymbol{H}(\mathrm{j}\omega)\right]=\left[1+\lambda_1(\mathrm{j}\omega)\right]\left[1+\lambda_2(\mathrm{j}\omega)\right]\cdots \tag{F.2}$$

where $\lambda_i(j\omega)$ are the eigenvalues of the $\boldsymbol{G}(j\omega)\boldsymbol{H}(j\omega)$ matrix. The stability of the closed-loop system can be guaranteed by ensuring that the loci of the eigenvalues, termed *characteristic loci*, do not encircle the $(-1,0)$ point. Despite this simple stability condition, the concepts of gain and phase margin, and therefore robust stability with respect to SISO systems, do not translate directly to the multichannel case unless there is a simultaneous change in the gain and phase of every element of the plant response matrix [154]. In general this limits the practical usefulness of equation F.2, even though it has been shown by Serrand and Elliott [193] that in a particular example of a simple two channel vibration isolation system the eigenvalues of the open-loop response may be related to the heave and pitching modes of the beam structure.

An alternative condition for multichannel stability is the small-gain theorem, which states that if the largest singular value of the plant matrix multiplied by largest singular value of

controller matrix is less than unity at all frequencies then the multichannel feedback system will be stable [132]. This can be expressed as

$$\bar{\sigma}[\boldsymbol{G}(j\omega)]\,\bar{\sigma}[\boldsymbol{H}(j\omega)] < 1 \qquad \forall\omega, \tag{F.3}$$

where $\bar{\sigma}[\cdots]$ indicates the maximum singular value of the associated matrix. In general this gives an overly restrictive condition for stability, but it is useful in defining robust stability constraints for the mutichannel system below [132].

The condition for robust stability in a multichannel feedback control system is significantly more complex than for the SISO case [154, 132]. In a SISO system, plant uncertainty from multiple sources can be lumped together into a single perturbation [154]. However, in a MIMO system, the effects of input and output perturbations are different and, therefore, cannot always be combined to provide a simple description of the plant uncertainty [154]. This will be shown following the derivation in [132], however, an equivalent formulation can also be found in [154] and both of these are based on work presented in [194].

A multiplicative input uncertainty can be described as

$$\boldsymbol{G}(j\omega) = \boldsymbol{G}_0(j\omega)\,[\boldsymbol{I} + \boldsymbol{\Delta}_I(j\omega)]\,, \tag{F.4}$$

where $\boldsymbol{G}_0(j\omega)$ is the matrix of nominal plant responses and $\boldsymbol{\Delta}_I(j\omega)$ is the multiplicative input uncertainty. This form of uncertainty may be produced, for example, by variations in the positions of the control sources [132]. A multiplicative output uncertainty can be described as

$$\boldsymbol{G}(j\omega) = [\boldsymbol{I} + \boldsymbol{\Delta}_O(j\omega)]\,\boldsymbol{G}_0(j\omega), \tag{F.5}$$

where $\boldsymbol{\Delta}_O(j\omega)$ is the multiplicative output uncertainty. This form of uncertainty may be produced, for example, by variations in the positions of the error sensors [132]. It is helpful, as in the SISO case, to define an upper bound on the magnitude of the plant uncertainties and this may be calculated for the multiplicative input and output uncertainties respectively as

$$\bar{\sigma}[\boldsymbol{\Delta}_I(j\omega)] \leqslant B_I(j\omega), \tag{F.6}$$

$$\bar{\sigma}[\boldsymbol{\Delta}_O(j\omega)] \leqslant B_O(j\omega), \tag{F.7}$$

where B_I and B_O are the bounds on the magnitude of the input and output uncertainties respectively. If it is assumed that the plant has an equal number of inputs and outputs, then the input and output uncertainties can be written by rearranging equations F.4 and F.5 as

$$\boldsymbol{\Delta}_I(j\omega) = \boldsymbol{G}_0(j\omega)^{-1}\,[\boldsymbol{G}(j\omega) - \boldsymbol{G}_0(j\omega)]\,, \tag{F.8}$$

$$\boldsymbol{\Delta}_O(j\omega) = [\boldsymbol{G}(j\omega) - \boldsymbol{G}_0(j\omega)]\,\boldsymbol{G}_0(j\omega)^{-1}. \tag{F.9}$$

The output uncertainty can then be rewritten in terms of the input uncertainty to give

$$\boldsymbol{\Delta}_O(j\omega) = \boldsymbol{G}(j\omega)\boldsymbol{\Delta}_I\boldsymbol{G}(j\omega)^{-1}. \tag{F.10}$$

Taking the maximum singular value, or 2-norm of equation F.10 and using the property of the 2-norm that $\bar{\sigma}[\boldsymbol{AB}] \leqslant \bar{\sigma}[\boldsymbol{A}]\,\bar{\sigma}[\boldsymbol{B}]$ gives an indication of the relative sizes of the input and output uncertainties

$$\bar{\sigma}[\boldsymbol{\Delta}_O(j\omega)] \leqslant \bar{\sigma}[\boldsymbol{G}(j\omega)]\,\bar{\sigma}[\boldsymbol{\Delta}_I]\,\bar{\sigma}\left[\boldsymbol{G}(j\omega)^{-1}\right]. \tag{F.11}$$

The condition number of a matrix is given by the ratio of its largest to its smallest singular values and, therefore, equation F.11 can be rewritten in terms of the condition number of the nominal plant matrix as

$$\bar{\sigma}[\boldsymbol{\Delta}_O(j\omega)] \leqslant \kappa[\boldsymbol{G}_0(j\omega)]\,\bar{\sigma}[\boldsymbol{\Delta}_I], \tag{F.12}$$

where $\kappa[\boldsymbol{G}_0(j\omega)]$ is the condition number of the nominal plant. Since the largest singular values of the input and output uncertainties are governed by equations F.8 and F.9, equation F.12 can be written for the maximum uncertainty in both input and output as

$$B_O(j\omega) \leqslant \kappa[\boldsymbol{G}_0(j\omega)]\,B_I(j\omega). \tag{F.13}$$

From this it can be seen that if an input uncertainty were modelled as an output uncertainty, then for a plant with a large condition number the bound on the output uncertainty would have to be much higher than the original input uncertainty. For this reason it is not reliable to lump input and output uncertainties, particularly when the plant condition number is large [154]. To achieve a reliable bound on the multiplicative uncertainty of a multichannel plant it is, therefore, necessary to model the plant uncertainty where it physically occurs [132, 154].

Despite the highlighted problems of lumping input and output uncertainty in a multichannel system, it is convenient to assume that the plant uncertainty can be modelled as output uncertainty. In the simulation scenario any plant uncertainty is artificially defined and, therefore, defining the multichannel plant uncertainty as output uncertainty looses no generality, but does allow a convenient condition for robust stability. The condition for robust stability in the case of unstructured output uncertainty is given as [132]

$$\bar{\sigma}[\boldsymbol{T}_0(j\omega)] < \frac{1}{B(j\omega)} \qquad \forall\omega, \tag{F.14}$$

where $\boldsymbol{T}_0(j\omega)$ is the multichannel complementary sensitivity function of the nominal plant and is given by

$$\boldsymbol{T}_0(j\omega) = [\boldsymbol{I} + \boldsymbol{G}_0(j\omega)\boldsymbol{H}(j\omega)]^{-1}\boldsymbol{G}_0(j\omega)\boldsymbol{H}(j\omega). \tag{F.15}$$

Appendix G

Multi-Modal Controller Formulation

In Chapter 4 a multi-source, multi-sensor, single mode feedback control system has been defined and its performance has been investigated. In many practical applications there may be a need for a higher-order controller that can control multiple modes. For example, it has been shown in Chapter 6.3 through offline simulations of a fully MIMO feedback controller that it is possible to achieve significant levels of global control of road noise in a car cabin using the error sensors and loudspeakers already provided for a feedforward engine noise controller. However, the practical implementation of this multichannel feedback controller is potentially difficult to achieve due to the computational requirements and the need for a high sampling rate, as discussed in Chapter 6. The computational requirements of the multichannel system may be reduced by employing a multi-modal feedback control system and, therefore, providing a compromise between the fully multichannel feedback controller and the single mode controller. The equations governing a multi-modal feedback control system will, therefore, be presented in order to support future work in this area.

A block diagram of the multi-sensor, multi-source, multi-modal feedback control system is presented in Figure G.1. The feedback control system consists of M loudspeakers and L_e discrete error sensors and may be used to control N_T targeted acoustic modes. An $(N_T \times 1)$ vector of composite error signals, $\boldsymbol{p}_c$, is generated through the weighted summation of the signals from the L_e discrete error microphones. This weighted summation is implemented via the $(L_e \times N_T)$ matrix of real, frequency independent, error sensor weightings, $\boldsymbol{W}_L$, and can be expressed in terms of the $(L_e \times 1)$ vector of pressures at the error sensors, $\boldsymbol{p}_e$, as

$$\boldsymbol{p}_c = \boldsymbol{W}_L^T \boldsymbol{p}_e, \tag{G.1}$$

where ^{T} denotes the matrix transpose and the vector of pressures at the error sensors is given by the summation of the $(L_e \times 1)$ vectors of pressures due to the primary disturbance, $\boldsymbol{p}_p$, and the control, or secondary sources, $\boldsymbol{p}_s$, so that

$$\boldsymbol{p}_e = \boldsymbol{p}_p + \boldsymbol{p}_s. \tag{G.2}$$

The composite error signal, $\boldsymbol{p}_c$, is filtered by the $(N_T \times N_T)$ negative feedback controller matrix, $-\boldsymbol{H}$, to give the vector of composite secondary source strengths

$$\boldsymbol{q}_c = -\boldsymbol{H}\boldsymbol{p}_c. \tag{G.3}$$

The composite source strengths are then sent to the M loudspeakers, or secondary sources, via the $(M \times N_T)$ matrix of real, frequency independent source weightings, $\boldsymbol{W}_M$, which gives the vector of secondary source strengths as

$$\boldsymbol{q}_s = \boldsymbol{Y}_L \boldsymbol{W}_M \boldsymbol{q}_c, \tag{G.4}$$

where $\boldsymbol{Y}_L$ is the matrix of volume velocity produced per unit input current to the control loudspeakers. The secondary source strengths are related to the vector of pressures due to the secondary sources, $\boldsymbol{p}_s$, via the $(L_e \times M)$ matrix of acoustic transfer impedances between the secondary sources and the error sensors, $\boldsymbol{Z}_s$, and thus equation 4.2 can be expanded to give,

$$\boldsymbol{p}_e = \boldsymbol{p}_p + \boldsymbol{Z}_s \boldsymbol{q}_s. \tag{G.5}$$

Substituting equations 4.1, 4.3 and 4.4 into equation 4.5 and rearranging gives the vector of error sensor pressures as

$$\boldsymbol{p}_e = \left[\boldsymbol{I} + \boldsymbol{Y}_L \boldsymbol{Z}_s \boldsymbol{W}_M \boldsymbol{H} \boldsymbol{W}_L^T\right]^{-1} \boldsymbol{p}_p, \tag{G.6}$$

where $\boldsymbol{I}$ is an $(L_e \times L_e)$ identity matrix. The $(L \times L)$ matrix sensitivity function of the L_e input, M output feedback controller is given by

$$\boldsymbol{S} = \left[\boldsymbol{I} + \boldsymbol{Y}_L \boldsymbol{Z}_s \boldsymbol{W}_M \boldsymbol{H} \boldsymbol{W}_L^T\right]^{-1}, \tag{G.7}$$

and the open-loop response is given by

$$\boldsymbol{Y}_L \boldsymbol{Z}_s \boldsymbol{W}_M \boldsymbol{H} \boldsymbol{W}_L^T, \tag{G.8}$$

where the M input, L_e output plant response is given by $\boldsymbol{G} = \boldsymbol{Y}_L \boldsymbol{Z}_s$ and the L_e input, M output controller response is given by $\boldsymbol{W}_M \boldsymbol{H} \boldsymbol{W}_L^T$. However, substituting equations 4.3, 4.4 and 4.5 into equation 4.1 gives the composite error signal as

$$\boldsymbol{p}_c = \left[\boldsymbol{I} + \boldsymbol{Y}_L \boldsymbol{W}_L^T \boldsymbol{Z}_s \boldsymbol{W}_M \boldsymbol{H}\right]^{-1} \boldsymbol{W}_L^T \boldsymbol{p}_p, \tag{G.9}$$

where $\boldsymbol{I}$ is an $(N_T \times N_T)$ identity matrix in this case, and the $(N_T \times N_T)$ matrix sensitivity function of the composite system is given as

$$\boldsymbol{S}_c = \left[\boldsymbol{I} + \boldsymbol{Y}_L \boldsymbol{W}_L^T \boldsymbol{Z}_s \boldsymbol{W}_M \boldsymbol{H}\right]^{-1}. \tag{G.10}$$

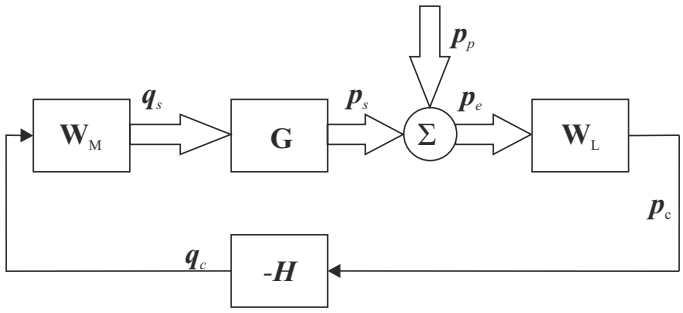

Figure G.1: Block diagram of the multi-source, multi-sensor, multi-modal feedback control system.

The open-loop response of the composite system is given by

$$\boldsymbol{Y}_L \boldsymbol{W}_L^T \boldsymbol{Z}_s \boldsymbol{W}_M \boldsymbol{H}, \tag{G.11}$$

where the N_T input, N_T output composite plant is given by $\boldsymbol{Y}_L \boldsymbol{W}_L^T \boldsymbol{Z}_s \boldsymbol{W}_M$ and the controller response is simply given by $\boldsymbol{H}$.

Appendix H

Alternative Modal Controller Design Strategy

H.1 Spatial Filtering

In a rigid walled, rectangular enclosure the selection of the transducer weightings is relatively straightforward, as described in Section 4.1 with reference to Figure 4.5. However, in a more complex system such as the car cabin or even the non-rigid walled enclosure investigated in Chapter 2, the process of selecting the transducer weightings is not so straightforward due to the potentially complex characteristics of the acoustic mode shapes. As detailed in Section 4.1, previous work on acoustic modal control has overcome this problem by defining the sensor weightings for a given acoustic mode as the real part of the acoustic transfer response between the error sensors and an arbitrarily positioned loudspeaker at the frequency of the targeted mode [146]. In the system presented in [146], due to the use of approximately collocated sources and sensors, the source weightings are then set equal to the associated sensor weightings.

For the modal feedback control system described in Chapter 4, the error sensors and secondary sources are not collocated in order to allow integration with a feedforward engine noise control system. Therefore, it is not possible to simply set the source weightings equal to the sensor weightings as in [146]. The systematic weighting method proposed by Lane *et al* [146] can be extended to the non-collocated source-sensor system by defining the source weightings for a given acoustic mode as the real part of the transfer response between each of the secondary sources and a sensor collocated with the arbitrarily positioned source at the frequency of the targeted mode. Although this method of defining the transducer weightings may be effective, it is in fact sensitive to the position of the collocated source and sensor used in the weighting calculation. For example, if the transducer pair was positioned on the nodal line of the targeted mode then the resulting transducer weightings would be subject to random variability due to the low coupling between the transducers and the targeted mode and the consequent potential dominance of noise in a measured value. This presents the worst case scenario and could be avoided by sensible source-sensor positioning. For example, in the rectangular enclosure,

which has been investigated in Chapter 2, if the source-sensor pair were positioned in the corner of the enclosure then this effect would be avoided for a significant number of modes and, in particular, the low frequency modes that could be targeted with an active control system.

Although it is possible to use an extension of the transducer weighting method proposed by Lane *et al* [146], this method requires the measurement of at least an additional set of transfer responses compared to the plant identification already required. In a complex acoustic enclosure such as the car cabin, it may also be difficult to chose an appropriate location for the collocated source-sensor pair and, therefore, an alternative method of systematically selecting the transducer weightings when disturbance rejection is required over a specific frequency range will be presented. An earlier version of this work has been presented in [159].

The aim of the transducer weightings is to ensure that the sensitivity function is small at frequencies where disturbance rejection is required and close to unity at all other frequencies. That is, the spatial filtering should produce a distributed array that is sensitive at frequencies where disturbance rejection is required and insensitive at all other frequencies. From equation 4.11 it can be seen that to achieve a sensitivity function that meets these requirements it is necessary to maximise the open-loop response over the targeted frequency range whilst minimising it elsewhere. The open-loop response for the single mode controller is given by

$$\begin{aligned} G(j\omega)H(j\omega) &= Y_L(j\omega)\boldsymbol{w}_L^T\boldsymbol{Z}_s(j\omega)\boldsymbol{w}_M H(j\omega) \\ &= \boldsymbol{w}_L^T\boldsymbol{G}(j\omega)\boldsymbol{w}_M H(j\omega), \end{aligned} \tag{H.1}$$

where $\boldsymbol{G(j\omega)} = Y_L(j\omega)\boldsymbol{Z}_s(j\omega)$.

H.1.1 Source Weighting Optimisation

Based on the desired characteristics of the open-loop response, one method of defining the source weightings is to maximise the response between the composite source strength and the pressure produced at the error sensors by the secondary sources over the targeted frequency range, whilst minimising this response at all other frequencies. The response between the composite source strength and the pressure produced at the error sensors for a single mode controller is given by

$$\frac{\boldsymbol{p}_s(j\omega)}{q_c(j\omega)} = \boldsymbol{G}(j\omega)\boldsymbol{w}_M, \tag{H.2}$$

and the definition of the source weightings can be achieved by maximising the ratio

$$\frac{\sum_{f=f_1}^{f_2}\boldsymbol{w}_M^T\boldsymbol{G}^H(j\omega_f)\boldsymbol{G}(j\omega_f)\boldsymbol{w}_M}{\sum_{f=0}^{f_1-1}\boldsymbol{w}_M^T\boldsymbol{G}^H(j\omega_f)\boldsymbol{G}(j\omega_f)\boldsymbol{w}_M + \sum_{f=f_2+1}^{N_f}\boldsymbol{w}_M^T\boldsymbol{G}^H(j\omega_f)\boldsymbol{G}(j\omega_f)\boldsymbol{w}_M}, \tag{H.3}$$

where a total of N_f discrete frequencies are considered and f_1 and f_2 are the lower and upper bounds of the acoustic mode targeted for disturbance rejection. The maximisation of the ratio

given by equation H.3 can be cast as a constrained optimisation problem where the aim is to

$$\text{maximise: } \sum_{f=f_1}^{f_2} \boldsymbol{w}_M^T \boldsymbol{G}^H(j\omega_f)\boldsymbol{G}(j\omega_f)\boldsymbol{w}_M, \tag{H.4}$$

$$\text{subject to: } \sum_{f=0}^{f_1-1} \boldsymbol{w}_M^T \boldsymbol{G}^H(j\omega_f)\boldsymbol{G}(j\omega_f)\boldsymbol{w}_M + \sum_{f=f_2+1}^{N_f} \boldsymbol{w}_M^T \boldsymbol{G}^H(j\omega_f)\boldsymbol{G}(j\omega_f)\boldsymbol{w}_M = c, \tag{H.5}$$

where c is a constant. Defining the summation over the targeted and rejected bandwidths as

$$\boldsymbol{T}_M = \sum_{f=f_1}^{f_2} \boldsymbol{G}^H(j\omega_f)\boldsymbol{G}(j\omega_f), \tag{H.6}$$

and

$$\boldsymbol{R}_M = \sum_{f=0}^{f_1-1} \boldsymbol{G}^H(j\omega_f)\boldsymbol{G}(j\omega_f) + \sum_{f=f_2+1}^{N_f} \boldsymbol{G}^H(j\omega_f)\boldsymbol{G}(j\omega_f), \tag{H.7}$$

allows this optimisation to be written more concisely. The cost function to be maximised can be expressed using the method of Lagrange multipliers as [177]

$$J_M = \boldsymbol{w}_M^T \boldsymbol{T}_M \boldsymbol{w}_M + \lambda\left(\boldsymbol{w}_M^T \boldsymbol{R}_M \boldsymbol{w}_M - c\right), \tag{H.8}$$

where λ is the real positive Lagrange multiplier. Since the source weightings are constrained to be real, it can be shown that the cost function to be maximised is [195]

$$J_M = \boldsymbol{w}_M^T \Re\{\boldsymbol{T}_M\}\boldsymbol{w}_M + \lambda\left(\boldsymbol{w}_M^T \Re\{\boldsymbol{R}_M\}\boldsymbol{w}_M - c\right). \tag{H.9}$$

Differentiating this cost function with respect to $\boldsymbol{w}_M$, equating to zero and rearranging gives

$$\boldsymbol{w}_M = -\lambda \Re\{\boldsymbol{T}_M\}^{-1} \Re\{\boldsymbol{R}_M\}\boldsymbol{w}_M. \tag{H.10}$$

To maximise the cost function, J_M, the vector of source weightings must thus be the eigenvector of the matrix $\Re\{\boldsymbol{T}_M\}^{-1}\Re\{\boldsymbol{R}_M\}$ corresponding to its largest eigenvalue.

H.1.2 Sensor Weighting Optimisation

The sensor weightings can be defined using a similar approach to the method used to define the source weightings. In this case, however, the weightings are defined to maximise the response between the composite source strength and the composite pressure due to the secondary sources over the targeted frequency range, whilst minimising this response at all other frequencies. The response between the composite source strength and the composite pressure due to the secondary sources for a single mode controller is given by

$$\frac{p_{c_s}(j\omega)}{q_c(j\omega)} = \boldsymbol{w}_L^T \boldsymbol{G}(j\omega)\boldsymbol{w}_M, \tag{H.11}$$

and the optimisation of the source weightings can be achieved by maximising the ratio

$$\frac{\sum_{f=f_1}^{f_2} \boldsymbol{w}_L^T \boldsymbol{G}(j\omega_f)\boldsymbol{w}_M \boldsymbol{w}_M^T \boldsymbol{G}^H(j\omega_f)\boldsymbol{w}_L}{\sum_{f=0}^{f_1-1} \boldsymbol{w}_L^T \boldsymbol{G}(j\omega_f)\boldsymbol{w}_M \boldsymbol{w}_M^T \boldsymbol{G}^H(j\omega_f)\boldsymbol{w}_L + \sum_{f=f_2+1}^{N_f} \boldsymbol{w}_L^T \boldsymbol{G}(j\omega_f)\boldsymbol{w}_M \boldsymbol{w}_M^T \boldsymbol{G}^H(j\omega_f)\boldsymbol{w}_L}, \tag{H.12}$$

where the source weightings, $\boldsymbol{w}_M$, have been pre-defined according to equation H.10. Defining the summation over the targeted and rejected bandwidths as

$$\boldsymbol{T}_L = \sum_{f=f_1}^{f_2} \boldsymbol{G}(j\omega_f)\boldsymbol{w}_M \boldsymbol{w}_M^T \boldsymbol{G}^H(j\omega_f), \tag{H.13}$$

and

$$\boldsymbol{R}_L = \sum_{f=0}^{f_1-1} \boldsymbol{G}(j\omega_f)\boldsymbol{w}_M \boldsymbol{w}_M^T \boldsymbol{G}^H(j\omega_f) + \sum_{f=f_2+1}^{N_f} \boldsymbol{G}(j\omega_f)\boldsymbol{w}_M \boldsymbol{w}_M^T \boldsymbol{G}^H(j\omega_f), \tag{H.14}$$

and following the method used in the optimisation of the source weightings gives the cost function to be maximised as

$$J_L = \boldsymbol{w}_L^T \boldsymbol{T}_L \boldsymbol{w}_L + \lambda \left(\boldsymbol{w}_L^T \boldsymbol{R}_L \boldsymbol{w}_L - c \right), \tag{H.15}$$

where λ is again the real positive Lagrange multiplier. Since the sensor weightings are constrained to be real, it can be shown that the cost function to be maximised is [195]

$$J_L = \boldsymbol{w}_L^T \Re\{\boldsymbol{T}_L\} \boldsymbol{w}_L + \lambda \left(\boldsymbol{w}_L^T \Re\{\boldsymbol{R}_L\} \boldsymbol{w}_L - c \right). \tag{H.16}$$

Differentiating this cost function with respect to $\boldsymbol{w}_L$, equating to zero and rearranging gives

$$\boldsymbol{w}_L = -\lambda \Re\{\boldsymbol{T}_L\}^{-1} \Re\{\boldsymbol{R}_L\} \boldsymbol{w}_L. \tag{H.17}$$

To maximise the cost function, J_L, the vector of sensor weightings must thus be the eigenvector of the matrix $\Re\{\boldsymbol{T}_L\}^{-1}\Re\{\boldsymbol{R}_L\}$ corresponding to its largest eigenvalue.

H.1.3 Discussion

The proposed approach to defining the transducer weightings, although computationally undemanding compared to the method presented in Chapter 4, has a number of potential limitations. Firstly, the definition of the source and sensor weightings requires two separate stages and, therefore, does not necessarily provide the optimal set of transducer weightings. The proposed approach is also only capable of defining the weightings for a single mode, single channel system. In order to use this method to calculate the transducer weightings for a multi-mode controller, where the transducer weightings are matrices, $\boldsymbol{W}_M$ and $\boldsymbol{W}_L$, the weighting vectors for each individual mode must be set independently and then combined to form the required matrices. This approach assumes that the interactions between the modes in a multi-mode control system are negligible. This would only be the case in a system with low modal density and

damping and, therefore, this method does not guarantee an optimal solution in the majority of practical problems. Despite the potential limitations of the proposed method of optimising the spatial filtering, it does provide a computationally efficient and systematic method of defining the transducer weightings and, therefore, it has been included here for reference. The application of this method to the road noise control problem has been employed in [159], however, it is shown that the performance is limited due to the multiple resonances present in the road noise control problem.

Appendix I

Simulink Feedforward Controller Implementation

In Chapter 6 the design and performance of the feedforward first engine order controller have been presented. This appendix provides additional details of the Simulink implementation of the controller.

I.1 Feedforward Controller

Figure I.1 shows the main block diagram of the feedforward controller implemented in Simulink. The inputs to the controller are shown by the blocks labelled *ADC TACHO* and *ADC Error 1*, which relate to the tachometer input signal and the four error microphone signals respectively. The three outputs from the controller are shown by the three blocks on the right-hand side labelled *DAC 1, 2* and *3*. Inputs to the controller are all multiplied by a factor of 10 and the outputs are multiplied by a factor of $1/10$, which is related to the operation of the DS1103 processor board.

The tachometer input can be seen at the top left hand side of the block diagram and this is connected to *Tacho_Processing* block, which calculates the frequency of the first engine order and the contents of this block are shown in more detail in Figure I.2 and discussed in Section I.2. The frequency of the first engine order is used to produce the in-phase and quadrature reference signals, using the *sin* and *cos* blocks. The frequency of the first engine order is also sent to the block labelled *alpha_scheduling*, which calculates the current value of the convergence coefficient, $\alpha(n)$, based on the multiplication of the frequency independent value of α_g, given in the block diagram by the block labelled *alpha*, and the frequency dependent convergence coefficient α_f, which is determined from a look-up table within the *alpha_scheduling* block.

The generated reference signals are sent along with the four error microphone signals to the two blocks labelled *Acoustic_LMS* and *Acoustic_LMS1*, which implement the adaptive LMS filters whose operation is described in the first subsection of Section 6.2.2. The details of these two blocks are shown in Figure I.3 and briefly discussed in Section I.3.

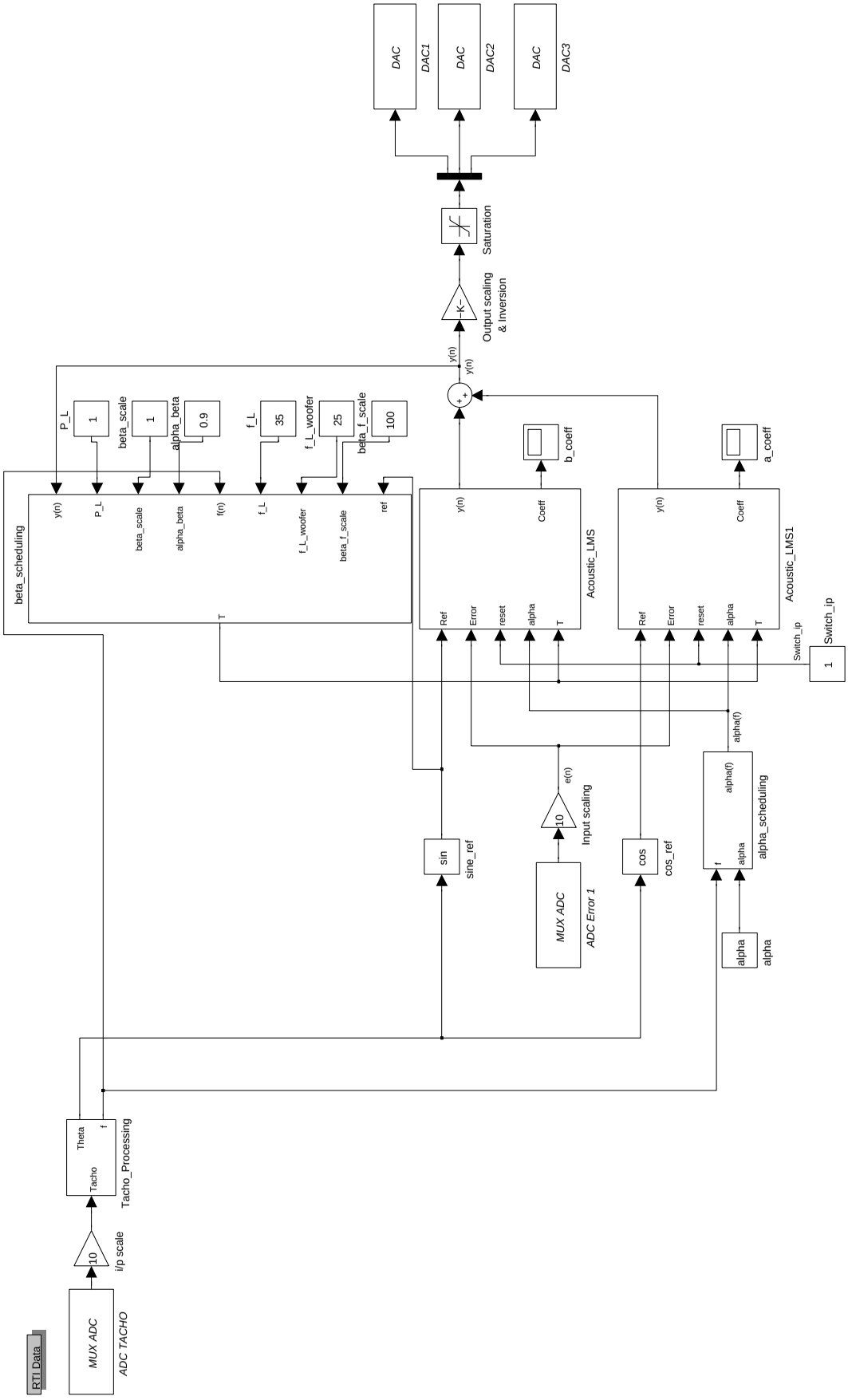

Figure I.1: The multi-input, multi-output first engine order feedforward controller implementation in Simulink.

The outputs of the LMS blocks are summed to form the complete control signals and these are sent to the outputs via a saturation block, which provides protection to the loudspeakers and amplifiers in the case of controller instability. The control signal is also sent to the *beta_scheduling* block, which calculates the control effort weighting parameters. The detailed contents of this block are provided in Figures I.4 and I.5.

I.2 Tacho reference signal processing

The tachometer signal processing block is presented in Figure I.2. This block receives the unprocessed tachometer signal, which is a once-per-rev pulse, and calculates the frequency of the first engine order. The first three blocks on the left of the block diagram take the unprocessed tachometer signal and remove noise that may produce false triggering by outputting a signal from the switch which is either zero or one. The *Edge Detector* block receives this signal and outputs an impulse for each positive going transition. The *Counter* block then counts the number of samples between consecutive pulses to give an instantaneous estimate of the period measured in samples. The next three blocks, which consist of two sample and hold blocks for the current and previous counter values and an *Error stopper* block, remove any significant variations in the estimated period. That is, if the current period is either unrealistically larger or smaller than the previous period then it is assumed that a false trigger or missed trigger has occured and the algorithm maintains the previous period estimate for an additional iteration. The following group of blocks implement a moving average filter which ensures unrealistic rapid variations in the estimate do not occur. The divide block the calculates the frequency of the first engine order and this is the second output of the *Tacho_Processing* block. To calculate the in-phase and quadrature reference signals it is necessary to calculate the angle of the reference signal, which depends on the rate of change of the engine speed rather than simply its instantaneous frequency. This is calculation is performed by the remaining blocks including the *Running Sum* block.

I.3 Least Mean Squares Adaptive Filters

The LMS adaptive filter block is presented in Figure I.3. The operation of the LMS adaptive filter is detailed in Section 6.2.2. It is helpful to highlight the main elements of the algorithm implemented in Simulink. The four main inputs to this block are the reference signal, the vector of error signals, the convergence coefficient and the control effort weighting parameter. The reference signal is filtered by the *Plant Model* block to produce the matrix of reference signals, the rest of the operation is described in conjunction with the work presented in Section 6.2.2.

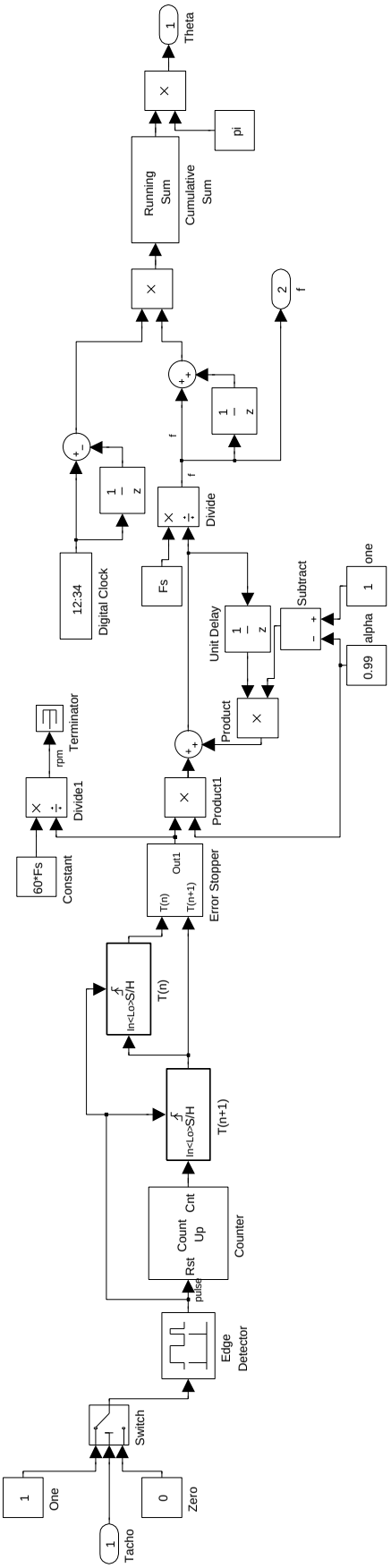

Figure I.2: Tacho signal processing implementation in Simulink.

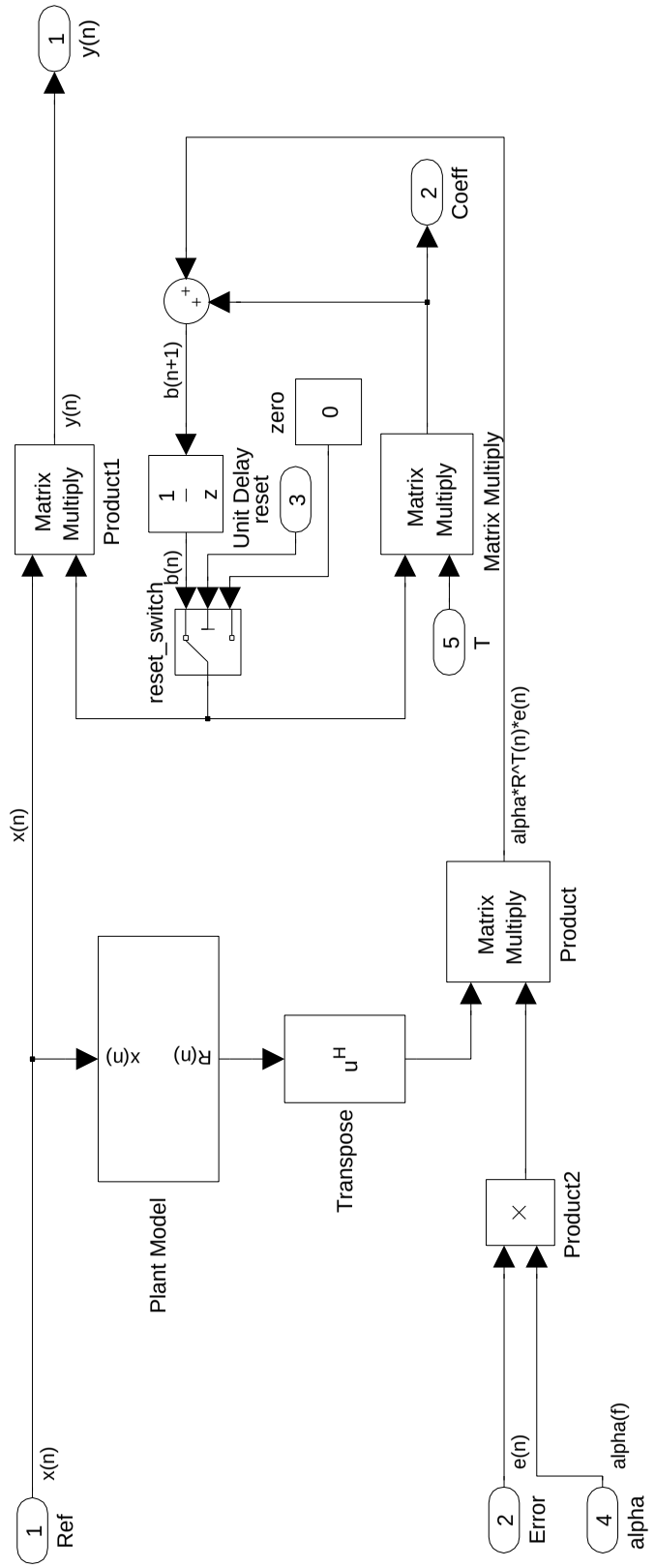

Figure I.3: Least mean squares adaptation algorithm implementation in Simulink.

I.4 Control Effort Weighting Scheduling

The control effort scheduling, or *beta_scheduling* block, is presented in Figure I.4. The first input to this block is the vector of control signals and the first operation on this signal is to calculate the modulus squared value and perform a running root mean square (RMS) over each period of the signal, which is determined based on the sine reference signal. This is necessary due to the oscillatory nature of the signal and scheduling the control effort weighting parameters on the instantaneous signal result in an oscillating control effort parameter. The average value of the control signals at each period is then split into the three independent signals and sent to the sub-blocks labelled *beta1_scheduling*; the details of which are shown in Figure I.5. These three blocks calculate the control effort weighting parameters for each control output, as detailed below, and their outputs are combined to form the matrix $(1-\alpha(n)\mathbf{\Delta})$, which is used in the LMS update algorithms.

The three *beta1_scheduling* blocks calculate the three control effort weighting parameters. Each control effort weighting parameter consists of a term due to the modulus squared control signal averaged over a period and a term due to the frequency of control. The control effort weighting scheduled on the modulus squared control signal is calculated according to equation 6.30, which is implemented in the *Embedded MATLAB Function*. The output of this function is multiplied a constant scaling term that sets the magnitude of the control effort weighting for the specific system and then this value is passed through a moving average filter to ensure that rapid variations in the control effort weighting parameter do not occur. The frequency dependent control effort parameter is scheduled according to equation 6.32 and this is implemented in the lower half of the block diagram shown in Figure I.5. The frequency dependent and control effort scheduled control effort weighting parameters are then summed before being output into to the main block diagram shown in Figure I.4.

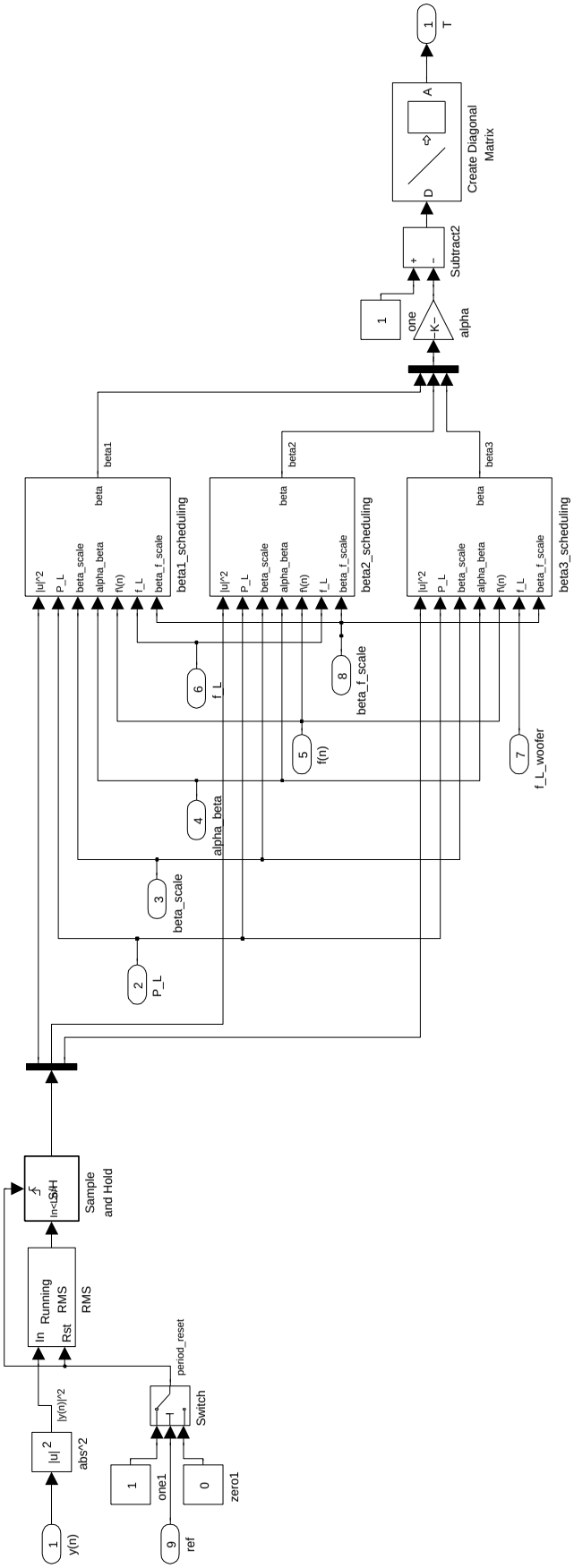

Figure I.4: Control effort weight scheduling implementation in Simulink.

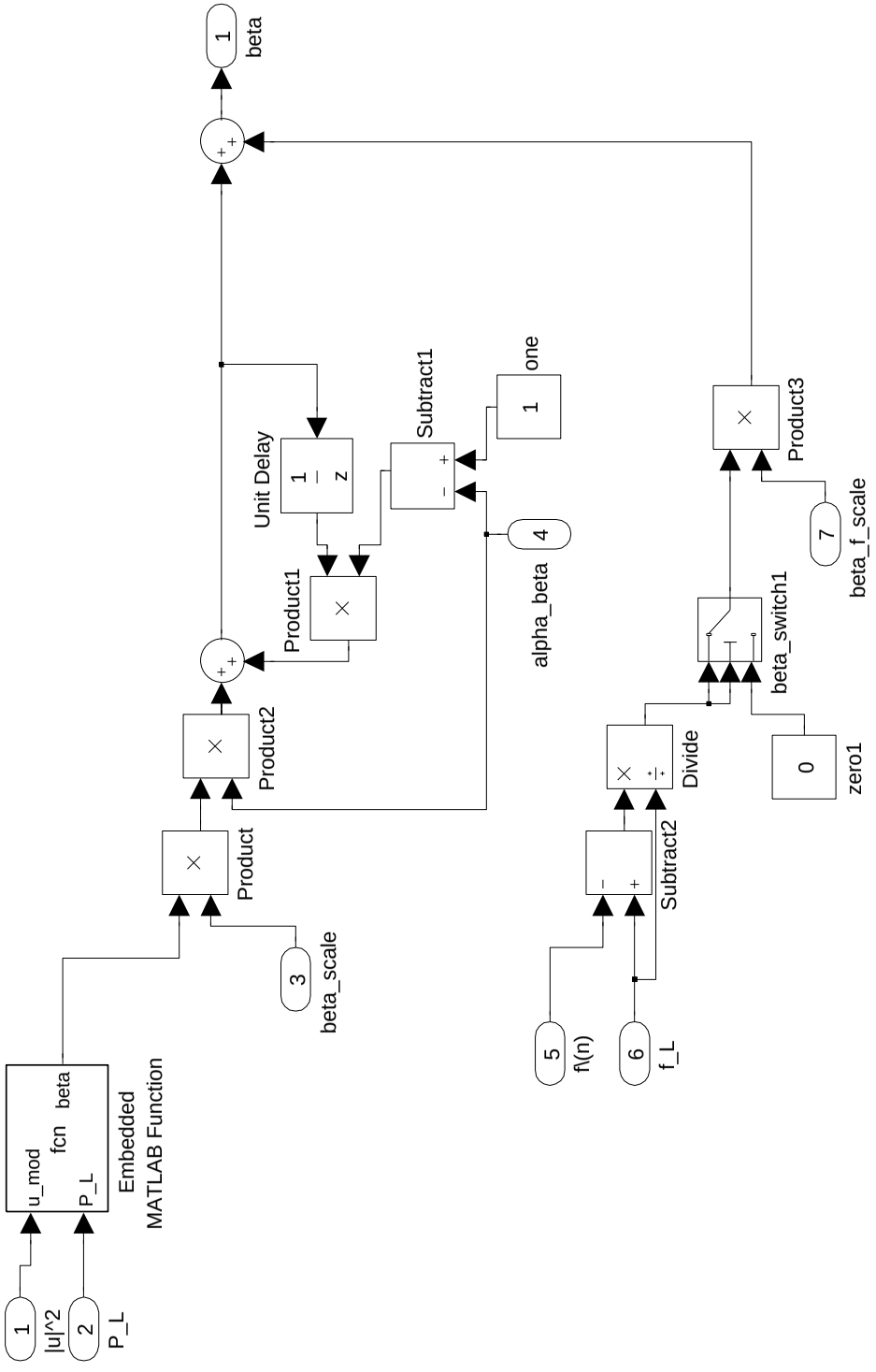

Figure I.5: Sub section of the control effort weight scheduling implementation in Simulink.

Appendix J

The Effect of Structural-Acoustic Coupling on Personal Audio

It has been shown in Chapter 3 that feedforward active noise control is largely unaffected by structural-acoustic coupling. Therefore, due to the similarity in the operating principles of the personal audio systems that will be investigated in the Chapter 7, it is unlikely that the significant increase in computation time that is required to compute the response of the structural-acoustic coupled enclosure will provide any additional understanding of the operation and physical limitations of a personal audio system. In order to confirm this assumption, and therefore justify the use of the standard rigid walled enclosure model to conduct the numerical investigation in Chapter 7, a brief comparison between the performance of a personal audio system in a rigid and non-rigid walled enclosure will be presented.

For a distributed source array with eight sources, one positioned in each corner of the rectangular enclosure shown in Figure 2.1, Figure J.1 shows the acoustic contrast performance and required array effort when the array is optimised to produce a bright zone in the front seating area and a dark zone in rear seating area shown in Figure 7.2 in both the rigid and non-rigid walled enclosures. The acoustic contrast and array effort are plotted in decibels relative to the acoustic contrast and array effort achieved when the eight corner sources are driven in-phase with equal amplitude whilst producing the same mean square pressure in the bright zone. From the acoustic contrast plot it can be seen that the general level of performance and characteristics are not affected by structural-acoustic coupling, although the specific details are altered by the variation in modal frequencies and addition of vibrating structures as discussed in Chapter 2. Similarly, the required array effort is only affected in detail and the general power requirement remains consistent between the rigid and non-rigid enclosures. This is consistent with the conclusions drawn regarding the effect of structural-acoustic coupling on feedforward active noise control and, therefore, due to reduced computational complexity, it is reasonable to employ the rigid walled model to investigate the implementation of a personal audio system in an enclosure in Chapter 7.

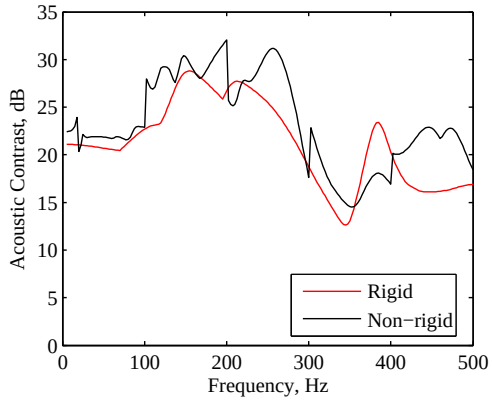

(a) Acoustic contrast

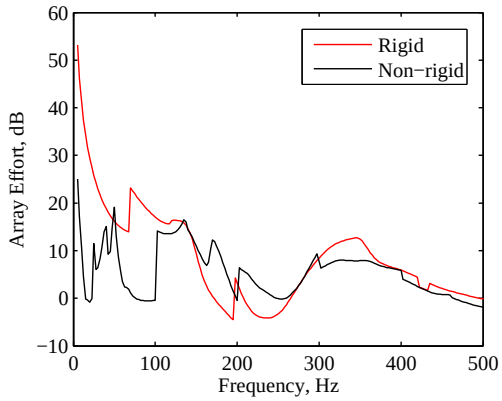

(b) Array effort

Figure J.1: The acoustic contrast and array effort achieved in the rigid (—) and non-rigid (—) enclosures for an array of eight sources positioned in the corners of the enclosure attempting to produce a bright zone in the front seating region and a dark zone in the rear seating region in the rectangular enclosure, as depicted in Figure 7.2. The acoustic contrast and array effort are plotted in decibels relative to the acoustic contrast and array effort achieved when the eight corner sources are driven in phase with equal amplitude whilst producing the same mean square pressure in the bright zone.

References

[1] A. Miskiewicz and T. Letowski, "Pschoacoustics in the automotive industry," *Acta Acustica*, vol. 85, pp. 646–649, 1999.

[2] X. Wang, "Rationale and history of vehicle noise and vibration refinement," in *Vehicle Noise and Vibration Refinement* (X. Wang, ed.), pp. 3–17, Cambridge: Woodhead Publishing, 2010.

[3] Staff Writer, "Automotive audio quality," *Journal of the Audio Engineering Society*, vol. 53, no. 6, pp. 542–548, 2005.

[4] D. Vigé, "Vehicle interior noise refinement – cabin sound package design and development," in *Vehicle Noise and Vibration Refinement* (X. Wang, ed.), pp. 286–317, Cambridge: Woodhead Publishing, 2010.

[5] S. J. Elliott, "Active noise and vibration control in vehicles," in *Vehicle Noise and Vibration Refinement* (X. Wang, ed.), pp. 235–251, Cambridge: Woodhead Publishing, 2010.

[6] O. A. Kutlar, H. Arslan, and A. T. Calik, "Methods to improve efficiency of four stroke, spark ignition engines at part load," *Energy Conversion and Management*, vol. 46, no. 20, pp. 3202 – 3220, 2005.

[7] T. G. Leone and M. Pozar, "Fuel ecoonomy benefit of cylinder deactivation-sensitvity to vehicle application and operating constraints," *Society of Automotive Engineers*, no. 2001-01-3591, 2001.

[8] S. J. Elliott, I. M. Stothers, P. Nelson, M. A. McDonald, D. C. Quinn, and T. J. Saunders, "The active control of engine noise inside cars," in *Proceedings of INTER-NOISE 88* (M. Bockhoff, ed.), vol. 2, (Poughkeepsie, New York), pp. 987–990, 1988.

[9] T. J. Sutton, S. J. Elliott, M. A. McDonald, and T. J. Saunders, "Active control of road noise inside vehicles," *Journal of Noise Control Engineering*, vol. 42, pp. 137–146, Jul-Aug 1994.

[10] S. J. Elliott and P. Nelson, "Multiple-point equalization in a room using adaptive digital-filters," *Journal of the Audio Engineering Society*, vol. 37, pp. 899–907, November 1989.

[11] S. J. Elliott, L. P. Bhatia, F. S. Deghan, A. H. Fu, M. S. Stewart, and D. W. Wilson, "Pracitcal implementation of low-frequency equalization using adaptive digital-filters," *Journal of the Audio Engineering Society*, vol. 42, pp. 988–998, December 1994.

[12] A. Carini, S. Cecchi, F. Piazza, I. Omiciuolo, and G. Sicuranza, "Multiple position room response equalization in frequency domain," *IEEE Transactions on Audio, Speech, and Language Processing*, vol. 20, pp. 122 –135, January 2012.

[13] M. J. Smithers, "Improved stereo imaging in automobiles," in *123rd Audio Engineering Society Convention*, (New York, USA), 2007.

[14] M. R. Bai and C.-C. Lee, "Comparative study of design and implementation strategies of automotive virtual surround audio systems," *Journal of the Audio Engineering Society*, vol. 58, no. 3, pp. 141–159, 2010.

[15] K. E. Heber, "Mobile internet audio: A report on the state of technology," in *36th International Audio Engineering Conference: Automotive Audio*, June 2009.

[16] B. Crockett, E. Benjamin, and M. Smithers, "Next generation automotive sound research and technologies," in *120th Audio Engineering Society Convention*, (Paris, France), 2006.

[17] S. Goose and F. Arman, "System and method for creating personalized sound zones." United States Patent, US 2006/0262935, November 2006.

[18] F. Bozzoli, E. Armelloni, A. Farina, and E. Ugolotti, "Effects of the background noise of the perceived quality of car audio systems," in *112th Audio Engineering Society Convention*, (Munich, Germany), 2002.

[19] F. Rumsey, "Orchestrating automotive audio," *Journal of the Audio Engineering Society*, vol. 56, no. 4, pp. 303–307, 2008.

[20] D. Thompson and J. Dixon, "Vehicle noise," in *Advanced Applications in Acoustics, Noise and Vibration* (F. Fahy and J. Walker, eds.), ch. 6, London: Spon Press, 2004.

[21] L. Wang, W. S. Gan, and S. M. Kuo, "Integration of bass enhancement and active noise control system in automobile cabin," *Advances in Acoustics and Vibration*, 2008.

[22] P. A. Nelson, "Active control of acoustic fields and the reproduction of sound," *Journal of Sound and Vibration*, vol. 177, no. 4, pp. 447–477, 1994.

[23] W. F. Druyvesteyn, R. M. Aarts, A. J. Asbury, P. Gelat, and A. Ruxton, "Personal sound," in *Proceedings of the Institute of Acoustics*, vol. 16, p. 571, 1994.

[24] J.-W. Choi and Y.-H. Kim, "Generation of an acoustically bright zone with an illuminated region using multiple sources," *Journal of the Acoustical Society of America*, vol. 111, pp. 1695–1700, April 2002.

[25] T. M. Nelson and T. H. Nilsson, "Comparing headphone and speaker effects on simulated driving," *Accident Analysis and Prevention*, vol. 22, no. 6, pp. 523 – 529, 1990.

[26] F. P. Thigpen, "Vehicle audio system with directional sound and reflected audio imaging for creating a personal sound stage." United States Patent, US 2004/0109575 A1, June 2004.

[27] S. Kuo and M. Ji, "Development and analysis of an adaptive noise equalizer," *IEEE Transactions on Speech and Audio Processing*, vol. 3, pp. 217 –222, May 1995.

[28] L. Rees and S. Elliott, "Adaptive algorithms for active sound-profiling," *IEEE Transactions on Audio, Speech, and Language Processing*, vol. 14, pp. 711 – 719, March 2006.

[29] J. Romm, "The car and fuel of the future," *Energy Policy*, vol. 34, no. 17, pp. 2609 – 2614, 2006.

[30] Honda, "Honda's VCM: Combining ample power with outstanding fuel economy." http://world.honda.com/automobile-technology/VCM/, 2011 (last accessed 8/10/2012).

[31] Fiat, "Twin-air – 85 hp, world preview." http://www.fiat.ie/cgi-bin/pbrand.dll/FIAT_IRELAND/news/news.jsp?session=no&contentOID=1074863311, 2009 (last accessed 8/10/2012).

[32] S. Elliott and P. Nelson, "Active noise control," *IEEE Signal Processing Magazine*, vol. 10, pp. 12–35, Oct 1993.

[33] P. Nelson and S. J. Elliott, *Active Control of Sound*. London: Academic Press, 1992.

[34] S. Hasegawa, T. Tabata, and T. Kinoshita, "The development of an active noise control system for automobiles," *Society of Automotive Engineers Technical Paper*, no. 922 086, 1992.

[35] Honda, "2005 honda accord hybrid sedan interior." http://www.honda.com/newsandviews/article.aspx?id=2004091736965, September 2004 (last accessed 8/10/2012).

[36] K. Ogawa, "Toyota cuts 'muffled noise' in crown hybrid." http://techon.nikkeibp.co.jp/english/NEWS_EN/20080619/153489/, June 2008 (last accessed 8/10/2012).

[37] C. Trout, "GM shows off terrain suv with noise cancellation, says silence equals fuel efficiency." http://www.engadget.com/2011/02/25/gm-shows-off-terrain-suv-with-noise-cancellation-says-silence-e/, February 2011 (last accessed 8/10/2012).

[38] Acura, "Acura tsx video: Active sound control." http://www.acura.com/Innovations.aspx#/Active-Sound-Control, January 2012 (last accessed 8/10/2012).

[39] R. Schirmacher, R. Kunkel, and B. M., "Active noise control for the 4.0 TFSI with cylinder on demand technology in Audi's S-series," *Society of Automotive Engineers*, no. 2012-01-1533, 2012.

[40] Bose, "Active sound management." http://www.bose.com/controller?url=/automotive/innovations/asm.jsp, January 2012 (last accessed 8/10/2012).

[41] S. Kuo, "Multiple-channel adaptive noise equalizers," in *Signals, Systems and Computers*, vol. 2, pp. 1250–1254, 1995.

[42] M. de Diego, A. Gonzalez, M. Ferrer, and G. Piñero, "Multichannel active noise control system for local spectral reshaping of multifrequency noise," *Journal of Sound and Vibration*, vol. 274, no. 1-2, pp. 249 – 271, 2004.

[43] X. Kong and S. Kuo, "Analysis of asymmetric out-of-band overshoot in narrowband active noise control systems," *IEEE Transactions on Speech and Audio Processing*, vol. 7, pp. 587 –591, Sept. 1999.

[44] L. Wang and W. S. Gan, "Analysis of misequalization in a narrowband active noise equalizer system," *Journal of Sound and Vibration*, vol. 311, no. 3-5, pp. 1438 – 1446, 2008.

[45] A. Gonzalez, M. de Diego, M. Ferrer, and G. Piñero, "Multichannel active noise equalization of interior noise," *IEEE Transactions on Audio, Speech, and Language Processing*, vol. 14, pp. 110 – 122, January 2006.

[46] S. M. Kuo, A. Gupta, and S. Mallu, "Development of adaptive algorithm for active sound quality control," *Journal of Sound and Vibration*, vol. 299, no. 1-2, pp. 12 – 21, 2007.

[47] Y. Kobayashi, T. Inoue, H. Sano, A. Takahashi, and K. Sakamoto, "Active sound control in automobiles," in *Proc. Inter-noise*, 2008.

[48] K. Tanaka, Y. Nishio, T. Kohama, and K. Ohara, "Technological development for active control of air induction noise," in *Proceedings of SAE*, no. 951301, 1995.

[49] W. Kropp, "An active helmholtz resonator for an exhaust noise control system." Personal Correspondence, September 2010.

[50] J. Krueger, M. Pommerer, and M. Conrathm, "Efficient exhast silencers for downsized gasoline engines," *Society of Automotive Engineers*, no. 2012-01-1563, 2012.

[51] R. Bernhard, "Active control of road noise inside automobiles," in *Proceedings of ACTIVE 95*, pp. 21–32, 1995.

[52] S.-H. Oh, H. suk Kim, and Y. Park, "Active control of road booming noise in automotive interiors," *Journal of the Acoustical Society of America*, vol. 111, no. 1, pp. 180–188, 2002.

[53] C. J. Heatwole and R. Bernhard, "Reference transducer selection for active control of structure-borne road noise in automobile interiors," *Noise Control Engineering Journal*, vol. 44, pp. 35–43, 1996.

[54] S. J. Elliott, P. Joseph, A. J. Bullmore, and P. A. Nelson, "Active cancellation at a point in a pure tone diffuse sound field," *Journal of Sound and Vibration*, vol. 120, pp. 183–189, 1988.

[55] P. Joseph, S. J. Elliott, and P. Nelson, "Near-field zones of quiet," *Journal of Sound and Vibration*, vol. 172, pp. 605–627, May 1994.

[56] Harman, "HALOsonic Noise management solutions." `http://www.halosonic.co.uk/`, January 2012 (last accessed 8/10/2012).

[57] S. Adachi and H. Sano, "Application of two-degree-of-freedom type active noise control using imc to road noise inside automobiles," in *Proceedings of the 35th IEEE conference on Decision and Control.*, vol. 3, pp. 2794–2795 vol.3, Dec 1996.

[58] S. Adachi and H. Sano, "Active noise control system for automobiles based on adaptive and robust control," in *Proceedings of the 1998 IEEE International Conference on Control Applications*, vol. 2, pp. 1125–1129, Sep 1998.

[59] H. Sano, T. Inoue, A. Takahashi, K. Terai, and Y. Nakamura, "Active control system for low-frequency road noise combined with an audio system," *IEEE Transactions on Speech and Audio Processing*, vol. 9, pp. 775–763, October 2001.

[60] G. Cerrato, "Automotive Sound Quality - Powertrain, Road and Wind Noise," *Sound and Vibration*, vol. 43, pp. 16–24, APR 2009.

[61] I. M. Stothers, T. J. Saunders, M. A. McDonald, and S. J. Elliott, "Adaptive feedback control of sun roof flow oscillations," in *Proceedings of the Institute of Acoustics*, vol. 15, pp. 383–393, 1993.

[62] F. Rumsey, *Spatial Audio*. Oxford: Focal Press, 2001.

[63] M. R. Bai and C. C. Lee, "Development and implementation of cross-talk cancellation system in spatial audio reprodiction based on subband filtering," *Journal of Sound and Vibration*, vol. 290, pp. 1269–1289, 2006.

[64] T. Takeuchi and P. A. Nelson, "Optimal source distribution for binaural synthesis over loudspeakers," *Journal of the Acoustical Society of America*, vol. 112, pp. 2786 – 2797, 2002.

[65] A. J. Berkhout, D. de Vries, and P. Vogel, "Acoustic control by wave field synthesis," *Journal of the Acoustical Society of America*, vol. 93, pp. 2764–2778, May 1993.

[66] T. Ricker, "Marantz returns with opsodis es7001 home theater system." http://www.engadget.com/2007/05/23/marantz-returns-with-opsodis-es7001-home-theater-system/, May 2007 (last accessed 8/10/2012).

[67] Audi, "New approaches to perfect sound – hi-fi expertise at audi." http://www.audiusanews.com/newsrelease.do;jsessionid=C3617A6EF93C583762EB3BBD5804F9DC?&id=1831, June 2010 (last accessed 8/10/2012).

[68] ITU-R BS.775-1, "Multi-channel stereophonic sound system with or without accompanying picture." International Telecommunications Union, Geneva, Switzerland, 1992-1994.

[69] P. Coleman, M. Møller, M. Olsen, M. Olik, P. Jackson, and J. Pedersen, "Performance of optimized sound field control techniques in simulated and real acoustic environments," in *Proceedings of Acoustics 2012 in Journal of the Acoustical Society of America*, vol. 131, (Hong Kong, China), p. 3465, 2012.

[70] J. Francombe, R. Mason, M. Dewhist, and S. Bech, "Determining the threshold of acceptability for an interfering audio programme," in *132nd Audio Engineering Society Convention*, (Budapest, Hungary), April 2012.

[71] W. F. Druyvesteyn and J. Garas, "Personal sound," *Journal of the Audio Engineering Society*, vol. 45, no. 9, pp. 685–701, 1997.

[72] I. Wolff and L. Malter, "Directional radiation of sound," *Journal of the Acoustical Society of America*, vol. 2, no. 2, pp. 201–241, 1930.

[73] K. Holland, "Principles of sound radiation," in *Loudspeaker and headphone handbook* (J. Borwick, ed.), Oxford: Focal Press, 3rd ed., 2001.

[74] J. M. Kates and M. R. Weiss, "A comparison of hearing-aid array-processing techniques," *Journal of the Acoustical Society of America*, vol. 99, pp. 3138–3148, May 1996.

[75] H. Cox, R. Zeskind, and M. Owen, "Robust adaptive beamforming," *IEEE Transactions on Acoustics, Speech and Signal Processing*, vol. 35, pp. 1365 – 1376, oct 1987.

[76] M. Jones and S. J. Elliott, "Personal audio with multiple dark zones," *Journal of the Acoustical Society of America*, vol. 124, no. 6, pp. 3497–3506, 2008.

[77] M. Shin, S. Lee, F. Fazi, P. Nelson, D. Kim, S. Wang, P. K.H., and J. Seo, "Maximization of acoustic energy difference between two spaces," *Journal of the Acoustical Society of America*, vol. 128, pp. 121–131, July 2010.

[78] M. F. Simón Gálvez, S. J. Elliott, and J. Cheer, "A superdirective array of phase-shift sources," *Journal of the Acoustical Society of America*, vol. 132, no. 2, pp. 746–756, 2012.

[79] J.-H. Chang and F. Jacobsen, "Sound field control with a circular double-layer array of loudspeakers," *Journal of the Acoustical Society of America*, vol. 131, no. 6, pp. 4518–4525, 2012.

[80] S. J. Elliott, J. Cheer, H. Murfet, and K. R. Holland, "Minimally radiating arrays for mobile devices," *Journal of the Acoustical Society of America*, vol. 128, pp. 1721–1728, November 2010.

[81] S. J. Elliott and M. Jones, "An active headrest for personal audio," *Journal of the Acoustical Society of America*, vol. 119, no. 5, pp. 2702–2709, 2006.

[82] S. J. Elliott and J. Cheer, "Regularisation and robustness of personal audio systems." ISVR Technical Memorandum, No. 995, December 2011.

[83] J.-H. Chang, C.-H. Lee, J.-Y. Park, and Y.-H. Kim, "A realization of sound focused personal audio system using acoustic contrast control," *Journal of the Acoustical Society of America*, vol. 125, pp. 2091–2097, April 2009.

[84] M. F. Simón Gálvez, "Loudspeaker arrays for family television," Master's thesis, University of Southampton, UK, 2011.

[85] J. Cheer, S. J. Elliott, Y. Kim, and J.-W. Choi, "The effect of finite sized baffles on mobile device personal audio," in *130th Audio Engineering Society Convention*, (London, UK), 2011.

[86] J. Cheer, S. J. Elliott, Y.-T. Kim, and J.-W. Choi, "Practical implementation of personal audio in a mobile device," *Journal of the Audio Engineering Society*, provisionally accepted September 2012.

[87] J.-H. Chang, J.-Y. Park, and Y.-H. Kim, "Scattering effect on the sound focused personal audio system," *Journal of the Acoustical Society of America*, vol. 125, pp. 3060–3066, May 2009.

[88] J.-Y. Park, J.-H. Chang, and Y.-H. Kim, "Generation of independent bright zones for a two-channel private audio system," *Journal of the Audio Engineering Society*, vol. 58, no. 5, pp. 382–393, 2010.

[89] M. Yoneyama, J. Fujimoto, Y. Kawamo, and S. Sasabe, "The audio spotlight - an application of non-linear interaction of sound-waves to a new type of loudspeaker design," *Journal of the Acoustical Society of America*, vol. 73, no. 5, pp. 1532–1536, 1983.

[90] Y. Nakashima, T. Yoshimura, and T. Ohya, "Prototype of parametric array loudspeaker on mobile phone and its acoustical characteristics," in *118th Audio Engineering Society Convention*, (Barcelona, Spain), 2005.

[91] C. Howard, C. Hansen, and A. Zander, "Review of current recommendations for airborne ultrasound exposure limits," in *Acoustics*, (Busselton, Western Australia), 2005.

[92] T. J. Holmes, "The acoustic resistance box - a fresh look at an old principle," *Journal of the Audio Engineering Society*, vol. 34, no. 12, pp. 981–989, 1986.

[93] J. Cheer, "Designing loudspeaker directivity for mobile devices," Master's thesis, University of Southampton, UK, 2009.

[94] H. J. Lim, Y.-T. Kim, J. Cheer, and S. J. Elliott, "Method and apparatus for creating personal sound zone." Patent Pending, 2012.

[95] E. Mabande and W. Kellermann, "Towards superdirective beamforming with loudspeaker arrays," in *19th International Congress on Acoustics* (A. Calvo-Manzano, A. Péréz-Lopéz, and J. S. Santiago, eds.), (Madrid, Spain), September 2007.

[96] E. N. Gilbert and S. P. Morgan, "Optimum design of directive antenna arrays subject to random variations," *Bell System Technical Journal*, vol. 34, pp. 637–663, 1955.

[97] H. Cox, R. Zeskind, and T. Kooij, "Practical supergain," *IEEE Transactions on Acoustics, Speech, and Signal Processing*, vol. 34, pp. 393 – 398, June 1986.

[98] M. M. Boone, W.-H. Cho, and J.-G. Ih, "Design of a highly directional endfire loudspeaker array," *Journal of the Audio Engineering Society*, vol. 57, pp. 309–325, May 2009.

[99] S. J. Elliott, J. Cheer, Y.-T. Kim, and J.-W. Choi, "Robustness and regularisation of personal audio systems," *IEEE Transactions on Audio, Speech, and Language Processing*, vol. 20, pp. 2123–2133, September 2012.

[100] Y. Wen, J. Yang, and W.-S. Gan, "Strategies for an acoustic-hotspot generation," *IEICE Transactions on Fundamentals of Electronics, Communications and Computer Sciences*, vol. E88, pp. 1739–1746, July 2005.

[101] B. V. Veen and K. Buckley, "Beamforming: A versatile approach to spatial filtering," *IEEE ASSP Magazine*, vol. 5, pp. 4–24, April 1988.

[102] H. Kutruff, *Room Acoustics*. London: Spon Press, 2000.

[103] D. J. Nefske, J. A. Wolf, and L. J. Howell, "Structural-acoustic finite element analysis of the automobile passenger compartment: A review of current practice," *Journal of Sound and Vibration*, vol. 80, no. 2, pp. 247–266, 1982.

[104] J. Cheer and S. J. Elliott, "The effect of structural-acoustic coupling on the active control of sound in vehicles," in *Proceedings of Eurodyn 2011*, (Leuven, Belgium), 2011.

[105] J. Cheer, M. Abbott, and S. J. Elliott, "Structural-acoustic coupling and psychophysical effects in the active control of noise in vehicles," in *Proceedings of the Institute of Acoustics*, vol. 33, September 2011.

[106] A. Craggs, "An acoustic finite element approach for studying boundary flexibility and sound transmission betwen irregular surfaces," *Journal of Sound and Vibration*, vol. 30, no. 3, pp. 343–357, 1973.

[107] S. H. Kim, J. M. Lee, and M. H. Sung, "Structural-acoustic modal coupling analysis and application to noise reduction in a vehicle passenger compartment," *Journal of Sound and Vibration*, vol. 225, no. 5, pp. 989 – 999, 1999.

[108] S. W. Kang, J. M. Lee, and S. H. Kim, "Structural-acoustic coupling analysis of the vehicle passenger compartment with the roof, air-gap, and trim boundary," *Journal of Vibration and Acoustics - Transactions of the ASME*, vol. 122, no. 3, pp. 196–202, 2000.

[109] E. H. Dowell and H. M. Voss, "The effect of a cavity on panel vibration," *AIAA Journal*, vol. 1, no. 2, pp. 476–477, 1963.

[110] S. M. Kim and M. J. Brennan, "A compact matrix formulation using the impedance and mobility approach for the analysis of structural-acoustic systems," *Journal of Sound and Vibration*, vol. 223, no. 1, pp. 97 – 113, 1999.

[111] F. Fahy and P. Gardonio, *Sound and Structural Vibration*. Oxford: Academic Press, 2nd ed., 2007.

[112] J. H. Ginsberg, "On dowell's simplification for acoustic cavity-structure interaction and consistent alternatives," *Journal of the Acoustical Society of America*, vol. 127, no. 1, pp. 22–32, 2010.

[113] E. H. Dowell, G. F. Gorman, and D. A. Smith Smith, "Acoustoelasticity: General theory, acoustic natural modes and forced response to sinusoidal exciatation, inclusing comparisons with experiments," *Journal of Sound and Vibration*, vol. 52, no. 4, pp. 519–542, 1977.

[114] E. H. Dowell, "Comment on "on dowell's simplification for acoustic cavity-structure interaction and consistent alternatives" [j. acoust. soc. am. [127], 22–32 (2010)]," *Journal of the Acoustical Society of America*, vol. 128, no. 1, pp. 1–2, 2010.

[115] J. H. Ginsberg, "Response to "comments on 'on dowell's simplification for acoustic cavity-structure interaction and consistent alternatives [j. acoust. soc. am. [127], 22–32 (2010)]' "," *Journal of the Acoustical Society of America*, vol. 128, no. 1, pp. 3–4, 2010.

[116] A. J. Bullmore, *The active minimisation of harmonic enclosed sound fields, with particular application to propeller induced cabin noise*. PhD thesis, University of Southampton, Southampton, UK, 1987.

[117] S.-M. Kim, *Active control of sound in strucutral-acoustic coupled systems*. PhD thesis, University of Southampton, UK, April 1998.

[118] P. Gardonio and M. J. Brennan, "Mobility and impedance methods in structural dynamics," in *Advanced Applications in Acoustics, Noise and Vibration* (F. Fahy and J. Walker, eds.), ch. 9, pp. 389–447, London: Spon Press, 2004.

[119] S.-M. Kim and M. J. Brennan, "Active control of harmonic sound transmission into an acoustic enclosure using both structural and acoustic actuators," *Journal of the Acoustical Society of America*, vol. 107, no. 5, pp. 2523–2534, 2000.

[120] J. I. Mohammad, *The active control of random sound inside cars*. PhD thesis, University of Southampton, UK, October 2006.

[121] F. Fahy, "Vibration of containing structures by sound in the contained fluid," *Journal of Sound and Vibration*, vol. 10, pp. 490–512, 1969.

[122] M. Tanaka and Y. Masuda, "Boundary element method applied to certain structural-acoustic coupling problems," *Computer Methods in Applied Mechanics and Engineering*, vol. 71, no. 2, pp. 225 – 234, 1988.

[123] J. Pan and D. A. Bies, "The effect of fluid–structural coupling on sound waves in an enclosure—theoretical part," *Journal of the Acoustical Society of America*, vol. 87, no. 2, pp. 691–707, 1990.

[124] J. Pan and D. A. Bies, "The effect of fluid–structural coupling on sound waves in an enclosure—experimental part," *Journal of the Acoustical Society of America*, vol. 87, no. 2, pp. 708–717, 1990.

[125] J. Pan, "The forced response of an acoustic-structural coupled system," *Journal of the Acoustical Society of America*, vol. 91, no. 2, pp. 949–956, 1992.

[126] S. Srinivasan and R. Rajamani, "Analytical modelling of structural acoustic vibrations in a panelled box," *Mathematical and Compute Modelling of Dynamical Systems*, vol. 2, pp. 148–161, 1998.

[127] J. I. Mohammad, S. J. Elliott, and A. Mackay, "The performance of active control of random noise in cars," *Journal of the Acoustical Society of America*, vol. 123, no. 4, pp. 1838–1841, 2008.

[128] D. Anthony and S. J. Elliott, "A comparison of three methods of measuring the volume velocity of an acoustic source," *Journal of the Audio Engineering Society*, vol. 39, pp. 355–366, May 1991.

[129] J. Pan, "Active control of noise transmission through a panel into a cavity: I. analytical study," *Journal of the Acoustical Society of America*, vol. 87, no. 5, pp. 2098–2108, 1990.

[130] J. Pan and C. H. Hansen, "Active control of noise transmission through a panel into a cavity. II: Experimental study," *Journal of the Acoustical Society of America*, vol. 90, no. 3, pp. 1488–1492, 1991.

[131] J. Pan and C. H. Hansen, "Active control of noise transmission through a panel into a cavity. III: Effect of the actuator location," *Journal of the Acoustical Society of America*, vol. 90, no. 3, pp. 1493–1501, 1991.

[132] S. J. Elliott, *Signal Processing for Active Control*. London: Academic Press, 2001.

[133] G. F. Franklin, J. D. Powell, and A. Emami-Naeini, *Feedback control of dynamic systems*. Massachusetts: Addison-Wesley, 2nd ed., 1991.

[134] B. Rafaely, S. J. Elliott, and J. Garcia-Bonito, "Broadband performance of an active headrest," *Journal of the Acoustical Society of America*, vol. 106, pp. 787–793, August 1999.

[135] P. D. Wheeler, *Voice Communications in the Cockpit Noise Environment - The Role of Active Noise Reduction*. PhD thesis, University of Southampton, UK, 1986.

[136] S. J. Elliott and T. Sutton, "Performance of feedforward and feedback systems for active control," *IEEE Transactions on Speech and Audio Processing*, vol. 4, pp. 214–223, May 1996.

[137] J. Fanson and T. Caughey, "Positive position feedback-control for large space structures," *AIAA Journal*, vol. 28, pp. 717–724, April 1990.

[138] L. Meirovitch and H. Baruh, "Control of self-adjoint distributed-parameter systems," *Journal of Guidance Control and Dynamics*, vol. 5, no. 1, pp. 60–66, 1982.

[139] D. R. Morgan, "An adaptive modal-based active control system," *Journal of the Acoustical Society of America*, vol. 89, pp. 248–256, January 1991.

[140] C. R. Fuller, S. J. Elliott, and P. A. Nelson, *Active Control of Vibration*. London: Academic Press, 1996.

[141] S. Daley, F. A. Johnson, J. B. Pearson, and R. Dixon, "Active vibration control for marine applications," *Control Engineering Practice*, vol. 12, pp. 465–474, 2004.

[142] M. J. Balas, "Active control of flexible systems," *Journal of Optimization Theory and Applications*, vol. 25, no. 3, pp. 415–436, 1978.

[143] L. Meirovitch and H. Baruh, "On the problem of observation spillover in self-adjoint distributed-parameter systems," *Journal of Optimization Theory and Applications*, vol. 39, pp. 269–291, 1983.

[144] M. J. Balas, "Finite-dimensional controllers for linear distributed parameter systems: Exponential stability using residual mode filters," *Journal of Mathematical Analysis and Applications*, vol. 133, pp. 283–296, August 1988.

[145] R. L. Clark and G. P. Gibbs, "Analysis, testing, and control of a reverberant sound field within the fuselage of a business jet," *Journal of the Acoustical Society of America*, vol. 105, no. 4, pp. 2277–2286, 1999.

[146] S. A. Lane, R. L. Clark, and S. C. Southward, "Active control of low frequency modes in an aircraft fuselage using spatially weighted arrays," *Journal of Vibration and Acoustics – Transactions of the ASME*, vol. 122, pp. 227–233, July 2000.

[147] S. Lane, J. Kemp, S. Griffin, and R. Clark, "Active acoustic control of a rocket fairing using spatially weighted transducer arrays," *Journal of Spacecraft and Rockets*, vol. 38, pp. 112–119, Jan-Feb 2001.

[148] R. L. Clark, K. D. Frampton, and D. G. Cole, "Phase compensation for feedback control of enclosed sound fields," *Journal of Sound and Vibration*, vol. 195, no. 5, pp. 701–718, 1996.

[149] M. A. Creasy, D. J. Leo, and K. M. Farinholt, "Adaptive collocated feedback for noise absorption in payload fairings," *Journal of Spacecraft and Rockets*, vol. 45, pp. 592–599, May-Jun 2008.

[150] M. Creasy, D. Leo, and K. Farinholt, "Adaptive positive position feedback for actively absorbing energy in acoustic cavities," *Journal of Sound and Vibration*, vol. 311, no. 1-2, pp. 461 – 472, 2008.

[151] J. B. Bisnette, A. K. Smith, J. S. Vipperman, and D. D. Budny, "Active noise control using phase-compensated, damped resonant filters," *Journal of Vibration and Acoustics – Transactions of the ASME*, vol. 128, no. 2, pp. 148–155, 2006.

[152] A. K. Smith, "Adaptive resonant mode active noise control," Master's thesis, University of Pittsburgh, Pittsburgh, 2005.

[153] M. Nyquist, "Regeneration theory," *Bell System Technical Journal*, vol. 11, pp. 126–147, 1932.

[154] S. Skogestad and I. Postlethwaite, *Multivariable feedback control, analysis and design*. Wiley, 1996.

[155] M. Morari and E. Zafiriou, *Robust process control*. London: Prentice Hall, 1989.

[156] B. Rafaely and S. J. Elliott, "H_2/H_∞ active control of sound in a headrest: Design and implementation," *IEEE Transactions on Control Systems Technology*, vol. 7, pp. 79–84, January 1999.

[157] W.-K. Tseng, B. Rafaely, and S. J. Elliott, "Performance limits and real-time implementation of a virtual microphone active headrest," in *Active 2002* (P. Gardonio and B. Rafaely, eds.), vol. 2, pp. 1231–1250, 2002.

[158] D. McFarlane and K. Glover, "A loop shaping design procedure using H_∞ synthesis," *IEEE Transactions on Automatic Control*, vol. 37, pp. 759–769, June 1992.

[159] J. Cheer and S. J. Elliott, "Spatial and temporal filtering for feedback control of road noise in a car," in *Proceedings of the 19th International Congress on Sound and Vibration*, (Vilnius, Lithuania), July 2012.

[160] S. J. Elliott and B. Rafaely, "Frequency-domain adaptation of feedforward and feedback controllers," in *Proceedings of ACTIVE 97*, pp. 771–788, 1997.

[161] S. Boyd, V. Balakrishnan, C. Barratt, N. Khraishi, X. Li, D. Meyer, and S. Norman, "A new CAD method and associated architectures for linear controllers," *IEEE Transactions on Automatic Control*, vol. 33, pp. 268 –283, mar 1988.

[162] P. Titterton and J. Olkin, "A practical method for constrained-optimization controller design: H_2 or H_∞ optimization with multiple H_2 and/or H_∞ constraints," in *Proceedings of the 29th Asilomar Conference on Signals, Systems and Computers*, vol. 2, pp. 1265 –1269, November 1995.

[163] S. Boyd and L. Vandenberghe, *Convex optimisation*. Cambridge: Cambridge University Press, 2004.

[164] B. Rafaely, *Feedback control of sound*. PhD thesis, University of Southampton, Southampton, UK, October 1997.

[165] A. Gonzalez, A. Albiol, and S. Elliott, "Minimization of the maximum error signal in active control," *IEEE Transactions on Speech and Audio Processing*, vol. 6, pp. 268 –281, may. 1998.

[166] MateSMC, "Fiat 500 3d model." `http://www.3dcadbrowser.com/preview.aspx?ModelCode=30810`, October 2009.

[167] D. C. Baillie, "Noise and vibration refinement of powertrain systems in vehicles," in *Vehicle Noise and Vibration Refinement* (X. Wang, ed.), pp. 252–285, Cambridge: Woodhead Publishing, 2010.

[168] B. Reef, "Noise and vibration refinement of chassis and suspension," in *Vehicle Noise and Vibration Refinement* (X. Wang, ed.), pp. 318–350, Cambridge: Woodhead Publishing, 2010.

[169] S. J. Elliott, I. M. Stothers, and P. A. Nelson, "A multiple error LMS algorithm and its application to the active control of sound and vibration," *IEEE Transactions on Acoustics, Speech, and Signal Processing*, vol. 35, pp. 1423–1434, October 1987.

[170] B. Widrow, J. R. Glover, M. McCool, J. Kaunitz, C. S. Williams, R. H. Hern, J. R. Zeidler, E. Dong, and R. C. Goodlin, "Adaptive noise cancelling: Principles and applications," *Proceedings of the IEEE*, vol. 63, pp. 1692–1716, December 1975.

[171] M. Ferrer, A. Gonzalez, M. De-Diego, and G. Pinero, "Convex combination filtered-x algorithms for active noise control systems," *IEEE Transactions on Audio, Speech, and Language Processing*, vol. 21, no. 1, pp. 154–165, 2012.

[172] S. Elliott and K. H. Baek, "Effort constraints in adaptive feedforward control," *IEEE Signal Processing Letters*, vol. 3, pp. 7 –9, January 1996.

[173] S. Kuo and M. Ji, "Passband disturbance reduction in periodic active noise control systems," *Speech and Audio Processing, IEEE Transactions on*, vol. 4, pp. 96 –103, mar 1996.

[174] S. Daley and I. Zazas, "A recursive least squares based control algorithm for the suppression of tonal disturbances," *Journal of Sound and Vibration*, vol. 331, no. 6, pp. 1270–1290, 2012.

[175] D. R. Hush, N. Ahmed, R. David, and S. D. Stearns, "An adaptive IIR structure for sinusoidal enhancement, frequency estimation, and detection," *IEEE Transactions on Acoustics, Speech, and Signal Processing*, vol. 34, no. 6, pp. 1380–1390, 1986.

[176] J. Backman, "Mobile Phone Audio: The Shape of Things to Come," in *34th International Audio Engineering Society Conference*, (Jeju Islands, Korea), August 2008.

[177] R. Fletcher, *Practical Methods of Optimization*. John Wiley & sons, 2nd ed., 2000.

[178] J.-W. Choi and Y.-H. Kim, "Active control for the enhancement of sound field," in *Proceedings of Active 04*, (Williamsburg, Virginia), Sept. 20-22 2004.

[179] P. Nelson, F. Orduna Bustamante, and H. Hamada, "Multichannel signal processing techniques in the reproduction of sound," *Journal of the Audio Engineering Society*, vol. 44, pp. 973–989, November 1996.

[180] J. Garcia-Bonito and S. J. Elliott, "Local active control of diffracted diffuse sound fields," *Journal of the Acoustical Society of America*, vol. 98, no. 2, pp. 1017–1024, 1995.

[181] M. Jones, *Personal Audio in a Headrest*. PhD thesis, University of Southampton, Southampton, UK, 2007.

[182] F. Fazi and P. A. Nelson, "The ill-conditioning problem in sound field reconstruction," in *130th Audio Engineering Society Convention*, (New York, USA), 2007.

[183] F. Fazi, *Sound field reproduction*. PhD thesis, University of Southampton, Southampton, UK, February 2010.

[184] J. H. Wilkinson, *The algebraic eigenvalue problem*. Clarendon Press, 1965.

[185] G. H. Golub and C. F. V. Loan, *Matrix computations*. The John Hopkins University Press, 1996.

[186] J. H. Wilkinson, "Notes on matrices with a very ill-conditioned eigenproblem," *Numerical Mathematics*, vol. 19, pp. 176–178, 1972.

[187] Ford, "Ford S-Max – spacious and versatile interior design - ford UK." `http://www.ford.co.uk/Cars/S-MAX/Interiordesign`, 2012 (last accessed 8/10/2012).

[188] P. Marins, F. Rumsey, and S. Zielinski, "The relationship between basic audio quality and selected artefacts in perceptual audio codexs - part II: validation experiment," in *122nd Audio Engineering Society Convention*, (Vienna, Austria), May 2007.

[189] S. J. Elliott and M. E. Johnson, "Radiation modes and the active control of sound power," *Journal of the Acoustical Society of America*, vol. 94, pp. 2194–2204, Oct 1993.

[190] V. Georgiev, V. Kylov, and R. Winward, "Simplified modelling of vehicle interior noise: Comparison of analytical, numerical and experimental approaches," *Journal of Low Frequency Noise, Vibration and Active Control*, vol. 25, pp. 69–92, June 2006.

[191] A. Berry and J. Nicolas, "Structural acoustics and vibration behavior of complex panels," *Applied Acoustics*, vol. 43, no. 3, pp. 185 – 215, 1994. Structural Acoustics and Vibrations.

[192] Visaton, "Visaton." `http://www.visaton.com/en/industrie/breitband/sc4_7nd_8.html`, September 2012 (last accessed 8/10/2012).

[193] M. Serrand and S. J. Elliott, "Multichannel feedback control for the isolation of base-excited vibration," *Journal of Sound and Vibration*, vol. 234, no. 4, pp. 681 – 704, 2000.

[194] J. Doyle and G. Stein, "Multivariable feedback design: Concepts for a classical/modern synthesis," *IEEE Transactions on Automatic Control*, vol. 26, pp. 4 – 16, Feb. 1981.

[195] P. A. Nelson, A. R. D. Curtis, S. J. Elliott, and A. J. Bullmore, “The minimum power output of free field point sources and the active control of sound,” *Journal of Sound and Vibration*, vol. 116, no. 3, pp. 397–414, 1987.